VIBRATIONS
IN PHYSICAL SYSTEMS

Volume XXV

Editors

Czesław CEMPEL, Marian W. DOBRY

Poznan 2012

VIBRATIONS IN PHYSICAL SYSTEMS
Vol. 25, 2012

ISBN 978-83-89333-43-8

ACCOUNT HOLDER
Polish Society of Theoretical and Applied Mechanics
Poznan University of Technology, Institute of Applied Mechanics
ul. Jana Pawła II 24, 60-965 Poznan, Poland, NIP 526-17-23-674

ACCOUNT NUMBER
IBAN PL 58 1020 4027 0000 1402 0312 9962
Bank name PKO BP SA, Oddzial I, Poznan
SWIFT code BPKOPLPW

PUBLISHED AND PRINTED
Agencja Reklamowa COMPRINT
ul. H. Rzepeckiej 26 A, 60-465 Poznan, Poland
Tel. +48 602 26 64 26, e-mail: comprint@data.pl, www.comprint.com.pl

The volume was published in the cooperation of the Institute of Applied Mechanics at Poznan University of Technology and Polish Society of Theoretical and Applied Mechanics.

This journal has been indexed in the list of Ministry of Science and Higher Education (6 points).

POZNAN UNIVERSITY OF TECHNOLOGY
MECHANICAL ENGINEERING AND MANAGEMENT FACULTY
INSTITUTE OF APPLIED MECHANICS
POLISH SOCIETY OF THEORETICAL AND APPLIED MECHANICS

XXV Jubilee Symposium

VIBRATIONS IN PHYSICAL SYSTEMS

2012

XXV JUBILEE SYMPOSIUM VIBRATIONS IN PHYSICAL SYSTEMS
Będlewo (near Poznań), May 15-19, 2012

Present edition of Symposium Vibrations in Physical Systems is under auspices of

President of Poznan University of Technology
Adam HAMROL

Dean of Mechanical Engineering and Management Faculty
Jan ŻUREK

FINANCIAL SUPPORT

Ministry of Science and Higher Education
Mechanical Engineering and Management Faculty

SPONSORS

EC Test Systems Sp. z o.o.
Bruel & Kjaer Polska Sp. z o.o.
Klimatest Trzymadłowski i Wspólnicy Sp. j.
ENVIBRA Sp. z o.o.

CONTENTS

INVITED PAPERS

PAPERS

XXV Symposium *Vibrations in Physical Systems,* Poznan – Bedlewo, May 15-19, 2012

New Method of Analysis of Non-Linear Stochastic and Random Vibrations

Jan KICINSKI
Institute of Fluid-Flow Machinery, Polish Academy of Sciences (IFFM PAS)
Fiszera 14, 80-952 Gdansk
University of Warmia and Mazury, Olsztyn, POLAND
kic@imp.gda.pl

Abstract

Topic discussed in the hereby paper is an assessment of the influence of a random character of certain input data – in this case – changes of external excitations of the system. This problem is related to the so-called **heuristic models** often placed in opposition to widely used **algorithmic models**. The main issue concerned the question whether the heuristic methodology can move to the techniques, in this case, the rotor dynamics. The objects of investigations were the high-speed rotor of a micro turbine being an element of the micro power plant in dispersed power engineering based on renewable energy sources.

Keywords: rotor dynamics, nonlinear vibrations, heuristic problems, computer simulation

1. Research tools and their verification

The MESWIR computer code, based on nonlinear models of complex systems rotor-bearings, was applied in research. Theoretical models, basic equations as well as the system itself have been presented already several times during the conferences and in publications [1, 2, 3]. Due to that and having in mind the paper space limitation and its different aims, the MESWIR series code will not be presented here in details. For the purposes of this paper we present only a block diagram of computing systems MESWIR – Fig. 1. However, it is worth mentioning that the most useful feature of this system is the possibility of description of the rotor machine state both in a linear and nonlinear range by means of the same tool, thereby describing new vibration forms at transition of the stability limit. The MESWIR code was experimentally verified both at the research stand and with using real systems such as large power turbo-sets – Fig. 2, 3 [1]. We can see here only one example of **model tuning procedure** performed on real large 200 MW Turboset and the measurements results and calculation results in the form of so called diagnostic cards, that means in the form of setting-up absolute vibration velocity and relative shaft displacement for all 7 bearings. In this picture only for bearing No 6.

Taking into account that we have to deal with so complicated object, **the agreement between experiment and theory** we can recognize as qualitative and thereby as satisfactory.

2. Object of investigation

Problems related to ecological energy generation at a small and dispersed scale have become very important in recent years. A dispersed power engineering requires building micro power plants which means also micro turbines of a power from a few to a dozen or so KW. The idea of building micro turbines for low-boiling agents ORC, which ensures small dimensions of devices and easiness of servicing, has become attractive.

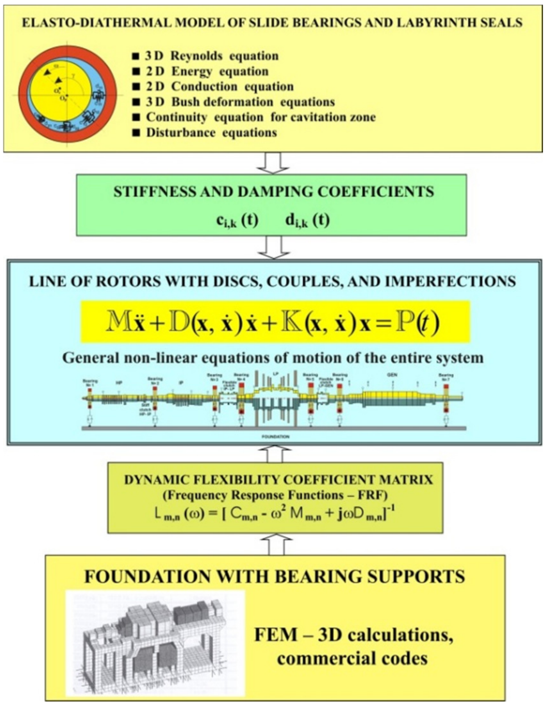

Figure 1. Block diagram of computer program MESWIR. The set of differential equations[1]

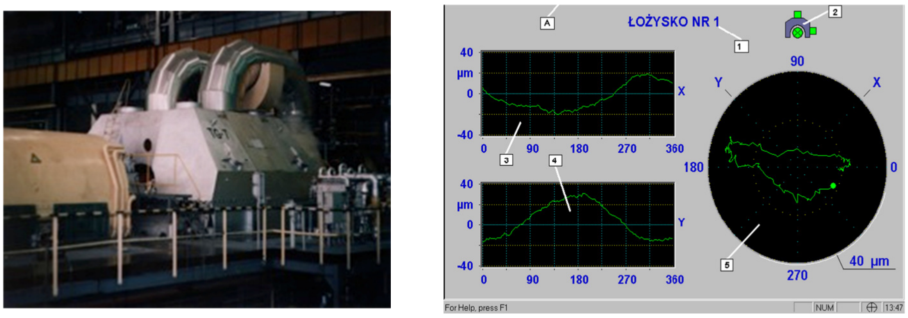

Figure 2. Experimental verification on real objects of the computer program MESWIR. On the left: photo of 200MW turbo-set, right: sample journal displacements in the bearing No. 1[1]

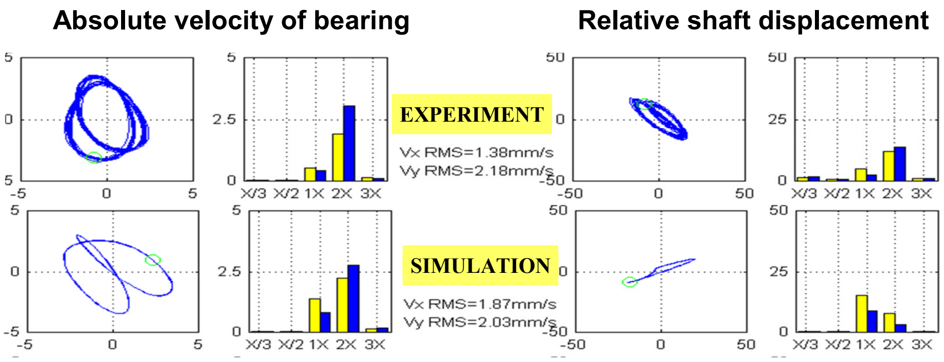

Figure 3. Sample results of the program MESWIR verification on the real 200 MW turbine set shown in Fig. 2.

Unfortunately it is obtained at the cost of a high rotational speed of the rotor, approaching 100 000 rpm. Thus, the main problem becomes ensuring the stable operation of the device within the entire rotational speed range of the rotor. This type of devices are most often coupled with boilers supplied with renewable energy sources.

A concept of such micro power plant (100 KW Power) developed in the IFFM PAS in Gdansk is shown in Fig. 4 [4, 5, 7]. Another example of microturbines with much less power (3 KW) is shown in Fig. 5. In both cases essential elements of the micro turbine constitute slide bearings of special characteristics ensuring a high stability of a system.

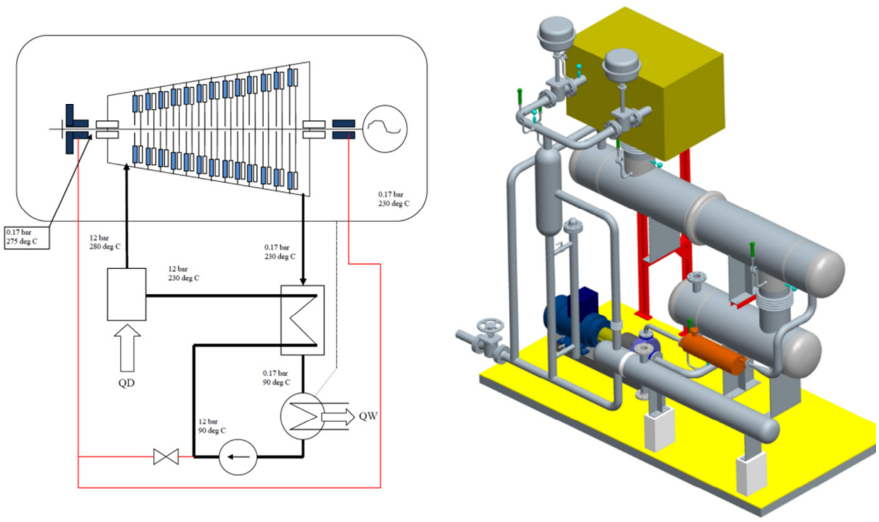

Figure 4. Micro power plant (100 KW electric power) with the rotor speed 3000 rpm developed in the IFFM PAS in Gdansk. One approach adopted for the analysis [7].

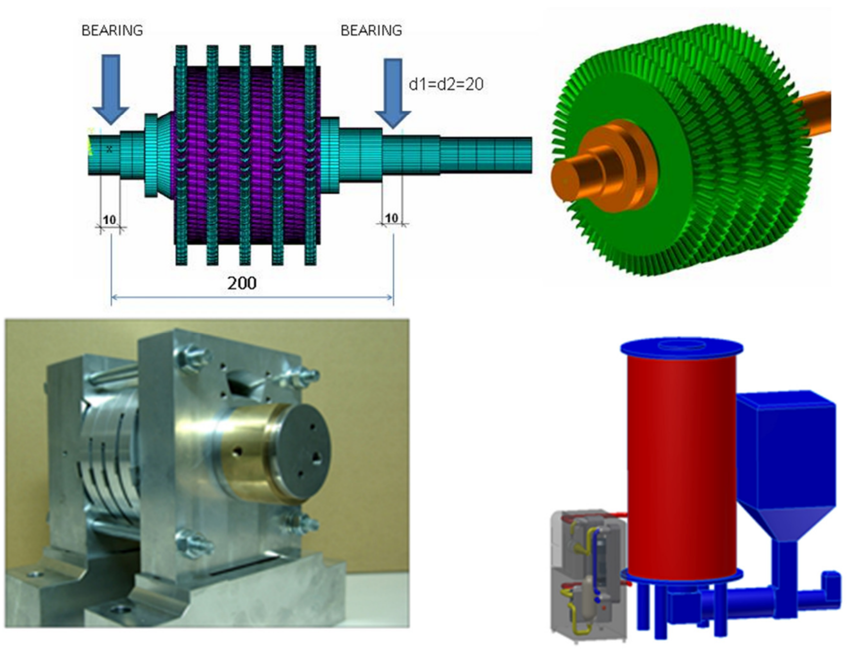

Figure 5. Micro power plant (3 KW electric power) with the rotor speed 8000 rpm developed in the IFFM PAS in Gdansk. One approach adopted for the analysis [4,5].

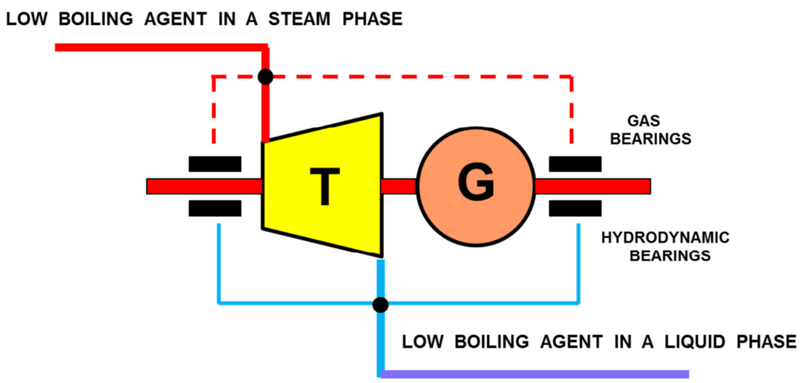

Figure 6. Two options for lubrication of journal bearings by means of low boiling agent: as a steam phase and as a liquid phase.

Regarding the microturbines, our main idea was to assume the application of low boiling agent both in the thermodynamic cycle of microturbine as well as for lubrications purposes in bearings system – Fig. 6.

For the lubrication purposes we can take the lubricant from the **liquid phase** and then we should use **hydrodynamic journal** bearings (classical or foil bearings) or we can take the lubricant from **steam phase** and then we can use only the **gas bearings**.

In the first stage under consideration we assume the liquid phase and hydrodynamic journal bearings. The micro-turbine is driven of course always by steam of low boiling medium.

Such idea has the followings advantages: eliminations of additional system for lubrication and isolation problem in bearing interspaces.

High speed microturbines in which the bearings are lubricated with low boiling agents are particularly sensitive to erroneous data or changes in some parameters. Stochastic and random vibration problems becomes in such cases very important.

3. Stochastic variability of input data in heuristic modeling of rotors

A classic, traditionally applied for many years, approach to the state modeling of various kinds of machines is the **algorithmic** approach, i.e. the one in which for the known set of input data we obtain the same, precisely repeatable, set of output data (results). This is the obvious consequence of calculation capability of computers and the applied programs. However, this type of 'traditional' research tools, often highly advanced and applicable in practice, are neither able to correct the already introduced data nor to modify the assumed model depending on external conditions during the calculation procedure being in progress.

Meanwhile natural phenomena and a human nature (and thereby objects created by it) are of a **heuristic** character**,** which means possible feedbacks occurring in processes, intrinsic data and the previously assumed methodology of state assessment corrections. It also means the necessity of taking into account influences of various errors and the uncertainty of input data, what is often intuitively done – Fig. 7.

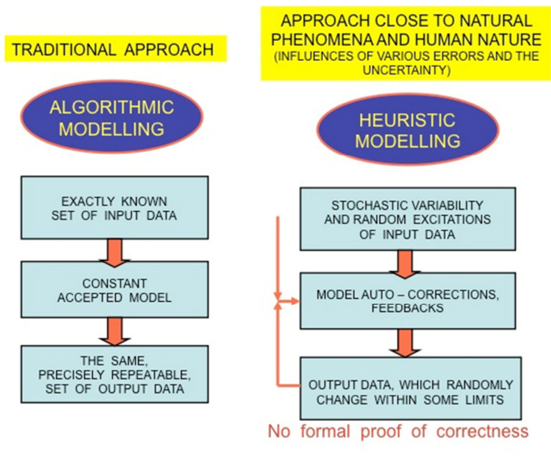

Figure 7. Fundamental differences in algorithmic and heuristic approach

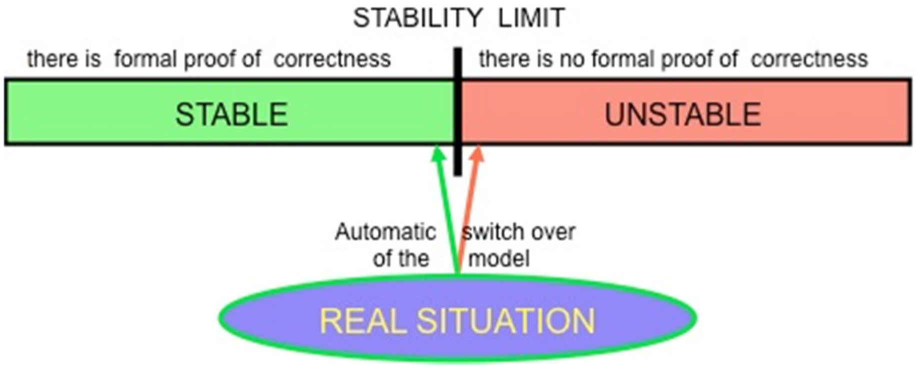

Figure 8. Real situation taking place in rotor dynamics. Justify the benefits of the use of heuristics.

Why the introduction of heuristic methodology for rotor dynamics can be fruitful? Because the two reasons are very important here:

- the possible work in unstable region – the need of model auto- corrections
- stochastic variability of input data. Random excitations

In both cases there is no formal proof of correctness. Despite of this we have to find the acceptable solution!

It is worth to mention that the trial of heuristic modeling means the necessity of having highly advanced 'traditional' research tools. The so called **nonlinear description** is extremely important since heuristic models are nonlinear by nature. Another substantial feature is the possibility of a smooth transition from the linear to nonlinear description applying the same research tools (the Superposition Principle cannot be used in this case). In consideration of the above, the MESWIR series code was applied in investigations.

Figure 9 presents the concept of random changes of external excitation forces acting on a bearing and rotor disc. The randomness of changes was assumed (random-number generator was applied) although within limits +/-ΔP in proportion to the basic value P. Calculations were performed for different ΔP values simulating in this way various possible situations (e.g.: displacement of rotating masses, influence of magnetic fields, etc.). External rotating excitation forces, which can randomly change within limits +/-20 % in proportion to the basic value, P, was assumed for the analysis.

The calculation results for the rotor shaft rotational speed from 300 rpm to 5550 rpm are shown in Fig. 10 and 11 [6]. The trajectory of the rotor centre loaded by a constant force (basic) – rotating synchronously – is shown for the comparison on the left-hand side of each figure, whereas the trajectory of the rotor loaded by randomly changing force – within limits +/-ΔP = 20 % in proportion to the basic force P – is shown on the right-hand side of the figure. Images of trajectories in co-ordinate systems related to the maximum value of bearing clearance are placed in the upper part, while images of trajectories magnified as much as possible to exhibit clearly the phenomena are shown in the lower part of the figure.

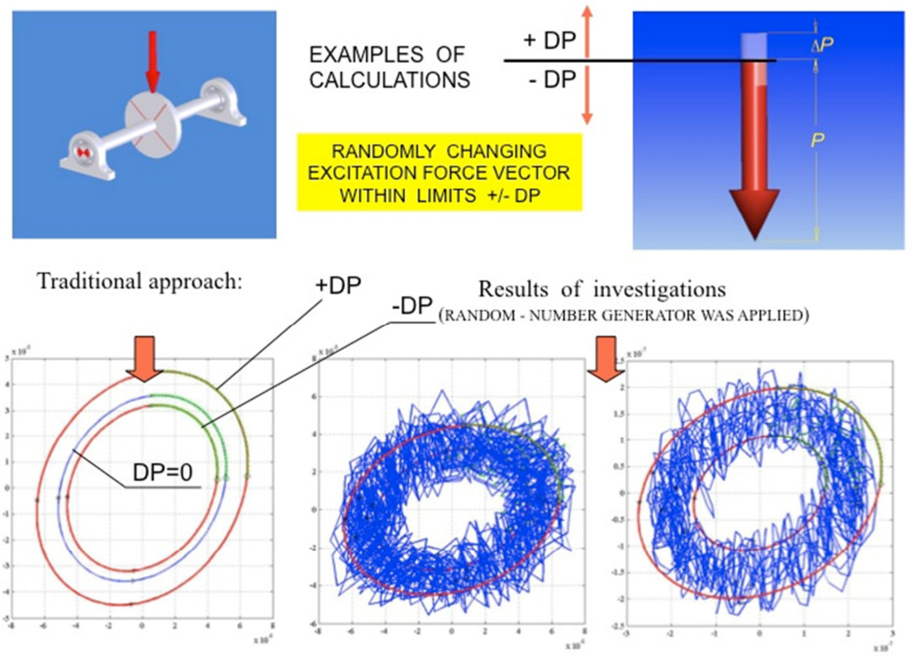

Figure 9. Concept of random changes of external excitation forces acting on a bearing and rotor disc. From left: traditional calculation, calculation with randomly changing vector for relative bearings and disc vibrations.

The analysis of the figure indicates that influence of randomly changing values of the external excitation force is significant in the case of small rotational speeds of the rotor. When the speed increases this influence diminishes, what can be explained by the influence of rotor inertial forces generally attenuating a time-history. At the very stability limit a certain increase in the trajectory disturbance can be observed. However, disturbances caused by the stochastic variability of input data decay when the rotor rotational speed increases, it means when the hydrodynamic instability develops Fig. 11. This is rather a startling result, since it could have been expected that such perturbations – after exceeding the stability limit – would intensify the instability of the entire system since it has been already unstable. Similar conclusions were found when investigations were performed for various ΔP values and various algorithms of random excitations. Thus, a system defect in the form of the hydrodynamic instability attenuates to a certain degree the defect caused by stochastic effects of input data. It is an interesting observation resulting from the performed research.

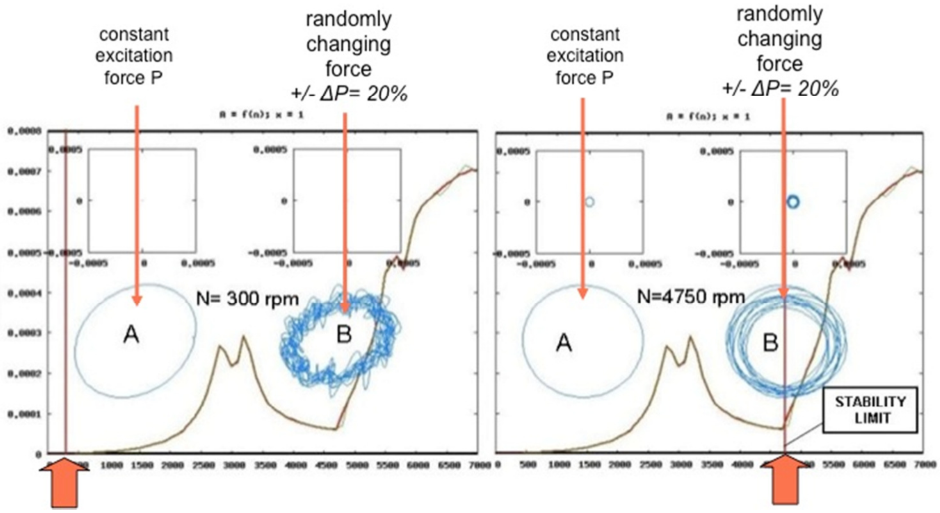

Figure 10. Displacement trajectories of the rotor centre – within a stable operation range – calculated for the constant excitation force (basic) P (part A) and for the randomly changing – within limits +/-ΔP = 20 % (part B) shown at the background of the rotor amplitude-frequency response [6]

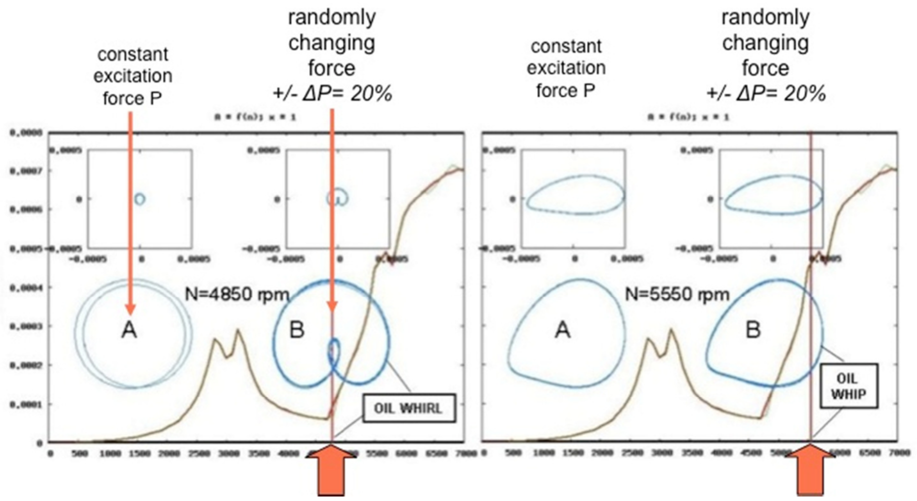

Figure 11. Displacement trajectories of the rotor centre after the system exceeded the stability limit calculated for the constant basic force P (part A) and for the randomly changing – within limits +/-ΔP = 20 % (part B) shown at the background of the rotor amplitude-frequency response [6]

4. Final conclusions

Preliminary considerations concerning heuristic modeling of rotors are included in the paper. In such modeling we took into account uncertainty and randomness of the calculation input data and mutual couplings. It was found that an influence of the stochastic variability of input data decreases after the system has exceeded the stability limit. This indicates that the defect of the hydrodynamic instability type can attenuate – to a certain degree – the defect in the form of a random scatter of input data.

References

1. Kicinski, J., *Rotor Dynamics*, IFFM Publishers, Gdansk 2006.
2. Batko, W., Dabrowski, Z. and Kicinski, J., *Nonlinear Effects In Technical Diagnostics*, Publishing and Printing House of the Institute for Sustainable Technologies, Warsaw 2008.
3. Kicinski, J., *Materials and Operational Imperfections in Rotating Machinery*, IFToMM – Seventh International Conference on Rotor Dynamics, Vienna 2006, Paper-ID 307.
4. Zywica, G., *Simulation Investigation of the Effect of a Supporting Structure Defect on the Dynamic State of the Rotor Supported on Slide Bearings*, ASME International Design Engineering Technical Conference, Las Vegas 2007, DETC2007-34415.
5. Kiciński, J., Żywica, G., Banaszek, S., Bogulicz, M. and Czoska, B., *Modelling of Thermo-Elastic Deformations of the Foil Bearing Bush with the Application of Authors' Own and Commertial Calculation Codes* (in polish), Internal Report of the IF-FM PAS, no. 22/08, Gdansk 2008.
6. Pietkiewicz, P., Kiciński, J., Czoska, B. and Markiewicz, A., *Development of Defect Models – with Uncertainty of Input Data Taken into Account* (in polish), Internal Report IF-FM PAS, Gdansk 2008.
7. Artur Fiuk, Sebastian Bykuć, *Koncepcja prototypowego stanowiska badawczego do analizy pracy obiegu ORC o mocy do 100 kw wykorzystującego ciepło z procesu spalania i innych procesów technologicznych*, Opracowanie wewnętrzne IMP PAN, Gdansk, 2011.

XXV Symposium *Vibrations in Physical Systems,* Poznan – Bedlewo, May 15-19, 2012

Damage Induced by Viscoplastic Waves Interaction

Tomasz ŁODYGOWSKI
Poznan University of Technology, Institute of Structural Engineering Centre for Mechatronics, Biomechanics and Nanotechnology Poznan, Poland
tomasz.lodygowski@put.poznan.pl

Wojciech SUMELKA
Poznan University of Technology, Institute of Structural Engineering Centre for Mechatronics, Biomechanics and Nanotechnology Poznan, Poland
wojciech.sumelka@put.poznan.pl

Abstract

Viscoplastic waves interaction plays a fundamental role in a strain localisation phenomenon especially during highly dynamic processes occurring for example during car or orbiting space objects crashes (strain rates locally reach the values of order $10^7\,s^{-1}$ In zones of localised deformation an intensive evolution of damage occurs which is undoubtedly directional (anisotropic) and finally may cause failure (loss of continuity). Such processes are highly influenced by the temperature (reaching often melting points) and mostly under adiabatic conditions. Mathematical description of the mentioned phenomena formulated in terms of Perzyna's thermo-viscoplasticity is considered in this paper.

Keywords: constitutive modelling, damage anisotropy, viscoplastic waves

1. Introduction

Very short dynamic events whose time duration is of the order of few micro-seconds like e.g. car or orbiting space objects crashes are highly influenced by the deformation waves and their interactions [3, 4]. In metallic ductile materials, central point in herein considerations, shortly after the beginning of a such dynamic process the deformation wave becomes viscoplastic one. Dependently of the geometry, boundary and initial conditions and the type of the material in which the wave is induced a strain localisation zones occurs. In those zones of severe plastic deformations an intensive evolution of damage occurs leading to failure of the material if the amount of the energy causing the deformation is sufficient.

The phenomena mentioned can be described by the Perzyna's type viscoplasticity theory [19], [6] whose development including full range of damage anisotropy influence was presented in [23]. This phenomenological model belongs to the class of simple materials with fading memory, and due to its final form and the way of incorporating the fundamental variables, belongs to the rate type materials with internal state variables [25].

The discussion of the fundamental concepts of the constitutive structure mentioned with its example application for dynamic test presented in [8] including HSLA-65 steel and the discussion on anisotropic damage induced by viscoplastic waves interaction is considered in this paper.

2. Constitutive model

2.1 Fundamental concepts

From mathematical point of view the constitutive model is a kind of theory, based on certain postulates, which ensures that the obtained evolution problem is well-posed, so it gives unique solution. Such model should also enable to describe any motion, thus the description should be invariant with respect to any diffeomorphism (so called covariant model [10]). To achieve such mathematical structure, in continuum mechanics, one should apart of fulfil certain conservation laws, choose proper mathematical space, use appropriate objective rates and regular material functions.

From physical point of view, to describe most important phenomena which occur in metallic materials during highly dynamic processes one should include: sensitivity to the rate of deformation, finite elasto-viscoplastic deformations, plastic non-normality, dissipation effects (anisotropic description of damage), thermo-mechanical couplings and length scale sensitivity. To emphasise the importance of the description of damages as anisotropic one, the main add and achievement of the authors to classical Perzyna's model, notice that such approach enables us to keep good global damage approximation (GDA) (strain-stress curves fitting from experiment and mathematical model) but especially good local damage approximation (LDA) (GDA plus coincidence in: macrodamage initiation time, velocity of macrodamage evolution and the geometry of macrodamage pattern) [24] Notice that variable which describes damage, microdamage tensor $\boldsymbol{\xi}$ has the physical interpretation that the Euclidean norm of the microdamage field defines the scalar quantity called the *volume fraction porosity* or simply *porosity* [19] while its principal values are proportional to the ratio of the damaged area to the assumed characteristic area of the representative volume element [23], thus they indicate damage plane as one perpendicular to maximal principal value of $\boldsymbol{\xi}$ (cf. Fig. 2). Compare also experimentally observed damage anisotropy (cf. [21, 20, 7, 11]) observed during e.g. plane-to-plane impact test [2].

2.2 Adiabatic process

Kinematics

To include the above mentioned properties of proper material behaviour description we propose as follows.

The abstract body is a differential manifold. To describe the finite elasto-viscoplastic deformations we use the multiplicative decomposition of the total deformation gradient to the elastic and viscoplastic parts [9]

$$\mathbf{F}(\mathbf{X},t) = \mathbf{F}^e(\mathbf{X},t) \cdot \mathbf{F}^p(\mathbf{X},t), \tag{1}$$

where $\mathbf{F} = \frac{\partial \phi(\mathbf{X},t)}{\partial \mathbf{X}}$ is the deformation gradient, ϕ describes the motion, $\mathbf{X}$ denotes material coordinates, t is time and $\mathbf{F}^e$, $\mathbf{F}^p$ are elastic and viscoplastic parts of the deformation gradient, respectively.

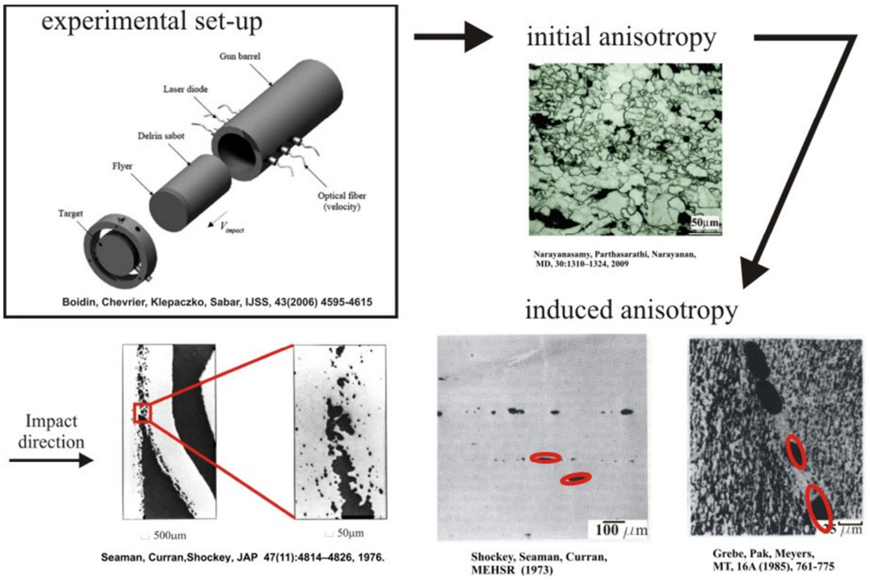

Figure 1. Experimentally observed anisotropy: initial and induced by the process of deformation

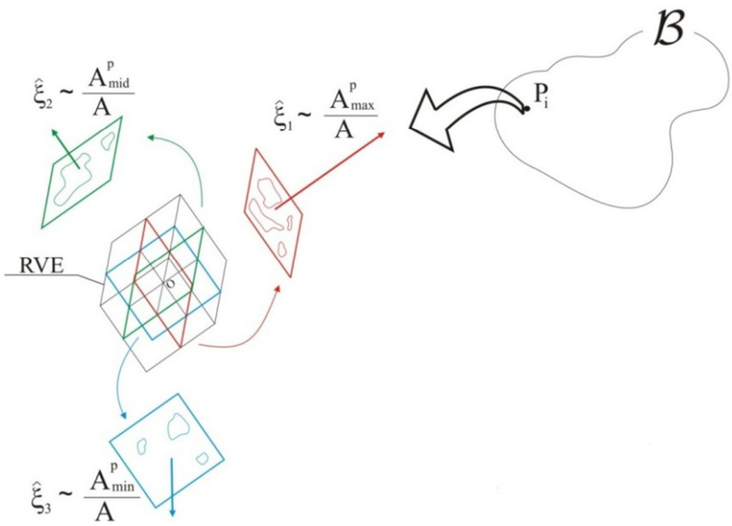

Figure. 2 The concept of microdamage tensor

Using spatial deformation gradient, denoted by **l**,

$$\mathbf{l}(\mathbf{x},t) = \frac{\partial \boldsymbol{\upsilon}(\mathbf{x},t)}{\partial \mathbf{x}}, \tag{2}$$

we obtain well known additive decompositions

$$\mathbf{l} = \mathbf{d} + \mathbf{w} = \mathbf{d}^e + \mathbf{w}^e + \mathbf{d}^p + \mathbf{w}^p, \tag{3}$$

$$\mathbf{d} = \frac{1}{2}\left(\mathbf{l} + \mathbf{l}^T\right), \tag{4}$$

$$\mathbf{w} = \frac{1}{2}\left(\mathbf{l} - \mathbf{l}^T\right), \tag{5}$$

where $\boldsymbol{\upsilon}$ denotes spatial velocity, **x** are spatial coordinates, **d** is the symmetric part and **w** is the antisymmetric part, of **l**, respectively.

Now, using objective Lie derivative of the strain we have the fundamental relation showing that **d** describes truly rate of deformation

$$\mathbf{d}^{\mathrm{b}} = \mathrm{L}_{\boldsymbol{\upsilon}}(\mathbf{e}^{\mathrm{b}}), \tag{6}$$

and simultaneously

$$\mathbf{d}^{e\mathrm{b}} = \mathrm{L}_{\boldsymbol{\upsilon}}(\mathbf{e}^{e\mathrm{b}}), \quad \mathbf{d}^{p\mathrm{b}} = \mathrm{L}_{\boldsymbol{\upsilon}}(\mathbf{e}^{p\mathrm{b}}), \tag{7}$$

where $\mathrm{L}_{\boldsymbol{\upsilon}}$ stands for Lie derivative, **e** for the Euler-Almansi strain, b indicates that a tensor has all its indices lowered [10], indices *e* and *p* denotes the elastic and viscoplastic parts, respectively.

Constitutive postulates

Assuming that the balance principles hold, namely: conservation of mass, balance of momentum, balance of moment of momentum and balance of energy and entropy production, we define four constitutive postulates [16, 18]:

- Existence of the free energy function ψ. Formally we apply it in the following form

$$\psi = \hat{\psi}(\mathbf{e}, \mathbf{F}, \vartheta; \boldsymbol{\mu}), \tag{8}$$

  where $\boldsymbol{\mu}$ denotes a set of internal state variables governing the description of dissipation effects and ϑ denotes temperature. Notice that we have used semicolon to separate the last variable due to its different nature (it introduces a dissipation to the model), without $\boldsymbol{\mu}$ the presented model describes thermoelasticity.
- Axiom of objectivity (spatial covariance). The material model should be invariant with respect to any superposed motion (diffeomorphism).

- The axiom of the entropy production. For every regular process the constitutive functions should satisfy the second law of thermodynamics.
- The evolution equation for the internal state variables vector $\boldsymbol{\mu}$ should be of the form

$$\mathrm{L}_{\upsilon}\boldsymbol{\mu} = \hat{\mathbf{m}}(\mathbf{e}, \mathbf{F}, \vartheta; \boldsymbol{\mu}), \tag{9}$$

  where evolution function $\hat{\mathbf{m}}$ has to be determined based on the experimental observations.

Initial boundary value problem

Assuming that the above holds, the deforming body under adiabatic regime is governed by the following set of equations. They state the initial boundary value problem (IBVP).

Find ϕ, $\boldsymbol{\upsilon}$, ρ, $\boldsymbol{\tau}$, $\boldsymbol{\xi}$, ϑ as functions of t and position $\mathbf{x}$ such that [17, 13, 14, 15]:

- the field equations

$$\begin{aligned}
&\dot{\phi} = \boldsymbol{\upsilon},\\
&\dot{\boldsymbol{\upsilon}} = \frac{1}{\rho_{Ref}}\left(\operatorname{div}\boldsymbol{\tau} + \frac{\boldsymbol{\tau}}{\rho}\cdot\operatorname{grad}\rho - \frac{\boldsymbol{\tau}}{1-(\xi:\xi)^{\frac{1}{2}}}\operatorname{grad}(\xi:\xi)^{\frac{1}{2}}\right),\\
&\dot{\rho} = -\rho\operatorname{div}\boldsymbol{\upsilon} + \frac{\rho}{1-(\xi:\xi)^{\frac{1}{2}}}(\mathrm{L}_{\boldsymbol{\upsilon}}\boldsymbol{\xi}:\mathrm{L}_{\boldsymbol{\upsilon}}\boldsymbol{\xi})^{\frac{1}{2}},\\
&\dot{\boldsymbol{\tau}} = \mathcal{L}^{e}:\mathbf{d} + 2\boldsymbol{\tau}\cdot\mathbf{d} - \mathcal{L}^{th}\dot{\vartheta} - (\mathcal{L}^{e} + \mathbf{g}\boldsymbol{\tau} + \boldsymbol{\tau}\mathbf{g}):\mathbf{d}^{p},\\
&\dot{\boldsymbol{\xi}} = 2\xi\cdot\mathbf{d} + \frac{\partial g^{*}}{\partial\boldsymbol{\tau}}\frac{1}{T_m}\langle\Phi^{g}[\frac{I_g}{\tau_{eq}(\boldsymbol{\xi},\vartheta,\in^{p})} - 1]\rangle,\\
&\dot{\vartheta} = \frac{\chi^{*}}{\rho c_p}\boldsymbol{\tau}:\mathbf{d}^{p} + \frac{\chi^{**}}{\rho c_p}\mathbf{k}:\mathrm{L}_{\boldsymbol{\upsilon}}\boldsymbol{\xi},
\end{aligned} \tag{10}$$

- the boundary conditions
  - displacement ϕ is prescribed on a part Γ_{ϕ} of $\Gamma(\mathcal{B})$ and tractions $(\boldsymbol{\tau}\cdot\mathbf{n})^{a}$ are prescribed on a part $\Gamma_{\boldsymbol{\tau}}$ of $\Gamma(\mathcal{B})$, where $\Gamma_{\phi}\cap\Gamma_{\boldsymbol{\tau}} = 0$ and $\Gamma_{\phi}\cup\Gamma_{\boldsymbol{\tau}} = \Gamma(\mathcal{B})$
  - heat flux $\mathbf{q}\cdot\mathbf{n} = 0$ is prescribed on $\Gamma(\mathcal{B})$,
- the initial conditions ϕ, $\boldsymbol{\upsilon}$, ρ, $\boldsymbol{\tau}$, $\boldsymbol{\xi}$, ϑ given for each particle $\mathbf{X}\in\mathcal{B}$ at $t = 0$,

are satisfied. In above, we have denoted: ρ_{Ref} as a referential density, $\boldsymbol{\tau}$ as the Kirchhoff stress tensor, ρ as a current density, $\mathcal{L}^{e}$ as an elastic constitutive tensor, $\mathcal{L}^{th}$ as a thermal operator, $\mathbf{g}$ as a metric tensor, $\frac{\partial g^{*}}{\partial\boldsymbol{\tau}}$ as the evolution directions for anisotropic micro-damage growth processes, T_m as a relaxation time of mechanical disturbances, I_g as a stress intensity invariant, τ_{eq} as the threshold stress, χ^{*}, χ^{**} as the irreversibility coefficients and c_p as a specific heat.

The details concerning material functions definitions can be found in e.g. [23, 5, 24].

3. Numerical Example

3.1 Implementation

The discussed material model is implemented into Abaqus/Explicit finite element code by taking advantage of a user subroutine VUMAT, which is coupled with Abaqus system [1]. Let us mention that the Abaqus/Explicit utilises central-difference time integration rule along with the diagonal ("lumped") element mass matrices. We use, so called element deletion method to remove damaged elements from mesh [22] – elements in which for every integration point fracture porosity was reached. This requires the proper density of meshes used in computations to ensure the convergence of the results.

The details concerning implementation can be found in e.g. [23, 5] – let us emphasise that the implementation keeps the Lie objective rate.

3.2 Identification

To solve the IBVP defined by Eqs (10), one has to determine material parameters that characterise analysed material (steel). In Tabel 1 we present a complete set of parameters (identified in sense of numerical calibration) for HSLA-65 steel. The identification procedure uses the results obtained experimentally in [12] and in general could be the topic of a separate paper.

Table 1. Material parameters for HSLA-65 steel

$\lambda = 121.154$ GPa	$\mu = 80.769$ GPa	$\rho_{Ref} = 7800$ kg/m^3	$m_{md} = 1$
$c = 0.067$	$b_1 = 0$	$b_2 = 0.5$	$b_3 = 0$
$\xi^{F*} = 0.36$	$\xi^{F**} = 0$	m_F –	$\|\|L_v\xi_c\|\|$ – s^{-1}
$\delta^{*} = 6.0$	$\delta^{**} = 1.4$	$T_m = 2.5$ μs	$m_{pl} = 0.14$
$\kappa_s^{*} = 570$ MPa	$\kappa_s^{**} = 129$ MPa	$\kappa_0^{*} = 457$ MPa	$\kappa_0^{**} = 103$ MPa
$\beta^{*} = 11.0$	$\beta^{**} = 2.5$	$n_1 = 0$	$n_2 = 0.25$
$\chi^{*} = 0.8$	$\chi^{**} = 0.1$	$\theta = 10^{-6}$ K^{-1}	$c_p = 470$ J/kgK

Figure 3 shows the adjustment of the model predictions to experimental data. Notice that the numerical solution is obtained from 3D thermomechanical analysis accounting for an anisotropic intrinsic microdamage process mentioned – in other words the presented numerical results – take into account the whole local process. The curve fitting shows that using presented material model one can obtain the numerical simulations in very good agreement with experimental observations.

3.3 Results

Let us consider 3D thermomechanical analysis under adiabatic regime being an idealisation of the experiment presented in [8]. In the experiment rectangular prism specimen with notch at the center is impacted by the cylindrical projectile with initial velocity 60 ms^{-1} (cf. Fig. 4).

The high impact of the projectile causes viscoplastic wave evolution through the specimen, soon after the beginning of the process. Due to notch at the specimen the deformation localises near the tip and failure (loss of the continuity) begins to evolve with velocity around 250 ms^{-1}.

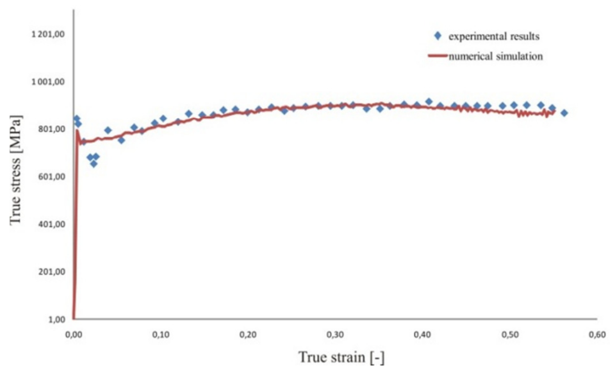

Figure 3. The comparison of the experimental [12] and numerical results for strain rate 3000 s^{-1} and initial temperature 296 K

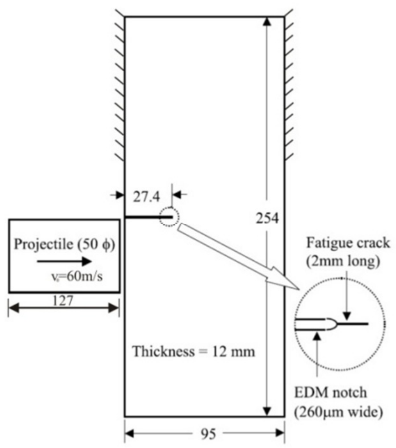

Figure 4. The set-up for dynamic test [8]

The evolution of HMH stresses, temperature and porosity are presented in Figs 5, 6 and 7, respectively. It is worth noticing, that temperature can reach locally close to 800 *K* (initial temperature was 296 *K*). Wave induced damage evolution is clearly proved by analysis of near tip porosity evolution due to the fact that failure development is proceeded by porosity growth slightly ahead of existing failure tip (cf. Fig. 7).

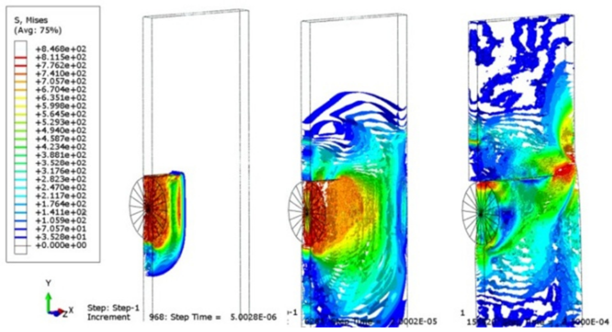

Figure 5. The HMH stress wave for time points: 5, 20, 250 μs from left respectively

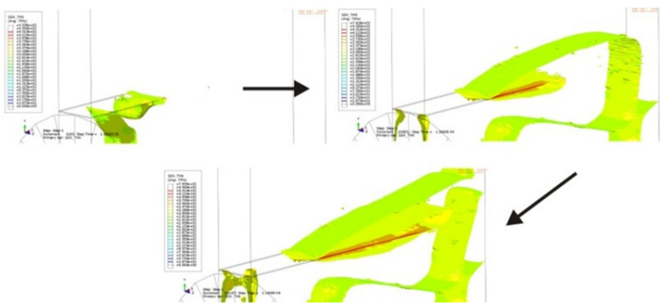

Figure 6. The temperature evolution for time points: 20, 130, 215 μs from top respectively (black arrow indicate time growth)

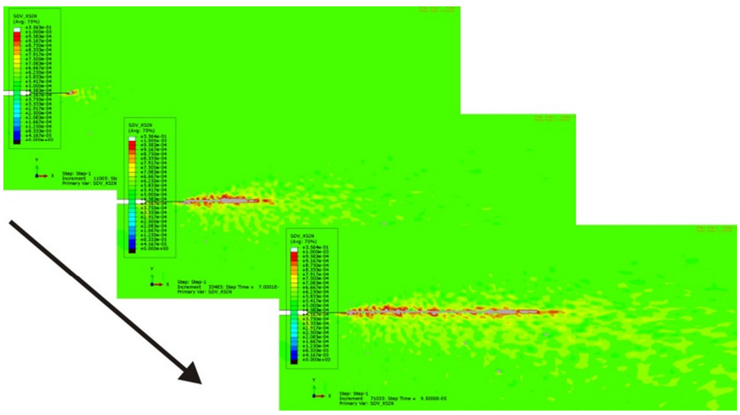

Figure 7. The near fatigue tip porosity evolution for time points: 30, 70, 95 μs from left respectively (black arrow indicate time growth)

4. Conclusions

Viscoplastic waves interaction plays a dominant role in a strain localisation as well as damage phenomena, especially during highly dynamic processes. It was shown that those phenomena can be described by the Perzyna's type viscoplasticity theory. The interactions of waves in dynamics contrary to some known results for quasistatic formulations causes the choice of the places and directions of localisation patterns. Using the proper densities of meshes assures the uniquness and convergence of the results. A results from a 3D numerical model, being an idealisation of a real set-up presented in [8], are used for verification.

Acknowledgements

The support of the Polish Ministry of Science and Higher Education under grant R00 0097 12 is kindly acknowledged.

References

1. Abaqus Version 6.11 *Theory Manu*al. 2011.
2. X. Boidin, P. Chevrier, J.R. Klepaczko, and Sabar H. *Identification of damage mech-anism and validation of a fracture model based on mesoscale approach in spalling of titanium alloy*. International Journal of Solids and Structures, **43**(14-15) (2006) 4029-4630.
3. A. Glema. *Analiza natury falowej zjawiska lokalizacji odkształceń plastycznych wciałach stałych*, volume **379** of *Rozprawy*. Publishing House of Poznan University of Technology, 2004. (in Polish).
4. A. Glema, T. Łodygowski, and P. Perzyna. *Numerical investigation of dynamic shearbands in inelastic solids as a problem of mesomechanics*. Computational Mechanics,**41**(2) (2008) 219-229.
5. A. Glema, T. Łodygowski, and W. Sumelka. *Nowacki's double shear test in the framework of the anisotropic thermo-elasto-vicsoplastic material model*. Journal of Theoretical and Applied Mechanics, **48**(4) (2010) 973-1001.
6. A. Glema, T. Łodygowski, W. Sumelka, and P. Perzyna. *The numerical analysis ofthe intrinsic anisotropic microdamage evolution in elasto-viscoplastic solids*. Inter-national Journal of Damage Mechanics, **18**(3) (2009) 205-231.
7. H.A. Grebe, H.-R. Pak, and Meyers M.A. *Adiabatic shear localization in titanium and Ti-6 pct Al-4 pct V alloy*. Metallurgical and Materials Transactions A, **16**(5) (1985) 761-775.
8. P.R. Guduru, A.J. Rosakis, and G. Ravichandran. *Dynamic shear bands: an investigation using high speed optical and infrared diagnostic*. Mechanics of Materials, **33** (2001) 371-402.
9. E.H. Lee. *Elastic-plastic deformation at finite strain*. ASME Journal of Applied Mechanics, **36** (1969) 1-6.
10. J.E. Marsden and T.J.H Hughes. *Mathematical Foundations of Elasticity*. Prentice-Hall, New Jersey, 1983.

11. R. Narayanasamy, N.L. Parthasarathi, and C.S. Narayanan. *Effect of microstructureon void nucleation and coalescence during forming of three different HSLA steelsheets under different stress conditions*. Materials and Design, **30** (2009) 1310-1324.
12. S. Nemat-Nasser and W.-G. Guo. *Thermomechanical response of HSLA-65 steelplates: experiments and modeling*. Mechanics of Materials, **37** (2005) 379-405.
13. T. Łodygowski. *Theoretical and numerical aspects of plastic strain localization*, volume **312** of D.Sc. Thesis. Publishing House of Poznan University of Technology, 1996.
14. T. Łodygowski and P. Perzyna. *Localized fracture of inelastic polycrystalline solidsunder dynamic loading process*. International Journal Damage Mechanics, **6** (1997) 364-407.
15. T. Łodygowski and P. Perzyna. *Numerical modelling of localized fracture of inelasticsolids in dynamic loading process*. International Journal for Numerical Methods in Engineering, **40** (1997) 4137-4158.
16. P. Perzyna. *Internal state variable description of dynamic fracture of ductile solids*. International Journal of Solids and Structures, **22** (1986) 797-818.
17. P. Perzyna. *Instability phenomena and adiabatic shear band localization in thermoplastic flow process*. Acta Mechanica, **106** (1994) 173-205.
18. P. Perzyna. *The thermodynamical theory of elasto-viscoplasticity*. Engineering Transactions, **53** (2005) 235-316.
19. P. Perzyna. *The thermodynamical theory of elasto-viscoplasticity accounting for microshear banding and induced anisotropy effects*. Mechanics, **27**(1) (2008) 25-42.
20. L. Seaman, D.R. Curran, and D.A. Shockey. *Computational models for ductile and brittle fracture*. Journal of Applied Physics, **47**(11) (1976) 4814-4826.
21. D.A. Shockey, L. Seaman, and D.R. Curran. *Metallurgical effects at high strain rates*, volume **473**. Plenum Press, New York, r.w. rohde, b.m. butchler, j.r. holland and c.h. karbes edition, 1973.
22. J-H Song, H. Wang, and T. Belytschko. *A comparative study on finite element methods for dynamic fracture*. Computational Mechanics, **42** (2008) 239-250.
23. W. Sumelka. *The Constitutive Model of the Anisotropy Evolution for Metals with Microstructural Defects*. Publishing House of Poznan University of Technology, Poznań, Poland, 2009.
24. W. Sumelka and T. Łodygowski. *The influence of the initial microdamage anisotropyon macrodamage mode during extremely fast thermomechanical processes*. Archiveof Applied Mechanics, **81**(12) (2011) 1973-1992.
25. C. Truesdell and W. Noll. *The non-linear field theories of mechanics*. In: Handbuchder Physik, vol. III/3. Springer-Verlag, Berlin, S. Flügge Ed, 1965.

XXV Symposium *Vibrations in Physical Systems,* Poznan – Bedlewo, May 15-19, 2012

Topological Wave Features near Degeneracies in Acoustics and Optics of Absorptive Crystals

Vladimir ALSHITS
A.V. Shubnikov Institute of Crystallography, Russian Academy of Sciences
Leninskii pr. 59,119333 Moscow, Russia
Polish-Japanese Institute of Information Technology
Koszykowa 86, 02-008 Warsaw, Poland, alshits@ns.crys.ras.ru

Vasilii LYUBIMOV
A.V. Shubnikov Institute of Crystallography, Russian Academy of Sciences
Leninskii pr. 59,119333 Moscow, Russia, lyubvn36@mail.ru

Andrzej RADOWICZ
Kielce University of Technology, Al. Tysiaclecia P.P. 7, 25-314 Kielce, Poland
radowicz@tu.kielce.pl

Abstract

The unified formalism for description of acoustic and optic properties is developed for directions close to degeneracies in absorbing crystals. The absorption splits a conical degeneracy which causes topological transformations in polarization and geometrical features of degenerate branches. Polarization ellipses distributions gain singularities at the degeneracy points characterized by the Poincaré indices $n = \pm 1/4$. The slowness surfaces acquire lines of self-intersection connecting the split degeneracy points where the wedge of intersection has infinitely sharp tips. Geometrical and polarization singularities due to absorption create non-trivial features in conical refraction. For any direction of propagation in the vicinity of the split axes the ray velocity precesses along the universal cone of refraction. Kinematics of this precession appreciably depends on the propagation direction. Conditions for experimental observation of the predicted effects are discussed.

Keywords: Acoustics, optics, absorption, degeneracies, polarization singularities, conical refraction

1. Introduction

Basic equations of optics and acoustics are substantially different. Accordingly the most characteristics and properties of electromagnetic and elastic waves in crystals differ from each other. For instance, along any non-degenerate direction $\mathbf{m}$ of propagation in optics only two isonormal waves are allowed, both purely transverse, whereas in acoustics along $\mathbf{m}$ three waves may exist, one quasi-longitudinal and two quasi-transverse. Hence in optics we deal with a two-sheet phase-velocity surface, and in acoustics such wave surface has three sheets. Along directions $\mathbf{m}_0$ of degeneracy of phase speeds (the so-called optic or acoustic axes) the mentioned sheets have points of contact. In optics all crystals are divided into the two groups: uniaxial (with one optic axis related to a tangent contact between degenerate sheets) or biaxial (with two optic axes of conical type) [1].

In acoustics, crystals may have up to 16 degeneracies or none (though only model crystals without acoustic axes are yet known). Points of degeneracy are again conical or tangent, but in this case degeneracy lines related to intersection of phase velocity sheets are also possible and really present in some hexagonal crystals [2]. Tangent acoustic axes must occur along 4- and 6-fold symmetry axes. A conical degeneracy is obligatory along a 3-fold symmetry axis [3]. But it may also exist in non-symmetric directions.

Along the direction $\mathbf{m}_0$ of optic or acoustic axis a propagation of any wave polarized in the degeneracy plane is allowed. The latter plane is orthogonal, respectively, to optic axis or to the polarization vector of non-degenerate elastic wave along acoustic axis. Vector polarization fields of degenerate branches near isolated optic or acoustic axes form singular patterns. For conical and tangent points they are respectively characterized by the Poincaré indices ½ and 1 (in optics) and ±½ and ±1 (in acoustics) [1,3].

Absorption splits conical degeneracies not coinciding with a 3-fold symmetry axis. This splitting provides non-trivial topological transformations of wave characteristics both in optics [4] and in acoustics [5-9]. And in spite of fundamental difference of basic equations describing electromagnetic and elastic waves, the main features of the above topological changes are remarkably similar. In this paper we shall formulate a universal formalism and describe on this basis those transformations in same terms.

2. Statement of the Problem and Formulation of the Universal Formalism

Consider in parallel the two plane waves in an absorbing crystal, the wave of elastic displacements $\mathbf{u}$ and electromagnetic wave formed by electric and magnetic fields ($\mathbf{e}$, $\mathbf{h}$):

$$\mathbf{u}(\mathbf{r},t) = C\mathbf{U}\exp[ik(\mathbf{m}\cdot\mathbf{r} - vt)], \quad \begin{pmatrix}\mathbf{e}(\mathbf{r},t)\\ \mathbf{h}(\mathbf{r},t)\end{pmatrix} = C\begin{pmatrix}\mathbf{E}\\ \mathbf{H}\end{pmatrix}\exp[ik(\mathbf{m}\cdot\mathbf{r} - vt)]. \tag{1}$$

The first wave field is combined with the dynamic elasticity equation where the elastic moduli tensor $\hat{c}$ is replaced by $\hat{c} - i\omega\hat{\eta}$ ($\hat{\eta}$ is the viscosity tensor) [10]). And the other wave field is substituted to the standard Maxwell equations with the inverse permittivity tensor $\hat{\varepsilon}^{-1}$ replaced by $\hat{\varepsilon}^{-1} - i\hat{\delta}$, where $\hat{\delta}$ is the tensor of absorption in optics [11]. From the obtained system of Maxwell's equations we exclude the electric polarization $\mathbf{E}$. After these manipulations we obtain two basic wave equations, for acoustics,

$$[\mathbf{m}(\hat{c} - i\omega\hat{\eta})\mathbf{m}]\mathbf{U} = \rho v^2\mathbf{U}, \tag{2}$$

and for optics,

$$-\{\mathbf{m}[\hat{e}(\hat{\varepsilon}^{-1} - i\hat{\delta})\hat{e}]\mathbf{m}\}\mathbf{H} = (v^2/c^2)\mathbf{H}, \tag{3}$$

where $\hat{e}$ is the Levi-Civita antisymmetric tensor of 3rd rank and c is the speed of light.

The derived equations (2) and (3) become identical if to introduce notation

$$\mathbf{A} = \begin{cases}\mathbf{U} \ \text{(ac)},\\ \mathbf{H} \ \text{(opt)};\end{cases} \quad \hat{\Lambda}' = \begin{cases}\hat{c}/\rho \quad \text{(ac)},\\ -c^2\hat{e}\hat{\varepsilon}^{-1}\hat{e} \ \text{(opt)};\end{cases} \quad \hat{\Lambda}'' = \begin{cases}\omega\hat{\eta}/\rho \ \text{(ac)},\\ -c^2\hat{e}\hat{\delta}\hat{e} \ \text{(opt)}.\end{cases} \tag{4}$$

In these terms one obtains the extended form of the Christoffel equation describing propagation of both elastic and electromagnetic waves in absorbing anisotropic media:

$$(\hat{Q}' - i\hat{Q}'')\mathbf{A} = v^2\mathbf{A}, \tag{5}$$

where the tensors $\hat{Q}'$ and $\hat{Q}''$ are defined by

$$\hat{Q}' = \mathbf{m}\hat{\Lambda}'\mathbf{m}, \quad \hat{Q}'' = \mathbf{m}\hat{\Lambda}''\mathbf{m}. \tag{6}$$

Certainly, complex equation (5), in general, determines complex eigenvectors and eigenvalues. In other words, we shall deal with complex phase velocities v_α and elliptic polarizations $\mathbf{A}_\alpha$ (α=1, 2, 3 for acoustics and α=1, 2 for optics):

$$v_\alpha = v'_\alpha - iv''_\alpha, \qquad \mathbf{A}_\alpha = \mathbf{A}'_\alpha + i\mathbf{A}''_\alpha. \tag{7}$$

3. Solutions in the Vicinity of Conical Degeneracy

In this paper we are interested in analysis of eigenproblem (5) in a close neighbourhood of the direction $\mathbf{m}_0$ of conical degeneracy:

$$\Delta\mathbf{m} = \mathbf{m} - \mathbf{m}_0, \quad |\Delta\mathbf{m}| << 1. \tag{8}$$

Let us start our consideration from the choice of optimized reference systems for optics and acoustics adequate to the problem of wave description in the vicinity of degeneracy. In region (8) polarizations of degenerate branches form vector fields distributed close to degeneracy planes D. Fig. 1 shows these planes and polarizations allowed for $\mathbf{m} = \mathbf{m}_0$ at zero damping for acoustics and optics. In both cases $\mathbf{A}_{03} \perp D$ are eigenvectors of $\hat{Q}'$. However only in acoustics $\mathbf{A}_{03}$ has a physical sense of polarization vector of non-degenerate wave along $\mathbf{m}_0$. In optics the eigenvalue corresponding to $\mathbf{A}_{03}$ vanishes. So, with phase speed v_{03}= 0 this solution is purely static and has nothing to do with our wave problem. Still in both cases the vectors $\mathbf{A}_{03}$ can be chosen as orts of our reference systems (Fig. 1). The other two vectors $\mathbf{A}_{01}$ and $\mathbf{A}_{02}$ can be arbitrarily chosen in the planes D where any direction is allowed for polarization (when attenuation vanishes).

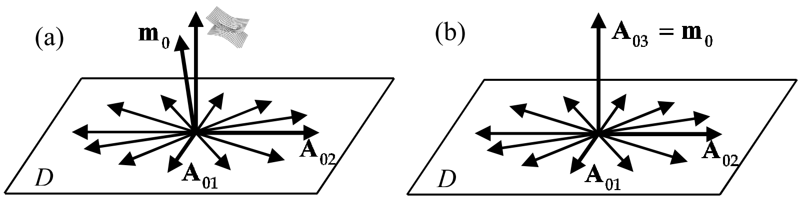

Figure 1. Allowed polarizations along the direction $\mathbf{m}_0$ of degeneracy at "switched off" absorption and reference systems {$\mathbf{A}_{01}$, $\mathbf{A}_{02}$, $\mathbf{A}_{03}$} for acoustics (a) and optics (b).

Analysis of eigenproblem (5) under condition (8) may be done in complete analogy with known solutions [9] of the purely acoustic equation. We present the results:

$$\Delta v_{1,2} = \mathbf{s}^0 \cdot \Delta\mathbf{m} - is'' \mp R,$$
$$\mathbf{A}_{1,2} \parallel -(\mathbf{q}\cdot\Delta\mathbf{m} - iq'')\mathbf{A}_{01} + (\mathbf{p}\cdot\Delta\mathbf{m} - ip'' \pm R)\mathbf{A}_{02}; \tag{9}$$

$$R = \sqrt{(\mathbf{p}\cdot\Delta\mathbf{m} - ip'')^2 + (\mathbf{q}\cdot\Delta\mathbf{m} - iq'')^2}, \tag{10}$$

where the vectors $\mathbf{s}^0$, $\mathbf{p}$, $\mathbf{q}$ and the small scalar parameters s'', p'', q'' are defined by

$$\left.\begin{matrix}\mathbf{s}^0\\ \mathbf{p}\end{matrix}\right\} = \frac{1}{2v_0}\left(\hat{\Lambda}_{11} \pm \hat{\Lambda}_{22}\right)\mathbf{m}_0, \quad \mathbf{q} = \frac{1}{2v_0}\left(\hat{\Lambda}_{12} + \hat{\Lambda}_{21}\right)\mathbf{m}_0,$$
$$\hat{\Lambda}_{ij} = \mathbf{A}_{0i}\hat{\Lambda}'\mathbf{A}_{0j}; \tag{11}$$

$$\left.\begin{matrix}s''\\ p''\end{matrix}\right\} = \frac{Q''_{11} \pm Q''_{22}}{4v_0}, \qquad q'' = \frac{Q''_{12}}{2v_0},$$
$$Q''_{ij} = \mathbf{A}_{0i}\cdot\hat{Q}''_0\mathbf{A}_{0j}, \quad \hat{Q}''_0 = \hat{Q}''(\mathbf{m}_0). \tag{12}$$

Here v_0 is the unperturbed degenerate speed along $\mathbf{m}_0$ before switching on the damping. One can easily check that $\mathbf{s}^0\cdot\mathbf{m}_0 = v_0$ and $\mathbf{p}\cdot\mathbf{m}_0 = \mathbf{q}\cdot\mathbf{m}_0 = 0$.

Consider the particular case when the initial direction $\mathbf{m}_0$ of the degeneracy belongs to the symmetry plane S of crystal. In this case, the polarization vector $\mathbf{A}_{03}$ of the nondegenerate branch obviously also lies in plane S. Then, it is convenient to choose vectors $\mathbf{A}_{01}$ and $\mathbf{A}_{02}$ so that the vector $\mathbf{A}_{02}$ is directed along the normal to plane S, while vector $\mathbf{A}_{01}$ lies in plane S together with $\mathbf{m}_0$ and $\mathbf{A}_{03}$ (Fig. 2a). In this case the relations

$$q'' = 0, \quad \mathbf{q} \parallel \mathbf{A}_{02}, \quad \mathbf{p} \parallel \mathbf{A}_{02}\times\mathbf{m}_0 \tag{13}$$

take place. In optics, due to the tensor $\hat{\varepsilon}$ symmetry, even simpler formulae for $\mathbf{p}$ and $\mathbf{q}$,

$$\mathbf{p}_{op} = \lambda v_0\mathbf{A}_{01}, \quad \mathbf{q}_{op} = \lambda v_0\mathbf{A}_{02}, \quad \lambda = \frac{1}{2}\sqrt{\frac{(\varepsilon_3-\varepsilon_2)(\varepsilon_2-\varepsilon_1)}{\varepsilon_1\varepsilon_3}}. \tag{14}$$

are valid even for a triclinic crystal. Here ε_i are diagonal components of the tensor $\hat{\varepsilon}$.

4. Split of Conical Degeneracy due to Absorption

The condition for a degeneracy $v_1 = v_2$ in terms of (9) is reduced to the complex equation $R = 0$, which is, by (10), satisfied along the two directions

$$\mathbf{m}_\pm \equiv \mathbf{m}_0 + \Delta\mathbf{m}_\pm, \qquad \Delta\mathbf{m}_\pm = \pm\frac{\mathbf{m}_0\times(p''\mathbf{p} + q''\mathbf{q})}{\mathbf{m}_0\cdot(\mathbf{p}\times\mathbf{q})}. \tag{15}$$

In the particular case $\mathbf{m}_0 \subset S$ when (13) is valid, one has $\Delta\mathbf{m}_\pm = \pm(p''/q)\mathbf{A}_{02}$ (Fig. 2b).

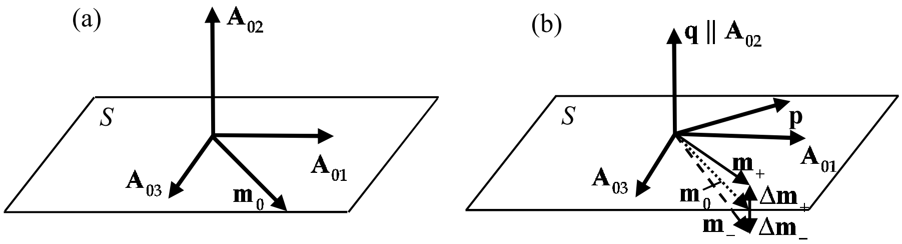

Figure 2. Degeneracy direction $\mathbf{m}_0$ in symmetry plane S (a), and its split (b).

5. Geometrical Features of Slowness Surface near Split Degeneracies

As follows from (10), at the line connecting the degeneracy points $\mathbf{m}^+$ and $\mathbf{m}^-$ on the unit sphere $\mathbf{m}^2 = 1$, the radical R is purely imaginary. Hence, on this line, the real components $v_1'(\mathbf{m})$ and $v_2'(\mathbf{m})$ of the phase velocity should coincide. This defines the lines of self-intersection both of the phase velocity surface $v_{1,2}'(\mathbf{m})$ and of slowness surface $1/v_{1,2}'(\mathbf{m})$. Figure 3a shows schematically the fragment of the slowness surface with the self-intersection line and split degeneracy points situated at its ends.

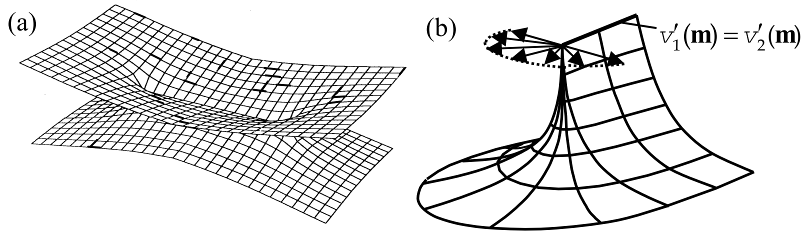

Figure 3. Fragment of the slowness surface with the split degeneracies and self-intersection line between them (a) and the form of a sharp tip at the end of this line (b).

Apart from such new topological feature as self-intersection line arising completely due to absorption, the geometry of this surface in the near vicinity of the degeneracy points at the ends of this line has additional specificity shown in Fig. 3b. The normals to the slowness surface in these points form flat “fans” which corresponds to the infinitely sharpened “noses” of the slowness surface at the ends of the self-intersection wedge.

6. Features of Polarization Fields near Split Degeneracies

Complex polarization vectors $\mathbf{A}_{1,2}(\mathbf{m})$ given by (9) describe on the unit sphere $\mathbf{m}^2 = 1$ in the vicinity of split axes quite non-trivial distribution of isonormal polarization ellipses. After a full bypass over a small circle Γ around one of the points $\mathbf{m}^{\pm}$, the identical transformation of the polarization field $\mathbf{A}_{1,2}$ to itself is realized in the form

$$\mathbf{A}_1(2\pi) = \mathbf{A}_2(0), \qquad \mathbf{A}_2(2\pi) = \mathbf{A}_1(0). \tag{16}$$

In other words, each of the two orthogonal polarization ellipses rotates through $\pi/2$ after going around the singular point, transforming to the polarization of the other isonormal wave. Such singularity of the polarization field can be described by Poincaré index [5,9]

$$n = \tfrac{1}{4}\operatorname{sgn} g, \qquad g = \mathbf{m}_0(\mathbf{p}\times\mathbf{q}) \tag{17}$$

(in optics $g > 0$). After going around a pair of split points, the index becomes twice more, $n = (1/2)\operatorname{sgn} g$, and coincides with the index for a conical singularity (Fig. 4a).

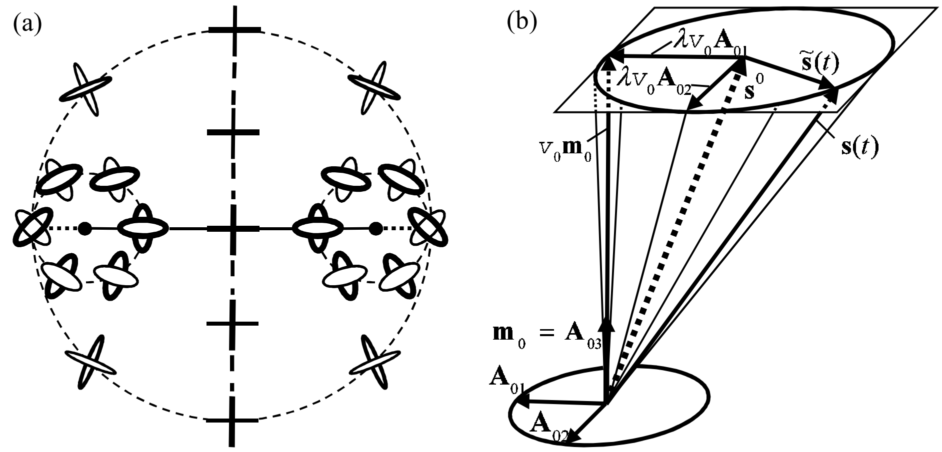

Figure 4. Field of elliptic polarizations of degenerate branches in the vicinity of a pair of singular points (the case g>0) (a); and cone of internal conical refraction for optics (b).

7. Internal Conical Refraction in Absorbing Crystals

In crystal without absorption a circular (or elliptically) polarized wave directed along the conical degeneracy $\mathbf{m}_0$ propagates as a cone of rays. This is the phenomenon known in optics and acoustics as internal conical refraction. It occurs because the ray velocity $\mathbf{s}$ of the wave is directed along the normal to the slowness surface, and in the conical contact point on this surface, the normals to it also form a cone. The corresponding cone of rays,

$$\mathbf{s}(t) = \mathbf{s}^0 + \tilde{\mathbf{s}}(t), \tag{18}$$

arises when the polarization moves along the circle (or ellipse) in the degeneracy plane (Figure 4b). During the wave period, the end of the vector

$$\tilde{\mathbf{s}}(t) = \mathbf{p}\cos 2\varphi(t) \pm \mathbf{q}\sin 2\varphi(t) \tag{19}$$

runs twice along the elliptic (or circular – in optics) cut of the refraction cone (Fig. 4b). Both signs are possible and the phase in (19) is just twice more than the wave phase, i.e.

$$\varphi(t) = v_0\mathbf{m}\cdot\mathbf{r} - \omega t. \tag{20}$$

Along split axes $\mathbf{m}_\pm$ of an absorbing crystal, formulae (18)-(20) remain valid with $\pm$ related to $\mathbf{m}_\pm$. In the same crystal beyond the degeneracy points but still in the zone (8), equations (18) and (19) retain their form however with an addition of wave indications $(\mathbf{s}, \widetilde{\mathbf{s}} \to \mathbf{s}_{1,2}, \widetilde{\mathbf{s}}_{1,2})$ and with replacing the phase (20) by some appropriate functions $\varphi_{1,2}(t)$.

Thus in absorbing crystal for any direction $\mathbf{m}$ satisfying condition (8) the forms of the refraction cone (18) and the cut ellipse (19) remain unchanged. However the kinematics of ray precession over the same cone strongly depends on the ellipticity of the wave polarization for a given $\mathbf{m}$. The less ellipticity, the less uniformity of precession occurs. The motion of the polarization $\mathbf{A}$ and ray velocity $\mathbf{s}$ will be slowest when $\mathbf{A}$ passes the points of maximum curvature on the polarization ellipse. As is seen in Fig. 4a, in the middle of the intersection line the polarization is linear (i.e. the ellipticity is zero) and the vectors $\mathbf{s}_{1,2}$ become static taking the positions of opposite generators of the cone. Hear the conical refraction transforms into wedge refraction.

8. Conclusions

Thus, the role of absorption in crystals is not simply reduced to the trivial decay of elastic or electromagnetic waves during their propagation. We have seen that the switching on of absorption drastically transforms the geometry of wave surfaces and topology of vector polarization fields by splitting the conical degeneracies of the general position. In this case, self-intersection line appears on the slowness surface and geometrical singularities arise at its ends (Fig. 3).

The plane field of linear polarization vectors having a singularity with the Poincaré index $n = (1/2)\mathrm{sgn}g$ at the conical degeneracy point is transformed after the axis splitting to the plane distribution of polarization ellipses which has two singular points $\mathbf{m}_\pm$ with equal Poincaré indices $n = (1/4)\mathrm{sgn}g$ (see Fig. 4a) and circular polarizations at these points.

Topological changes in wave surfaces and polarization fields give rise to principally new features of the internal conical refraction. It must now occur not only along the axes $\mathbf{m}_\pm$ but also for any direction $\mathbf{m}$ in the vicinity of split axes with the same universal cone of refraction for ray velocity precession and the same universal ellipse as a trajectory of motion of the ray vector end (Fig. 4b). But the kinematics of this motion over standard trajectories depends on the choice of the direction $\mathbf{m}$, being rather sensitive to an ellipticity of the wave polarization.

Formally, the discussed effect has no threshold absorption. But the weaker the absorption, the smaller the solid angle within which all the above described processes proceed. If this angle is smaller than the divergence angle of an acoustic or optic beam, we will see neither the splitting of degeneracies nor the effects related to splitting. Therefore, to observe these phenomena, the split angle should exceed the diffraction divergence of the beam of the order of λ/d, where λ is the wavelength and d is the beam diameter.

In the case of acoustics this requirement is reduced [9] to the following condition on the frequency $\nu = \omega/2\pi$ in future experiments:

$$\nu > \nu_{th} \sim \sqrt{\frac{c_s \mu}{2\pi\eta d}} \,, \tag{21}$$

where c_s is the speed of sound, μ is the shear modulus, and η is viscosity. Substituting here relevant magnitudes of physical parameters we obtain the estimate of the threshold frequency ν_{th} ~ 100 MHz. Although this estimate is rather rough, it shows that subtle effects discussed in this paper can be observed.

Acknowledgments

V.I. Alshits and V.N. Lyubimov are grateful to the Kielce University of Technology for a hospitality and support.

References

1. Yu.I. Sirotin, M.P. Shaskol'skaya, *Principles of Crystal Physics,* Nauka, Moscow 1979; Mir, Moscow, 1983 (English translation).
2. F.I. Fedorov, *Theory of Elastic Waves in Crystals,* Nauka, Moscow, 1965; Plenum, New York 1968 (English version).
3. V.I. Alshits, A.V. Sarychev, A.L. Shuvalov, *Classification of degeneracies and analysis of their stability in the theory of elastic waves in crystals,* Sov. Phys. JETP, **62** (3) (1985) 531-539.
4. V.I. Alshits, V.N. Lyubimov, *Wedge refraction of electromagnetic waves in absorbing crystals,* JETP **98** (5) (2004) 870-881.
5. V.I. Alshits, V.N. Lyubimov, *Elastic waves in absorptive media: peculiarities of wave surfaces and singularities in the polarization fields,* 2nd Workshop "Dissipation in Physical Systems", Borkow, Poland, September 1–3, 1997, Ed. by A. Radowicz, Politechnika Swiętokrzyska, Kielce, Poland 1998, 15-43.
6. A.L. Shuvalov, P. Chadwick, Degeneracies in the theory of plane harmonic wave propagation in anisotropic heat-conducting elastic media, Phil. Trans. R. Soc. Lond., **A 355** (1997) 156-188.
7. A.L. Shuvalov, N.H. Scott, On the properties of homogeneous viscoelastic waves, Q. J. Mech. Appl. Math., **52** (1999) 405-417.
8. A.L. Shuvalov, N.H. Scott, On singular features of acoustic wave propagation in weakly dissipative anisotropic thermoviscoelasticity, Acta Mech. **140** (2000) 1-15.
9. V.I. Alshits, V.N. Lyubimov, A. Radowicz, Topological singularities in acoustic fields due to absorption of a crystal, Intern. Monography: Acoustic Waves – From Microdevices to Helioseismology, Ed. by Marco G. Beghi, INTECH, Vienna, Austria 2011, 21-48; ISBN: 978-953-307-572-3.
10. L.D. Landau, E.M. Lifshitz, *Course of Theoretical Physics*, Vol. 7: *Theory of Elasticity,* Nauka, Moscow 1987; Butterworth–Heinemann, Oxford 1995.
11. F.I. Fedorov, *Optics of Anisotropic Media,* Editorial, Moscow 2004 (in Russian).

XXV Symposium *Vibrations in Physical Systems,* Poznan – Bedlewo, May 15-19, 2012

On the Human Arm Motion Camera Tracking System

Tomasz ANDRYSIAK
Technical University of Łódź, Departament of Automation and Biomechanics, Stefanowskiego str. 1/15, 90-924 Łódź, tomasz.andrysiak@gmail.com

Jan AWREJCEWICZ
Technical University of Łódź, Departament of Automation and Biomechanics, Stefanowskiego str. 1/15, 90-924 Łódź, jan.awrejcewicz@p.lodz.pl

Michał LUDWICKI
Technical University of Łódź, Departament of Automation and Biomechanics, Stefanowskiego str. 1/15, 90-924 Łódź, michal.ludwicki@p.lodz.pl

Bartłomiej ZAGRODNY
Technical University of Łódź, Departament of Automation and Biomechanics, Stefanowskiego str. 1/15, 90-924 Łódź, b.zagrodny.pl@gmail.com

Abstract

This paper presents results of research devoted to tracking human arm trajectories in sagittal plane by means of motion capture. One camera tracking system was developed. Co-ordinates of upper limb joints (distincted by light reflecting markers) were obtained via tracking software. Markers were illuminated coaxially to the optical axis of the lens to obtain maximum of reflectivity. Positions, linear velocities and accelerations of a shoulder, elbow, wrist and palm in a sagittal plane were presented. Obtained results in the form of points (in Cartesian co-ordinate system) can be adopted for control of mechanism and robots with kinematics similar to that of a human arm. The obtained results show that in studied biological systems there are no fixed trajectories. All movement co-ordinates (including velocities, accelerations and joints angles) are slightly different for each time selected until movement task is completed. Presented method is relatively inexpensive and non-invasive and can be adopted for other types of motion capture.

Keywords: human arm, motion capture, joints trajectories, biomechanics

1. Introduction

Examination of the animal and human motor system using vision apparatus is carried out (see examples [1-2] of coaching application). Significant number of publications and research is dedicated to this topic, as for example [3-7], being usually focused on a four and two legged moving animal with a particular emphasis on a human biped locomotion [1]. Human movement serves often as a model for robots and other mechanisms. Usually one camera set is used for motion capture and recognition (see for instance [2]), since this is relatively easy and cheap procedure. Computation and tracking of movement trajectories of body segments and their parameters can serve for remote control (like in the case of reference [8]).

Five volunteers were examined. Their task was to raise their arm in the following manner: (i) start from point on the level of their knees; (ii) finish at a specific point above their heads; (iii) complete the motion while sitting, without standing up; (iv) complete the motion ten times.

Points were marked on the rack. No other restriction in arm movements were applied. Luminescent markers were placed on the shoulder joint, elbow, wrist and small finger. Markers were illuminated coaxially to the optical axis of the camera. Images were recorded by one camera with following parameters: (i) 50 Hz frequency (50 frames per second); (ii) Full HD resolution (1920x1080, 50p); (iii) camera was mounted 3 meters from the subject; (iv) an rectilinear lens was used to avoid image distortion.

Recorded videos were analysed using a software to obtain co-ordinates of each marker from all recorded frame. On this basis, other parameters were calculated, i.e. linear velocities and accelerations of the shoulder, elbow, wrist and palm in a sagittal plane.

2. Results

Figure 1 shows trajectories of each marker for one of the volunteer. It is clearly seen, that each cycle was different from previous one. They were made with different velocities and accelerations (see Figure 3 and Figure 4).

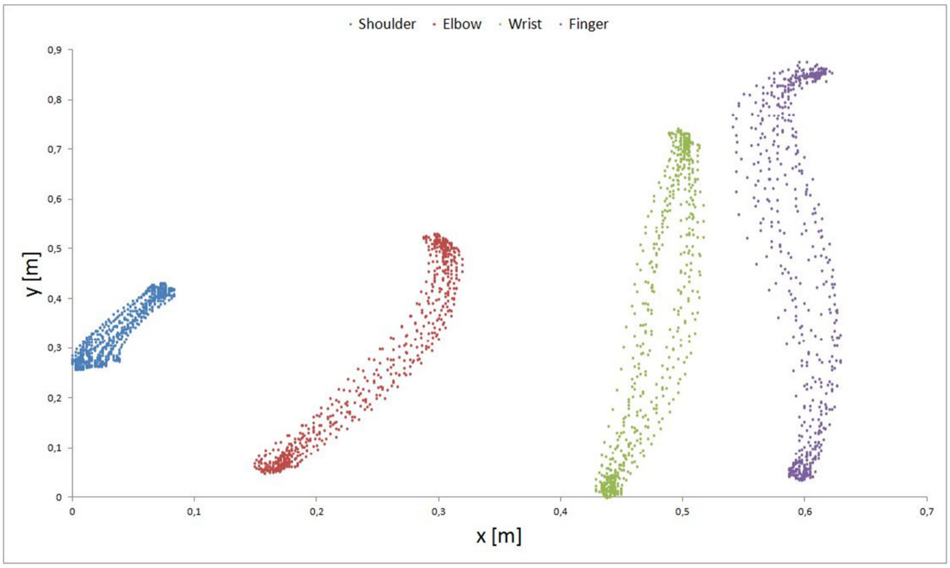

Figure 1. Shoulder, elbow, wrist and finger trajectories (an example)

As expected, the main components of displacements were in Y direction in comparison to X direction (see Fig. 2). Repeatability and differences between movements are clearly seen.

Figure 3 shows markers linear velocities and accelerations computed from the captured positions. Differences between each cycle are seen.

Maximal linear velocities and accelerations were obtained for a palm, accordingly 3.4 m/s and 29.8 m/s^2 (during arm lifting). For arm lowering these values were 2.8 m/s and 23.6 m/s^2, respectively. Table 1 shows mean values of velocities and accelerations.

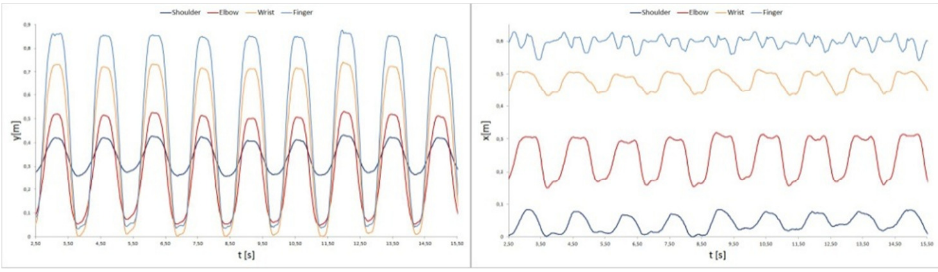

Figure 2. Shoulder, elbow, wrist and finger displacements in Y (left) and in X (right) direction (an example)

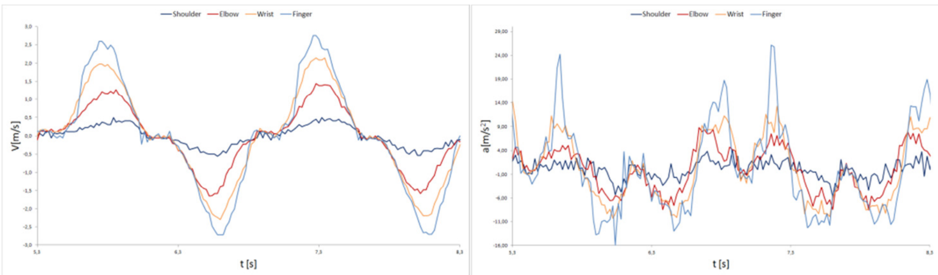

Figure 3. Shoulder, elbow, wrist and finger velocities (left) and accelerations (right) in movement direction (an example).

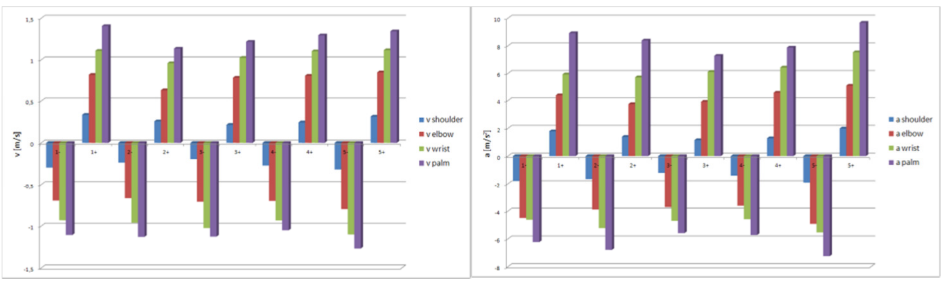

Figure 4. Average velocities (m/s) (left) and accelerations (m/s^2) (right) for each volunteer ("+" for lifting, "-" for lowering).

Table 1. Average velocities and accelerations.

		Arm lifting				Arm lowering			
		Shoulder	Elbow	Wrist	Palm	Shoulder	Elbow	Wrist	Palm
v [m/s]	EX	0.27	0.78	1.06	1.27	0.26	0.71	0.98	1.13
	SD	0.05	0.08	0.06	0.1	0.049	0.049	0.072	0.080
a [m/s^2]	EX	1.52	4.36	6.34	8.42	1.59	4.12	4.92	6.31
	SD	0.35	0.55	0.71	0.92	0.28	0.56	0.43	0.7

3. Conclusions

The obtained results in the form of points, after some interpolations, can be easily adopted for control of mechanism and robots, with kinematics similar to human arm. It was shown that in biological systems there are no fixed trajectories. Because of many disruptions, imperfection of central nervous system, muscle fatigue and other human and environment dependent influences, each trajectory was different. This result is similar to the data presented in reference [9] or [10]. In the first paper the movement was traced in transverse plane, in the second the movement was dependent from wrist position. Also it was clearly seen that each of the volunteers had different movement strategy, i.e. in some cases the raising phase was faster and in other the lowering phase was faster. This indicates a different muscle cooperation in each movement, what can serve as an illustration of muscle indeterminacy collaboration problem (see [11]). In each movement the same goal was obtained in a different way (with different velocities, different joint bending angles, etc.). In this case we have so many solutions as many combination in the system we can obtained to realised the goal. In this particular case we have some biological and physiological restrictions like maximum muscle force, maximal angle of joint bending and straightening, and many others. During analysis of the results a hypothesis was taken under consideration that differences in arm velocities during lifting and lowering of the arm (also in other types of movement) are connected with muscle system condition, possible injuries and diseases.

Presented method and software can be easy modified for other types of movement (like a gait) or mechanisms control. Authors have undertaken the effort to develop three dimensional movement tracking system. However due to our experience only one camera system can be also applied to follow tracking properly.

Motion capture method is relatively cheap and noninvasive, which indicates an advantage in comparison with other methods, where goniometers or EMG electrodes are needed (for example [12], [13]). Increase in measurements accuracy can be easily obtained by changes in the software or by using a camera with higher frame rate (slow motion camera).

It is also possible to use a method of movement tracking that does not need any markers (see [3], [6]). Those methods require some changes in the analyzing software (like phase detection algorithm).

Acknowledgments

This research is supported by "Mistrz" Programme of Foundation for Polish Science.
Videos were analyzed using a software created by Michał Ludwicki.

References

1. Y. Hong, R. Bartlett, *Handbook of Biomechanics and Human Movement Science*, Routledge international Handbooks, London, New York, 2008.
2. V. Filova, F. Solina, J. Lenarcic, *Automatic reconstruction of 3D human arm motion from a monocular image sequence*, Machine Vision and Applications, **10** (1998) 223-231.
3. V. Lepetit, P. Fua, *Monocular Model – Based 3D Tracking of Rigid Objects: A Survey*, Foundation and Trends in Computer Graphics and Vision, **1(1)** (2005) 1-89.
4. C. Bregler, J. Malik, K. Pullen, *Twist based Acquisition and Tracking of Animal and Human Kinematics*, International Journal of Computer Vision, **56(3)** (2004) 179-194.
5. J. Rosen, J. Perry, N. Manning, S. Burns, B. Hannaford, *The Human Arm Kinematics and Dynamics During Daily Activities – Toward a 7 DOF Upper Limb Powered Exoskeleton*, ICAR '05. Proceedings, (2005) 532-539.
6. Y. Azoz, L. Devi, M. Yesin, R. Sharma, *Tracking the human arm using constraint fusion and multiple-cue localization*, Machine Vision and Applications, **13** (2003) 286-302.
7. E. Rostkowska, P. Benz, L. B. Dworak, *AVI Image – video motion analysis software for tests of biomechanical movement characteristics*, Acta of Bioengineering and Biomechanics, **8(1)** (2006) 13-25.
8. D. Kim, J. Kim, K. Lee, Ch. Park, J. Song, D. Kang, *Excavator Tele-operation system using a human arm*, Automation in Construction, **18** (2009) 173-182.
9. T. Okadome, M. Honda, *Kinematic construction of the trajectory of sequential arm movements*, Biological Cybernetics, **80** (1999) 157-169.
10. X. Wang, *Three-dimensional kinematic analysis of influence of hand orientation and joint limits on the control of arm postures and movements*, Biological Cybernetics, **80** (1999) 449-463.

11. A. Siemieński, *Odwrotne zagadnienie optymalizacji dla współdziałających mięśni szkieletowych*, Studia i Monografie AWF, Wrocław 2007.
12. C. G. Meskers, H.M. Vermeulen, J. H. de Groot, F. C. T. van der Helm, P. M. Rozing, *3D shoulder position measurements using a six-degree-of-freedom electromagnetic tracking device*, Clinical Biomechanics, **13** (1998) 280-292.
13. K. Manal, R. V. Gonzalez, D. G. Lloyd, T. S. Buchanan, *A Real-time EMG-driven virtual arm*, Computers in Biology and Medicine, **32** (2002) 25-36.

Modelling, Simulation and Experimental Studies of the Axially Excited Spatial Double Physical Pendulum Coupled by Universal Joints

Jan AWREJCEWICZ
Department of Automation and Biomechanics, Technical University of Lodz
1/15 Stefanowski St., 90-924 Lodz, Poland, jan.awrejcewicz@p.lodz.pl

Grzegorz KUDRA
Department of Automation and Biomechanics, Technical University of Lodz
1/15 Stefanowski St., 90-924 Lodz, Poland, grzegorz.kudra@p.lodz.pl

Michał LUDWICKI
Department of Automation and Biomechanics, Technical University of Lodz
1/15 Stefanowski St., 90-924 Lodz, Poland, michal.ludwicki@p.lodz.pl

Abstract

We are aimed on developing the physical and mathematical model of a novel, spatial, double physical pendulum being coupled by two universal joints. The active part of first joint is axially excited by a non-constant periodic torque. In addition, the influence of gravitational field and viscous damping force of joint's bearings is taken into account. The numerical simulation, as well as the experimental studies revealed a wide spectrum of nonlinear phenomena. Chaotic, quasi-periodic and periodic orbits are detected and studied.

Keywords: double spatial physical pendulum, chaotic dynamics, universal joint, computer simulation

1. Introduction

This work is a part of summary of most important results presented in the author's[3] PhD thesis. The concept of this work raised on development of the mathematical model of a novel, spatial, double physical pendulum being coupled by two universal joints. The active part of first joint is axially excited by a vertically mounted drive with constant or periodic angular velocity. The model includes all mechanical properties of all rigid bodies in the system. In addition, the influence of gravitational field and viscous damping force of joint's bearings are taken into account. Moreover, the experimental setup is developed and constructed by the author[3] to perform detailed verification of the computer simulation results.

Since the first applications of physical pendulum, e.g. a clock by C. Huygens in 1657, a number of research directions based on dynamics of this simple mechanism has appeared. The evolution of pendulum analysis starts from the measurement and experiment, e.g. Foucault's pendulum, 1851, showing the effects of rotation of the Earth [1] or Kater's reversible pendulum [2] used for measuring the gravitational acceleration.

Nowadays single pendulums or systems of pendulums (mathematical and physical ones) are more often used as components to model (simplify) complex mechanisms.

For instance, to develop methods of dynamic vibration absorption and/or control systems [3]. Important part of research includes also theoretical investigations concerning pendulums dynamics [4-5]. Multiple pendulum systems are mostly simplified either to planar space [6] or they concerning only mathematical pendulums [7]. Physical pendulums are insufficiently examined in their multiple configurations.

Here, mathematical model of a 3D double physical pendulums system is introduced. The results of numerical computations, as well as possible applications of the original simulation program are discussed. A rich spectrum of regular and chaotic dynamics of the system is detected. In addition, some results of the experimental setup are presented.

2. The Pendulum Model

A multiple pendulum system being proposed is shown on Figure 1. It consists of two cylindrical-shaped rigid bodies combined by universal joint O_2 and hung on a second universal joint O_1. This joint is also externally driven so it actuates the entire mechanical system axially with either constant or non-constant angular velocity.

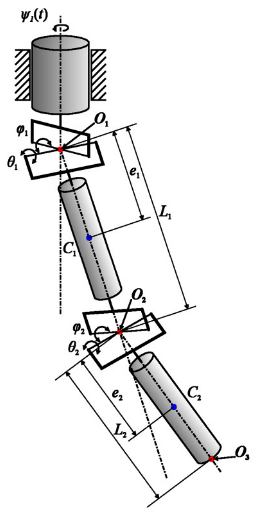

Figure 1. Coupled pendulums

Angles of deflection of each universal joint's shaft have been described by three Euler angles φ_i, θ_i and ψ_i, where i is an index of each joint. The rotation matrices are derived, as well as positions of each body centers, theirs linear and angular velocities and energy are defined. Analytically determined set of nonlinear ODEs governing the pendulum dynamics follows

$$\mathbf{M}(\mathbf{q})\ddot{\mathbf{q}} + \mathbf{A}(\mathbf{q})\mathbf{a} + \big(\omega(t)\mathbf{B}(\mathbf{q}) + \mathbf{C}\big)\dot{\mathbf{q}} + \mathbf{r}_g(\mathbf{q}) + \omega^2(t)\,\mathbf{r}_\omega(\mathbf{q}) = \mathbf{0}, \tag{1}$$

where $\mathbf{q} = [\theta_1\ \varphi_1\ \theta_2\ \varphi_2]^T$, $\mathbf{a} = \big[\dot\theta_1^2\ \dot\varphi_1^2\ \dot\theta_2^2\ \dot\varphi_2^2\ \dot\theta_1\dot\varphi_1\ \dot\theta_1\dot\theta_2\ \dot\theta_1\dot\varphi_2\ \dot\theta_2\dot\varphi_1\ \dot\varphi_1\dot\varphi_2\ \dot\theta_2\dot\varphi_2\big]^T$, and **M**, **A**, **B**, **C**, $\mathbf{r}_g$, $\mathbf{r}_\omega$ devote matrices and vectors (here not defined explicitly).

Analytical (symbolic) *Wolfram Mathematica*® computer package has been carried out, during process of derivation of equation (1).

In the study, simple model of viscous damping of joints is assumed in form:

$$\mathbf{M}_d = \begin{bmatrix} M_{d\theta_1} - M_{d\theta_2} & M_{d\varphi_1} - M_{d\varphi_2} & M_{d\theta_2} & M_{d\varphi_2} \end{bmatrix}^T, \tag{2}$$

where M_i are corresponding damping torques proportional to the angular velocities.

Angular velocity of the axial excitation is as follows:

$$\dot{\psi}_1 = \omega(t) = \omega_0 + q\sin(\Omega t), \tag{2}$$

where ω_0 is a constant part of velocity, q is the amplitude and Ω states for frequency.

3. Computations and results

According to the *User manual* of *Wolfram Mathematica*® package, the ODEs solving algorithm is based on higher order Runge-Kutta methods with automatic step control. Results, as well as the plots, are automatically interpolated to any chosen time steps.

Results presented in this paper concerns the following fixed parameters: weight of the pendulums $m_1 = m_2 = 0.5$ kg, length $L_1 = L_2 = 0.2$ m, position of the mass center $e_1 = e_2 = 0.1$ m, viscous damping coefficient $c = 0.1$, moments of inertia $I_x = I_y = 0.002$ kg·m and $I_z = 0.0001$ kg·m, which correspond to cylindrical shape of both identical pendulum links. The exemplary angular velocity parameters of the excitation are set to $\omega_0 = 0$ rad/s and $q = 12$ N·m (for the periodic excitation) and $\omega_0 = 12.5$ rad/s (for the constant excitation). The frequency of periodic excitation Ω (bifurcation parameter) is described in the figures' captions. For each Poincaré section 400 time steps were ignored as transient motion and 400 were qualified as significant for the analysis.

The first part of performed analysis concerned finding stable positions of the system under constant excitation. The example of the obtained results is shown in Fig. 2.

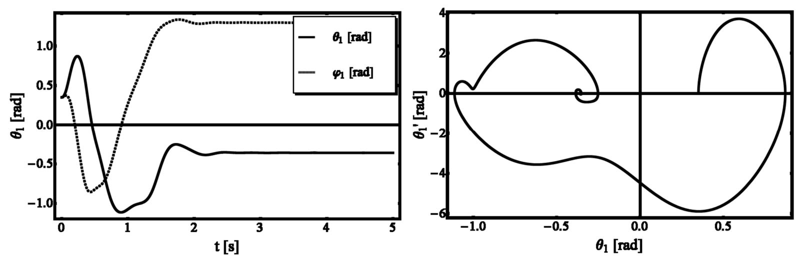

Figure 2. Time series and phase plots of deflection angle θ_1 of first pendulum for $\omega_0 = 12.5$ rad/s and initial coordinates $\varphi_1 = \theta_1 = 0.35$ rad

Presented position is one of many stable positions found in performed investigation. It is expectable that there are infinite number of such configurations possible to achieve from many initial conditions and in many angular velocities. It is also worth mentioning that this non-trivial configuration appears only above some value of angular velocity of excitation. Lower velocity corresponds to trivial axial rotation, while each pendulum hangs freely under the influence of the gravity, without an exhibition of any vibrations.

The second part of the research concerns analysis of the system subjected to periodic external excitation. Since one could predict much more complicated movement, possibly a periodic or chaotic one, the driven universal joint rotates axially with periodic angular velocity governed by the formula (3). We initiate a study by computations of bifurcation diagrams with excitation frequency Ω as a control parameter for each angle of deflection. This global method of analysis revealed many interesting nonlinear dynamics phenomena (example of regular and chaotic behaviour is shown in Fig. 3).

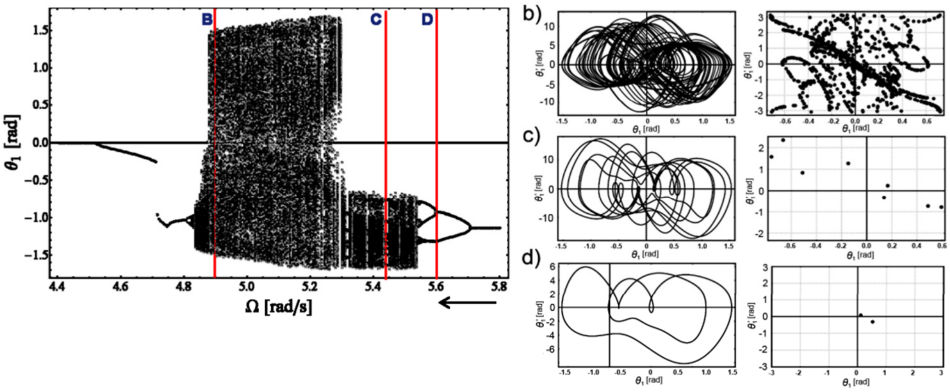

Figure 3. Bifurcational diagram regarding angle θ1 in range $\Omega \in \langle 4.4, 5.8 \rangle$ rad/s with step -0.005 rad/s, series of phase plots and Poincaré maps (vertical lines (B-D) correspond to parameters used in further analysis)

During the bifurcation analysis we were lowering the value of control parameter Ω with constant step size. Over 5.7 rad/s the system performs harmonic vibrations. Changing the value of Ω one can observe the first bifurcation and double period bifurcation (see Fig. 3d, which corresponds to line D in Fig. 3a).

After a further reducing the value of Ω, the period doubles several times tending to chaos. The illustration of one of the periodic windows between chaotic behaviour is presented in Fig. 3c. Figure 3b shows an example of chaos (see line B in Fig. 3a). It is worth to mention that the performed detailed analysis (with smaller value of control parameter steps) shows that changes in the character of movement dynamics occurred in each angle of deflection simultaneously. Moreover, in a region of higher angular velocities of excitation a few regions of quasi-periodics have been found and studied.

4. The experimental stand

The experimental part of the project consisted of planning, designing and constructing the stand to perform verification and validation of the numerical results. In order to compare the numerical results with those obtained experimentally the original measurement and acquisition software has been developed. The photo of the stand and a scheme of its construction are shown in Fig. 4.

The orientation of each pendulum is measured by means of four incremental encoders and the dedicated PCI acquisition card. Special slip ring is used to transmit signals between rotating pendulums equipped with the encoders and mounting frame. The external angular velocity excitation is provided by the PC-controlled servomotor.

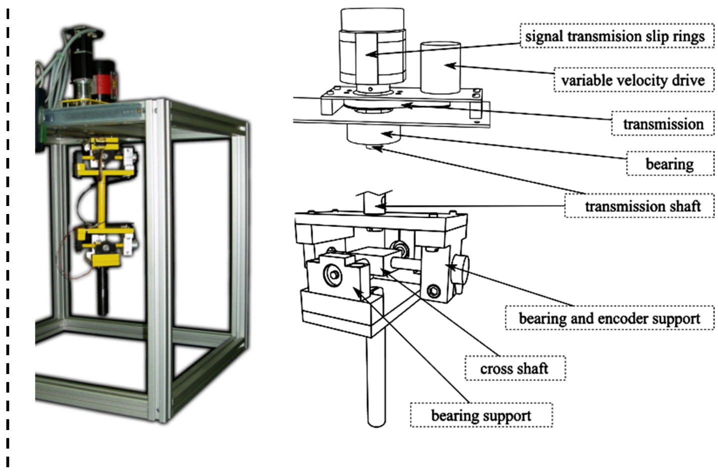

Figure 4. A part of the designed experimental stand

One should notice that the stand has some limitations in comparison with the mathematical model. Due to the construction details it is impossible to realize pendulums rotations in more than about 30 degrees in each direction. Exceeding these limits will result in impacts that could damage the stand. For this reason the first measurements have been focused on real damping coefficients of the bearing identification and verification of the analytically calculated mechanical parameters, like moments of inertia, etc. Currently, the procedure of searching stable configurations of pendulums is under development and improvement. The measurement data averaged to avoid incidental errors have been shown in Fig. 5.

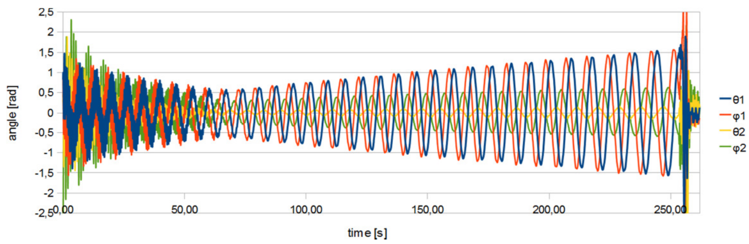

Figure 5. The results for measuring constant angular velocity of excitation (3.7 rad/s)

The pendulum has been accelerated to a constant angular velocity and pushed out of balance in an accidental way. One can observe damped vibrations transforming to more regular movement with growing amplitude due to a centrifugal force, ending with impacts that immediately stopped the experiment. The collisions are the main inconvenience of the measurement. Increasing the damping of the first pendulum may improve this situation and is under development. Additionally, the control software for the servomotor is developed so as to vary the excitation angular velocity.

5. Conclusions

Performed simulation investigation revealed a wide spectrum of nonlinear effects, periodic, quasi-periodic and chaotic orbits have been detected and discussed, among others. The experimental research is still being improved, mainly to avoid impacts that can be dangerous, where chaotic character of movement is expected. It is also worth mentioning, that the experimental work showed potential additional applications, i.e. a real-time analysis of some types of driving shafts or robots dynamics.

Acknowledgments

This work has been supported by the Ministry of Science and Higher Education of Poland, co-financed from the European Social Fund and the State Budget within the Activity 2.6 of the Integrated Operational Program for Regional Development. The research after PhD thesis defence were supported by "*MASTER*" Programme of Foundation for Polish Science.

References

1. N. Phillips, *What Makes the Foucault Pendulum Move among the Stars?*, Science & Education, **13** (2004) 653- 661.
2. M. Rossi, L. Zaninetti, *The cubic period-distance relation for the Kater reversible pendulum*, Central European Journal of Physics, **3(4)** (2005) 636- 659.
3. S.-T. Wu, *Active pendulumvibration absorbers with a spinning support*, Journal of Sound and Vibration, **323(1-2)**, (2009) 1-16.
4. O. Gottlieb, G. Habib, *Non-linear model-based estimation of quadratic and cubic damping mechanisms governing the dynamics of a chaotic spherical pendulum*, Journal of Vibration and Control, doi: 10.1177/1077546310395969 (2011).
5. J. Shen, A.K. Sanyal, N.A. Chaturvedi, D. Bernstein, H. McClamroch, *Dynamics and control of a 3D pendulum*, 43rd IEEE CDC, **1** (2004) 323-328.
6. J. Awrejcewicz, G. Kudra, G. Wasilewski, *Chaotic zones in triple pendulum dynamics observed experimentally and numerically*, Applied Mechanics and Materials, **9** (2008) 1-17.
7. J.E. Marsden, J. Scheurle, *Lagrangian reduction and the double spherical pendulum*, Z. Angew. Math. Phys., **44**(1) (1993) 17- 43.

XXV Symposium *Vibrations in Physical Systems,* Poznan – Bedlewo, May 15-19, 2012

On Some Aspects of Multiple Scale Method in Problems of Nonlinear Dynamics

Jan AWREJCEWICZ
Łódź University of Technology, Department of Automation and Biomechanics
Stefanowskiego 1/15, 90-924 Łódź, Poland, awrejcew@p.lodz.pl

Roman STAROSTA, Grażyna SYPNIEWSKA-KAMIŃSKA
Poznan University of Technology, Institute of Applied Mechanics
ul. Piotrowo 3, 60-965 Poznań, Poland
roman.starosta@put.poznan.pl, grazyna.sypniewska-kaminska@put.poznan.pl

Abstract

Nonlinear vibrations of the two degree-of-freedom system near resonances are studied. The system is externally and kinematically driven. The dynamical problem is solved by an analytical multiple scales method (MS). This analytical approach gives very good results in solving problems of nonlinear dynamics and is more and more popular in last decades. The investigations are focused on correctness of MS method using various number of considered time scales. Namely, we show that in some cases the use of only two time scales is insufficient to detect all possible resonances exhibited by the studied system.

Keywords: resonances, asymptotic method, multiple time scale

1. Introduction

The great advantage of asymptotic methods relies on their analytical character. A solution obtained by asymptotic methods in contrary to numerical solutions possesses a more universal character. This allows to deduce a system behaviour without the need to solve very large number of problems. In turn, the powerful computer algebra systems that are used to implement these methods, significantly help us to carry out all computations using symbolic algebra manipulations. The multiple scales method (MS) is used in the paper to solve the dynamical problem of the two degrees-of-freedom mechanical object. Many authors take into account only two time scales to simplify the mathematical complexity of the problem. However, in this paper we show that the introduction of the additional time scale allows to obtain more information about behavior of the system. Similar analysis using three time scales has been carried out in reference [1]. Influence of the number of time scales in the MS method on qualitative and quantitative properties of the solutions is now discussed.

2. Formulation of the problem

The spring pendulum having the movable suspension point O is analyzed (Fig. 1). The equations of motion in non-dimensional form are as follows [1]:

$$\begin{gathered}\ddot{z}(\tau)+c_1\dot{z}(\tau)-\left(1+z(\tau)\right)\left(\dot{\varphi}(t)\right)^2+z(\tau)+w^2\left(1-\cos(\varphi(\tau))\right)-\\-r_x p_x^2\cos\left(\tau\, p_x\right)\cos\left(\varphi(\tau)\right)-r_y p_y^2\sin\left(\tau\, p_y\right)\sin\left(\varphi(\tau)\right)=f_1\cos(p_1\tau)\end{gathered}\tag{1}$$

$$
\begin{gathered}
(1+z(\tau))^2\ddot{\varphi}(\tau)+\left(c_2+2(1+z(\tau))\dot{z}(\tau)\right)\dot{\varphi}(\tau)+w^2\sin(\varphi(\tau))(1+z(\tau))- \\
r_y p_y^2(1+z(\tau))\sin(\tau\, p_y)\cos(\varphi(\tau))+r_x p_x^2(1+z(\tau))\cos(\tau\, p_x)\sin(\varphi(\tau))=f_2\cos(p_2\tau)
\end{gathered}
\tag{2}
$$

with the following initial conditions for non-dimensional generalized co-ordinates and their first derivatives

$$
z(0)=z_0,\ \dot{z}(0)=v_0,\ \varphi(0)=\varphi_0,\ \dot{\varphi}(0)=\omega_0\,. \tag{3}
$$

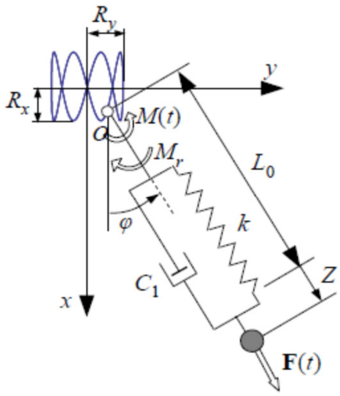

Figure 1. Spring pendulum moving on a prescribed path

3. Multiple scale method

The multiple scale method is applied to solve the governing equations and to obtain the resonance conditions. The amplitudes of vibrations are assumed to be of the order of a small parameter $0<\varepsilon<<1$. Let us introduce some new variables ζ and ϕ in the following form

$$
z(\tau)=\varepsilon\,\zeta(\tau;\varepsilon),\ \ \varphi(\tau)=\varepsilon\,\phi(\tau;\varepsilon). \tag{4}
$$

The smallness of some other parameters occurring in (2) is also assumed [2]. The functions ζ and ϕ are sought in the form

$$
\begin{gathered}
\zeta(\tau;\varepsilon)=\sum_{k=1}^{k=N}\varepsilon^k\zeta_k(\tau_0,\tau_1,\tau_2,...,\tau_N)+O(\varepsilon^N), \\
\phi(\tau;\varepsilon)=\sum_{k=1}^{k=N}\varepsilon^k\phi_k(\tau_0,\tau_1,\tau_2,...,\tau_N)+O(\varepsilon^N),
\end{gathered}
\tag{5}
$$

where $\tau_0=\tau$, $\tau_i=\varepsilon^i\,\tau,\ i=1,...,N-1$ are various time scales.

Derivatives with respect to time τ are calculated in terms of the new time scales as follows

$$\frac{d}{d\tau}=\frac{\partial}{\partial\tau_0}+\varepsilon\frac{\partial}{\partial\tau_1}+\varepsilon^2\frac{\partial}{\partial\tau_2}+...,$$
$$\frac{d^2}{d\tau^2}=\frac{\partial^2}{\partial\tau_0^2}+2\varepsilon\frac{\partial^2}{\partial\tau_0\partial\tau_1}+\varepsilon^2\left(\frac{\partial^2}{\partial\tau_1^2}+2\frac{\partial^2}{\partial\tau_0\partial\tau_2}\right)+.... \tag{6}$$

Introducing (4)–(6) into (1)–(2) we obtain two partial differential equations, in which the small parameter ε appears. After ordering each of the equations due to the powers of ε and omitting all terms of the order higher than ε^N, a set of N equations is derived. The obtained hierarchy sequence is solved recursively [1, 2].

4. Approximate analytical solution

MS method allows to obtain the approximate solution in an analytical form. Its correctness depends, among others, on the number of time scales used in the method. Below are presented solutions of equations (1)–(2) using two and three time scales.

- the solution for two time scales

$$z(\tau)=a_1\cos(\eta_1)-\frac{f_1\cos(p_1\tau)}{p_1^2-1}+\frac{p_x^2r_x\cos(p_x\tau)}{\left(p_x^2-1\right)}+\frac{w^2a_2^2\left(4w^2-1+3\cos(2\eta_2)\right)}{4\left(4w^2-1\right)} \tag{7}$$

$$\varphi(\tau)=a_2\cos\eta_2-\frac{p_y^2r_y\sin p_y\tau}{p_y^2-w^2}-\frac{f_2\cos p_2\tau}{p_2^2-w^2}+\frac{wa_1a_2\left(-3w\cos\eta_1\cos\eta_2+2\left(w^2-1\right)\sin\eta_1\sin\eta_2\right)}{4w^2-1} \tag{8}$$

- the solution for three time scales

$$\begin{aligned}z(\tau)=a_1\cos(\eta_1)&-\frac{f_1\cos(p_1\tau)}{p_1^2-1}+\frac{8wa_1a_2^2\left(3w\cos\eta_1\cos2\eta_2+\left(1+2w^2\right)\sin\eta_1\sin2\eta_2\right)}{4w^2-1}\\&+\frac{4p_x^2r_x\left(1-4w^2\right)\cos(p_x\tau)+\left(p_x^2-1\right)w^2a_2^2\left(4w^2-1+3\cos(2\eta_2)\right)}{4\left(p_x^2-1\right)\left(4w^2-1\right)}\\&-\frac{p_y^4r_ya_2\left(\left(p_y^2+w^2-1\right)\cos\eta_2\sin p_y\tau-2p_yw\cos p_y\tau\sin\eta_2\right)}{p_y^6-w^2\left(w^2-1\right)^2-p_y^4\left(2+3w^2\right)+p_y^2\left(1+3w^4\right)}.\end{aligned} \tag{9}$$

$$\begin{aligned}\varphi(\tau)=a_2\cos\eta_2&-\frac{p_y^2r_y\sin p_y\tau}{p_y^2-w^2}+\frac{wa_1a_2\left(-3w\cos\eta_1\cos\eta_2+2\left(w^2-1\right)\sin\eta_1\sin\eta_2\right)}{4w^2-1}-\\&-\frac{\left(13w^2-1\right)a_2^3\cos3\eta_2}{192\left(4w^2-1\right)}-\frac{p_y^4r_ya_1\left(\left(1+p_y^2-w^2\right)\cos\eta_1\sin p_y\tau-2p_y\cos p_y\tau\sin\eta_1\right)}{p_y^6-w^2\left(w^2-1\right)^2-p_y^4\left(2+3w^2\right)+p_y^2\left(1+3w^4\right)}+\\&-\frac{f_2\cos p_2\tau}{p_2^2-w^2}+\frac{p_xr_x\left(p_x^2+w^2-1\right)a_2\left(p_x\cos p_x\tau\cos\eta_2+2w\sin p_x\tau\sin\eta_2\right)}{\left(p_x^2-1\right)\left(p_x^2-4w^2\right)}-\\&-\left(24wa_1^2a_2\left(w\left(1+2w^2\right)\cos^2\eta_1\cos\eta_2-w\left(1+2w^2\right)\sin^2\eta_1\cos\eta_2+\right.\right.\\&\left.\left.+\left(2-5w^2\right)\sin2\eta_1\sin\eta_2\right)\right)\Big/192\left(4w^2-1\right),\end{aligned} \tag{10}$$

where $\eta_1 = \tau + \psi_1(\tau)$, $\eta_2 = w\tau + \psi_2(\tau)$.

As we can see higher number of time scales causes that the solution is much more complicated in comparison to the results obtained through two scales procedure. The carried out numerical tests confirm that the three scales solution improved slightly the results. However, in majority of cases appeared in non-linear mechanics and physics two time scales are sufficient to describe very well time histories of generalized co-ordinates. On the other hand solutions (9)–(10) yield more deep qualitative information about dynamics of the studied system, which will be shown further.

5. Resonance cases

It should be emphasized that the solutions (7)–(10) are not valid for the cases, when their denominator values tend to zero. These cases are responsible for the resonance occurrence. All possible resonances can be identified as the external, kinematic, internal or combined ones.

Resonance cases obtained from the two time scales solution (7)–(8) ($N = 2$) follow: $p_1 \approx 1$, $p_2 \approx w$, $p_x = 1$, $p_y = w$, $1 = 2w$

Resonance cases obtained from the three time scales solution (9)–(10) ($N = 3$) follow: $p_1 \approx 1$, $p_2 \approx w$, $p_x = 1$, $p_y = w$, $p_x = 2w$, $1 = 2w$, $p_y = \pm(1 - w)$, $p_y = \pm(1 + w)$.

As we can see some resonance cases cannot be detected by the two time scales approach. For example, the case $p_x = 2w$ is not exhibited by formulas in (7)–(8), but the numerically obtained time history of the z and φ indicates the intensive energy exchange proving that such resonance exists in the system (Fig. 2).

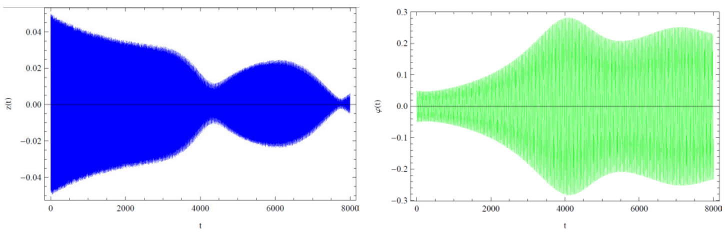

Figure 2. Time history of the z and φ in kinematical resonance $p_x = 2w$

It is worth to underline that all resonance cases which appear as result of (7)–(8) are included in the set of the cases detected using (9)–(10).

6. Two resonances appearing simultaneously

Let us examine parametric and primary resonances appearing simultaneously, i.e.

$$p_x \approx 1,\ p_2 \approx w. \tag{11}$$

In order to study the resonances, we introduce the new so-called detuning parameters σ_1 and σ_2 as a measure of the distance from the strict resonance:

$$p_x = 1 + \sigma_1 = 1 + \varepsilon\tilde{\sigma}_1 \text{ and } p_2 = w + \sigma_2 = w + \varepsilon\tilde{\sigma}_2 . \tag{12}$$

Resonance conditions (12) in equations (1)–(2) yield occurrence of secular terms, allowing for derivation of the frequency response functions:

- using two time scales

$$\left(c_1^2+4\sigma_1\right)a_1^2-r_x^2\left(1+\sigma_1\right)^4=0\,, \tag{13}$$

$$a_2^2w^2\left(c_2^2+4\sigma^2\right)-f_2^2=0\,, \tag{14}$$

- using three time scales

$$a_1^2\left(\frac{w^2\left(7w^2-1\right)a_2^2}{4\left(1-4w^2\right)}-\sigma_1\right)^2+\frac{c_1^2}{4}a_1^2-\frac{r_x^2\left(1+\sigma_1\right)^4}{4}=0\,, \tag{15}$$

$$a_2^2\left(-\sigma_2+\frac{\left(7w^2-1\right)wa_1^2}{4\left(1-4w^2\right)}+\frac{\left(1-5w^2+8w^4\right)wa_2^2}{16\left(1-4w^2\right)}\right)^2+\frac{c_2^2}{4}a_2^2-\frac{f_2^2}{4w^2}=0\,, \tag{16}$$

where a_1 and a_2 are amplitudes of the longitudinal and swing vibrations, respectively.
There are some crucial differences between frequency response governed by equations (13)-(14) and (15)-(16). In the first set, equations are simpler and uncoupled but do not describe a certain sophisticated behavior of the system in a strict resonance. Especially some additional steady state solutions are detected only using more than two time scales in the asymptotic approach.
The resonant responses are presented in Figure 3 obtained from (13)-(14), and in Figure 4 obtained from (15)-(16).

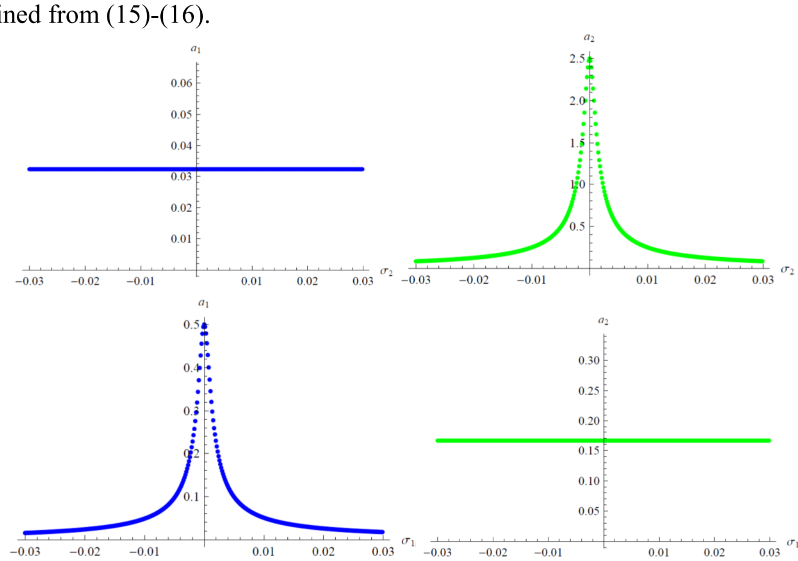

Figure. 3 Amplitude curves versus σ_1 for σ_2 = -0.03

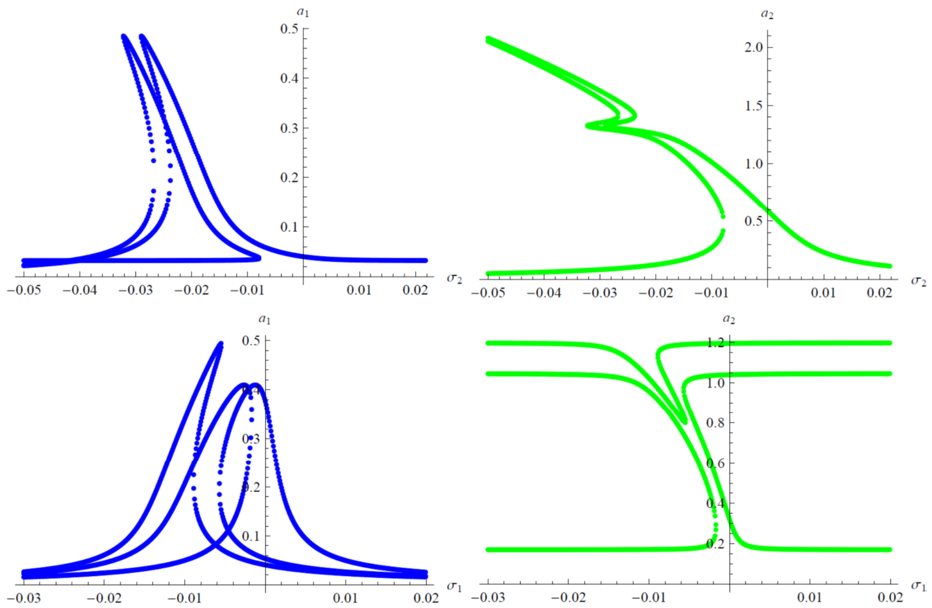

Figure 4. Amplitude curves versus σ_2 for σ_1=-0.005

All curves in Figs. 3 and 4 are reported for the same values of parameters.

7. Conclusions

The nonlinear non-autonomous two degree of freedom system has been studied. The analytical approximate solution has been obtained using multiple scales method in time domain.

The comparison between solutions obtained with the help of two and three time scales has been illustrated and discussed.

Very strong differences have been noticed in the case of a steady state response near the resonance. Therefore, it has been shown that in some cases simpler and easier to obtain solution with two time scales is insufficient to describe properly very complicated behaviour of the system. Moreover, more dangerous resonance cases in the system can be detected applying more time scales.

References

1. Starosta. R., Sypniewska-Kamińska G., Awrejcewicz J., *Asymptotic analysis of kinematically excited dynamical systems near resonances,* Nonlinear Dynamics, DOI: **10.1007/s11071-011-0229-6**; 2011.
2. Awrejcewicz J., Krysko V.A., *Introduction to Asymptotic Methods,* Chapman and Hall, Boca Raton, 2006.

XXV Symposium *Vibrations in Physical Systems,* Poznan – Bedlewo, May 15-19, 2012

Problems of In-Situ Vibroacoustic Testing of Low-Vibroactive Devices

Roman BARCZEWSKI
Poznan University of Technology, Institute of Applied Mechanics
CMBN ul Jana Pawła II 24 60-965 Poznań, laboratoria@tlen.pl

Bartosz JAKUBEK
Poznan University of Technology, Mechanical Engineering and Management Faculty
ul Piotorowo 3, 60-965 Poznań, bartosz.jakubek@student.put.poznan.pl

Abstract

This paper article outlines the problems of in situ vibroacoustic testing of low-vibroactive devices. Moreover a comparison of selected methods of object's surface velocity mapping was carried out in the paper. Primary features, advantages and limitations of these methods are stated here. On the example of tests on a refrigerator the methodology and specifics of testing of this type of devices using a laser vibrometer is also shown.

Keywords: noise of refrigerators, laser vibrometry, vibroactivity assessment,

1. Introduction

The competition on the market and growing consumers demands are creating the necessity of minimization of the noise emitted by machinery, devices and especially by household appliances. Low vibroactivity of these devices is important primarily from the point of view of comfort of use. Bearing this in mind, most of appliances are tested at the final stage of production. Besides checking the operating parameters, the level of the emitted noise is also checked in some classes of devices. The necessity of measuring the noise and the vibrations of devices results mostly from directives or standards. In many cases, the noise level can also be treated as a global measure of product quality (e.g. quality of assembly, proper operating of device subsystems, etc.). In case of devices with high noise levels, the measurement is relatively easy. Then the tests can be carried out in situ, in an industrial conditions e.g. in a separated and acoustically adopted area of a production hall. To obtain correct results it is necessary to take into account required corrections resulting from the influence of the measurement environment.

On the other hand, carrying out the tests of low-vibroactive devices is problematic. The level of noise emitted by them may be in many cases lower than the level of the acoustic background. Obtaining reliable results of the tests would require to carry them out in an anechoic chamber or at least in the testing environment that takes into account the standard's recommendations (general or branch). Practically, it is not possible to examine all produced units in the laboratory conditions. It comes out both from the time limitations related to the production cycle and economic reasons. This solution is also not possible to apply in case of mass production (e.g. the production line). An example of low-vibroactivity appliances is a refrigerator. The noise level emitted by the refrigerator should meet the requirements of the branch or company standards. It is also important that the average sound level (L_A for steady noise) or an equivalent sound level ($L_{A,eq}$. for unsteady noise) in the living environment (e.g. kitchen) is lower than the limit values of 35 dB in the day and 25 dB in the night time (according to standard PN-87/B02151/2 [1]).

This article introduces the method of carrying out the identification vibroacoustic tests of refrigerators with a laser vibrometer. The results of tests show that the method may be used for comparative evaluation of vibroactivity of this class of devices.

2. Alternative testing method

Because of the typically high level of acoustic background in an in-situ testing environment the measurement of the refrigerator's noise with microphone or matrix of microphones may be not effective enough. Carrying out the tests even in the near acoustic field does not guarantee to obtain reliable measurement results. It is worth to mention that there are no subassemblies or elements of the cooling system visible from outside in refrigerators produced nowadays. They are covered by the rear wall of the refrigerator or they are combined with the rear wall. A refrigerator creates then a quasi-surface source of noise.

Table 1. The ccomparison of the characteristics of measuring systems from the viewpoint of velocity mapping

	Measuring system/ transducer type		
	laser vibrometer	eddy current probe (proximitor)	accelerometer
Measuring type	non-contact relative vibration	non-contact relative vibration	contact absolute vibration
Measured vibration quantity	Velocity	Displacement	Acceleration
Features, Advantages and Disad-vantages	• High costs of devices • High sensitivity of the measuring system • Very good linearity of signal conversion • Wide frequency range • Most effective techniques (in case of a scanning system) • A laser head vibroisolation and an object stabilization is recommended • Problem with laser beam focusing	• Low or medium cost of equipment • Velocity signal is crated by displacement signal differentiation • Limited frequency range • Transducer supporting and/or positioning system is necessary • Measurement interference of close located sources of a magnetic field • Suitable for measuring significant vibration sources	• Low or medium cost of equipment • Velocity signal is created by acceleration signal integrating • Resonances of a transducer and its mounting systems (linearization of frequency characteristic is necessary) • Manual transducer positioning or an industrial robot is needed • transducer presence on the object may interfere with measurement results

One of the ways to solve this problem is an estimation of object's vibroactivity with an indirect method. The proposed method includes creation of a velocity map of the device's case vibration, then determination of the distribution of a sound power (or the sound power level) on the surface of the object. Basing on such a form of a result it is possible to estimate the noise in the near field. Mapping could be based on the contact vibration measurement. However, practically a non-contact method is better e.g. using a scanning vibrometer (see Table 1).

This approach is also justified by the terms of application procedures e.g. the final product quality control. Velocity or sound power level maps created on the basis of the identification tests, firstly enables to locate the main sources of noise and vibration in the device. Secondly, it allows simplifying the product testing procedures. It means that the number of measuring points can be reduced only to the areas with the greatest vibroactivity.

3. Testing procedure

The vibroacoustic identification test of a refrigerator was performed by scanning its case using the Polytec laser vibrometer (type OFV-5000). The scanning procedure consisted of a multi-point, non-contact measurement (laser beam) of rear wall of the refrigerator. In this area the main sources of vibration (condenser, expansion valve, evaporator unit, compressor and fans) are located. Manual positioning of the laser beam was used.

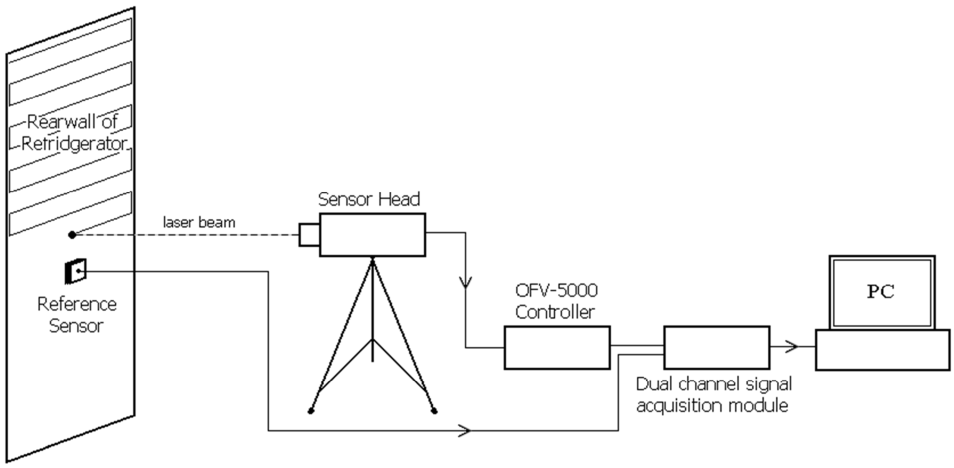

Figure 1. Measuring system used for scannning the surface of the refrigerator and VA signal acquisition [3]

A simplified algorithm of object vibroactivity identification is shown in Fig. 2. The testing process was carried out in five stages. In the first stage vibration of refrigerator's rear wall velocity was measured sequentially (according to the grid). The digital signal processing of recorded signals was done in the second stage. In the result the set of RMS values of vibration velocity in octave frequency bands for all measuring points has been created. The third stage of the procedure included the amplitude correction. It resulted from scanning the surface at different angles. In the fourth stage, for each elementary surface acoustic power and sound power level were determined. The last stage included visualization of the tests results.

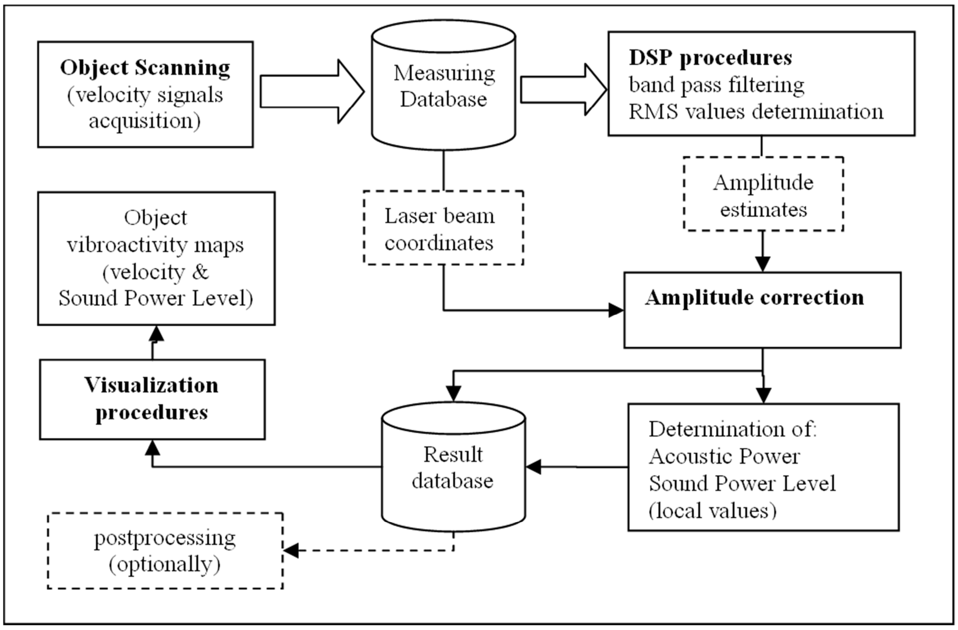

Figure 2. Simplified algorithm of object vibroactivity identification

A signal from the laser vibrometer was pre-filtered and AD converted in a dual channel signal acquisition module. The correction of the RMS vibration velocity was based on the equation (1).

$$v_R = v_P \cdot \cos\left(atc\tan\frac{\sqrt{x^2 + y^2}}{a} \right) \tag{1}$$

where:

v_P is the measured vibration velocity

v_R is corrected vibration velocity

x, y are horizontal and vertical shift of the laser beam,

a is the distance between refrigerator and sensor head.

The matrix of the corrected vibration velocity $v_{R\,i,j}$ (the RMS values) was used to determine the matrix of sound power, basing on equation (2)

$$N_{i,j} = \rho \cdot c_a \cdot v_{i,j}^2 \cdot \frac{S}{n}, \tag{2}$$

where
- ρ is a medium density (air) ,
- c_a is the sound speed in the air,
- $v_{i,j}$ are the RMS values of vibration velocity in the points i,j,
- S is the total area of the vibration emitting surface,
- n is the number of measurement points on the surface.

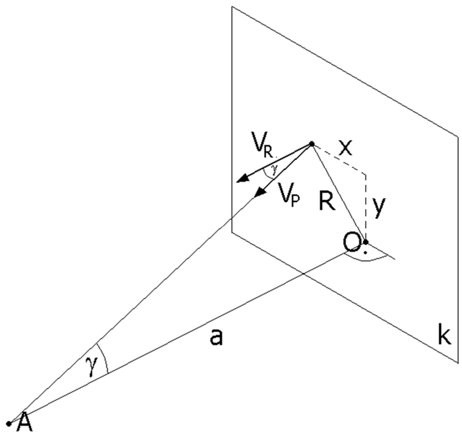

γ is an angle between V_P and V_R vectors,
R is the distance between point O and measurement point,
k is the refrigerator's rear wall surface,
a is a distance between refrigerator and sensor head,
A is the source of laser beam
O is a reference point.

Figure 3. Relation between vibration velocity vectors: normal and measured [3]

The sound power level $L_{i,j}$ was determined in reference to $N_0 = 10^{-12}$W :

$$L_{i,j} = 10\log_{10}\frac{N_{i,j}}{N_0} \tag{3}$$

The sample of refrigerator's test results in the form of the sound power level map in the hearing range and RMS vibration velocity map is given in Fig. 4.

4. Conclusions

Tests carried out in the room without special acoustic adaptation allowed to draw the following conclusions:

- The applied measurement system was very sensitive. Processes such as: a conversation in the room, the floor vibrations caused by movement of personnel, working elevator or closing the door had been reflected in the vibration signal. The influence of these effects on final results should be taken into account.

- The logarithmic scale of the vibroactivity maps is an optimal form of the results presentation, especially for identification of both the high-energy and the low-energy phenomena. (see Figure 3 b).
- Basing on the analysis of the contour map of the sound power level it is possible to localize the main noise sources of the device.
- The identification of vibroacoustic processes, the determination of emitted noise nature and noise evaluation is possible on the basis of map sets created for each octave frequency band.
- Using additional simulation tools e.g. the SYSNOISE system also creates the possibility of the virtual noise analysis and the noise assessment without the use of an anechoic chamber.

a) b)

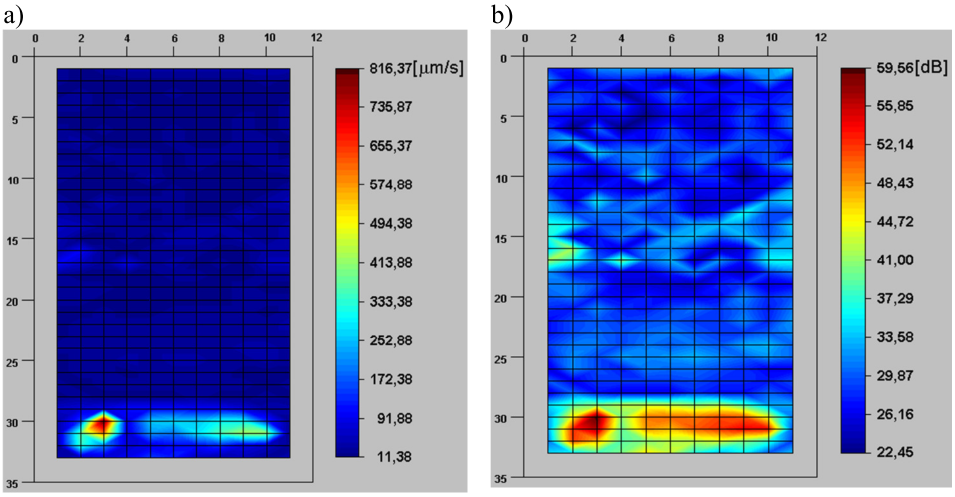

Figure 4. Maps of the refrigerator vibroactivity created on the basis of the vibration velocity (a) and the sound power level (b) (rear wall) [3]

References

1. *Handbook for sound engineers*, editor Ballou G.M., Focal Press, Elsevier 2005.
2. Cempel. C., *Wibroakustyka stosowana*, PWN, Warszawa-Poznań 1978.
3. Jakubek. B., *Vibroacoustig testing of a refrigerator*, Poznan Univ. of Technology Faculty of Mechanical Engineering and Management, Poznań 2012, (promoter Barczewski R.)

.

XXV Symposium *Vibrations in Physical Systems,* Poznan – Bedlewo, May 15-19, 2012

Some Problems on Thin Walled Wooden Structures Modeling

Roman BARCZEWSKI
Poznań University of Technology, Institute of Applied Mechanics
Jana Pawła II 24, Poznań, laboratoria@tlen.pl

Andrzej KABAŁA
Poznań University of Technology, kabalaandrzej@gmail.com

Abstract

The paper presents some problems on thin-walled wooden structures modal investigations. Dynamic experimental method is used to determine Young's modulus of the chosen wooden specimens. Numerical FEM simulations (ABAQUS/Standard) are applied to the Young's modulus tests, obtained by experiment, as well as to simulate modal behaviour of simple wooden plates with arbitrary oriented annual rings.

Keywords: wooden structures, module of elasticity, modeling, experiment, numerical simulation

1. Introduction

Wood and wooden materials have very wide range of elasticity modulus values. Thus, precious experimental determinations of the Young's modulus are necessary to realize numerical investigation of the CAD wooden structures. In case of modal investigation of thin walled structures the recommended methods used to determine modulus of elasticity are dynamical vibration methods. One of them, the free vibration method, is applied to determine the elasticity modulus of several wooden specimens.

Numerical modal simulation of the specimen is used to test the Young's modulus determined by experiment.

2. The Method

The free vibration technique of determination of elasticity modulus is an alternative to standard method based on four or three-point static flexure test. The standard test method determines the modulus of elasticity within the linear region of the stress-strain curve. The vibration method is based on measure of natural frequency (first mode) of the beam (see Figure 1b). The Young's modulus is calculated from the following equation

$$E = \alpha \cdot m \cdot \left(\frac{l}{h} \right)^3 \cdot b \cdot f^2 \tag{1}$$

where

f is measured frequency (first mode)

b, h, l are width, height and length of the specimen (beam)

α is the numerical value

Recordings of the specimen free vibration have been made using the Polytec laser vibrometer (type OFV-5000). After ADC conversion the signals have been software processed. The natural frequency of the specimen has been received from the high resolution spectral analysis of the captured vibration signal. Elaborated DSP system (created in the DasyLab environment) automatically calculates the average value of modulus of elasticity. The measuring system, aside from the vibration signal, requires input data such as: beam width (b) beam height (h) - beam overall length (l_c), active length of the beam (l), total mass of the beam (m) to be introduced.

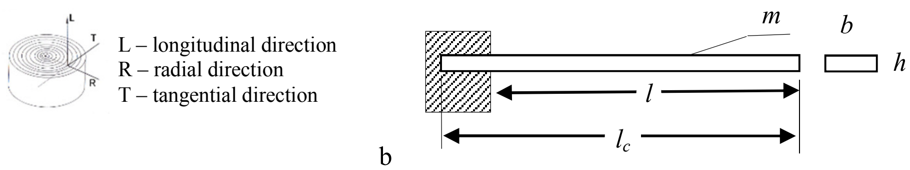

Figure 1. Local coordinate system to which wooden properties are related (a), dimensions of the specimen (b)

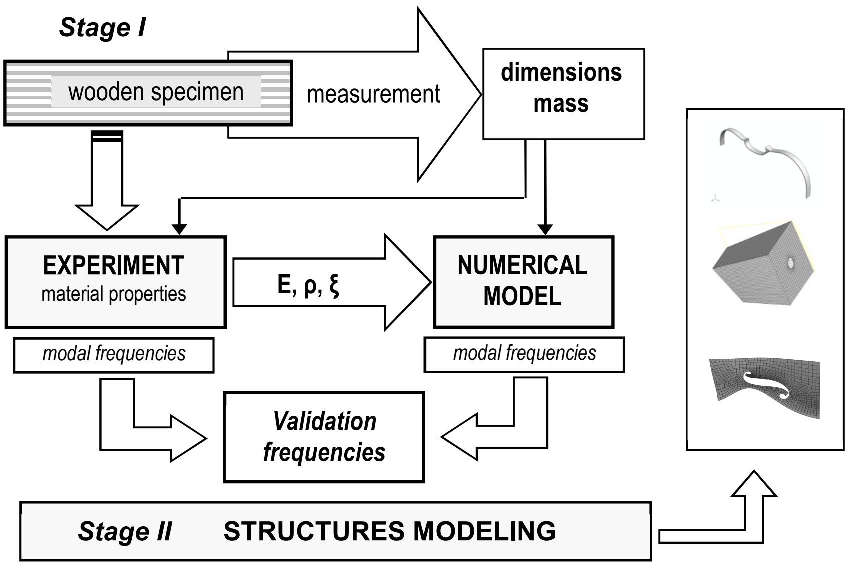

Figure 2. Dynamical method of Young's modulus determination and numerical simulations test algorithm

3. Experimental Determination of Wooden Young's Modulus and Numerical Simulation Tests

Several numerical simulations are done to test Young's modulus experimental determination, according to algorithm shown in Figure 2. Spruce, great maple, nut wood, pine, beach wood and oaken specimen modal behaviour are investigated. Some of the specimens are modeled as shell models and same as solid 3D models. The specimens are modeled as elastic material with the Young's modulus and the density determined by experiment. The basic description of the specimens is shown in Table 1.

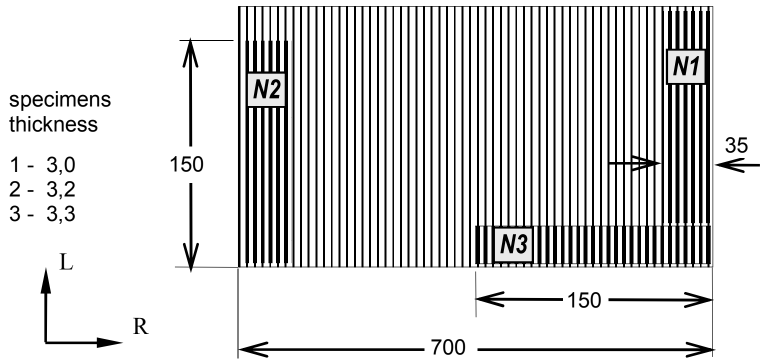

Figure 3. Three specimens of spruce plate used to build guitar – dimensions in [mm]

The main orientation of the specimens is LR-plain (see Figure 1a), thickness orientation is T-direction. All rectangular specimens described in Table 1 consist of 4-node shell elements type S4R with the mesh layout as shown in Figure 6. Figure 3 illustrates the spurs sheet and positions of specimens N1, N2, N3. Position of specimen N3 is oriented (RL) perpendicular to orientation of specimens N1 and N2 (LR).

Table 1. Results of Young's modulus experimental determination and results of frequency numerical simulation (ABAQUS)

specimen	material	orient.	*q* kg/m^3	***E* [GPa]** exper.	reference		$f_{w(1)}$ [Hz] exper.	ABAQUS	Δ [%]
A(ar)	spruce	L	499,69	14,011			57,860	57,649	*0,36*
B(ar)	spruce	L	548,57	14,235	7.3 - 21.0		55,660	55,459	*0,36*
N1	spruce	L	478,82	10,997	16[1)]		104,740	104,54	*0,19*
N2	spruce	L	431,55	9,268			108,030	107,81	*0,20*
N3	spruce	***R***	*489,67*	***0,656***	0.701[1)]		27,830	27,776	*0,19*
N4	great maple	L	645,11	6,296	6.4 - 15.2		31,860	31,834	*0,08*
N5	nut	L	687,97	5,778	12.3[2)]		71,780	71,624	*0,22*

[1)] Aszkenazi [2)] walnut

Material properties of the specimens are experimentally determined and introduced into input files of the numerical models. One of the specimen short edges is clamped as boundary condition. In ABAQUS/Standard FEM System the *FREQUENCY procedure is used to extract the modes and natural frequencies of the specimens.

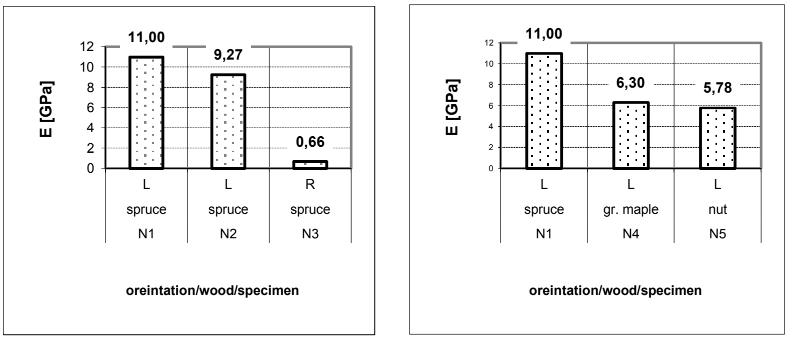

Figure 4. Comparison of Young’s modulus experimental results of the chosen specimens

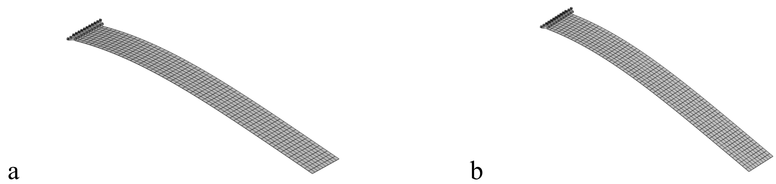

Figure 5. 1st mode shape of the spruce specimen No 1 (E = 10.997 GPa) – 104.54 [Hz](a)
1st mode shape of the spruce specimen No 3 (E = 0.66 GPa) – 27.78 [Hz] (b)

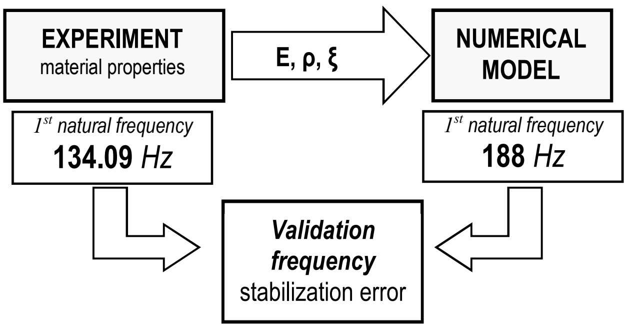

Figure 6. Comparison of experimental and numerical 1st natural frequencies – investigation of the incompatibility reason (see Fig. 7)

The first natural frequency of the specimen extracted by numerical simulation is compared with the specimen frequency measured by experiment. Comparison of the frequencies is presented in Table 1 as error Δ. In case when the error is too large the investigation of the reason must be done. The example of unsatisfactory frequencies comparison is shown in Figure 6 and the reason of incompatibility is shown in Fig. 7.

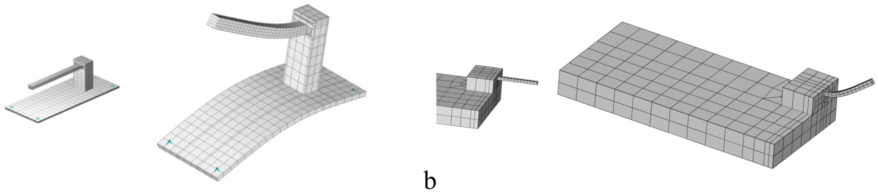

a b

Figure 7 Invalid (a) and valid (b) specimen stabilization examples,
a - specimen stabilization in thin-walled steel structure, b - specimen stabilization in concrete and metal heavy structure

4. Examples of Wooden Plates Experimental Investigations and Numerical Simulations

The first example is square plate vibration shown in Fig.8. All edges are free and harmonic displacement excitation perpendicular to the plate surface is applied at the center of the plate.

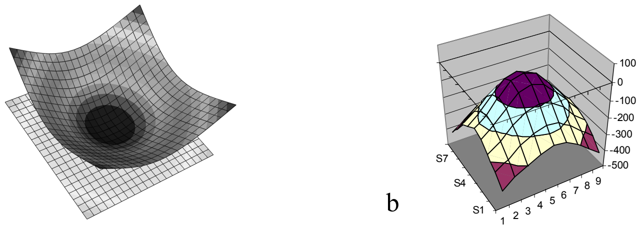

a b

Figure 8. Mode III of brazen square plate (100x100x1 mm)
a – ABAQUS 204,4 [Hz], b – experiment 202,8 [Hz]

a b

Figure 9. Mode III of wooden (pine) plate - 116x117x5.7 mm. Plate edge is parallel to L-dir.; a – ABAQUS 348.8 [Hz], b – experiment 342.3 [Hz]

In the next example the boundary condition and the load (harmonic displacement excitation) is the same as in the first one. Material of the plate is pine and two plate edges are parallel to L axis direction (see Fig. 1a). Dimensions of the plate and results of numerical and experimental investigations are shown in Fig. 9.

a b

Figure 10. Mode III of wooden (pine) plate - 116x116x5.7 mm.
Plate edge is 45^{o} skew to L-dir.; a – ABAQUS 313 [Hz], b – experiment

The third example is the same as previous but edges of the plate are 45^{o} skew to L direction (see Fig. 1a). Dimensions of the plate and results of numerical and experimental investigations are shown in Fig. 10.

5. Conclusions

Dynamic experimental method that is used to determine Young's modulus satisfies requirements of wooden thin-walled structures numerical investigation. Graphical representation of the method algorithm allows validation experimental and numerical investigation results. All results of the investigation as well as presented in the paper examples confirm practical application of the method. It is necessary to experimentally determine wooden Young's modulus for designed thin-walled wooden structure materials individually.

References

1. Е. К. Ашкенази, *Анизотропия древесины и древестных материалов,* Издателство „Лесная Промќшленность", Москва 1978
2. R. Barczewski, A. Kabała, *Uwarunkowania wyznaczania modułu sprężystości drewna metodami wibroakustycznymi,* II Kongres Mechaniki Polskiej, Poznań 2011.
3. Haines W., Leban J., Herbe C., Determination of Young's modulus for spruce, fir and isotropic materials by the resonance flexure method with comparisons to static flexure and other dynamic methods Wood Science and Technology 30 (1996) 253-263 Springer-Verlag 1996.
4. W. Kokociński, *Drewno pomiary właściwości fizycznych i mechanicznych,* PRO-DRUK, Poznań 2004
5. H. Petersson and other, *Moisture Distortion Modelling of Wood and Structural Timber,* International Conference of COST Action E8 Mechanical Performance of Wood Products Theme Wood-water relations, Copenhagen Denmark 1997
6. ABAQUS/Standard v.6.1, *User's Manual, Theory Manual,* Hibbit, Karlsson & Sorensen, Inc., Pawtucket, USA.

XXV Symposium *Vibrations in Physical Systems,* Poznan – Bedlewo, May 15-19, 2012

Dynamic Analysis of Collision of Beam With Rough Obstacle

Tomasz BARTKOWIAK
Poznań University of Technology, Institute of Applied Mechanics
Piotrowo 3, 60-965 Poznań, Poland
tomaszbartkowiak88@gmail.com

Henryk KAMIŃSKI
Poznań University of Technology, Institute of Applied Mechanics
Piotrowo 3, 60-965 Poznań, Poland
henryk.kaminski@put.poznan.pl

Grażyna SYPNIEWSKA-KAMIŃSKA
Poznań University of Technology, Institute of Applied Mechanics
Piotrowo 3, 60-965 Poznań, Poland
grazyna.kaminska@put.poznan.pl

Abstract

Beam collision with an obstacle is studied in the work. It is presumed that the conditions, under which the motion of the beam before, during and after the collision is planar, are fulfilled. Friction forces between contacting surfaces of both objects are taken into consideration. The problem is solved using the Rigid Finite Element Method. Interaction between the beam and the obstacle, taking into account the elastic properties and surface roughness of the latter one, is modelled using the elastic element. Three different models of the interaction, corresponding to various conditions governing the process, have been presented. Numerical simulations for the three possible variants of collision have been conducted. The results for the three considered cases of the collision have been compared with data obtained using Routh method.

Keywords: collision, modelling, rigid finite element method

1. Introduction

The study considers collision of a beam with motionless plane. Before the collision beam is in transitional motion at a constant velocity of $\vec{v}$, β is an angle between the beam axis and the direction of the velocity. At the initial moment of contact the beam axis is at an angle of α measured from the plane. The beam is characterized by its mass m, length L and its cross-section is a rectangle which has length h and width b.

Conditions under which before, during and after the collision, the beam is in planar motion are fulfilled. The obstacle with which the beam collides is permanently motionless and its surface is rough, what implies that friction forces must be considered during the collision. Friction force is modeled basing on Coulomb-Moren friction law.

Moreover, it is assumed that the contact between the both colliding objects takes place at the point O. Gravity is not considered in the model due to its non-pulse character.

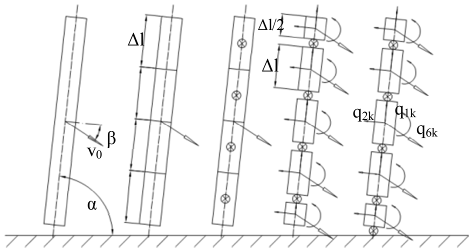

Figure 1. The model of considered collision.

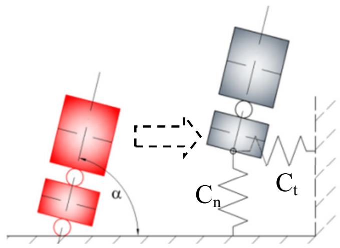

Figure 2. Modelling the contact.

2. Psysical model of the collision

The problem is solved using rigid finite element method (RFEM). In this method beam is divided into rigid and elastic elements which represent accordingly inertial and elastic characteristics of divided segments [2]. The beam was initially divided into *n* equally long pieces in the centre of which elastic element was placed. Between every two subsequent elastic elements rigid element was put. The contact between the beam and the surface is modeled by elastic element which bending stiffness is zero allowing the beam to rotate freely around the contact point (Fig.1).

Furthermore, it is presumed that slip occurs from the very beginning of the collision, which implies that the linear velocity of the beam in the point O projected on the collided plane is not equal to zero. The slip continues until one of the following events occurs:

- normal force at the point of collision changes its value to negative,
- slipping speed, understood as linear speed at the point of collision reaches value of zero, which means either that the contact changes its character into non-slip or the slip continues but in reverse direction. The first situation happens when ratio between tangential and normal force at the point of collision, at the moment of zeroing the sliding speed, is below the frictional coefficient. The latter situation occurs when the ratio is above this value.

The stiffness of contact element is described in coordinate system associated with the surface, which enables to apply stiffness referring to the normal and tangential to the plane directions (Fig. 2). However, the motion of the beam is described in the coordinate systems placed in the geometrical centre of rigid elements. Therefore, displacements at the contact elements are transformed into to the coordinate system of the first rigid element according to the following equations:

$$\vec{w}_{k1} = \begin{cases} w_{11} = q_{11} \cdot cos(\alpha) \; - \; q_{21} \cdot sin(\alpha) \\ w_{21} = q_{11} \cdot sin(\alpha) \; + q_{21} \cdot cos(\alpha), \\ \qquad w_{61} = q_{61} \end{cases} \tag{1}$$

where q_{11}, q_{21}, q_{61} are the generalized coordinates associated with the first rigid element, referring accordingly to translation along local x- and y- axis as well as rotation around z -axis; w_{11} w_{21}, w_{61} are the displacements of contact elastic element.

Motion equations when slip contact occurs are derived from Lagrange's equation as it follows:

$$\frac{d}{dt}\left(\frac{\partial E}{\partial \dot{q}_{rk}}\right) - \left(\frac{\partial E}{\partial q_{rk}}\right) + \left(\frac{\partial V}{\partial q_{rk}}\right) = P, \quad r=1,2,\dots,u, \quad k\in\{1,2,6\}, \tag{2}$$

where $E -$ kinetic energy of the system, $V -$ a potential energy of the system, P force derived from the friction, q_{rk} $-$ generalized coordinate of r-th element, u $-$number of rigid elements.

Kinetic energy of the system can be represented as sum of kinetic energy of particular rigid elements

$$E = \frac{1}{2}\left(\sum_{r=1}^{u} m_r \cdot \dot{q}_{1r}^2 + \sum_{r=1}^{u} m_r \cdot \dot{q}_{2r}^2 + \sum_{r=1}^{u} I_r \cdot \dot{q}_{6r}^2\right), \tag{3}$$

where m_r – mass of element, I_r $-$ mass moment of inertia of element.

Potential energy of the system is expressed as a sum of particular energies of particular elastic elements

$$V = \sum_{k=1}^{m} \frac{1}{2}\left(C_n \cdot \Delta w_{1k}^2 + C_t \cdot \Delta w_{2k}^2 + C_g \cdot \Delta w_{6k}^2\right), \qquad \text{for } k \neq 1 \tag{4}$$

where C_n – axial stiffness of the particular beam segment, C_t – shear stiffness of the particular beam segment, C_g – bending stiffness of the beam segment, Δw_{1k}, $\Delta w_{2k}, \Delta w_{6k}$ $-$ accordingly axial, shear and bending deformation at the r elastic element.

Potential energy accumulated in the contact element is added to the total potential energy and can be written as it follows

$$V_1 = \frac{1}{2}(a \cdot C_n \cdot \Delta w_{k1}^2) \tag{5}$$

where a is coefficient which characterizes the stiffness of the surface.

Substituting the equation (1) to (5), potential energy of the contact element takes a form

$$\begin{aligned} V = {} & \frac{1}{2} a \cdot C_n (q_{11} \cdot \sin\alpha + q_{21} \cdot \cos\alpha)^2 + \frac{1}{2} C_n \cdot (q_{12} - q_{11})^2 + \\ & + C_t \cdot \left(q_{22} - q_{62}\frac{\Delta l}{2} - (q_{21} + q_{61}\frac{\Delta l}{4}\right)^2 + C_g \cdot (q_{62} - q_{61})^2 \\ & + \frac{1}{2}\sum_{k=3}^{v-1} C_n \cdot (q_{1k} - q_{1\,k-1})^2 + \frac{1}{2} C_n \cdot (q_{1v} - q_{1\,v-1})^2 + \\ & + \frac{1}{2}\sum_{k=3}^{v-1} (C_t \cdot \left(q_{2k} - q_{6k}\frac{\Delta l}{2} - (q_{2\,k-1} + q_{6k-1}\frac{\Delta l}{2}\right)^2 + C_g \\ & \cdot (q_{6k} - q_{6k-1})^2) \\ & + C_t \cdot \left(q_{2v} - q_{6v}\frac{\Delta l}{4} - (q_{2\,v-1} + q_{6\,v-1}\frac{\Delta l}{2}\right)^2 + C_g \cdot (q_{6v} - q_{6\,v-1})^2 \end{aligned} \tag{6}$$

Friction force is proportional to the value of normal force at the point of O

$$N = a \cdot C_n \cdot (q_{11} \cdot \sin\alpha + q_{21} \cdot \cos\alpha). \tag{7}$$

In order to substitute the friction force to the set of Lagrange's equations (2), it must be projected on the coordinates of the first rigid element

$$P = \begin{bmatrix} k \cdot \mu \cdot a \cdot C_n \cdot \left(q_{11} \cdot \sin\alpha \cdot \cos\alpha + \left(q_{21} - q_{61}\frac{\Delta l}{4}\right) \cdot cos^2\alpha\right) \\ -k \cdot \mu \cdot a \cdot C_n \cdot \left(q_{11} \cdot sin^2\alpha + \left(q_{21} - q_{61}\frac{\Delta l}{4}\right) \cdot \sin\alpha \cdot \cos\alpha\right) \\ k \cdot \mu \cdot a \cdot C_n \cdot \left(q_{11} \cdot \sin\alpha \cdot \cos\alpha + \left(q_{21} - q_{61}\frac{\Delta l}{4}\right) \cdot cos^2\alpha\right) \cdot \frac{\Delta l}{4} \cdot \sin\alpha \\ 0 \\ \vdots \\ 0 \end{bmatrix}, \tag{8}$$

where k takes value 1 or 0 depending on the direction of the frictional force.
Finally, motion differential equations have a form

$$A \cdot \ddot{q} + (C - P^*) \cdot q = 0,$$

where P^* –vector of coefficients derived from the force vector according to $P = P^* \cdot q$, A – matrix of inertia coefficients, C – matrix of stiffness coefficients. (9)

The solution of the equations (2) takes a following form

$$q_{js} = \sum_{i=1}^{3(n+1)} \left(E_i \cdot \xi_{ijs}^0 \cdot sin(\omega_{0is}t) + F_i \cdot \xi_{ijs}^0 \cdot cos(\omega_{0is}t)\right), \tag{10}$$

where E_i, F_i – vectors of coefficients dependent on the initial conditions, ω_{0is} – angular frequencies of the system, ξ_{ijs}^0 – modes of vibrations.

As far as non-slip contact is concerned, the motion equation are derived from Langrange's equation as it follows

$$\frac{d}{dt}\left(\frac{\partial E}{\partial \dot{q}}\right) - \left(\frac{\partial E}{\partial q}\right) + \left(\frac{\partial V}{\partial q}\right) = 0. \tag{11}$$

Further deliberations are similar to slip contact example, therefore it can be written that motion differential equations take a form

$$A \cdot \ddot{q} + C \cdot q = 0. \tag{12}$$

The solution of (12) is as it follows

$$q_{jn} = \sum_{i=1}^{3(n+1)} \left(G_i \cdot \xi_{ijn}^0 \cdot sin(\omega_{0in}t) + H_i \cdot \xi_{ijn}^0 \cdot cos(\omega_{0in}t)\right), \tag{13}$$

where G_i, H_i – vectors of coefficients dependent on the initial conditions.

3. Numerical experiments

Let us consider three different situations leading to three different cases:

- when sliding velocity does not change its direction during the collision,
- when sliding velocity does change its direction to opposite during the collision,
- when contact changes its character from slip to non-slip during the collision.

Initial parameters were adjusted in other to obtain particular situation. In all three cases, the beam is equally long – 0.5 m, has the same cross section (0.02 m x 0.06 m) and is made of the same material – carbon steel.

Firstly, the case when the sliding velocity does not change its direction during the collision is considered. The results presented in Fig. 3a have been obtained for the following parameters and initial conditions: $v_0 = 5\ \frac{m}{s}, \omega_0 = 0\ \frac{m}{s}\ \ \alpha = 70°,\ \beta = 0°,\ \mu = 0.05$. Comparing the time history of slide velocity with the normal force during the collision confirms that its direction has not been changed during the contact.

Secondly, the situation when the sliding velocity does change its direction during the collision is examined. The results presented in Fig. 3c have been obtained for the following parameters and initial conditions: $v_0 = 1\ \frac{m}{s}, \omega_0 = 0.2\ \frac{m}{s}\ \ \alpha = 30°,\ \beta = 10°,\ \mu = 0.5$. Comparing the time history of slide velocity with the normal force during the collision confirms that the its direction has been changed during the contact. Furthermore, the ratio between normal and tangent force is compared to friction coefficient in order to determine the fact that contact character has not been changed to non–slip. The ratio value is greater than the friction coefficient.

Finally, the case when contact between the beam and the surface changes from slip to non-slip during the collision. The results presented in Fig. 3e have been obtained for the following parameters and initial conditions: $v_0 = 30\ \frac{m}{s}, \omega_0 = 0\ \frac{m}{s}\ \ \alpha = 10°, \beta = 0°,\ \mu = 0.85$. Comparing the time history of slide velocity with the normal force during the collision confirms that the its direction has been changed during the contact. In addition, the ratio between normal and tangent force is compared to friction coefficient in order to determine the fact that contact character has been changed to non–slip. The ratio value is lower than the friction coefficient.

The results gained by RFEM have been compared with the results given by Routh method for the same initial conditions and parameters. Pulses of normal and tangent force during the impact have been shown in Fig. 3b, Fig. 3d and Fig. 3f. Comparisons of the results by the two method is presented in Table 1.

Table 1. Comparison of the results obtained by the two different methods.

Case	RFEM			Routh	
	$\mathcal{T}$ [-]	$\mathcal{N}$ [-]	t_{col} [s]	$\mathcal{T}$ [-]	$\mathcal{N}$ [-]
1. Sliding velocity does not change its direction during the collision	-0,25	4,96	$1{,}03 \cdot 10^{-4}$	-0,11	2,28
2. Sliding velocity changes its direction to opposite during the collision	-0,05	0,12	$5{,}51 \cdot 10^{-6}$	-0,09	0,38
3. Contact changes its character from slip to non-slip during the collision	0,18	1,07	$4{,}45 \cdot 10^{-6}$	0,33	4,05

4. Conclusion

The results obtained by the RFEM are proved by Routh method as far as the character of the collision is concerned. The values of force pulses are similiar.

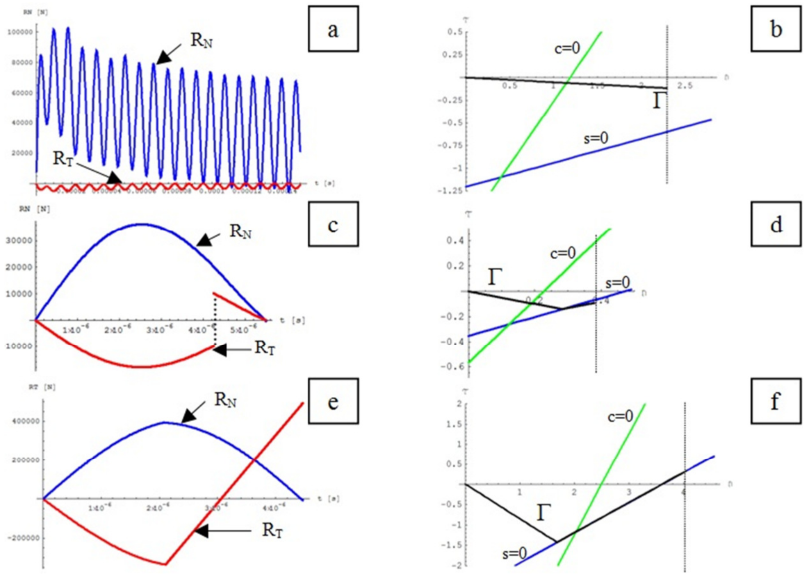

Figure 3. a) Normal and tangential force during the collision when sliding speed does not change its direction, b) pulses of normal and tangential force during the collision when sliding speed does not change its direction, c) normal and tangential force during the collision when sliding speed changes its direction, d) pulses of normal and tangential force during the collision when sliding speed changes its direction, e) normal and tangential force during the collision when contact changes its character from slip to non-slip, f) pulses of normal and tangential force during the collision when contact changes its character from slip to non-slip.

References

1. J. Awrejcewicz, G. Kudra, C.H. Lamarque, *Investigation of Triple Physical Pendulum with Impacts Using Fundamental Solution Matrices.* Int. J. Bifurcation and Chaos **14**(2) (2004) 4191–4213.
2. T. Bartkowiak, *Analiza naprężeń i odkształceń wywołanych zderzeniem belki z chropowatą przeszkodą*, praca dyplomowa, Poznań 2012.
3. J. Kruszewski, S. Sawiak, E. Wittbrodt, *Metoda sztywnych elementów skończonych w mechanice konstrukcji*, WNT 1999.
4. G. Sypniewska-Kamińska, Ł. Rosiński, *Application of the Routh Method in Computer Simulation of Selected Problems in Collision Theory*, Computational Methods in Science and Technology **14**(2) (2008) 123-131.

XXV Symposium *Vibrations in Physical Systems,* Poznan – Bedlewo, May 15-19, 2012

A Simple Model of Sound in Enclosures with a Low Frequency Harmonic Excitation

Andrzej BŁAŻEJEWSKI
Institute of Mechatronics, Nanotechnology and Vacuum Technique
Racławicka 15-17, Building F, 75-620 Koszalin, andrzej.blazejewski@tu.koszalin.pl

Tomasz KRZYŻYŃSKI
Institute of Mechatronics, Nanotechnology and Vacuum Technique
Racławicka 15-17, Building F, 75-620 Koszalin, tkrzyz@tu.koszalin.pl

Abstract

In the paper the problem of a room with a sound source inside is investigated. The effect, an acoustic field inside is affected by two factors: the shape and the boundaries of the enclosure. In order to evaluate the acoustic field, modal analysis assumption has been applied to describe the room's pressure distribution. Thus, the sum over a set of the room's eigenfunctions and proper time components represents the values of the acoustic field. Eigenfunctions can be obtained by solving the Helmholtz equation for rigid walls. Time components can be determined applying Green's theorem. This approach allows boundary conditions to be adjoined to time components and thereafter obtain a set of ordinary differential equations for each specified time component correlated with corresponding eigenfunction. Assuming a harmonic excitation, time components are harmonic as well. Therefore, the values of coefficients of each time component (i.e. the modal amplitudes) are required. Directly, one can evaluate the modal amplitudes by solving simple algebraic equations. As a result of this calculation, the finite set of eigenfunctions of an enclosure and modal amplitudes has been obtained. In this case of an additional assumption of high enough boundary impedance, the modal coupling can be neglected and consecutive formula reduction is possible. Under frequency limitation, the modal approach to a room's acoustic field modelling, involves much less computational effort than the alternative, for instance applying Finite Element Method (FEM) or Boundary Element Method (BEM).

Keywords: acoustic field, enclosure, modal analysis, modal amplitudes, harmonic source

1. Introduction

An acoustic field in an enclosure is a specific case of acoustic wave propagation. After the source of sound starts to emit a signal (sound wave), at the room's boundaries appears a loss of acoustic energy caused by absorption. This attenuation in the short term is equalized by the energy from the source. After this transient period the steady state behaviour dominates in an enclosure. The steady-state of an acoustic field, as characterized by the specific acoustic pressure distribution is reached. In order to describe this distribution inside a room, one can use modal analysis formulation under several restrictions [1]. The first factor in modal approach states that the enclosure can be considered a resonator and acoustic field distribution inside is dependent on its normal modes (eigenfunctions). It was assumed that one can use the eigenfunctions in the case of a room with perfectly rigid walls i.e. Neuman's boundary condition equals zero. Simultaneously, orthogonality and normalization of eigenfunctions are required [2]. The second factor is that the time components describe acoustic pressure variation in time.

On the other hand the acoustic field inside the room with a source describes a linear, inhomogeneous wave equation and the specific boundary conditions most often characterized by the wall's acoustic impedance. In order to solve such a formulated problem, the Finite Element Method (FEM) or Boundary Element Method (BEM) is needed. These methods are computationally expensive. Let's consider a modal approach.

2. Mathematical model of an acoustic field in an enclosure

Let's consider the acoustic field inside an arbitrary enclosure V with a vibro-acoustical source which is located in a determinate area (points), characterised by its power or outflow f. The field is described by a well-known wave equation:

$$\Delta p - \frac{1}{c^2}\frac{\partial^2 p}{\partial t^2} = f \tag{1}$$

where c is the sound velocity in air. The Neumann's impedance boundary conditions on each i part of the boundary S of the limited enclosure V are in the form:

$$\frac{\partial p}{\partial n} = -\rho_0 \frac{1}{Z_i}\frac{\partial p}{\partial t} \tag{2}$$

where Z_i is the impedance on the surface i. In order to solve the problem described by (1) and (2) and eventually obtain p(r,t), a FEM or BEM method is needed. The function p(r,t) represents values of acoustic pressure at a point r(x,y,z) of an enclosure in specific time t. In some cases modal analysis can be applied and the solution is directly assumed in the form:

$$p(r,t) = \sqrt{V}\sum_{m=0}^{\infty} T_m(t)\Psi_m(r) \tag{3}$$

where $T_m(t)$ are the time components, describing variation of an acoustic pressure in a time and $\Psi_m(r)$ are the eigenfunctions of an enclosure, which satisfies the Helmholtz equation in the general form:

$$\Delta\Psi_n(r) + \lambda_n \Psi_n(r) = 0 \tag{4}$$

under the following boundary conditions:

$$\frac{\partial \Psi_n}{\partial n} = 0 \tag{5}$$

In Eq.(4) λ_n's are the eigenvalues correlated with the eigenfrequencies ω_n of an enclosure by the formula $\omega^2_n=\lambda_n c^2$. In this case index n means the particular eigenvalue and eigenfunction of an enclosure. According to Green's theorem, if one considers an enclosure with volume V and boundary S as a bounded, positively-oriented domain, then both functions p(r,t) in Eq. (1) and $\Psi_n(r)$ in Eq. (4) should satisfy the following equation:

$$\int_V (p\Delta\Psi_n - \Psi_n \Delta p)dV = \int_S (p\frac{\partial \Psi_n}{\partial n} - \Psi_n \frac{\partial p}{\partial n})dS \tag{6}$$

In order to get more transparency here, variable t in the time components and r in the eigenfunctions were omitted.

Modifying Eq. (1) and (4) properly in order to obtain Δp and $\Delta\Psi_n$ respectively enables the application of the Laplasians into the left side of Eq. (6). Simultaneously, introducing the boundary conditions described by Eq. (2) and Eq. (5) into the right side of Eq. (6), eventually one can get the formula as follows:

$$\int_V (-p\lambda_n \Psi_n - \frac{1}{c^2}\frac{\partial^2 p}{\partial t^2}\Psi_n - f\Psi_n)dV = \int_S (\frac{\rho_0}{Z}\frac{\partial p}{\partial t}\Psi_n)dS \tag{7}$$

The integrand on the right hand side of Eq.(7) contains the boundary condition formulation for all boundaries of the enclosure. The first and second time pressure derivatives, calculated based on Eq. (3) take the form:

$$\frac{\partial p}{\partial t} = \sqrt{V}\sum_{m=0}^{\infty} \dot{T}_m \Psi_m \qquad \frac{\partial^2 p}{\partial t^2} = \sqrt{V}\sum_{m=0}^{\infty} \ddot{T}_m \Psi_m \tag{8}$$

where $\dot{T}_m$ and $\ddot{T}_m$ mean first and second time component, T_m, time derivatives respectively. Using both formulae, Eq. (7) it can be rewritten as follows:

$$\int_V (-\lambda_n \Psi_n \sqrt{V}\sum_{m=0}^{\infty} T_m \Psi_m - \frac{\sqrt{V}}{c^2}\Psi_n \sum_{m=0}^{\infty} \ddot{T}_m \Psi_m - f\Psi_n)dV = \int_S (\frac{\rho_0\sqrt{V}}{Z}\Psi_n \sum_{m=0}^{\infty} \dot{T}_m \Psi_m)dS \tag{9}$$

Simultaneously, modal analysis assumes the eigenfunctions should have been orthogonal and normalised. That means:

$$\int_V \Psi_n \Psi_m dV = \begin{cases} 0 \; n \neq m \\ 1 \; n = m \end{cases} \tag{10}$$

It enables Eq.(9) to be simplified to the form:

$$-\lambda_n \sqrt{V} T_n - \frac{\sqrt{V}}{c^2}\ddot{T}_n - \int_V f\Psi_n dV = \rho_0 \sqrt{V}\sum_{m=0}^{\infty} \dot{T}_m \int_S \frac{\Psi_m \Psi_n}{Z} dS \tag{11}$$

Grouping factors with time components and its derivatives on the left side hand and factors including the source term on the right, using simple algebraic operations, one can obtain a formula similar to the equation of the forced vibration with a damping. It takes the form:

$$\ddot{T}_n + \omega_n^2 T_n + \rho_0 c^2 \sum_{m=0}^{\infty} \dot{T}_m \int_S \frac{\Psi_m \Psi_n}{Z} dS = -\frac{c^2}{\sqrt{V}}\int_V f\Psi_n dV \tag{12}$$

The time components T_n can be obtained by solving the sets of Eq.(12). However, the eigenvalue problem of an enclosure with volume V, described by Eq.(4) and Eq.(5) has to initially be solved. Hence, the correlated eigenfunctions and eigenfreqencies are known. Eventually, applying Eq.(3), the values of acoustic pressure and its distribution in the enclosure could be determined. But in this case two main problems arise from summation on the left hand side of Eq.(12). The first problem appears because of the time component derivates summation and the second arises from the infinity of this sum. But in some cases one can solve this problem.

3. Harmonic excitation

In many cases properties of a sound source, describe by function f(r,t) and dimension of an enclosure V, make it possible to consider this source as harmonic, located at an exact point. Let's assume that a harmonic sound source described by function $f(r_0,t)=f_\omega\, e^{j\omega t}$. Where f_ω represents the power or outflow of the source with the frequency ω. The source is located at point r_0 of an enclosure. Considering only the steady-state of the acoustic field, the time components have to be harmonic as well i.e. $T_n=A_n\, e^{j\omega t}$. Introducing the assumption of the sound source harmonic behaviour enables Eq.(12) to be rewritten in the form:

$$\omega_n^2 A_n - \omega^2 A_n + j\omega\rho_0 c^2 \sum_{m=0}^{\infty} A_m \int_S \frac{\Psi_m \Psi_n}{Z}\, dS = -\frac{c^2}{\sqrt{V}} f_\omega \Psi_{n0} \tag{13}$$

where Ψ_{n0} is the eigenfinction value at a point r_0 (the sound source location). It is possible to extract the factor related to amplitude A_n from the sum ΣA_m and again the rewrite takes effect:

$$\omega_n^2 A_n - \omega^2 A_n + j\omega\rho_0 c^2 A_n \int_S \frac{\Psi_n^2}{Z}\, dS + j\omega\rho_0 c^2 \delta_{nm} \sum_{m=0}^{\infty} A_m \int_S \frac{\Psi_m \Psi_n}{Z}\, dS = -\frac{c^2}{\sqrt{V}} f_\omega \Psi_{n0} \tag{14}$$

where $\delta_{nm}=1$ if $n\neq m$ and $\delta_{nm}=0$ if n = m. Solving the Eq.(14) with respect to the A_n, one can obtain the modal amplitudes values in the form :

$$A_n = \frac{-\dfrac{c^2}{\sqrt{V}} f_\omega \Psi_{n0} - j\omega\rho_0 c^2 \delta_{nm} \displaystyle\sum_{m=0}^{\infty} A_m \int_S \frac{\Psi_m \Psi_n}{Z}\, dS}{\omega_n^2 - \omega^2 + j\omega\rho_0 c^2 \displaystyle\int_S \frac{\Psi_n^2}{Z}\, dS} \tag{15}$$

The surface integral represents damping in the acoustic system. One can see that damping is different for each modal amplitude and is dependent on the factor in the form:

$$d_{mn} = \rho_0 c^2 \int_S \frac{\Psi_m \Psi_n}{Z}\, dS \tag{16}$$

Eq.(15) is simplified to:

$$A_n = \frac{-\dfrac{c^2}{\sqrt{V}} f_\omega \Psi_{n0} - j\omega\rho_0 c^2 \delta_{nm} \displaystyle\sum_{m=0}^{\infty} A_m d_{mn}}{\omega_n^2 - \omega^2 + j\omega\rho_0 c^2 d_{nn}} \tag{17}$$

In order to evaluate all modal amplitudes described by Eq.(17), the factor contained in the summation has to be computed first. Initially, using an iteration method, all modal amplitudes for terms n = m are computed. The modal amplitudes A_0, A_1,A_2,..., in the case when the modal coupling is neglected, are determined. Eventually, its values are applied in sums in Eq.(17). In some cases, the boundary impedance Z reaches high values. In that situation one can utilise modal amplitude values without modal coupling.

4. Application of the method and limitation

Evaluating Eq.(3), infinite series need infinite numbers of the eigenfunctions and the time components. In the case of the harmonic excitation, the denominator in Eq.(17) includes the differences between the specific eigenfrequency and the source frequency. It indicates that the modal amplitudes tend to zero for eigenfrequencies, which are significantly bigger than the source frequency. It means one can modify formulation Eq.(3) and apply finite series:

$$p(r,t) = \sqrt{V}\sum_{m=0}^{N} T_m(t)\Psi_m(r) \tag{18}$$

where N is the number of the eigenfunctions taken into consideration. Eq.(18) represents the eigenfunctions correlated with the eigenfrequencies „be low and above" the source frequency. The values of the modal amplitudes diminish with the eigenfrequency and source frequency distance. Hence, for low range of frequency of excitation, there is the finite number N of the eigenfrequencies, which allows the acoustic field inside of the enclosure to be evaluated with acceptable accuracy. Simultaneously, the higher the frequency of an excitation is the bigger number N is needed. It results from the higher density of eigenfrequencies in a higher range compared to a low range of the eigenmodes.

5. Example of the method application and comparison with FEM

In order to compare accuracy of the method and the formulae, the same problem was solved, applying FEM and modal method. As the FEM the commercial software Comsol Muliphysics was used. The example object, the room bounded by 15 different walls, was shown in the Fig.1. The walls were characterized by the real and complex acoustic impedance. The results, i.e. acoustic pressure distribution, for the simple harmonic source characterized by power f=0.00015W, placed inside at two points r_{01}(4.5, 2.51, 1.31) and r_{02} (1.08, 2.51, 1.43) were considered. The two source frequency 100Hz and 300Hz were applied respectively. In the Fig. 1 the dimensions of the object are shown in meters and acoustic pressure in Pascal units.

6. Conclusions

The both FEM and modal model results comparison, as it is presented in the Fig. 1, indicates high convergence. The simple modal model presented in the paper is based on a evaluation of the eigenfunctions and the eigenfrequencies in accordance with Eq.(4) and the time components up to Eq.(12) (for the harmonic source Eq.(17)) and next acoustic pressure distribution using Eq.(18). Simply one has to solve acoustic eigenproblem for the enclosure first, next use the results in order to evaluate the damping in system (damping coefficients) and eventually evaluate the values of the modal amplitudes. Holding this numeric data one can simply simulate the acoustic field in the room in case of the different boundary condition and the source configuration. But one has to be aware that is not possible evade numerical methods solving this kind of problems. Solution of the egienproblems in case of irregular objects shapes and consequently integration in order to get damping coefficients require numerical method.

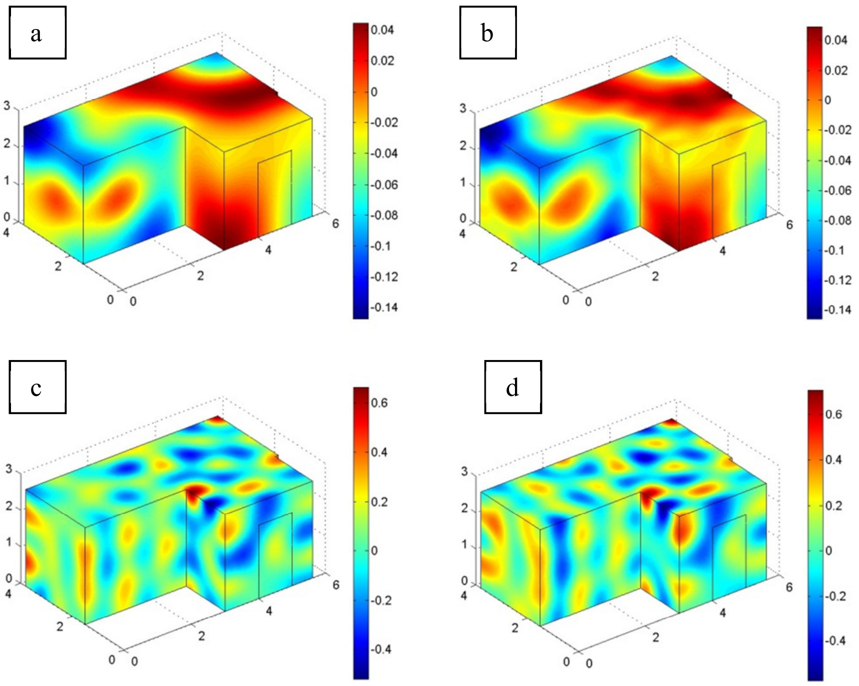

Figure 1. The acoustic field inside the example object obtained applying: a) FEM model and b) modal model in case of the source with frequency 100Hz at the point r_{01} and c) FEM model and d) modal model the source at the point r_{02} with frequency 300Hz

References

1. P.M. Morse, K.U. Ingard, *Theoretical acoustics,* Mc Graw-Hill, New York, 1968.
2. M. Meissner, *Zastosowanie analizy modalnej do wyznaczania rozkładu pola akustycznego i czasu pogłosu w pomieszczeniu o złożonym kształcie,* 50 Otwarte Seminarium z Akustyki. (2003) 110 – 113.
3. A. Marciniec, S.Noga, *Natural Frequencies and mode shapes of a composite annular membrane,* Vibration in Physical Systems, Volume XXIV, Poznań 2010.

XXV Symposium *Vibrations in Physical Systems,* Poznan – Bedlewo, May 15-19, 2012

The Evaluation of the Crack-Like Damage Parameter of Blades at the Vibroacoustical Diagnosis of the Gas-Turbine Engines

Nadiia BOURAOU
National Technical University of Ukraine "Kiev Polytechnic Institute"
37 Peremogy Pr., Kyiv, Ukraine, 03056, burau@pson.ntu-kpi.kiev.ua

Sergiy IGNATOVICH
National Aviation University
1 Kosmonavta Komarova Pr., Kyiv, Ukraine, 03058, ignatovich@nau.edu.ua

Abstract

This work is devoted to vibroacoustical condition monitoring of the gas-turbine engines (GTE) blades and diagnosis of the crack-like damages at the steady-state and non-steady-state modes of GTE. For detection of the mentioned damages we proposed the application and further development of the low-frequency vibroacoustical diagnostic methods which use vibrating and acoustical noise as diagnostic information. The following amplitude dimensionless characteristics are used as fault features: probability factor, peak factor and factor of background. The evaluation of the crack-like damage of the blades is carried out at the steady-state and non-steady-state modes by using the generalized likelihood method. The statistical quality of the received estimations is investigated.

Keywords: nondestructive evaluation, gas-turbine engine, crack-like damage, likelihood method

1. Introduction

The problems of condition monitoring of the gas-turbine engines (GTE) at the steady-state and non-steady-state modes of GTE, on-line crack-like damages detection and evaluation may be solved by using the vibroacoustical diagnosis methods. The creation of the condition monitoring system is based on improvement and further development of the low-frequency (0-25 kHz) vibroacoustical diagnostic methods which use vibrating and acoustical noise as diagnostic information [1]. This noise is radiated by the turbine and compressor stages during operation of the GTE. The diagnostic information is characterized by complexity and variety, and the measured signals are the local or essential non-steady-state processes. In case of the crack-like damages of GTE blades the components containing the information on faults are characterized by small vibratory energy. This restricts the application of traditional spectral-correlative methods of signal analysis for the early fault detection, estimation of their parameters and prediction of the further evolution.

The initiation and increase of a fatigue crack in the blade lead to the instantaneous change of its stiffness. Usually the change of stiffness is modeled by the piecewise-linear characteristic of the restoring force. Non-linearity leads to variation of the oscillation parameters and to the occurrence of local non-stationary component in the measured signal. We created the dynamic model of gas-turbine engine as the object for fatigue cracks diagnostic in turbine blades and compressors [1]. This model is used for simulation and analysis of vibroacoustical processes which occur at the steady-state and non-steady-state modes of GTE in the absence and presence of small fatigue cracks in one blade of the turbine stage (the relative rigidity changing at the crack presence is considered $\vartheta = 0.01,\ldots,0.1$). Three modes of GTE are simulated and investigated: m1 – steady-state (constant value of the rotor rotation frequency); m2 – non-steady-state (the fast increase of the rotor rotation frequency); m3 – non-steady-state (the decrease of the rotor rotation frequency). The simulated signals were processed using preliminary Wavelet-transformation and the amplitude dimensionless characteristics of the vibroacoustical signals. The following amplitude dimensionless characteristics are used as fault features: probability factor J_2, peak factor J_3 and factor of background J_4 [1, 2]. All features represent random quantities, the probability distribution law of features is close to normal. Pattern recognition of the blades condition may be carried out by way of estimation of the current value of fault parameter ϑ, and then making the decision based on comparison of the obtained estimations with the values of the reference level established in advance.

The purpose of this work is the evaluation of the relative rigidity changing ϑ as the fault parameter at the crack-like damage presence in turbine blades during operation of the GTE.

2. Analytic definition of maximum-likelihood estimations of the fault parameter

The maximum-likelihood method (MLM) is used for estimation of the nonrandom parameters in practice [3]. Generally, the equation of the maximum-likelihood is of the form:

$$\frac{\partial}{\partial\lambda}\ln L(\lambda) = 0\,, \tag{1}$$

where $L(\lambda)$ is the functional of likelihood; λ is the evaluated parameter.

The maximum-likelihood estimation $\hat{\lambda}_n$ of the unknown nonrandom parameter is asymptotically effective, the minimum dispersion of an estimation corresponds to Rao-Cramer boundary and defines a potential precision of an estimation. The dispersion of the estimation of the evaluated parameter is used as a measure of precision:

$$m\{(\hat{\lambda}_n - \lambda)^2\} \ge \sigma^2_{\hat{\lambda}} \ge [1 + b'_n\ (\lambda)]\big/I_n(\lambda)\,, \tag{2}$$

where $\sigma^2_{\hat{\lambda}}$ is dispersion of an estimation; $m\{\cdot\}$ is sign of mathematical expectation; $b'_n(\lambda)$ is a derivative on parameter λ from magnitude of a deviation of the obtained estimation from value of the evaluated parameter; $I_n(\lambda)$ is the information on Fisher which is contained in sample; n is the sample length.

For the estimation of fault parameter ϑ we use the above mentioned features at three modes of GTE: J_3^{m1} and J_4^{m1} at the m1 mode; J_2^{m2}, J_3^{m2} and J_4^{m2} at the m2 mode; J_3^{m3} and J_4^{m3} at the m3 mode.

We consider the mentioned features J_r^{mk} (the index r determines the type of the amplitude dimensionless characteristic) obtained in the ith measurement, as random values ξ_{ir} characterized by the normal probability distribution:

$$p(\xi_{ir}) = \frac{1}{\sigma_r\sqrt{2\pi}} e^{-\frac{(\xi_{ir}-m_r)^2}{2\sigma_r^2}} . \tag{3}$$

The mathematical expectations of the fault features m_r are the functions of the fault parameter ϑ, these dependencies are approximated by the following polynomials:

- the first-order with respect to ϑ for m1 and m3 modes:

$$m_r = \mu_{r0} + \mu_{r1}\vartheta ; \tag{4}$$

- the second-order with respect to ϑ for m2 mode:

$$m_r = \mu_{r0} + \mu_{r1}\vartheta + \mu_{r2}\vartheta^2 . \tag{5}$$

The dispersions of the fault features σ_r^2 are supposed to be independent from the parameter of a fault ϑ for all considered conditions. Maximum magnitudes of dispersions are:

- 10^{-2} for J_3^{m1} and $2.5 \cdot 10^{-2}$ for J_4^{m1};
- 10^{-2} for J_2^{m2}, $1.5 \cdot 10^{-2}$ for J_3^{m2} and $1.8 \cdot 10^{-2}$ for J_4^{m2};
- $1.4 \cdot 10^{-2}$ for J_3^{m3} and $1.5 \cdot 10^{-2}$ for J_4^{m3}.

Taking into account equation (3), we obtain the following expressions for the logarithmic functional of likelihood:

- in the ith measurement:

$$\ln p(\xi_{ir}, \vartheta) = -\ln\sigma_r - 0.5\ln 2\pi - \frac{(\xi_{ir} - m_r)^2}{2\sigma_r^2} ;$$

- for the general case of n measurements:

$$L(\xi_r, \vartheta) = \sum_{i=1}^{n} \ln p(\xi_{ir}, \vartheta) = -n(\ln\sigma_r + 0.5\ln 2\pi) - \frac{1}{2\sigma_r^2}\sum_{i=1}^{n}(\xi_{ir}^2 - 2\xi_{ir}m_r + m_r^2) . \tag{6}$$

After transforming expression (6) we obtain the equation of the maximum-likelihood (1) in the following form:

$$\frac{1}{\sigma_r^2}\left(nm_r\frac{\partial m_r}{\partial\vartheta} - \sum_{i=1}^{n}\xi_{ir}\frac{\partial m_r}{\partial\vartheta} \right) = 0 . \tag{7}$$

With due account of (4) or (5), the solution of the equation (7) is the maximum-likelihood estimation $\hat{\vartheta}_r$ of the fault parameter ϑ for the mentioned features J_r^{mk} :

- for m1 and m3 modes:

$$\hat{\vartheta}_r = \frac{\sum_{i=1}^{n} \xi_{ir} - \mu_{r0}}{\mu_{r1}}; \tag{8}$$

- for m2 mode estimation $\hat{\vartheta}_r$ is obtained as a solution of equation:

$$\sum_{j=0}^{3} \mathrm{M}_{rj} \vartheta^j = 0, \tag{9}$$

where $\mathrm{M}_{r3} = 2\mu_{r2}^2$; $\mathrm{M}_{r2} = 3\mu_{r1}\mu_{r2}$; $\mathrm{M}_{r1} = 2\mu_{r0}\mu_{r2} + \mu_{r1}^2 - 2\mu_{r2}\sum_{i=1}^{n} \xi_{ir}$;

$\mathrm{M}_{r0} = \mu_{r1}(\mu_{r0} - \sum_{i=1}^{n} \xi_{ir})$.

3. Calculation and analysis of the fault parameter maximum-likelihood estimations

The maximum-likelihood estimations $\hat{\vartheta}_r$ of the fault parameter ϑ were calculated by using formulas (8) and (9) for $n = 5$. The maximum values of the estimation dispersion $\sigma_{\hat{\vartheta}}^2$ are given in Table 1 for a considered range of values of the evaluated parameter ϑ and for each of the considered modes of GTE. Values of the dispersion are defined according to the left part of an inequality (2) and they are the measure of precision of the received estimations.

Table 1. The maximum values of the estimation dispersion $\sigma_{\hat{\vartheta}}^2$ with respect to J_r^{mk}

Mode of GTE	Fault features	Values of evaluated parameter				
		$\vartheta = 0,01$	$\vartheta = 0,03$	$\vartheta = 0,05$	$\vartheta = 0,07$	$\vartheta = 0,1$
m1	J_3^{m1}	$2.5\cdot10^{-5}$	$8.9\cdot10^{-4}$	$3.2\cdot10^{-4}$	$2.5\cdot10^{-5}$	$8.4\cdot10^{-4}$
	J_4^{m1}	$3.2\cdot10^{-5}$	$8.1\cdot10^{-4}$	$9\cdot10^{-5}$	$1\cdot10^{-4}$	$8.5\cdot10^{-5}$
m2	J_2^{m2}	$1.5\cdot10^{-5}$	$1.4\cdot10^{-4}$	$1.6\cdot10^{-4}$	$6.4\cdot10^{-5}$	$1.4\cdot10^{-3}$
	J_3^{m2}	$2.2\cdot10^{-5}$	$2.6\cdot10^{-5}$	$6.3\cdot10^{-4}$	$1\cdot10^{-4}$	$1\cdot10^{-5}$
	J_4^{m2}	$2.4\cdot10^{-5}$	$1.2\cdot10^{-4}$	$4\cdot10^{-6}$	$1.4\cdot10^{-4}$	$9\cdot10^{-6}$
m3	J_3^{m3}	$2.6\cdot10^{-3}$	$1.6\cdot10^{-3}$	$1\cdot10^{-3}$	$1.6\cdot10^{-3}$	$9\cdot10^{-4}$
	J_4^{m3}	$1.85\cdot10^{-3}$	$6.8\cdot10^{-4}$	$1.3\cdot10^{-3}$	$5.8\cdot10^{-4}$	$1\cdot10^{-6}$

For the received estimations we generate the following vectors of fault parameter estimations for the considered modes of GTE:

$$\hat{\Theta}_{m1} = \{\hat{\vartheta}_{J_3^{m1}}; \hat{\vartheta}_{J_4^{m1}}\};\ \hat{\Theta}_{m2} = \{\hat{\vartheta}_{J_2^{m2}}; \hat{\vartheta}_{J_3^{m2}}; \hat{\vartheta}_{J_4^{m2}}\};\ \hat{\Theta}_{m3} = \{\hat{\vartheta}_{J_3^{m3}}; \hat{\vartheta}_{J_4^{m3}}\}, \tag{10}$$

which allow defining the mathematical expectation $m_{\hat{\Theta}}$ and dispersion $\sigma^2_{\hat{\Theta}}$ of the estimates of the fault parameter ϑ for the given measurement and each mode of GTE.

For the statistical analysis estimations we use the statistical parameter Q, which is defined as a ratio:

$$Q(\vartheta) = \sigma^2_{\hat{\vartheta}(\hat{\Theta})} \Big/ m^2_{\hat{\vartheta}(\hat{\Theta})} \,. \tag{11}$$

The parameter Q is the inverted signal-to-noise ratio and is directly related to the statistical stability of the estimate, and values $Q << 1$ correspond to the smooth estimates with small dispersion. Graphs plotting 20lg Q as a function of the evaluated parameter ϑ for estimations which are received by using separate features J_r^{mk} and for vectors (10) are shown in Fig. 1 (for mode m1), Fig. 2 (for mode m2) and Fig. 3 (for mode m3).

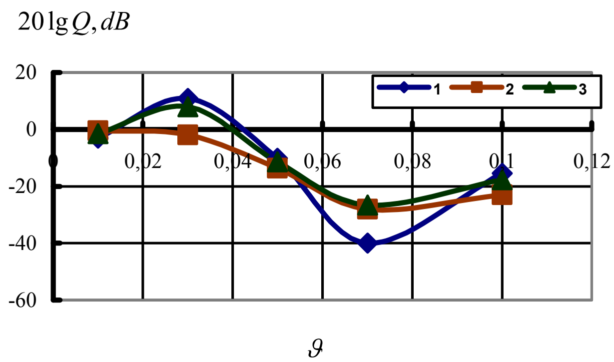

Figure 1. Dependencies of estimations statistical parameter on ϑ for mode m1 at an estimation on the basis of features J_3^{m1} (1), J_4^{m1} (2) and vector $\hat{\Theta}_{m1}$ (3)

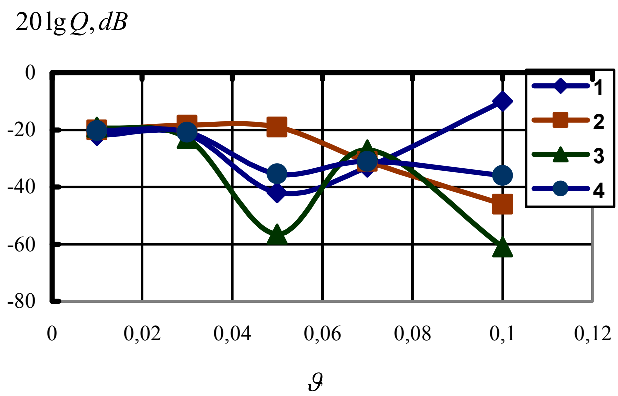

Figure 2. Dependencies of estimations statistical parameter on ϑ for mode m2 at an estimation on the basis of features J_2^{m2} (1), J_3^{m2} (2), J_4^{m2} (3) and vector $\hat{\Theta}_{m2}$ (4)

One can see that the estimation of parameter ϑ is ineffective for small faults ($\vartheta \leq 0.05$) at the steady-state mode of GTE (mode m1). Let the threshold value of estimations statistical parameter be -20 dB, then the received estimations are tolerant and steady for features J_3^{m2} and J_4^{m2}, and vector $\hat{\Theta}_{m2}$ in all range of considered values of the evaluated parameter ϑ at the non-steady-state mode of GTE with the fast increase of the rotor rotation frequency (mode m2). At the modes m1 and m3 the estimations statistical parameter is not higher than the above-mentioned threshold value for the evaluated parameter range $\vartheta \leq 0.06$.

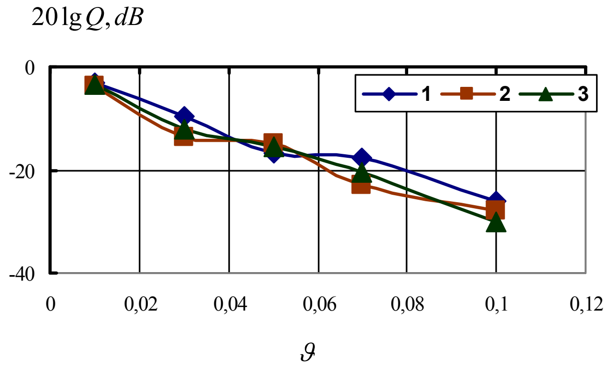

Figure 3. Dependencies of estimations statistical parameter on ϑ for mode m3 at an estimation on the basis of features J_3^{m3} (1), J_4^{m3} (2) and vector $\hat{\Theta}_{m3}$ (3)

4. Conclusions

The evaluation of the relative rigidity changing ϑ as the crack-like fault parameter is carried out at the steady-state and non-steady-state modes of GTE. The received results show that the non-steady-state mode of GTE with the fast increase of the rotor rotation frequency (mode m2) is the most informative diagnostic mode of GTE and that the estimations of fault parameter are tolerant and steady in all considered range of small values of the evaluated parameter. The received results allow detecting crack-like damages based on comparison of the obtained estimations with the values of the reference level established in advance.

References

1. N. Bouraou, Iu. Sopilka, *Vibroacoustical diagnosis of the crack-like damages of aircraft engine blades at the steady-state and non-steady-state modes*, Vibrations in Physical Systems, **24** (2010) 69-74.
2. C. Cempel *Diagnostically Oriented Measures of Viroacoustical Process*, J. of Sound and Vibration, **73**(4) (1980) 547-561.
3. B. Levin, *Theoretical principles of radio-electronics*, Sovetskoe radio, Moscow 1975.

XXV Symposium *Vibrations in Physical Systems,* Poznan – Bedlewo, May 15-19, 2012

Dynamic Model of the Drum of the Washing Machine SAMSUNG WF0804

Jacek BUŚKIEWICZ
Politechnika Poznańska, Wydział Budowy Maszyn i Zarządzania
Instytut Mechaniki Stosowanej, ul. Jana Pawła II 24, 60-965 Poznań
jacek.buskiewicz@put.poznan.pl

Grzegorz PITTNER
Politechnika Poznańska, Wydział Budowy Maszyn i Zarządzania
Instytut Technologii Mechanicznej, ul. Jana Pawła II 24, 60-965 Poznań
grzegorz.pittner@put.poznan.pl

Abstract

The paper deals with vibrations of the washing machine Samsung WF0804. The motion equations of the washing machine drum were derived. The vibration of the drum caused by the unbalanced mass was examined. The presented analysis will make up the basis for experimental studies aimed at validating the theoretical model and finding the most effective way of balancing of the drum vibration.

Keywords: washing machine, motion equations, vibrations

1. Introduction

The last phase of the washing process is the spin cycle which consists in accelerating the drum to about 1200 rpm in order to drain the laundry using centrifugal force. Effectiveness of this process is directly proportional to the drum rotational speed. The mass center of the drum with laundry is displaced with respect to the axis of rotation. As a result the unbalanced force occurs and significantly affects the washing machine work. It causes noise, mechanical degradation, and drum vibration. In extreme case it can lead to the collision of the drum with the frame. The unbalanced force can also be the reason of oscillatory walking of the washing machine [2].

Many models of the washing machine drum have been elaborated. The simplest ones describe the drum as a solid body. In the paper [2] the motion of the mass center in the plane parallel to the front of a washing machine was analysed. The drum is a solid body of two degrees of freedom (dof). The problem of washing machine oscillatory walking was analysed too. In the paper [4] the drum was also described as a solid body moving in plane motion. More sophisticated model of 6 dof is considered in the paper [3] using NLP (Non Linear Programming) method. The results of numerical simulations have shown that the stiffness of the drum material may be neglected and, in consequence, the drum can be modeled as a rigid body. The papers [1, 5] describe the drum as a mechanical system of 12 dof. The equations of motion are derived using Lagrange's equations of the second type. The kinetic and potential energies are written separately for rotating and non rotating parts of the drum unit. The point of difference is that the paper [5] considers a front loaded washing machine unit with 4 dampers and 4 springs whereas the paper [1] deals with the suspension consisting of 2 dampers and 2 springs. In [5] the flexibility of the drum shaft and bearings was taken into account. In [1] additional four dof were added to consider the elastic deformation of the drum and tub during the rotational motion.

The washing machine WF0804 produced by Samsung Inc. is considered in the paper. It is the frontloaded horizontal drum type domestic washing machine (Fig. 1). The aim is to describe the dynamics of the washing machine drum with an unbalanced mass. The support of the drum allows for translational and rotational motions. Analysing the support conditions and the motor characteristics the drum was modeled as a four dof object consisting of the rotating and non rotating parts. The objective of the further researches is to validate the model by comparing with experimental results.

2. The washing machine description

The motor of the washing machine is BLDC direct drive type without any reduction like a transmission belt. The rotor shaft of the motor is connected directly to the drum. The maximum allowed rotational speed of the drum is 1600 rpm. The maximum laundry load is 8 kg. Suspension of the drum consists of a system with two springs attached at the top and two dampers attached at the bottom of the drum.

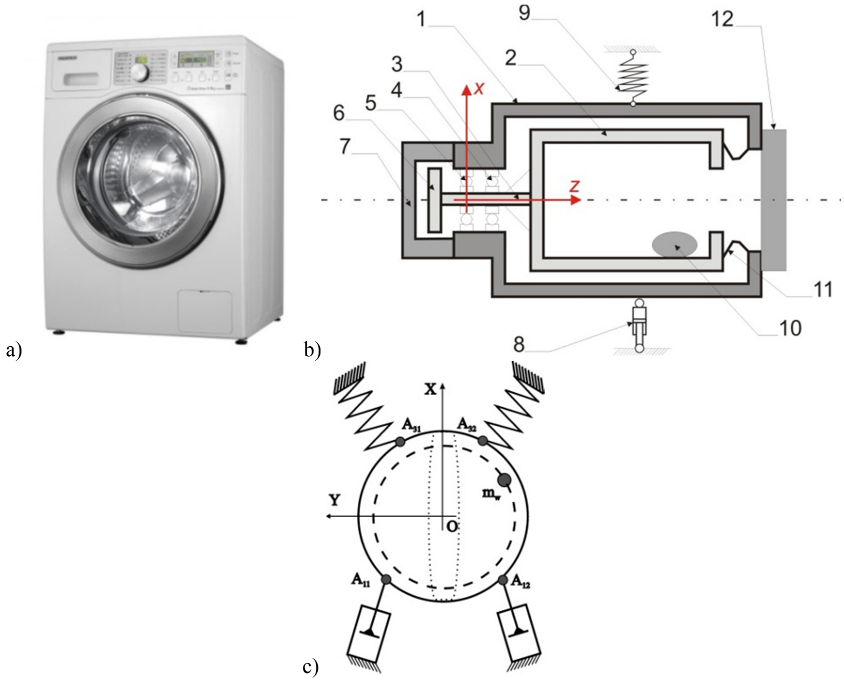

Figure 1. Frontloaded horizontal drum type domestic Washing machine WF0804 (a).
The schemes of the washing machine WF0804 (c, b).

As illustrated in figure 1, the drum unit of the machine consists of steel drum (2) contained the laundry (10) and connected with the rotor (6) of the motor by the shaft (3). The shaft is connected to two bearings (4) and (5) with plastic container tube (1), which does not rotate. The stator of the motor (7) is also connected to the tube. Two concrete blocks (12) are mounted at the loading front of the drum to increase the global mass of the system and reduce the vibration. Nonetheless, the presence of the blocks implicates higher cost of transport and increases the size of the machine. The suspension of the drum has been designed using two springs (9) attached at the top of the tube and two friction dampers (8) mounted at the bottom of the tube. A rubber lip (11) at the front window of the drum prevents the tube from the water leakage.

For the further considerations the origin of the coordinate system has been located at the center of the back bearing, as shown in Figure 1. For the purposes of the dynamic analysis, the drum system is divided into the rotating part, called the drum unit, and non rotating part, called the tube unit. The unbalanced forces are generated by rotating parts and transmitted to the tube unit through the bearings. As a result the tube unit sets on displacing inside the washing machine frame. If the suspension of the tube is too stiff, the frame vibrates and, in the extreme case, a washing machine can even move itself on the floor. On the other hand flexible suspension gives a risk of the collision of the tube and frame which can damage the machine.

For the purposes of the object modeling the characteristic of the suspension elements must be given. In order to study the damper characteristics, it has been dismounted from the washing machine and mounted in the laboratory stand for the automotive dampers validation. The result of the research enables to assume that the force is S-shaped function that achieves $b = 40$ N when the velocity of the damper rod is non zero:

$$F_{tl}(v) = -\frac{2}{\pi} b \arctan(\lambda v)\,. \tag{1}$$

λ is a parameter dependent on many factors, e.g. temperature of the damper. The spring stiffness $k = 9090.91$ [N/m] has been read from the characteristic force – extension.

3. Derivation of motion equations and numerical solutions

Theoretical foundations for the derivation of motion equations may be found in [6]. The following assumptions were taken to describe the dynamics of the drum:

- The rotating part of the drum – the drum unit (DU) moves in general motion that is the superposition of the translation and rotation about some point. The coordinate system fixed to the DU is referred to as the DUS (Fig. 2). The drum shaft does not bend.
- The mass center of the drum unit does not translate along the drum axis
- The position of the drum unit is described by: the coordinates of the mass center x_{c1}, y_{c1}, φ - precession angle, θ - nutation angle, ψ - spin angle.
- The motion of the tube unit (TU) is described by means of the position coordinates of its mass center x_{c2}, y_{c2}, and, introduced above, the nutation and preces-

sion angles. The tube unit does not spin around its horizontal axis, i.e. $\dot{\psi} = 0$. The coordinate system fixed to the tube unit is referred to as the TUS (Fig. 2).

The global fixed reference frame (GS) is introduced (Fig. 2). The horizontal axis of the GS coincides with the axis of the drum in its stationary position. The origin of the system and the center of the bearings $O(x_o,y_o)$ coincide when the washing machine does not work. The translational non rotating coordinate system (TNRS) has the origin at $O(x_o,y_o)$ at any instant. The axes of the TNRS are parallel to the axes of the GS. With the motor rotating at constant angular velocity, the washing machine drum has four dof: x_o, y_o, φ, θ.

T is the transformation matrix from the DUS to TNRS. $\mathbf{T_I} = \mathbf{T}^{-1}$ is the inverse transformation matrix.

$$\mathbf{T} = \mathbf{A_{zp} A_{xp} A_x}, \tag{2}$$

where:

$$\mathbf{A_Z}=\begin{bmatrix} \cos(\varphi) & \sin(\varphi) & 0 \\ -\sin(\varphi) & \cos(\varphi) & 0 \\ 0 & 0 & 1 \end{bmatrix},\ \mathbf{A_{xp}}=\begin{bmatrix} 1 & 0 & 0 \\ 0 & \cos(\theta) & \sin(\theta) \\ 0 & -\sin(\theta) & \cos(\theta) \end{bmatrix},\ \mathbf{A_{Zp}}=\begin{bmatrix} \cos(\psi) & \sin(\psi) & 0 \\ -\sin(\psi) & \cos(\psi) & 0 \\ 0 & 0 & 1 \end{bmatrix}.$$

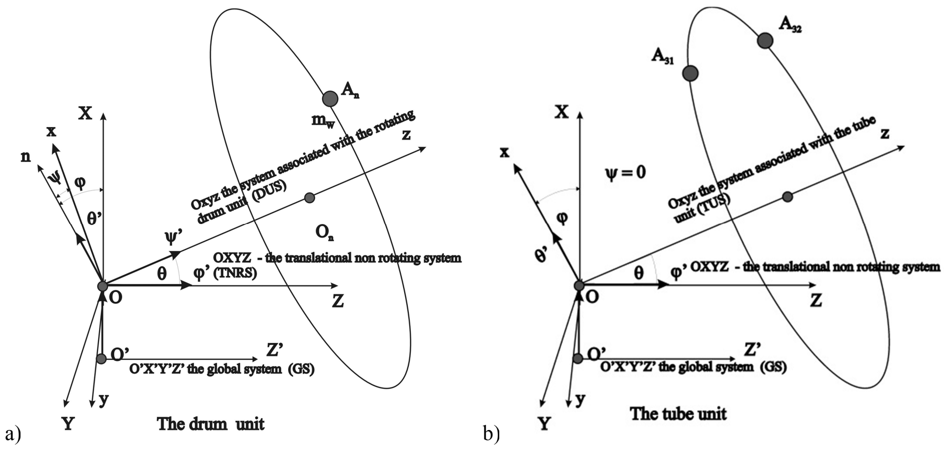

Figure 2. The coordinate systems fixed to the drum unit (a) and tube unit (b).

To determine matrix **T'**, that transforms from the TUS to TNRS, one has to take ψ=0 in matrix **T**. $\mathbf{T_I'}$ transforms from TNRS to TUS.

The angular velocity of the rotating drum has the following components in the DUS.

$$\boldsymbol{\omega}_{wb} = \left[\cos(\psi)\dot{\theta} + \sin(\theta)\sin(\psi)\dot{\varphi} \quad -\sin(\psi)\dot{\theta} + \sin(\theta)\cos(\psi)\dot{\varphi} \quad \cos(\theta)\dot{\varphi} + \dot{\psi}\right].$$

The angular velocity of the tube in the TUS $\boldsymbol{\omega}_{nb} = \left[\dot{\theta} \quad \sin(\theta)\dot{\varphi} \quad \cos(\theta)\dot{\varphi}\right]$.

The kinetic energy of the drum unit and tube unit equals to:

$$E_{K1} = \frac{1}{2}\left(M_{wb}\mathbf{v}_{wb}\cdot\mathbf{v}_{wb} + M_{nb}\mathbf{v}_{nb}\cdot\mathbf{v}_{nb} + \boldsymbol{\omega}_{wb}\cdot\mathbf{I}_{wb}\cdot\boldsymbol{\omega}_{wb} + \boldsymbol{\omega}_{nb}\cdot\mathbf{I}_{nb}\cdot\boldsymbol{\omega}_{nb}\right) \qquad (3)$$

where: $\mathbf{I_{wb}}$ and $\mathbf{I_{nb}}$ - the inertia tensors of the drum in the DUS and of the tube in the TUS, M_{wb}, M_{nb} - the masses of the drum and tube, respectively, $\mathbf{v}_{wb}$ - the velocity of the drum mass center, $\mathbf{v}_{nb}$ - the velocity of the tube mass center.

The unbalanced mass mw is attached at the circumference of the drum. The coordinates of this mass in the DUS are $\mathbf{A}_n = [A_{nx}, A_{ny}, A_{nz}]$. The coordinates of this mass in the GS are: $\mathbf{A}_{np} = [x_o, y_o, 0] + \mathbf{T}^{-1}\mathbf{A}_n$. The kinetic energy of the unbalanced mass is $E_{K2} = \frac{1}{2}\left(m_w\dot{\mathbf{A}}_{np}\cdot\dot{\mathbf{A}}_{np}\right)$.

The dampers and springs are fixed to the tube at points A_{11}, A_{12} and A_{31}, A_{32}, respectively. The coordinates of these points in the TUS as well as the versors of the springs $\mathbf{n}_{31}$, $\mathbf{n}_{32}$ and dampers $\mathbf{n}_{11}$, $\mathbf{n}_{12}$.are given. In order to determine the deformation of the springs one can compute the displacement of the spring pins, by which they are fixed to the tube, in the GS. The displacements are computed as the transformation of these points from the TUS to the GS: $\mathbf{A}_{31p} = [x_o, y_o, 0] + \mathbf{T}'^{-1}\mathbf{A}_{31}$, $\mathbf{A}_{32p} = [x_o, y_o, 0] + \mathbf{T}'^{-1}\mathbf{A}_{32}$. Then, the absolute displacements are: $\mathbf{r}_{31} = \mathbf{A}_{31p} - \mathbf{A}_{31}$, $\mathbf{r}_{32} = \mathbf{A}_{32p} - \mathbf{A}_{32}$. Assuming that the displacements are small, the spring deformation is computed as the projection of the absolute displacements onto spring axis (in its undeformed state): $\mathbf{du}_1 = \mathbf{r}_{31}\cdot\mathbf{n}_{31}$, $\mathbf{du}_2 = \mathbf{r}_{32}\cdot\mathbf{n}_{32}$. The absolute displacements of the dampers pins, by which they are fixed to the tube, are: $\mathbf{A}_{11p} = [x_o, y_o, 0] + \mathbf{T}'^{-1}\mathbf{A}_{11}$, $\mathbf{A}_{12p} = [x_o, y_o, 0] + \mathbf{T}'^{-1}\mathbf{A}_{12}$. The absolute velocities are: $\mathbf{v}_{11} = \dot{\mathbf{A}}_{11p}$, $\mathbf{v}_{12} = \dot{\mathbf{A}}_{12p}$. The projections of these velocities onto damper axes are: $\mathbf{v}_{11R} = \mathbf{v}_{11}\cdot\mathbf{n}_{11}$, $\mathbf{v}_{12R} = \mathbf{v}_{12}\cdot\mathbf{n}_{12}$.

The potential energy of the system is:

$$V = \frac{1}{2}k(du_1^2 + du_2^2) + M_{wb}gx_{C1} + M_{nb}gx_{C2}\,. \qquad (4)$$

Qualitatively one can describe the other dissipative forces during machine motion by means of Rayleigh function:

$$R_A = \frac{1}{2}\left(b_r(\dot{x}_o^2 + \dot{y}_o^2) + b_\theta\dot{\theta}^2 + b_\varphi\dot{\varphi}^2 + b_\psi\dot{\psi}^2\right), \qquad (5)$$

where b_r, b_θ, b_φ, b_ψ - dissipation coefficients

The angular velocity of the motor is constant $\dot{\psi} = \omega$. The dynamic equations are derived using Lagrange equations of the second type for each generalized coordinate $q = x_o, y_o, \theta, \varphi$.

$$\frac{d}{dt}\left(\frac{\partial L}{\partial \dot{q}}\right) - \frac{\partial L}{\partial q} + \frac{\partial R_A}{\partial \dot{q}} = F_{tl}(v_{11R})\frac{\partial v_{11R}}{\partial \dot{q}} + F_{tl}(v_{12R})\frac{\partial v_{12R}}{\partial \dot{q}}, \tag{6}$$

where $L = E_{K1} + E_{K2} - V$. In the foregoing equations $\frac{\partial v_{ijR}}{\partial \dot{q}}$ is the displacement of point A_{ij} caused by the change in generalized coordinate q. Zero initial conditions are taken.

For the purposes of numerical analysis, the physical properties of the drum and tube were determined. The masses, centers of the masses and mass moments of inertia has been measured (the coordinates of positions are in [m]).
Masses: m_w = 0.1 kg, M_{nw} = 28.4 kg, M_w = 8.41 kg.
The rotational speed of the motor n = 600 rev/min.
The coordinates of the unbalanced mass fixation in the DUS: A_n = (0.479;0;0.254).
The drum unit and tube unit mass centers: C_1(0;0;0.092), C_2 (0;0;0.289).
The coordinates of the points of dampers and springs fixation in the TUS are:
1st damper - A_{11} (-0.2446;0.1762;0.254), A_{110} (-0.4173;0.2722;0.2778).
2nd dampers - A_{12} (-0.2446;-0.1762;0.25462), A_{120} (-0.4173;-0.2722;0.2778).
1st spring - A_{31} (0.1477;0.2479;0.2546), 2nd spring - A_{32} (0.1477;-0.2479;0.2546).
The mass moments of inertia of the drum unit in the DUS are (the axes of the DUS are the principal axes of inertia): I_{x1} = 0,21 kgm^2, I_{y1} = 0,12 kgm^2, I_{z1} = 0.256 kgm^2.
The mass moments of inertia of the tube unit in its TUS are (the axes of the TUS are the principal axes of inertia): I_{x2} = 1.91 kgm^2, I_{y2} = 1.91 kgm^2, I_{z2} = 1.254 kgm^2.
Dissipation coefficients: b_r = 1000 Ns/m, $b_\varphi = b_\psi = b_\theta$ = 1000 Ns.

The figure 3 presents the displacements of the points at which the springs are attached to the tube.

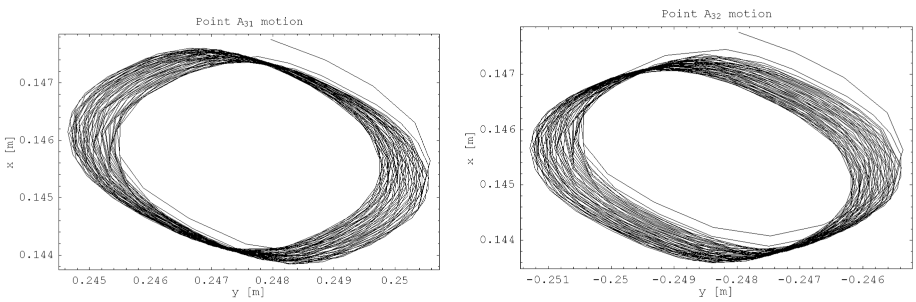

Figure 3. The displacements of the points of spring fixation to the tube.

4. Conclusions

The authors aim at verifying the model with the data obtained in experiments. If the results are satisfactory the model will be used to examine the influence of the suspension parameters on the drum vibrations. Using the model one can simulate the drum motion in order to examine the effectiveness of various methods of active and semi-active vibration elimination, e.g. dampers with variable characteristic or force inductors. The solution, which gives the best result, will be applied to the washing machine and verified experimentally.

Acknowledgments

The work was supported by The National Centre for Research and Development (project nr 22.0404).

References

1. Hee-Tea Lim, Weui-Bong Jeong, Keun Joo Kim, *Dynamic Modeling and Analysis of Drum-Type Washing Machine*, International Journal of Precision Engineering and Manufacturing, **11**(3) (2010) 407-417.
2. D. C. Conrad, W. Soedel, *On The Problem of Oscillatory Walk of Automatic Washing Machines*, Journal of Sound and Vibration, **188**(3) (1995) 301-314.
3. B. Kiray, A. K. Tugcu, I. T. Sumer, *Formulation and Implementation of Parametric Optimisation of a Washing Machine Suspension System*, Mechanical Systems And Signal Processing **9**(4) (1995) 359-377.
4. E. Papadopoulos, I. Papadimitriou, *Modeling, Design and Control of a Portable Washing Machine During The Spinning Cycle*, National Technical University Of Athens, Proceedings of The 2001 IEEE/ASME International Conference On Advanced Intelligent Mechatronics Systems (AIM 2001), 8–11 July 2001, Como, Italy, 899-904.
5. T. NygÍrds, V. Berbyuk, *Multibody Modeling and Vibration Dynamics Analysis of Washing Machines*, Multibody System Dynamics **27**(2012) 197–238.
6. J. Awrejcewicz, *Mechanika techniczna i teoretyczna*, Wydawnictwa Politechniki Łódzkiej, Łódź 2011.

XXV Symposium *Vibrations in Physical Systems,* Poznan – Bedlewo, May 15-19, 2012

Machine Condition Monitoring with Inventive System TRIZ[1]

Czesław CEMPEL
Institute of Applied Mechanics, Poznan University of Technology
3 Piotrowo Street, PL-60-965 Poznań, czeslaw.cempel@put.poznan.pl

Abstract

The machine condition monitoring has not been approached by TRIZ[2] practitioners, as yet, so the knowledge of TRIZ methodology has not been applied there. But it seems to be a need to make such an approach in order to see if some new knowledge and new technology will emerge from this study. In doing this we need at first to define the ideal final result (*IFR*). As a next we need to describe the problem of system condition monitoring (CM) in terms of TRIZ problem (*engineering*) parameters and to look for respective inventive principles. This means we should present the machine CM problem by the main tool of TRIZ, it means the contradiction matrix. When specifying the problem parameters and inventive principles, one should use analogy and metaphorical thinking, which by definition is not exact but fuzzy, and leads sometimes to unexpected results and outcomes, especially when doing it first time. The paper undertakes this important application problem and brings some fresh insight into system and machine CM problems. This may mean for example the minimal dimensionality of TRIZ engineering parameter set for the description of machine CM problems, and of course the ideal final result of TRIZ methodology.

Keywords: machine condition monitoring, TRIZ, ideal final result, engineering parameters, inventive principles, contradiction matrix.

1. Introduction

Condition monitoring of machines (*systems*) is the science and technology for the assessment of condition of running machine by means of observation of machine phenomenal field, where some symptom of condition can be captured and measured (*see for example [1]*). This means that we are trying to determine the fault space of the machine, its dimensionality and fault advancement, by some observed symptoms of condition, creating in this way our observation space. The fault space of a system (*machine*) can be assumed by some prior knowledge taken from the experience with the other running machines, and the same concerns with symptom observation space.

As fault space of every machine is multidimensional, for example we have unbalance, misalignment, bearing faults, etc., the same multidimensionality is needed in our observation space, and as usually it needs some redundancy too. This is because the symptom which we measure are interdependent, and by means of some symptom processing procedures we can determine the dimensionality of fault space and the intensity (*advancement*) of the main faults which evolve during the machine lifetime.

Condition monitoring is mostly applied to critical machinery, where by special monitoring system we can monitor thermo and vibroacoustical phenomena carrying the needed information on system condition. This means that by some measurements of these

[1] Paper partially supported by NCN grant No7028/B/T02/2011/40
[2] TRIZ -Russian acronym for Inventive Problem Solving

phenomena and respective signal processing we can create symptom of condition, like for example the velocity vibration amplitude measured at the bearing pedestal, or some other location of machine casing. What is important here that by means of special signal and symptom processing procedures, one can determine the type of fault, its advancement, and also the symptom limit value and symptom reliability, which is analogous to lifetime reliability of machine.

In summary one can say, that having some experience on machine life and running, a and prior knowledge concerning processing of received signals and measured symptoms of condition, we can asses the current machine condition and make forecasting of future condition, the fault type and date of stopping machine for the renewal, etc.

2. The ideal final result in diagnostics of machinery

This type of thinking, looking explicit for final ideal result (IFR) in condition monitoring is new in machine condition monitoring (MCM). Hence let us imagine, what we really need here? Self repairing machine, it seems to be too early. But if we integrate advanced CM system with the machine, our resultant **IFR** can be as follows.

The machine itself is signaling the approaching system breakdown, a type of fault, and the time, when it should be stopped for renewal.

In order to do this one can imagine that integrated CM system should contain vibration transducers with signal preprocessing to form several symptoms of condition $\mathbf{S_i}$. In this way machine observation space is created, which is monitored continuously, and symptom readings are taken with the proper life time distance, depending on the machine type and the wearing intensity [2]. The successive symptom readings form the so called symptom observation matrix (SOM) with columns presenting different type of monitored symptoms and rows giving the values of discrete symptom readings. This rectangular matrix is the only source of information concerning the condition of the machine, and one can extract this information applying singular value decomposition (SVD) [4], or principal component analysis (PCA) [3]. The processing of SOM can give the symptom **limit value** $\mathbf{S_l}$ which control the stopping of the machine [2], and also can give symptom reliability **R(S)** which assesses the potency of running or functional ability of the machine.

Knowing this one can say that by proper SOM processing method, SVD for example, we are **projecting** the observation space to the fault space. In this way we are transferring the wanted information concerning fault evolution, its type and the advancement.

As many symptoms of condition depends on the current machine load, which is controlled by production process, special processing of SOM should be elaborated and taken into account [6], [5], which gives the results being almost immune against the load variability and other disturbances as well.

When these precaution and preparations are successfully applied into the processing of signals, symptoms, and the SOM too, the defined above IFR seems to be under the reach of contemporary technology of machine monitoring and signal / symptom processing and computation.

3. The contradiction matrix for machine condition monitoring

One of the main Altshuller idea is the **contradiction matrix** enabling to resolve contradiction by means of the use of inventive principles and other TRIZ tools and operators [9], [8]. The space of contradiction matrix is defined by engineering parameters describing every innovation problem in given area of engineering. We will take into account the 39 engineering parameters used in mechanical engineering in its broad meaning, as described in many books and articles concerning TRIZ methodology. Introductory analysis [7] connected with a broad interpretation convinces us, that out of these 39 parameters ten or nine will be enough to describe CM problem properly.

Special comment should be given to choose new parameters, describing fault space and observation space, the most important entities in CM. As normally parameters No 3 and 4 of TRIZ describes the length of stationary and moving parts of the machine, and length is some dimension coordinate. And when the dimension is taken with plural we will have **fault space** of the machine (***Dimension–I***), the primary entity in condition monitoring with the coordinates being the faults evolving in the machine during its life. The same reasoning lead us to the second parameter **Dimension-II**, which symbolizes **observation space** of phenomenal field of the machine, with coordinates being the measured symptoms of condition. The rest eight engineering parameters of CM are as follows; symptom reliability, accuracy in detection and measurement, information loss, energy loss, durability or lifetime, ease of use or running, repairability (*maintainability*), and the temperature. Considering the information carried by thermo field of the machine one can notice it is multidimensional spatial information source. While thinking about energy loss as an engineering parameter we see it is only one dimensional and in many practical cases its dynamics is very low. Hence, we can drop from the consideration this engineering parameter and concentrate our diagnostic problem around 9 dimensional description of any diagnostic problems.

This means we will take into consideration here **9** by **9** contradiction matrix, but if needed in some special cases, this dimensionality can be extended easily or diminished a little (*see temperature*). It is well known in methodology of invention and TRIZ as well, that the change of one engineering parameter in the direction of improvement may be the source of worsening of another one, and the only way outside of this loop is to apply some of 40 **inventive principles**. Which one to use is usually the matter of careful analogy thinking and the prior knowledge in the given area of science and engineering. Some introductory thinking in this direction was given in our last paper [7], but without presenting the definite contradiction matrix.

To solve contradictions seen in the table above we will use inventive principles of Altshuller, giving them the meaning taken with mechanical engineering area and extended with the knowledge of metrology and the diagnostic signal / symptom processing.

Table. Contradiction matrix of TRIZ methodology for vibration machine condition monitoring area

Improving ⇒ / ⇓ Worsening	Dimension.I (*fault space*)	Dimension.II (*observation space*)	Reliability (*symptom reliability*)	Accuracy in (*detection/ measurement*)	Information loss	Durability/lifetime	Ease of use/running	Repairability, mainten.	Temperature	*No of invent. rincipl.*
Dimension -I (*fault space*)	X	5, 10	11		16	15				5 (*5*)
Dimension -II (*observation space*)	5, 10	X	1,2,16, 19, 20, 23, 26	5, 10, 19,26	3	3	20	16, 20	26	19 (*10*)
Reliability (*symptom reliab.*)	11	1, 2, 16, 19, 20, 23, 26	X	9, 10, 15,16	1, 9	11, 16	11, 20	16	3	20 (*12*)
Accuracy in (*detection/ measure.*)		5, 10, 19,26	9, 10, 15,16	X	9, 15			16	1	12 (*8*)
Information loss	16	3	1, 9	9, 15	X					6 (*4*)
Durability/ lifetime	15	3	11, 16			X	34, 35			6 (*6*)
Ease of use/running		20	11, 20			34, 35	X			5 (*4*)
Repairability, maintenance		16, 20	16	16				X		4 (*2*)
Temperature		26	3	1					X	3 (*3*)
No of inventive principles applied (*different*)	5 (*5*)	19 (*10*)	20 (*12*)	12 (*8*)	6 (*4*)	6 (*6*)	5 (*4*)	4 (*2*)	3 (*3*)	X

The numbering of inventive principles shown in Tab. is in accordance with that given in TRIZ references, and its diagnostic meaning and prescribed actions are described below.

1. Segmentation – segmentation of the frequency spectrum of vibration process, band analysis and /or Fourier spectral analysis.

2. Extraction, rejection – rejection filters for cutting of unwanted signal interferences, for example the mains frequency 50Hz, the meshing frequency in gearbox diagnosis, etc.

3. Local quality – the use of thermal, light or acoustic barrier, the hardening of the shaft ends,etc.

5. Integration, merging – the vibration transducers with preamplifier, signal preprocessing, and wireless transmission, integrated with machine at specially chosen points and directions.

9. Prior counter-action – the forecast of signal distortion and compensation before its transmission and processing.

10. Prior action – introductory analysis of a fault space and symptom observation space of the machine in order to chose probable faults, observed diagnostic processes and location of vibration transducers, along the machine body.

11. Prior cushioning – safe shut down procedure in rotating machinery diagnostic systems.

15. Dynamics – elastic mounts or spacers in order to diminish or filter vibration transmission inside **a** machine body, immunity to the load change.
16. Partial or excessive action – use SVD / PCA analysis of SOM to filter noise and obtain singular components /values, also signal demodulation for detection of diagnostic information.
19. Periodic action – synchronous averaging of signal, signal sampling with preprocessing, over-sampling of vibration process to detect periodicity and reduce the noise.
20.Continuity of useful action – constant load in a production process, constant use of condition monitoring subsystem.
23. Feedback – monitoring of diagnostic oriented residual processes in the phenomenal field of the machine for the assessment of the machine condition and the increase of its reliability.
26. Copying – infrared picture of the machine and / or acoustic map of its surrounding; symbolic or mathematical model of machine symptoms evolution to make its condition forecast.
34. Discarding and recovering – self balancing systems in rotating machinery, small regulations and repairs during the machine running.
35. Parameters changes – passive or active change of; mass, stiffness and damping, in order to reduce excessive and harmful vibration and noise.

One can notice from the above that for the solution of 9 by 9 contradiction matrix in machine condition monitoring we can use at least 15 inventive principles interpreted in terms of machine use and signal / symptom processing knowledge and technology. They can be used altogether for the best, or some of them can be omitted due to lack of knowledge (*see principle 9*), technology (*see principle 5*), or lack of need (*see principle 2 and 15*).

Looking once more for the inventive principles allocated in the contradiction matrix, and described broadly in above listing, one can say, they present **already known** knowledge and technology of MCM. This includes the broad meaning of the inventing principle No 26, where **Copy** may mean also the **model** of the symptoms evolution to make condition assessment and forecast.

What is important here, that first time it was possible to describe MCM problem by means of minimal number of engineering parameters, and to notice importance of abstract entities of fault space and observation space. To notice also their common definition and influence on symptom reliability, the ease of running and repairability (*maintainability*) of the machine. Concerning the problem of minimal dimensionality of engineering parameter set to describe MCM problem, it seems that minimal dimension of engineering parameter set, for the TRIZ description of MCM problems, can be reduced to a number of **nine parameters** only. But it is possible to extend this number on other engineering parameters like accuracy of production (manufacturability-32), productivity (39), or harmful side effects (31) noise and/or other pollution types of the machine.

Applying TRIZ first time to MCM area it is also interesting to know which engineering parameters are the most important to define and solve the problem of obtaining IFR? To answer this question a special row and column was appended to contradiction matrix, which enumerate the number of different inventive principles possible to apply in order to improve, or worsen the given parameter. As we can see from the contradiction matrix, there are two of them, the **reliability** of the machine and its **observation space**, having both 10 and 12 inventive principles as the way to improvement. This is important message, which means that we should be very careful in defining and using the observation space and calculating (*assessing*) the machine reliability.

4. Conclusion

As it follows from the above it was possible to transfer creatively the current science and technology of machine vibration condition monitoring into the formal TRIZ tools that means to the ideal final result (IFR) and contradiction matrix. Due to that, the relative importance of the definition of machine fault space and observation space has been elucidated, and taken into account. Also it has been proposed that the minimal number of engineering parameters for MCM problem description and solution can be taken as nine parameters, including the most important observation space and the reliability of the machine. And when using proper dimensionality of observation space and software for signal and SOM processing we can make machine condition assessment and forecasting with a good accuracy.

References

1. R. A., Collacott, *Mechanical Fault Diagnosis*, Chapman&Hall, London, 1977, pp 405.
2. C. Cempel, *Vibroacoustic Condition Monitoring*, E. Horwood, London 1991, pp 212.
3. I. Y., Tumer, E. M., Huff *Principal component analysis of tri-axial vibration data from helicopter transmission*, 56th Meeting of the Society of Machine Failure Prevention Technology, 2002.
4. C., Cempel, M. Tabaszewski, *Multidimensional condition monitoring of the machines in non-stationary operation*, Mechanical Systems and Signal Processing, **21** (2007) 1233-1247.
5. C. Cempel, M. Tabaszewski, *Optimization of dimensionality of symptom space in machine condition monitoring*; Mechanical Systems and Signal Processing, **24** (2010) 1129-1137.
6. C. Cempel, *The evolution of generalized fault symptoms and fault intensities as indicators of observation redundancy and coming system breakdown*, Invited lecture, Proceedings of 38 Machine Diagnostic Conference, Wisła – Poland, 2011.
7. A. Skoryna, C. Cempel, *Some possibilities of TRIZ application in machine condition monitoring*, Diagnostyka No 3, (2010) 69-77.
8. M. A. Orlov, *Inventive Thinking through TRIZ*, 2 edit., Springer Verlag 2006, pp 351.
9. S. D. Savransky, *Engineering of Creativity*, CRC Press, New York 2002, pp 394.

XXV Symposium *Vibrations in Physical Systems,* Poznan – Bedlewo, May 15-19, 2012

Rolling Contact Problems with Nonhomogeneous Materials

Andrzej CHUDZIKIEWICZ
Institute of Transport, Warsaw University of Technology
ul. Koszykowa 75, 00-662 Warsaw, ach@it.pw.edu.pl

Andrzej MYŚLIŃSKI
Systems Research Institute, ul. Newelska 6, 01-447 Warsaw
myslinsk@ibspan.waw.pl

Abstract

Numerous laboratory experiments indicate that graded materials layers or coatings covering the conventional steel body can reduce the magnitude of contact and/or thermal stresses as well as the noise and the rolling contact fatigue. The paper is concerned with the numerical solution of the wheel-rail elastic contact problem assuming that the surface of the rail consists from layers having distinct constant material parameters and a functionally graded material layer between them which mechanical properties are dependent on its depth. The contact phenomenon includes friction as well as wear. Quasistatic numerical approach is used to solve numerically this problem. Numerical results are provided and discussed.

Keywords: rolling contact problem, functionally graded materials, quasistatic method

1. Introduction

This paper deals with the numerical solution of the two-dimensional rolling contact problems including friction and wear. The contact of a rigid wheel with an elastic rail lying on a rigid foundation is considered. The friction between the bodies is described by Coulomb law [1,2,3]. We employ Archard's law of wear [4]. In the model the wear is identified as an increase in the gap between bodies. The elastic or thermoelastic rolling contact problems were considered by many authors (see references in [1,3,5,6]). Numerous laboratory experiments indicate [2,7] that the use of a coating material attached to the conventional steel body reduce the magnitude of residual or thermal stresses. It leads to the reduction of the rolling contact fatigue and noise. However in a conventional coating structure homogeneous materials are used. The abrupt change in the mechanical properties of the materials at the surface coating-substrate interface results in stress concentration or degraded bonding strength [8].

Therefore in this paper we solve numerically this contact problem with friction and wear assuming more complicated model of coating layer than used in [9]. We assume that between the homogeneous coating layer and the homogeneous substrate there exists the graded interlayer which properties depend on its depth according to the exponential law [8]. In the paper we take special features of this rolling contact problem and use so-called quasistatic approach [10] to solve this problem. In this approach the inertial term is replaced by the stationary term reflecting the dynamics of the body rather than completely neglected as in classical quasistatic formulation. Therefore, after brief introduction of the elastic model of the rolling contact problem with friction and wear in the framework of two-dimensional linear elasticity theory the general coupled time dependent system describing this physical phenomenon is formulated. This system is transformed into equivalent stationary system in so-called quasistatic formulation. To solve numerically this stationary system we will transform it into equivalent optimization problem. Finite element method is used as a discretization method. The numerical results are provided and discussed.

2. Problem formulation

Consider deformations of an elastic strip lying on a rigid foundation (see Fig. 1). The strip has constant height h and occupies domain $\Omega \subset R^2$ with the boundary Γ. A wheel rolls along the upper surface Γ_C of the strip. The wheel has radius r_0, rotating speed ω and linear velocity V. The axis of the wheel is moving along a straight line at a constant altitude h_0 where $h_0 < h + r_0$, *i.e.*, the wheel is pressed in the elastic strip. It is assumed, that the head and tail ends of the strip are clamped, i.e., we assume that the length of the strip is much bigger than the radius of the wheel. Moreover it is assumed, that there is no mass forces in the strip. The body is clamped along a portion Γ_0 of the boundary Γ of the domain Ω. The contact conditions are prescribed on a portion Γ_C of the boundary Γ. Moreover, $\overline{\Gamma}_0 \cap \overline{\Gamma}_C = \varnothing$ $\overline{\Gamma} = \overline{\Gamma}_0 \cup \overline{\Gamma}_C$.

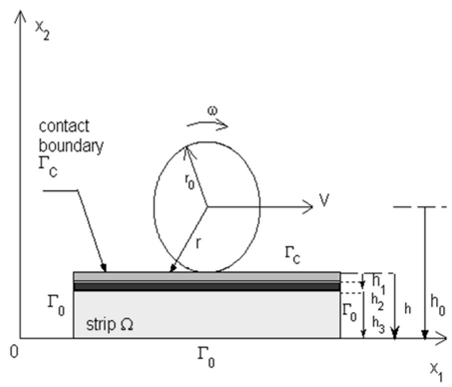

Figure 1. Wheel rolling over the strip

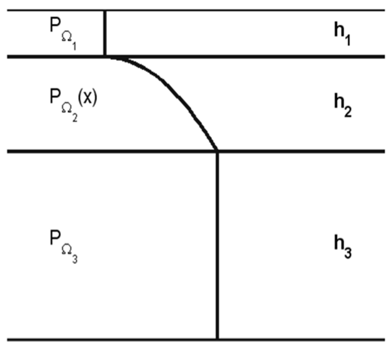

Figure 2. Three-layers model

We denote by $u = (u_1, u_2)$, $u = u(x, t)$, depending on the spatial variables $x = (x_1,x_2) \in \Omega$, and time variable $t \in [0,T]$, $T > 0$, a displacement of the strip. Assume $\Omega = \Omega_1 \cup \Omega_2 \cup \Omega_3$ where Ω_1, Ω_2 and Ω_3 denote the homogeneous coating layer, graded interlayer, and substrate layer, respectively. The heights of these layers are h_1, h_2, h_3, respectively. In the middle layer Ω_2 material parameters depend on the height of the layer according to the exponential law. The displacement u of the strip satisfies the evolution equation [9] in the cylinder $\Omega \times (0,T)$:

$$\rho \frac{\partial^2 u}{\partial t^2} = A^* D A u \,, \tag{1}$$

The following initial and boundary conditions are imposed:

$$u(0) = u_{0i}\,, \quad u'(0) = u_{1i}\,, \quad i = 1,2, \quad \text{in} \quad \Omega, \tag{2}$$

$$u = 0 \;\text{ on }\; \Gamma_0 \times (0,T) \quad \text{and} \quad B^*D\,Au = F \;\text{ on }\; \Gamma_C \times (0,T), \tag{3}$$

where $u(0)=u(x,0)$, $u' = du/dt$, u_{0i} and u_{1i} are given functions, ρ is a mass density of the strip material, $\Gamma_0 = \Gamma \setminus \Gamma_C$. The operators A, B and D are defined as follows [10]

$$A = \begin{pmatrix} \frac{\partial}{\partial x_1} & 0 & \frac{\partial}{\partial x_2} \\ 0 & \frac{\partial}{\partial x_2} & \frac{\partial}{\partial x_1} \end{pmatrix}^*, \quad B = \begin{pmatrix} n_1 & 0 & n_2 \\ 0 & n_2 & n_1 \end{pmatrix}^*, \quad D = \begin{pmatrix} \lambda + 2\gamma & \lambda & 0 \\ \lambda & \lambda + 2\gamma & 0 \\ 0 & 0 & \gamma \end{pmatrix}, \tag{4}$$

where $n = (n_1,n_2)$ is the outward normal versor to the boundary Γ of the domain Ω, λ and γ are Lame coefficients, A* denotes a transpose of A. In Ω_2 operator D is assumed to depend on the depth of the graded interlayer according to the exponential law. By $\sigma = (\sigma_{11}, \sigma_{22}, \sigma_{12})$ and F we denote the stress tensor in domain Ω and surface traction vector on the boundary Γ, respectively. The surface traction vector $F = (F_1, F_2)$ on the boundary Γ_C is a priori unknown and is given by conditions of contact and friction. Under the assumptions that the strip displacement is small the contact conditions on the boundary $\Gamma_C \times (0,T)$ take a form:

$$u_2+g_r + w \le 0, \quad F_2 \le 0, \quad (u_2+g_r + w)F_2 = 0, \quad g_r = h - h_0 + \sqrt{r_0^2 - (u_1 + x_1)^2}\,, \tag{5}$$

$$| F_1 | \le \mu | F_2 |, \quad F_1 \frac{du_1}{dt} \le 0, \quad (| F_1 | - \mu | F_2 |) \frac{du_1}{dt} = 0, \tag{6}$$

where μ is a friction coefficient. Conditions (5)-(6) describe the non penetration condition as well as Coulomb law of friction, respectively [1,6]. Assuming that the dimensional wear coefficient $k > 0$ is given the wear $w = w(x,t)$ is governed by the equation [4]:

$$\frac{dw}{dt} = k\,V\,F_2. \tag{7}$$

In (5) the wear w increases the gap between the contacting surfaces.

2.1 Material properties of functionally graded materials

In subdomains Ω_1 and Ω_3 the operator D characterizing the properties of the material occupying strip Ω takes different constant values, respectively (see Figure 2). In the subdomain Ω_2 the operator D is assumed to depend on the depth of the layer. This dependence is governed by the exponential law [8, 9]:

$$P(x_2) = P_{\Omega 1}\ \exp(\eta\ \frac{x_2 + h_1}{h_2}),\quad x_2 \in [-h_2\text{-}h_1, -h_1], \tag{8}$$

where $\eta = \log(P_{\Omega 1}/P_{\Omega 3})$, h_1, h_2 are given parameters, x_2 denotes the spatial variable and $P(x_2)$, $P_{\Omega 1}$, $P_{\Omega 3}$ denote the height dependent material property (material density or Young modulus) of layer Ω_2 as well as the material properties of layers Ω_1 and Ω_3, respectively. The continuity of the displacements and the stresses along the interfaces $\partial\Omega_1 \cap \partial\Omega_2$ and $\partial\Omega_2 \cap \partial\Omega_3$ are assumed.

3. Quasistatic formulation

Taking into account the special features of the contact problem (1)-(8) one can reformulate it in the framework of the quasistatic approach. This approach is based on the assumption that for the observer moving with a wheel its displacement does not depend on time [10].

Consider an observer moving with the wheel with the constant linear velocity V. We introduce the new Cartesian coordinate system $O'x_1'x_2'$ hooked in the middle of the wheel. The systems $O'x_1'x_2'$ and Ox_1x_2 are related by: $x_1' = x_1 - V\,t$ and $x_2' = x_2$. Since by the above assumptions (a)-(d) the displacement $u(x_1', x_2')$ does not depend on time we obtain:

$$\frac{du}{dt}(x_1',x_2') = \frac{du}{dt}(x_1 - V\,t, x_2) = 0. \tag{9}$$

It implies:

$$\frac{du}{dt} = -V\ \frac{du}{dx_1} \quad \text{and} \quad \frac{d^2u}{dt^2} = V^2\ \frac{d^2u}{dx_1^2}. \tag{10}$$

Using these assumptions the inertial term in equation (1) is replaced by the stationary term depending on the wheel velocity and spatial derivatives of displacement and reflecting the dynamics of the moving body rather than completely neglected it as in the classical quasistatic formulation [1]. Taking into account (10), quasistatic approximation of the contact problem (1)-(8) takes the form: find displacement u satisfying:

$$A^*D(x)Au - \rho V^2 u_{1,1} = 0 \quad \text{in } \Omega, \tag{11}$$

as well as

$$u = 0 \quad \text{on } \Gamma_0, \qquad B^*D(x)\,Au = F \quad \text{on } \Gamma_C, \tag{12}$$

$$u_2+g_r + w \le 0, \quad F_2 \le 0, \quad (u_2+g_r + w)F_2 = 0, \qquad \text{on } \Gamma_C, \tag{13}$$

$$|F_1| \le \mu\,|F_2|, \quad F_1\,u_{1,1} \le 0, \quad (|F_1| - \mu\,|F_2|)\,u_{1,1} = 0, \quad \text{on } \Gamma_C, \tag{14}$$

$$\frac{dw}{dx_1} = -k\ F_2, \qquad \text{on } \Gamma_C, \tag{15}$$

where $u_{i,j} = \frac{\partial u_i}{\partial x_j}$, $u_{i,jk} = \frac{\partial^2 u_i}{\partial x_i \partial x_k}$, i,j,k=1,2. Moreover in (2) $u_{0i} = u_{1i} = 0$ is set.

3.1 Friction Regularization

In order to ensure the existence of solutions to the problem (11)-(15) we have to regularize it, *i.e.*, we will consider it as the problem with the prescribed friction. Let $\varepsilon > 0$ be a regularization parameter. We use the following formula relating tangential and normal tractions on the contact boundary Γ_C [10]:

$$F_1 = F_1(\varepsilon, F_2, u_1) = -\mu \mid F_2 \mid \arctan \frac{V u_{1,1}}{\varepsilon}. \tag{16}$$

4. Numerical methods and results

Finite element method is used to approximate problem (11)-(16) as the approximation method. The discretized contact problem is reformulated as a quadratic optimization problem in terms of tangent and normal tractions. For details of the method see [10].

The obtained distributions of normal contact and longitudinal stress along the contact boundary for different values of parameter η=0.5, 0, -0.3 are displayed in Fig. 3 and 4, respectively. These distributions are strongly dependent on parameter η. As it is shown in Fig. 3 and Fig. 4 the decrease of the parameter η reduces the maximum normal contact pressure at a cost of widening the contact zone as well as reduces the maximum longitudinal stress.

5. Conclusions

The elastic rolling contact problem where the properties of the elastic layer between the homogeneous surface coating and the substrate of the rail are dependent on its depth is solved numerically using the quasistatic approach. The material properties of the graded layer are assumed to be governed by the exponential law. The obtained numerical results indicate that the elastic graded layer may reduce the values of the normal contact stress in the contact zone comparing to the pure homogeneous case. The dependence of the obtained stress distributions on the parameter η is stronger than on the nonhomogenity index in power law (see [9]). Remark also, that using the quasistatic approach we can observe dynamic phenomena of the rolling wheel. In future one can consider plastic layers in the neighborhood of the rail surface rather than elastic layers considered in this paper.

Acknowledgments

The research work of the second author is partially supported by the National Center for Research and Development of Poland under grant No. NR02-009-06.

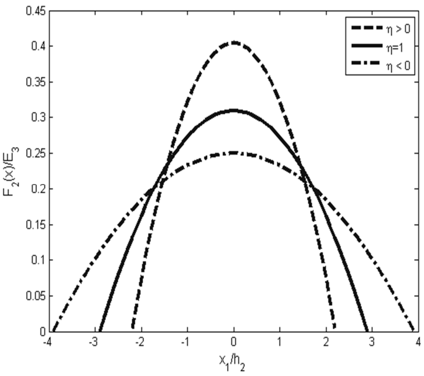

Figure 3. Normal contact stress distribution

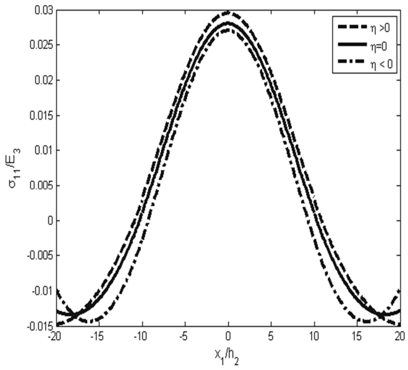

Figure 4. Longitudinal stress distribution σ_{11} at interface $x_2 = 0$.

References

1. W. Han, M. Sofonea, *Quasistatic contact problems in viscoelasticity and viscoplasticity*, AMS and IP 2002.
2. M. Hiensch et al., *Two-material rail development field test results regarding rolling contact fatigue and squeal noise behavior*, Wear, **258** (2005) 964-972.
3. M. Shillor, M. Sofonea, J.J Telega, *Models and analysis of quasistatic contact: variational methods*, Springer, Berlin 2004.
4. H.C. Meng, K.C. Ludema, *Wear models and predictive equations: their form and content*, Wear, **181-183** (1995) 443-457.
5. W. Sextro, *Dynamical contact problems with friction*, Springer, Berlin 2007.
6. P. Wriggers, *Computational contact mechanics*, Second Edition, Springer, Berlin 2006.
7. S. Suresh, *Graded materials for resistance to contact deformation and damage*, Science, **292** (2001) 2447-2451.
8. J. Yang, L.L Ke, *Two-dimensional contact problem for a coating-graded layer - substrate structure under a rigid cylindrical punch*, International Journal of Mechanical Sciences, **50** (2008) 985-994.
9. A. Chudzikiewicz, A. Myśliński, *Thermoelastic Wheel-Rail Contact Problem with Elastic Graded Materials*, Wear, **271** (2011) 417-425.
10. A. Chudzikiewicz, A. Żochowski, A. Myśliński, *Quasistatic versus Kalker approach for Solving Rolling Contact Problems*, The Archive of Transport, **4** (1992) 103-120.

XXV Symposium *Vibrations in Physical Systems,* Poznan – Bedlewo, May 15-19, 2012

Natural Frequency Analysis of Piezoelectric Rods and their Assemblies by Compliance Method

Piotr CUPIAŁ
AGH University of Science and Technology, Department of Process Control
Al. Mickiewicza 30, 30-059 Krakow, pcupial@agh.edu.pl

Abstract

The vibrations of one-dimensional structures that consist of several interconnected members are conveniently analysed by matrix methods that include: the compliance (receptance) method, the mobility approach, dynamic stiffness method or the transfer matrix method. The paper presents the generalization of the classical receptance method to the coupled electromechanical vibrations of piezoelectric rods. Several compliance matrices are derived for piezoelectric rods undergoing longitudinal vibrations. These matrices can then be used in the derivation of the characteristic equations of rods with different boundary conditions as well as piezoelectric rod assemblies. The approach is illustrated by deriving the characteristic equation for a single piezoelectric rod with one end fixed and a spring and capacitor attached to its other end, as well as a two-rod assembly.

Keywords: vibration, continuous systems, coupled piezoelectricity, matrix methods

1. Introduction

In the analysis of one-dimensional continuous systems that consist of several interconnected members, matrix methods show important advantages over an alternative approach, in which the equations are solved for each member and the boundary and interface conditions are then applied. In any of the matrix method, the matrices that relate some quantities specified at the end of a member are derived. Unlike in the finite element method the matrices used are exact and do not make use of numerical approximations.

Several matrix methods of vibration analysis have been used for studying the behaviour of elastic structures, which include the receptance (or compliance) method [1,2], the mobility approach [3,4], the dynamic stiffness method [5,6] and the transfer matrix method [2]. The receptance and mobility approaches have the same principle, but they differ in the measure of vibration used (displacement and velocity is used, respectively).

The aim of the paper is to discuss the generalization of the classical receptance method to the coupled electromechanical vibrations of piezoelectric rods. The equations that describe the longitudinal vibration problem of piezoelectric rods have been discussed in [7], and they consist of two coupled electromechanical partial differential equations. Since the necessary compliance matrices of piezoelectric elements are not available in the literature, an outline of their derivation is provided in Section 2, for rods with two different boundary conditions. The compliance matrices of piezoelectric members contain both mechanical and electrical degrees of freedom.

In Section 3 the effectiveness of the compliance method in deriving the characteristic equations of one-dimensional systems is illustrated on two examples. The first one is a single piezoelectric rod fixed at its left end with the other end restrained by a spring.

Additionally, a capacitor is connected to the right end to allow modelling of a class of electrical boundary conditions. The second example will consider a piezoelectric rod consisting of two members with different mechanical and electrical properties.

2. Compliance matrices of piezoelectric rods

The receptance (compliance) method has been used for rod and beam assemblies in [1,2]. For elastic rods that undergo longitudinal vibration the receptance is defined as the ratio of the amplitude of displacement at some point of the rod to the magnitude of the driving harmonic force. Many receptances have been tabulated for elastic rods and beams in [1]. For rods that are described by coupled piezoelectricity theory the corresponding matrices were discussed in the author's monograph [7]. The essential elements of the derivation of these matrices for two different boundary conditions are given below. Since in the analysis of piezoelectric rods the corresponding matrices include both mechanical and electrical degrees of freedom, the term 'compliance matrix' rather than 'receptance matrix' will be used.

The set of coupled electromechanical equations of the longitudinal vibration of a slender rod has the following form [7]:

$$\rho F \frac{\partial^2 u}{\partial t^2} - \frac{\partial}{\partial z}\left(c\frac{\partial u}{\partial z} + e\frac{\partial \phi}{\partial z} \right) = 0,$$

$$\frac{\partial}{\partial z}\left(e\frac{\partial u}{\partial z} - \kappa\frac{\partial \phi}{\partial z} \right) = 0. \qquad (1)$$

Here u and ϕ stand, respectively, for the displacement and electric potential, and:

$$c = F\left(c_{33} - \frac{2c_{13}^2}{c_{11}+c_{12}} \right), \quad e = F\left(e_{33} - \frac{2c_{13}e_{31}}{c_{11}+c_{12}} \right), \quad \kappa = F\left(\kappa_{33} + \frac{2e_{31}^2}{c_{11}+c_{12}} \right). \qquad (2)$$

In Eq. (2), c_{11}, c_{12}, c_{13}, c_{33} are the elastic stiffness coefficients, κ_{33} is the electric permittivity in the direction of the rod axis, and e_{31}, e_{33} are the piezoelectric constants of the rod (more details about the constitutive equation of linear piezoelectricity can be found in [7, 8]). The symbol F denotes the area of the rod cross-section. The boundary conditions relevant to Eq. (1) are prescribed as follows:

$$u = 0 \quad \text{or} \quad N = \hat{N}; \qquad \phi = 0 \quad \text{or} \quad D_n = -\hat{q}. \qquad (3)$$

Here, $N = c\dfrac{\partial u}{\partial z} + e\dfrac{\partial \phi}{\partial z}$ is the normal force and $D_n = \pm\left(e\dfrac{\partial u}{\partial z} - \kappa\dfrac{\partial \phi}{\partial z} \right)$ is the normal component of the electric displacement vector (the plus sign corresponds to the right end of the rod and the minus sign the left end). $\hat{N}$ (positive when it acts in the direction of the normal) is the applied force and $\hat{q}$ is the free charge prescribed at a rod end.

According to the approach used in [2] for elastic rods and beams, in the following derivations of the compliance matrices it is assumed that the rod undergoes steady-state harmonic vibration with frequency ω. In order to illustrate the derivation of the compliance matrices for piezoelectric rods, we consider a rod that is fixed at the left end and free to move at the other end. In steady-state vibration with frequency ω the general solution of Eq. (1) is given by:

$$U(z) = A\sin(\lambda z) + B\cos(\lambda z),$$
$$\Phi(z) = \frac{e}{\kappa}\left[A\sin(\lambda z) + B\cos(\lambda z) + G\frac{z}{L} + H\right], \tag{4}$$

where: $\omega = \lambda\sqrt{\dfrac{c + e^2/\kappa}{\rho F}}$. For the fixed-free rod the boundary conditions are defined as follows:

$$U(0) = 0, \quad \Phi(0) = \phi_L,$$
$$p_R = cU'(L) + e\Phi'(L) = A(c + e^2/\kappa)\lambda\cos(\lambda L) + \frac{e^2}{\kappa}\frac{G}{L}, \tag{5}$$
$$q_R = -[eU'(L) - \kappa\Phi'(L)] = \frac{eG}{L}.$$

It has been assumed that the longitudinal force $p_R = N(L)$ and a charge with amplitude q_R have been applied to the right end of the rod. For physical reasons, since the electrostatic potential cannot be determined in a unique way, an arbitrary value ϕ_L is prescribed at the left end of the rod. Solving the set of equations (5) for A one obtains:

$$A = \frac{1}{(c + e^2/\kappa)\lambda\cos(\lambda L)}p_R - \frac{e}{\kappa}\frac{1}{(c + e^2/\kappa)\lambda\cos(\lambda L)}q_R, \tag{6}$$

and the solution for $U(z)$ and $\Phi(z)$ can be written in the following matrix form:

$$\begin{Bmatrix} U(z) \\ \Phi(z) - \phi_L \end{Bmatrix} = \begin{bmatrix} \alpha_{11}(z) & \alpha_{12}(z) \\ \alpha_{21}(z) & \alpha_{22}(z) \end{bmatrix} \begin{Bmatrix} p_R \\ -q_R \end{Bmatrix} \tag{7}$$

Here, α_{11}, α_{12}, α_{21}, α_{22} are the components of the compliance matrix defined by the following expressions:

$$\alpha_{11}(z)=\frac{\sin(\lambda z)}{(c+e^2/\kappa)\lambda\cos(\lambda L)},\quad \alpha_{12}(z)=\alpha_{21}(z)=\frac{e}{\kappa}\frac{\sin(\lambda z)}{(c+e^2/\kappa)\lambda\cos(\lambda L)},$$
$$\alpha_{22}=\frac{e^2}{\kappa^2}\frac{\sin(\lambda z)}{(c+e^2/\kappa)\lambda\cos(\lambda L)}-\frac{z}{\kappa}. \tag{8}$$

The compliance matrix of a free-free rod can be obtained in a similar manner. In this case the solution is expressed as follows:

$$\begin{Bmatrix} U(z) \\ \Phi(z)-\phi_L \end{Bmatrix}=\begin{bmatrix} \beta_{11}(z) & \beta_{12}(z) \\ \beta_{21}(z) & \beta_{22}(z) \end{bmatrix}\begin{Bmatrix} p_L \\ q_L \end{Bmatrix} \tag{9}$$

Here, $p_L = -N(0)$ is the component of the force that acts in the positive direction of the z-axis (the sign convention used here is typical of matrix methods and is the same as in [2]). The components of the compliance matrix of a free-free rod are given by the following expressions:

$$\beta_{11}(z)=-\frac{\cos[\lambda(L-z)]}{(c+e^2/\kappa)\lambda\sin(\lambda L)},\quad \beta_{12}(z)=\frac{e}{\kappa}\frac{\{\cos[\lambda(L-z)]-\cos(\lambda z)\}}{(c+e^2/\kappa)\lambda\sin(\lambda L)},$$

$$\beta_{21}(z)=-\frac{e}{\kappa}\frac{\{\cos[\lambda(L-z)]-\cos(\lambda L)\}}{(c+e^2/\kappa)\lambda\sin(\lambda L)}, \tag{10}$$

$$\beta_{22}(z)=\frac{e^2}{\kappa^2}\frac{\{\cos[\lambda(L-z)]-\cos(\lambda z)-\cos(\lambda L)+1\}}{(c+e^2/\kappa)\lambda\sin(\lambda L)}-\frac{z}{\kappa}.$$

It is to be noted that $\beta_{12}(z) \neq \beta_{21}(z)$, but the following symmetry condition holds: $\beta_{12}(0) = \beta_{21}(L)$.

3. Applications

In order to demonstrate the application of the compliance matrices to the derivation of the characteristic equations, two examples will be discussed: a single piezoelectric rod and an assembly that consists of two interconnected rods.

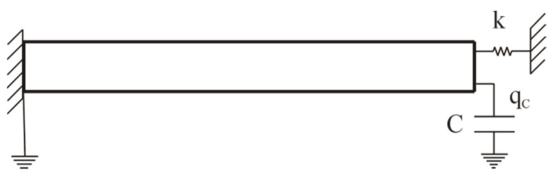

Figure 1. A piezoelectric rod restrained by a spring with a capacitor attached

In the first example, the rod shown in Fig. 1 is considered, where the left end of the rod is fixed and the other end is restrained by a spring of stiffness *k*. Electrically, the left end is grounded and the right end is connected to ground through capacitance *C*. Making use of Eq. (7) the displacement and electrostatic potential of the right end of the rod are expressed as follows:

$$\begin{aligned} u_R^{(1)} &= u = \alpha_{11}(L)p_R^{(1)} + \alpha_{12}(L)(-q_R^{(1)}) = \alpha_{11}(L)p_R^{(1)} + \alpha_{12}(L)q_C, \\ \phi_R^{(1)} &= \alpha_{21}(L)p_R^{(1)} + \alpha_{22}(L)(-q_R^{(1)}) = \alpha_{21}(L)p_R^{(1)} + \alpha_{22}(L)q_C. \end{aligned} \tag{11}$$

In writing these expressions the value of the electrostatic potential of the left end has been set equal to zero and use has been made of the fact that in order to ensure the conservation of electric charge the charge at the rod right end is the negative of the charge at the top plate of the capacitor: $q_R = -q_C$. Moreover: $\phi_R^{(1)} = \frac{1}{C}q_C$, where $\phi_R^{(1)}$ is the potential of the right end of the rod relative to the ground. Making use of these facts, Eq. (11) reduces to:

$$\begin{cases} \alpha_{11}(L)p_R^{(1)} + \alpha_{12}(L)q_C = u, \\ \alpha_{21}(L)p_R^{(1)} + \left[\alpha_{22}(L) - \dfrac{1}{C}\right]q_C = 0. \end{cases} \tag{12}$$

Solving this equation for $p_R^{(1)}$ one finds that:

$$p_R^{(1)} = \frac{\alpha_{22}(L) - 1/C}{\alpha_{11}(L)[\alpha_{22}(L) - 1/C] - \alpha_{12}(L)\alpha_{21}(L)}u. \tag{13}$$

Now, assume that a harmonic external force with amplitude *P* acts on the right end of the rod. From the balance of forces it follows that:

$$p_R^{(1)} + p_L^{(2)} = P \Leftrightarrow \left\{\frac{\alpha_{22}(L) - 1/C}{\alpha_{11}(L)[\alpha_{22}(L) - 1/C] - \alpha_{12}(L)\alpha_{21}(L)} + k\right\}u = P, \tag{14}$$

where: $p_L^{(2)} = ku$ is the force that acts on the left end of the spring. By solving Eq. (14) for u, the characteristic equation is obtained by setting the denominator of the resulting expression equal to zero. The characteristic equation has the following form:

$$\alpha_{22}(L) - 1/C + k\alpha_{11}(L)[\alpha_{22}(L) - 1/C] - k\alpha_{12}(L)\alpha_{21}(L) = 0. \tag{15}$$

Making use of the expressions for the elements of the compliance matrix, the characteristic equation has the following explicit form:

$$\left[\frac{e^2}{\kappa^2}\frac{\tan(\lambda L)}{(c + e^2/\kappa)\lambda} - \frac{1}{C_e}\right]\left[1 + k\frac{\tan(\lambda L)}{(c + e^2/\kappa)\lambda}\right] - k\frac{e^2}{\kappa^2}\frac{\tan^2(\lambda L)}{(c + e^2/\kappa)^2\lambda^2} = 0, \tag{16}$$

where: $C_e = \dfrac{(\kappa / L)C}{(\kappa / L) + C}$ is the equivalent capacitance of a series connection of capacitance C and that of the piezoelectric rod. A number of special cases that correspond to different mechanical and electrical boundary conditions can be obtained from Eq. (16), by setting limiting values of k and C. The characteristic equations for such cases have been obtained in [7] by solving the differential equations with appropriate boundary conditions.

As a second example we consider a piezoelectric rod that consists of two interconnected members, shown in Fig. 2. From Eqs. (7) and (9) one finds the

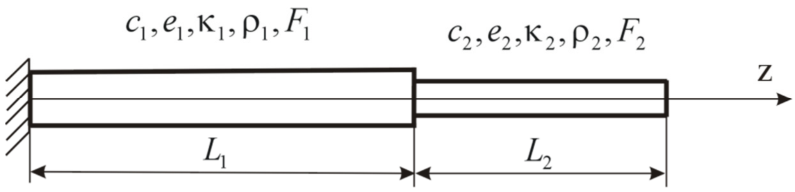

Figure 2. A two-member piezoelectric rod

displacement of the right end of the first member and the left end of the second one:

$$u_R^{(1)} = \alpha_{11}(L_1) p_R^{(1)} + \alpha_{12}(L_1)(-q_R^{(1)}), \quad u_L^{(2)} = \beta_{11}(0) p_L^{(2)} + \beta_{12}(0)(q_L^{(2)}). \tag{17}$$

The elements of the compliance matrices are calculated using the properties of the respective member.

Open-circuit electrical boundary conditions are assumed, in which case there are no charges at the ends of the composite rod. The electrostatic potential at one point is arbitrary, and if potential distribution needs to be calculated, this value can be set as equal to zero at the left end of the first member. Considering the second member, since the free charge at its right end is equal to zero: $q_R^{(2)} = 0$, the free charge is also equal to zero at its left end: $q_L^{(2)} = 0$. Using this fact and the conservation of charge at the interface of the two rods, the following equation also holds true:

$$q_R^{(1)} + q_L^{(2)} = 0 \Leftrightarrow q_R^{(1)} = 0. \tag{18}$$

Using the above argument that concerns the charges, equation (17) reduces to:

$$u_R^{(1)} = \alpha_{11}(L_1) p_R^{(1)}, \quad u_L^{(2)} = \beta_{11}(0) p_L^{(2)}. \tag{19}$$

Denoting the common displacement at the interface point by u, then expressing $p_R^{(1)}$ and $p_L^{(2)}$ in terms of u using Eq. (19), and making use of the force balance in precisely the same way as was described in the previous example, one obtains the following equation:

$$u = \frac{\alpha_{11}(L_1)\beta_{11}(0)}{\alpha_{11}(L_1) + \beta_{11}(0)} P. \tag{20}$$

The characteristic equation follows by setting the denominator as equal to zero, and it has the following form:

$$\left(c_2 + \frac{e_2^2}{\kappa_2}\right)\lambda_2 \sin(\lambda_1 L_1)\sin(\lambda_2 L_2) - \left(c_1 + \frac{e_1^2}{\kappa_1}\right)\lambda_1 \cos(\lambda_1 L_1)\cos(\lambda_2 L_2) = 0. \tag{21}$$

In Eq. (21), λ_1 and λ_2 are related to ω by the formulas (see the definition following equation (4)):

$$\lambda_1 = \frac{\omega}{\sqrt{\dfrac{c_1 + e_1^2/\kappa_1}{\rho_1 F_1}}}, \quad \lambda_2 = \frac{\omega}{\sqrt{\dfrac{c_2 + e_2^2/\kappa_2}{\rho_2 F_2}}} \tag{22}$$

The characteristic equation (21) has been derived independently in [7], by finding the solution in each member and imposing the boundary and interface conditions.

4. Conclusions

The paper has discussed the compliance approach to the calculation of the natural frequencies of piezoelectric rods. Compliance matrices have been derived for two different mechanical boundary conditions: the fixed-free and the free-free rod. Two examples were given illustrating the usefulness of the method in the calculation of the natural frequencies of a single rod and a two-member piezoelectric rod. For more complex assemblies, the Holtzer method was proposed for elastic structures in Refs. [1, 2]. The compliance approach discussed in the paper can also be used to calculate the steady-state forced response of undamped rod assemblies under mechanical and electrical excitation.

References

1. R.E.D. Bishop, D.C.. Johnson, *The Mechanics of Vibration*, Cambridge University Press, 1960.
2. R.E.D. Bishop, G.M.L. Gladwell, S. Michaelson, *Macierzowa analiza drgań (The Matrix Analysis of Vibration)*, WNT, Warszawa 1972.
3. L. Cremer, M.Heckl, *Structure-born Sound: Structural Vibrations and Sound at Audio Frequencies*, Springer, 2nd ed., Berlin 1988.
4. J.C. Snowdon, *Vibration and Shock in Damped Mechanical Systems*, John Wiley & Sons, New York 1968.
5. R.W. Clough, J. Penzien, *Dynamics of Structures*, Mc-Graw-Hill, New York 1993.
6. T. Chmielewski, Z. Zembaty, *Podstawy dynamiki budowli (Principles of Structural Dynamics)*, Arkady, Warszawa 1998.

7. P. Cupiał, *Coupled Electromechanical Vibration Problems for Piezoelectric Distributed-parameter Systems*, Monografia 362, Seria Mechanika, Politechnika Krakowska, Kraków 2008.
8. W. Nowacki, *Efekty elektromagnetyczne w stałych ciałach odkształcalnych (Electromagnetic Effects in Deformable Solids)*, PWN, Warszawa 1983.

XXV Symposium *Vibrations in Physical Systems,* Poznan – Bedlewo, May 15-19, 2012

Vibroacoustic Properties and Interactions of an Urban Tram

Bartosz CZECHYRA
Poznan University of Technology, Institute of Combustion Engine and Transport
Division of rail Vehicle, Piorowo Str. No.3, 61-965 Poznan
bartosz.czechyra@put.poznan.pl

Abstract

Complex acoustic climate of urban space is an integral part development of civilization. It is well known also that the ambient noise level significantly affect the quality of life in the city. There is also a factor negatively affecting your body reducing the comfort of living and productivity. At the same time some of the annoying sound sources, we can not eliminate. Because the vibration and noise generated by trams are a regular part of urban vibroacoustic climate their impact on the environment must be recognized and minimized.
In this article author defines the concept of the vehicle vibroacoustic activity and submit use the pass-by test in description of vehicle features under normal operating conditions. This paper presents the assumptions and methodology of the proposed experimental research. A preliminary study on the possibility of a comprehensive description of vibroacoustic properties of various types of trams in the study in situ condition is presented. Author also presents selected results of research carried out on trams operated in Poznan (Poland).

Keywords: vibroacoustic activity, tram, experimental research

1. Introduction

The new tram is placed in service after positive verification of the requirements as to the external noise level generated by vehicle. The main document in this area is **EN ISO 3095:2005** *Railway applications – Acoustics. Measurement of noise emitted by rail-bound vehicles.* The document gives a detailed methodology for normative testing of external noise. There are indicated conditions for locating of the measuring place, the measuring points and environmental and other conditions that must be met for the comparison of measurements.

This document also provides a methodology of sound level calculation for a representative sample in the pass-by test. An example of determining the sound level generated by the tram during pass-by test is presented graphically in Fig. 1.

As is shown on Fig. 1 the reference point is the beginning and end of the tram (square marker). The time window set by the length of the vehicle determines the average sound level. After a first phase of calculation the time window is expand to time before and behind the vehicle edges so as to capture a moment when the current sound level is 10dB lower than the average level fixed in first step. Only the sound level of such an extended time window is assessed and compared as normative value.

The only thing this rule does not specify is the sound level limits. These values are determined in each individual case by the Employer/Contractor. Often Employer/Contractor benefits from the experience of those involved in rail vehicles. In Poland, very frequently is invoked of German VDV standard No 154 [1]. They set the sound level limits and are treated as a reference point for the construction of new vehicles.

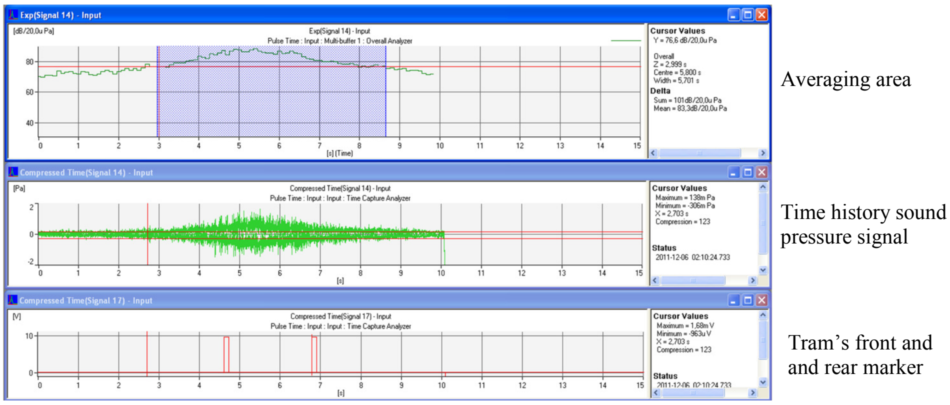

Figure 1. Graphical representation of the sound level calculation according to EN ISO 3095:2005

In our cities we can find many types of modern tram which meet the cited standard. This does not mean that all trams are equally friendly to the ear of inhabitants and the urban environment. Each vehicle is different under real operating conditions and thus different influences on the vibroacoustic climate of our cities. Therefore, it is still actual question how to choose the best vehicle for our city with taking into account:

- the geographical specificity of the tram network,
- the technology of infrastructure,
- Passenger flows in normal operating conditions,
- the model of rail/wheel wearing
- the real dynamic effects as a results of vehicle/infrastructure interaction.

All these factors affect the general vibroacoustic phenomena accompanying of the vehicle under normal operating conditions. This measure, as information about the global vibroacoustic impact of vehicle on environment is defined by the author as Vibroacoustic Activity of Vehicle. This volume - unlike vibroactivity presented in [2] - describes tram noise and vibration effects in a quantitative and qualitative way at environmental impact aspect and it takes into account:

- Tram acoustic signature
- Dynamic wheel-rail interaction at the micro-geometry level
- Dynamic vehicle interaction with infrastructure – para-seismic vibration.

The individual elements consist the vibroacoustic activity of the vehicle are presented below.

2. Tram acoustic signature

Acoustic signature is a unique and characteristic sound fingerprint of a described object enabling its identification and location in the space. Originally this term was created for the army to describe ships and submarines [3]. Later the idea of acoustic signature was successfully used in a civil technique to identify sources of vibroacoustic signals and machinery diagnostics [4, 5]. The idea of using the acoustic signature for description and identification different types of Poznan tram was presented in papers [6, 7].

Exemplary results of the investigation and analyses of two characteristic for Poznan types of trams: 105 Na and Siemens Combino are presented below. A time-spectrum map was the basis to work out the utile acoustic signature. The signals were filtered in accordance with weighting curve A. The results are presented in Fig. 2.

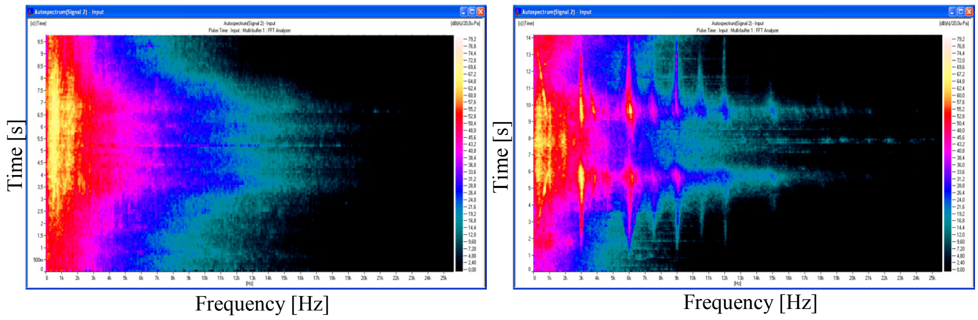

Figure 2. Time-spectrum map for a ride of tram type 105Na (left side) and Siemens Combino (right side)

Presented spectrum characteristics of registered signals differ considerably. In Fig. 2 it is difficult to identify certain wheel sets as main sources of noise. After more detailed analysis it is only possible to identify vehicle subsequent bogies. In this signal no characteristic tonal components dominate, except for broadband excitation.

On the contrary, in case of tram type Siemens Combino, distinct and characteristic existence of tonal components, resulting from inverter running in the drive system, can be unequivocally identified in the spectrum. Although, just like in the previous example, certain wheels cannot be identified, subsequent bogies can be unequivocally pointed – especially driving bogies. At the same time it was noticed that unlike in car type 105 Na, in tram type Siemens Combino a middle bogie is mostly responsible for generating overall noise. This is a rolling bogie and does not transfer driving force into the vehicle. Additionally this bogie enables gentle fitting of tram in the curve and that is why it should have better possibility to dislocate against the body – bigger construction clearance.

A common feature of both objects generating analyzed signals is focusing larger part of acoustic energy in lower frequency bands. On the basis of comparative analysis it can be indicated that wheel/rail cooperation generates noise in the frequency typical for mechanical interactions *i.e.* up to 2 kHz. For tram type 105 Na nearly 85% of signal acoustic energy generated during a pass-by is comprised in band up to 2 kHz. Slightly different values characterize tram type Siemens Combino. In this case participation of mechanical wheel/rail interactions constitutes barely 50% of energy participation in the whole signal registered during a pass-by. Electroacoustic sources constitute a considerable energy participation in signal generated by tram type Siemens Combiono at a test pass-by. Inverter is a main source of sounds of harmonic components 3, 6, and 9 kHz, high amplitude and inconvenience. Acoustic features of this element of drive system perform well the identifying function of this means of transport.

3. Dynamic wheel-rail interaction at the micro-geometry level

Generated noise is a secondary effect of processes occurring on wheel/rail contact, particularly micro-slippages resulting from changeable location of contact point of both profiles and changes in meshing area of both elements [8]. Additionally vibroacoustic effects are determined by construction of tram bogie. In this case many different details influence on quality of rolling and thus sound and vibration generated during tram operations. Simultaneously these parameters will change during operation because of wearing, too. The elements like dumpers, rubber-metal joints and suspension parts, etc. change their mechanical properties in service. That mean different construction interact differently on infrastructure.

In the case of rail vehicles the primary criterion for assessing the safety of driving in the track is Nadal's criterion. Nadal's criterion is based on the ratio of lateral and vertical forces acting on the wheel and rail just prior to derailment. Probability of derailment is higher in quasi-static conditions. So, the value of vibration energy in the two dimension in dynamic condition can be a base for assess global, dynamic interaction between wheel and rail in normal operational conditions. Because the vibration level strongly depends on speed of ride experimental data was collected for different speed. An example of comparing the vehicles based on the rail vibration is shown on Fig. 3.

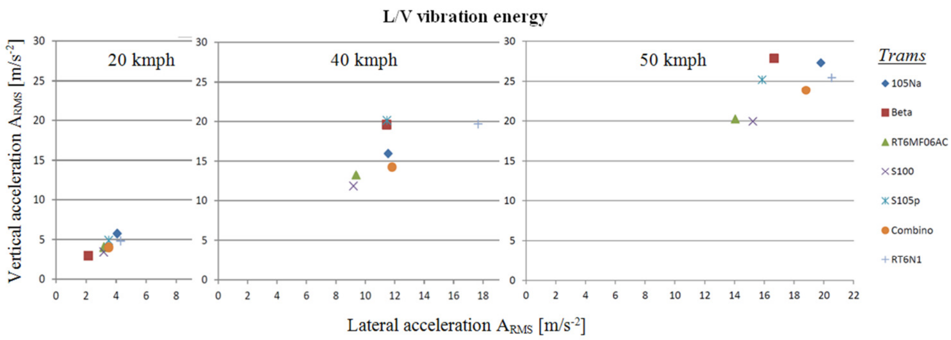

Figure 3. Energy of rail acceleration (lateral and vertical) measured for 7 tram types

As can be seen on figure 3 the levels of impact on the rail strongly depends on the type of tram – design features and construction details. Depending on vehicle type the differences range is from 6% to 50% and it is correlated on the speed of ride. These results clearly show that it is possible to indicate such a vehicle, which generates the slightest impact on the infrastructure at the micro level of inequality (rail/wheel interaction) and has the lowest influence on rolling noise.

4. Dynamic vehicle interaction with infrastructure – para-seismic vibration

Para-seismic vibrations are another, very important and undesirable effect of trams operating. These vibrations can adversely affect the infrastructure of tramway and buildings surrounding the tramway net. The energy of vibration which propagate thru the ground layers are endanger for homes and other engineer buildings in the city, like a bridges, overpasses, tunnels, water pipes, sewage system, etc.

In the experiment the level of generated para-seismic vibrations was analyzed. The vibrations were recorded for the same types of trams presented in Fig. 3. Seismic accelerometer (B&K type 8340) was placed at a distance of 1 meter from the rail. Visualization and comparison of chosen measurement results are shown in Fig. 4.

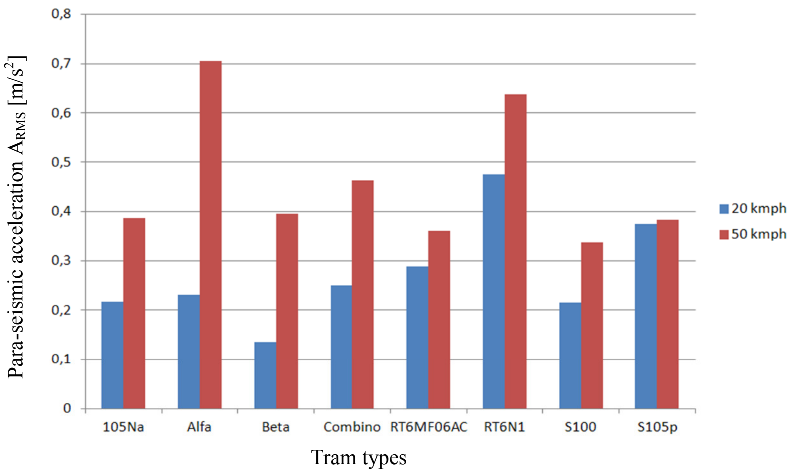

Figure 4. Para-seismic vibration acceleration caused by riding trams

As can be seen in Fig. 4 the level para-seismic vibrations generated by trams are different. Depending on the vehicle type RMS value of acceleration vibration reaches 0.47 ms^{-2} at 20 kmph and exceeds 0.7 ms^{-2} for speed 50 kmph. Simultaneously is noticed the increase of energy para-seismic vibrations generated by the tram, depending on the speed. In critical cases (Alfa) is a more than threefold increase the acceleration RMS value.

5. Conclusions

Noise and vibration generated by tram are unique characteristics of its functional features in terms of environmental sustainability. It is appropriate to introduce a new quantitative measure for assessing global impact the tram on the environment under normal operating conditions. It is proposed to introduction of the term vibroacoustic activity of the tram as a global measure of vehicle quality. This measure can be used for quick diagnosis of the vehicle and the dynamic, pro-environmental management of the rolling stock [9].

Acknowledgments

This research project would not have been possible without the support of many people. Special thanks to management and the entire leadership of Local Tram Operator – Miejskie Przedsiębiorstwo Komunikacyjne w Poznaniu – for help and involvement in the research program.

The author wishes to express her gratitude to students of Mass Transportation specialization (Eng. Przemysław Szymański and Eng. Michał Szaroleta) who were abundantly helpful and offered invaluable assistance.

References

1. VDV Schriften 154; 08/02*, Geräusche von Nahverkehrs-Schienenfahrzeugen nach BOStrab.* Verband Deuscher Verkehrsunternehmen Köln, Deutschland
2. Łączkowski R.: *Wibroakustyka maszyn i urządzeń*, WNT, Warszawa 1983
3. McGraw-Hill *Dictionary of Scientific and Technical Terms*, 6th edition, published by The McGraw-Hill Companies, Inc.
4. Randall R.B.: *Vibration Signature Analysis – Techniques and Instrument Systems* Noise, Shock and Vibration Conference at Monash Uniyersity, Melbourne, 1974
5. Czechyra B.: *The use of vibration signature to assessment the propriety of diesel engine running*. 28th International Scientific Conference, Technical Diagnostics of Machines and Manu-facturing Equipment, 27 – 28. January 2009, Rožnov pod Radhoštěm, Czech Republic
6. Czechyra B., Tomaszewski F.: *Acoustic signature of trams*, 16th International Congress on sound and Vibration, Krakow, 5-9 July 2009
7. Czechyra B., Skrodzka E., Tomaszewski F.: *The use of a tram acoustic signature in orientation and mobility of blind persons*, 56 Otwarte Seminarium Akustyki OSA2009, Goniądz nad Biebrzą 15-18 września 2009
8. Czechyra B., Firlik B., Tomaszewski F.: *Technical state monitoring method of light rail track wear*, Proceedings of the Fourth European Workshop on Structural Health Monitoring 2008, Edited by: UHL, OSTROWSKI, HOLNICKI-SZULC; DEStrech Publications, Inc., Pennsylvania, USA; page 167-174; ISBN 978-1-932078-94-7
9. Czechyra B., Kwaśnikowski J., Tomaszewski F.: *Możliwości wykorzystania metod w procesie oceny własności eksploatacyjnych tramwaju.* Logistyka, 4/2011 (materiały na CD)

XXV Symposium *Vibrations in Physical Systems,* Poznan – Bedlewo, May 15-19, 2012

Effective Damping of Energy Flow in 3D Biomechanical Human – Breaker Systems with the Application of Wosso Vibration Damping

Marian Witalis DOBRY
Institute of Applied Mechanics, Poznan University of Technology
3 Piotrowo Street, PL-60-965 Poznań, marian.dobry@put.poznan.pl

Abstract

The article concerns the dynamic energy analysis in a Human–Breaker (H–B) system with the application of spatial WoSSO vibration damping. The analysis required the development of a spatial mathematical energy model of a biomechanical system in which the Constant-Force Vibration Damping (WoSSO) system is applied; this model was solved by means of a simulation prepared with the use of a special programme created with the MATLAB/simulink software. The obtained results indicated that the innovative WoSSO system applied in this case effectively dampens the flow of energy to the human operator while retaining the full energy of blows to the base under the breaker.

Keywords: power distribution, energy flow, biomechanical systems, energy damping, WoSSO system

1. Introduction

Figure 1. Breaker during laboratory tests

Large mechanical hand tools (breakers) are often part of the equipment used in the building construction industry or for the construction and repair of roads and bridges – see Fig. 1. The breakers are characterised by the high blow energy required to perform the given task, e.g. break concrete. The impact of these tools on the human operator is also high and results in the vibration-induced white finger syndrome. Reports of occupational medicine institutes contain a quantitative and qualitative documentation of the cases of vibration-induced white finger syndrome amongst the operators of these tools. The disease usually results in damage to upper limb joints. According to the reports, the most commonly damaged joints are the elbow joints – 69%, wrist and carpal joints – 25% and shoulder joints – 4%. For many years, attempts have been made to reduce the levels of vibration in the handles of these tools. Simple classical methods of vibration damping did not produce the expected results. Permissible weighted acceleration values on the handles of these tools were never achieved.

At the Division of Vibroacoustics and Biodynamics of Systems (ZWiBDS) of the Institute of Applied Mechanics at the Poznan University of Technology, an attempt was made to provide the spatial damping of breaker vibrations using the innovative WoSSO vibration damping method. This method had already proven effective in the reduction of vibrations in smaller tools, with the mass of 5.6–8.5 kg and with the energy of breaker ram blows ranging from 10 to 30 [J].

In order to obtain the design guidelines for the design of **l**arge **m**echanical **h**and **t**ools (LMHT) which are innovative in terms of vibration damping and energy-safe, virtual experimental simulative investigations of vibrations, power distribution and flow of energy in the biomechanical Human – LMHT system (see Fig. 1) have been performed. Such investigations at the ZWiBDS precede the implementation of the production of innovative tools. The implementation begins with the preparation of technical documentation, development of the investigative model and performance of experimental tests. The results of these investigations allow for final modifications of the design and for the creation of a production prototype for specific type of batch production.

The results of the virtual investigations concerning the dynamics, power distribution and energy flow in the investigated H – LMHT biomechanical system with the application of the innovative vibration damping system are the subject of the present article.

2. Description of investigations

The procedure of the energy investigations of biomechanical systems begins with the analysis of the dynamic structure of the actual object and sources of vibrations and the structure of its physical (Fig. 2) and mathematical model [2]. The physical model of the human submodel was prepared on the basis of dynamic human parameters for three directions, specified in ISO 10086 [4].

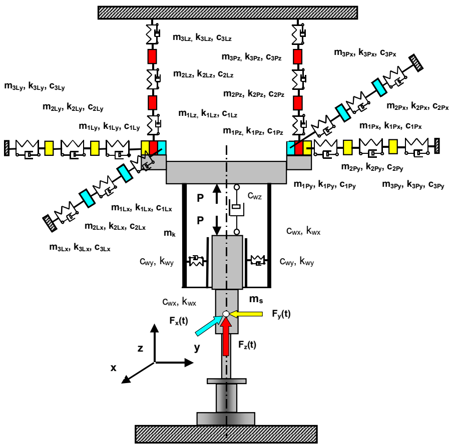

Figure 2. Physical model of the Human–Breaker system with WoSSO vibration damping

Then, through the application of two energy principles developed by the author [1], an energy model – in the form of integral equations of the energy flow in the entire structure of the investigated biomechanical system – is obtained [2].

In the investigated case, the energy model consisted of 18 integral equations describing the flow of energy in the entire structure of the biomechanical H – LMHT system [2].

The energy model was solved using the method of digital simulation of energy flow, with the use of a specially developed programme for the dynamics, power distribution and energy flow in the biomechanical H – LMHT system with WoSSO vibration damping. In this programme, the power distribution, energy flow and dynamics of the system are solved synchronously, allowing for the advanced dynamic analysis of the investigated system.

3. Results of investigations

The simulation was preceded by experimental tests in order to identify the sources of the vibrations of the breaker and its dynamics, including the determination of the accelerations of the vibrations of breaker motor body. The obtained functions of instantaneous accelerations in time and their RMS values were used to fine-tune the developed physical model to the actual investigated object, i.e. H – LMHT [2]. The values of the dynamic parameters for the physical model of the human submodel were adopted on the basis of ISO 10068 [4]. The RMS values of accelerations, velocities and displacements in three directions obtained in the digital simulation of the dynamics of the investigated system are included in Table 1, and Figs. 3–6 depict sample energy portraits of the individual points of reduction along the most important direction – "z" [2].

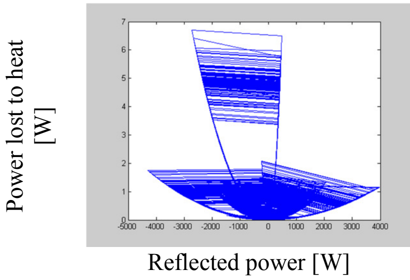

Figure 3. Energy portrait of the point of reduction "Motor Body z" (MBz) in the H–B System with WoSSO vibration damping – direction "z" [2]

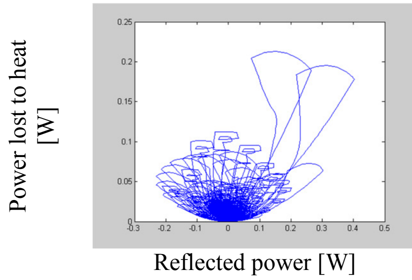

Figure 4. Energy portrait of the point of reduction "Handle-Hand z" (H-Hz) in the H–B System with WoSSO vibration damping – direction "z" [2]

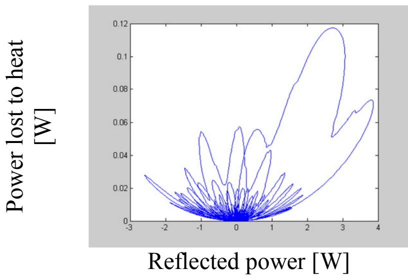

Figure 5. Energy portrait of the point of reduction "Forearm-Elbow z" (F-Ez) in the H–B System with WoSSO vibration damping – direction "z" [2]

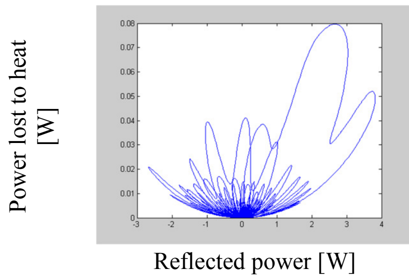

Figure 6. Energy portrait of the point of reduction "Arm-Shoulder z" (A-Sz) in the H–B System with WoSSO vibration damping – direction "z" [2]

Subsequent rows of Table 1 include the energy doses and mean power calculated on the basis of these doses for the Motor Body (MB) point of reduction, as the synchronous sum of three types of doses: dose of inertial energy, loss energy and elastic strain energy. The motor body in the investigated case is separated from the human operator by the spatial WoSSO vibration damping system – Fig. 2.

Mean power values in the part of the physical model related with the human body are specified in subsequent rows. These are, successively: Casing and two hands (C–H), Forearm–Elbow (F–E) and Arm–Shoulder (A–S). Due to the symmetrical position of the human operator, the mean power values for the left hand and right hand are identical. The comparison of mean power values indicated that for BC – H points of reduction, the mean power is highest for the point of reduction in direction “x,” then in direction “y” and finally in direction “z.”

The sequence of directions for points of reduction is different in case of F–E and A–S points. In these points of reduction, the most dangerous direction for this case of WoSSO vibration damping is direction “y,” then direction “x” and finally direction “z.” The influence of WoSSO vibration damping is evident, particularly in direction “z.” This dominant direction for the motor of a conventional breaker after the application of WoSSO vibration damping system is characterised by the smallest load measured as synchronous mean power in [W]. This testifies to the high effectiveness of energy damping of the WoSSO vibration damping system.

Higher value of mean power in the F–E point indicates the concentration of energy flow in this point – this is consistent with the reports concerning occupational medicine [3]. In this point, the highest percentage of elbow joint damage – i.e. 69% of the damage to all joints of the upper limb – was recorded.

Table 1 also includes the values of the total dose of energy in [J] flowing through all points of reduction for the 30 [s] duration of the simulation of energy flow in the investigated system. The mean power calculated on the basis of the energy confirms the results obtained on the basis of the sum of mean power values from all points of reduction specified in the table above.

4. Risk assessment in the energy domain

In the conducted investigations, the key problem was to achieve mean power values in the individual points of reduction lower than the permissible level of power established for a human operator within 8 hours of work. The permissible mean power value was determined based on the knowledge of energy flow and permissible duration of exposure to vibrations in case of an MS13 pneumatic hammer commonly used to clean off castings in foundries and steel mills [1]. The permissible value of mean power is 0,1 [W] – this value is also specified in Table 1.

The simulated mean power values for the individual vibration directions divided by the permissible power value that the ratio of calculated mean power to permissible power is lower than 1. The following values have been achieved for x, y and z directions, respectively: 0,71, 0,82 and 0,14. This means that the breaker equipped with WoSSO vibration damping system fulfils the energy damping criteria for all vibration directions and that this innovative breaker is energy-safe for human operators.

The mean power values for the source of energy and the sum of the power in the point of reduction of the human protected by the WoSSO vibration damping system can be used to calculate the **e**nergy **d**amping **e**ffectiveness (EDE) of the vibration damping system. The calculated values of the EDE were as follows: for direction “x” – $EDE_{WoSSO\ X}$ = 0,43/0,072 = 6, for direction “y” – $EDE_{WoSSO\ Y}$ = 0,52/0,082 = 6,3 and for direction “z” – $EDE_{WoSSO\ Z}$ = 0,5976/0,014 = 42,7 – see last row in Table 1.

Table 1. Results of digital simulation of the dynamics and energy flow in the biomechanical Human–Breaker System with the application of innovative WoSSO vibration damping system

<table>
<tr><th colspan="7">DIGITAL SIMULATION OF THE DYNAMICS – VIBRATION DIRECTIONS</th></tr>
<tr><td>Points of reduction</td><td colspan="6">Vibration directions</td></tr>
<tr><td>Motor Body – MB</td><td colspan="2">x</td><td colspan="2">y</td><td colspan="2">z</td></tr>
<tr><td>Acceleration (RMS)</td><td colspan="2">48.82</td><td colspan="2">79.17</td><td colspan="2">150.5</td></tr>
<tr><td>Velocity (RMS)</td><td colspan="2">0.067</td><td colspan="2">0.074</td><td colspan="2">0.1986</td></tr>
<tr><td>Displacement (RMS)</td><td colspan="2">0.00043</td><td colspan="2">0.00102</td><td colspan="2">0.0046</td></tr>
<tr><th colspan="7">DIGITAL SIMULATION OF POWER DISTRIBUTION AND ENERGY FLOW</th></tr>
<tr><td colspan="7">ENERGY DOSES in [J] and POWER in [W]</td></tr>
<tr><td>Pneumatic motor body</td><td colspan="2">x</td><td colspan="2">y</td><td colspan="2">z</td></tr>
<tr><td>Energy dose [J]</td><td colspan="2">13.01</td><td colspan="2">15.59</td><td colspan="2">17.93</td></tr>
<tr><td>Mean power [J/s]</td><td colspan="2">0.43</td><td colspan="2">0.52</td><td colspan="2">0.5976</td></tr>
<tr><td>Points of reduction / Left hand and right hand</td><td>Left hand</td><td>Right hand</td><td>Left hand</td><td>Right hand</td><td>Left hand</td><td>Right hand</td></tr>
<tr><td>Body-Casing – Handle–Hand (H–H) [W]</td><td colspan="2">0.042</td><td colspan="2">0.0383</td><td colspan="2">0.00632</td></tr>
<tr><td>Forearm–Elbow (F–E) [W]</td><td>0.0152</td><td>0.0152</td><td>0.036</td><td>0.036</td><td>0.0021</td><td>0.0021</td></tr>
<tr><td>Arm–Shoulder (A–S) [W]</td><td>0.000005</td><td>0.000005</td><td>0.0003</td><td>0.0003</td><td>0.0018</td><td>0.0018</td></tr>
<tr><td>Synchronous sum of mean power values in [W]</td><td colspan="2">0.072</td><td colspan="2">0.082</td><td colspan="2">0.014</td></tr>
<tr><td>Energy dose in [J] within 30 [s]</td><td colspan="2">2.165</td><td colspan="2">2.472</td><td colspan="2">0.4281</td></tr>
<tr><td>Mean power [J/s] = [W]</td><td colspan="2">0.072</td><td colspan="2">0.082</td><td colspan="2">0.014</td></tr>
<tr><td>Permissible level for 8 h of work [W]</td><td colspan="2">0.10</td><td colspan="2">0.10</td><td colspan="2">0.10</td></tr>
<tr><td>Ratio of calculated mean power to permissible power</td><td colspan="2">0.72</td><td colspan="2">0.82</td><td colspan="2">0.14</td></tr>
<tr><td>Energy damping effective-ness (EDE) of WoSSO vibration damping</td><td colspan="2">5.9</td><td colspan="2">6.3</td><td colspan="2">42.7</td></tr>
</table>

At this point, we can observe the high effectiveness of energy damping in direction “z,” where the innovative WoSSO subsystem was used. In effect, the lowest flow of energy was achieved in this direction, despite the fact that this direction is exposed to the strongest pulse source of vibration energy. This testifies to very good damping properties of the WoSSO system.

5. Conclusions

The conducted energy investigations of the H – LMHT system demonstrated that the innovative spatial WoSSO vibration damping system applied in this case effectively protects human operators against the excessive flow of vibrational energy generated by the operating breaker through their body.

In all directions, the achieved mean power values were lower from the permissible value established for 8-hour work [2] at the level of 0.1 [W]. The energy damping effectiveness of the vibration damping system in directions x, y and z are as follows: $EDE_{WoSSO\,X} = 6$, $EDE_{WoSSO\,Y} = 6.3$, $EDE_{WoSSO\,Z} = 42.7$. This is equivalent to the development of energy-safe and ergonomic breakers.

The commenced investigations, intended to develop entire ranges of energy-safe and ergonomic large powered hand tools, will be continued as part of further research projects. Their purpose will be to develop the design of such tools, commence production and implement them for actual use. The tools should prevent the vibration-induced white finger syndrome amongst operators, which is currently a major social problem around the globe.

Acknowledgements

The investigations were made possible owing to partial funding by the Ministry of Science and Higher Education in research project no. N503 017 32/2558, 2007–2011 [2].

References

1. M. W. Dobry, *Optymalizacja przepływu energii w systemie Człowiek – Narzędzie – Podłoże (CNP)* [Optimisation of energy flow in the Human – Tool – Base (HTB) System], Seria: Rozprawy Nr 330 ISSN 0551-6528, Wyd. Politechniki Poznańskiej 1998; Poznań 1998.
2. M. W. Dobry, M. Wojsznis, *Innowacyjna metoda redukcji przepływu energii do człowieka-operatora od dużych zmechanizowanych narzędzi ręcznych* [Innovative method for the reduction of energy flow to the human operator of large mechanical hand tools], Raport końcowy projektu badawczego nr N503 017 32/2558, 2007-2011, Politechnika Poznańska, IMS, Poznań 2011.
3. K. Marek, *Choroby zawodowe* [Occupational diseases], Wydawnictwo Lekarskie PZWL, Warszawa 2003
4. International Standardization organization, ISO/FDIS 10068:1998, *Mechanical vibration and shock – Free mechanical impedance of human hand-arm system at the driving point.*

XXV Symposium *Vibrations in Physical Systems,* Poznan – Bedlewo, May 15-19, 2012

Energy Flow as a Base of New Energy Approach to Fatigue Strength

Marian Witalis DOBRY
Poznan University of Technology, Institute of Applied Mechanics
3 Piotrowo Street, 60-965 Poznan, POLAND
marian.dobry@put.poznan.pl

Emil MACIEJEWSKI
Poznan University of Technology, Institute of Applied Mechanics
3 Piotrowo Street, 60-965 Poznan, POLAND
emil.maciejewski@put.poznan.pl

Abstract

This paper deals with the question of applying a new energy method in fatigue strength. The concept of using the equations of vibrations theory and two energy principles of Dobry to describe the process of material degradation was proposed. The main idea of this approach with the indication of these features which differ it from the other energy method was presented. The way of using MATLAB/Simulink models to carry out the simulation and the general idea of real experiment were described.

Keywords: fatigue strength, energy method , energy flow , power distribution

1. Bases of the new energy approach

Energy method which is described in the paper below bases on analysis of energy flow in mechanical systems. What is very important, this is such an analysis which take into consideration instantaneous values of energy. It will be conducted basing on energy principles of Dobry. The detailed description of this method one can find in [1], where the application of such a type of analysis was presented. It is necessary to underline, that in those article the application of these principles to carry out the analysis and energy assessment of the vibroisolation system for pneumatic hammer in whole system human being – tool – base was described. So this is completely different application than this one which determines the subject of this paper. Nevertheless, the results obtained by Dobry were in accordance with the results of experimental energy investigations, what places this kind of energy approach in the line from the point of view of the other applications. The leading idea of this paper is the conception of application of the computational procedures which were verified while vibroisolation systems designing and computing to analyze the process of materials fatigue.

The attempt of finding the connections between fatigue strength and the quantity of energy which flow by system in the whole balance will be undertaken. This is the feature which make the fundamental difference between this method and the other methods called “energy method of fatigue strength” in commonly accessible publications. The method described below could be defined as “macro” approach to fatigue process. “Macro” means: without the connection with fracture mechanics methods and without connections with method involving microscopic researches. This approach, which is for the moment on the stage of preparing and elaborating simulation models (with use of MATLAB/Simulink program), will be verified during the experiment which is planned in the near future.

The two energy principles, which will make the base of investigations, run as follows:

First Principle of Energy Flow in Mechanical System [1]:

“The sum of increment the internal energy of mechanical system and the energy in the output of system is equal to work of external forces which act on system in the input diminished by the increment of energy of dissipation”

While using the principle above, it is necessary to take in consideration the following assumption [1]: there is no accumulation and no heat flow in its pure form in the system. Assuming that the increment of heat provided to system is equal zero ($Q_{dop} = 0$) one can write the first Thermodynamic Principle for mechanical system as follows [1]:

$$\Delta E_{syst} = L_{sz} - \Delta E_{wy} = \Delta(E_k + U) + \Delta E_{str} \tag{1}$$

The equation above can be rewrite in the other form [1]:

$$L_{sz} - \Delta E_{str} = \Delta(E_k + U) + \Delta E_{wy} \tag{2}$$

In this formula one can distinguish: E_k - kinetic energy (internal), U - potential energy (internal), $\Delta(E_k + U)$ - the increment of internal energy, L_{sz} - work of external forces on the input to system, ΔE_{wy} - increment of output energy.

The consideration above can be written down with use only of energy increments. Below, one can find the equation which is mathematical note of First Principle of Energy Flow in Mechanical Systems [1]:

$$\Delta E_{we} - \Delta E_{str} = \Delta E_{od} - \Delta E_{wy} \tag{3}$$

ΔE_{od} - the increment of reflected energy

What called attention is the term: reflected energy, which is the sum of inertial energy and spring energy. First Principle of Energy Flow, after double-sided differentiation, and its application to system with one degree of freedom, enables to show the instantaneous values of energy flow i.e. the power. One can obtain in such a way the equation (4) which shows the power distribution in mechanical system:

$$W(t)\dot{x}(t) - c[\dot{x}(t)]^2 = m\ddot{x}(t)\dot{x}(t) + kx(t)\dot{x}(t) \tag{4}$$

The equation (4) expresses the First Principle of Power Distribution in Mechanical Systems [1]. This principle can be derived from First Principle of Energy Flow in Mechanical Systems and it was demonstrated above.

As far as the general form of energy equation is concerned, it is necessary to remark, that this is the increment of dissipation energy which poses the biggest problem to be identified. Input energy, output energy and reflected energy are possible to be observed by using the vibrations measurements. On the contrary, the dissipation energy must be calculated from the equation, what is possible when one know the value of these three mentioned above. The basic problem, which must be solved before using the both principles is to elaborate the proper dynamic model. Before simulation, it was necessary to prepare the conception of real system which will be subjected to vibrations. Than the reduction point was chosen and the physical and mathematical model were elaborated. The problem of reduction point concerns the problem of replacing the system with the continuous parameters by the system with discrete parameters. The point on the end of semi-beam subjected to vibrations was chosen as reduction point.

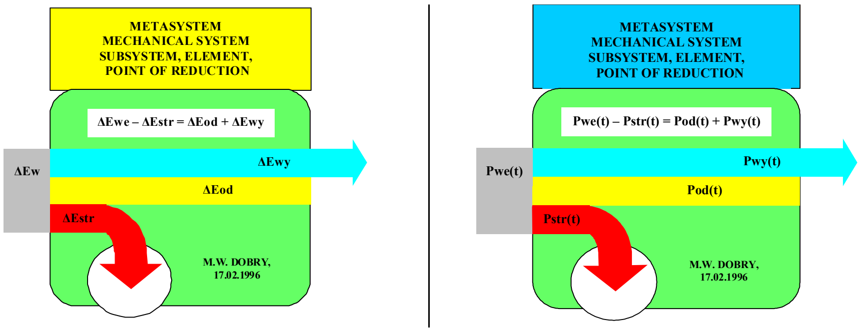

Figure 1. At left side: graphic interpretation of First Principle of Energy Flow in Mechanical System; at right side: graphic interpretation of First Principle of Power Distribution [1]

The physical model of the system is the spring-mass-dissipative system with one degree of freedom excited to movement by kinematic input function. The rate of dissipation is depending on internal dissipation in material and on the dissipation in the holder. In the investigated system the damping ratio were assumed to be equal ξ = 0,01, that is the standard value for steel.

The differential equation of motion for the system runs as follow:

$$m_z \ddot{x}_1(t) + c_z \dot{x}_1(t) + k_z x_1(t) = k_z x_0(t) + c_z \dot{x}_0(t) \tag{5}$$

The idea of practical application of the principles described above consist on using the equation (4) for harmonic input function[1]:

$$E_{we}[P(t)] = \int_0^T P(t)V(t)dt = \int_0^{2\pi/p} P_0 \sin(pt) A_0 p \cos(pt - \varphi)dt = ... = \pi \cdot P_0 A_0 \sin\varphi \tag{6}$$

P_0 – Force amplitude, A_0 – Velocity amplitude, φ –Phase shift,

By multiplying the instantaneous value of force which is exerted on reduction point by instantaneous value of velocity, one can obtain the instantaneous input power which in the moment fall on the reduction point. Then, by integrating such a product of instantaneous values, one can obtain the value of energy dose which flowed in the specified period of time.

The term “flowed” does not determine if the energy was dissipated, accumulated or if maybe it leave out the system. To could conduct this analysis it is necessary to divide the whole energy into three types of structural energies. Viz. in the mechanical system one can distinguish: spring energy, inertial energy, and dissipation energy.

The distribution of input energy on three types mentioned above and the proportion of this distribution depend on the proportion of force function frequency to natural frequency of the system (nondimensional frequency) and it depends on the dynamic parameters of system. The range for which $\delta > 1$ is called above-resonance, the range for which $\delta < 1$ is called under-resonance and the exact value $\delta = 1$ means the movement in resonance. This terminology will be used in the next part of article.

The correlation of terminology used in energy principles of Dobry with commonly known theory of damped oscillator may require some additional explanations. While considering the damped oscillator the terms of kinetic energy, potential energy and work of friction force are used. It is very important to underline the difference between kinetic energy and inertial energy in Dobry meaning. The first one depends from velocity and mass while The Principles of Dobry concern the acceleration. Inertial energy depends on mass and acceleration and there is no direct connection with velocity. Noticing this fundamental difference is very important to proper comprehension of the energy discussion below.

3. Simulation models

In order to implement the new energy method the simulation models in Matlab/Simulink were prepared. On the input to model the data concerning the sample are introduced. These data are: the length of beam, the height and the width of cross-section (for rectangular section), the degree of damping (which covers internal damping in material and in the holder) and the weight of the mass which is attached to the tip of the beam. The parameters of kinematic function are defined (the frequency of vibrations and the amplitude of displacements exerted by vibrator). The main element of the program created in MATLAB/Simulink is MWD Elementary Energy Flow Processor. On the input of this subsystem the dynamical parameters of the system are introduced. The second sort of data are signals representing the instantaneous values of displacements, velocities and accelerations which are the results of solving the differential equation of motion. The suitable operations make it possible to calculate (basing on these data) the instantaneous values of power. The analysis of percent share of every type of structural energy is possible too. So far, the simulations experiments that were conducted, confirmed the conception of change of share of every type of energy in the whole energy depending on the range of work (above-resonance or under-resonance). It can be noticed on the chart (figure nr 2). One can observe that if the sample is subjected to vibration that the frequency is lower than its natural frequency, the biggest share in all power is for spring power. It is worth to say, that the emergency situations taking place during the operating processes of many technical objects, confirm this energy theory. The damages take place very often in low frequency range. The energy methods provide the possibility to explain this phenomena by the fact that in the low frequency range there is the biggest share of spring energy in the whole energy dose. The chart shows that the share of spring power and inertial power is equal for the resonance.

The future aim of experiment is to calculate the exactly dose of energy that is introduced to the system by the specified way of exerting load on the system. It is necessary to underline that the energy which flows by system depends not only from the parameters of exciting function but from the dynamical parameters of investigated system also (investigated system is the sample subjected the experiment). The simulation models make it possible to calculate the dynamical stresses in material. For example for the steel sample: length of 250 mm, height and the width of cross-section (rectangular section): 2,5x25 mm one can obtain the stresses about 200 MPa for the frequency of 8 Hz.

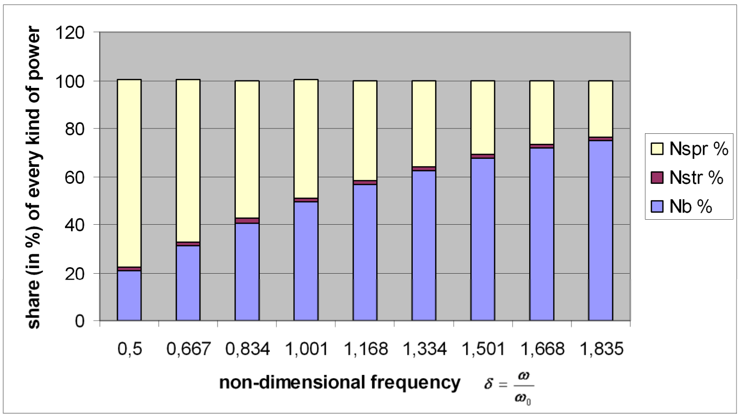

Figure 2. Chart showing how the share of every kind of structural power depends on non-dimensional frequency

As it was mentioned, as far, the experiment which is conducted only as the simulation is planned to be conducted in reality. At the beginning, it is planned to carry out the experiment with use of materials for which the fatigue parameters and the load curves are known and accessible in literatures and publications. It will be some kind of validation of the method. The main idea which is tied up with implementation of new energy method is to indicate, that the term “dose of energy” can be equivalent to the term of quantity of cycles for the specified level of stresses. In that way the energy method could be treated as alternative in relation to the approach employed up to now, and consisting on conducting the classical fatigue analysis. The term “Classical fatigue analysis” means all the measures having on aim to find the relation between the quantity of cycles that material can support and the value of stresses, the type and the shape of exciting force function.

Commonly accessible literature concerning the fatigue process employs the terms: energy of plastic strain and energy of elastic strain. The object of conducted fatigue investigation will be subjected the loads evoking the stresses below the yield point. Nevertheless it does not permit to neglect the plastic strain. It is known and very well described in literature that the process of material degradation bring about the structure change, which manifests itself by the change of dynamic parameters of sample [6]. The fracture mechanics provides the knowledge about how is the structure of the front of fracture [5], [7]. There is the zone of plastic strain. This problem can be taken into consideration by the appropriate approach to energy of dissipation. The fatigue process evokes the increment of damping ratio and the dissipation energy depends on this ratio.

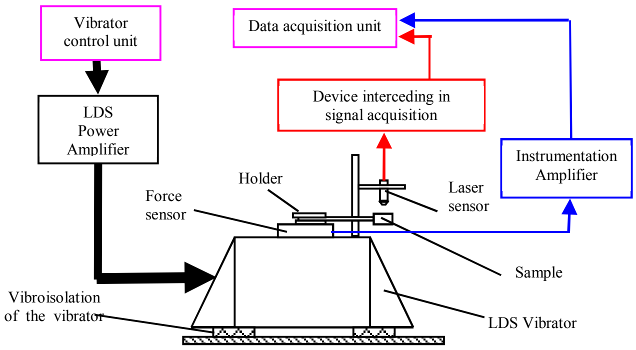

Figure 3. The test stand scheme

3. Conclusions

In the paper above the new concept of approach to fatigue calculation was presented. The look from the new point of view is expected to bring the possibility of work out the new energy criterion of material fatigue assessment. One of the main aim of the investigations will be the recognize the range of unlimited fatigue strength. As it is very well describe in the literature some materials (for example: many non-ferrous alloys) do not have the range of unlimited fatigue strength. The Wohler Diagram for these materials is descending in the whole range. Meanwhile the steel for example is the material, for which it is possible to indicate such a value of load, for which even the infinite quantity of cycles will not bring about its destruction. The look on this problem from the point of view of energy flow may provide the possibility to make this phenomena more clear.

References

1. M. W. Dobry, *Optymalizacja przepływu energii w systemie Człowiek – Narzędzie – Podłoże (CNP)*, seria: Rozprawy Nr 330, Wyd. Politechniki Poznańskiej, Poznań 1998
2. M.W. Dobry, *Pierwsza Zasada Przepływu Energii jako podstawa uogólnionej metody analizy dynamicznej systemów mechanicznych*, Konferencja Napędy'99 Szczyrk 1999
3. M.W. Dobry, W. Marciniak, *Metoda energetyczna analizy obciążeń dynamicznych systemu mechanicznego*, XIV Konferencja naukowa WIBROTECH, Kraków 2008
4. Z. Dyląg, Z. Orłoś, *Wytrzymałość zmęczeniowa materiałów*, WNT, Warszawa 1962
5. S. Kocańda,, J. Szala, *Podstawy obliczeń zmęczeniowych*, PWN, Warszawa 1997
6. S. Kocańda, *Zmęczeniowe pękanie metali*, WNT, Warszawa 1985
7. A. Neimitz, *Mechanika pękania*, PWN, Warszawa 1998

XXV Symposium *Vibrations in Physical Systems,* Poznan – Bedlewo, May 15-19, 2012

General Numerical Description of a Mass Moving Along a Structure

Bartłomiej DYNIEWICZ
Institute of Fundamental Technological Research, Polish Academy of Sciences
Pawińskiego 5b, 02-106 Warsaw, Poland, bdynie@ippt.gov.pl

Czesław BAJER
Institute of Fundamental Technological Research, Polish Academy of Sciences
Pawińskiego 5b, 02-106 Warsaw, Poland
The Faculty of Automotive and Construction Machinery Engineering
Warsaw University of Technology, Narbutta 84, 02-524 Warsaw, Poland
cbajer@ippt.gov.pl

Abstract

The paper deals with vibrations of structures under a moving inertial load. The space-time finite element approach has been used for a general description of the moving mass particle. Problems occur when we perform computer simulations. In the case of wave problem numerical description of the moving inertial loads requires great mathematical care. Otherwise we get a wrong solution. There is no commercial computing packages that would enable us direct simulation of moving loads, both gravitational and inertial.

Keywords: space-time finite element method, moving mass, vibrations

1. Introduction

Engineering structures under moving loads is the important research topic in many diverse fields of engineering. Moving loads are widely used i. a. in transportation. A vehicle travelling along a road plate or airfield plate is one of numerous practical applications. A complete description of the problem should contain both gravitational and *inertial* action of moving load. Implementation of gravitational moving forces is simple in analytical and numerical approaches. Since it does not depend on solution, it requires only an ad hoc modification of the load vector. Much more complex are moving inertial loads. Inclusion of inertia of the moving load requires not only modification of the right-hand side vector, but also affects selected parts of global matrices of inertia, damping and stiffness of the system. Acceleration of the moving mass particle is described by the well known Renaudot formula

$$\frac{d^2 w(\mathbf{v}t,t)}{dt^2} = \left.\frac{\partial^2 w(x,t)}{\partial t^2}\right|_{x=\mathbf{v}t} + 2\mathbf{v}\left.\frac{\partial^2 w(x,t)}{\partial x \partial t}\right|_{x=\mathbf{v}t} + \mathbf{v}^2 \left.\frac{\partial^2 w(x,t)}{\partial x^2}\right|_{x=\mathbf{v}t} . \tag{1}$$

Adequate terms correspond to the transverse, Coriolis and centrifugal acceleration. Several papers [1, 2, 3, 4] discuss a numerical description of the moving mass in the finite element formulation, applied to the Euler beam and Kirchhoff plate. Interpolation of displacements by 3rd order polynomials is simple. It facilitates the derivation of the matrices describing the traveling mass particle (1). Matrices known from the literature are not comprehensive. They are not suitable for general applications. In the case of the wave equations (string, Timoshenko beam, Mindlin plate) we take into account a linear relationship between displacements and angles of rotation in neighbouring nodes. In the paper [5] classical finite element formulation of the moving mass travelling along the Timoshenko beam was proposed.

This paper presents a space-time approach to the moving mass problem. Characteristic matrices in the case of thin and thick plates were derived.

2. Finite element carrying a moving mass

Numerical formulation of a moving mass is performed by space-time finite elements method [6, 7, 8]. This method consists of discretization of equations of motion both in space and time. In this case velocity variant and stationary mesh was used. Finally we obtain the system of algebraic equations $\mathbf{K}^* \mathbf{v} + \mathbf{e} = 0$ with velocities as unknowns. In order to calculate nodal displacements vector we use the following formula

$$\mathbf{w}_{i+1} = \mathbf{w}_i + h\left[\beta \mathbf{v}_i + (1-\beta)\mathbf{v}_{i+1}\right]. \tag{2}$$

Let us consider space-time finite element carrying mass m moving at a constant speed $\mathbf{v}$. Virtual energy in the domain $\Omega = \{(x,t)\colon 0 \le x \le b,\ 0 \le t \le h\}$, is written by the equation

$$\Pi_m = \int_0^h \int_0^b v^* \cdot \delta(x - x_0 - \mathbf{v}t)\, m \frac{d^2 w(\mathbf{v}t, x)}{dt^2} dx dt\,. \tag{3}$$

Dirac delta δ defines the position of the moving mass. v^* is the virtual velocity. However, the acceleration of the moving mass is given by (1). We apply linear interpolation of the nodal velocity

$$v(x,t) = \sum_{i=1}^{4} N_i(x,t) v_i\,. \tag{4}$$

where the shape function takes the following form

$$\mathbf{N} = \left[\frac{1}{bh}(x-b)(t-h),\ -\frac{1}{bh}x(t-h),\ -\frac{1}{bh}(x-b)t,\ \frac{1}{bh}xt\right]. \tag{5}$$

Displacement function is a result of the integration of (4)

$$w(x,t) = w(x,0) + \int_0^t \mathbf{N}\mathbf{v} dt\,. \tag{5}$$

The virtual velocity is described with Dirac function

$$v^* = \delta(t - \alpha h)\left[\left(1 - \frac{x}{b}\right) v_3 + \frac{x}{b} v_4\right]. \tag{5}$$

Linear interpolation of nodal physical parameters with shape functions unables determination of a centrifugal acceleration of the moving mass particle. We rewrite (1) in the equivalent form

$$\frac{d^2 w(\mathbf{v}t,t)}{dt^2} = \left.\frac{\partial v(x,t)}{\partial t}\right|_{x=\mathbf{v}t} + \mathbf{v}\left.\frac{\partial v(x,t)}{\partial x}\right|_{x=\mathbf{v}t} + \mathbf{v}\frac{d}{dt}\left[\left.\frac{\partial w(x,t)}{\partial x}\right|_{x=\mathbf{v}t}\right]. \tag{8}$$

We assume the backward difference formula to the third term of (8). We have then

$$\frac{d}{dt}\left[\left.\frac{\partial w(x,t)}{\partial x}\right|_{x=\mathbf{v}t}\right] = \frac{1}{h}\left[\left.\frac{\partial w(x,t)}{\partial x}\right|_{x=\mathbf{v}t}\right]^{t+h} - \frac{1}{h}\left[\left.\frac{\partial w(x,t)}{\partial x}\right|_{x=\mathbf{v}t}\right]^{t}. \tag{9}$$

The upper indices indicate time at which the respective terms are defined. At~time of transition of the moving load between the elements k and $k+1$ (Fig. 1), the current

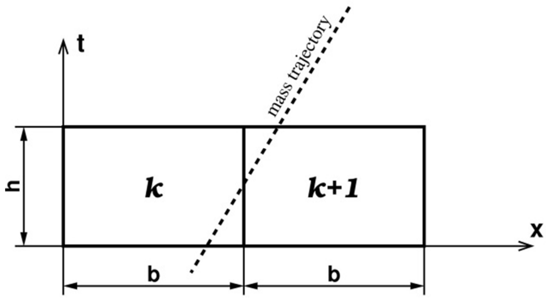

Figure 1. The transition mass between elements.

displacements are computed based on displacements the neighbouring element $k+1$

$$\left[\left.\frac{\partial w(x,t)}{\partial x}\right|_{x=\mathbf{v}t}\right]^{t+h} = \frac{1}{b}\left(w_4^{k+1} - w_3^{k+1}\right), \tag{10}$$

however, the initial displacement in the element k equals

$$\left[\left.\frac{\partial w(x,t)}{\partial x}\right|_{x=\mathbf{v}t}\right]^{t} = \frac{1}{b}\left(w_2^{k} - w_1^{k}\right). \tag{11}$$

The lower indices indicate the number of nodes. According to (2), (10), and (11) the finite difference scheme (9) is written as follows

$$\begin{aligned}\frac{d}{dt}\left[\left.\frac{\partial w(x,t)}{\partial x}\right|_{x=\mathbf{v}t}\right] &= \frac{1}{bh}\left(w_2^{k+1} - w_2^{k} - w_1^{k+1} + w_1^{k}\right) + \\ &+ \frac{1}{b}\left[-\beta v_1^{k+1} + \beta v_2^{k+1} - (1-\beta)v_3^{k+1} + (1-\beta)v_4^{k+1}\right].\end{aligned} \tag{12}$$

The accurate solution is obtained with β = 1 – α [9]. Therefore, we can write

$$\frac{d}{dt}\left[\left.\frac{\partial w(x,t)}{\partial x}\right|_{x=\mathbf{v}t}\right]=\frac{1}{bh}\left(w_2^{k+1}-w_2^k-w_1^{k+1}+w_1^k\right)+ \\ +\frac{1}{b}\left[-(1-\alpha)v_1^{k+1}+(1-\alpha)v_2^{k+1}-\alpha v_3^{k+1}+\alpha v_4^{k+1}\right]. \tag{13}$$

Classical minimization of the energy (3) results in the following matrices

$$\mathbf{M}_m=\frac{m}{h}\left[\begin{array}{cc|cc} -(1-\kappa)^2 & -\kappa(1-\kappa) & (1-\kappa)^2 & \kappa(1-\kappa) \\ -\kappa(1-\kappa) & -\kappa^2 & \kappa(1-\kappa) & \kappa^2 \end{array}\right], \tag{14}$$

$$\mathbf{C}_m=\frac{2m\mathbf{v}}{b}\left[\begin{array}{cc|cc} (\kappa-1)(1-\alpha) & (1-\kappa)(1-\alpha) & (\kappa-1)\alpha & (1-\kappa)\alpha \\ -\kappa(1-\alpha) & \kappa(1-\alpha) & -\kappa\alpha & \kappa\alpha \end{array}\right], \tag{15}$$

and vector of nodal forces at the beginning of the time interval

$$\mathbf{e}_m=\frac{m\mathbf{v}}{bh}\left[\begin{array}{c} (1-\kappa)\left(w_2^{k+1}-w_2^k-w_1^{k+1}+w_1^k\right) \\ \kappa\left(w_2^{k+1}-w_2^k-w_1^{k+1}+w_1^k\right) \end{array}\right], \tag{16}$$

The coefficient κ describes the instantaneous position of the mass in the spatial element

$$\kappa=\frac{x_0+\mathbf{v}\alpha h}{b} \quad 0<\kappa\le 1\,. \tag{17}$$

We must emphasize here that the centrigugal forces are contributed in the vector $\mathbf{e}_m$ and is not described by a separate term. In the case of direct differentiation of (1) we lose information of nodal forces represented by (16). Vector $\mathbf{e}_m$ has nonzero values during the transition of the mass between neighbouring space-time elements. It can not be omitted since it contributes vital mathematical quantity, even if it mostly equals zero. The matrices (14)-(15) and the vector (16) contribute only the moving inertial particle effect. The matrices of the mass influence in a finite element of a structure must be added to the global system of equations.

3. Numerical examples

First we will consider a thin plate. Respective finite element formulation related to the plate can be found for example in [10]. We use thin plate elements in the simulation of a plate vibrations under a mass moving along the symmetry axis of the plate. The data assumed: thickness $t = 0.4$ m, dimensions $l_x = l_y = 12$ m, Young modulus E = 30 MPa, Poisson coefficient $\nu = 0.2$, mass density $\rho = 2400$ kg/m^3, the moving load composed of the mass $m = 10^4$ kg and related force P = 9.81 · 10^4 N.

In the case of thick plate we consider the Mindlin model of the plate. We use the formulation given for example in [11, 12]. We assume linear distributions of both displacements and rotations along the element, according to the interpolation functions. Comparisons of numerical and semi-analytical solution were done. The excellent coincidence is exhibited. Influence of inertia of the moving load solutions are depicted in Figs. 2 and 3. Displacements of the contact point and the center of the plates are depicted. w_0 denotes the static displacement of the center of the Kirchhoff plate.

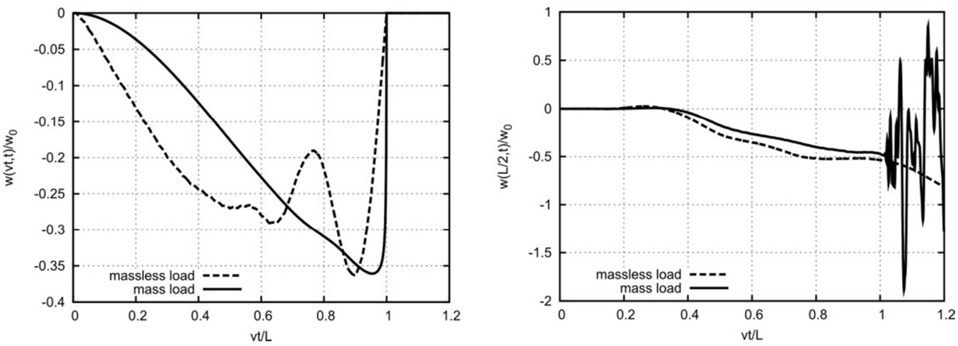

Figure 2. Vertical displacements at the contact point and at the middle of the Kirchhoff plate (thickness = 0.1 m, v = 360 km/h)

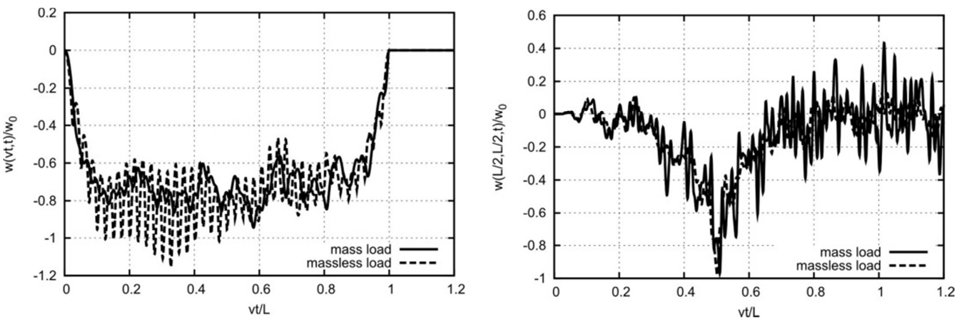

Figure 3. Vertical displacements at the contact point and at the middle of the Mindlin plate (thickness = 1 m, v = 360 km/h)

4. Conclusions

Original finite elements carrying a moving mass particle were elaborated. The presented approach is general and allows the accurate modelling of the point mass traveling with a constant velocity in numerical computations by using the space-time finite element method. The results confirm the significant influence of the inertia of the moving load on the solutions.

Acknowledgment

This work has been supported by The National Centre for Research and Development (NCBiR) under the grant No. LIDER/26/40/L-2/10/NCBIR/2011 and by the Foundation for Polish Science.

References

1. D. M. Yoshida and W. Weaver. *Finite-element analysis of beams and plates with moving loads*. Intl. Assoc. Bridge Struc. Engr. **31**(1) (1971) 179-195.
2. F. V. Filho. *Finite element analysis of structures under moving loads*. The Shock and Vibration Digest, **10**(8) (1978) 27-35.
3. A. O. Cifuentes. *Dynamic response of a beam excited by a moving mass*. Finite Elem. Anal. and Des., **5**(3) (1989) 237-246.
4. J. R. Rieker, Y. H. Lin, and M. W. Trethewey. *Discretization considerations in moving load finite element beam models*. Finite Elem. Anal. and Des., **21** (1996) 129-144.
5. B. Dyniewicz and C. I. Bajer. *Numerical methods for vibration analysis of Timoshenko beam subjected to inertial moving load*. In C. Cempel, editor, Vibrations in Physical Systems, pages 87-92, 2010.
6. M. E. Gurtin. *Variational principles for linear elastodynamics*. Arch. Rat. Mech. Anal., **16** (1964) 34-50.
7. M. E. Gurtin. *Variational principles for linear initial – value problems*. Quart. Appl. Math., **22** (1964) 252-256.
8. I. Herrera and J. Bielak. *A simplified version of Gurtin's variational principles*. Arch. Rat. Mech. Anal., **53** (1974) 131-149.
9. C. Bajer. *Space-time finite element formulation for the dynamical evolutionary process*. Appl. Math. and Comp. Sci., **3**(2) (1993) 251-268.
10. O. C. Zienkiewicz. *The finite element method in engineering science*. McGraw-Hill, London 1971.
11. R. Cook, D. S. Malkus, and M. E. Plesha. *Concepts and applications of finite element analysis*. John Willey & Sons, third edition 1989.
12. M. Petyt. *Introduction to finite element vibration analysis*. Cambridge University Press, Cambridge 1990.

XXV Symposium *Vibrations in Physical Systems,* Poznan – Bedlewo, May 15-19, 2012

Non-Hertzian Contact Model in Wheel/Rail or Vehicle/Track System

Bartłomiej DYNIEWICZ
Institute of Fundamental Technological Research, Polish Academy of Sciences
Pawińskiego 5b, 02-106 Warsaw, Poland
bdynie@ippt.gov.pl

Czesław BAJER
Institute of Fundamental Technological Research, Polish Academy of Sciences
Pawińskiego 5b, 02-106 Warsaw, Poland
and Faculty of Automotive and Construction Machinery Engineering
Warsaw University of Technology, Narbutta 84, 02-524 Warsaw, Poland
cbajer@ippt.gov.pl

Abstract

In the paper the spring-mass system describing the moving load, determined with the Hertz theory, was replaced with the spring-mass system with an inertial part being in contact with the beam, rail, or a track. Computational problems can be reduced significantly. Results are qualitatively and quantitatively improved, especially at higher range of the speed, related to critical values.

Keywords: wheel/rail contact, train-track system, moving loads

Introduction

Numerical dynamic analysis of engineering problems nowadays successfully replace experimental or real scale investigations. Unfortunately there exist several problems that can not be easily treated by computer means. Such are problems with moving loads, especially with inertial moving loads. There are two main reasons of difficulties. The first one concerns problems with numerical description of inertial particles moving along finite elements. Despite the massless load can be applied to the system in an extremely simple way, the inertia attached to the moving force vector require modification of matrices in the system of differential equations describing the motion of the whole system. The second problem occurs when we compute frequencies of the response of the structure subjected to a moving load system with required accuracy. In engineering practice quantitative results start to be essential in numerical simulations. This is a fundamental reason why we push our research from cost experiments towards numerical analysis.

Preliminary calculations exhibit significant difference of results obtained with the use of a massless load acting to the track and with the use of the inertial moving load. The point mass increasing the inertia of the continuous track significantly changes the dynamic response. The fundamental question then is what part of a wheel or wheelset can be attached to the track to give more realistic response. More realistic means in our case more accurate amplitudes of displacements or accelerations, and more accurate frequencies of vibrations under the load moving at high speed, comparing with experimental measurements. We consider the speed in the near critical range, both under and over-critical. The contributing numerical observations must last a few seconds of the real time to enable the vehicle pass a few hundred meters. The dynamic analysis of a long-term response of the track to a moving vehicle or a train can be successfully carried on with the use of multi-scaled numerical computations. The analysis of the wheel-rail system allowed us to determine the partition of the wheel between the part moving along the rail, being in contact with the rail, and a part that subjects the rail through an elastic massless element, considered as a part of the spring-mass system that describes the vehicle.

In the paper we intend to demonstrate the dynamic analysis of vehicle–track system, with the influence of the inertia of the load. The monograph by Fryba [1] treats problems of structures only under moving massless loads. The theoretical analysis of the problem of an inertial load is presented in [2, 3, 4]. Numerical analysis could not be previously efficiently performed. Existing examples of a beam vibrations published in literature concern relatively low moving velocity and even in this case exhibit significant errors. At higher speed presented solutions differ significantly with accurate results. In the case of pure hiperbolic differential equations which describe a string or a bar vibrations, integrated numerically by the step-by-step schemes resulting solutions diverge. In a series of papers [5, 6, 7] we explain how to derive elemental matrices that carry a moving mass particle and apply them to the finite element method or space-time finite element method. In all cases displacements of the contact point in the static equilibrium state are equal, although dynamic responses differ.

The next important feature is related to the interesting property of the differential equation describing the Timoshenko beam or simpler case, the string. The detailed analysis of the solution exhibits discontinuity of the inertial particle trajectory in the neighbourhood of the rear support, in the case of simply supported span. The phenomenon was first analysed in the case of a string, mathematically proved and published in [2]. It is also observed in the case of of a Timoshenko beam or a thick plate. We can discuss whether this effect of the shock is noticably in reality. Practics gives the positive answer. Examples of the effect can be noticed in the case of electric cables of the train traction being in contact with a moving pantograph power receiver. As another example we can consider road plates. During the motion of vehicles significant force jumps are registred at final stage of the passage.

Let us compare trajectories of contact points under the load. Figure 1 depicts the comparison of mass and massless load moving on the Euler and Timoshenko beam. In this comparison dimensionless unitary data were assumed.

Left-hand side plot exhibit the mass trajectory while the right-hand side plots depict deflection in the middle of the span. Results obtained for the case of both types of beams differ considerably. Other structures, i.e. strings, plates etc. exhibit similar differences in the case on pure force and the force with a point mass as a load.

In the paper we will demonstrate, that the computational model should be assumed with attention. Detailed analysis of one phenomenon in micro-scale could be less valuable if the model of a whole structure is far from the real one. We will demonstrate that results obtained with different numerical tools differ significantly and, what is more, differ from the real registered signal. The classical track will be considered. However, the identical analysis can be performed for the ballast-less track and track with Y-type sleepers.

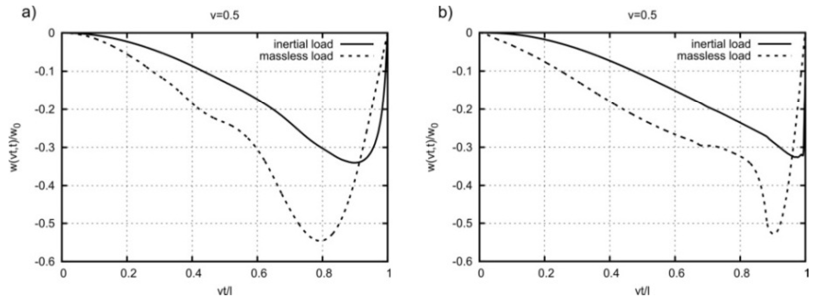

Figure 1. Comparison of the load trajectories on the (a) Euler and (b) Timoshenko beam in the case of inertial and massless load for the speed v = 0.5.

2. Analysis of the attached mass

Classical approach to the whel-rail contact analysis is based on the Hertz theory. The contact between the rail and the wheel is then nonlinear and is massless (Fig. 2a). The contact stiffness between the wheel ring and the rail head depends on the type of the wheel and equals 500–580 MN/m. The wheel disc has the rigidity equal 500 MN/m in the case of tyred wheel and overpass 900 MN/m in the case of the monoblock wheel. The averaged stiffness of the entire wheel equals 250 MN/m for tyred wheel and 355 MN/m for monoblock wheel.

At the first stage we must establish the percentage of the wheel that influences the track motion. The aim is not easy. We should solve the inverse problem to determine parameters of the problem: attached mass, sprung mass, and spring stiffness. Moreover, the identification of parameters depends on the velocity of the motion and may be influenced by other vehicle and track parameters. We must emphasize here that the contact between the wheel and the rail is non-linear.

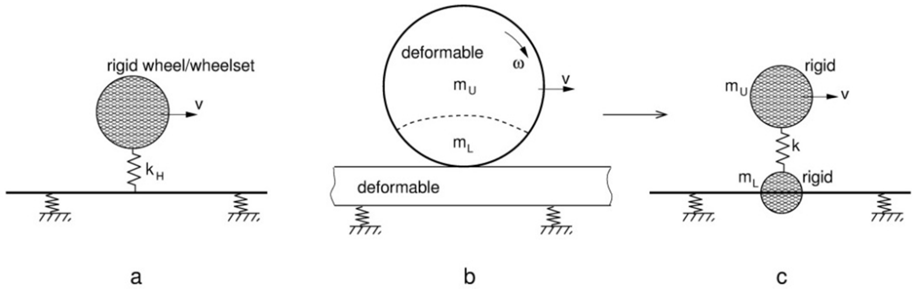

Figure 2. Replacement of a continuous system with a rigid-body system: a) classical Hertz contact model, b) and c) proposed approach.

We solved two problems to determine unknown parameters m_L, m_U, and the stiffness k of the alternative simplified model of the wheel placed on the rail (Fig. 2). In the first one we assume the velocity $v = 0$. In this case displacements in time of the contact point A $u_A(t)$ and accelerations $\ddot{u}_A(t)$ are registered. In the simplified model excited with the same initial conditions appropriate quantities $\tilde{u}_A(t)$ and $\tilde{\ddot{u}}_A(t)$ are measured in the same point, i.e. in the point of a beam at the center of the mass m_L. The objective function that estimates the quality of the selection of parameters is as follows:

$$I_1 = \int_0^{t_f} \alpha(t)\,[u_A(t) - \tilde{u}_A(t)]^2 dt + \int_0^{t_f} \beta(t)\,[\ddot{u}_A(t) - \tilde{\ddot{u}}_A(t)]^2 dt \tag{1}$$

$\alpha(t)$ and $\beta(t)$ are weight functions that determine validity of consideration of displacements and accelerations in time.

In the second problem we assume rolling of a wheel. Appropriate objective function is similar:

$$I_2 = \int_0^{t_f} \alpha(t)\,[u(vt,t) - \tilde{u}(vt,t)]^2 dt + \int_0^{t_f} \beta(t)\,[\ddot{u}(vt,t) - \tilde{\ddot{u}}(vt,t)]^2 dt \tag{2}$$

3. Numerical model

We assume the spring-beam system model of a vehicle. This is a simplified model, however it sufficiently represents the dynamic properties of the real vehicle. Proper stiffness, inertia and damping allows us to obtain dynamical response coinciding with a real response.

The track model can be composed of plates, beam, grid or frame elements and springs. Simple or complex track structure can be considered. Below we will consider the simplest classical track, built of grid elements placed on the elastic Winkler foundation, springs which model elastic pads and grid elements describing the geometry of rails, straight or curved.

4. Examples

Now let us have a look at a real example of vibrations of a carriage moving on a classical track. We use custom computer software implementing the numerical approach presented in this paper. We assume geometric and material data from [8]. In the Fig. 4 in the case of a non-inertial load (lower diagrams) we can notice the strong influence of the sleepers. In the case of the inertial load (upper plots) this influence is moderate and the dynamic response is more realistic.

We can compare our results with the reference [8], Fig. 3. Both the inertial load in Fig. 4 and Fig. 3 exhibit a similar range of accelerations of the axle box. The signal in Fig. 3 shows a low frequency mode which is difficult to explain. The response of our simulation has the same level of accelerations and is characteristic of more realistic higher frequency oscillations.

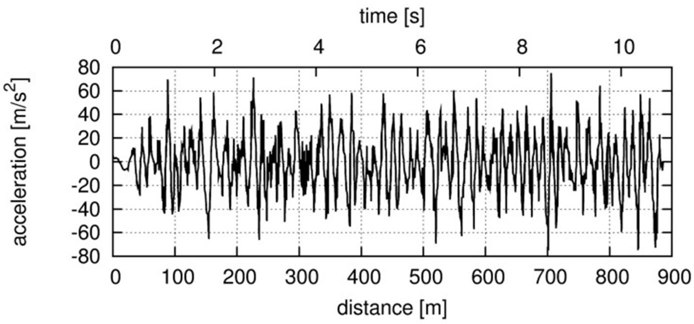

Figure 3. Acceleration of the axle box 290 km/h taken from [8]

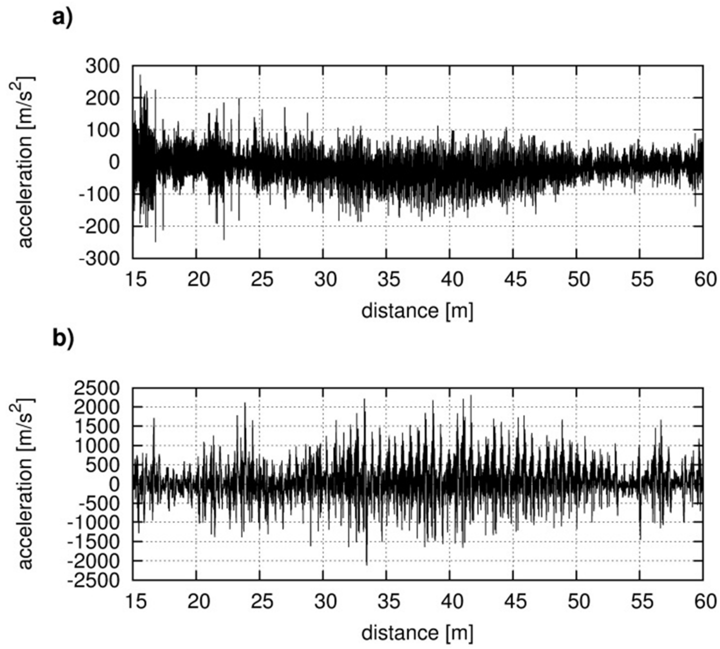

Figure 4. Vertical acceleration of the axle box at 290 km/h with inertial and non-inertial load assumed in the model with rigid ballast: a) inertial load, b) non-inertial load

5. Conclusions

In the paper we explained why the massless load should not be taken to computer simulations. Moreover, the rigid Hertz spring in computational practice is usually chosen arbitrary. Qualitative results can be obtained, but they differ quantitatively in all ranges of vehicle velocity. The inertial load in rigid body models is recommended.

References

1. L. Fryba, *Vibrations of solids and structures under moving loads*. Thomas Telford House 1999.
2. B. Dyniewicz and C. I. Bajer, *Paradox of the particle's trajectory moving on a string*. Arch. Appl. Mech., **79**(3) (2009) 213-223.
3. B. Dyniewicz and C. I. Bajer, *Discontinuous trajectory of the mass particle moving on a string or a beam*. Machine Dyn. Probl., **31**(2) (2007) 66-79.
4. B. Dyniewicz and C. I. Bajer, *New feature of the solution of a Timoshenko beam carrying the moving mass particle*. Arch. Mech, **62**(5) (2010) 327-341.
5. C. I. Bajer and B. Dyniewicz, *Space-time approach to numerical analysis of a string with a moving mass*. Int. J. Numer. Meth. Engng., **76**(10) (2008) 1528-1543.
6. C. I. Bajer and B. Dyniewicz, *Virtual functions of the space-time finite element method in moving mass problems*. Comput. and Struct., **87** (2009) 444-455.
7. C. I. Bajer and B. Dyniewicz, *Numerical modelling of structure vibrations under inertial moving load*. Arch. Appl. Mech., **79**(6-7) (2009) 499-508. DOI: 10.1007/s00419-008-0284-8.
8. G. Diana, F. Cheli, S. Bruni, and A. Collina, *Dynamic interaction between rail vehicles and track for high speed train*. Vehicle System Dynamics, **24** (1995) 15-30.

XXV Symposium *Vibrations in Physical Systems,* Poznan – Bedlewo, May 15-19, 2012

Semi-Active Control of Track Subjected to an Inertial Moving Load

Bartłomiej DYNIEWICZ
Institute of Fundamental Technological Research, Polish Academy of Sciences
Pawińskiego 5b, 02-106 Warsaw, Poland, bdynie@ippt.gov.pl

Dominik PISARSKI
Institute of Fundamental Technological Research, Polish Academy of Sciences
Pawińskiego 5b, 02-106 Warsaw, Poland, dpisar@ippt.gov.pl

Robert KONOWROCKI
Institute of Fundamental Technological Research, Polish Academy of Sciences
Pawińskiego 5b, 02-106 Warsaw, Poland, rkonow@ippt.gov.pl

Abstract

The paper deals with the problem of stabilization of vibrations of the load carrying structure via adaptive damping performed with a smart material. The properties of such a material must ensure reduction of vibrations, especially accelerations and displacements of selected stationary or follower points in a higher range than in the case of the material with homogeneous bilateral characteristics. Analytical calculations and numerical simulations proved the efficiency of the approach. Results obtained with the testing system equipped with magnetorheological controlled dampers will allow us to prove experimentally assumed control strategies and rheological properties of the filling material.

Keywords: control, moving inertial load, vibrations, smart materials

1. Introduction

Historic buildings and buildings founded on grades are particularly vulnerable to vibrations. Historic brick buildings are fragile, very susceptible to deformation. The low susceptibility of the material, which does not succumb to excessive momentary or long-term deformation is the main reason of damages. The negative impact of infrastructure on the surrounding buildings, particularly historic, forces us to take action to reduce the adverse external effects. In this aim, we assume the concept of modification of the track structure, to enable influencing its dynamic properties.

Pioneering concepts of integration semi-active control systems with engineering design, transportation and robotics date back several decades. Systems based on semi-active electro or magnetorheological dampers are an attractive alternative to passive and active systems. Correctly designed algorithms for semi-active control systems produce better results than the passive ones. The low power requirements are a strong competitive with active control systems. Over the years, semi-active systems are replacing passive and active systems. This is thanks to the emergence of more and more interesting design solutions of semi-active vibration absorbers. Today, not only rheological fluids, but also significantly cheaper air foam can be used as a medium of such absorbers. Wealth of properties of actuator opens up new possibilities in the design of control algorithms. Problems associated with optimal control methods of semi-active systems are still open. Mainly due to their nonlinear (bilinear) characteristics.

One of the first concept of semi-active control in mechanical systems was proposed by Karnopp, Crosby and Harwood [1]. In their work they presented the idea of active suppression of the oscillator with one degree of freedom, moving over uneven ground. Damping coefficient was a decision parameter. Solutions developed by the Skyhook algorithm is today one of the most widely used in active suspension control systems for vehicles. The idea was designed to improve comfort of passengers. Giraldo and Dyke [2], and Chen, Tan, Bergman, Tsao [3], showed that Skyhook method also gives good results for the oscillator moving over the simply supported continuum. Semi-active systems have also found numerous applications in structures subjected to seismic excitation. We should mention here works, e.g. Soong [4], and Yoshida, Fujio [5]. The task for semi-active control system was to stabilize the system when lost the equilibrium state.

The paper deals with the concept and the preliminary development of optimal control strategy of a track. Practical verification of received control algorithms requires dynamic measurements on the test stand. The description of the test stand has been done.

2. Optimization of the semi-active track

In this section we present in brief the methodology for solving optimal control problem for the semi-active track. For more details see [6].

The governing equation for the track system is given as follows

$$\dot{x} = Ax + \sum_{i=1}^{m} u_i B_i x + F(x), \quad x(0) = x_0 \ . \tag{1}$$

Here x, u stand for the state vector (composed of vertical displacements and velocities) and the input vector (composed of damping coefficients), respectively. The impact of a moving load on the system is described by $F(x)$. Matrices A and B_i result from both the method of discretization and dampers placement. In (1) the decision parameters u_i are given in nonlinear (bilinear) terms and therefore, none of the standard optimal control method, that leads to close loop solution (for instance LQR), can be here applied. In this project, at first we use the gradient methods to obtain the open loop optimal solutions. As preliminary results showed, the structures of these solutions are in fact the copies of some simple switching patterns. Therefore, it might be possible to synthesize them later in order to get the close loop system. However, experimental validation will be crutial here.

Now we give a general procedure to obtain the open loop solutions. We consider the following optimal control problem

$$\begin{aligned} &u^* = \arg\min_u J(x,u) = \frac{1}{2}\int_0^T \left(\bar{x}^T Q \bar{x} + u^T R u\right) dt, \\ &\text{s.t.} \quad \dot{x} = Ax + \sum_{i=1}^{m} u_i B_i x + F(x), \quad x(0) = x_0, \quad u \in \mathcal{U} = [u_{min}, u_{max}]^m. \end{aligned} \tag{2}$$

By $\bar{x}$ we denote here the vector of displacements, velocities or accelerations, depending on the objective of control. Under the assumption, that the problem (2) is convex and the optimal solution u^* is in the interior of $\mathcal{U}$ we can apply the first order necessary condition. For that purpose we introduce the Hamiltonian $\mathcal{H}$ and the adjoint state p as follows

$$\mathcal{H} = p^T \left(Ax + \sum_{i=1}^{m} u_i B_i x + F(x) \right) - \frac{1}{2}\left(\bar{x}^T Q \bar{x} + u^T R u\right), \quad \dot{p} = -\frac{\partial \mathcal{H}}{\partial x}, \quad p(T) = 0 \tag{3}$$

The necessary optimality condition states that

$$\Delta_{u^*} J = -\frac{\partial \mathcal{H}}{\partial u^*} = 0 \tag{4}$$

Numerical computations, based on the method of steepest descent, can be performed by proceeding the following steps

S1 Guess initial control u_0, set $k \leftarrow 0$.

S2 Solve the state x equation (1) by substituting $u \leftarrow u_k$.

S3 Solve the adjoint state p equation (3) by backward integration.

S4 Compute the descent direction $d_k = \frac{\partial \mathcal{H}}{\partial u}$. If $\|d_k\| < \varepsilon$, then $u^* \leftarrow u_k$ and terminate the procedure.

S5 Choose step size λ_k such that $u_{k+1} = u_k + \lambda_k d_k$ respects the constraints i.e. $u_{k+1} \in [u_{min}, u_{max}]^m$. Optionally perform the line search.

S6 Set $u_{k+1} \leftarrow u_k + \lambda_k d_k$, $k \leftarrow k + 1$ and go to S2.

3. Experimental research

The numerical model was first elaborated. It should enable verification of both real objects and our model stand. A simplification of a moving vehicle to a single point load is excessive. In practice we require much more complex mathematical model to approach a physical object. Vibration of wheelsets and the coupling of vibrations through wheelsets must be taken into account. Analytical solution of the extended model is practically impossible. Approach methods applied to the correct numerical model enable us to obtain sufficiently accurate results. In the project we developed and applied the numerical formulation of the inertial moving load to wave problems [7, 8, 9], at the variable speed of motion. For this purpose, we applied the space-time element method. It allows us a relatively simple and direct description of the moving point mass in time. Numerical simulation in the case of wave approach, i.e. in the case of around critical speed, requires great mathematical care. Otherwise we obtain wrong solutions. Commonly used commercial software packages do not support simulations of the inertial moving load problems.

Models of a track are based on a system of continuous beams (Euler or Timoshenko model). Semi-active dampers are placed between two parallel beams – a supporting and a contact one. They are spread over the length of a track or placed just in selected points. Forces generated by dampers are proportional to the relative speed of its two ends. Damper can generate at least two different values of damping, so parameters in the system can be switched. In addition, the switching possibility should be performed within a short distance of the load passage, several to tens centimeters.

Verification of optimal control algorithms for MR dampers requires experimental investigation of the real object. For this purpose, the concept and design of the experimental test stand has been developed. The model of a boogie was accelerated to a fixed speed, then travelled with a constant speed and after a certain distance decelerated to zero on the final support. Due to the deflection of the rail guideways are selected without the supporting beams. The stiffness of the rail results in the vertical displacements in the range ±17 mm for the mass load 6 kg moving at the constant speed 4 m/s. The limit displacements of the dampers are ±25 mm and the same are limit displacements of the guideway. The efficiency of the experiment is ensured when the amplitude of damped points increases 5 mm. In such a case we can fix our dampers directly to the beams, without supplementary leverage increasing their range of work. The LORD's magnetorheological dampers were used in the stand. Manufacturer of the dampers provides only minimal information about his product. All the other required dynamical data must be determined experimentally at start, i.a. the longitudinal stiffness of the damper caused by gas cushion located in its interior. The gas spring stiffness of the damper was $K_s = 2.66 \div 9.47$ kN. The largest value of the rigidity corresponds to the displacement of 12 mm and the smallest one corresponds to the maximum range of motion of the piston 50 mm.

In addition, the analysis of boogie carrying a moving inertial load was done. The relatively large deflection of the rail could jam the trolley. The drive will be performed with a stepping motor. It is powered by pulse electric current, which means that its rotor is not rotating in a continuous movement, but does the rotation angle of a strictly fixed at every time step. The advantage is the possibility of very rapid acceleration and braking the moving object. This engine via a toothed belt would enable to disperse and stop the weight of 6 kg through 4 m.

The foundation of the test stand is the steel frame. The proposed design of the frame is a multi-section truss. It consists of two-meter components. This allows a simple modification of the test stand, adjusting them to the longer track. In this case, we only need to replace the guide rail and a toothed belt and add a simple truss segment. In the case of foundation plate would not have such possibilities. In addition, taking a lighter frame with the independent ballast will provide greater mobility of the test stand.

The results obtained by numerical simulation enabled the selection of appropriate displacement and acceleration sensors in the track measurement in the test stand. Complete diagram of the measurement sensors has been developed. Measurement of the vertical rail displacement caused by the moving mass will be used laser displacement sensors. These transducers are the best solution. This follows from the fact that laser sensors measure the non-contact method, so it does not introduce disorders into the investigated system. In addition to the laser displacement sensors will be used acceleration sensors with very low weight. Computer model of the test stand with the measurement instrumentation is performed on Fig. (1).

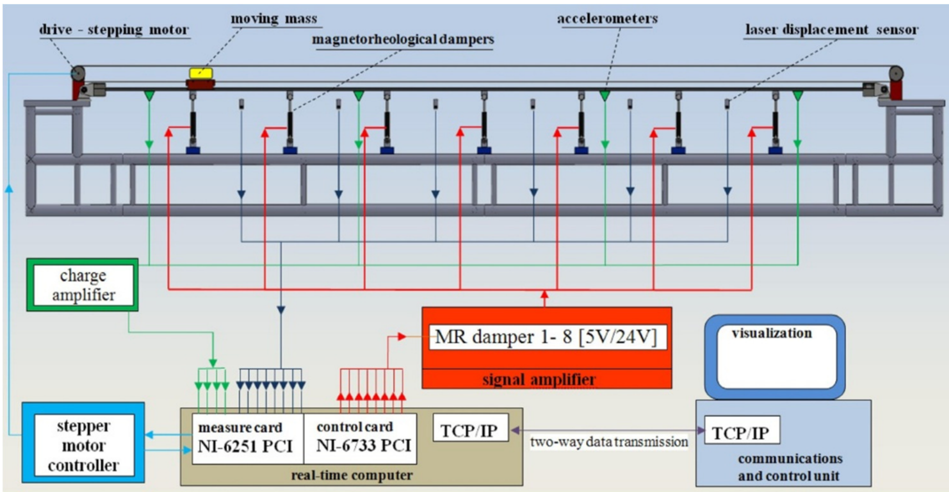

Figure 1. Scheme of the test stand

4. Conclusions

As a result of the project we will elaborate a proposal for a new design of a track. Well designed semi-active control system can be an attractive solution for building protection against surrounding infrastructure. In particular for many priceless monuments, located in town centers and exposed to destructive action of the public railway transport, only the additional smart damping system can be a successful solution to maintain their viability. The low susceptibility of the material, that the monuments are built of, does not succumb to excessive momentary or long-term deformation. The solution for this problem is a concept of modification of the track structure. Semi-active damping layer incorporated into the track can reduce vibration levels propagating into the ground in more efficient way than the traditional vibroisolation.

Acknowledgment

This work has been supported by The National Centre for Research and Development (NCBiR) under the grant No. LIDER/26/40/L-2/10/NCBIR/2011.

References

1. R. Harwood, D. Karnopp, and M. Crosby. *Vibration control using semi-active force generators*. ASME Journal of Engineering for Industry, **96** (1974) 619-626.
2. Sh. J. Dyke and D. Giraldo. *Control of an elastic continuum when traversed by a moving oscillator*. Journal of Structural Control and Health Monitoring, **14** (2002) 197-217.
3. L. A. Bergman, T. C. Tsao, Y. Chen, and C. A. Tan. *Smart suspension systems for bridge-friendly vehicles*. SPIE Proceedings Series, 4696 (2002) 52-61.
4. T. Soong. *Active hybrid and semi-active strucural control*. John Wiley and Sons, 2005.
5. T. Fujio and K. Yoshida. *Semi-active base isolation for a building structure*. International Journal of Computer Applications in Technology, **13** (2000) 52-58.
6. D. Pisarski and C. Bajer. *Smart suspension system for linear guideways*. Journal of Intelligent and Robotic Systems, **62** (3-4) (2001) 451-466.
7. C. I. Bajer and B. Dyniewicz. *Space-time approach to numerical analysis of a string with a moving mass*. Int. J. Numer. Meth. Engng., **76**(10) (2008) 1528-1543.
8. C. I. Bajer and B. Dyniewicz. *Virtual functions of the space-time finite element method in moving mass problems*. Comput. and Struct., **87** (2009) 444-455.
9. C. I. Bajer and B. Dyniewicz. *Numerical modelling of structure vibrations under inertial moving load*. Arch. Appl. Mech., **79**(6-7) (2009) 499-508.

XXV Symposium *Vibrations in Physical Systems,* Poznan – Bedlewo, May 15-19, 2012

Effectiveness of Vibration Reduction of a Nonlinear Dynamic Vibration Eliminator

Zdzisław GOLEC
Poznan University of Technology, Institute of Applied Mechanics
ul. Piotrowo 3 Street, PL 60-965 Poznan
zdzislaw.golec@put.poznan.pl

Abstract

The paper presents the research aimed at effectiveness of elimination of the mechanical system vibration with the use of a nonlinear dynamic vibration eliminator. The considered object has been modeled as a discrete system with two degrees of freedom subjected to force excitation. Nonlinearity of elastic and dissipative properties of the protected object and the eliminator is defined by 3rd order polynomials. Solutions of the equations of motion have been obtained by simulation research with the use of MATLAB® software. Effectiveness of the vibration reduction has been assessed based on the function of the elimination effectiveness defined as the ratio of rms values of the vibration amplitudes of the protected object without the eliminator to the ones occurring with it, in the case of steady motion.

Keywords vibration eliminators, dynamic eliminator, nonlinear vibration, simulation investigation

1. Introduction

The task of elimination of the mechanical vibration consists in minimizing the vibration of the protected object by joining it to an additional mechanical system [1]. Considering a simple model (a discrete one, with two degrees of freedom) of the protected object with the eliminator (Fig. 1) the elastic and dissipative properties *R* of the protected object depend on the deformation *x* and the deformation velocity $\dot{x}$, while the forces *S* acting between the protected object *M* and the eliminator *m* is a function of deformation of the

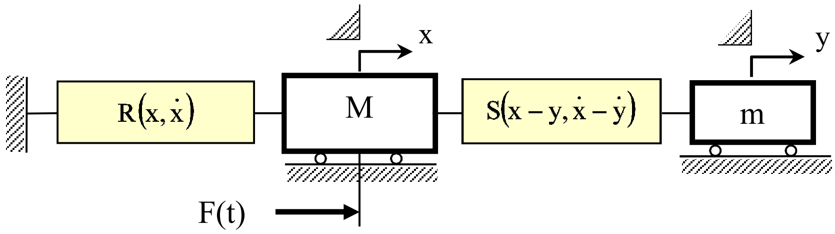

Figure 1. A physical model of protected object with vibration eliminator

coupling element (*x-y*) and the deformation velocity $(\dot{x} - \dot{y})$ of the coupling element

$$R = R(x, \dot{x}),$$
$$S = S[(x - y), (\dot{x} - \dot{y})] \tag{1}$$

According to the form of the *R* and *S* relationships various models of the protected objects and various models of the vibration eliminators may be formulated [2,3,4].

2. Physical model of the protected object provided with dynamic vibration eliminator

The considered object is modeled as a discrete system of two degrees of freedom, with harmonic force excitation (Fig. 2).

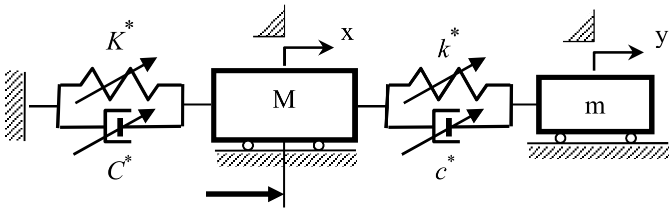

Figure 2. Physical model of the protected object provided with nonlinear dynamic vibration eliminator

The elastic and dissipative properties of the protected object are described by 3rd order polynomials, being the functions of the deformation and deformation velocity:

$$R(x,\dot{x}) = Kx\left(1 + Bx^2\right) + C\dot{x}\left(1 + W\dot{x}^2\right), \tag{2}$$

while the elastic and dissipative properties of the coupling between the protected object and the eliminator are described by 3rd order polynomials, being the functions of the deformation and deformation velocity of the coupling element

$$S(x-y,\dot{x}-\dot{y}) = k(x-y)\left[1 + b(x-y)^2\right] + c(\dot{x}-\dot{y})\left[1 + w(\dot{x}-\dot{y})^2\right] \tag{3}$$

where K, C and k, c are the stiffness and damping coefficients of the protected object and the eliminator, respectively, while B, W and b, w are coefficients of nonlinearity of stiffness and damping of the protected object and the eliminator, respectively

Hence, equations of motion of the whole system take the form:

$$\begin{aligned} &M\ddot{x} + C\dot{x}\left(1 + W\dot{x}^2\right) + Kx\left(1 + Bx^2\right) + \\ &\quad + c(\dot{x}-\dot{y})\left[1 + w(\dot{x}-\dot{y})^2\right] + k(x-y)\left[1 + b(x-y)^2\right] = F_0\sin(\omega t), \\ &m\ddot{y} - c(\dot{x}-\dot{y})\left[1 + w(\dot{x}-\dot{y})^2\right] - k(x-y)\left[1 + b(x-y)^2\right] = 0. \end{aligned} \tag{4}$$

They make a basis for the simulation model of the system.

3. Simulation model of the main system provided with vibration eliminator

The simulation model is constructed based on the dimensionless equations of motion:

$$\begin{aligned} \frac{d^2x_1}{d\tau^2} &= F_1\sin(2\pi\delta\tau) - 4\pi\xi\frac{dx_1}{d\tau}\left[1 + \alpha_M\left(\frac{dx_1}{d\tau}\right)^2\right] - 4\pi^2x_1\left(1 + \beta_M x_1^2\right) + \\ &- 4\pi\xi\gamma\left(\frac{dx_1}{d\tau} - \frac{dy_1}{d\tau}\right)\left[1 + \alpha_m\left(\frac{dx_1}{d\tau} - \frac{dy_1}{d\tau}\right)^2\right] - 4\pi^2\varepsilon(x_1 - y_1)\left[1 + \beta_m(x_1 - y_1)^2\right], \end{aligned}$$

$$,\frac{d^2 y_1}{d\tau^2}=4\pi\frac{\xi\gamma}{\mu}\left(\frac{dx_1}{d\tau}-\frac{dy_1}{d\tau}\right)\left[1+\alpha_m\left(\frac{dx_1}{d\tau}-\frac{dy_1}{d\tau}\right)^2\right]+4\pi^2\frac{\varepsilon}{\mu}(x_1-y_1)\left[1+\beta_m(x_1-y_1)^2\right]=0. \tag{5}$$

where the following dimensionless denotations are adopted:

$$F_1=\frac{F_0}{Mg/K},\ \delta=\frac{\omega}{\omega_0},\ \omega_0=\sqrt{\frac{K}{M}},\ \tau=\frac{\mathrm{t}}{\mathrm{T}_0},\ \mathrm{x}_1=\frac{x}{Mg/K},\ \mathrm{y}_1=\frac{y}{Mg/K},$$

$$\xi=\frac{C}{2\sqrt{KM}},\ \alpha_M=W\left(\frac{Mg}{KT_0}\right)^2,\ \ \gamma=\frac{\mathrm{c}}{\mathrm{C}},\ \alpha_\mathrm{m}=w\left(\frac{Mg}{K}\right)^2,$$

$$\beta_\mathrm{M}=B\left(\frac{Mg}{K}\right)^2,\ \ \varepsilon=\frac{k}{K},\ \ \beta_\mathrm{m}=b\left(\frac{Mg}{K}\right)^2,\ \mu=\frac{\mathrm{m}}{\mathrm{M}}.$$

The simulation model of the considered system has been developed based on the equations of motion with the use of the MATLAB® software with SIMULINK package [5, 6] (Fig. 3)

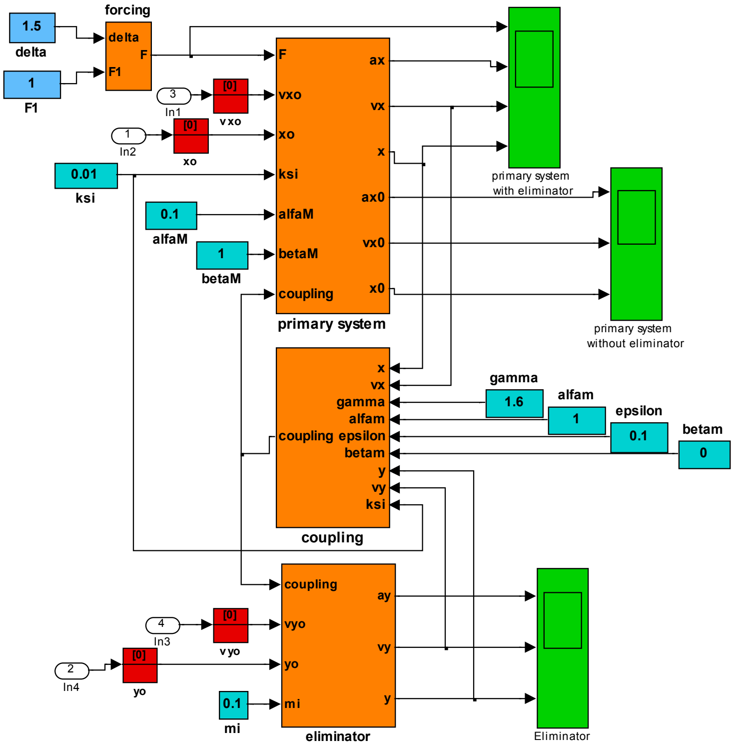

Figure 3. Simulation diagram of the protected object provided with dynamic vibration eliminator

The model allows to investigate dynamics of the system with varying parameters of the forcing– F_1, δ of the protected object – ξ, α_M, β_M, and the eliminator – $\mu, \gamma, \alpha_m, \varepsilon, \beta_m$.

4. Efficiency of vibration reduction of a nonlinear dynamic vibration eliminator

Efficiency of vibration reduction for the task of vibration elimination has been estimated on the grounds of the function of vibration elimination effectiveness defined in the present paper, being equal to the ratio of rms values of the vibration displacements of the protected object without the eliminator to the ones occurring with it, in the case of steady motion.

$$E = \sqrt{\frac{\sum_{j=n}^{j=n+r} x_{01}^2(\tau_j)}{\sum_{j=n}^{j=n+r} x_1^2(\tau_j)}}, \tag{6}$$

where $\tau_j = j \cdot \Delta\tau$

It was found during the tests that steady motion of the system for various values of the dynamic parameters occurs for the simulation time:

$\tau_n = n \cdot \Delta\tau$ for $n = 90000$ and $\Delta\tau = 0.01$, with $r = 10000$.

The investigation includes analysis of the system dynamics and effectiveness of vibration elimination with the use of nonlinear dynamic vibration eliminator for the following values of the dynamic parameters:

- dimensionless amplitude of the exciting force – $F_1 = 0.1,\ 1,$
- dimensionless frequency of the excitation – $\delta = 0.9,\ 1.0,\ 1.1,$
- damping degree of the protected system – $\xi = 0.01,$
- dimensionless parameter of damping nonlinearity of the protected system – $\alpha_M = 0,\ 0.01,\ 0.05,\ 0.1,$
- dimensionless parameter of stiffness nonlinearity of the protected system – $\beta_M = 0,\ 0.01,\ 0.05,\ 0.1,$
- dimensionless damping of the eliminator – $\gamma = 1.0,$
- dimensionless parameter of damping nonlinearity of the eliminator – $\alpha_m = 0,\ 0.01,\ 0.05,\ 0.1,$
- dimensionless parameter of stiffness nonlinearity of the eliminator – $\beta_m = 0,\ 0.01,\ 0.05,\ 0.1,$
- dimensionless mass of the eliminator – $\mu = 0.1,$

as the functions of the dimensionless stiffness of the eliminator $0.04 \le \varepsilon \le 0.2$.

Results of calculation of effectiveness of the vibration elimination E for exemplary constant values of the system parameters:

$$F_1 = 0.1, \quad \xi = 0.01, \quad \alpha_M = \beta_M = 0, \quad \mu = 0.1, \quad \gamma = 1.0$$

and the other parameters varying as follows

$$\delta = 0.1, \; 1, \; 1.1, \quad \alpha_m = 0, \; 0.01, \; 0.05, \; 1, \quad \beta_M = 0, \; 0.01, \; 0.05, \; 1$$

are presented below as the functions of dimensionless stiffness of the eliminator.

a) $\delta = 0.9$ b)

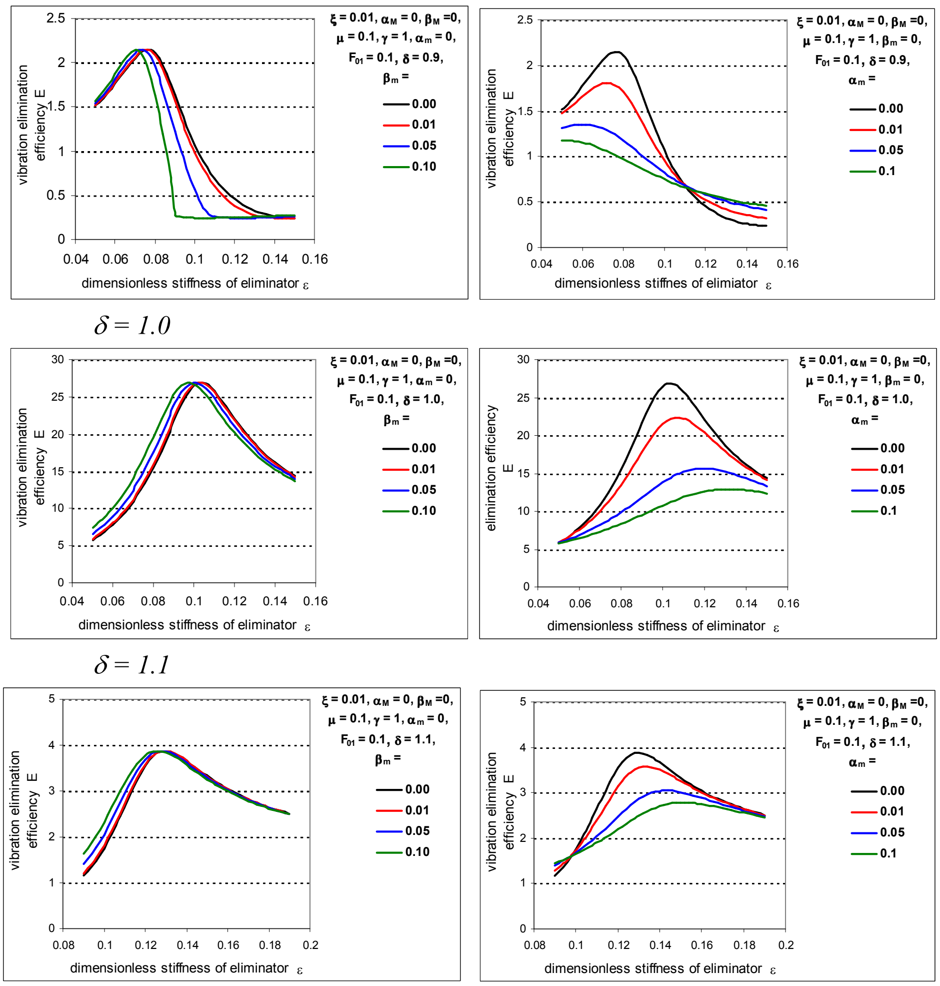

Figure 4. Effectiveness of vibration reduction attained with the help of dynamic eliminator in the case of linear protected system $(\alpha_M = \beta_M = 0)$ as the function of ε; a) linear damping of the eliminator; b) linear stiffness of the eliminator for various values of dimensionless excitation frequency δ

4. Summary

The numerical research allows to formulate the following conclusions (related to the above presented results):

- nonlinear stiffness of the coupling between the protected system and the eliminator results only in inconsiderable changes in effectiveness of the vibration reduction of the dynamic eliminator (with linear damping of the coupling $\alpha_m = 0$ – Fig. 4a);
- nonlinear damping of the coupling between the protected system and the eliminator results in remarkable changes in effectiveness of vibration reduction of the dynamic eliminator (with linear stiffness of the coupling $\beta_m = 0$ – Fig. 4b);

References

1. Zb. Osiński [red.] *Tłumienie drgań mechanicznych*, PWN, Warszawa 1986.
2. Z. GOLEC, M. GOLEC, *Model of Damper of Vibration with interaction described by Means of Fractional Derivatives*, Proceedings of XIXth Symposium Vibrations in Physical Systems, Poznań – Błażejewko, May 23 – 27,2000.
3. Awrejcewicz J., *Drgania deterministyczne układów dyskretnych*, WNT,Warszawa 1996.
4. Batko W., Dąbrowski Z., Kiciński J., *Zjawiska nieliniowe w diagnostyce wibroakustycznej*, Wydawnictwo Naukowe Instytutu Technologii Eksploatacji, Radom 2008.
5. A. Zalewski, R. Cegieła, *Matlab – obliczenia numeryczne i ich zastosowania*, Wydawnictwo Nakom, Poznań 1997.
6. B. Mrozek, Z. Mrozek, *Matlab i Simulink. Poradnik użytkownika*, Wydawnictwo Helion, Gliwice 2004.

XXV Symposium *Vibrations in Physical Systems,* Poznan – Bedlewo, May 15-19, 2012

Synchronization of Rotating Double Pendula System

Juliusz GRABSKI
Technical University of Łódź, 90-924 Łódź, Stefanowskiego 1/15, julgrabs@p.lodz.pl

Jarosław STRZAŁKO
Technical University of Łódź, 90-924 Łódź, Stefanowskiego 1/15, jstrzalk@poczta.onet.pl

Jerzy WOJEWODA
Technical University of Łódź, 90-924 Łódź, Stefanowskiego 1/15
jerzy.wojewoda@.p.lodz.pl

Tomasz KAPITANIAK
Technical University of Łódź, 90-924 Łódź, Stefanowskiego 1/15, tomaszka@p.lodz.pl

Abstract

Theoretical and experimental analysis of a set of four double pendula located on a vertically excited platform is analysed. The pendula can rotate in different directions. The main interest is concentrated on the phenomenon of synchronization. It has been shown that different types of phase synchronization between pendula can be observed. The experimental results are confirmed by the numerical simulations.

Keywords: synchronization, rotating pendulum, kinematic excitation

1. Introduction

Synchronization is understood as an adaptation of the system's dynamics due to the interaction between its subsystems, which is achieved by coupling the system's variables. For the first time the synchronisation of two pendulum clocks hanging on the wall was observed by Huygens [1]. The phenomenon of coupled harmonic oscillators is studied nowadays by many authors [2, 3, 4]. The synchronisation of horizontally moving beam and n identical mathematical pendulums hanging from the beam has been presented in [5].

In this work the system of four almost identical physical double pendula located on a common base is analysed. We investigate possibility of the synchronization of the rotating motion of the pendula. We give experimental evidence that the rotating pendula can synchronize even in the case when some of them rotate in different directions. We show that the appearance of the particular synchronous state strongly depends on the system parameters and its initial conditions.

2. Mathematical model of double pendulum kinematically excited

Figure 1 presents experimental rig and 3-D model of $n = 4$ double pendula kinematically excited. One of the double pendulum from the set is presented in Fig. 2, where the main dimensions and parameters are shown.

Excitation of the pendulum in the considered case is performed through driving the base vertically. Pendulum's horizontal axis throw the point (C_1) moves but its motion is not given directly nor analytically. Equations of dynamics of the double pendulum excited kinematically ($y_{A1} = A\cos\omega t$) attempt:

$$\begin{gathered}\left(J_2+m_2\xi_2^2\right)\ddot{\varphi}_2 + m_2\xi_2\,(A\,\omega^2\cos\omega t+g)\sin\varphi_2 + \\ + m_2\xi_2\left(\xi_1\left(\dot{\varphi}_1^2\cos(\varphi_1-\varphi_2)+\ddot{\varphi}_1\sin(\varphi_1-\varphi_2)\right)\right)+\frac{1}{3}k_c\eta_2^3\dot{\varphi}_2^2=0\,,\end{gathered} \tag{1}$$

$$\begin{gathered}\left(J_1+\left(m_1+m_2\right)\xi_1^2\right)\ddot{\varphi}_1 + \frac{1}{2}\eta_1^2k_s\sin\left(2\varphi_1\right)+m_2\xi_1\left(\xi_2\left(\ddot{\varphi}_2\sin\left(\varphi_1-\varphi_2\right)\right)-\dot{\varphi}_2^2\cos\left(\varphi_1-\varphi_2\right)\right)- \\ -\left(m_1+m_2\right)\xi_1\cos\left(\varphi_1\right)(A\,\omega^2\cos\omega t+g)=0\,.\end{gathered} \tag{2}$$

a) 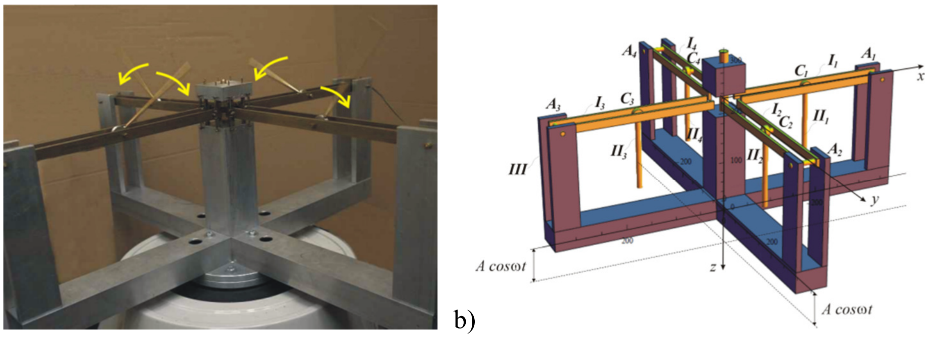 b)

Figure 1. Experimental rig (a) and 3-D model of *4* kinematically excited double pendula (b)

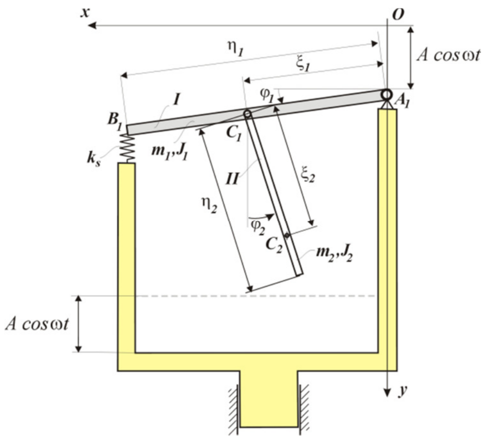

Figure 2. Model of the system of two bodies (pendula) elasticallly supported and kinematically excited

3. Experimental observation and numerical results

The system parameters have been identified as: ξ_{i1} = 0.153 m, ξ_{i2} = 0.078 m, η_{i1} = 0.315 m, η_{i2} = 0.145 m, m_{i1} = 0.4 kg, m_{i2} =0.0166 kg. The estimated values of the stiffness coefficients: k_{1s} = 4664 N/m, k_{2s} = 4115 N/m, k_{3s} = 4535 N/m, k_{4s} = 4325 N/m, and the damping coefficients: k_{1c} = 0.070 kg/ms, k_{2c} = 0.035 kg/ms, k_{3c} = 0.035 kg/ms, k_{4c} = 0.050 kg/ms.

Using the experimental rig we have identified different types of synchronization of rotating pendula, i.e., we have observed synchronization of pendula rotating both, in the same or opposite directions, respectively. The most interesting case is when all four pendula rotate. In this case one can observe various types of pendula synchronization. For the qualitative classification of the pendula behavior we use the following nomenclature: the pendula which rotate clockwise or counterclockwise are marked respectively by +1 (blue points) and –1 (red points), the pendula which are at rest are marked by 0 (yellow points). An example of synchronization observed is shown in Fig. 1(a) where yellow arrows indicate direction of rotation. Figure 1(a) presents the case when two pair of pendula rotate in the opposite direction, i.e. (+1,+1,–1,–1) and the values of the angular velocities of all pendula are the same.

Some examples of numerical solution results are presented in Fig. 3–5. Figure 3(a) shows different types of individual pendulum's behaviour on the A and ω plane and synchronization map for the system.

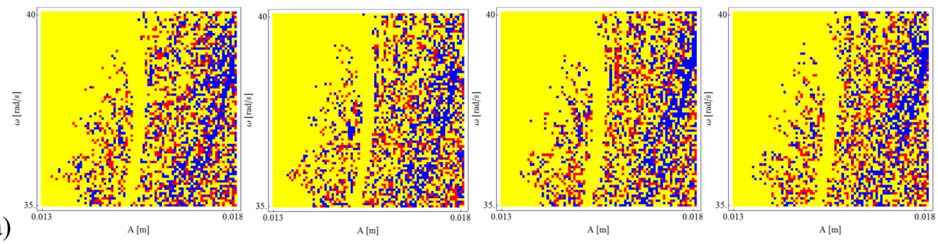

a)

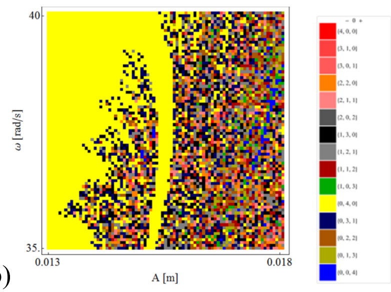

b)

Figure 3. Different types of pendula's behavior on the A and ω plane for $\varphi_2(0) = \pi/2$ (a) (blue regions – clockwise rotation, red regions – counterclockwise rotation, yellow regions – no regular rotation) and synchronization map for the system (b)

In Figure 4 the regions of synchronized rotation (+1,+1,+1,+1) and (–1,–1,–1,–1) for values of initial angular speed equal to *10*, *15* and *20* are compared for two cases of initial rotation: clockwise and counterclockwise. We have found that for nonzero initial pendula’s angular speed the synchronization region of rotating pendula expands and shifts up in the assumed coordinate system.

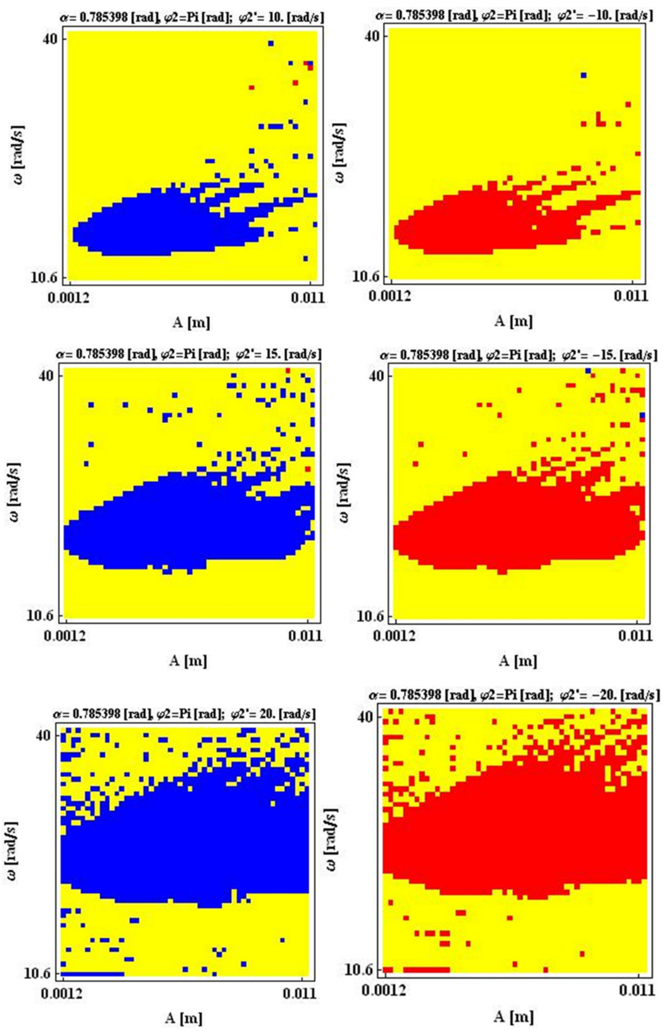

Figure 4. Different types of pendula's behavior on the A and ω plane for nonzero initial angular speed (blue regions – clockwise rotation, red regions – counterclockwise rotation, yellow regions – no regular rotation)

Time series of rotating pendula position (φ) and angular speed (ω_2) are depicted in Fig. 5 for equal initial phase (*0.024* rad) and different initial angular speed (for three pendula *40* rad/s and fourth *27* rad/s). In this case three pendula rotate with mean angular speed $\omega_2 = 60$ rad/s and rotation speed of the fourth (Fig. 5(c)) is $\omega_2 = 20$ rad/s.

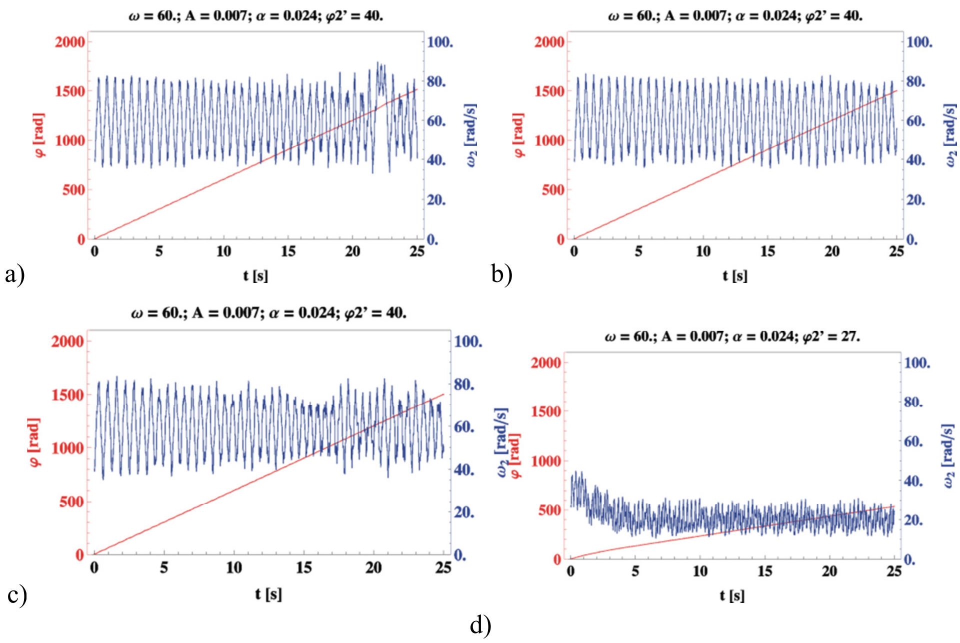

Figure 5. Time series of rotating pendula position (φ) and angular speed (ω_2)

4. Conclusions

The existence of experimentally observed synchronous states is confirm in the numerical simulations. We have observed synchronous motion with all pendula rotating in the same direction (clockwise and counterclockwise rotation), the case when two pairs of pendula rotate in the different directions (clockwise and counterclockwise rotation), and the case when 3 pendula rotate in the same direction, while the fourth in the opposite one. Rotating pendula can be 1:1 and 1:2 synchronized with the oscillations of the platform.

We have found the extreme sensibility of the synchronized state on the system parameters and initial conditions.

Acknowledgments

This work has been supported by the Polish Department for Scientific Research (DBN) under project No. N N501 249238.

References

1. Huygens, C. Horoloqium Oscilatorium, (Apud F. Muquet, Paris, 1673); English translation: *The pendulum clock*, (Iowa State University Press, Ames).
2. Blekham, I.I. *Synchronization in Science and Technology*, ASME, New York 1988.
3. Pogromsky, A. Yu., Belykh, V.N. & Nijmeijer, H. *Controlled synchronization of pendula,* Proceedings of the 42nd IEEE Conference on Design and Control (2003) 4381-4385.
4. Czołczyński, K., Perlikowski, P., Stefański, A. & Kapitaniak, T. *Clustering and synchronization of n Huygens' clocks*, Physica A **388** (2009) 5013-5023.
5. Czołczyński, K., Perlikowski, P., Stefański, A. & Kapitaniak, T. *Clustering of Huygens' clocks*, Prog. Theor. Phys. **122** (2009) 1027-1033.

XXV Symposium *Vibrations in Physical Systems,* Poznan – Bedlewo, May 15-19, 2012

Evaluation of Technical Condition of Belt Conveyor FAGOR 20943

Magdalena GRYGOROWICZ, Przemysław BRZEZIŃSKI
Poznan University of Technology, PL 60-965Poznan Piotrowo street No. 3
magdalena.grygorowicz@put.poznan.pl

Abstract

This paper presents an evaluation of the technical condition of the belt conveyor FAGOR 20943. The four bearing nodes had been diagnosed. Vibration measurement in these nodes was performed according to the standard PN-ISO 10816:1. Comparing the results with standard criteria, the condition of conveyor was defined as a state B - satisfactory condition. Machinery whose vibrations are in this zone can work long term without restrictions. Diagnostic of machine and it result showed the management board of the company, how important is regular evaluation of technical condition of machinery. This can reduce the cost of production downtime caused by equipment failures.

Keywords: technical condition, PN standard, reduce of cost

1. Introduction

Any break down of machinery in production companies is associated with downtime costs. This applies to small as well large companies. Every break in production process is equal to delay of realization date of orders. In consequence the brand of company loses on its value.

Systematically control of the technical condition of machinery is very important in order to maintain continuity of production. The management of a large manufacturing company around Września has been convinced to the benefits of such controls. The management reserved the protection of data including information on production profile.

The research and analysis of the results were made in the thesis.

2. Evaluation of technical condition of belt conveyor FAGOR 20943

2.1. Characteristic of production

The company works on producing large quantities of flat steel elements [1]. Work is performed in three shifts. In production are used various parameters presses, finishing equipment and conveyors for the transportation of blank. The evaluation of technical condition has been done for belt conveyor FAGOR 20943. Its immobility would stop the entire production process.

2.2. Belt conveyor FAGOR 20943

Device was presented on Fig. 1. It construction is easy. The main element is the belt tension by two rollers: active and passive. The active roller was driven by an external electric motor. Fig. 2 shows the data plate of the motor. The whole construction was mounted in a steel frame [1].

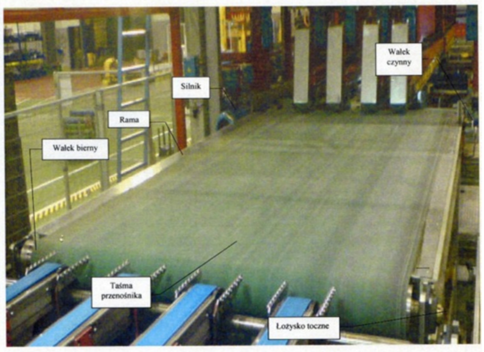

Figure 1. Construction of belt conveyor FAGOR 20943 [1]

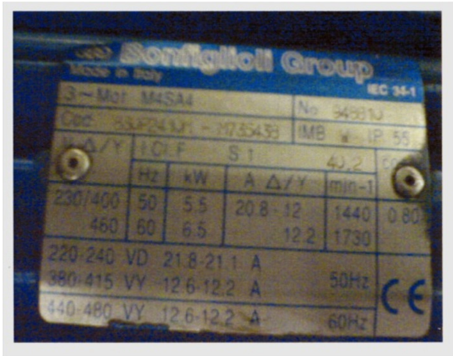

Figure 2. The data plate of motor [1]

2.3. Classification of the device due to the power and installation method

In order to properly assess the state of the conveyor first the device had been classified on the base of standard PN-90/N-01358 (table 1). The power of the motor was taken from its data plate. It was 5.5 [kW].

Table 1. The division into groups of machines due to their size and power [2]

Grupe	Power and installation methode
1	Machinery, including engines up to 15 [kW]
2	Machinery, including engines up to 15 till 75 [kW] without special foundation and machinery up to 300 [kW] placed on foundation
3	Machinery up to 300 [kW], including engines up to 75 [kW], founded on the foundations satisfy the stiffening conditions
4	Machinery up to 300 [kW], including engines up to 75 [kW], founded on foundations satisfy the conditions of setings of elastic

Due to the standard the belt conveyor had been classified to the firs group – machinery up to 15 [kW]. This information was very helpful when the evaluation of the device had been done.

2.4. Criteria for evaluation the condition of the machine due to the generated vibration

The evaluation of the technical condition of device has been done due to criteria from the standard PN-ISO 10816:1 (tab. 2).Below is an explanation of letter designations contained in Table 2:

A – very good condition – in this area should be vibration machines newly placed in service,

B – satisfactory condition – machinery whose vibrations are in this zone can work long term without restrictions, *C – temporarily allowing condition* – machinery whose vibrations are in this zone is usually considered not suitable for long–term continuous operation. In general, the machine can operate for a limited period of time until it is able to take preventive action,

D – unacceptable condition – vibration values in this zone is generally regarded as sufficient serious and indicated the possibility of damage to the machine. After reaching this level of vibration, the machine should be switch off immediately.

Table 2. Criteria for the evaluation of technical condition of the device due to the generated vibration [3]

<table>
<tr><td colspan="2">The RMS value of velocity $V[mm/s]x10^{-3}$ in the $10 \div 1000[Hz]$</td><td colspan="4">Group</td></tr>
<tr><td>up to</td><td>till</td><td>1</td><td>2</td><td>3</td><td>4</td></tr>
<tr><td></td><td>0,71</td><td>A</td><td rowspan="2">A</td><td rowspan="3">A</td><td rowspan="4">A</td></tr>
<tr><td>0,71</td><td>1,12</td><td rowspan="2">B</td></tr>
<tr><td>1,12</td><td>1,80</td><td rowspan="2">B</td></tr>
<tr><td>1,80</td><td>2,80</td><td rowspan="2">C</td><td rowspan="2">B</td></tr>
<tr><td>2,80</td><td>4,50</td><td rowspan="2">C</td><td rowspan="2">B</td></tr>
<tr><td>4,50</td><td>7,10</td><td rowspan="4">D</td><td rowspan="2">C</td></tr>
<tr><td>7,10</td><td>11,20</td><td rowspan="3">D</td><td rowspan="2">C</td></tr>
<tr><td>11,20</td><td>18</td><td rowspan="2">D</td></tr>
<tr><td>18</td><td></td><td>D</td></tr>
</table>

2.5. The study of vibration level in bearing nodes used in belt conveyor

According to the standard PN-90/N-01358, the study had been done for all bearing nodes used in belt conveyor. Figure 3 shows one of the bearings nodes and bearing used in it. As you can see, access to the bearing wasn't difficult. There was possibility to make measurement directly on bearing or its housing. Figure 4 shows diagram of typical rolling bearing.

Wideband measurements of velocity V [mm/s] performed in frequency range $10 \div 1000$ [Hz], in three orthogonal directions (horizontally, vertically and axially). Research work was done during normal use, five times for each measuring point. The time of single measuring was 5 [s]. Works were made according to the plan of measure shows in Table 3.

The diagram of measurement system is shown in figure 5. The four bearing nodes (point 1, 2, 3, 4) were marked on this diagram.

At node No. 3 was mounted electrical motor driving the active roller of belt conveyor. Measurements were made by using CMD-3vibration meter. Figure 6 shows velocity measurement in axial direction [1].

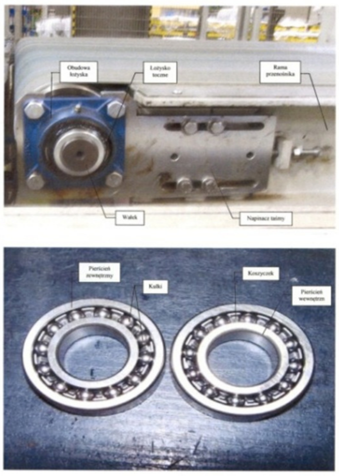

Figure 3. The bearing node and bearing used in conveyor FAGOR 20943 [1]

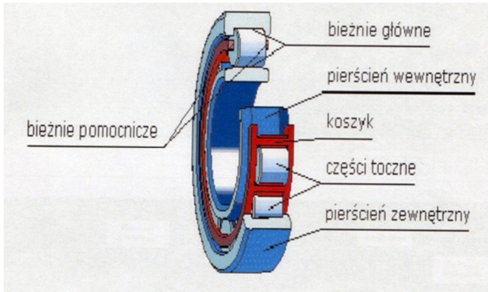

Figure 4. The construction of rolling bearing [4]

Table 3. The plan of vibration measurement at the workplace [1]

Place of measurement	Przedsiębiorstwo produkcyjne we Wrześni
Goal of measurement	Diagnostic of technical conditio of device
Object of reaserch	Belt conveyor FAGOR 20943
Measured values	Velocity in horisontal, vertical and axial direction
Equipment of measurement	Vibration meter CMD-3
Proces of measurement	Vibration measurement V [mm/s] in 4 bearing nodes; 5 series of measurement for each bearing, measured in 3 directions; duration time of single measurement about 5 [sec]

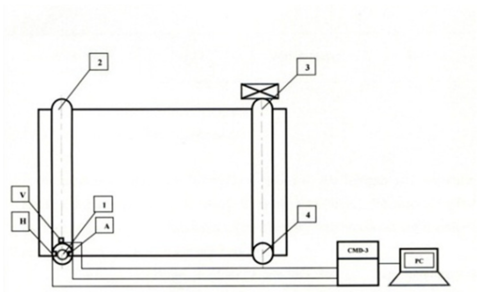

Figure 5. The diagram of device and measurement system [1]

Figure 6. The velocity measurement in axial direction [1]

2.6. Analysis of the results

The results of measurement shows Fig. 7. The diagram of values results in every direction was made for each measuring point.

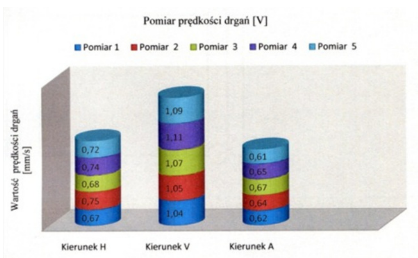

Measuring point: node 1 – the highest value: 1,11 [mm/s]

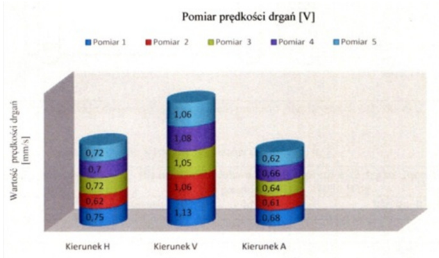

Measurning point: node 2 – the highest value: 1,13 [mm/s]

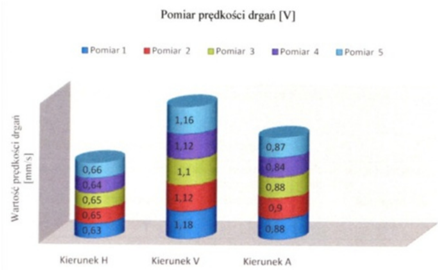

Measuring point: node 3 – the highest value: 1,18 [mm/s]

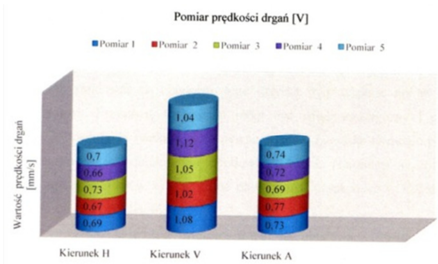

Measuring point: node 4 – the highest value: 1,12 [mm/s]

Figure 7. Summary of results velocity measurements at all nodes [1]

According above the highest velocity values were measured in vertical direction for each node. The results of velocity for bearing nodes No. 1, 2, and 4 were very similar (1,11 ÷ 1,13 [mm/s]). The highest value, 1.18[mm/s], was measured for node No. 3. The cause of this value could be an electric motor driving an active roller.

Based on this result and evaluation criteria of technical condition of machine, the state of investigated belt conveyor has been evaluated for acceptable (B), which allows for long work without restrictions.

3. Conclusions

The regular evaluation of technical condition of machine can prevent long-term disruptions in production caused by the sudden failure of machines. Such research has underestimates the factory, where the vibration of bearing nodes were measured.

The management of company considered it advisable to introduce a cyclic diagnostic of machinery. The more that proposed method proved to be simple to make and machines does not have to be stopped, as in the case of three shift system of work is very valuable. Prevention of accidents was much cheaper than repair or replace any machine. The economic results and the company's marked has not been shattered.

References

1. Brzeziński P., *The evaluation of technical condition of belt conveyor Fagor 20943*, Poznan University of Technology, Faculty of Mechanical Engineering and Management, 2010.
2. Polish Standard PN-90/N-01358 *Vibration. Method of measurement and evaluation of machinery vibration*.
3. PN-ISO 10186:1 *Machine vibrations Evaluation based on measurements on parts of the non-spinning*.
4. Construction of rolling bearing http://pcws.ia.polsl.pl

XXV Symposium *Vibrations in Physical Systems,* Poznan – Bedlewo, May 15-19, 2012

Biomechanical Couple Interactions

Tadeusz J. HOFFMANN
Poznan University of Technology, Institute of Applied Mechanics
ul. Piotrowo 3, 60-965 Poznan
tadeusz.hoffmann@put.poznan.pl

Michał Wojciech POŚPIECH
Poznan University of Technology, Institute of Applied Mechanics
ul. Piotrowo 3, 60-965 Poznan
michal.wojciech.pospiech@gmail.com

Marta CHUDZICKA-ADAMCZAK
Polytechnic Institute, Higher Vocational State School in Pila
10 Podchorążych Street, 64-920 Piła
martachudzicka@wp.pl

Abstract

Micropolar continuous medium theory from the beginning was modeling theory. It predicted in that medium existing of mass angular momentum, asymmetrical stress forces, stress moments and mass force momentum. On the beginning there was no able to interpret angular momentum, stress moments and mass force momentum on physical matter known base. In 70's of XX age there were provided an examples for ferromagnetic, paramagnetic and dielectric bodies. This paper gives attention to interpret those effects in biological structures. On example of human blood there is showed application of Langevin's paramagnetism classical theory and its mechanical results. In the paper there are presented interesting examples of biological structures which had mechanical results using electric dipole moments.

Keywords: micropolar continuous medium, couple stress

1. Introduction

In the paper the two processes are analyzed: implants' bio-degradation in human cardiovascular system and gecko's paw moulting in biotic process. These processes can be modeled as an environmental impact on material medium. In mechanical modeling this impact means that forces and force moments act on the examined medium and its mass changes. In thesis a closed dynamic system model is used, where subsystems exchange mass, momentum, angular momentum and energy. Integrated component systems which occupy the same finite volume are: electro-magnetic field and material continuum. According to mechanics principles it is known that when forces act, then momentum changes. Next, when forces moments act, angular momentum changes as well as the energy of loaded system changes. What is more, in the description of these actions it is essential to study the balances of mass, momentum, angular momentum and energy.

Implants' bio-degradation in human cardiovascular system occurs in a process, where erythrocytes having mass create electro-magnetic field. Implants' bio-degradation products are absorbed by cardiovascular system. [2], [3]. Therefore, there is the process of mass exchange between the subsystems: implant – cardiovascular system. In modeling this process the characteristics of electromagnetic field should be taken into account.

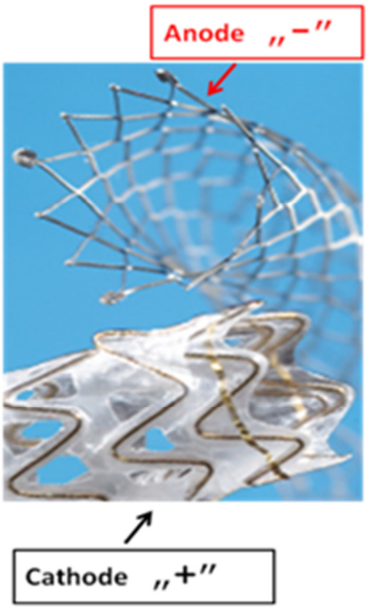

Figure1. Stent – visible polymer releasing antibiotic influenced by corrosion (source: http://www.elektro-oxigen.pl/nowa/stenty_zolciowe.php)

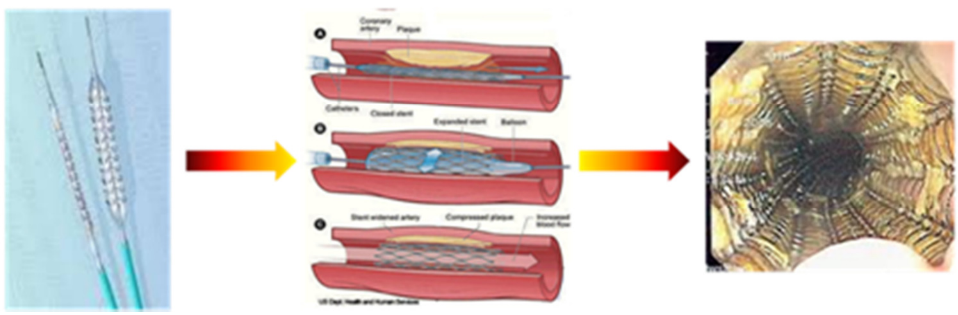

Figure2. Practical application of stents (source: Wikipedia)

In gecko's paw moulting process there is a situation, where moulting process causes the reduction in number of dipoles creating the force field. There is the decrease of mass creating electric field (hairloss means that electrical dipoles create electrical field. Adherence is the effect of the force of hair close contact action – dipoles with induced electrical dipoles of material medium). Decreasing mass is not, however, transmitted to subsystem – material medium, where gecko climbs. In this process, the mass creating electromagnetic field drops and leaves all the system.

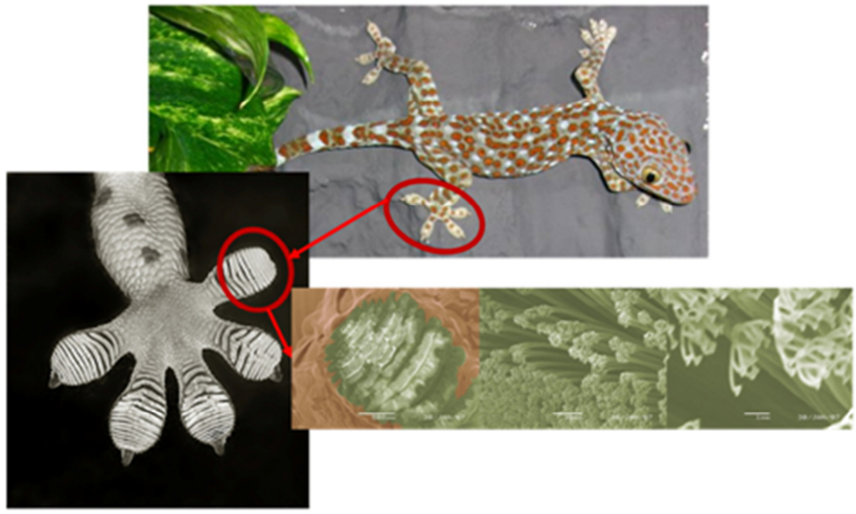

Figure3. Gecko's paw structure (source: Wikipedia)

In the considered processes, the mass change of system proceeds in two different ways. In the process of implants' bio-degradation in human cardiovascular, the change in mass of material medium occurs, while in the process of gecko's paw moulting there is the decrease of mass in the external field.

The process of implants' bio-degradation in human cardiovascular system there is material medium mass change, but in gecko's paws moulting process there is external field mass decrease.

In the mathematical modeling, there is a popular and experimentally proved in physiochemical processes law [1], [4]:

Let's assume the decrease in mass continuum. It is known that the mass is mass decrease in mathematical modeling, very popular and confirmed by experiments in physical-chemical processes [1], [4] is the law:

$$\frac{dm}{dt} = -\alpha m, \tag{1}$$

where:

$m = [kg]$ - current mass,

$\alpha = \left[\frac{1}{s}\right]$ - process characteristic constant value.

Let's assume the decrease in material continuum. It is known that the mass is determined by the density of medium in the determined volume. Hence, the following equation based on equation (1) is obtained:

$$\frac{d}{dt}\int_V \rho dV = -\alpha \int_V \rho dV, \tag{2}$$

where

ρ – medium density,

V – deformable domain volume.

Applying [9] on p.85 it is obtained:

$$\int_V \left\{ \frac{\partial \rho}{\partial t} + \partial_k (v_k \rho) \right\} dV = -\alpha \int_V \rho dV, \tag{3}$$

where

v_k - the component of the current velocity of the point in medium,

t - time.

Transforming the above equation the following form is obtained:

$$\int_{\mathrm{V}} \left[\left\{ \frac{\partial \rho}{\partial t} + \partial_k (v_k \rho) \right\} + \alpha\rho \right] dV = 0. \tag{4}$$

which effects (towards the freedom and finiteness of the area) in the differential form mass decrease:

$$\frac{D\rho}{Dt} + \rho \, \partial_k \, v_k + \alpha\rho = 0, \tag{5}$$

hence mass decrease can be presented finally as the equation of the form:

$$\frac{\partial \rho}{\partial t} + v_k \, \partial_k \, \rho + \rho \, \partial_k \, v_k = -\alpha\rho \, . \tag{6}$$

Equations (5) and (6) are assumed as the differential (local) of the mass balance form.
From the balance equation point of view:

$$\frac{D\rho}{Dt} + \rho \, \partial_l \, v_l - \partial_l \, j_l(\rho) - \sigma(\rho) - r(\rho) = 0, \quad \sigma(\rho) = -\alpha\rho . \tag{7}$$

As a result, the above equation takes a form:

The same mechanism of mass decrease, according to equation (6), can be applied to external field, where the following is assumed:

$$\sigma\left(\rho^{ext}\right) = -\beta\rho^{ext} \, . \tag{8}$$

It means that balance equation:

$$\sigma\left(\rho^{ext}\right) = -\beta\rho^{ext} \, , \tag{8}$$

$$\frac{D\rho^{ext}}{Dt} + \rho^{ext}\partial_l v_l - \partial_l j_l(\rho^{ext}) - \sigma(\rho^{ext}) + r\,(\rho^{ext}) = 0 \, , \tag{9a}$$

gets a new form:

$$\frac{D\rho^{ext}}{Dt} + \rho^{ext}\partial_l v_l - \partial_l j_l(\rho^{ext}) + \beta\rho^{ext} + r\,(\rho^{ext}) = 0 \, . \tag{9b}$$

The above assumptions have a big influence on the form of the balance equations of system in the described processes. It is later analyzed more specifically.

2. Implants' bio-degradation process in human cardiovascular system

The mass balance – in this process mass exchange between subsystems has a balanced character [7], it means that mass balance is described by equation:

$$\frac{D}{Dt}(\rho^{ext}+\rho)+(\rho^{ext}+\rho)\partial_l v_l-\partial_l[j_l(\rho^{ext})+j_l(\rho)]=0\cdot \tag{10}$$

The momentum balance – [6], [7] takes a form:

$$\rho\frac{Dv_k}{Dt}+v_k[\partial_l j(\rho)_l-\alpha\rho+r(\rho)]-\partial_l(T_{kl}+t_{kl})-(f_k^{ext}+f_k^{mech})=0\cdot. \tag{11}$$

The angular momentum balance – it takes the following form:

$$\begin{aligned}&\rho\frac{D}{Dt}\left[\chi_i^{(ext)}+\chi_i\right]+\left[\chi_i^{(ext)}+\chi_i\right]\left[\partial_s\, j_s(\rho)-\alpha\rho+r(\rho)\right]+\varepsilon_{ijk}\left(T_{kl}+t_{kl}\right)-\partial_l\left(M_{il}+m_{il}\right)+\\&+\varepsilon_{ijk}x_j f_k^{ext}+\rho k_i=0.\end{aligned} \tag{12}$$

The energy balance – it gets a form:

$$\begin{aligned}&\frac{D\mathrm{E}^{ext}}{Dt}+\mathrm{E}^{ext}\partial_l v_l-\partial_l j_l\left(E^{ext}\right)+\rho\frac{D\mathrm{E}}{Dt}+\\&+\left[\mathrm{E}+\frac{1}{2}\left(v_k^2+\omega_k\omega_l I_{kl}\right)\right]\left[\partial_s\, j_s(\rho)-\alpha\rho+r(\rho)\right]=t_{kl}\,\partial_l\, v_k+m_{il}\,\partial_l\,\omega.\end{aligned} \tag{13}$$

The precise description of symbols is presented in [8].

3. Gecko's paw moulting process

The mass balance – in this process there is mass decrease (the number of electric dipoles), so in balance equations it is assumed that: $\sigma(\rho^{ext})=-\beta\rho^{ext}$.

This modifies the mass balance:

$$\frac{D}{Dt}(\rho^{ext}+\rho)+(\rho^{ext}+\rho)\partial_l v_l-\partial_k[j_k(\rho^{ext})]-\sigma(\rho^{ext})=0, \tag{14a}$$

leading to a following form:

$$\frac{D}{Dt}(\rho^{ext}+\rho)+(\rho^{ext}+\rho)\partial_l v_l-\partial_k[j_k(\rho^{ext})]+\beta\rho^{ext}=0. \tag{14b}$$

The momentum balance – in momentum balance the influence of the external field is omitted with the following effect:

$$\rho\frac{Dv_k}{Dt}-\partial_l\left(T_{kl}+t_{kl}\right)-f_k^{mech}=0. \tag{15}$$

The angular momentum – in angular momentum balance we take into account the spin angular momentum of external field, taken from inducing electrical dipoles. The form is presented below:

$$\rho \frac{D}{Dt}[\chi_i^{(ext)} + \chi_i] + \varepsilon_{ijk}(T_{kl} + t_{kl}) - \partial_l (M_{il} + m_{il}) - \rho k_i = 0, \tag{16}$$

The energy balance – a form is obtained:

$$\frac{D\mathrm{E}^{ext}}{Dt} + \mathrm{E}^{ext}\partial_k v_k - \sigma(\mathrm{E}^{ext}) + \rho \frac{DE}{Dt} = t_{kl}\partial_l v_k + m_{kl}\partial_l \omega_l \cdot \tag{17}$$

Equations (15) and (16) are dynamical motion equations of material body. The energy balance (17) describes work and energy equivalence.

4. Conclusions

In the obtained equations it can be observed how the classical Cosserats' theory equations evolved in the described processes. The cause of moment impacts is electromagnetic field thanks to local angular momenta. Additionally, mass change mechanisms expand balance equations. The balance equations creating basis system dynamics are achieved. It is a wide foundation where different ideas can be raised thanks to constitutive equations. The authors are conscious that formulating the above equations is not easy, however, it can be useful to apply the suggested theory in the areas difficult to foresee. The similar problems would occur while formulating the boundary conditions.

References

1. J. Dereń, J. Haber, R. Pampuch, *Chemistry of Solids*, PWN, Warszawa 1975.
2. A. Antczak, M. Myśliwiec, P. Pruszczyk, edited by A. Dmoszyńska, *Internal Medicine. Haematology*, Medical Tribune Polska, Warszawa 2011.
3. G. M. Fuller, D. Shields, *Molecular Basic of Medical Cell Biology*, Medical Publishing House in Poland PZWL, Warszawa 2005
4. T. J. Hoffmann, B. Niechciałkowska *Foundations of mechanics of corroding materials*, Archives of mechanics **51** (1999) 391.
5. T.J. Hoffmann, *Fundamentals of Engineering Mechanics*, Publishing House of Poznan University of Technology, Poznan 2000.
6. T.J. Hoffmann, M. Chudzicka-Adamczak, *The Maxwell Stress Tensor for Magnetoelastic Materials,* Int. J. Engng Sci. **47** (2009) 735-739.
7. W. Kosiński, *Field Singularities and Wave Analysis in Continuum Mechanics*, PWN, Poznan 1981.
8. M. Pośpiech *Dynamika ośrodków o zmiennej masie w niesymetrycznej sprężystości,* PhD thesis, Poznan University of Technology, 2012.
9. C. Rymarz, Mechanics *of Continuous Media*, PWN Warszawa 1993.

XXV Symposium *Vibrations in Physical Systems,* Poznan – Bedlewo, May 15-19, 2012

Survey of Some Constitutive Models for Arterial Walls under Uniaxial and Biaxial Loading

Malgorzata A. JANKOWSKA
Poznan University of Technology, Institute of Applied Mechanics, Jana Pawła II 24
malgorzata.jankowska@put.poznan.pl

Romuald BĘDZIŃSKI
Wroclaw University of Technology
Biomedical Engineering and Experimental Mechanics Department, Łukasiewicza 7/9
romuald.bedzinski@pwr.wroc.pl

Abstract

The paper deals with some constitutive equations for arterial walls subjected to uniaxial and biaxial extension tests. In spite of a great number of various approaches to development of the strain-stress relations, the models selected for presentation seems to be good representatives of the most characteristic and fundamental ones.

Keywords: constitutive equations, arterial walls, uniaxial and biaxial extension

1. Introduction

A great many constitutive relations for arterial walls were proposed for a few last decades. We can start studying them from some comparative positions in the literature such as e.g. [Humphrey, 1995], [Humphrey, 2002], [Fung, 1993] or [Holzapfel, Grasser and Ogden, 2000]. Most of constitutive relations are phenomenological. Hence, they are strongly dependent on the experimental data. Specific forms of the appropriate mathematical expressions are also closely related to a kind of experiment performed and description of stress and strain state used in the model. In the paper we limit our considerations to the constitutive relations corresponding to the most common types of stretching tests, i.e. uniaxial and biaxial loading experiments.

2. Fundamentals of the Arterial Walls Structure and its Mechanical Behaviour

Blood vessels, in particular arteries considered, belong to the class of soft tissues. The mechanical behavior of arterial walls is first of all featured in Hooke's law disobeying, the nonlinear stress-strain relationships and the existence of hysteresis. Such behavior has some structural bases.

The basic structural elastic materials present in the arterial walls are elastin and collagen [Fung, 1993], [Holzapfel, 2001]. They are both proteins. Elastin is arranged in a form of thin strands. It is essentially a linearly elastic material. A three-dimensional network of long flexible elastin molecules may be stretched to about 2.5 times the initial length in the unloading configuration. Furthermore, it displays very small relaxation effects. Collagen is the main load carrying element in the arterial walls. Its molecules are wound together into fibrils and the fibrils are organized into fibers. In the arterial walls structure collagen appears as concentrically arranged fibers.

Consider the structure of the arterial wall. From the microscopic point of view the arterial walls consists of three layers [Fung, 1993], [Holzapfel, Gasser, Ogden, 2000]. The innermost layer is the intima. It is a single layer made of endothelial cells lining the arterial wall and located on a thin basal membrane. There are elastin and collagen fibers present in the intima. The orientation of collagen fibers is dispersed. The intima is very thin in young healthy individuals and its contribution to the mechanical behavior of the arterial wall is insignificant. Nevertheless, this layer stiffens and thickens with age. Note that in the intima we can also distinguish a subendothelial layer. Its thickness varies with such factors as topography, state of health and age. It almost does not exist in healthy young muscular arteries.

Next we have the middle layer of the artery called the media. It consists of a complex three-dimensional network of elastin, collagen fibrils and smooth muscle cells. The constituents considered are organized in a varying number of medial lamellar units (e.g. an average of 40 in the human abdominal aorta). The number of elastic laminae decreases toward the periphery and in muscular arteries the elastic laminae are hardly present. Note that the media is separated from the intima and the adventitia (i.e. the outermost layer of the artery) by the internal and external elastic lamina, respectively. The medial layer is concentrically fiber-reinforced and well-defined. Such a specific structure [Holzapfel, 2002] makes it the most significant layer in a healthy artery. It has the ability to resist high loads in the longitudinal and circumferential direction.

The outermost layer of the artery is called the adventitia. It consists of fibroblasts and fibrocytes (i.e. the cells producing the collagen and elastin), ground substance and thick bundles of collagen fibrils that form a fibrous tissue. It is surrounded by loose connective tissue [Holzapfel, Gasser, Ogden, 2000], [Holzapfel, 2002]. The thickness of the layer depends on the physiological function of the blood vessel, its type (elastic or muscular) and the topographical site. The collagen fibrils, arranged in helical structures, reinforce the arterial wall and contribute to its stability and strength.

From the experimental results is was concluded that biological tissues, with the arteries included, are not perfectly elastic. Their behaviour can be described by the following characteristic features [Fung, 1993]. The stress is affected by the history of strain and we can notice a significant difference in the stress response between loading and unloading. They show hysteresis. When they are held at a constant strain, they show stress relaxation (i.e. decreasing stress) and when are held at a constant stress, they show creep (i.e. increasing strain). The arterial walls are anisotropic and their stress-strain relationship is nonlinear. Their properties differ along the arterial tree and they also depend on age, state of health, lifestyle and many different environmental conditions.

3. Constitutive Models for Arterial Walls

Constitutive equations specify the properties of materials and can be determined by experiments. Knowledge of constitutive equations of biological tissues is also of great importance because of their necessity for boundary-value problems formulation, making the appropriate detailed analysis and evaluation of some predictions.

3.1. Stress-Strain Relationships in Uniaxial Extension

Description of the stress-strain state

Consider the arterial wall as a membrane. We can study its behaviour under uniaxial extension experiment of a longitudinal or circumferential strip of tissue with the shape of a rectangular parallelepiped [Tanaka and Fung, 1974], [Fung, 1993], [Hayashi, 1993]. Let us denote by L_0, W_0 and H_0 the length, the width and the thickness of the specimen, respectively. Under the load F, the length becomes L. Hence, we can define the stretch ratio λ as, $\lambda = L/L_0$. Furthermore, the tensile stress T is given as $T = F/A_0$, where A_0 is the initial cross-sectional area. With the assumption about incompressibility of the arterial walls [Chuong and Fung, 1984], when the length of the specimen is increased by a given stretch ratio λ, the cross-sectional area of a specimen is reduced by $1/\lambda$. Hence, for the Eulerian stress σ we have $\sigma = F/A = (F\cdot\lambda)/A_0 = T\cdot\lambda$.

Stress-strain relationship by Fung et al.

Consider the relationship between the load and the stretch ratio in the uniaxial extension process. The stress-strain relationship of the artery wall can be of the form [Fung, 1967], [Fung, 1993]

$$T = f(\lambda). \tag{1}$$

We can examine the function f if we plot $\mathrm{d}T/\mathrm{d}\lambda$ against T (i.e. the variation of the Young's modulus with stress at a given strain). The experimental curve can be fit, as a first approximation, by a straight line given by the equation

$$dT/d\lambda = \alpha(T+\beta) = \alpha T + \gamma\,, \tag{2}$$

where α, β, $\gamma = \alpha\cdot\beta$ are some constants; α represents a rate of increase of the Young's modulus with respect to increasing tension, γ is the intercept of the straight line segment to $T = 0$. Note that α, β can be determined with the experimental data, see [Fung, 1993].

An integration of (2) gives

$$T = \left(T^* + \beta\right)\exp\left\{\alpha\left(\lambda - \lambda^*\right)\right\} - \beta\,, \tag{3}$$

where T^*, λ^* correspond to one point on the curve in the region of validity of (2).

Furthermore, let us note that it is also a good practice to represent the experimental data with several straight line segments [Fung, 1993].

As pointed out in [Tanaka and Fung, 1974] the relationship considered is valid only if the stress is sufficiently large. For low stress levels the experimental data are fit with a power law [Wylie, 1966]. Tanaka and Fung examined the experimental data obtained from the uniaxial extension tests of longitudinal and circumferential strips of aortic wall tissue of the dog. The exponential stress-strain relation (3) were used for the description of the elastic behaviour of the aortic wall if $20 < T < 60$ [kPa] (i.e. within a physiological range but much below the breaking strength of the aorta).

3.2. Constitutive Equations in Biaxial Extension

Although in the section we study constitutive equations for arterial walls in biaxial experiments, we start from the description of the three-dimensional stress-strain states on the basis of a rectangular plate. Such plate can be treated as a model of a rectangular element of an arterial wall. Then, we introduce the fundamentals of the strain-energy function. Finally, the assumptions and mathematical formulation of the constitutive equations for arterial walls proposed in [Fung, Fronek and Patitucci, 1979] are given.

Description of the stress-strain state

Consider a rectangular plate (see Figure 1) of uniform thickness, made of orthotropic material as in [Fung, 1993], [Tong and Fung, 1976], [Fung, Fronek and Patitucci, 1979].

In the zero stress state the original size of the rectangle is determined by L_{10}, L_{20}. Furthermore, its thickness and density are equal to h_0 and ρ_0, respectively. If we impose forces F_{11}, F_{22} to the plate, then its edge lengths become L_1, L_2. The thickness and the density of the deformed plate are h and ρ, respectively. Since there is no shear stress acting on the edges of the plate, then the coordinates x, y are the principal axes.

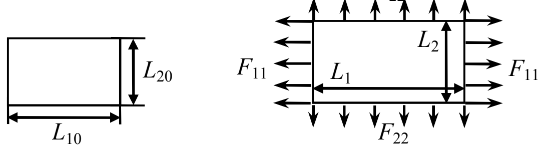

Figure 1. Deformation of a rectangle membrane subjected to tensile forces in a load-free (left) and a deformed (right) configuration

We can define the stress components of the Cauchy stress tensor $\boldsymbol{\sigma}$, the first Piola-Kirchhoff stress tensor **T** and the second Piola-Kirchhoff stress tensor **S**. Hence, we have

$$\begin{aligned} &\sigma_{11} = F_{11}/(L_2 h), \quad \sigma_{22} = F_{22}/(L_1 h), \quad T_{11} = F_{11}/(L_{20} h_0), \quad T_{22} = F_{22}/(L_{10} h_0), \\ &S_{11} = T_{11}/\lambda_1 = (\rho_0 \sigma_{11})/(\rho \lambda_1^2), \quad S_{22} = T_{22}/\lambda_2 = (\rho_0 \sigma_{22})/(\rho \lambda_2^2). \end{aligned} \tag{4}$$

Furthermore, the deformation can be measured by the principal stretch ratios $\lambda_1 = L_1/L_{10}$, $\lambda_2 = L_2/L_{20}$ and the strain components of the Green-Lagrange strain tensor **E** and the Euler-Almansi strain tensor **e**, i.e.

$$E_1 = (\lambda_1^2 - 1)/2, \quad E_2 = (\lambda_2^2 - 1)/2, \quad e_1 = (1 - 1/\lambda_1^2)/2, \quad e_2 = (1 - 1/\lambda_2^2)/2. \tag{5}$$

Furthermore, we can use infinitesimal strains given as follows

$$\varepsilon_1 = (L_1 - L_{10})/L_{10} = \lambda_1 - 1, \quad \varepsilon_2 = (L_2 - L_{20})/L_{20} = \lambda_2 - 1. \tag{6}$$

Strain-energy function (strain potential)

As we know (see [Fung, Fronek and Patitucci, 1979], [Fung, 1965]), if there is a one-to-one relationship between stresses and strains, then within the theory of elasticity, it can be shown that there exists a strain-energy function from which stresses can be computed from strains by differentiation.

We denote by W and ρ0 the strain energy (per unit mass of the tissue) and the mass density in the zero stress state, respectively. Then, ρ0W is the strain energy (per unit volume) in the zero stress state. Let W be expressed in terms of the nine strain components Eij, i,j = 1,2,3, and in a form that is symmetric in the symmetric components E12 and E21, E13 and E31, E23 and E32. If such a strain-energy function ρ0W exists, the stress components Sij, i,j = 1,2,3 can be obtained as derivatives of ρ0W. We have

$$S_{ij} = \partial(\rho_0 W)/\partial E_{ij}\ , \tag{7}$$

where the strain components E_{ij} are treated as independent variables [Fung, 1965].

Remarks [Fung, 1993]

Note that not all elastic materials have a strain-energy function. Such a function exists for perfectly elastic materials (the justification can be based on the thermodynamics). Living tissues, including arteries, are not perfectly elastic and we cannot obtain a strain-energy function in the thermodynamic sense. They are inelastic. As pointed out in e.g. [Fung, 1993], after preconditioning the stress-strain relationship does not vary very much with the strain rate. Moreover, if we also ignore the strain-rate effect, then the loading and unloading curves (which are not equal) can be treated separately as a uniquely defined stress-strain relationships. Such relationship is associated with a strain-energy function. Each curve is called a pseudoelasticity curve. Similarly, each strain-energy function is called a pseudoelasticity strain-energy function.

Constitutive equations by Fung et al.

For the constitutive model proposed in [Fung, Fronek and Patitucci, 1979], [Fung, 1993] an artery is represented in a form of a circular cylindrical tube. The artery is subjected to a biaxial loading of an internal pressure and a longitudinal stretch. The description of stress and strain state is given in accordance with polar coordinates (r,θ,z) in the radial, circumferential and axial directions, respectively. Note that the z axis is located at the center of the tube.

The simplifying assumptions are made with respect to stress distribution, i.e. the normal stress σ_{rr} in the radial direction is negligible in comparison with the normal stress $\sigma_{\theta\theta}$ in the circumferential direction. The stresses $\sigma_{\theta\theta}$ and σ_{zz} are approximately uniform throughout the wall thickness. The transverse shear stresses $\sigma_{z\theta}$, $\sigma_{r\theta}$ and σ_{rz} are assumed to be zero. The reasoning behind such assumptions can be seen in e.g. [Fung, Fronek and Patitucci, 1979], [Fung, 1993].

Then, the problem can be reduced to a two-dimensional case and we have

$$S_{\theta\theta} = \sigma_{\theta\theta}/\lambda_\theta^2 = \partial\left(\rho_0 W\right)/\partial E_{\theta\theta}, \quad S_{zz} = \sigma_{zz}/\lambda_z^2 = \partial\left(\rho_0 W\right)/\partial E_{zz}, \tag{8}$$

where $\rho_0 W$ is the strain-energy function given in terms of $E_{\theta\theta}$, E_{zz} and λ_θ, λ_z are the stretch ratios of the middle surface of the arterial wall in the circumferential and axial directions, respectively. Furthermore, we have

$$E_{\theta\theta} = \left(\lambda_\theta^2 - 1\right)/2, \quad E_{zz} = \left(\lambda_z^2 - 1\right)/2. \tag{9}$$

We introduce the following notations: R_i, R_0 and r_i, r_0 are the inner and outer radii in the load-free and deformed configuration, respectively; $H = R_0 - R_i$, $h = r_0 - r_i$, are the thicknesses of the wall in the load-free and deformed configuration; P_i, P_0 are the inner and outer pressures; F is the force applied at the ends of the artery. We also take $P_0 = 0$.

The pseudoelastic stress-strain relationship [Fung, Fronek and Patitucci, 1979], [Fung, 1993] for an artery subjected to an internal pressure and a longitudinal stretching within the physiological rage is given in the following exponential form

$$\rho_0 W = \frac{C}{2}\exp\left[\, a_1\left(E_{\theta\theta}^2 - E_{\theta\theta}^{*2}\right) + a_2\left(E_{zz}^2 - E_{zz}^{*2}\right) + 2a_4\left(E_{\theta\theta}E_{zz} - E_{\theta\theta}^{*}E_{zz}^{*}\right)\right], \tag{10}$$

where C is a stress-like material parameter and a_1, a_2, a_3 are dimensionless material parameters. Moreover, $E^*_{\theta\theta}, E^*_{zz}$ are strains corresponding to an arbitrary pair of stresses (usually chosen in the physiological range) $S^*_{\theta\theta}$, S^*_{zz}.

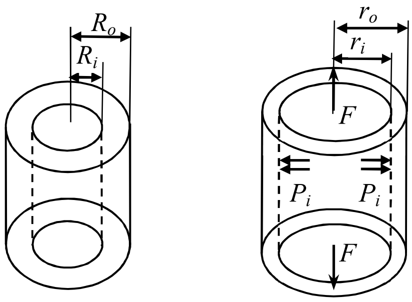

Figure 2. Deformation of a circular cylindrical tube subjected to an internal pressure and tensile longitudinal forces in a load-free (left) and a deformed (right) configuration

Note that there is another form of the constitutive equation (10) given as follows

$$\rho_0 W = \frac{C'}{2} \exp\left[a_1 E_{\theta\theta}^2 + a_2 E_{zz}^2 + 2a_4 E_{\theta\theta} E_{zz} \right]. \tag{11}$$

In the constant C' used in (11) the quantities with the asterisk from (10) are included.

The constants C or C', a_1, a_2, a_3 are calculated on the basis of the mean values of stresses obtained from the equilibrium condition, see [Fung, Fronek and Patitucci, 1979]. Defining $\lambda_\theta = r_o/R_o$, we have

$$\sigma_{\theta\theta} = \left(P_i r_o \lambda_\theta\right)/H - P_i, \quad S_{\theta\theta} = \left(P_i r_o\right)/\left(H\lambda_\theta\right) - P_i/\lambda_\theta^2, \tag{12}$$

$$\sigma_{zz} \doteq F/\left(\pi H\left(2R_o - H\right)\right) + \sigma_{\theta\theta}/2, \quad S_{zz} \doteq F/\left(\lambda_z^2 \pi H\left(2R_o - H\right)\right) + \left(S_{zz}\lambda_\theta^2\right)/\left(2\lambda_z^2\right). \tag{13}$$

In [Fung, Fronek and Patitucci, 1979], the constitutive equation (10) is used to describe the mechanical properties of rabbit arteries along the arterial tree.

3.3. Multi-Layer Constitutive Models by Holzapfel et al.

Now we describe multi-layer constitutive models proposed by Holzapfel at al. In the approach presented in [Holzapfel, Gasser and Ogden, 2000] the artery is treated as a two-layer thick-walled nonlinearly elastic circular cylindrical tube, with residual stresses, subjected to axial extension, inflation and torsion. Two layers represent the media and the adventitia. Each layer is composed of a non-collagenous matrix (treated as an isotropic material) and two families of collagen fibres (helically wound along the arterial axis, symmetrically dispersed with respect to the axis). The anisotropy in the mechanical response is induced by these fibres. In this way the overall response of each layer is orthotropic and can be accounted for the constitutive theory of fiber-reinforced solids. Since the model involves two layers and within each of them we consider information about the orientation of the collagen fibers obtained from histological tests, then we can say that the model is structural. Finally, for each arterial layer we assume that it is incompressible.

With details concerning the stress-strain state [Holzapfel, Gasser and Ogden, 2000], the constitutive equation that models each layer of the artery can be given as follows

$$\Psi = \frac{c}{2}\left(\bar{I}_1 - 3\right) + \frac{k_1}{2k_2}\sum_{i=4,6}\left\{\exp\left[k_2\left(\bar{I}_i - 1\right)^2 - 1\right]\right\}, \tag{14}$$

where Ψ is the isochoric strain-energy function (per unit volume), $c > 0$, $k_1 > 0$ are stress-like material parameters, $k_2 > 0$ is a dimensionless parameter and $\bar{I}_1, \bar{I}_4, \bar{I}_6$ are some invariants defined in [Holzapfel, Gasser and Ogden, 2000]. Since each layer responds with similar mechanical characteristic, we can use the same constitutive equation (14) with different sets of three material parameters (c, k_1, k_2).

Another approach is proposed [Holzapfel, Sommer, Gasser and Regitnig, 2005]. As previously, we assume that each arterial sample is incompressible, which require that $\lambda_r \lambda_\theta \lambda_z = 1$, where λ_r, λ_θ, λ_z are the principal stretches of the deformation corresponding to the radial, circumferential and axial directions (when there is no shear). The general mechanical characteristic of the arterial walls can be modelled with the strain-energy function Ψ (per unit volume) that is an extension of the constitutive model proposed in [Holzapfel, Gasser, Ogden, 2000], [Holzapfel, Gasser, Ogden, 2004]. We have

$$\Psi = \mu\left(I_1 - 3\right) + \frac{k_1}{k_2}\left(\exp\left\{k_2\left[(1-\rho)\left(I_1 - 3\right)^2 + \rho\left(I_4 - 1\right)^2\right]\right\} - 1\right), \tag{15}$$

where $I_1 = \lambda_\theta^2 + \lambda_z^2 + \left(\lambda_\theta \lambda_z\right)^{-2}$, $I_4 = \lambda_\theta^2 \cos^2\varphi + \lambda_z^2 \cos^2\varphi$, $I_4 > 1$ are invariants, $k_2 > 0$, $\rho \in [0,1]$ are dimensionless parameters and $\mu > 0$, $k_1 > 0$ are stress-like parameters. Note that φ is a phenomenological parameter and it is equal to the angle between the fiber reinforcement and the circumferential direction in a layer. Similarly as before, we can use (15) with different sets of five material parameters (μ, k_1, k_2, φ, ρ) for each layer.

In [Holzapfel, Sommer, Gasser and Regitnig, 2005] the modified constitutive equation (15) is applied for determination of layer-specific mechanical properties of human coronary arteries with nonatherosclerotic intimal thickening. The arteries from the individual layers in axial and circumferential directions are subjected to cyclic quasi-static uniaxial tension tests.

4. Conclusions

The paper presents some constitutive equations for arterial walls by Fung and Holzapfel et al. subjected to uniaxial and biaxial extension tests. Since the constitutive relations provide a useful tool for investigation of some biomaterial properties, then it seems of great importance to acquaint with the well-known models. The most recent approaches are directed towards taking into consideration also the specific architecture of arterial walls. Hence, the models are based on data obtained from some statistical analysis of histological sections. The direction seems to be very promising. Nevertheless, from the authors point of view, a complex nature of arterial walls with anisotropic and nonlinear elastic behaviour, makes the subject of the constitutive relations very important and still not well-known area of scientific research demanding continuous investigations.

References

1. C.J. Chuong, Y.C. Fung, *Compressibility and Constitutive Equation of Arterial Wall in Radial Compression Experiments*, Journal of Biomechanics, **17** (1984) 35-40.
2. Y.C. Fung, *Foundations of Solid Mechanics*. Prentice Hall 1965
3. Y.C. Fung, *Elasticity of soft tissues in simple elongation*, American Journal of Physiology, **28 (**1967) 1532-1544.
4. Y.C. Fung, *Biomechanics: Mechanical Properties of Living Tissues*, Springer 1993
5. Y.C. Fung, K. Fronek, P. Patitucci, *Pseudoelasticity of arteries and the choice of its mathematical expression*. American Journal of Physiology, **237**(5) (1979) H620-H631.
6. K. Hayashi, *Experimental approaches on measuring the mechanical properties and constitutive laws of arterial walls*. Journal of Biomechanical Engineering, **115 (1993)** 481-488.
7. G.A. Holzapfel, T.C. Gasser, R.W. Ogden, *A new constitutive framework for arterial wall mechanics and a comparative study of material models*. Journal of Elasticity, **61** (2009) 1-48.
8. G.A. Holzapfel, T.C. Gasser, R.W. Ogden, *Comparison of a multi-layer structural model for arterial walls with a Fung-type model, and issues of material stability*. ASME Journal of Biomechanical Engineering, **126** (2004) 264-275.
9. G.A. Holzapfel, G. Sommer, C.T. Gasser, P. Regitnig, *Determination of layer-specific mechanical properties of human coronary arteries with non-atherosclerotic intimal thickening, and related constitutive modeling*. American Journal of Physiology - Heart Circulation Physiology, **289** (2005) H2048-2058.
10. G.A. Holzapfel, *Biomechanics of soft tissue*. In: J. Lemaitre (ed.), The Handbook of Materials Behavior Models, Vol. 3, Multiphysics Behaviors, Chapter 10, Composite Media, Biomaterials, Academic Press: Boston 2001, 1049-1063.
11. G.A. Holzapfel, *Biomechanics of soft tissues with application to arterial walls*. In: J.A.C. Martins and E.A.C. Borges Pires (eds.), Mathematical and Computational Modeling of Biological Systems, Chapter 1, Centro Internacional de Matemática CIM: Coimbra, Portugal 2002, 1-37.
12. J.D. Humphrey, *Mechanics of arterial walls: Review and directions*. Critical Reviews in Biomedical Engineering, **23** (1995) 1-162.
13. J.D. Humphrey, *Cardiovascular Solid Mechanics: Cells, Tissues, and Organs*. Springer 2002.
14. T.T. Tanaka, Y.C. Fung, *Elastic and inelastic properties of the canine aorta and their variation along the aortic tree*. Journal of Biomechanics, **7** (1974) 357-370.
15. P. Tong, Y.C. Fung, *The Stress-Strain Relationship for the Skin*. Journal of Biomechanics, **9** (1976) 649-657.
16. E.R. Wylie, *Flow through taped tubes with nonlinear wall properties*. In Biomechanics Symposium (Y.C. Fung ed.), American Society of Mechanical Engineering, New York 1996, 82-95.

XXV Symposium *Vibrations in Physical Systems,* Poznan – Bedlewo, May 15-19, 2012

Microlocal Modelling in Elastodynamic of Periodically Compound Plates

Katarzyna JELENIEWICZ
Warsaw University of Life Sciences - SGGW
ul. Nowoursynowska 159, 02-776 Warszawa, k.jeleniewicz@tlen.pl

Wiesław NAGÓRKO
Warsaw University of Life Sciences – SGGW
ul. Nowoursynowska 159, 02-776 Warszawa, wieslaw_nagorko@sggw.pl

Abstract

In the paper, we will present certain method of modelling of elastic, heterogeneous, anisotropic and periodically multicomponent plates. The method is called the microlocal homogenization or the homogenization with microlocal parameters. It differs from the currently known methods in the fact that it does not consist in solving the problem on the basic cell. The system of assumptions and set of modeling relationships is different from that in the classical method of asymptotic homogenization. There occur not only displacement and stress fields in a body, but also some new fields – microlocal parameters – that describe the behavior of a plate inside the basic cell. In the constructed model, there is 1 + *n* coupled equations, corresponding to three displacements and *n* microlocal parameters. Moreover, the model equations depend on some postulated functions called *shape functions*, which must be known. In the paper, we will propose such functions and carry out an analysis of free vibrations of multicomponent plates.

Keywords: elastodynamics of plates, methods of homogenization, periodically compound plates

1. Introduction

Let the reference configuration of the plate be a region $\Omega = \Pi \times (0,h)$, where $h > 0$ and $\Pi = (0,L_1)\times(0,L_2) \subset R^2$. The Cartesian coordinate system will be assumed in such a way that $x_\alpha \in \Pi$, $\alpha = 1,2$, $x \in (0,h)$. Moreover, we assume that the plate is periodically heterogeneous and a repeating element is a rectangle determined by straight lines $x_1 = nl_1$, $x_2 = ml_2$, $n = 0,1,2,...n_1$, $m = 0,1,2,...n_2$, and $l_\alpha << L_\alpha$, $\alpha = 1,2$.

A basic cell in a point (x_1, x_2) will be the set

$$\Delta(x_1,x_2) = \left(x_1 - \frac{l_1}{2}, x_1 + \frac{l_1}{2}\right)\times\left(x_2 - \frac{l_2}{2}, x_2 + \frac{l_2}{2}\right)$$

Furthermore, let the basic cell $\Delta(l/2, l_2/2)$ be divided by straight lines $x_1 = al_{1a}$, $x_2 = bl_{2b}$, $a = 1,2,... a_0$, $b = 1,2,... b_0$, into rectangles Δ_{ab}, for which we assume that their material is homogeneous (Fig. 1).

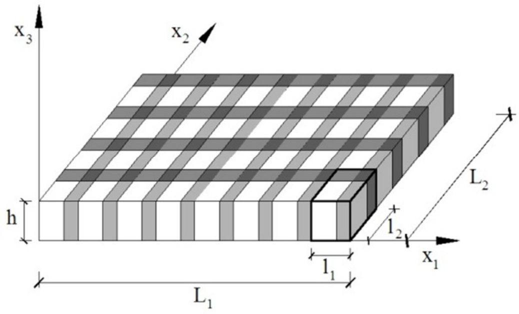

Figure 1. A multicomponent plate

We define the stiffness moduli as

$$B_{\alpha\beta\gamma\delta} = \int_0^h \left(C_{\alpha\beta\gamma\delta} - \frac{C_{\alpha\beta 33} C_{\gamma\delta 33}}{C_{3333}} \right) x_3^2 dx_3 \tag{1}$$

where $C_{\alpha\beta\gamma\delta}$, $C_{\alpha\beta 33}$, C_{3333} , $\alpha, \beta, \gamma, \delta = 1{,}2$ are the material functions.

The mass density and moduli (1) of the plates under consideration will be defined as:

$$\begin{aligned} \rho &= \rho(x_1, x_2)\big|_{(x_1,x_2)\in\Delta_{ab}} = \rho^{ab}, \\ B_{\alpha\beta\gamma\delta} &= B_{\alpha\beta\gamma\delta}(x_1, x_2)\big|_{(x_1,x_2)\in\Delta_{ab}} = B^{ab}_{\alpha\beta\gamma\delta} \end{aligned} \tag{2}$$

where $\rho^{ab}, B^{ab}_{\alpha\beta\gamma\delta}$, $a = 1,2,...,a_0$, $b = 1,2,...,b_0$, $\alpha, \beta, \gamma, \delta = 1{,}2$ are constant for all combinations of subscripts and superscripts.

If there exist at least two rectangles Δ_{ab}, Δ_{cd} for which $\rho^{ab} \neq \rho^{cd}$ or $\boldsymbol{B}^{ab} \neq \boldsymbol{B}^{cd}$ where $\boldsymbol{B} = (B_{\alpha\beta\gamma\delta})$, $\alpha, \beta, \gamma, \delta = 1{,}2$ then the plate will be called *multicomponent*.

Let $w = w(x_1, x_2, t)$, $(x_1, x_2) \in \Pi$, $t \in \langle t_0, t_1 \rangle$ be a plate deflection.

The equation describing dynamic problems in multicomponent plates has the form

$$\rho\ddot{\omega} + (B_{\alpha\beta\gamma\delta} w,_{\alpha\beta}),_{\gamma\delta} = p \tag{3}$$

where ρ is the mass density and p is an external load of the plate.

After defining a functional

$$L = \frac{1}{2}\rho(\dot{w})^2 - \frac{1}{2} B_{\alpha\beta\gamma\delta} w,_{\alpha\beta}\, w,_{\gamma\delta} - pw \tag{4}$$

the equation (3) can be written in the form of the Euler-Lagrange equation

$$\left(\frac{\partial L}{\partial w,_{\alpha\beta}} \right),_{\gamma\delta} + \frac{\partial}{\partial t}\frac{\partial L}{\partial \dot{w}} - \frac{\partial L}{\partial w} = 0 \tag{5}$$

For the multicomponent plates, the solution of the equation (3), also numerical, is difficult. It is reasonable, in this situation, to search for simpler models, where the equation coefficients are constant. In this paper, we count averaged coefficients by the use of the method of microlocal parameters [1-2].

2. Averaged model of multicomponent plates

According to [1] we assume the plate deflection in a form

$$w(x_1,x_2,t)=u(x_1,x_2,t)+h^A(x_1,x_2)v^A(x_1,x_2,t) \\ (x_1,x_2)\in\Pi,\ t\in\langle t_0,t_1\rangle \tag{6}$$

Substitution of the decomposition of plate deflection (6) to the functional (4) and its asymptotical averaging gives:

$$\langle L\rangle=\frac{1}{2}\langle\rho\rangle(\dot{u})^2-\frac{1}{2}\langle B_{\alpha\beta\gamma\delta}\rangle u,_{\alpha\beta}u,_{\gamma\delta}-\frac{1}{2}\langle B_{\alpha\beta\gamma\delta}h,^A_{\alpha\beta}h,^B_{\gamma\delta}\rangle v^Av^B \\ -\langle B_{\alpha\beta\gamma\delta}h,^A_{\gamma\delta}\rangle u,_{\alpha\beta}v^A-pu \tag{7}$$

where, for an arbitrary function *f*, we denoted by $\langle f\rangle$:

$$\langle f\rangle=\frac{1}{|\Delta|}\int_\Delta f(\boldsymbol{x})\,d\Delta \tag{8}$$

The Euler-Lagrange equations in this case assume a form

$$\left(\frac{\partial\langle L\rangle}{\partial u_{k,l}}\right)_{,l}+\frac{\partial}{\partial t}\frac{\partial\langle L\rangle}{\partial\dot{u}_k}-\frac{\partial\langle L\rangle}{\partial u_k}=0 \\ \frac{\partial\langle L\rangle}{\partial v_k^A}=0 \tag{9}$$

thus the equation of motion for multicomponent plate assumes a form

$$\langle\rho\rangle\ddot{u}-\langle B_{\alpha\beta\gamma\delta}\rangle u,_{\alpha\beta\gamma\delta}-\langle B_{\alpha\beta\gamma\delta}h,^A_{\gamma\delta}\rangle v,^A_{\alpha\beta}+p=0 \\ \langle B_{\alpha\beta\gamma\delta}h,^A_{\alpha\beta}h,^B_{\gamma\delta}\rangle v^B+\langle B_{\alpha\beta\gamma\delta}h,^A_{\gamma\delta}\rangle u,_{\alpha\beta}=0 \tag{10}$$

Let us introduce denotations

$$\eta_{1a}=\frac{l_{1a}}{l_1},\quad \eta_{2b}=\frac{l_{2b}}{l_2},\quad \eta^{ab}=\eta_{1a}\eta_{2b},\quad \eta^{abA}_{\alpha\beta}=\frac{1}{l_1l_2}\iint_{\Delta_{ab}}h,^A_{\alpha\beta}\,d\Delta, \\ \eta^{abAB}_{\alpha\beta\gamma\delta}=\frac{1}{l_1l_2}\iint_{\Delta_{ab}}h,^A_{\alpha\beta}h,^B_{\gamma\delta}\,d\Delta \tag{11}$$

then the coefficients appearing in the equations (10) are equal

$$\begin{aligned}
&\langle \rho \rangle = \eta^{ab}\rho^{ab} = \rho^{eff} \\
&\langle B_{\alpha\beta\gamma\delta} \rangle = \eta^{ab} B^{ab}_{\alpha\beta\gamma\delta} \equiv D_{\alpha\beta\gamma\delta} \\
&\langle B_{\alpha\beta\gamma\delta} h,^{A}_{\gamma\delta} \rangle = \eta^{abA}_{\alpha\beta} B^{ab}_{\alpha\beta\gamma\delta} \equiv D^{A}_{\alpha\beta} \\
&\langle B_{\alpha\beta\gamma\delta} h,^{A}_{\alpha\beta}\, h,^{B}_{\gamma\delta} \rangle = \eta^{abAB}_{\alpha\beta\gamma\delta} B^{ab}_{\alpha\beta\gamma\delta} \equiv D^{AB}
\end{aligned} \tag{12}$$

and the equations (10) can be written as

$$\begin{cases} \rho^{eff}\ddot{u} - D_{\alpha\beta\gamma\delta} u,_{\alpha\beta\gamma\delta} - D^{A}_{\alpha\beta} v,^{A}_{\alpha\beta} + p = 0, \\ D^{A}_{\alpha\beta} u,_{\alpha\beta} + D^{AB} v^{B} = 0 \end{cases} \tag{13}$$

Let a matrix D^{AB} be a nonsingular matrix; then we can determine fluctuation v^{A} from the equation $(13)_2$

$$v^{A} = -(D^{AB})^{-1} D^{B}_{\alpha\beta} u,_{\alpha\beta} \tag{14}$$

Substitution of (14) to the equation $(13)_1$ gives

$$\rho^{eff}\ddot{u} - D^{eff}_{\alpha\beta\gamma\delta} u,_{\alpha\beta\gamma\delta} + p = 0 \tag{15}$$

where

$$D^{eff}_{\alpha\beta\gamma\delta} = D_{\alpha\beta\gamma\delta} - D^{A}_{\alpha\beta} (D^{AB})^{-1} D^{B}_{\gamma\delta} \tag{16}$$

The quantities defined by the equations (16) are the effective stiffness moduli obtained as a result of microlocal averaging. The equation (15) has the analogical form to the well-known equation of plate deflection, but there occur not stiffness moduli $B_{\alpha\beta\gamma\delta}$, which are functions, but the efficient stiffness moduli, which, due to averaging process, are constant.

3. Example of a four-component plate

As a special case of multicomponent plate we consider a representative element consisting of four components. The component dimensions are denoted in Fig. 2.

The decomposition of plate deflection (4) will be assumed in a form, [2]:

$$w(x_1, x_2, t) = u(x_1, x_2, t) + h^1(x_1) v^1(x_1, x_2) + h^2(x_2) v^2(x_1, x_2)$$

where the shape function h^1:

$$h^1(x_1) = \begin{cases} \frac{l_1}{4} x_1 (2x_1 - l_1), & x_1 \in \left(0, \frac{l_1}{2}\right) \\ -\frac{l_1}{4}(2x_1 - l_1)(x_1 - l_1), & x_1 \in \left(\frac{l_1}{2}, l_1\right) \end{cases} \tag{17}$$

The function $h^2 = h^2(x_2)$ can be defined analogically to $h^1 = h^1(x_1)$. The functions h^A , A = 1, 2, are periodic and oscillating.

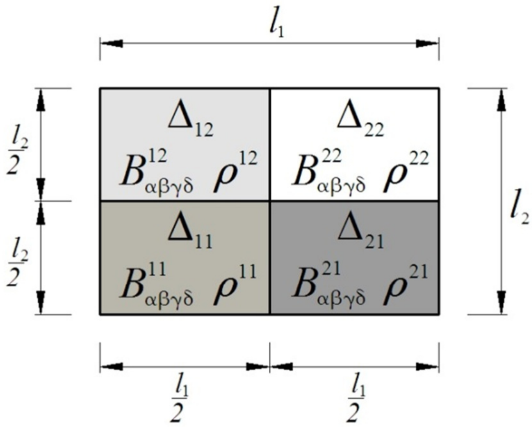

Figure 2. Four-component element

The quantities (11) appearing in the equations (13) are then equal

$$\begin{gathered} \eta^{11} = \eta^{12} = \eta^{21} = \eta^{22} = \frac{1}{4} \\ \eta^{111}_{11} = \eta^{121}_{11} = -\eta^{211}_{11} = -\eta^{221}_{11} = \frac{l_1}{4} \\ \eta^{112}_{22} = \eta^{122}_{22} = -\eta^{212}_{22} = -\eta^{222}_{22} = \frac{l_2}{4} \\ \eta^{1111}_{1111} = \eta^{1211}_{1111} = \eta^{2111}_{1111} = \eta^{2211}_{1111} = \frac{l_1^2}{4} \\ \eta^{1122}_{2222} = \eta^{1222}_{2222} = \eta^{2122}_{2222} = \eta^{2222}_{2222} = \frac{l_2^2}{4} \\ \eta^{1112}_{1122} = \eta^{1212}_{1122} = \eta^{2112}_{1122} = \eta^{2212}_{1122} = \eta^{1121}_{2211} = \eta^{1221}_{2211} = \eta^{2121}_{2211} = \eta^{2221}_{2211} = \frac{l_1 l_2}{4} \end{gathered} \tag{18}$$

The remaining coefficients are equal 0.

Now let us assume that the plate is heterogeneous only in the x_1 direction, Fig. 3.

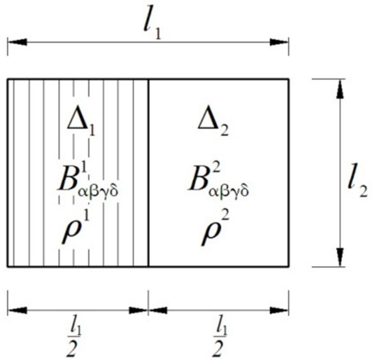

Figure 3. Two-component element

This means that

$$B^{11}_{\alpha\beta\gamma\delta} = B^{12}_{\alpha\beta\gamma\delta} = B^{1}_{\alpha\beta\gamma\delta}\,,\; B^{21}_{\alpha\beta\gamma\delta} = B^{22}_{\alpha\beta\gamma\delta} = B^{2}_{\alpha\beta\gamma\delta}$$

$$\rho^{11} = \rho^{12} = \rho^{1}\,,\; \rho^{21} = \rho^{22} = \rho^{2}$$

The coefficients (11) have now a form

$$\eta^{11} = \eta^{21} = \frac{1}{2}, \quad \eta^{111}_{11} = -\eta^{211}_{11} = \frac{l_1}{2}, \quad \eta^{1111}_{1111} = \eta^{2111}_{1111} = \frac{l_1^2}{2} \tag{19}$$

Substitution the quantities (19) to the equations (13) gives

$$\begin{gathered} \rho^{eff}\ddot{u} + \left(\frac{B^1_{\alpha\beta\gamma\delta} + B^2_{\alpha\beta\gamma\delta}}{2}\right)u,_{\alpha\beta\gamma\delta} + \frac{l_1}{2}(B^1_{11\gamma\delta} - B^2_{11\gamma\delta})v_{1,\gamma\delta} = p \\ \frac{l_1}{2}(B^1_{11\gamma\delta} - B^2_{11\gamma\delta})u,_{\gamma\delta} + \frac{l_1^2}{2}(B^1_{1111} + B^2_{1111})v_1 = 0 \end{gathered} \tag{20}$$

The equation $(20)_2$ enables to determine the fluctuation v_1:

$$v_1 = -\frac{(B^1_{11\gamma\delta} - B^2_{11\gamma\delta})}{l_1\,(B^1_{1111} + B^2_{1111})}u,_{\gamma\delta} \tag{21}$$

then the equation $(18)_1$ assumes a form

$$\rho^{eff}\ddot{u} + B^{eff}_{\alpha\beta\gamma\delta}u,_{\alpha\beta\gamma\delta} = p \tag{22}$$

where

$$B^{eff}_{\alpha\beta\gamma\delta} = \frac{B^1_{\alpha\beta\gamma\delta} + B^2_{\alpha\beta\gamma\delta}}{2} - \frac{(B^1_{11\gamma\delta} - B^2_{11\gamma\delta})^2}{2(B^1_{1111} + B^2_{1111})}.$$

If $B^1_{\alpha\beta\gamma\delta} = B^2_{\alpha\beta\gamma\delta}$ and $\rho^1 = \rho^2$ (homogeneous cell), the equation takes the form of the classical plate equation.

In the case of a cell consisting of isotropic components we have

$$\begin{aligned} &B^1_{1111} = B^1_{2222} = \lambda_1 + 2\mu_1, \quad B^1_{1122} = \lambda_1 \;\; B^1_{1212} = \mu_1 \\ &B^2_{1111} = B^2_{2222} = \lambda_2 + 2\mu_2, \quad B^2_{1122} = \lambda_2 \;\; B^2_{1212} = \mu_2 \end{aligned} \tag{23}$$

where $\lambda_\alpha, \eta_\alpha$ are the Lamé parameters.

The coefficients B^{eff} are equal

$$\begin{aligned} B^{eff}_{1111} &= \frac{\lambda_1 + 2\mu_1 + \lambda_2 + 2\mu_2}{2} + \left[\frac{\lambda_1 - \lambda_2 + 2\mu_1 - 2\mu_2}{2(\lambda_1 + 2\mu_1 + \lambda_2 + 2\mu_2)} \right] \\ B^{eff}_{2222} &= \frac{\lambda_1 + 2\mu_1 + \lambda_2 + 2\mu_2}{2} + \left[\frac{\lambda_1 - \lambda_2}{2(\lambda_1 + 2\mu_1 + \lambda_2 + 2\mu_2)} \right] \\ B^{eff}_{1122} &= \frac{\lambda_1 + \lambda_2}{2} + \left[\frac{\lambda_1 - \lambda_2}{2(\lambda_1 + 2\mu_1 + \lambda_2 + 2\mu_2)} \right] \\ B^{eff}_{1212} &= \frac{\mu_1 + \mu_2}{2}. \end{aligned} \tag{24}$$

The components in the square brackets in the formulas (24) describe the impact of the microlocal parameter v_1 on the plate behavior.

Now let us assume that the plate heterogeneity is of a chessboard-type (Fig. 4). It means that

$$B^{11}_{\alpha\beta\gamma\delta} = B^{22}_{\alpha\beta\gamma\delta} = B^1_{\alpha\beta\gamma\delta}, \; B^{21}_{\alpha\beta\gamma\delta} = B^{21}_{\alpha\beta\gamma\delta} = B^2_{\alpha\beta\gamma\delta}$$

$$\rho^{11} = \rho^{22} = \rho^1, \; \rho^{21} = \rho^{12} = \rho^2.$$

The coefficients (11) are in this case identical with the coefficients (18) and the quantities (12) are then equal

$$\begin{aligned} D_{\alpha\beta\gamma\delta} &= \frac{B^1_{\alpha\beta\gamma\delta} + B^2_{\alpha\beta\gamma\delta}}{2} \\ D^A_{\alpha\beta} &= 0, \quad A = 1,2 \end{aligned} \tag{25}$$

Substitution of the quantity (25) to the equations (13) gives

$$\begin{aligned}
&\rho^{eff}\,\ddot{u} + \left(\frac{B^1_{\alpha\beta\gamma\delta} + B^2_{\alpha\beta\gamma\delta}}{2}\right) u,_{\alpha\beta\gamma\delta} = p \\
&D^{AB} v^B = 0
\end{aligned} \tag{26}$$

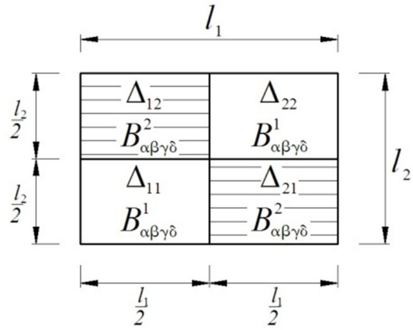

Figure 4. Representative element with the chessboard-type heterogeneity

From the equation $(26)_2$ we can conclude $v_1 = 0$, $v_1 = 0$. In this case, the heterogeneous and anisotropic body behaves like a homogeneous anisotropic body, considering the fact that the mass density and material constants of this homogeneous body are the arithmetic means of the mass density and material constants of the heterogeneous body components.

4. Conclusions

The method of averaging of discontinuous function coefficients of the equation of plate deflection, used in the work, led to a model with $1+n$ equations with the constant effective coefficients. The unknowns in this set of equations are the averaged deflection *u* and *n* microlocal parameters describing the plate heterogeneity. This system is convenient for the analysis of dynamic problems in plates, particularly free vibrations, which will be discussed at the conference.

References

1. *Mathematical modelling and analysis in continuum mechanics of microstructured media*, ed. Woźniak Cz. et al., Wyd. Politechniki Śląskiej, Gliwice 2010.
2. Nagórko W., *Microlocal modelling of periodic elastic plates*, (in:) Mathematical methods in continuum mechanics, Wyd. Politechniki Łódzkiej, Łódź 2011, 317-329.

XXV Symposium *Vibrations in Physical Systems,* Poznan – Bedlewo, May 15-19, 2012

Vibrations of Microstructured Functionally Graded Plates

Jarosław JĘDRYSIAK
Technical University of Łódź, Department of Structural Mechanics
al. Politechniki 6, 90-924 Łódź, Poland, jarek@p.lodz.pl

Abstract

Functionally graded plates with a microstructure are considered. The size of the microstructure is assumed to be of an order of the plate thickness. To take into account the effect of the microstructure on vibrations of these plates the tolerance modelling method is applied. Using this method we obtain model equations with smooth functional coefficients involving terms dependent of the microstructure size.

Keywords: functionally graded plates, microstructure, vibrations, tolerance modelling

1. Introduction

In this note plates with constant thickness d made of two materials are objects under consideration. On the microlevel these materials are tolerance-periodic distributed along only one direction $x \equiv x_1$, cf. Figure 1. Averaged properties of these plates are assumed to be slowly-varied along this direction, which is normal to interfaces between the materials. Hence, these plates consist of many small elements on the microlevel. Every element is treated as a plate band with a span l, called *the microstructure parameter*. Moreover, adjacent elements are nearly identical, but distant elements can be very different. Hence, plates of this kind are treated to be made of a certain *functionally graded material* (*FGM*), cf. [8], and are called *functionally graded plates*, cf. [4, 5]. The thickness d is assumed to be the same order of the microstructure parameter l, $d \sim l$, cf. [3, 2, 7, 1], and material properties of these plates to be tolerance-periodic functions in x and independent of x_2.

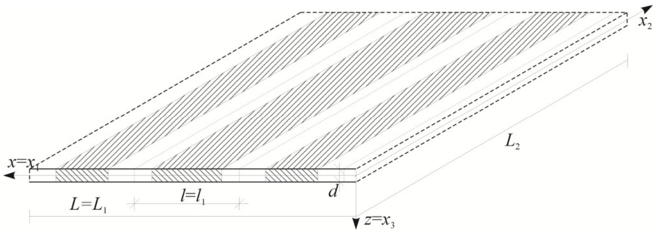

Figure 1. A fragment of a functionally graded plate under consideration

Plates of this kind can be analysed using various kinematic assumptions. In this contribution two various model equations are presented – one based on the Kirchhoff-type plates theory relations and other – based on the Hencky-Bolle-type plates theory relations. Unfortunately, obtained governing equations have highly-oscillating, tolerance-periodic, non-continuous functional coefficients of x. These equations are not good tools to analyse various special problems of these plates. However, in order to investigate thermomechanical problems of FGM-type structures (also for plates) modelling methods for periodic structures can be used, cf. [8, 6]. Unfortunately, the effect of the microstructure size is neglected in governing equations of these models.

The main aim of this contribution is to show averaged equations of *tolerance models of functionally graded plates*, having smooth, slowly-varying coefficients of x. These equations are obtained in the framework of *the tolerance modelling*, cf. [10, 9, 2], and involve terms describing the effect of the microstructure size. Similar tolerance models for thin transversally graded plates under the condition $d<<l$ is shown in [4, 2, 5].

2. Fundamental relations

Let $\mathbf{x}\equiv(x_1,x_2)$, $x=x_1$ and $z\equiv x_3$. The undeformed plate occupies the region denoted by $\Omega \equiv \{(\mathbf{x},z): -d/2 \le z \le d/2, \mathbf{x} \in \Pi\}$, where Π is the midplane and d is the constant plate thickness. Denote by ∂_α derivatives of x_α, and also $\partial_{\alpha\ldots\delta}\equiv\partial_\alpha\ldots\partial_\delta$. The "basic cell" on Ox_1x_2 is defined as $\Delta \equiv [-l/2, l/2] \times \{0\}$, with cell length dimension along the x-axis equal l, cf. Figure 2. The length l satisfies conditions $d\sim l$ and $l<<\min(L_1,L_2)$, and is called *the microstructure parameter*. All material and inertial properties of the plate, as mass density $\rho=\rho(\cdot,x_2,z)$ and elastic moduli $a_{ijkl}=a_{ijkl}(\cdot,x_2,z)$, are assumed to be tolerance-periodic functions in x, even functions in z and independent of x_2. Let $a_{\alpha\beta\gamma\delta}$, $a_{\alpha\beta33}$, a_{3333} be the non-zero components of the elastic moduli tensor. Denote $c_{\alpha\beta\gamma\delta}\equiv a_{\alpha\beta\gamma\delta}-a_{\alpha\beta33}a_{\gamma\delta33}(a_{3333})^{-1}$.

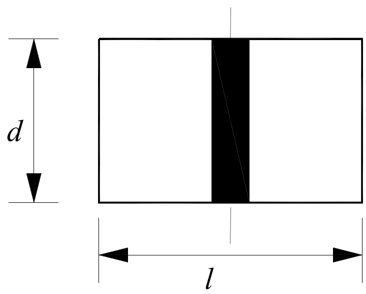

Figure 2. "Basic cell" of the plate under consideration

Properties of these plates are described by tolerance-periodic functions of x: a mass density per unit area μ, a rotational inertia ϑ and stiffnesses $b_{\alpha\beta\gamma\delta}$, $d_{\alpha\beta}$, defined as:

$$\mu \equiv \int_{-d/2}^{d/2} \rho dz, \quad \vartheta \equiv \int_{-d/2}^{d/2} \rho z^2 dz, \quad b_{\alpha\beta\gamma\delta} \equiv \int_{-d/2}^{d/2} c_{\alpha\beta\gamma\delta} z^2 dz, \quad d_{\alpha\beta} \equiv \tfrac{5}{6}\int_{-d/2}^{d/2} c_{\alpha 3\beta 3} dz.$$

Let us denote plate displacements by u_i (i=1,2,3), loads normal to the midplane by p.

Applying the kinematic assumptions of the Kirchhoff-type plates theory, dynamics of the functionally graded plates under consideration is described by the following equation:

$$\partial_{\alpha\beta}(b_{\alpha\beta\gamma\delta}\partial_{\gamma\delta}w) + \mu\ddot{w} - \partial_\alpha(\vartheta\partial_\beta\ddot{w})\delta_{\alpha\beta} = p, \tag{1}$$

for the plate deflection $w=u_3$.

However, from the kinematic assumptions of the Hencky-Bolle-type plates theory the system of three equations is derived:

$$\begin{aligned} &\partial_\beta(b_{\alpha\beta\gamma\delta}\partial_\delta\phi_\gamma) - d_{\alpha\beta}(\partial_\beta w + \phi_\beta) - \vartheta\ddot{\phi}_\alpha = 0, \\ &\partial_\alpha[d_{\alpha\beta}(\partial_\beta w + \phi_\beta)] - \mu\ddot{w} = -p, \end{aligned} \tag{2}$$

where w is the plate deflection and ϕ_α, α=1,2, are rotations.

The governing equations (1) and (2) have highly-oscillating, tolerance-periodic, non-continuous functional coefficients of x. Hence, these equations are not good tools to analyse special problems of the plates under consideration. To derive model equations with smooth continuous coefficients the tolerance averaging method is applied.

3. Tolerance modelling

Basic concepts of the tolerance averaging method are presented in [10, 9, 2]. There are: an averaging operator, a slowly-varying function, a tolerance-periodic function, a highly-oscillating function, a fluctuation shape function. Here, we mention only two of them. Let $\Delta(\mathbf{x}) \equiv \mathbf{x} + \Delta$, $\Pi_\Delta = \{\mathbf{x} \in \Pi : \ \Delta(\mathbf{x}) \subset \Pi\}$, be a cell at $\mathbf{x} \in \Pi_\Delta$. *The averaging operator* for an arbitrary integrable function f is defined by

$$< f > (x) = \tfrac{1}{l}\int_{\Delta(\mathbf{x})} f(y)dy. \tag{3}$$

For the tolerance-periodic of x function f its averaged value by (3) is a slowly-varying function in x. The important concept of this method is also the fluctuation shape function, which is assumed in the form shown in Figure 3.

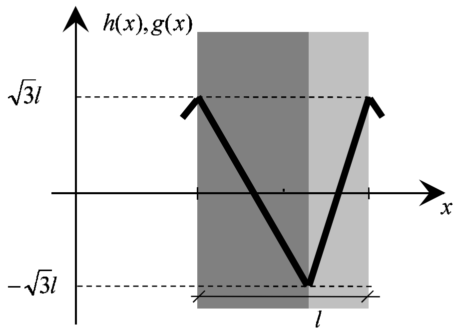

Figure 3. A fragment of fluctuation shape functions

Using the aforementioned concepts the fundamental assumptions of the tolerance modelling for the plates under consideration can be formulated.

The main assumption is *the micro-macro decomposition* of a basic unknown field in the problem under consideration. Here, there are formulated two independent those assumptions, which lead to various tolerance models of functionally graded plates.

The micro-macro decomposition for the Kirchhoff-type plates.

Displacements of the plate midplane u_i (i=1,2,3) are assumed that they can be decomposed in the form similar to that for periodic plates, cf. [7], or functionally graded shells, cf. [3, 2]:

$$u_3(\mathbf{x},z,t)=w(\mathbf{x},t)=W(\mathbf{x},t), \qquad u_\alpha(\mathbf{x},z,t)=-z[\partial_\alpha W(\mathbf{x},t)+h(x)V_\alpha(\mathbf{x},t)], \tag{4}$$

with new unknowns: a *macrodeflection* W and *fluctuation variables* V_α (α=1,2), which both of them are slowly-varying functions in x; and the known fluctuation shape function h, assumed in the form of a saw-like function, cf. Figure 3.

The micro-macro decomposition for the Hencky-Bolle-type plates.

Displacements of the plate midplane u_i (i=1,2,3) are assumed to be decomposed in the form similar to that for periodic plates, cf. [1]:

$$u_3(\mathbf{x},z,t)=w(\mathbf{x},t)=W(\mathbf{x},t), \qquad u_\alpha(\mathbf{x},z,t)=z[\Phi_\alpha(\mathbf{x},t)+g(x)\Theta_\alpha(\mathbf{x},t)], \tag{5}$$

with new unknowns: a *macrodeflection* W, *macrorotations* Φ_α (α=1,2), *fluctuation variables* Θ_α (α=1,2), which all of them are slowly-varying functions in x; and the known fluctuation shape function g, which has the form of a saw-like function.

The next main assumption of the tolerance averaging method is the tolerance averaging approximation in which it is assumed that in the modelling terms of an order of the tolerance parameter δ are negligibly small, e.g.:

$$\begin{aligned}
&< f > (x) =< \bar{f} > (\mathbf{x}) + O(\delta), \qquad < fF > (x) =< f > (x)F(x) + O(\delta),\\
&< f\partial_\alpha (hF) > (x) =< f\partial_\alpha h > (x)F(x) + O(\delta),\\
&x \in (0, L_1);\ \alpha = 1,2; 0 < \delta << 1,
\end{aligned} \tag{6}$$

where f is a tolerance-periodic function of x, F is a slowly-varying function of x and h is the known fluctuation shape function.

Using the above concepts and assumptions we can make some manipulations by using various tolerance modelling procedures, cf. [11, 10, 9]. Here, the procedure shown in [11] is applied, which can be divided on four steps. The first of them is to substitute micro-macro decompositions (4) or (5) to equations (1) or (2), respectively. In the second step these equations are averaged by using the averaging operator (3). The third step is a formulation of the problem to find the fluctuation variables. In order to obtain these unknowns the orthogonal method can be used, i.e. the governing equations (1) or (2) are multiplied by the fluctuation shape function and then averaged by formula (3). In the fourth step micro-macro decompositions (4) or (5) are substituted into obtained equations.

4. Governing equations of tolerance models

Using the aforementioned tolerance modelling procedure, after some manipulations governing equations of two different tolerance models are derived.

4.1. The tolerance model equations of the Kirchhoff-type functionally graded plates

The tolerance averaging procedure leads from thin plates equations (1) to the following governing equations:

$$
\begin{aligned}
&\partial_{\alpha\beta}(<b_{\alpha\beta\gamma\delta}>\partial_{\gamma\delta}W+<b_{\alpha\beta\gamma1}\partial_1 h>V_\gamma)+<\mu>\ddot{W}-<\vartheta>\partial_{\alpha\beta}\ddot{W}\delta_{\alpha\beta}=<p>,\\
&<b_{\alpha1\gamma\delta}\partial_1 h>\partial_{\gamma\delta}W+<b_{\alpha1\gamma1}\partial_1 h\partial_1 h>V_\gamma-\underline{<b_{\alpha2\gamma2}hh>}\partial_{22}V_\gamma+\underline{<\vartheta hh>}\ddot{V}_\alpha=0.
\end{aligned}
\tag{7}
$$

Equations (7) stand a system of differential equations – one for the macrodeflection $W(\cdot,x_2,t)$ and two equations for the fluctuation variables $V_\alpha(\cdot,x_2,t)$.

4.2. The tolerance model equations of the Hencky-Bolle-type functionally graded plates

The tolerance averaging procedure applied for medium-thickness plates equations (2) makes it possible to arrive at the following governing equations:

$$
\begin{aligned}
&\partial_\beta(<b_{\alpha\beta\gamma\delta}>\partial_\delta\Phi_\gamma)+\partial_\beta(<b_{\alpha\beta\gamma1}\partial_1 g>\Theta_\gamma)-\\
&\qquad\qquad -<d_{\alpha\beta}>(\partial_\beta W+\Phi_\beta)-<\vartheta>\ddot{\Phi}_\alpha=0,\\
&\partial_\alpha(<d_{\alpha\beta}>(\partial_\beta W+\Phi_\beta))-<\mu>\ddot{W}=-<p>,\\
&-<b_{\alpha1\gamma\delta}\partial_1 g>\partial_\delta\Phi_\gamma-\\
&-(<b_{\alpha1\beta1}\partial_1 g\partial_1 g>+\underline{<d_{\alpha\beta}gg>})\Theta_\beta+\underline{<b_{\alpha2\gamma2}gg>}\partial_{22}\Theta_\gamma-\underline{<\vartheta gg>}\ddot{\Theta}_\alpha=0.
\end{aligned}
\tag{8}
$$

This is a system of differential equations – two for the macrorotations $\Phi_\alpha(\cdot,x_2,t)$, one for the macrodeflection $W(\cdot,x_2,t)$ and two equations for the fluctuation variables $\Theta_\alpha(\cdot,x_2,t)$.

It can be observed that in the above equations (7) and (8) the effect of the microstructure size is described by the underlined terms, which depend on the microstructure parameter l. Moreover, conditions of application of the both models are formulated, i.e. equations (7) or (8) have physical sense for unknowns W, V_α or W, Φ_α, Θ_α, respectively, being slowly-varying functions in x, for every t. These conditions can be treated as a certain *a posteriori* criterion of physical reliability for the models of dynamic problems for functionally graded plates under consideration. Boundary conditions have to be formulated only for macrofunctions: *the macrodeflection W* and *the macrorotations* Φ_α on all edges. However, boundary conditions for *the fluctuation variables* V_α and Θ_α can be defined only on edges x_2=0, L_2.

5. Conclusions

Using the tolerance averaging method for governing equations of various functionally graded media with a microstructure we can pass from the equations with tolerance-periodic, non-continuous functional coefficients to equations with averaged, smooth, slowly-varying functional coefficients.

It can be observed that both the derived systems of the governing equations together with the aforementioned conditions for the unknowns and the specified fluctuation shape functions stand the tolerance model of functionally graded plates with microstructure. Using various kinematic assumptions we arrive at: the system (7) – for the Kirchhoff-type plates, the system (8) – for the Hencky-Bolle-type plates. Coefficients of these equations are slowly-varying functions in x.

Moreover, it has to be emphasized that these equations involve the underlined terms, which describe the effect of the microstructure size on dynamics of functionally graded plates under consideration.

Some applications of these models will be presented separately. However, to obtain some calculational results in the framework of these models, e.g. free vibrations frequencies – lower and higher, some known approximation methods can be applied, e.g. the Ritz method, the orthogonalisation method.

References

1. E. Baron, *Mechanics of periodic medium thickness plates*, Sci. Bul. Silesian Tech. Univ., No 1734, Wydawnictwo Politechniki Śląskiej, Gliwice 2006, (in Polish).
2. J. Jędrysiak, *Thermomechanics of laminates, plates and shells with functionally graded properties*, Wydawnictwo Politechniki Łódzkiej, Łódź 2010, (in Polish).
3. J. Jędrysiak, Cz. *Woźniak, Elastic shallow shells with functionally graded structure*, PAMM, **9** (2009) 357–358.
4. M. Kaźmierczak, J. Jędrysiak, *Free vibrations of thin plates with transversally graded structure*, EJPAU, Civ. Eng., 13, 4 (2010).
5. M. Kaźmierczak, J. Jędrysiak, *Tolerance modelling of vibrations of thin functionally graded plates*, Thin Walled Struct., **49** (2011) 1295-1303, doi:10.1016/j.tws.2011.05.001.
6. R.V. Kohn, M. Vogelius, *A new model of thin plates with rapidly varying thickness*, Int. J. Solids Struct., **20** (1984) 333-350.
7. K. Mazur-Śniady, Cz. Woźniak, E. Wierzbicki, *On the modelling of dynamic problems for plates with a periodic structure*, Arch. Appl. Mech., **74** (2004) 179-190.
8. S. Suresh, A. Mortensen, *Fundamentals of functionally graded materials*, The University Press, Cambridge 1998.
9. Cz. Woźniak, et al. [eds], *Mathematical modelling and analysis in continuum mechanics of microstructured media*, Wydawnictwo Politechniki Śląskiej, Gliwice 2010.
10. Cz. Woźniak, B. Michalak, J. Jędrysiak [eds], *Thermomechanics of microheterogeneous solids and structures*, Wydawnictwo Politechniki Łódzkiej, Łódź 2008.
11. Cz. Woźniak, E. Wierzbicki, *Averaging techniques in thermomechanics of composite solids. Tolerance averaging versus homogenization*, Wydawnictwo Politechniki Częstochowskiej, Częstochowa 2000.

XXV Symposium *Vibrations in Physical Systems,* Poznan – Bedlewo, May 15-19, 2012

Tolerance Modeling of Three-Layered Plates with a Periodic Structure

Jarosław JĘDRYSIAK
Technical University of Lodz, Faculty of Engineering, Architecture and Environmental Engineering, Politechniki 6, 90-924 Łódź, jarek@p.lodz.pl

Agata ZALESKA
Technical University of Lodz, Faculty of Engineering, Architecture and Environmental Engineering, Politechniki 6, 90-924 Łódź, zaleska.agata@gmail.com

Abstract

In this note there are considered three-layered plates with periodic structure. These plates consist of many small elements, called periodicity cells. The size of the cell is assumed to determine the microstructure parameter. In this paper the tolerance modeling is applied to derive governing equations with constant coefficients, which take into account the effect of the microstructure size.

Keywords: three-layered plates, periodic structure, tolerance modeling, effect of microstructure size

1. Introduction

The main objects under consideration are three-layered plates with a periodic microstructure. In this plate it can be distinguished a small repetitive element called the periodicity cell. The diameter of the cell is assumed to determine the size of the microstructure of these plates.

Plates of this kind are described by partial differential equations with highly-oscillating, periodic, non-continuous functional coefficients, cf. [5, 2, 1]. Hence, these governing equations are not a proper tool to investigate special engineering problems of these plates. In order to obtain equations with constant coefficients there are proposed various methods. Among them it is necessary to mention models which are based on the asymptotic homogenisation method, cf. [5]. Extended list of publications of applications of this method is shown in monographs [11, 2, 10, 9]. However, the equations of these asymptotic models usually neglect the effect of the microstructure size on the overall behaviour of periodic structures under consideration.

In order to take into account this effect the tolerance averaging method can be applied. This method was proposed for periodic composites and structures by Woźniak, cf. [11], and was developed and used to various problems of these media and also so called functionally graded structures in a series of papers. It can be mentioned applications of this method for: thin periodic plates by Jędrysiak [2, 3], wavy-type plates by Michalak [6], medium thickness periodic plates by Baron [1], thin periodic shells by Tomczyk [8], thin functionally graded plates by Kaźmierczak and Jędrysiak [4]. The extended list of papers can be found in [10, 9].

Hence, in this contribution the tolerance averaging method is applied to investigate vibrations of three-layered periodic plates. It is assumed that the plates under consideration are made of three layers. The upper and the bottom layers are identical and treated as thin plates. However, the middle layer is assumed to be made of an elastic Winkler's-type material. Hence, we can distinguish the symmetry plane, which is equally distance from the upper and the bottom planes of the plate.

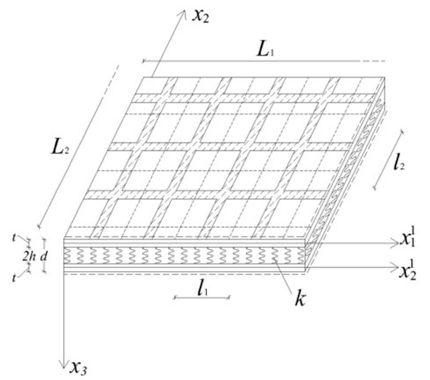

Figure 1. Illustration of three-layered plate with periodic structure

The main aim of this contribution is to formulate governing equations of three-layered periodic plates under consideration in the framework of the tolerance averaging method. These equations are based on a simplified approach of these plates, proposed by Szcześniak [7]. It has to be emphasised that these equations describe the effect of the microstructure size on the overall behaviour of the plates.

2. Fundamental relations

Let $Ox_1x_2x_3$ be an orthogonal Cartesian coordinate system. The time coordinate is denoted by t. Subscripts i, j, k, l run over 1, 2, 3; α, β, γ, δ run over 1, 2 and A, B, K, L=1,…,N. Setting $\mathbf{x}=(x_1,x_2)$ and $z=x_3$ it is assumed that the undeformed plate occupies the region $\Omega\equiv\{(\mathbf{x},z): d/2\leq z\leq d/2,\ \mathbf{x}\in\Pi\}$, with midplane Π and plate thickness d.

The periodicity cell is defined as a plane region $\Delta\equiv[-l_1/2, l_1/2]\times[-l_2/2, l_2/2]$, with l_1, l_2 being the cell dimensions along the x_1- and x_2-axis, respectively. The diameter of the periodicity cell, given by $l=[(l_1)^2+(l_2)^2]^{1/2}$, is called *the microstructure parameter*. It is assumed that $d<<l<<\min(L_1,L_2)$, where L_1, L_2 are characteristic dimensions of the plate along the x_1- and x_2-axis. Here and further the partial derivative with respect to a space coordinate is denoted by $\partial\alpha=\partial/\partial x\alpha$, and the derivative with respect to time t is denoted by an overdot.

Denote deflections of the upper and the bottom plates by $u_1(\mathbf{x},t)$ and $u_2(\mathbf{x},t)$, respectively, and loads along axis z as $p_1(\mathbf{x},t)$ and $p_2(\mathbf{x},t)$, the mass density of the plate material per unit area by:

$$\mu(\mathbf{x}) \equiv \mu^1(\mathbf{x}) = \mu^2(\mathbf{x}) = \int_{-t/2}^{t/2} \rho(\mathbf{x}, z)dz, \tag{1}$$

the elastic module tensor by C_{ijkl} and bending stiffnesses tensor by

$$B_{\alpha\beta\gamma\delta}(\mathbf{x}) \equiv B^1_{\alpha\beta\gamma\delta}(\mathbf{x}) = B^2_{\alpha\beta\gamma\delta}(\mathbf{x}) = \int_{-t/2}^{t/2} C_{\alpha\beta\gamma\delta}(\mathbf{x}, z) z^2 dz. \tag{2}$$

Taking into account the effect of the elastic Winkler's middle layer, with the Winkler's coefficients $k(\cdot)$, under Kirchhoff-type plates theory assumptions we can write two equations of motion for the upper and the bottom plate, respectively:

$$\begin{aligned} &\partial_{\alpha\beta}(B^1{}_{\alpha\beta\gamma\delta}\partial_{\gamma\delta}u_1) + \mu^1\ddot{u}_1 + k(u_1 - u_2) = p_1, \\ &\partial_{\alpha\beta}(B^2{}_{\alpha\beta\gamma\delta}\partial_{\gamma\delta}u_2) + \mu^2\ddot{u}_1 + k(u_2 - u_1) = p_2. \end{aligned} \tag{3}$$

Deflections $u_\alpha(\mathbf{x},t)$, α=1,2, $\mathbf{x} = (x_1, x_2) \in \overline{\Pi}$, $t \in (t_0, t_1)$, have to satisfy regularity conditions. We assume p_2=0 and denote p=p_1. Hence the system of equations (3) can be written in the form:

$$\begin{aligned} &\partial_{\alpha\beta}(B_{\alpha\beta\gamma\delta}\partial_{\gamma\delta}u_1) + \mu\ddot{u}_1 + k(u_1 - u_2) = p, \\ &\partial_{\alpha\beta}(B_{\alpha\beta\gamma\delta}\partial_{\gamma\delta}u_2) + \mu\ddot{u}_2 + k(u_2 - u_1) = 0. \end{aligned} \tag{4}$$

Equations (4) are partial differential equations with highly oscillating, periodic, non-continuous functional coefficients. They stand a starting point for our considerations.

3. Tolerance modeling

In order to obtain averaged equations with constant coefficients for the periodic plates under consideration we apply the tolerance averaging method in the form presented in Woźniak and Wierzbicki [11] and for plates by Jędrysiak, [2]. Introductory concepts of tolerance modeling defined and explained in these books are used. Some of them are recalled below.

One of the introductory concepts is *an averaging operation*, which can be defined for arbitrary function f in the form:

$$< f > (\mathbf{x}) = \frac{1}{l_1 l_2} \int_{\Delta(\mathbf{x})} f(\mathbf{y}) d\mathbf{y}, \qquad \mathbf{x} \in \overline{\Pi}. \tag{5}$$

For periodic function f its averaging value is constant.

Other introductory concepts of the tolerance modeling are: slowly-varying function, periodic-like function, highly oscillating function, fluctuation shape function, cf. [11, 9, 8] and for plates cf. [2, 1].

Using the aforementioned concepts two fundamental assumptions of the tolerance averaging.

The first of them is *micro-macro decomposition* for deflections of thin plates $u_\alpha(\mathbf{x},t)$, α=1,2:

$$u_1(\mathbf{x},t) = w_1(\mathbf{x},t) + h_1{}^A(\mathbf{x})v_1{}^A(\mathbf{x},t),$$
$$u_2(\mathbf{x},t) = w_2(\mathbf{x},t) + h_2{}^K(\mathbf{x})v_2{}^K(\mathbf{x},t), \qquad t \in (t_0,t_1), \tag{6}$$

where the basic kinematic unknowns w_α, α=1, 2, are called *the macro-deflections*, and additional basic kinematic unknowns v_α^A, A=1,…,N, are called *the fluctuation amplitudes*; h_α^A are the known fluctuation shape functions. It is assumed that the basic unknowns w_α, α=1, 2, and v_α^A, A=1,…,N, are slowly-varying functions.

The tolerance averaging approximation is the second modeling assumption, in which it is assumed that some terms are negligibly small, e.g. in formulas:

$$<\varphi>(\mathbf{x}) = <\overline{\varphi}>(\mathbf{x}) + O(\delta), \qquad <\varphi\Psi>(\mathbf{x}) = <\varphi>(\mathbf{x})\Psi(\mathbf{x}) + O(\delta),$$
$$<\varphi\partial_\alpha(h\Psi)>(\mathbf{x}) = <\varphi\partial_\alpha h>(\mathbf{x})\Psi(\mathbf{x}) + O(\delta), \tag{7}$$
$$\mathbf{x} \in \Pi; \;\; \alpha = 1,2; 0 < \delta << 1,$$

where φ is a periodic function of $\mathbf{x}$, Ψ is a slowly-varying function of $\mathbf{x}$, h is the known fluctuation shape function and δ is a tolerance parameter.

The above assumptions are fundamental for the tolerance modeling of the plates under considerations.

4. Model equations

4.1. Tolerance model

Using the tolerance modeling procedure, cf. [2], and introduce denotations of averaged coefficients:

$$
\begin{aligned}
&\hat{B}_{\alpha\beta\gamma\delta} = < B_{\alpha\beta\gamma\delta} >, && \\
&B^A_{1\alpha\beta} = < B_{\alpha\beta\gamma\delta}\partial_{\gamma\delta}h_1{}^A >, && B_1{}^{AB} = B_{11}{}^{AB} = < B_{\alpha\beta\gamma\delta}\partial_{\alpha\beta}h_1{}^A\partial_{\gamma\delta}h_1{}^B >, \\
&\hat{\mu} = < \mu >, && \\
&\mu_1{}^{AB} = \mu_{11}{}^{AB} = l^{-4} < \mu h_1{}^A h_1{}^B >, && \\
&K \equiv < k >, && K_1{}^A \equiv l^{-2} < k h_1{}^A >, \\
&K_{11}{}^{AB} \equiv l^{-4} < k h_1{}^A h_1{}^B >, && K_{12}{}^{AL} \equiv l^{-4} < k h_1{}^A h_2{}^L >, \\
&B^K_{2\alpha\beta} = < B_{\alpha\beta\gamma\delta}\partial_{\gamma\delta}h_2{}^K >, && B_2{}^{KL} = B_{22}{}^{KL} = < B_{\alpha\beta\gamma\delta}\partial_{\alpha\beta}h_2{}^K\partial_{\gamma\delta}h_2{}^L >, \\
&\mu_2{}^{KL} = \mu_{22}{}^{KL} = l^{-4} < \mu h_2{}^K h_2{}^L >, && \\
&K_2{}^K \equiv l^{-2} < k h_2{}^K >, && K_{22}{}^{KL} \equiv l^{-4} < k h_2{}^K h_2{}^L >, \\
&K_{21}{}^{KB} \equiv l^{-4} < k h_2{}^K h_1{}^B >, && \\
&\hat{p} = < p >, && p^A = l^{-2} < p h_1{}^A >,
\end{aligned}
\tag{8}
$$

as a result we arrive at equations:

$$\partial_{\alpha\beta}(\hat{B}_{\alpha\beta\gamma\delta}\partial_{\gamma\delta}w_1 + B^{B}_{1\alpha\beta}v_1{}^{B}) + K(w_1 - w_2) + \underline{l^2(K_1{}^{B}v_1{}^{B} - K_2{}^{K}v_2{}^{K})} + \hat{\mu}\ddot{w}_1 = \hat{p},$$

$$B^{A}_{1\alpha\beta}\partial_{\alpha\beta}w_1 + B_1{}^{AB}v_1{}^{B} + \underline{l^2K_1{}^{A}(w_1 - w_2)} + \underline{l^4(K_{11}{}^{AB}v_1{}^{B} - K_{12}{}^{AK}v_2{}^{K})} + \underline{l^4\mu_1{}^{AB}\ddot{v}_1{}^{B}} = \\ = \underline{l^2p^{A}},$$

$$\partial_{\alpha\beta}(\hat{B}_{\alpha\beta\gamma\delta}\partial_{\gamma\delta}w_2 + B^{K}_{2\alpha\beta}v_2{}^{K}) + K(w_2 - w_1) + \underline{l^2(K_2{}^{K}v_2{}^{K} - K_1{}^{K}v_1{}^{K})} + \hat{\mu}\ddot{w}_2 = 0,$$

$$B^{K}_{2\alpha\beta}\partial_{\alpha\beta}w_2 + B_2{}^{KL}v_2{}^{L} + \underline{l^2K_2{}^{K}(w_2 - w_1)} + \underline{l^4(K_{22}{}^{KL}v_2{}^{L} - K_{21}{}^{KB}v_1{}^{B})} + \underline{l^4\mu_2{}^{KL}\ddot{v}_2{}^{L}} = 0. \tag{9}$$

The above equations are the system of 2N partial differential equations for the basic unknowns – macrodeflections w_α, α=1, 2, and fluctuation variables $v_\alpha{}^{A}$, , A=1,…,N. Coefficients of equations (9) are constant. These equations together with micro-macro decompositions (6) stand *the tolerance model of three-layered periodic plates*. It can be observed that boundary conditions have to be formulated only for macrodeflections w_α.

4.2. Asymptotic model

In order to evaluate obtained results we also write equations of *the asymptotic model*:

$$\begin{aligned}
&\partial_{\alpha\beta}(\hat{B}_{\alpha\beta\gamma\delta}\partial_{\gamma\delta}w_1 + B^{B}_{1\alpha\beta}v_1{}^{B}) + \hat{\mu}\ddot{w}_1 = \hat{p},\\
&B^{A}_{1\alpha\beta}\partial_{\alpha\beta}w_1 + B_1{}^{AB}v_1{}^{B} = 0,\\
&\partial_{\alpha\beta}(\hat{B}_{\alpha\beta\gamma\delta}\partial_{\gamma\delta}w_2 + B^{K}_{2\alpha\beta}v_2{}^{K}) + \hat{\mu}\ddot{w}_2 = 0,\\
&B^{K}_{2\alpha\beta}\partial_{\alpha\beta}w_2 + B_2{}^{KL}v_2{}^{L} = 0,
\end{aligned} \tag{10}$$

Equations (10) stand the system of two partial differential equations for macrodeflection w_α, α=1, 2, and 2N algebraic equations for fluctuation amplitudes $v_\alpha{}^{A}$, A=1,…,N. These equations can be derived using the formal asymptotic procedure, cf. [9, 4]. It can be observed that they can be also obtained from equations (9) by neglecting the underlined terms.

5. Remarks

For three-layered periodic plates the simplified modeling approach can be used, cf. [7], which leads to the system of differential equations for two deflections of thin plates. This system can be starting point to analyze vibrations of these plates in the framework of the tolerance averaging method. This modeling procedure makes it possible to replace the aforementioned equations with highly oscillating, periodic, non-continuous coefficients by equations with constant coefficients. The resulting equations take into account the effect of the microstructure size on the overall behaviour of the plates under consideration.

Some applications of the proposed tolerance and asymptotic models to special problems will be analyzed in the forthcoming papers.

References

1. E. Baron, *Mechanics of periodic medium thickness plates*, Sci. Bul. Silesian Tech. Univ., No 1734, Wydawnictwo Politechniki Śląskiej, Gliwice 2006, (in Polish).
2. J. Jędrysiak, *Dispersive models of thin periodic plates*, Scientific Bulletin of Technical University of Łódź , series: Sci. Trans. 289, Łódź 2001, (in Polish).
3. J. Jędrysiak, *Higher order vibrations of thin periodic plates*, Thin-Walled Struct., **47** (2009) 890-901.
4. M. Kaźmierczak, J. Jędrysiak, *Tolerance modelling of vibrations of thin functionally graded plates*, Thin-Walled Struc., **49** (2011) 1295-1303.
5. R.V. Kohn, M. Vogelius, *A new model of thin plates with rapidly varying thickness*, Int. J. Solids Struct., **20** (1984) 333-350.
6. B. Michalak, *Dynamics and stability of wavy-type plates*, Wydawnictwo Politechniki Łódzkiej, Łódź 2001, (in Polish).
7. W. Szcześniak, *Vibration of elastic sandwich and elastically connected double-plate system under moving loads*, Transactions of Technical University of Warszawa – Civil Engineering, **132** (1998), (in Polish).
8. B. Tomczyk, *On the modelling of thin uniperiodic cylindrical shells*, J. Theor. Appl. Mech., **41** (2003) 755-774.
9. Cz. Woźniak, et al. (eds), *Mathematical modelling and analysis in continuum mechanics of microstructured media*, Wydawnictwo Politechniki Śląskiej, Gliwice 2010.
10. Cz. Woźniak, B. Michalak, J. Jędrysiak (eds), *Thermomechanics of microheterogeneous solids and structures*, Wydawnictwo Politechniki Łódzkiej, Łódź 2008.
11. Cz. Woźniak, E. Wierzbicki, *Averaging techniques in thermomechanics of composite solids. Tolerance averaging versus homogenization*, Wydawnictwo Politechniki Częstochowskiej, Częstochowa 2000.

XXV Symposium *Vibrations in Physical Systems,* Poznan – Bedlewo, May 15-19, 2012

Mechanical Properties Modeling of Neoprene in the Contact Zone of Tool with the Soil

Andrzej KABAŁA
Poznan University of Technology, kabalaandrzej@gmail.com

Michał ŚLEDZIŃSKI
Poznan University of Technology, Chair of Machine Design Fundamentals
michal.sledzinski@put.poznan.pl

Florian MELER
Poznan University of Technology, Chair of Machine Design Fundamentals
florian.meler@put.poznan.pl

Abstract

The investigations concern neoprene behaviour with contact of impact tools. Experimental method is used to solve nonlinear Young's modulus of neoprene. The results of numerical simulation in FEM System ABAQUS/Explicit are compared with experimental results.

Keywords: FEM, neoprene, contact, numerical simulation, experiment

1. Introduction

Experimental investigation of soil consolidating tools, in the real conditions (progressive soil consolidation) can not guarantee obtaining repeatable results which are necessary to carry on comparative analysis of investigated tools. This is why investigations are performed on substitute soils. Neoprene is one of the materials enabling the performance of comparative investigations in conditions similar to the real work conditions of the tool. This material has been applied for several experimental investigations, presented in [3].

2. Experimental determination of neoprene Young's modulus.

Neoprene is elastomeric foam and has a property of nonlinear Young's modulus. Compression of uniaxial test data method is used to determine the neoprene modulus of elasticity. Formulation details of this experimental method are given in [5]. The neoprene test piece has dimensions of 20x20x20 mm. Results of experimental test are shown in Fig. 1.

3. Numerical investigation of a free fall of a rigid sphere onto neoprene plate

This numerical investigation simulates vertical impact of a rigid spherical surface onto a round neoprene plate with thickness of 20 mm. Discrete models of the sphere and the neoprene are shown in Fig. 2. The sphere has a diameter of 20 mm and is assumed to be rigid, with a mass of 0.2 kg localized in the sphere center. In initial condition the center of the sphere is at the distance of 210 mm above the neoprene surface and has zero velocity. Gravity acceleration of 9.81 m/s^2 initiates vertical free fall of the sphere mass in direction perpendicular to the neoprene center. Investigation is completed in the time of 0.9 second.

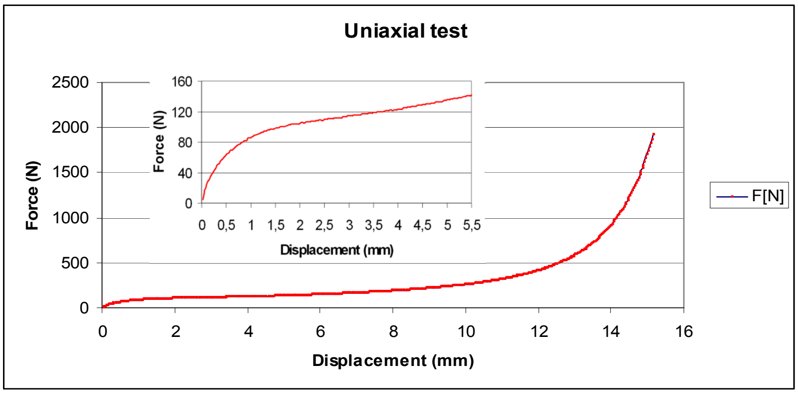

Figure 1. Force versus displacement curve. Neoprene compression test

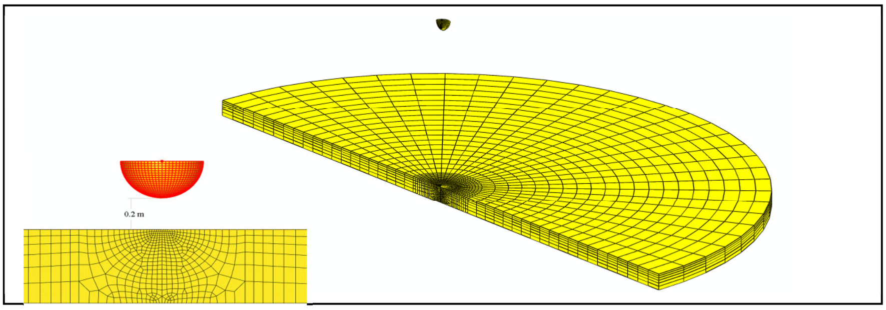

Figure 2. Spherical rigid surface and neoprene discrete model

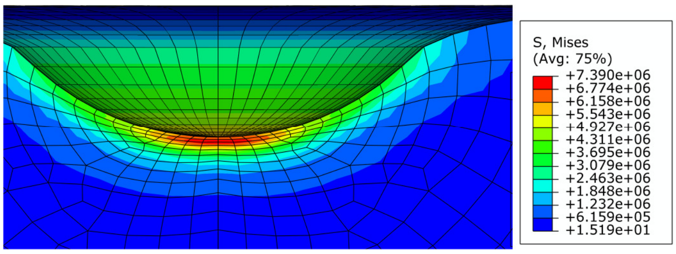

Figure 3. Deformed shape and Mises stress distribution at 146 milliseconds

The spherical rigid surface three times falls down onto the neoprene plate at the analyzed time of 0.9 second. Deformed mesh of the neoprene plate center and Mises stress distribution at 0.146 second is shown in Fig. 3.
The contact between the top of exterior surface of the neoprene plate and the rigid surface representing the point mass is modeled with *CONTACT PAIR option. Contact stresses distribution at the point time of 0.146 second is shown in Fig. 4.

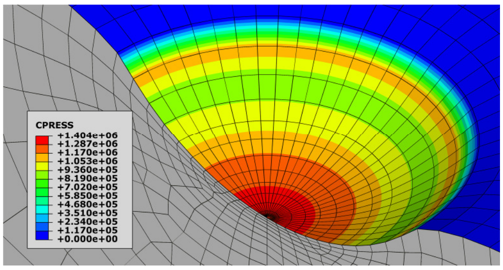

Figure 4. Contact stresses distribution at 146 milliseconds

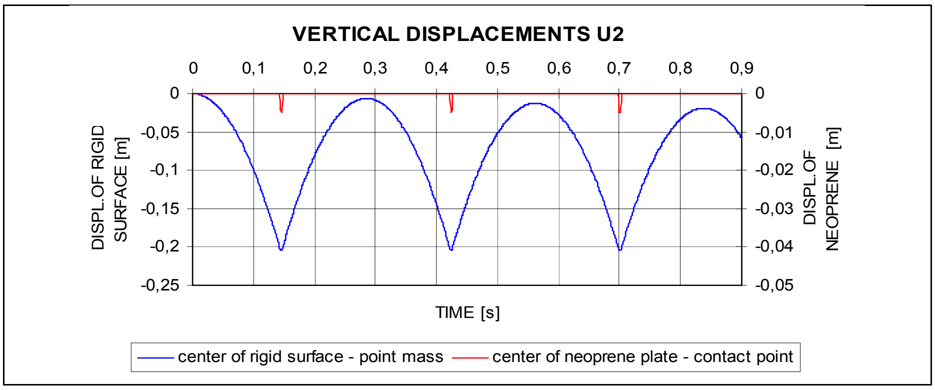

Figure 5. Vertical displacements of 0.2 kg point mass (center of rigid surface) at time range of 0.0 – 0.9 second

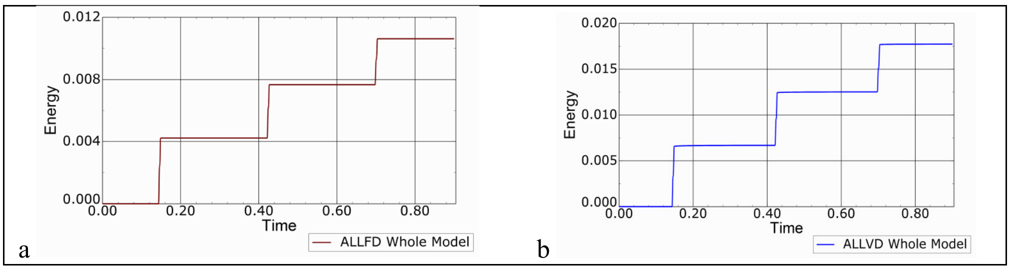

Figure 6. Frictional dissipation of energy (a), viscous dissipation of energy (b). Energy (J), time (seconds)

Vertical displacements of the rigid surface and the top center of the neoprene are shown in Fig. 5. Amplitudes of the point mass decrease during analysis time history. The reasons of the amplitudes decreasing are frictional and viscous dissipations of energy [1]. The histories of frictional energy dissipation and viscous energy dissipation are shown in Figure 6a and in Figure 6b, respectively.

4. Numerical simulations of cooperation the ram with neoprene

The base of numerical simulation of cooperation the ram with the neoprene were investigation results presented in [3]. The compatibility of numerical investigation results with experimental test results significantly increases investigation fields for chosen problems.

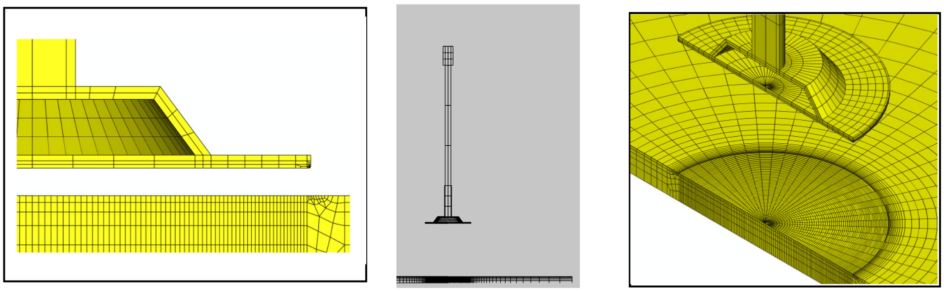

Figure 7. Discrete model of the tobol and neoprene plate

Numerical model of ram for soil consolidation as well as neoprene plate is shown in Fig. 7. Axisymetric elements of CAX4R type are applied. The ram is made of steel with elasticity modulus of E = 207 GPa, $\nu = 0.3$ and density of $\rho = 7850$ kg/m^3. In the model, instead of real soil the neoprene with density of $\rho = 350$ kg/ m^3 is applied.

Young's modulus of the neoprene – the elastomeric foam material is defined through the *HYPERFOAM option using experimental uniaxial test data – see Fig. 1.
Boundary conditions are described as:

- Vertical motion of the ram,
- Axisymetric motion of the deformed neoprene,
- Lower neoprene plate surface is fixed.

The piston (connected with ram) is forced by varying in time pressures: p1 – upper piston surface, p2 – lower piston surface. Gravity of 9.81 m/s^2 is applied for whole model. Variation of p1, p2 pressures in time domain is presented in Fig. 8.
Comparison of ram displacement in the form of three curves is presented in Fig. 9. The curves are obtained as:

- By experimental way [3] – described as „h – exper"
- By numerical simulation without hysteresis – described as „U2 abaqus"
- By numerical simulation with hysteresis – described as „U2 abaqus-hyst"

Comparison of ram velocity obtained by experimental way [2, 3] with numerical simulations is presented in Fig. 10.

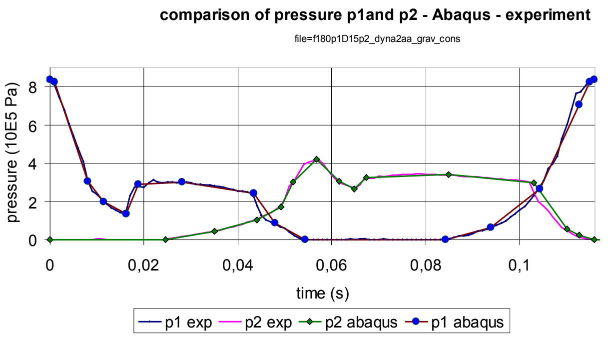

Figure 8. Comparison of pressures p1, p2; Abaqus - experiment

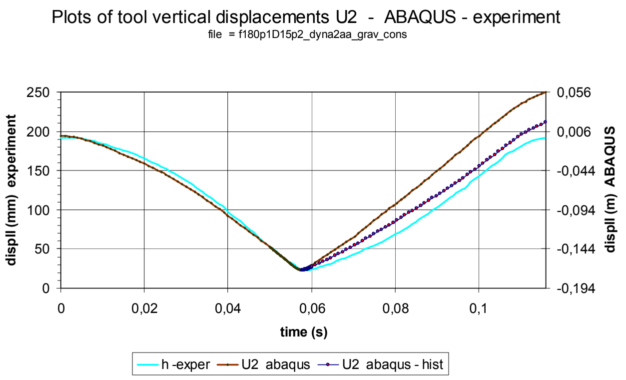

Figure 9. History of tool vertical displacements

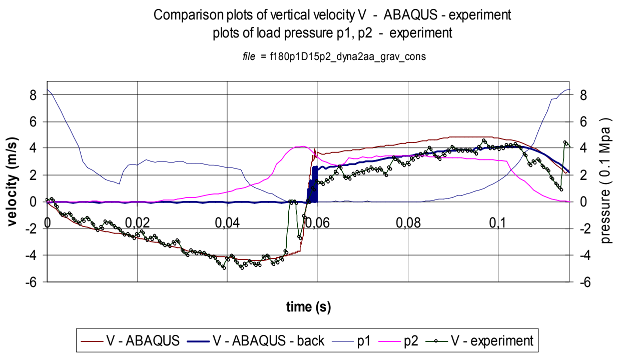

Figure 10. History of tool vertical velocities

5. Conclusions

Presented investigation results are of a great compatibility of numerical investigations with experimental ones [3]. It was necessary to consider neoprene hysteresis in simulation investigations. The curves „abaqus hyst" (Figure 9) and „ABAQUS – back" (Figure 10) confirm the necessity of hysteresis consideration. Additional important conclusion is the necessity of determination the neoprene hysteresis (in the dynamical way) which is used to determine the nonlinear elasticity modulus of the investigated material. Consideration of displacement changes frequency has also influence on the proper determination of the hysteresis concerning the material elasticity modulus.

References

1. Dobry M.W.: O*ptymalizacja przepływu energii w systemie Człowiek – Narzędzie – Podłoże (CNP)*, Seria: Rozprawy nr 330, Wyd. Politechniki Poznańskiej 1998.
2. Śledziński M., *Dynamika wewnętrzna ubijaka pneumatycznego – weryfikacja doświadczalna opisu teoretycznego*, Zeszyty Naukowe Politechniki Poznańskiej Nr 54, Poznań 2002.
3. Śledziński M.: *Kształtowanie cech konstrukcyjnych tłumika drgań ubijaka pneumatycznego*, rozprawa doktorska, Politechnika Poznańska WMRiP, Poznań 2005.
4. *Theory Manual, ABAQUS/Standard v.6.1*, Hibbit, Karlsson & Sorensen, Inc., Pawtucket, USA.
5. *User's Manual, ABAQUS/Standard v.6.1*, Hibbit, Karlsson & Sorensen, Inc., Pawtucket, USA.

XXV Symposium *Vibrations in Physical Systems,* Poznan – Bedlewo, May 15-19, 2012

Modelling of a Rope: Two Discrete Approaches

Henryk KAMIŃSKI
Institute of Applied Mechanics, Poznan University of Technology
24 Jana Pawła II Str., 60-965 Poznań, Poland, henryk.kaminski@put.poznan.pl

Paweł FRITZKOWSKI
Institute of Applied Mechanics, Poznan University of Technology
24 Jana Pawła II Str., 60-965 Poznań, Poland, pawel.fritzkowski@gmail.com

Abstract

Plane motion of a rope is considered. Two approaches to rope modelling are presented: the one based on classical concepts of analytical mechanics and the rigid finite element method. In both cases equations of motion are derived within the framework of the Lagrangian formalism, without the small displacement assumption. In a numerical experiment parameters matching of the two models is attempted, which cannot be performed in a straightforward manner. The rigid finite element method allows to consider the internal forces related to tension, shearing and bending, whereas the other approach, based strictly on rigid body mechanics, is much simpler.

Keywords: discrete model, ropes, numerical simulation, rigid finite element method

1. Introduction

Derivation of the partial differential equations describing dynamics of continuous systems may be a burdensome task, especially when dealing with bodies which undergo large displacements/deformations, e.g. ropes, cables, belts. In such a case the approach based on a discrete model approximating the continuous system seems to be very attractive.

The discrete model can be obtained by applying various theoretical formulations. In case of the rope, one can use classical concepts of analytical mechanics: a chain-like model is composed of rigid links connected by joints of different types. Then, equations of motion can be derived through the Lagrangian formalism. This approach, for instance, has been applied in the papers [1, 2]. On the other hand, the discretization may be embedded in a certain computational technique. For further purposes, we focus on the Rigid Finite Element Method (RFEM) developed by Kruszewski *et al.* [4, 5]. A physical model is composed of rigid bodies connected by massless elements, whose elastic-dissipative properties restrict motion of the non-deformable ones. The method has been used by the authors in [3].

In what follows, we compare the two approaches to rope modelling: (i) the one based on analytical mechanics, further referred to as AM approach, and (ii) the rigid finite element method, further referred to as RFE approach or simply RFEM.

2. Mathematical formulation

Consider a uniform rope of length L and mass M suspended from a support in a gravitational field. For sake of simplicity, we shall stick to the case of plane motion and neglect air resistance forces.

Let us firstly describe the discrete model derived in the framework of AM approach. The rope is approximated by a system of n identical rigid members connected by rotational joints (see Fig. 1). The rigid elements are assumed to be prismatic rods of a length $l = L/n$ and mass $m = M/n$. The joints, in turn, determine elastic-dissipative properties of the mechanical system: as a combination of a spring and damper, each joint is described by stiffness k and damping c. The stiffness coefficient k is equivalent to the flexural rigidity of the rope EI.

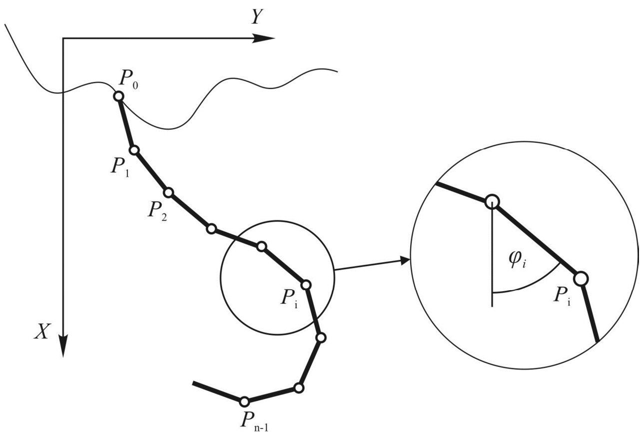

Figure 1. The discrete model of a rope based on AM approach

Using the angular generalized coordinates $\mathbf{q} = [\varphi_1, \varphi_2, ..., \varphi_n]^T$ and generalized velocities, one can express kinetic energy of the system T, potential energy of the system V, the dissipation function D, and apply the Lagrange equations:

$$\frac{\mathrm{d}}{\mathrm{d}t}\left(\frac{\partial T}{\partial \dot{\mathbf{q}}}\right) - \frac{\partial T}{\partial \mathbf{q}} + \frac{\partial D}{\partial \dot{\mathbf{q}}} + \frac{\partial V}{\partial \mathbf{q}} = \mathbf{0}\,, \tag{1}$$

For the given problem, the resulting equations of motion can be written concisely as

$$\mathbf{M}(\mathbf{q})\,\ddot{\mathbf{q}} = \mathbf{f}(t, \mathbf{q}, \dot{\mathbf{q}})\,. \tag{2}$$

The time-dependent mass matrix reflects inertial coupling of the system members. The right-hand side vector function $\mathbf{f}$ includes the components coming from generalized potential and dissipative forces.

It should be noted that the mathematical model (2) is an implicit system of ordinary differential equations (IODEs) and numerical integration may require some sophisticated strategies. A full description of the model can be found in [1, 2].

In the RFE approach a physical model of the system is created in two steps. First, the rope is divided into $\tilde{n}$ sections of equal length $l = L/\tilde{n}$. Their elastic-dissipative properties are concentrated in their centers and captured by massless spring-damping elements (SDEs). Next, $n = \tilde{n} + 1$ rigid finite elements (RFEs) are added: they are interconnected and connected to foundation via the SDEs as shown in Fig. 2. All the SDEs are characterized by stiffness and damping coefficients, while mass and inertial moments are associated with RFEs. The two elements RFE_0 and RFE_{n+1} can be regarded as a foundation or can be used for realization of rheonomic constraints. Motion of the rope with a free end is obtained as stiffness parameters of SDE_{n+1} have zero values.

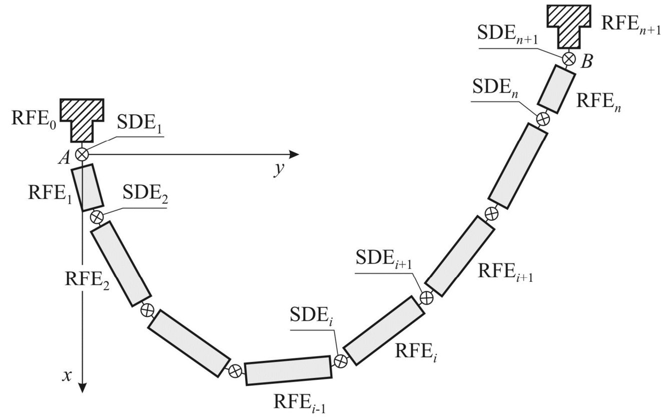

Figure 2. The discrete model of a rope in the framework of RFEM

In the case of plane motion, every RFE has three degrees of freedom and its position is specified by the generalized coordinate vector $\mathbf{q}_i = [q_{xi}, q_{yi}, q_{\varphi i}]^{\mathrm{T}}$; the entire system has $N = 3n$ degrees of freedom. However, to restrict freedom of the elements and make them create the coherent system, one should form the potential energy V, considering deformation of SDEs due to tension, shearing and bending. The respective stiffness coefficients are:

$$C_x = \frac{EA}{l}, \qquad C_y = \frac{GA}{l}, \qquad C_\varphi = \frac{EI}{l}, \tag{3}$$

where E denotes the Young's modulus, G is the shear modulus, A denotes the cross-sectional area of the rope and I is the second area moment the rope's cross-section. The subscripts x, y, φ correspond to the local coordinate systems associated with RFEs (see Fig. 3).

Similar, the dissipation function D can be expressed in terms of deformation velocities of SDEs and the following damping coefficients:

$$B_x = \frac{\eta A}{l}, \qquad B_y = \frac{\overline{\eta} A}{l}, \qquad B_\varphi = \frac{\eta I}{l}, \tag{4}$$

where η and $\overline{\eta}$ are material constants of normal and tangential damping, respectively.

Equations of motion can be derived using the Lagrange equations (1). Since the assumption of small vibrations is not introduced, the mathematical model is non-linear and is given by

$$\mathbf{A}\,\ddot{\mathbf{q}} = \mathbf{F}(t, \mathbf{q}, \dot{\mathbf{q}})\,, \tag{5}$$

where the mass matrix **A** is diagonal, because the local coordinate system associated with a RFE overlaps with its principal central axes of inertia. Hence, the system of differential equations (5) can be easily transformed to the explicit form

$$\ddot{\mathbf{q}} = \widetilde{\mathbf{F}}(t, \mathbf{q}, \dot{\mathbf{q}})\,, \tag{6}$$

where $\widetilde{\mathbf{F}} = \mathbf{A}^{-1}\mathbf{F}$.

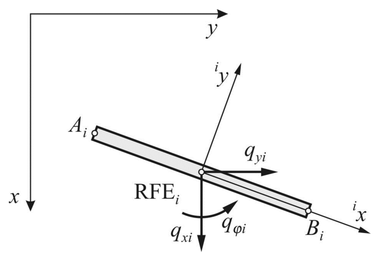

Figure 3. Local coordinate system and degrees of freedom of a RFE;
the axes ^ix and ^iy are related to the directions of normal and shear forces

3. Numerical experiment

The presented models have been derived in different theoretical frameworks. Consequently, the problem of parameters matching arises in comparative studies of these approaches. Below we show results of an attempt to select such parameters values that ensure possibly highest agreement of the two systems motion.

Table 1. Rope parameters

Quantity	Symbol	Unit	Value
Rope density	ρ	kg/m^3	6000
Rope length	L	m	1.0
Rope diameter	D	m	0.005
Young’s modulus	E	Pa	$35{\cdot}10^6$
Shear modulus	G	Pa	$14{\cdot}10^6$
Material constant of normal damping	η	Ns/m^2	10^4
Material constant of tangential damping	$\overline{\eta}$	Ns/m^2	$4{\cdot}10^3$

Consider motion of the rope which is initially deflected aside: the deflection angle $\alpha = 75°$ is equal for all the elements. Table 1 includes the rope parameters which relates directly to the RFE model. The damping material constants fulfil the relation [4, 5]:

$$\frac{\overline{\eta}}{\eta} = \frac{G}{E}. \tag{7}$$

In case of the AM model, the stiffness coefficient is calculated according to the formula $k = EI$. Selection of the damping values, c, has been performed by trial and error.

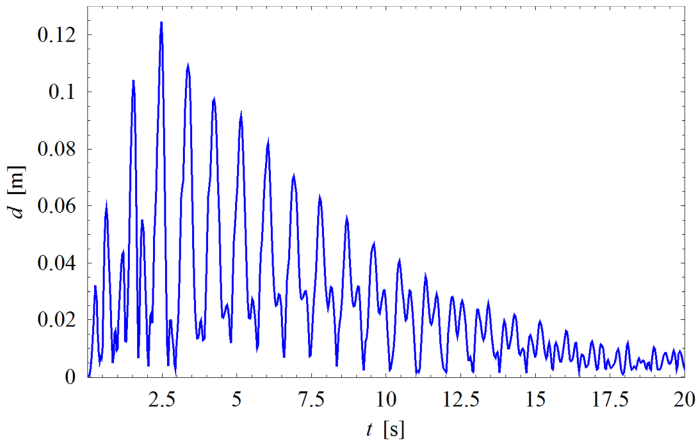

Figure 4. Distance between free ends of the two different physical models

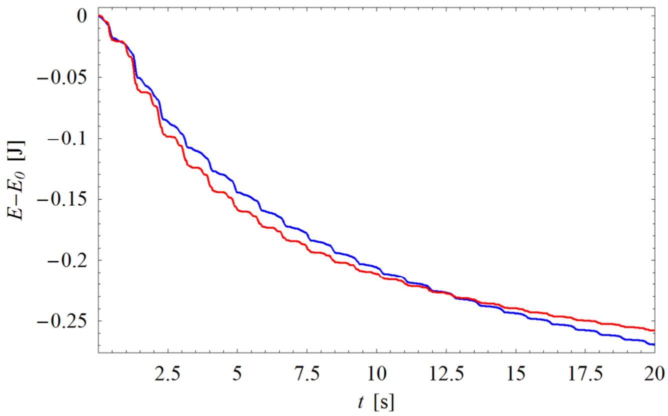

Figure 5. Total energy of the two systems: the model based on AM approach (blue) and the model based on RFEM (red)

Figure 4 illustrates the distance $d(t)$ between free ends of the two compared systems as $c = 2\cdot10^{-2}$ [Nm s]. The distance values are relatively high during the transient phase of motion, then the distance decreases gradually. However, the free end of the rope does not represent the entire mechanical system. Therefore, total energy of the systems $E = T+V$ is shown in Fig. 5. To make the two cases fully comparable, the initial energy E_0 is regarded as the zero level. The difference between energy of the systems should be minimized in more systematic comparative analysis.

4. Conclusions

The two approaches to rope modelling have been presented: the one based on classical ideas of analytical mechanics and the rigid finite element method. Without the assumption of small vibrations both the formulations lead to non-linear equations of motion. However, in the RFEM case the mathematical model is comprised of ordinary differential equations in the standard (explicit) form, which is advantageous from the numerical point of view. On the other hand, each RFE in a plane is assumed to have all three degrees of freedom, which increases the number of the unknown generalized coordinates.

When comparing behaviour of the two different models, parameters matching is not so straightforward. The rigid finite element method allows to consider the internal forces related to tension, shearing and bending, whereas the other approach, based strictly on rigid body mechanics, is much simpler. All in all, the comparative studies merit further attention.

Acknowledgments

This work has been supported by 21-381/2012 DS grant.

References

1. P. Fritzkowski, H. Kamiński, *Dynamics of a rope as a rigid multibody system*, J. Mech. Mater. Struct., **3** (2008) 1059-1075.
2. P. Fritzkowski, H. Kamiński, *A discrete model of a rope with bending stiffness or viscous damping*, Acta Mech. Sin., **27** (2011) 108-113.
3. H. Kamiński, P. Fritzkowski, *Application of the rigid finite element method to modelling of a rope*, Proceedings of the 11th Conference on Dynamical Systems – Theory and Applications, Dynamical Systems: Nonlinear Dynamics and Control, 435-440, Łódź 2011.
4. J. Kruszewski, S. Sawiak, E. Wittbrodt, *The rigid finite element method in dynamics of structures* [in Polish], WNT, Warsaw 1999.
5. E. Wittbrodt, I. Adamiec-Wójcik, S. Wojciech, *Dynamics of flexible multibody systems: rigid finite element method*, Springer-Verlag, Berlin 2006.

XXV Symposium *Vibrations in Physical Systems,* Poznan – Bedlewo, May 15-19, 2012

Asymptotic-Tolerance Modelling on Vibrations of Functionally Graded Thin Plates

Magda KAŹMIERCZAK
Department of Structural Mechanics, Technical University of Lodz
al. Politechniki 6, 90-924 Łódź, Poland, magda.kazmierczak@p.lodz.pl

Jarosław JĘDRYSIAK
Department of Structural Mechanics, Technical University of Lodz
al. Politechniki 6, 90-924 Łódź, Poland, jarek@p.lodz.pl

Abstract

In this note there are considered functionally graded plates. To describe vibrations of these plates and take into account the effect of the microstructure, the tolerance averaging method is applied, cf. [7, 8]. There are formulated governing equations of the asymptotic-tolerance model, cf. [8]. Calculational results obtained for a functionally graded plate band using the proposed model, are compared to results by the known – tolerance and asymptotic models.

Keywords: thin functionally graded plates, tolerance-periodic microstructure, tolerance modelling

1. Introduction

The main objects under consideration are thin plates with functionally graded macrostructure in planes parallel to the plate midplane. These plates have a tolerance-periodic microstructure along two directions on the microlevel, cf. Figure 1.

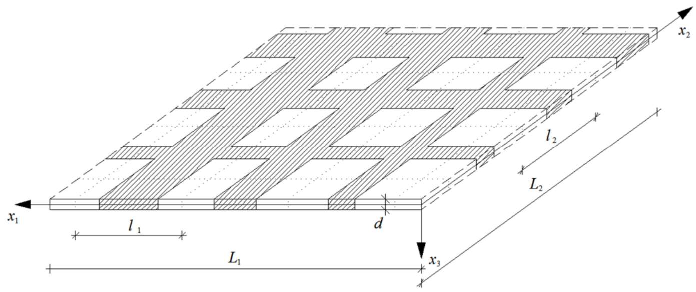

Figure 1. Fragment of a functionally graded plate

Plates of this kind are consisted of many small elements. Adjacent elements are nearly identical, however distant elements can be different. Every element is treated as a thin plate with spans l_1 and l_2 along the x_1- and the x_2-axis, respectively. The size of the microstructure is described by *the microstructure parameter l* defined as $l \equiv [(l_1)^2+(l_2)^2]^{1/2}$. In various problems of these plates *the effect of the microstructure* cannot be neglected.

The effect of the microstructure can be taken into account using *the tolerance averaging technique*, cf. [7-8]. Some applications of this method to the modelling of various periodic structures are shown in series of papers, e.g. [1,5,6]. In last years the tolerance modelling was adopted to functionally graded structures, e.g. [2-4].

The main aim of this paper is to show a new *asymptotic-tolerance model* of functionally graded plates. Equations of this model can be derived using both the asymptotic and the tolerance modelling procedures. Moreover, this model makes it possible to analyse macro- and micro-vibrations.

2. Modelling foundations

Denote a plate deflection by $w(\mathbf{x},t)$, loads normal by p. Set $\mathbf{x}\equiv(x_1,x_2)$ and $z\equiv x_3$. The region of the undeformed plate is defined as $\Omega\equiv\{(\mathbf{x},z):-d(\mathbf{x})/2\le z\le d(\mathbf{x})/2,\mathbf{x}\in\Pi\}$, with the midplane Π and the plate thickness $d(\cdot)$. The "cell" on Π is denoted by $\Omega\equiv[-l_1/2,l_1/2]\times[-l_2/2,l_2/2]$.

Define tolerance-periodic functions of $\mathbf{x}$: a mass density per unit area μ, a rotational inertia ϑ and bending stiffnesses $b_{\alpha\beta\gamma\delta}$ in the form:

$$\mu(\mathbf{x})\equiv\int_{-d/2}^{d/2}\rho(\mathbf{x},z)dz,\qquad \vartheta(\mathbf{x})\equiv\int_{-d/2}^{d/2}\rho(\mathbf{x},z)z^2dz,\qquad b_{\alpha\beta\gamma\delta}(\mathbf{x})\equiv\int_{-d/2}^{d/2}c_{\alpha\beta\gamma\delta}(\mathbf{x},z)z^2dz. \tag{1}$$

From the Kirchhoff-type plates theory assumptions the equation for deflection $w(\mathbf{x},t)$ of functionally graded plates with highly oscillating, tolerance-periodic, non-continuous coefficients is described by

$$\partial_{\alpha\beta}(b_{\alpha\beta\gamma\delta}\partial_{\gamma\delta}w)+\mu\ddot{w}-\partial_\alpha(\vartheta\partial_\alpha\ddot{w})=p. \tag{2}$$

Averaged equations for functionally graded plates will be obtained using the combined asymptotic-tolerance modelling, cf. [8], where basic concepts of these modelling procedures are defined and explained, e.g. an averaging operator, a tolerance-periodic function, a slowly-varying function.

In tolerance modelling two fundamental modelling assumptions are introduced, cf. [2,8]. The first of them is *the micro-macro decomposition*:

$$w(\mathbf{x},t)=U(\mathbf{x},t)+h^A(\mathbf{x})Q^A(\mathbf{x},t),\qquad A=1,\dots,N,\quad \mathbf{x}\in\Pi, \tag{3}$$

where functions $U(\cdot,t)$ and $Q^A(\cdot,t)$ are kinematic unknowns, called *the macrodeflection* and *the fluctuation amplitudes*, respectively, $h^A(\cdot)$ are the known *fluctuation shape functions*. The second assumption is *the tolerance averaging approximation*, i.e. terms of an order of $O(\delta)$ are negligibly small.

3. Asymptotic-tolerance modelling

In the asymptotic-tolerance modelling we have two fundamental steps, cf. [8], [2].

The first step is the application of the asymptotic procedure. Using the asymptotic decomposition $w_\varepsilon(\mathbf{x},\mathbf{y},t)=U(\mathbf{y},t)+\varepsilon^2\tilde{h}_\varepsilon^A(\mathbf{x},\mathbf{y})Q^A(\mathbf{y},t)$ in equation (2) and bearing in mind the limit passage $\varepsilon\to0$ terms $O(\varepsilon)$ are neglected in final equations. Making some manipulations we arrive at the system of equations: one differential equation for the macrodeflection U:

$$\partial_{\alpha\beta}((< b_{\alpha\beta\gamma\delta} > - < b_{\alpha\beta\gamma\delta}\partial_{\gamma\delta}h^{B} >< b_{\alpha\beta\gamma\delta}\partial_{\alpha\beta}h^{A}\partial_{\gamma\delta}h^{B} >^{-1}< b_{\alpha\beta\gamma\delta}\partial_{\alpha\beta}h^{A} >)\partial_{\gamma\delta}U) + \\ + < \mu > \ddot{U} - < \vartheta > \partial_{\alpha\alpha}\ddot{U} = < p >, \tag{4}$$

and the system of algebraic equations for fluctuation amplitudes Q^A:

$$Q^{B} = - < b_{\alpha\beta\gamma\delta}\partial_{\alpha\beta}h^{A}\partial_{\gamma\delta}h^{B} >^{-1}< b_{\alpha\beta\gamma\delta}\partial_{\gamma\delta}h^{A} > \partial_{\alpha\beta}U. \tag{5}$$

Equations (4) and (5) stand *the asymptotic model of thin functionally graded plates*. However, this model does not describe effects of the microstructure size.
Solving the equations of asymptotic model we have the known function which is the complete deflection of plate by the asymptotic model, i.e. $w \cong w_0$

$$w_0(\mathbf{x},t) = U(\mathbf{x},t) + h^{A}(\mathbf{x})Q^{A}(\mathbf{x},t). \tag{6}$$

In *the second step* we apply the tolerance procedure. Using the known tolerance-periodic function $w_0(\cdot,t)$ and the known fluctuation shape functions $g^K(\cdot)$, K=1,…,N, we assume the plate deflection as $w(\mathbf{x},t)=w_0(\mathbf{x},t)+g^K(\mathbf{x})V^K(\mathbf{x},t)$, where V^K are slowly-varying unknown functions in $\mathbf{x}$. After some transformations we arrive at the following system of differential equations for functions V^K:

$$< b_{\alpha\beta\gamma\delta}\partial_{\alpha\beta}g^{K}\partial_{\gamma\delta}g^{J} > V^{J} + \underline{(< \mu g^{K}g^{J} > + < \vartheta\partial_{\alpha}g^{K}\partial_{\beta}g^{J} >)\ddot{V}^{J}} = \\ = \underline{< pg^{K} >} - < b_{\gamma\delta\alpha\beta}\partial_{\alpha\beta}g^{K}\partial_{\gamma\delta}w_0 > . \tag{7}$$

Equations (4) and (7) represent *the asymptotic-tolerance model of thin functionally graded plates*. Equation (7) contains the microstructure parameter l which makes it possible to analyse the effect of the microstructure size.

3. Applications – free vibrations of transversally graded plate bands

Let us consider a thin plate band with span L along the x_1-axis, neglecting the loading p, p=0. The plate band has a functionally graded structure along its span, cf. Figure 2. The material properties of this plate are independent of the x_2-coordinate.

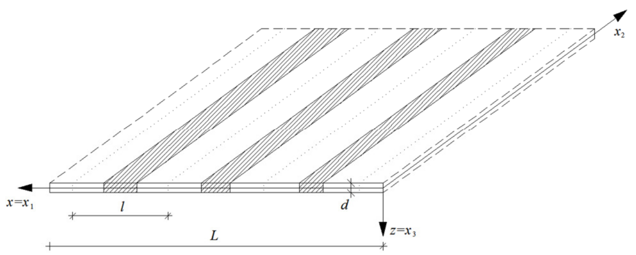

Figure 2. A fragment of the plate band

Denote $x=x_1$, $z=x_3$, $x \in [0,L]$, $z \in [-d/2,d/2]$, d – the constant plate thickness. The basic cell is defined as $\Delta \equiv [-l/2,l/2]$ in the interval $\Lambda \equiv [0,L]$, where l is the cell length.

It is assumed that the plate band is made of two different component materials. Their properties are described by Young's moduli E'', E' and mass densities ρ'', ρ':

$$E(\cdot,z) = \begin{cases} E', & \text{for} \quad z \in ((1-\gamma(x))l/2, (1+\gamma(x))l/2), \\ E'', & \text{for} \quad z \in [0,(1-\gamma(x))l/2] \cup [(1+\gamma(x))l/2, \lambda], \end{cases} \tag{8}$$

$$\rho(\cdot,z) = \begin{cases} \rho', & \text{for} \quad z \in ((1-\gamma(x))l/2, (1+\gamma(x))l/2), \\ \rho'', & \text{for} \quad z \in [0,(1-\gamma(x))l/2] \cup [(1+\gamma(x))l/2, l], \end{cases} \tag{9}$$

where $\gamma(x)$ is a distribution function of material properties, cf. Figure 3; the Poisson's ratio $\nu \equiv \nu'' = \nu'$ is constant.

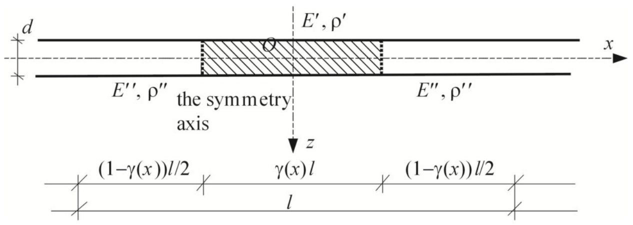

Figure 3. A cell of the plate band

To obtain the approximate formulas of free vibrations frequencies the known Ritz method can be applied, cf. [4]. In this method relations of the maximal strain energy Y_{max} and the maximal kinetic energy K_{max} are determined. For the plate band solutions (the macrodefletion and the fluctuation amplitudes) applied in the Ritz method can be assumed in the form:

$$\begin{aligned} &U(x,t) = A_U \sin(\alpha x)\cos(\omega t), \\ &V(x,t) = A_V \sin(\alpha x)\cos(\omega t), \qquad Q(x,t) = A_Q \sin(\alpha x)\cos(\omega t), \end{aligned} \tag{10}$$

where α is a wave number, ω is a free vibration frequency. The function $U(\cdot)$ satisfies the boundary conditions for the simply supported plate band for x=0, L. Using the conditions of the Ritz method:

$$\frac{\partial(\mathrm{Y}_{max} - \mathrm{K}_{max})}{\partial A_U} = 0, \qquad \frac{\partial(\mathrm{Y}_{max} - \mathrm{K}_{max})}{\partial A_Q} = 0, \qquad \frac{\partial(\mathrm{Y}_{max} - \mathrm{K}_{max})}{\partial A_V} = 0, \tag{11}$$

and make some manipulations we arrive at the following formulas:

$$(\omega_-^{AT})^2 \equiv \alpha^4 \frac{\breve{B}\widehat{B} - \overline{B}^2}{(\breve{\mu} + \breve{\vartheta}\alpha^2)\widehat{B}}, \qquad (\omega_+^{AT})^2 \equiv \frac{\widehat{B}}{l^2(l^2\overline{\mu} + \overline{\vartheta})}, \tag{12}$$

of *the lower frequency* ω_-^{AT} *of free macro-vibrations* and *the higher frequency* ω_+^{AT} *of free micro-vibrations*, respectively, in the framework of *the combined asymptotic-tolerance model*, where coefficients are:

$$\hat{B} = \frac{d^3}{12(1-\nu^2)}\int_0^L \{E''[1-\tilde{\gamma}(x)] + \tilde{\gamma}(x)E'\}\sin^2(\alpha x)dx,$$
$$\overline{B} = \frac{(\pi d)^3}{3(1-\nu^2)}\int_0^L \{(E'-E'')[2\pi\tilde{\gamma}(x) + \sin(2\pi\tilde{\gamma}(x))] + 2\pi E''\}\sin^2(\alpha x)dx, \tag{13a}$$

$$\widetilde{B} = \frac{\pi d^3}{3(1-\nu^2)}(E'-E'')\int_0^L \sin(\pi\tilde{\gamma}(x))\sin^2(\alpha x)dx,$$
$$\breve{\mu} = d\int_0^L \{[1-\tilde{\gamma}(x)]\rho'' + \tilde{\gamma}(x)\rho'\}\sin^2(\alpha x)dx,$$
$$\overline{\mu} = \frac{d}{4\pi}\int_0^L \{(\rho'-\rho'')[2\pi\tilde{\gamma}(x) + \sin(2\pi\tilde{\gamma}(x))] + 2\pi\rho''\}\sin^2(\alpha x)dx + \tag{13b}$$
$$+\frac{d}{\pi}(\rho'-\rho'')\int_0^L c(x)[\pi c(x)\tilde{\gamma}(x) - 2\sin(\pi\tilde{\gamma}(x))]\sin^2(\alpha x)dx +$$
$$+ d\rho''\int_0^L [c(x)]^2\sin^2(\alpha x)dx.$$

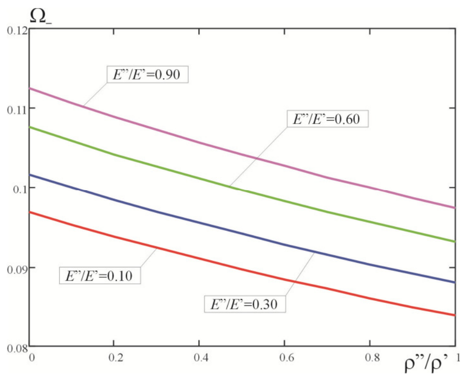

Figure 4. Diagrams of parameters Ω, Ω_-^{AT} for lower free vibration frequencies

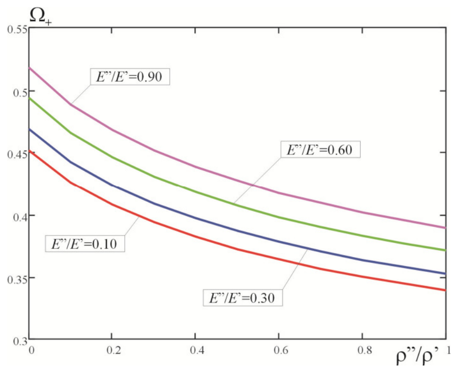

Figure 5. Diagrams of frequency parameter Ω_+^{AT} for higher free vibration frequencies

Calculational examples are made for simply supported plate bands for one distribution function of material properties $\gamma(x)$ given as

$$\gamma(x) = \sin^2(\pi x / L). \tag{14}$$

Let us also introduce dimensionless frequency parameters defined as:

$$(\Omega_-^{AT})^2 \equiv \tfrac{12(1-\nu^2)\rho'}{E'} L^2 (\omega_-^{AT})^2, \qquad (\Omega_+^{AT})^2 \equiv \tfrac{12(1-\nu^2)\rho'}{E'} L^2 (\omega_+^{AT})^2 \tag{15}$$

Results of calculations are shown as diagrams in Figure 4 and Figure 5; Poisson's ratio ν=0.3, ratio l/L=0.1, ratio d/l=0.1.

4. Conclusions

In this paper *the combined asymptotic-tolerance modelling procedure* is applied to the known differential equation of Kirchhoff-type plates with functionally graded macrostructure. This procedure makes it possible to replace the governing differential equation with non-continuous, tolerance-periodic coefficients by the system of differential equations with smooth, slowly-varying coefficients.

The equations of the tolerance model and the derived equations of the combined asymptotic-tolerance model describe the effect of the microstructure size in opposite of the equation of the asymptotic model, which neglects this effect.

Acknowledgments

This contribution is supported by the National Science Centre of Poland under grant No. 2011/01/N/ST8/07758.

References

1. J. Jędrysiak, *Higher order vibrations of thin periodic plates*, Thin-Walled Struct., **47** (2009) 890-901.
2. J. Jędrysiak, *Thermomechanics of laminates, plates and shells with functionally graded structure*, Łódź, Wyd. Politechniki Łódzkiej 2010 [in Polish].
3. M. Kaźmierczak, J. Jędrysiak, *Free vibrations of transversally graded plate bands*, EJPAU, Civ. Engrng., 13, 4 (2010) (online: www.ejpau.media.pl).
4. M. Kaźmierczak, J. Jędrysiak, *Tolerance modelling of vibrations of thin functionally graded plates*, Thin-Walled Struc., **49** (2011) 1295-1303.
5. B. Michalak, *Dynamics and stability of wavy-type plates*, Łódź, Wyd. Politechniki Łódzkiej 2001 [in Polish].
6. B. Tomczyk, *On the modelling of thin uniperiodic cylindrical shells*, J. Theor. Appl. Mech., **41** (2003) 755-774.
7. Cz. Woźniak, B. Michalak, J. Jędrysiak (eds.), *Thermomechanics of heterogeneous solids and structures*, Łódź, Wyd. Politechniki Łódzkiej 2008.
8. Cz. Woźniak, et al. (eds.), *Mathematical modelling and analysis in continuum mechanics of microstructured media*, Gliwice, Wyd. Politechniki Śląskiej 2010.

XXV Symposium *Vibrations in Physical Systems,* Poznan – Bedlewo, May 15-19, 2012

Influence of Nonlinear Damping on Dynamics of Mechanical System with a Pendulum

Krzysztof KĘCIK
Lublin University of Technology, k.kecik@pollub.pl

Abstract

Investigations of regular and chaotic vibrations of the autoparametric system suspended on a nonlinear coil spring and a magnetorheological damper are presented in the paper. Application of a semi-active damper together with the nonlinear spring allows controlling the dangerous motion and additionally gives new possibilities for designers. The investigations are curried out close to the main parametric resonance in the neighbourhood of the instability region which can appear inside the resonance. Obtained results show that the semi-active suspension may reduce dangerous motion and it also allows to maintain the pendulum at a given attractor or to jump to another one.

Keywords: chaos, MR damper, control, attractor

1. Introduction

Autoparametric systems represent a special class of nonlinear systems. Two or more degree of freedom systems with, so-called, inertial coupling sometimes characterized by vibration appearing without external source of energy supply. In such a case we deal with self-parametric vibrations called''autoparametric''. Autoparametric vibration systems have an interesting dynamics that result from at least two nonlinearly coupled subsystems interacting each other in order to transfer the energy. Mass-spring systems with an attached pendulum are common in many mechanical and civil engineering problems [1]. Gantry cranes, lifts or special dynamical absorbers, mounted in buildings and working as dynamical dampers against earthquake, are classical examples where interactions between the support and the pendulum occur [5]. Vibrations absorption of the mass-spring oscillator is possible in the system due to the pendulum swinging. However, for some parameters the situation may worsen and pendulum vibrations may increase dramatically, and then the protection of the structure (modelled as a mass-spring oscillator) is lost. Motion of the system can be regular or in some circumstances may become chaotic [2].

Intelligent and adaptive material systems and structures have become very important in engineering applications. A new class of materials with promising applications in structural and mechanical systems is the magnetorheological dampers (MRD). Application of a smart damper to regular and chaotic dynamics control and also for reduction of the force transmitted on the ground is investigated in this paper. It is shown numerically and experimentally that MR damping can effectively reduce chaotic oscillations without a lost of the dynamical vibration absorption.

2. Model and the Problem Formulation

The investigated system is shown in Fig. 1. The system consists of a pendulum and a body of mass suspended on a coil spring with linear or nonlinear characteristic and magnetorheological damper. The damping coefficient of pendulum is assumed viscous. The body of mass is subjected to a harmonic vertical excitation by linear spring – kinematic excitation. In Fig. 1 the scheme of an autoparametric pendulum-like system is showed.

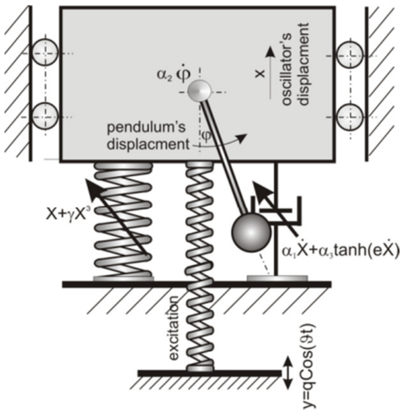

Figure 1. Model of an autoparmetric pendulum-like system with MR damper.

Based on dimensional form of equation of motion in paper [3], the non-dimensional equations can be written as:

$$\ddot{X}+\alpha_1\dot{X}+\alpha_3\tanh\left(e\dot{X}\right)+X+\gamma X^3+\mu\lambda\left(\ddot{\varphi}\sin\varphi+\dot{\varphi}^2\cos\varphi\right)=q\cos\vartheta\tau, \qquad (1)$$

$$\ddot{\varphi}+\alpha_2\dot{\varphi}+\lambda\left(\ddot{X}+1\right)\sin\varphi=0. \qquad (2)$$

In eqs. (1) and (2) α_1, α_3 and e describe the MR damper, α_2 denotes damping coefficient of the pendulum, γ is nonlinearity of oscillator's spring. Parameters μ and λ describe pendulum's parameters, while q and ϑ identify parameters of excitation. Due to coupling of both coordinates, x and φ, by sinus and cosines functions, the system is strongly nonlinear. Particular strong interactions between vibration modes occur if the natural frequency of the oscillator is twice higher than the pendulum frequency. Damping of the oscillator is studied in two variants, as linear viscous and nonlinear magnetorheological. Our concept on nonlinear damping is realized by application of the magnetorheological (MR) damper. I propose to use a smooth function of modified Bingham's model, to describe of MR damper behavior, suggested in paper [4]. In dimensionless form the dynamic force F_d in MR damper is expressed as

$$F_d=\alpha_3\tanh\left(e\dot{X}\right)+\alpha_1\dot{X}. \qquad (3)$$

The detailed derivation of equations (1) and (2), and transform them in dimensionless form you can find in book chapter [3]. This model consists of a combination of viscous damping (α_1) and a Coulomb friction (α_3). An analytical solution of equations (1)-(2) by harmonic balance method (HBM) is presented in [1].

3. Laboratory Pendulum-Like System with MR Damper

The experiment was performed on an autoparametrically two degree of freedom system presented in *Fig. 2a* and schematically in *Fig.1*. The laboratory rig consists of two main components: the pendulum which allows for full rotation and the oscillator. A main part of a nonlinear component of suspension i.e. MR damper *RD 10-97-01* is presented in *Fig. 2b*.

(a) (b)

Figure 2. Laboratory rig of an autoparametric system (a) and MR damper RD (b).

The spring which connects the oscillator and the base is considered in two variants, linear or nonlinear with different soft or hard stiffness characteristics. Nonlinearity of springs has been reached by designing of a special shape of springs: barrel shape and spiral hourglass helical shape. For data acquisition and for control the DasyLab system is used. The angle of rotation φ of the pendulum and the displacement x of the oscillator are measured in the considered system.

4. Influence of MR Damping

The presence of chaos in physical systems is very common and is a key feature of nonlinear systems. The parameters of an autoparametric system can be tuned in such a way that a small perturbation of initial conditions transits its response to dangerous motion, like a chaotic dynamics. If the pendulum plays a role of a dynamical absorber, this kind of motion is unwanted. In *Fig. 3a*, near the main parametric resonance, the three chaotic regions are discovered. In these analyses the following parameters are used: $\alpha_1=0.3054$, $\alpha_2=0.1$, $\mu=14.6863$, $\lambda=0.1342$, $q=2.3239$ and $\gamma=0$.

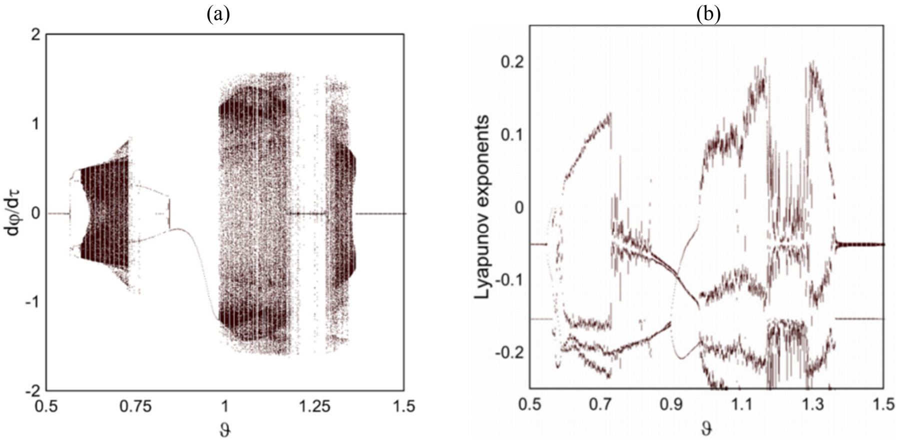

Figure 3. Bifurcation diagram (a) and Lyapunov exponents (b) versus frequency of excitation.

Chaotic regions are verified by positive value of Lyapunov exponent. Shape of strange attractors in *Figs. 4*, are presented. Comparing the attractors' set we can see that the pendulum motion reaches the highest velocity in the widest second chaotic region, the smallest velocity is obtained in the first chaotic zone.

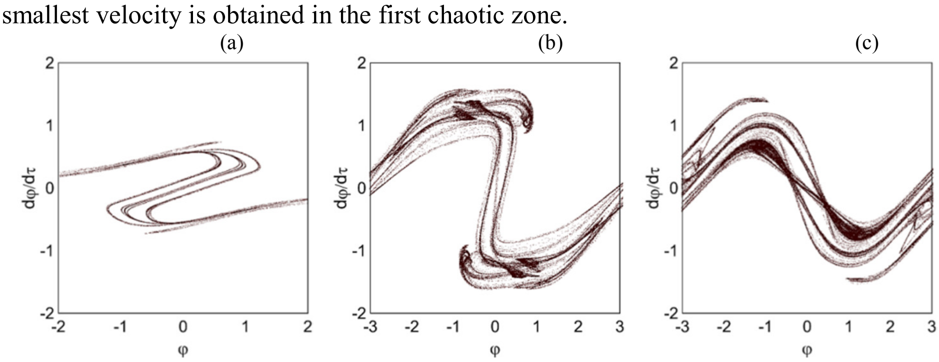

Figure 4. Strange attractors in chaotic regions for $\vartheta=0.7$ (a) $\vartheta=1.1$(b) and $\vartheta=1.32$(c).

Introducing MR damping during first chaotic motion *($\vartheta=0.7$),* we can observe that this irregular motion can be eliminate for $\alpha_3\approx0.25$ *(Fig. 5a),* while in second chaotic region this value is higher and equal $\alpha_3\approx0.3$*(Fig. 5b)*. This result from the fact, that in second chaotic region has a higher angular velocity of pendulum, therefore this motion is difficult to reduce. Additionally, the new chaotic region near the MR damping $\alpha_3=0.8$, appears. Theretofore, magnetorheological damping applied to elimination of dangerous motion should be earlier studied and checked.

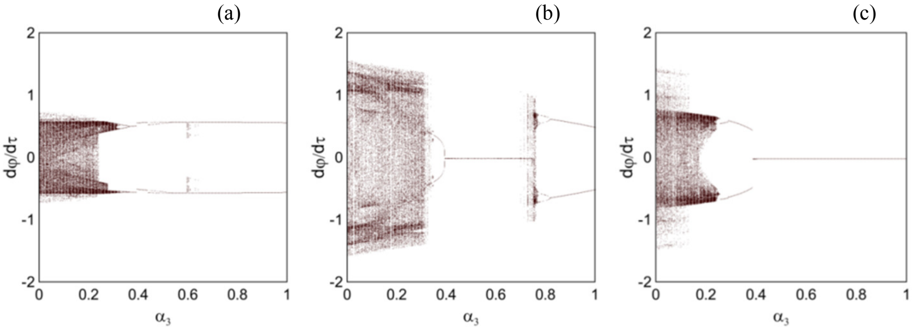

Figure 5. Influence MR damping of chaotic regions ϑ=0.7 (a) ϑ=1.1(b) and ϑ=1.32(c).

The autoparametric systems are very sensitive for initial and working conditions. Therefore, even very small and temporary change in working conditions or slight disturbance may influence on obtained response. Additionally, in this type of nonlinear systems, the existences of two or more solutions are possible. Dynamics control of an autoparametric structure is very important to keep the pendulum at a given, wanted pendulum, or if necessary change it. For this purpose, the MR damper is proposed.

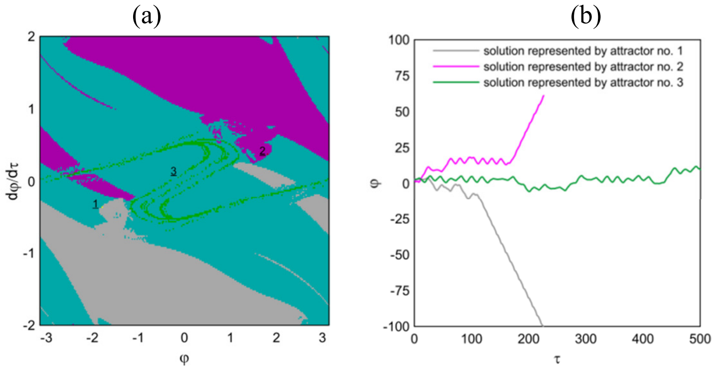

Figure 6. Basins of attractions for α_3=0 (a) and experimental time histories with impulse activation of MR damper (b).

Figure 6a shows basins of attractions for two sets of initial conditions of the pendulum, that is, its angular displacement *(φ)* and angular velocity *(dφ/dτ)*. The diagram indicates more than one coexisting attractor for the same set of parameters. For each attractor, the set of initial conditions leading to long-time behaviour is plotted in corresponding colours. Attractor *no. 1* (dark grey colour) and *no. 2* (pink colour) represent negative (clockwise direction) or positive rotation of pendulum, respectively. The attractor *no. 3* (blue colour set of initial conditions) represents a chaotic motion consist of a swings and rotation of pendulum. This kind of motions is represented by chaotic attractor, in *Fig. 4a*, and by blacked colour in *Fig. 5a*, confirmed by positive value of Lyapunov exponent (Fig. 3b). This example emphasises a very important aspect of the existence of possible multiple solutions in nonlinear structures. This observation has practical meaning in engineering and physical problems. *Figure 6b* shows experimental time histories of pendulum with impulse MR damping activated *(α_3=0.3)*. We observe that impulse turn on of MR damper (value α_3=0.5, activation lasts $\tau \approx 10$) causes change kind of motion (jump one attractor into another). The response of systems depends on moment (actual initial conditions of pendulum) in which MR damper is turn on.

5. Conclusions and Final Remarks

The paper presented the numerical and experimental results of the autoparametric system with applied MR damper. Activation of the MR damper allows for an open loop control of the system. Obtained results show, that the application of nonlinear damper may be an effective method of elimination of the chaotic motion, or if necessary to change one attractor into another. Moreover, by applying simple open-loop control, it is possible to fit on-line the structure response to the frequency and amplitude of external excitation. This suggests that MR damper can be used as special device in engineering applications as a system of dangerous motion preventive or as special control dynamics device of harvesting energy applications. The future work is planned, to use MR damper together with shape memory spring (SMA spring) and apply a closed loop control to prepare a smart dynamical absorber.

Acknowledgments

The work is financed by Grant from the Polish Ministry of Science and Higher Education in years 2012-2014.

References

1. J. Warminski, K. Kecik, Instabilities in the main parametric resonance area of mechanical system with a pendulum, Journal of Sound Vibration, 332 (2009) 612-628.
2. J. Warminski, K. Kecik, Regular and chaotic motions of an autoparametric real pendulum system with the use of a MR damper. Modeling, Simulation and Control of Nonlinear Engineering Dynamical Systems, Springer, 2009 267-276.
3. J. Warminski, K. Kecik, Autoparametric vibrations of an nonlinear system with a pendulum and magnetorheological damping. Nonlinear Dynamics Phenomena in Mechanics. Eds. J. Warminski, S. Lenci, M. P. Cartmell, G. Rega and M. Wiercigroch, 181 (2012), 1-62, Springer.
4. K. Kecik, J. Warminski, Dynamics of an autoparametric pendulum-like system with a nonlinear semiactive suspension. Mathematical Problems in Engineering, 2011, Article ID 451047.
5. H. Yoshioka, J.C. Ramallo, B.F. Spencer, Smart base isolation strategies employing magnetorheological dampers. Journal of Engineering Mechanics, 128(5), 540–551, 2002.

XXV Symposium *Vibrations in Physical Systems,* Poznan – Bedlewo, May 15-19, 2012

Dynamics of Spacecraft due to Elastic Ring Antenna Deployment

Viktor S. KHOROSHILOV
M. K. Yangel State Design Office "Youzhnoye"
3, Krivorozhskaja Street, Dniepropetrovsk, Ukraine, 49008, skh@ukr.net

Alexandr E. ZAKRZHEVSKII
S. P. Timoshenko Institute of mechanics National Academy of Science of Ukraine
3, Petra Nesterova Street, Kiev, Ukraine, 03057, alex.zakr@mail.ru

Abstract

This research deals with the study the dynamics of the spacecraft with the deployed flexible ring antenna. The deployment is performed after placing the spacecraft into orbit and completion of the preliminary damping by a special jet-propelled system, and after uncaging the gyros of the stabilization system. Primarily the antenna is a pre-stressed tape wound on a special drum. When the drum starts deploying the tape, it takes the shape of an elastic ring of variable diameter. The objective of the study is the mechanical and computational modelling of the spacecraft dynamics. The equations of motion are derived with the use of the Eulerian-Lagrangian formalism with the help of Mathematica 5©. Numerical simulations of the operational mode of the system are conducted. Numerical results indicate that the system used for attitude stabilization ensures the shape of the deployed design and prescribed accuracy of the orientation. Simulation results are presented for the spacecraft model in order to show the effectiveness of the spacecraft and deployment process stabilization.

Keywords: spacecraft, flexible ring antenna, deployment, gyro-gravitational stabilization.

1. Introduction

Spacecraft delivered into orbit in a compact form are one of the basic components of modern space systems. The deployment of the flexible appendages perturbs the attitude motion of the transformed spacecraft. The study of such configurations is required for minimization of deployment duration, weight, and power resources, for analysis of the effect of such constructions on the spacecraft attitude motion. There exist a large number of studies in the literature dedicated to the deployment of elastic appendages from the fixed basis as well as from a rotating spacecraft. A short review of these publications is contained in [1]. A special class of large structures to be deployed in space concerns the tethered spacecraft. Levin [2] gives a detailed analysis of basic aspects of this problem.

Here a spacecraft that includes gyro-gravitational system of stabilization is studied during deployment of a flexible ring antenna structure according to a commanded motion. The deployment mechanism dynamics is also taken into consideration. The spacecraft (SC) includes two gyro-dampers (GD) which are installed in order to reduce amplitudes of attitude oscillations. It includes also the elastic preliminarily stressed tape with memory of shape. The spacecraft is placed in a circular orbit about the Earth of radius 6600 km. Fig. 0 shows the spacecraft under consideration with the mechanism of the tape deployment and the gyro-gravitational system of stabilization.

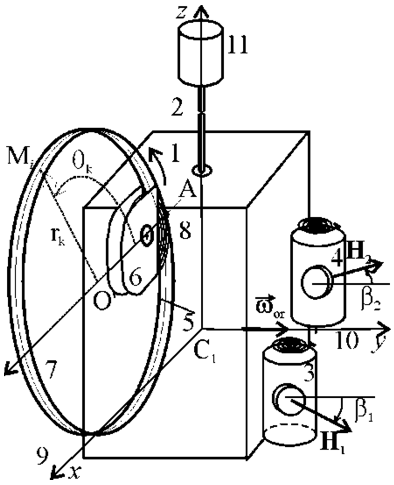

Figure 1. Basic elements of the spacecraft.

Here, element 1 is the SC main module, 2 is the gravi-stabilizer, 3, 4 are the GD, 5 is the tape wound on the drum, 6 is the case of the deployment device, 7 is the ring to be formed of the pre-stressed tape, 8 is the external end of the tape, 9 is the direction of flight, 10 is the direction along the orbit binomial, 11 is the local vertical. Deploying from the drum according to a commanded motion into the circular flexible antenna in the orbital plain, the tape takes the shape of an elastic ring of 30 meters in diameter. The external end of the tape is fixed close to the point where the tape leaves the drum. This point comes nearer to the drum surface as the tape is reeling out.

2. Mechanical model of system

For the case under consideration the generalized mechanical model may be represented as a main rigid body S_1 and body S_2 of variable configuration attached to it. The body S_1 is the gyro-static part and includes the GD, which do not change the rotational body inertia.

The following frames of reference may be useful for the problem statement: $\overline{C}\overline{X}\overline{Y}\overline{Z}$ is an earth-cantered inertial reference frame; C_1xyz is the body S_1 fixed reference frame (Fig. 1) with C_1z along the design position of the GS axis; the orbital frame of reference $Cx^{or}y^{or}z^{or}$ is fixed in the SC mass centre. These frames are introduced in a traditional way [4].

The position vector $\mathbf{r}$ defines the location of the arbitrary point P with respect to the reference frame $\overline{C}\overline{X}\overline{Y}\overline{Z}$, and the position vector $\mathbf{r}'$ – with respect to the reference frame *Oxyz*. In contrast to the problem of dynamics of relative motion of carried bodies described by Lurie [5], the problem under consideration is the more general one when the expression for $\mathbf{r}'$ depends on time t explicitly, not only through the generalized coordinates:

$$\mathbf{r}' = \mathbf{r}'(q_1, \ldots, q_n, t) \qquad (1)$$

as the deployment of the tape takes place in accordance with the prescribed in time law. As a result, $\mathbf{r}'$ changes in time in the process of deployment even when the magnitude of the generalized coordinates, which determine the relative elastic motion of the ring, are identically zero.

Since the deployment is supposed to be rather slow as compared with the maximal period of ring natural oscillations, the ring antenna may be modelled with use of classical modal analysis. Further, the relative displacements for two oscillation modes of the elastic ring fixed in one point in its plain and for its two modes in transversal direction are to be chosen as the generalized coordinates, which determine the relative motion of the ring.. The angles of rotation β_i (i=1,2) (Fig. 1) of gyro-dampers also must be considered as additional generalized coordinates.

3. Mathematical model of system

The equations of motion of the system under consideration become the most compact and convenient for numerical integration, if one chooses the instantaneous position of the mass centre C as an origin. Then one can obtain the following Lagrange's equations of the second kind for the generalized co-ordinates, q_s :

$$E_s(T_r^{C_1}) - M\overset{**}{\mathbf{r}}_C{}' \cdot \frac{\partial \mathbf{r}_C{}'}{\partial q_s} - \frac{1}{2}\boldsymbol{\omega} \cdot \frac{\partial \boldsymbol{\Theta}^C}{\partial q_s} \cdot \boldsymbol{\omega} + \dot{\boldsymbol{\omega}} \cdot \frac{\partial \mathbf{K}_r^C}{\partial \dot{q}_s} + \boldsymbol{\omega} \cdot E_s^*(\mathbf{K}^C{}_r) = Q_s . \qquad (2)$$

The equation of the attitude motion may be obtained as the Euler-Lagrange equation

$$\boldsymbol{\Theta}^C \cdot \dot{\boldsymbol{\omega}} + \overset{*}{\boldsymbol{\Theta}}{}^C \cdot \boldsymbol{\omega} + \boldsymbol{\omega} \times (\boldsymbol{\Theta}^C \cdot \boldsymbol{\omega}) + \boldsymbol{\omega} \times \mathbf{K}_r^C = \mathbf{m}^C . \qquad (3)$$

The following notations are used here: $\boldsymbol{\Theta}^C$ is the inertia tensor of the whole system with respect to point C; $\mathbf{K}_r^C = \int_m \mathbf{r}' \times \overset{*}{\mathbf{r}}{}' dm - M\,\mathbf{r}_C{}' \times \overset{*}{\mathbf{r}}_C{}'$ is the relative moment of momentum of the deployed part with respect to point *C*; $\mathbf{r}_C'$ is position vector of the instant position of the mass centre *C* in the main body fixed frame of reference; the symbol * denotes time differentiation in the reference frame C_1xyz; *M* is the total mass of the system; $T_r^{C_1}$ is the kinetic energy of the relative motion of the carried bodies calculated under condition of definition of relative velocities of their points with respect to C_1; $E_j(\cdot) = \frac{d}{dt}\frac{\partial(\cdot)}{\partial \dot{q}_j} - \frac{\partial(\cdot)}{\partial q_j}$ is the Euler's operator, $E_j^*(\cdot) = \frac{\partial}{\partial t}\frac{\partial(\cdot)}{\partial \dot{q}_j} - \frac{\partial(\cdot)}{\partial q_j}$ is also the Euler's operator, but the time differentiation is performed in the reference frame C_1xyz; Q_s are generalized forces that take into account the elastic and dissipative characteristics of the construction, and $\mathbf{m}^C$ is the gravitational torque.

If to supplement Eqs. (2), (3) by the kinematical equations, one obtains a closed system of equations of motion. The parameters of Rodrigues-Hamilton were chosen as the attitude parameters. Further, it is necessary to determine expressions for $\mathbf{r}_c'$, $\boldsymbol{\Theta}^C$, T_r^C, $\mathbf{K}_r^C$, Π, Q_s and all their derivatives with respect to time and generalized co-ordinates, which appear into expressions for coefficients of the equations (2), (3) . All this values may be defined if one knows the expressions for $\mathbf{r}'$ and $\mathbf{v}'$ for all points of the system under consideration.

During deployment, the material points of the tape make a compound motion. All these point are disposed always close to a ring of variable radius. Its centre is defined uniquely by three co-ordinates $a_{xr}(t)$, a_y, a_z in the main body fixed reference frame. Velocity of any material point of the tape which is passing through any point M_i of the circular trajectory with respect to this point at the given instant can be written in projections to C_1xyz as the following:

$$\tilde{v}'_x = (2\pi - \vartheta_k)\sin(\vartheta_k)\,\dot{r}_k; \quad \tilde{v}'_y = 0; \quad \tilde{v}'_z = (2\pi - \vartheta_k)\cos(\vartheta_k)\,\dot{r}_k. \tag{4}$$

One can write the following expression for the position vector of the material point M of the tape in the reference frame C_1xyz:

$$\begin{aligned} r'_x &= a_{\mathrm{xr}}(t) - \cos(\vartheta_k)\,r_k(t) + q_{u1}(t)\,uv1cs(\vartheta_k) + q_{u2}(t)\,uv2cs(\vartheta_k); \\ r'_y &= a_y + q_{w1}(t)\,w_1(\vartheta_k) + q_{w2}(t)\,w_2(\vartheta_k); \\ r'_z &= a_z + \sin(\vartheta_k)\,r_k(t) + q_{u1}(t)\,uv1sc(\vartheta_k) + q_{u2}(t)\,uv2sc(\vartheta_k). \end{aligned} \tag{5}$$

Here $uv1cs(\vartheta_k), uv2cs(\vartheta_k), uv1sc(\vartheta_k), uv2sc(\vartheta_k)$ are the first and second modes of oscillations of the ring with one fixed point in its plane in projections to the axes C_1x and C_1z taking into account both radial and tangential motions, $w_1(\vartheta_k), w_2(\vartheta_k)$ are the first and second modes of transversal oscillations of the ring in projections to the axis C_1y. Now one can write $\mathbf{v}_i' = \tilde{\mathbf{v}}_i' + \overset{*}{r_i}'$, where the last term is obtained as a result of time differentiation of the expression (5) in C_1xyz.

The original computation package was developed for the numerical integration of the obtained ordinary differential equations in the frame of the Cauchy problem. The majority of operators of the program was obtained in the form of Fortran-expressions in Mathematica5© with help of codes written specifically for the system studied, and after using a set of replacements of the bulky expressions obtained, by simple enough variables.

4. Simulations

Key system parameter values are: mass of main body $m_1 = 1400$ kg, tape bending stiffness $EJ = 1.5$ N m^2, $EJ_1 = 366{,}4$ N m^2, decrement of oscillations $\vartheta = 0.001$, components of the main body inertia tensor $J_{xx} = 10000$ kg m^2, $J_{yy} = 12000$ kg m^2, $J_{zz} = 2000$ kg m^2, angular momentum of one GD rotor $h_{rot} = 20$ kg m^2/s, GD damping coefficient $k_{3\beta_1,\beta_2} = 40$ N m / s^2, duration of deployment $T_f = 500$ s. The initial values of the attitude angles are taken to be zero, the initial values of the SC angular velocity components in orbital reference frame before the deployment are to be used within the range 0.0 – 0.0005 s^{-1}, the smooth enough law is taken as a basis for the deployment law in time that corresponds to the optimal slewing of the flexible SC with the minimal dynamic overloads of elastic elements in a relative motion, as is described in [6]. In the case under consideration, such a law also creates the minimum possible perturbations, inducing elastic oscillations, during the deployment.

The orbit parameters were accepted to be arbitrary. Though the SC movement along an orbit is not considered here, the orbit parameters are required to calculate the gravitational torque and for the monitoring of errors of the numerical integration of the initial value problem.

During deployment the diagonal components of the SC inertia tensor increase. The component $\Theta_{2,2}^{C}$ increases the most. If one tries to deploy the antenna on an SC, which does not contain the gyro-dampers, the SC begins to rotate around its pitch axis. This is visible in Fig. 2a, where the time history of the projections of the absolute angular velocity for such a case (Fig. 2a) is shown. Projection ω_2 becomes strongly less of its initial value and SC performs long-term spatial motion. But if GD are switched on, the SC does not enter into rotation around the pitch axis; here are only oscillations around this axis. With increase of the GD inertial and damping characteristics, the process of stabilization with regard to a local vertical considerably improves. Fig. 2b shows that the angular velocity of rotation around the pitch axis starts to oscillate about the orbital angular velocity in process of damping of the elastic and pitch oscillations. Oscillations of other two projections ω_1 and ω_3 also decrease step-by-step.

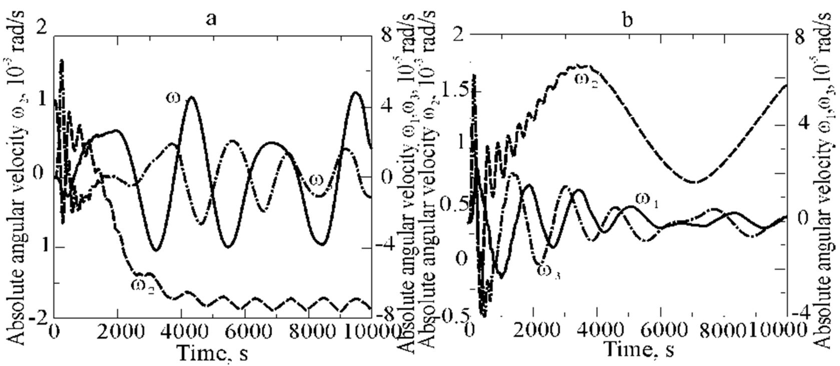

Figure 2. Time histories of absolute angular velocity projections

The plane vibrations of the ring (Fig. 3) have the maximum amplitude of approximately 1.8 m for the first oscillation mode q_{u1} (Fig. 3a), which then decreases as a result of the constructional damping and remains at a nearly constant level as a result of interaction with the SC attitude motion. The behaviour of the amplitude q_{u2} of the second plane mode is the same. The nature of the in-plain vibrations is not depends on the presence or lack of the GD. The transversal oscillations of the ring behave differently, though their amplitudes are much less in view of the higher bending stiffness. In Fig. 3b one can see difference in q_{w1} behaviour when the GD are absent (solid line) and when the GD are switched on (dot-and-dash line). During the deployment process these oscillations behave identically but with time as a result of interacting with the SC damped oscillations around the yaw axis they also are damping. The analyzed graphs show that deployment of the ring antenna from the SC in the presence of the gyro-gravitational stabilisation reduces to the nominal conditions of the SC motion.

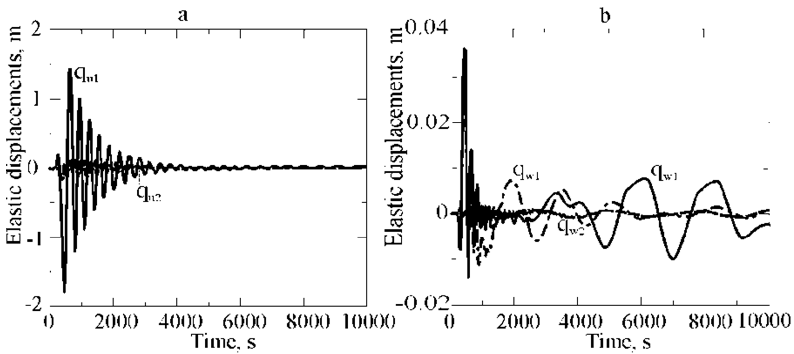

Figure 3. Relative elastic displacements

9. Conclusion

The present research deals with the exploration of the dynamics of the gyro-gravitational stabilized spacecraft in the mode of the deployment of the elastic ring antenna. The mathematical model developed for this case may be regarded as the generalization of the theory of a flexible multi-body system with the time dependent configurations. The approach may be successfully extended to the modelling of the dynamics of other space construction deployments with the significant change of the configuration in the process of exploitation. The computational Fortran-package developed for the numerical simulation has common characteristics, which may be easily adopted for other deployed systems. The obtained data permit to select the most appropriate deployment and gyro-dampers parameters.

References

1. V. Dranovskii, V. Khoroshylov, A. Zakrzhevskii, *Spacecraft dynamics with regard to elastic gravitational stabilizer deployment*, Acta Astronautica, **64** (2009) 50-513.
2. E. Levin, *Dynamic Analysis of Space Tether Missions*, Advances in the Astronautical Sciences, **126**, Univelt 2007.
3. V. Dranovskii, A. Zakrzhevskii, A. Kovalenko, V. Khoroshilov, *On the Dynamics of Deployment of an Orbital Structure with Elastic Elements*, *International Applied Mechanics*, **42** (2006) 959-965.
4. V. Beletsky, *Motion of an Artificial Satellite about its Center of Mass*, Israel Program for Scientific Translations, Jerusalem 1966.
5. A. Lurie, *Analytical mechanics*, Springer 2002.
6. A. Zakrzhevskii, *Slewing of Flexible Spacecraft with Minimal Relative Flexible Acceleration*, J. of Guidance, Control, and Dynamics, **31** (2008) 563-570.

XXV Symposium *Vibrations in Physical Systems,* Poznan – Bedlewo, May 15-19, 2012

Numerical Analysis of Vibration in a Brake System for High Speed Train

Robert KONOWROCKI
IPPT, Polish Academy of Sciences, Department of Intelligent Technologies
rkonow@ippt.gov.pl

Roman BOGACZ
Krakow University of Technology, Department of Civil Engineering
rbogacz@ippt.gov.pl

Abstract

The paper is devoted to a computer simulation of brake pad/brake disc dynamic interaction. The main purpose of the studies is a numerical analysis of friction pair dynamics, aiming at describe generation of vibration related to the process of transition phenomena associated with braking. To investigation will be used environment of Automatic Dynamic Analysis of Mechanical Systems. In the analysis is used two-dimensional friction model. The results show the slip-stick and creep phenomenon.

Keywords: vibrations excited by friction, self-excited of vibrations, slip-stick, creepage.

1. Introduction

Self-excitation of vibrations due to dry friction commonly found in brake systems. Many research connected with determination of causes of vibrations have been undertaken. In questions of that nature it is necessary to determine criteria for modelling such phenomena, considering the principal factor such as dynamic non-linear friction. Developing models of interact friction pair of brake systems in an era of increasing vehicle speed and increase their weight is very important. In the case of braking systems for high speed train introduced sintered pads (Fig. 1).

Figure. 1. Brake system for high speed train and sintered brake pads (*source: www.gobizkorea.com*).

Such a segmented structure can faster conduct and radiate the heat from the brake pad. The dynamic interaction between elements of the brake pad may increase or decrease the vibration depending on configuration. It seems to be dependent on mode of pad elements vibration (in-phase or out of phase).

Elaboration of a method of decrease and damping of unfavourable vibrations requires, among others, building of correct numerical model simulating, as far as possible, accurately the system under investigation. To identify the interactions of friction pairs requires understanding the dynamics of the friction transient process [1, 2]. Numerous investigation in research units all over the world are engaged in analysis of the

self-excited vibration in brake systems. Problem of "squeaking" brakes has been investigated to considerable extent in automotive industry. Author in paper [3] gave comprehensive preview on that phenomenon with regard to vibrations and contact forces. He presented both experimental and numerical study. Majority of projects connected with modelling of brake systems was based on finite elements method. The authors of paper [4] adopted the model with two degrees of freedom for disc brakes where the disc and pads are modelled as particular kinds of connections through the interface of friction and stability. In their approach also analysis of limit cycles was executed. Some methods of brake discs vibration analysis are presented in the studies [5] and [6]. Brake disc components were modelled with application of the plate finite elements. The influence of non-linearity of contact forces on generation of low and high frequency noise in brake discs was subjected to experimental and analytical investigation by authors [7]. The researchers observed that time-frequency analysis is very useful in identification of character of generated noise.

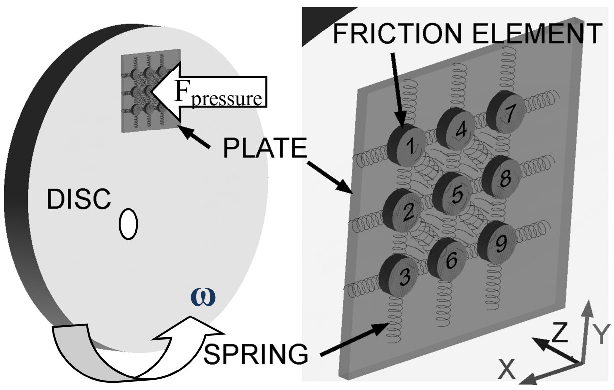

Figure. 2. Model of brake system.

2. Model of brake system

The model (Fig. 2) consider consist of 11 moving parts (friction elements, disc and plate); therefore the number of parameters describing configuration is 11 x 3 = 33 used by the pre-processor to build the set of equations of motion. The model of brake system contains: one revolution joints, one translation joint, nine planar joint and one rotation joint motion. The total number is 11, what make together 20 degrees of freedom. The friction elements are flexibly connected between each other. Outer elements are flexibly connected with a plate. A force F directed along the Z axis operates by the plate on all friction pairs.

2.1. Equations of motion

The brake model is based on a Cartesian coordinates approach for the assembly of the equations of motion. The Euler parameters are used to represent the rotational degrees of freedom and Lagrangian formulation for the assembly and generation of equations of motion. The joints between bodies are expressed in a set of algebraic equations, subsequently assembled in a second derivative structure, obtaining finally a set of Differential Algebraic Equations in the following packable form:

$$\begin{bmatrix} \mathbf{M}(\mathbf{q}) & \mathbf{\Phi}(\mathbf{q})^T \\ \mathbf{\Phi}(\mathbf{q}) & \mathbf{0} \end{bmatrix} \begin{bmatrix} \ddot{\mathbf{q}} \\ \boldsymbol{\lambda} \end{bmatrix} = \begin{bmatrix} \mathbf{F}(\mathbf{q}, \dot{\mathbf{q}}, t) \\ \chi \end{bmatrix} \tag{1}$$

The symbols **M** is the mass matrix, **q,** $\boldsymbol{\lambda}$ and **F** denote, respectively, the generalized coordinates, the Lagrange multipliers and the generalized forces applied to the rigid bodies vectors. Symbol χ the right-hand-side of the second derivative the constraint equations.

2.2. Description of contact

Model of contact used in our analysis lets you define a two-dimensional contact between a pair of geometric objects. Using the contact as a unilateral constraint, as a force that has zero value when no penetration between the specified elements exists, and a force that has a positive value when exists penetration between elements friction and disc. The model of contact describes the following formula (2).

Both the static and quasi-static equilibrium analysis modes use Newton-Raphson (NR) iterations to solve the nonlinear algebraic equations of force balance. The NR algorithm ensures that the system solution moves in the direction of most compliance (least stiffness). When a contact is active, the stiffness in the direction of the normal force is high, so the NR algorithm modifies the system states to decrease this force. If a contact is inactive, there is no stiffness in the direction of increasing contact.

$$F = \begin{cases} \max(k(x_p - x_k)^e - c\dot{x}, 0) & \text{for} \quad x_p \leq x_k \\ 0 & \text{for} \quad x_p > x_k, \end{cases} \tag{2}$$

$$c(p) = \begin{cases} 0 & \text{for} \quad b \le 0 \\ c_{max}\left(\frac{3}{l^2}b^2 - \frac{2}{l^3}b^3\right) & \text{for} \quad 0 < b \le l \\ c_{max} & \text{for} \quad b > l \end{cases}. \tag{3}$$

To describe the contact model following parameters are used: c is damping parameters of contact, k is contact stiffness, x_p initial displacement of contact, x_k is displacement of the penetration ($b=x_p- x_k$), p is the maximal value of penetration. Parameter of damping coefficient c corresponds to energy dissipation during the contact. From the above mentioned formula (3) it follows that the value of coefficient c depends on the penetration b the friction element in the disc. Damping coefficient c can reach a maximum value after reaching required penetration l. During the further penetration the damping is constant ($c = c_{\max}$).

2.3. Friction model

In order to determine the contact friction force in investigations used a velocity-based friction model of contact. The figure below shows how the coefficient of friction varies with slip velocity.

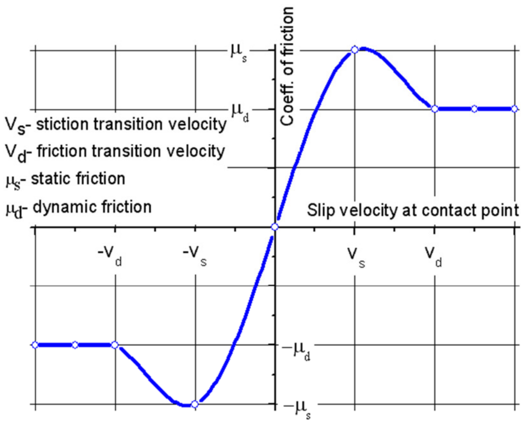

Figure. 3. Model of Friction.

In this model:

$$\begin{aligned}
&\mu(-v_s) = \mu_s \\
&\mu(v_s) = -\mu_s \\
&\mu(0) = 0 \\
&\mu(-v_d) = \mu_s \\
&\mu(v_d) = -\mu_d \\
&\mu(v) = -\text{sign}(v)\cdot\mu_d && \text{for } |v| > v_d \\
&\mu(v) = -\text{step}(|v|, v_d, \mu_d, v_s, \mu_s)\cdot\text{sign}(v) && \text{for } v_s < |v| < v_d
\end{aligned} \tag{4}$$

$\mu(v) = \text{step}(v,-v_s, \mu_s, v_s, -\mu_s)$ for $-v_s < v < v_s$.

Parameter v_s is the velocity at which full value of the static friction coefficient is applied. v_d is the velocity at which the value of the dynamic friction coefficient has fully transitioned from the static friction coefficient.

3. Computational example

The study on the numerical model provided us with some interesting observations shown in following graphs. For all results presented below assumed constant values of parameters: coefficients friction, stiffness of spring, force of pressure on the friction elements (normal force). They are μ_s=0.6, μ_d = 0.3, k_{spring} = 400 N/mm, F_{press}= 300 N. During the tests changed angular velocity of the disc ω, stiction friction transition velocity v_s and friction transition velocity v_d. Because the interaction of neighboring friction elements the amplitude of vibration of some the elements under consideration decreases with time (Fig. 3). Such behavior is confirmed by studies [1]. The authors introducing an external excitation, to reduce the vibration amplitude of the masses moving on the conveyor.

It was also found that reducing the angular velocity of the disc causes the phenomenon of stick-slip. Stick-slip phenomenon is also dependent on the value of the parameter v_d included in the model of friction. In case of increase in v_d above the 33 mm/s, this phenomenon disappears passing to periodic oscillations (Fig. 4).

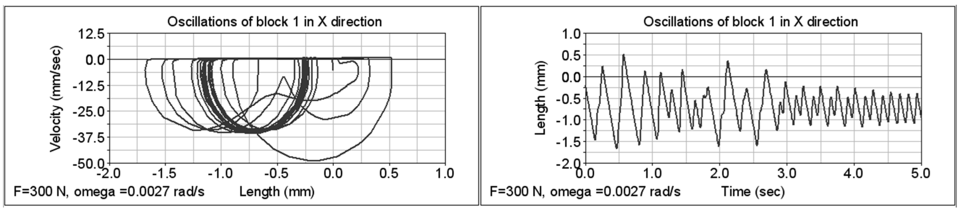

Figure. 3. Phase trajectory and time-histories of oscillation friction element no 1.

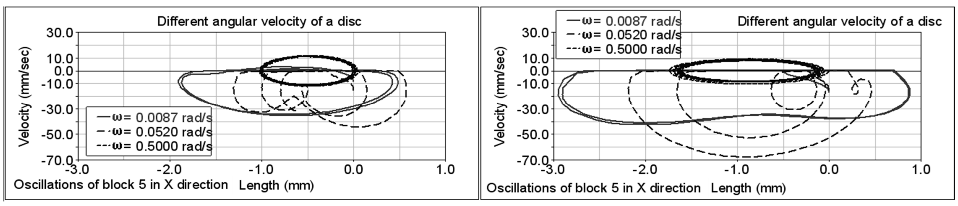

Figure. 4. Phase trajectory by different angular velocity of disc.

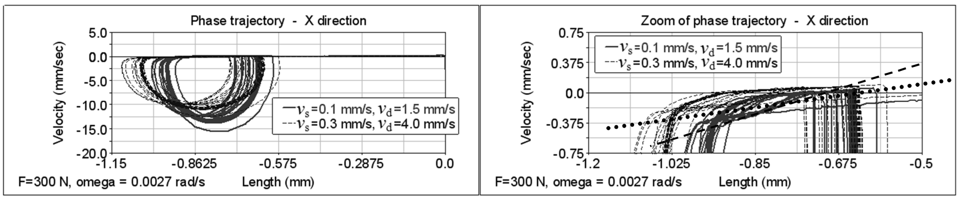

Figure. 5. Phase trajectory with creep effect at different velocity (v_s, v_d) describing curve of friction model– differences of creepage marked by dot and dashed lines.

In between the range of stick-slip and periodic vibration, creep phenomena can be observed (Fig. 5). This creepages is marked by dot and dashed lines. Differences in the creep process marked by straight lines on graphs phase trajectories (Fig. 5) are caused by different value of the velocity v_s and v_d of friction model. The values of these velocity affect on different slope of the curve of friction model (Fig. 3).

4. Conclusions

Stick-slip and creepage phenomena obtained in the numerical model of brake system has been presented. The studies also confirmed that introduction of an additional excitation to the system can reduce the amplitude of vibration of the system. In many papers the authors introduced external harmonic excitation into the system to reduce vibrations. In our case excitation generated by vibration of neighbouring friction elements of the model may reduce amplitude vibration depending on configuration of elements (Fig. 4).

References

1. Bogacz R., Ryczek B., Experimental and theoretical investigations of vibrations excited by dry friction. In: Dynamics of Rail Vehicles and Optimization of their Subsystems, Z. Jubil. Politechnika Krakowska, Nr 10, pp. 5-24
2. Bajer Cz., Konowrocki R. Friction rolling with lateral slip in railways. Journal of Theoretical and Applied Mechanics, 2009, 47(2), pp. 275-293,
3. Kinkaid, N. M., O'Reilly, O. M., and Papadopoulos, P. Automotive disc brake squeal. *J. Sound Vibr.*, 2003, 267(1), 105–166
4. Shin, K., Brennan, M. J., Oh, J. E., and Harris, C. J. Analysis of disc brake noise using a two-degree-of-freedom model. *J. Sound Vibr.*, 2002, 254(5), 837–848
5. Ouyang, H.,Cao, Q., Mottershead, J. E., and Treyde, T. Vibration and squeal of a disc brake: modeling and experimental results. Proc. I Mech. E, Part D: J. Automobile Engineering, 2003, 217(D10), 867–875. DOI:10.1243/095440703769683270
6. Cao, Q., Ouyang, H., Friswell, M.I., Mottershead, J.E. Linear eigenvalue an analysis of the disc-brake squeal problem. Int. J. Numer. Meth. Eng., 2004, 61(9), 1546–1563
7. Beloiu, D.M. and Ibrahim, R. A. Analytical and experimental investigations of disc brake noise using the frequency–time domain. J. Int. Assoc. Struct. Control Monit., 2005, 13(1), 277–300

XXV Symposium *Vibrations in Physical Systems,* Poznan – Bedlewo, May 15-19, 2012

Vibration Analysis of Irregularly Shaped Plates by the Spline-based Differential Quadrature Method

Artur KROWIAK
Cracow University of Technology, Institute of Computing Science, Al. Jana Pawła II 37, 31-864 Kraków, Poland, e-mail: krowiak@mech.pk.edu.pl

Abstract

The paper deals with the free vibration analysis of irregularly shaped plates using differential quadrature method (DQM). In the paper some effective approaches to deal with the problem of mapping irregular area into regular one are presented. These approaches are used in conjunction with a branch of the DQM based on spline interpolation to solve the free vibration problem of thin, isotropic plates. The use of this type of interpolation in the DQM ensures the stability of the method. As the results, the convergent tests of the natural frequencies are presented and compared with the results from conventional DQM.

Keywords: differential quadrature, irregularly shaped plates, blending functions, free vibration

1. Introduction

The differential quadrature method (DQM) is the discretization technique used to solve differential equations. It is characterized by very high rate of convergence, similar to spectral methods. In some particular cases, the method is identical to pseudospectral collocation method and finite difference method of the highest order of accuracy. Besides high rate of convergence, the DQM is characterized by high accuracy, little computational effort and is easy to implement due to its simple formulation. But this method has some limitations and drawbacks including computational instability and difficulties in handling the problems with irregular domains.

One of the ways to improve the stability of the method is the use of the spline functions to approximate the sought solution [1], instead of conventional interpolation polynomial [2]. There are also attempts to use the DQM in the case of problems with irregular domains. In paper [3], serendipity shape functions have been applied to map between regular and irregular area, similarly to finite element method. Another approach that allows exactly to map computational area into irregular one is the use of the blending functions, proposed by Gordon [4]. This approach, associated with the conventional DQM, has been employed to analyze thin, isotropic plates [5,6]. The aim of the present work is to examine the DQM based on spline interpolation in vibration problem of plates with irregular geometries. In the paper, the comparison between two ways of implementation of the DQM in this type of problems is also taken up.

2. Short description of the DQM

The basic idea of the DQM lies in the fact that the spatial derivative of a function at a given point is approximated by a linear weighted sum of the function values at all discrete points along the line that pass through the point of interest. It can be put as fol-follows

$$\frac{d^r f(\zeta)}{d\zeta^r}\Big|_{\zeta=\zeta_i} = \sum_{j=1}^{N} a_j^{(r)}(\zeta_i) f(\zeta_j) = \sum_{j=1}^{N} a_{ij}^{(r)} f_j \qquad i = 1,\ldots,N \tag{1}$$

where N denotes the number of grid points and $a_{ij}^{(r)}$ are the weighting coefficients of the rth order derivative.

By approximating all derivatives in the governing equation and/or boundary conditions according to formula (1) and collocating these equations at appropriate sampling points in the domain one obtains a set of algebraic equations. A key stage of the method is to determine the weighting coefficients. These coefficients depend on the way the sought solution is approximated. Therefore, they influence the convergence, accuracy and stability of the method.

The conventional DQM uses interpolation polynomial. On this basis the weighting coefficients are determined [7]. The latters are described by simple algebraic formulas, what makes the method very efficient. To overcome the main disadvantage of the DQM – computational instability – author proposed to approximate the sought solution by the spline functions [1]

$$f(\zeta) \approx \left\{ s_i(\zeta), \zeta \in \left[\zeta_i, \zeta_{i+1}\right],\ i = 1,\ldots,N-1 \right\} \tag{2}$$

In Equation (2) N is the number of nodes and the ith spline section $s_i(\zeta)$ of n degree can be written as

$$s_i(\zeta) = \sum_{j=0}^{n} c_{ij} (\zeta - \zeta_i)^j \tag{3}$$

where c_{ij} are spline coefficients. Expression (2) is correct for the odd spline degrees. In order to determine the weighting coefficients $a_{ij}^{(r)}$, one has to calculate spline coefficients at first. To this end, the set of algebraic equations has to be solved. The lack of explicit expressions for weighting coefficients is an inconvenience of the method comparing to conventional one. The spline-based DQM has been successfully applied in various mechanical problems including these where conventional DQM fails [8]. All details about spline-based DQM can be found in [1,9].

3. DQM for irregular geometries

Plates analyzed in the present paper are represented in general by curvilinear quadrilateral region, shown in Fig. 1a), called as physical domain. To employ the DQM in this case, a mapping between this region and computational regular area, presented in Fig. 1b), is required. To this end, the advantage of the blending functions [4] is taken and the mapping can be described as

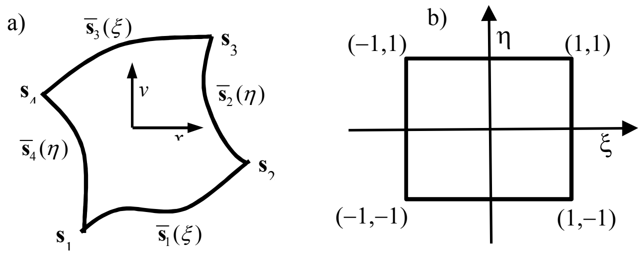

Figure 1. Domains: a) physical domain, b) computational domain

$$\begin{aligned}\mathbf{s} = \frac{1}{2}\left[(1-\eta)\,\overline{\mathbf{s}}_1(\xi) + (1+\xi)\,\overline{\mathbf{s}}_2(\eta) + (1+\eta)\,\overline{\mathbf{s}}_3(\xi) + (1-\xi)\,\overline{\mathbf{s}}_4(\eta)\right] - \\ -\frac{1}{4}\left[(1-\xi)(1-\eta)\,\mathbf{s}_1 + (1+\xi)(1-\eta)\,\mathbf{s}_2 + (1+\eta)(1+\xi)\mathbf{s}_3 + (1-\xi)(1+\eta)\mathbf{s}_4\right]\end{aligned} \tag{4}$$

where $\mathbf{s} = [x, y]^T$, $\overline{\mathbf{s}}_i$ are parametric curves that represent the boundaries and $\mathbf{s}_i$ are Cartesian coordinates of the corner points of the quadrilateral region.

There are two approaches to use the conventional DQM in this case. One of them is known as partial transformation [3,5] and transforms the weighting coefficients $a_{ij}^{(r)}$ for the DQM from computational domain to irregular one by the use of Equation (4). Further computations are carried out in original, physical domain. The second approach, known as complete transformation [6], transforms governing equation and associated boundary conditions from physical domain to computational one and uses original DQM weighting coefficients to discretize the problem in computational, rectangular domain. This approach requires less computational effort to obtain the solution but the stage of transformation is much more complicated. Below are the basic details of both methods.

Partial transformation

Taking advantage of the chain rule of differentiation

$$\frac{\partial f}{\partial x} = \frac{1}{|J|}\left(\frac{\partial y}{\partial \eta}\frac{\partial f}{\partial \xi} - \frac{\partial y}{\partial \xi}\frac{\partial f}{\partial \eta}\right), \quad \frac{\partial f}{\partial y} = \frac{1}{|J|}\left(-\frac{\partial x}{\partial \eta}\frac{\partial f}{\partial \xi} + \frac{\partial x}{\partial \xi}\frac{\partial f}{\partial \eta}\right) \tag{5}$$

where $|J|$ is the determinant of the Jacobian, given as $|J| = \dfrac{\partial x}{\partial \xi}\dfrac{\partial y}{\partial \eta} - \dfrac{\partial y}{\partial \xi}\dfrac{\partial x}{\partial \eta}$, the weighting coefficients $b_{mn}^{(1)}$ and $\overline{b}_{mn}^{(1)}$ that approximate first derivatives with respect to x and y in physical domain can be obtained as

$$\left(\frac{\partial f}{\partial x}\right)_m = \frac{1}{\left|J_{ij}\right|}\left[\left(\frac{\partial y}{\partial \eta}\right)_{ij}\sum_{k=1}^{N_\xi} a_{ik}^{(1)} f_{kj} - \left(\frac{\partial y}{\partial \xi}\right)_{ij}\sum_{l=1}^{N_\eta} \overline{a}_{jl}^{(1)} f_{il}\right] = \sum_{n=1}^{N_{\xi\eta}} b_{mn}^{(1)} f_n \tag{6}$$

$$\left(\frac{\partial f}{\partial y}\right)_m = \frac{1}{\left|J_{ij}\right|}\left[-\left(\frac{\partial x}{\partial \eta}\right)_{ij}\sum_{k=1}^{N_\xi} a_{ik}^{(1)} f_{kj} - \left(\frac{\partial x}{\partial \xi}\right)_{ij}\sum_{l=1}^{N_\eta} \overline{a}_{jl}^{(1)} f_{il}\right] = \sum_{n=1}^{N_{\xi\eta}} \overline{b}_{mn}^{(1)} f_n \tag{7}$$

In Equation (6)-(7) $m,n=(i-1)N_\eta + j,\ j=1,...,N_\eta, i=1,...,N_\xi$ and $N_{\xi\eta}=N_\xi \cdot N_\eta$. Taking into account that higher order derivatives obtained by the chain rule (5) are given by complicated formulas, weighting coefficients $b_{mn}^{(r)}$, $\overline{b}_{mn}^{(r)}$ for these derivatives and mixed one $c_{mn}^{(rs)}$ are obtained by matrix multiplication formula

$$B^{(r)} = B^{(1)}\, B^{(r-1)},\ \overline{B}^{(r)} = \overline{B}^{(1)}\, \overline{B}^{(r-1)},\ r=2,3,...,\ \ C^{(rs)} = B^{(r)}\, \overline{B}^{(s)},\ \ r,s=1,2,..., \tag{8}$$

Once the weighting coefficients in physical domain are determined, the DQM analog of governing equation and boundary conditions can be easily written.

Complete transformation

The governing equation end associated boundary conditions are transformed to computational domain. In the case of square, thin, isotropic plate, for which free vibrations are governed by the formula

$$\frac{\partial^4 W}{\partial X^4} + 2\frac{\partial^4 W}{\partial X^2 \partial Y^2} + \frac{\partial^4 W}{\partial Y^4} = \Omega^2 W \tag{9}$$

the transformed equation is as follows

$$\begin{aligned} &D^{(41)}W,_{\xi\xi\xi\xi} + D^{(42)}W,_{\xi\xi\xi\eta} + D^{(43)}W,_{\xi\xi\eta\eta} + D^{(44)}W,_{\xi\eta\eta\eta} + D^{(45)}W,_{\eta\eta\eta\eta} + D^{(31)}W,_{\xi\xi\xi} \\ &+ D^{(32)}W,_{\xi\xi\eta} + D^{(33)}W,_{\xi\eta\eta} + D^{(34)}W,_{\eta\eta\eta} + D^{(21)}W,_{\xi\xi} + D^{(22)}W,_{\xi\eta} + D^{(23)}W,_{\eta\eta} \\ &+ D^{(11)}W,_{\xi} + D^{(12)}W,_{\eta} = \Omega^2 W \end{aligned} \tag{10}$$

In Equation (10), the coefficients $D^{(ij)}$ depend on *x*, *y* coordinates that are taken from the mapping formula (4). The detailed description of these values is given in [6].
Similarly the boundary conditions are transformed, e.g. equation for clamped edges takes the form

$$W = W,_n = 0,\ \text{ where } n = \xi \text{ or } \eta \tag{11}$$

Using the DQM weighting coefficients determined in computational domain the discretized equation for (10) and (11) can be easily written.

4. Numerical example

In the work, the numerical experiment has been carried out in order to confirm usefulness of the spline-based DQM in vibration problems of plates with curvilinear boundaries. The plate presented in Fig. 2 has been considered. The physical domain from Fig. 2 can be described by the use of Equation (4), what yields

$$\begin{aligned} x(\xi,\eta) &= (0.6255\eta + 2.6255)\cos((\xi+1)\pi/4) \\ y(\xi,\eta) &= (0.8755\eta + 1.8755)\sin((\xi+1)\pi/4) \end{aligned} \tag{12}$$

Two approaches presented in section 3 have been employed to discretize the governing equitation of the plate as well as the clamped boundary conditions.

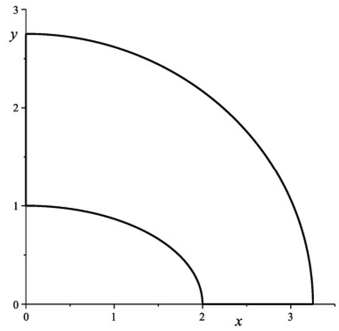

Figure 2. A quarter section of an elliptical plate

The weighting coefficients $a_{ij}^{(r)}$ have been obtained by the use of the spline functions of eleventh degree. The computation has been done applying Gauss-Lobatto pattern of point distribution. The results, depending on the number of points in both directions $N=N_\xi=N_\eta$, are shown in Table 1. The results from the conventional DQM are also provided for comparison.

Table 1. Convergent test on the base of natural frequencies of the clamped plate

	Ω_1		Ω_2		Ω_3		Ω_4	
N	SDQM	DQM	SDQM	DQM	SDQM	DQM	SDQM	DQM
Partial transformation								
11	10.756	10.757	14.209	14.204	18.625	18.722	23.615	24.587
18	9.955	9.955	13.171	13.171	17.342	17.343	23.091	23.093
22	9.826	9.826	13.008	13.008	17.126	17.126	22.794	22.794
26	9.756	9.757	12.920	12.920	17.009	17.009	22.635	22.635
Complete transformation								
11	9.600	9.598	12.722	12.742	16.712	16.910	22.261	22.145
18	9.595	9.595	12.717	12.717	16.744	16.743	22.276	22.275
22	9.595	9.595	12.717	12.717	16.743	16.743	22.275	22.274
26	9.595	9.595	12.717	12.717	16.743	16.743	22.275	22.274

The results contained in Table 1 show almost identical convergence even though different types of approximation are applied in the DQM. Moreover, the complete transformation approach leads to significantly higher convergence then partial transformation one. Only a few sampling points in each directions (e.g. N = 11) are sufficient to achieve acceptable accuracy. The same calculation has been carried out for simply supported plate and the same conclusion has been drawn. It should be noted that although complete transformation provides higher quality results and requires less computational effort [6], partial transformation seems to be more general method since only weighting coefficients are mapped to physical domain.

5. Concluding remarks

In the paper, the DQM based on spline interpolation is examined in the free vibration analysis of plates with curvilinear boundaries. Two approaches of handling this type of problem are presented. Although complete transformation approach gives faster convergence and requires less computational effort, this approach is more complicated since governing equation and boundary conditions have to be mapped to computational domain. In the second approach only DQM weighting coefficients are mapped, what simplifies problem definition.

The obtained results show the same rate of convergence of the spline-based DQM in comparison with conventional DQM. The present results and the fact that spline interpolation improves the stability of the DQM make this method competitive to conventional one in this type of problems.

References

1. A. Krowiak, *Symbolic computing in spline-based differential quadrature method, Commun*. Numer. Meth. Engng, **22** (2006) 1097-1107.
2. R. Bellman, J. Casti, *Differential quadrature and long term integration*, Journal of Mathematical Analysis and Application, **34** (1971) 235–238.
3. C.W. Bert, M. Malik, *The differential quadrature method for irregular domains and application to plate vibration*, Int. J. Mech. Sci., 38 (1996) 589 – 606.
4. W.J. Gordon, C.A. Hall, *Transfinite Element Methods: Blending Function Interpolation over Arbitrary Curved Element Domains*, Numer. Math., **21** (1973) 109 – 129.
5. M. Malik, C.W. Bert, *Vibration analysis of plates with curvilinear quadrilateral planforms by DQM using blending functions*, J. Sound Vib., **230** (2000) 949 – 954.
6. C. Shu, H. Du, *Free vibration analysis of curvilinear quadrilateral plates by the differential quadrature method*, J. Comp. Phys., **163** (2000) 452 – 466.
7. C. Shu, *Differential quadrature and its application in engineering*, Springer-Verlag, London 2000.
8. A. Krowiak, *The convergence and stability of the spline-based differential quadrature method applied to the vibration analysis of rectangular plates with free corners*, Vibration in Physical Systems, **22** (2006) 197 – 202.
9. A. Krowiak, *Modified spline-based differential quadrature method applied to vibration analysis of truncated conical shells*, Engineering Computations, in press

XXV Symposium *Vibrations in Physical Systems,* Poznan – Bedlewo, May 15-19, 2012

Analysis of the Dynamic Interaction Between the Pantograph and Catenary System

Anna KUMANIECKA
Institute of Mathematics,Cracow University of Technology
Warszawska 24, 31-155 Cracow, Poland, pukumani@cyf-kr.edu.pl

Abstract

The work presented in this paper emphasis the modeling and simulation of the dynamic interaction between the pantograph and a catenary system. The main aim of the paper is to present the influence of catenary stiffness on the overhead system dynamics. To investigate the effect of the catenary stiffness on the system vibration a new formula describing stiffness has been introduced. The limit uplift force which does not cause the contact loss was determined. General results are illustrated by numerical examples in which the effect of contact wire stiffness is observed. The comparison of the result of simulation and experiment, performed on especially built stand, is provided.

Keywords: dynamics, pantograph, catenary, stiffness

1. Introduction

At present, the collection of current from the overhead equipment is a problem of primary importance for high speed railway systems, and has become a challenging task for the development and exploitation of current electrical railway lines. It is generally known that the pantograph-catenary system, with its dynamic behaviour, is a crucial component of railway transportation. Therefore, research into understanding the current collection system dynamic characteristics is needed.

The dynamics of the pantograph-catenary system was studied mainly theoretically by simulation methods with numerical calculations. The pantograph was modelled as two - or three – dimensional lumped – mass system of two or four degrees of freedom. The catenary was considered as a continuous model, first of all as string or Bernoulli-Euler beam models. A review paper describing the pantograph-catenary systems has been presented by Poetsch et al. [2] and Kumaniecka [1]. In the present paper more attention is paid to catenary-pantograph models including contact wire stiffness.

The paper is organized in five sections. Following the introduction, the models of the catenary and pantograph are described in Section 2. The influence of contact wire stiffness on dynamic performance is discussed in Section 3. A comparison of the results of simulation and experiment is presented in Section 4. The concluding remarks are the subject of the Section 5.

2. Model of the catenary-pantograph system

The catenary is one of the most important parts of a railway electrification system. In railway transportation two types of catenary are in use, a simple catenary and compound catenary. The compound catenary is used for high-speed trains (above 250 km/h) and the simple catenary for mid-speed trains (below 150 km/h). In Poland the simple catenary is still in use. Many different pantograph designs have been proposed, see Fig. 1.

Figure1. Pantograph system: symmetric with one strip and asymmetric with two strips

The pantograph and the catenary together form a dynamically coupled vibrating system mutually affecting each other through the contact force. The contact force is composed of the static force that it called uplift force, and the dynamic force which depends on the running speed and the vibration of system.

The major source of vibration is the spatial stiffness variation of the catenary along the span in which this value is a minimum value in the middle and maximum value near the supports. The previous studies on the response of catenary-pantograph have shown that the variation of the contact force between the pantograph and the contact wire is principally caused by the stiffness variation along the span and the wave propagation in the catenary wires. Wu et al. [4] proved that the compound catenary has a smaller static stiffness variation in comparison with the simple catenary.

If the stiffness variation between the vertical droppers is omitted and the train is travelling at constant speed v, then the stiffness $k(t)$ can be approximated by the formula:

$$k(t) = k_0\left(1 + \alpha \cos\left(\frac{2\pi v}{L} t\right)\right) \tag{1}$$

with

$$k_0 = \frac{k_{\max} + k_{\min}}{2}, \alpha = \frac{k_{\max} - k_{\min}}{k_{\max} + k_{\min}}$$

where L is the length of one span and $k_{\max}$, $k_{\min}$ are the largest and smallest stiffness in the span, respectively. k_0 can be regarded as the average stiffness and α as the stiffness variation coefficient. It should be mentioned that several authors used the type of approximation shown in Eq. (1).

In Fig. 2 the physical model of the pantograph type WBL-85/3kV, which is commonly used in many countries in Europe, Asia and Africa, is shown. Displacement of the pantograph pan-head is the main factor for dynamic performance and it is related to the contact force directly. The static uplift force is applied to the pantograph to keep the proper working height. A smaller static uplift force may induce a contact loss, arcing and sparkle.

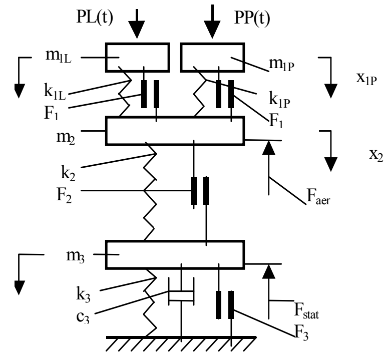

Figure 2. Model of the pantograph

To limit the scope of the problem of the dynamic pantograph behavior, in the presented study, only the vertical vibration in surrounding of static equilibrium state have been considered. It was assumed that damping in kinematic connections has a dry friction characteristic, and elastic connection elements of reduced masses of contact strips and upper arm have nonlinear characteristics. The aerodynamic force is taken into account. Some details are presented in the monograph [1]. The mathematical model for a physical model of the pantograph, adopted in Section 2, was discussed in [3]. To predict the dynamic behaviour of the system in question, the time varying static stiffness $k(t)$ should be replaced by the dynamic stiffness.

3. Influence of contact wire stiffness on the system dynamics

A proper description of stiffness needs unilateral constraints in the contact between the pantograph strip and wire to be taken into account. The function describing the contact force $F(t)$ should be written as follows:

$$F(t) = PL(t) + PP(t)$$

where:

$$PL(t) = k_0 \begin{cases} \left[1 - \alpha \cos\left(\dfrac{2\pi v}{L} t\right)\right]\left(x_{1L0} - x_{1L}\right) & \text{for} \quad x_{1L0} > x_{1L} \\ 0 & \text{for} \quad x_{1L0} \le x_{1L} \end{cases} \tag{2}$$

$$PP(t) = k_0 \begin{cases} \left[1 - \alpha \cos\left(\dfrac{2\pi}{L}(vt + x_{LP})\right)\right]\left(x_{1P0} - x_{1P}\right) & \text{for} \quad x_{1P0} > x_{1P} \\ 0 & \text{for} \quad x_{1P0} \le x_{1P} \end{cases}$$

In Figure 3 the program of simulation of minimal limit of uplift force F_{stat}, which does not cause a contact loss, is presented.

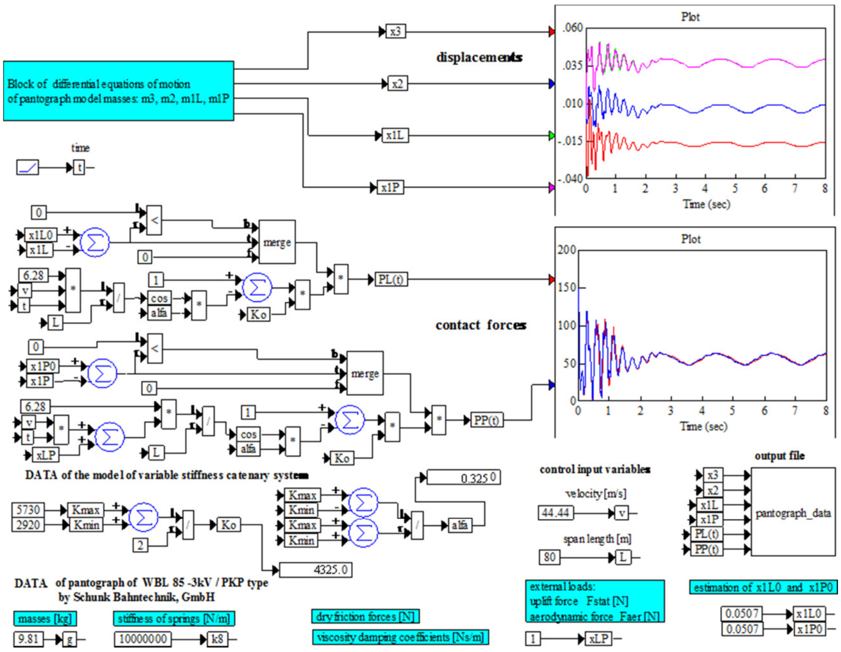

Figure 3. Minimal limit of uplift force F_{stat} = 560 [N] and at F_{aer} = 30 [N] with no loss of contact

Taking into account the limit value of uplift force F_{stat} = 560 [N] the calculations of the values of the contact forces on the strips of the pantograph were done.

To investigate the phenomena of the contact loss in the overhead system numerical simulations for the contact force less a limit force have been carried out. In Fig. 4 the contact force in the form of peak-to-peak and the range of loss of contact is shown.

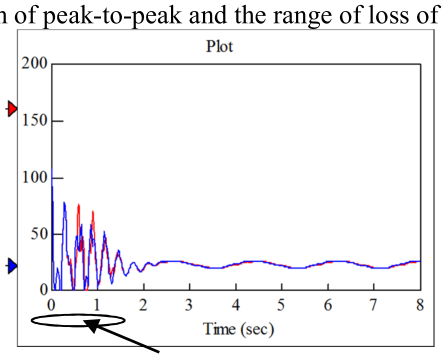

Figure 4. Contact forces on strips at too little value of uplift force F_{stat} = 500 [N]

The stiffness variability plays a key role at high speeds and it is responsible for higher contact force. The contact force is always positive, there exists contact between the catenary and pantograph, or zero when there is a contact loss.

Contact losses can be found when the peak-to-peak contact force is smaller than the minimum contact force.

The value of uplift force F_{stat} = 500 [N] is too little and the phenomena of contact loss appear. In order to highlight the influence of the train speed calculations for different values of operational speeds have been provided.

4. Experimental investigation

Theoretical models of the overhead system need to be verified experimentally. The testing facility for laboratory experiments was designed and built at the Faculty of Mechanical Engineering, Cracow University of Technology.

The main part of experiments was connected with the interaction between the moving oscillator and contact wire. Plan of the experiments included also testing of catenary stiffness.

The goal of the experiment provided was the measurement of forces between the pantograph strip and contact wire in different conditions of the given motion.

The analysis of the experimental results shows periodical variability of the local flexibility along the wire. The maximum value of variability is 40% of the mean flexibility value. In Fig. 5 the acceleration of vertical vibration of pantograph strips and spectrum of acceleration for vertical excitation are presented.

The measurements of dynamic vibration and interaction force between the pantograph and contact wire were taken for different initial loads and different velocity of the rail car. As a result, we could state that the loss of contact between pantograph and catenary is possible.

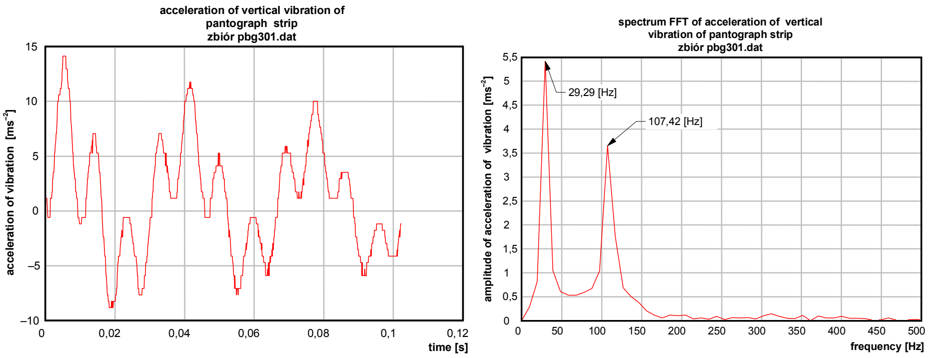

Figure 5. Acceleration of vertical vibration of pantograph strip and spectrum of acceleration for vertical excitation

5. Conclusions

On the basis of theoretical investigations and experiments the following conclusions can be drawn:

- Widely used formula (1) is too simple as a representation of the stiffness.
- The new formula describing stiffness proved to be introduced.
- The stiffness of the catenary varies significantly with train speed.
- Parallel analysis of results of investigation carried out on the physical and experimental model enables their mutual verification.

The computer simulation performed on the base of relevant theoretical models, verified in experiments with physical models are a useful tool for designers, both of the catenary and the pantograph.

References

1. A. Kumaniecka, *Methods of analysis of discrete-continuous systems vibration and their application to the railway transport problems*, Scientific Issue of Cracow University of Technology, Mechanics, Vol. 352 (2007).
2. G. Poetsch, J. Evans, R. Meisinger, W. Kortum, W. Baldauf, A. Veitl, J. Wallaschek, *Pantograph/ Catenary Dynamics and Control*, Vehicle System Dynamics, **28** (1997) 159-195.
3. M. Prącik, K. Furmanik, *Problems of modelling and simulation of catenary and pantograph cooperation*, Proc.VII-th Workshop PTSK, Warsaw, (2000), **7**, 242-250.
4. T. X. Wu, M. J. Brennan, *Dynamic stiffness of a railway overhead wire system and its effect on pantograph-catenary system dynamics*, Journal of Sound and Vibration, **219** 4 (1999) 483-502.

XXV Symposium *Vibrations in Physical Systems,* Poznan – Bedlewo, May 15-19, 2012

Free Vibrations of Layer Composite Plates Pliable to Transversal Shear and Compression

Oksana LESYK
Ternopil National Economic University, MESU
11, Lvivska Str., 46020 Ternopil, Ukraine
glesyk@mail.ru

Mykhaylo MARCHUK
Pidstryhach Institute for Applied Problems of Mechanics and Mathematics, NASU
L'viv, Ukraine, 3 b, Naukova Str., L'viv, 79053, Ukraine
mmv1956@hotmail.com; marchuk@iapmm.lviv.ua

Vira PAKOSH
Pidstryhach Institute for Applied Problems of Mechanics and Mathematics, NASU
L'viv, Ukraine, 3 b, Naukova Str., L'viv, 79053, Ukraine
v.pakosh@ukr.net

Abstract

A mathematical model of the process of linear free vibrations of layer plates with components pliable to transversal shear and compression is proposed. The analytical expression for the spectrum of natural frequencies of two-layer plate-strip is obtained. The influence of parameters of pliability to transversal shear and compression on their values is investigated.

Keywords: Layer plates, vibrations, natural frequencies, composite plates

1. Introduction

Composite plates of layer structure with regulated characteristics of strength and materials consumption are one of the most abundant bearing elements of constructions and technical means of different purpose. In most cases they are subjected to intensive dynamic, cyclic in particular, loadings. Therefore the reliable estimation of such dynamic characteristic as a spectrum of natural frequencies is an actual problem at their designing in order to prevent the resonance phenomena in operating conditions.

The pliability to transversal shear and compression is the most typical peculiarity of deformation of thin-walled elements from modern reinforced composites on the polymeric basis (both in static and dynamic cases) along with anisotropy of elastic characteristics [1]. It should be noted that today there are not many works on vibrations of composite plates with simultaneous accounting the pliability to transversal shear and compression, especially for their layer structure by the thickness when considering discretely the layers. The prevailing majority of our results have been obtained by means of numerical methods. In general same research conducted using the refined theories with the exact elastic characteristics of thickness [2, 3].

Below, basing on the variant of refined theory of plates, which takes into account explicitly the pliability to transversal shear and implicitly – to compression [4], we have suggested a mathematical model of the process of free vibrations of layer plates-strips to consider discretely the components of such structures. In the case of two-layer plate-strip an analytical expression for a spectrum of natural frequencies under condition of elongated edges, hinged on the lower face plane of the structure, has been obtained. The influence of physical-mechanical characteristics and geometric parameters of the structure components on the magnitudes of values of natural frequencies has been analyzed. The expression for a spectrum of natural frequencies of free vibrations of plate-strip with a thin protective coating, covered on the upper face surface, has been obtained as a special case [5].

2. Problem statement

Consider a layer structure consisting of thin composite plates with brought physical-mechanical characteristics and thickness $2h_i$ and densities ρ_i, respectively. If one of the tangential dimensions of the structure considered exceeds essentially the other then we have a two-layer plate-strip, the characteristics of the stressed-strained state of which can be considered to be dependent on two local coordinates of each plate only (Fig. 1).

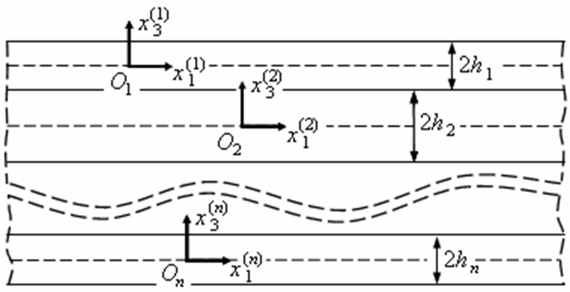

Figure 1. Layer structure of composite thin plates-strips

It is assumed that between the plates the conditions of perfect mechanical contact are satisfied. Due to the action of normal and tangential contact stresses on the interplate plane for the transverse vibrations of such a structure each component undergoes both bending and longitudinal deformations. The vibration process of each plate is described [4] by:

a) equilibrium equations (motion)

$$N_i' + 2\tau_i^- = 0\,, \quad M_i' - Q_i + 2h_i\tau_i^+ = 0\,, \quad Q_i' + 2\sigma_i^- = 2\rho_i h_i \ddot{w}_i\,, \tag{1}$$

where

$$\tau_i^\pm = \frac{1}{2}[\sigma_{13}^{(i)}(x_1^{(i)}, h_i, t) \pm \sigma_{13}^{(i)}(x_1^{(i)}, -h_i, t)]\,,$$

$$\sigma_i^- = \frac{1}{2}[\sigma_{33}^{(i)}(x_1^{(i)}, h_i, t) - \sigma_{33}^{(i)}(x_1^{(i)}, -h_i, t)];$$

b) elasticity relations

$$N_i = \overline{B}_i\, \varepsilon_{1i}^0, \quad M_i = \overline{D}_i\, \overline{\varepsilon}_{1i}^1, \quad Q_i = \Lambda_i\, \varepsilon_{13i}^0; \tag{2}$$

c) deformation relations

$$\varepsilon_{1i}^0 = u_i', \quad \overline{\varepsilon}_{1i}^1 = \varepsilon_{1i}^1 / h = \gamma_i'; \quad \varepsilon_{13i}^0 = \gamma_i + w_i'. \tag{3}$$

In equalities (1) – (3) the conventional notations are used for tensile N_i and intersecting Q_i forces, bending moments M_i in each plate, components of tensors of stresses $\sigma_{kn}^{(i)}$, displacements u_i of points of the midplane of the i th plate in tangentional direction, angles of rotation γ_i of the normal elements to the midplane before deformation, displacements of points of the midplane along the normal coordinate w_i, longitudinal ε_{1i}^0 and bending $\overline{\varepsilon}_{1i}^1$ deformations, deformation of transversal shear ε_{13i}^0 and also for the introduced rigidity characteristics of the plate: $\overline{B}_i = 2E_i h_i (1+\alpha_i)/3(1-\nu_i^2)$ – the generalized tensile rigidity, $\overline{D}_i = h_i^2\, \overline{B}_i / 3$ – the generalized bending rigidity, $\Lambda_i = 2k' h_i G_i'$ – shearing rigidity, $\alpha_i = ((1+\nu_i)(\nu_i')^2/(1-\nu-2\nu\nu'))(E_i/E_i')$, E_i, ν_i – Young's moduli and Poisson's ratios in the midplane and plane equidistant to it, E_i', ν_i' – the same values in the planes perpendicular to the midplane, G_i' – transversal shear moduli, $k' = 14/15$, $i = 1, n$, where n is the number of layers. The stroke denotes the coordinate derivative $x_1^{(i)}$, and the dot – the t derivative.

The boundary conditions at the ends $x = \pm l$ of a hinged lower plate along the elongated sides on the lower face surface read

$$N_i(\pm l, t) = 0, \quad M_i(\pm l, t) = 0,$$

$$w^{(1)}(\pm l, -h_1, t) = w^{(2)}(\pm l, h_2, t) = \ldots = w^{(n)}(\pm l, -h_n, t) = 0. \tag{4}$$

The equation (1), together with relations (2), (3) and boundary conditions (4) form a mathematical model of the process of small free vibrations of layer plate-strip. The pliability of material of the ith component to transversal compression is taken into account in this model due to the presence the coefficients depending on the transversal elastic constants E_i' and ν_i' in the expressions for their rigidity characteristics.

3. Construction of solution of the problem

Then consider in detail a case for $n = 2$ (Fig. 1).

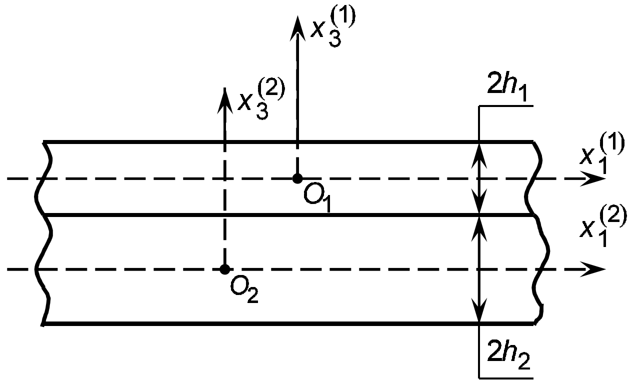

Figure 2. Two-layer plate-strip

For free vibrations of the layer structure under study on its face planes we have:

$$\sigma_{13}^{(1)}(x_1^{(1)}, h_1, t) = \sigma_{33}^{(1)}(x_1^{(1)}, h_1, t) = 0 \,,$$

$$\sigma_{13}^{(2)}(x_1^{(2)}, -h_2, t) = \sigma_{33}^{(2)}(x_1^{(2)}, -h_2, t) = 0 \,. \tag{5}$$

The relations

$$\sigma_{13}^{(1)}(x_1, -h_1, t) = \sigma_{13}^{(2)}(x_1, h_2, t) = \tau(x_1, t) \,,$$

$$\sigma_{33}^{(2)}(x_1, -h_1, t) = \sigma_{33}^{(2)}(x_1, h_2, t) = \sigma(x_1, t) \,, \tag{6}$$

$$u^{(1)}(x_1, -h_1, t) = u^{(2)}(x_1, h_2, t) \,, \quad w^{(1)}(x_1, -h_1, t) = w^{(2)}(x_1, h_2, t) \tag{7}$$

are the consequence of conditions of perfect mechanical contact between the plates at matching the origins of coordinate axes $x_1^{(1)}$ and $x_1^{(2)}$.

The eguations (1) of motion, after substitution the relations (5) and (6) into them, yield

$$N_1' - \tau = 0 \,, \quad N_2' + \tau = 0 \,,$$

$$M_1' - Q_1 + h_1\tau = 0 \,, \quad M_2' - Q_2 + h_2\tau = 0 \,,$$

$$Q_1' - \sigma = 2\rho_1 h_1 \ddot{w}_1 \,, \quad Q_2' + \sigma = 2\rho_2 h_2 \ddot{w}_2 \,. \tag{8}$$

Since on the face planes of each plate the tangential $u^{(i)}$ and normal $w^{(i)}$ displacements are determined by the formulas [4]

$$u^{(i)}(x_1, \pm h_i, t) = u_i(x_1, t) \pm h_i \gamma_i(x_1, t) \,, \quad w^{(i)}(x_1, \pm h_i, t) = w_i(x_1, t), \; i = 1,2 \,,$$

from equalities (7) we find:

$$u_1 = u_2 + h_1\gamma_1 + h_2\gamma_2, \quad w_1 = w_2 = w. \tag{9}$$

The relations (9) enable the elimination of the contact interlayer stresses τ and σ from equilibrium equations (8) and obtaining a system of three resolving equations:

$$(1+\beta_1)\gamma_1'' - \kappa_1^2 + \beta_{12}\gamma_2'' = \kappa_1^2 w',$$

$$\beta_{21}\gamma_1'' + (1+\beta_2)\gamma_2'' - \kappa_2^2\gamma_2 = \kappa_2^2 w',$$

$$\lambda_1\gamma_1^1 + \lambda_2\gamma_2^1 + w'' = \frac{1}{c_2^2}\ddot{w}, \tag{10}$$

where $\lambda_i = \Lambda_i/\Lambda$, $\kappa_i^2 = \Lambda/\overline{D}_i$, $\beta_i = 3\overline{B}_i/B$, $i=1,2$; $\Lambda = \Lambda_1 + \Lambda_2$; $B = \overline{B}_1 + \overline{B}_2$; $\frac{1}{c_2^2} = \frac{2(\rho_1 h_1 + \rho_2 h_2)}{\Lambda}$; $\beta_{12} = 3\,\frac{h_2}{h_1}\frac{\overline{B}_2}{B}$; $\beta_{21} = 3\,\frac{h_1}{h_2}\frac{\overline{B}_1}{B}$.

If the sought for functions w and γ_1, γ_2 we present in the form

$$w(x,t) = \left(\sum_{n=0}^{\infty} w_n \cos\lambda_n x\right) e^{i\omega t}, \quad \gamma_i(x,t) = \left(\sum_{n=0}^{\infty} \gamma_{in} \sin\lambda_n x\right) e^{i\omega t}, \quad i = 1, 2, \tag{11}$$

$$\lambda_n = \frac{2n+1}{2}\frac{\pi}{l},$$

then the boundary conditions (4) are satisfied. After substitution (11) into (10) we obtain an infinite system of algebraic equations to determine the coefficients w_n, γ_{1n}, γ_{2n}, which consists of independent third order subsystems

$$[(1+\beta_1)\lambda_n^2 + \kappa_1^2]\,\gamma_{1n} + \beta_{12}\,\lambda_n^2\,\gamma_{2n} = \kappa_1^2\lambda_n\; w_n,$$

$$\beta_{21}\,\lambda_n^2\,\gamma_{1n} + [(1+\beta_2)\lambda_n^2 + \kappa_2^2]\,\gamma_{2n} = \kappa_2^2\lambda_n\; w_n$$

$$\lambda_1\,\alpha_n\,\gamma_{1n} + \lambda_2\,\alpha_n\,\gamma_{2n} - \lambda_n^2\,w_n = -\frac{\omega_n^2}{c^2}w_n, \tag{12}$$

$n = \overline{1,\infty}$; ω_n is the n th natural frequency.

The expression for the squares of the values of natural frequencies

$$\omega_n^2 = \alpha_n^4\,\frac{c_2^2}{\alpha_n^2 + a^2/b^2}, \tag{13}$$

where

$$a^2 = \alpha_n^2\{[\lambda_1(1+\beta_2) - \lambda_2\beta_{21}]\kappa_1^2 + [\lambda_2(1+\beta_1) - \lambda_1\beta_{12}]\kappa_2^2\} + \kappa_1^2\kappa_2^2,$$

$$b^2 = 4\alpha_n^2 + [(1+\beta_2)(1-\lambda_1) + \lambda_2\beta_{21}]\kappa_1^2 + [(1+\beta_1)(1-\lambda_2) + \lambda_1\beta_{12}]\kappa_2^2,$$

$$\lambda_1 = \Lambda_1/\Lambda, \quad \lambda_2 = \Lambda_2/\Lambda, \quad \Lambda = \Lambda_1 + \Lambda_2,$$

is the consequence of condition for non-triviality of solution of the subsystem (12).

4. Special cases

4.1 Plate-strip with a thin coating

If the upper plate is assumed to be a thin protecting coating in comparison with the lower one then we can neglect the bending moment M_1 in it. Having introduced into consideration the expression for a spectrum of dimensionless frequencies by the formula

$$\overline{\omega}_n = l\,\omega_n\sqrt{\frac{\rho_2}{E_2}}, \tag{14}$$

from (13) for their values we obtain:

$$\overline{\omega}_n = \varepsilon\, k_n^2\, a_n\,, \tag{15}$$

where $\varepsilon = h_2/l$ is the parameter of a thin-walled plate, $k_n = \dfrac{2n+1}{2}\pi$,

$$a_n^2 = \frac{1+\alpha_2}{1+\eta}\,\frac{1+a^2+\beta^2}{(1+\beta^2)(1+\alpha_2)k_n^2\,\varepsilon^2(E_2/G_2) + 3(1-\nu_2^2)},$$

$$a^2 = \frac{3\overline{B}_1}{B_1+B_2}\,\frac{h_1}{h_2}\ , \quad \beta^2 = 3\overline{B}_1/\overline{B}_2\,.$$

4.2 Plate-strip pliable to transversal shear and compression

This case is obtained setting $h_1/h_2 = 0$. Then from (13) for the spectrum of dimensionless frequencies (14) we obtain

$$\overline{\omega}_n = k_n^2\varepsilon\sqrt{\frac{1+\alpha_2}{\delta^2 + k_n^2\varepsilon^2(1+\alpha_2)(E_2/G_2')/k'}}\ , \tag{16}$$

where $\delta^2 = 3(1-\nu_2^2)$.

4.3 Timoshenko shear model

Timoshenko shear model is obtained putting the values $E_2 / E'_2 = 0$ into the expression for coefficient α_2. Then the spectrum of dimensionless natural frequencies is determined by the formula

$$\overline{\omega}_n = k_n^2 \varepsilon \sqrt{\frac{1}{\delta^2 + k_n^2 \varepsilon^2 (E_2 / G'_2) / k'}} . \tag{17}$$

4.4 Classical theory

If the plate material is not pliable to transversal shear, that is $E_2 / G'_2 = 0$, then for $\overline{\omega}_n$ we have

$$\overline{\omega}_n = k_n^2 \varepsilon / \delta . \tag{18}$$

5. Analysis of results and conclusions

Numerical calculations are performed for a two-layer plate-strip for $E_1 / E_2 = 0,2,$ $\nu_1 = 0,2,$ $\nu_2 = 0,375,$ $E_i / G_i = 2(1+\nu_i)$, $\rho_1 / \rho_2 = 0,2,$ $h_1 / h_2 = 1,0,$ $\varepsilon = 0,05$. In the Table in the first line the values of dimensionless frequencies $\overline{\omega}_n$ for $n = 0,1,2$, calculated by the formula (17), are presented using the rigidity characteristics deduced by the thickness that is neglecting discreteness. The second line shows the values of the same natural frequencies calculated by the formula (13) for $E_i / E'_i = 0.$ The third line presents the same natural frequencies calculated by the formula (13) but for $E_i / E'_i = 1.$

$\overline{\omega}_n$ / Nos of the variant	$\overline{\omega}_0$	$\overline{\omega}_1$	$\overline{\omega}_2$
1	**0,1465**	**1,2089**	**2,9247**
2	**0,1288**	**1,0124**	**2,4822**
3	**0,1350**	**1,0956**	**2,6204**

From comparison of the 1st line with the 2nd one, we see that accounting the discreteness of construction by thickness causes the decrease of the values of natural frequencies, whereas accountig the pliability increases their values.

References

1. R.M. Christensen, *Mechanics of composite materials,* New York : Wiley, 1979.
2. S. Latheswary, K.V. Valsarajan, Y.V.K.S. Rao, *Free Vibrations Analysis of Laminated Plates using Higher-order Shear Deformation Theory*, IE (I) J.-AS, **85** (2004) 18–24.
3. Huu-Tai Thai, Seung-Eock Kim, *Free vibration of laminated composite plates using two variable refined plate theory,* International Journal of Mechanical Sciences, **52** (10) (2010) 626-623.
4. V.A. Osadchuk, M.V. Marchuk, *Mathematical model of dynamic deformation of pliable to shear and compression composite plates,* Applied Problems of Mechanics and Mathematics, **3** (2005) 43-50.
5. V.S. Pakosh, *Fundamental frequencies of pliable to transversal shear and compression plate-strip with a thin coating,* Applied Problems of Mechanics and Mathematics, **7** (2009) 94-98.

XXV Symposium *Vibrations in Physical Systems,* Poznan – Bedlewo, May 15-19, 2012

Dynamics of Mechanical Model of Implant-Tissue System in Ventral Hernia Repair

Izabela LUBOWIECKA
Gdansk University of Technology, ul. Narutowicza 11/1, 80-233 Gdansk, Poland
lubow@pg.gda.pl

Abstract

The paper deals with a finite element modelling of implants in the problem of ventral hernia repair. The synthetic mesh implanted in the abdomen during surgery is here modelled as a membrane structure. The system undergoes the internal abdominal pressure that occurs during the postoperative cough, the load identified in the literature as the main cause of the connection failure and hernia recurrence. The model can be used to estimate the forces appearing in the connections of tissue and implant for different materials of implants and different number of tacks. This can help to predict the fixing system, such as the number of tacks etc. to be provided during the surgery in order to resist the cough pressure and avoid the hernia recurrence. The dynamic analysis of the structure is compared to the laboratory experiments in a pressure chamber to demonstrate the accuracy of the proposed model.

Keywords: biomechanics, synthetic implant, membrane, dynamic analysis

1. Introduction

A hernia occurs when part of an internal organ protrudes through a weak area of muscle. Most hernias occur in the abdomen. Especially, the incisional hernias as large abdominal wall defects have been shown to have recurrence rates of between 25 to 52% when primarily repaired [1]. The usual treatment for a hernia is a repair surgery where the synthetic implants are fixed to the tissue called fascia in the human abdomen.

Even though the ventral hernia repair surgery is a common procedure, the mechanical properties of the tissue-implant system are unknown so the implantation of the repairing mesh depends on the surgeon knowledge and practice. Unfortunately, the recurrences of the illness still take place as shown e.g., in [2]. The number of the joints (called tacks) required for holding the implanted mesh correctly is undefined and their optimal position is only intuitive (Fig. 1). Moreover, the high number of joints can affect nerves and result in chronic pain, so the minimising of the tacks number standing the abdominal pressure is required.

For that, a mechanical model based on finite element method of implanted mesh is proposed here and its dynamic behaviour is studied to provide a methodology for the repair assessment. The model contains an orthotropic membrane structure of the material properties identified within the laboratory tests. The simple cable implant model of implanted mesh has been previously studied and presented in [3]. Also some attempts were undertaken to model implant behaviour as a membrane structure as shown in [4]. In addition a membrane model for a herniated rabbit abdominal wall with hernia orifice and implant was previously proposed and discussed in [5] but and any assessment method for the repair persistence was provided.

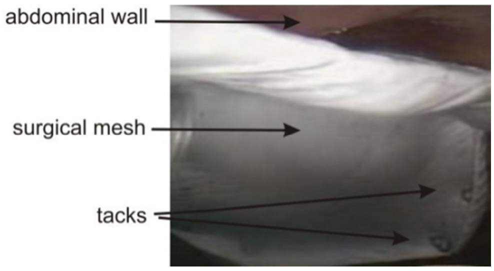

Figure 1. Hernia repair in human abdomen

The author pays considerable attention to the forces that appear in the connection between tissue and implant. These forces compared with the repair failure load identified in [6] are analysed to estimate the hernia repair persistence. For that reason, the mechanical model of whole abdomen is not necessary here. These forces should not exceed the experimental value of the strength of the tissue-implant connection that would mean that the hernia recurrence will not appear due to the appropriate load.

The finite element dynamic analysis of the system is performed and the results are compared to the laboratory tests on the implant-tissue system sample subjected to a pressure load in a specially prepared pressure chamber.

2. Mechanical model of implant. Materials and experimentation.

The surgical mesh Dual Mesh Gore® was taken to the analysis. Its material properties were identified on the basis of the one dimensional tensile tests on the machine Zwick Roel 020 as presented in [3-4] and [7-8].

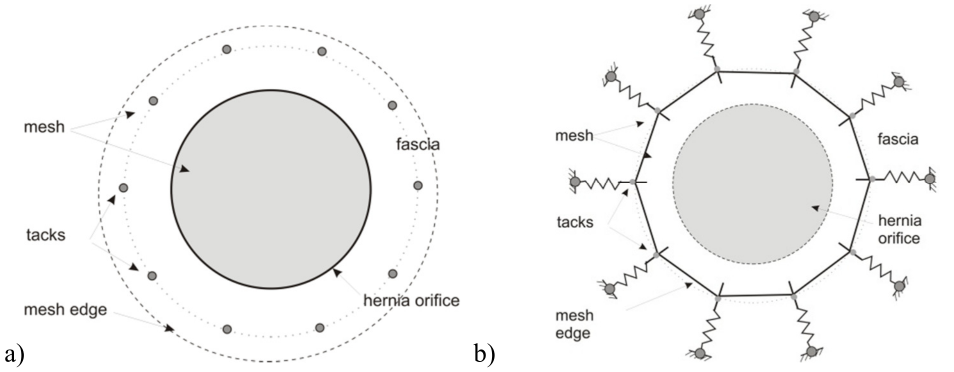

Figure 2. a) Scheme of repaired hernia; b) Implant model

The orthotropy of the surgical mesh material was observed as indicated in [9]. The material stiffness was described by bilinear elastic moduli $E_1 = 28.03$ N/mm and $E_2 = 25.54$ N/mm when the strain $\varepsilon \leq 0.3$ and $E_1 = 4.17$ N/mm and $E_2 = 2.84$ N/mm when $\varepsilon > 0.3$.

The model geometry (Fig. 2) refers to the clinical case of hernia with the 5 cm large orifice. As the common distance between joints differs from 2 to 4 cm, the largest as unfavourable one was considered in the model and also in the experiment. The membrane is a polygonal structure stretched out on 9 elastic supports every 4 cm, with 4 cm tissue overlap. This gives the membrane span equal to 0.12 m. The elastic supports, of the stiffness assuring the joints horizontal displacement observed within the experiment, represent the zone of interaction of the tissue and implanted membrane.

a) 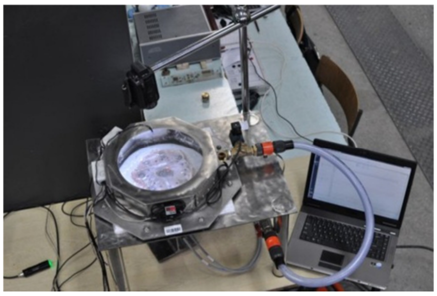 b) 

Figure 3. a) Experimental stand; b) Operated hernia specimen

The experiment was performed in a specially prepared pressure chamber where the air impact representing the cough pressure was applied to the specimen of implant fixed to the porcine tissue (Fig. 3). The pressure value was growing during 0.1 s until the value 270 mmHg identified in [10] as the cough pressure and then decreasing to 0 within next 0.1 s. The size and the fixing type referred to a real clinic case of hernia repair. The details of the experiments are presented in [8].

3. Finite element analysis and results

The nonlinear dynamic analysis was carried out by means of the MSC.Marc finite element commercial system. 469 (symmetric part) 4-node membrane element of type 18 (MSC.Marc) containing 3 translational degrees of freedom in each node was applied (see e.g. [11-12]), Fig. 4. The large strains and Total Lagrangean formulation were considered in the study. The implicit single step Houbolt algorithm (see e.g., [13]) was used to simulate the structure dynamics.

The dynamic analysis demonstrates relatively strong damping in the tissue-implant system, so the Rayleigh damping parameters were introduced also to the mechanical model. The parameters were estimated on the basis of modal analysis according to the formula (1)

$$\xi_i = \frac{\alpha}{2\omega_i} + \frac{\beta\omega_i}{2} \tag{1}$$

where α and β are respectively the mass and stiffness damping ω_i represents i-th natural frequency of the system [14]. For the tested implant, these two coefficients were estimated as α = 2 and β = 0.01, for which the simulation corresponds to the experi-experimental results.

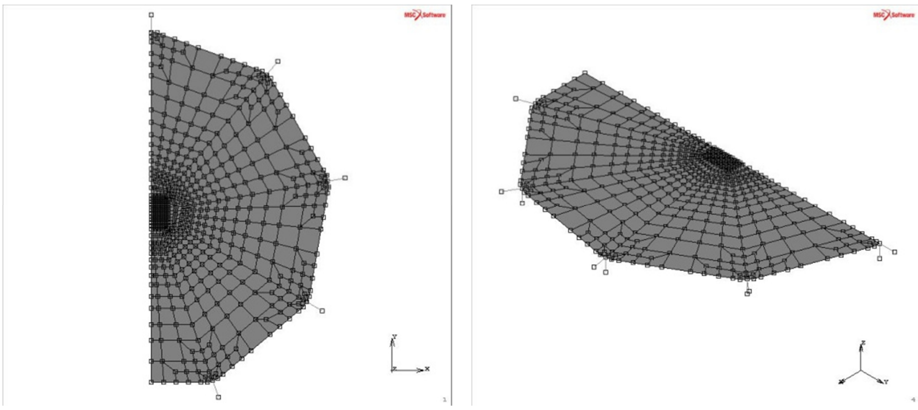

Figure 4. Finite element model of implant (symmetric part)

The dynamic analysis representing the experiment was conducted within the time of 2 s. The experimental and simulated results were compared on the example of the displacement functions.

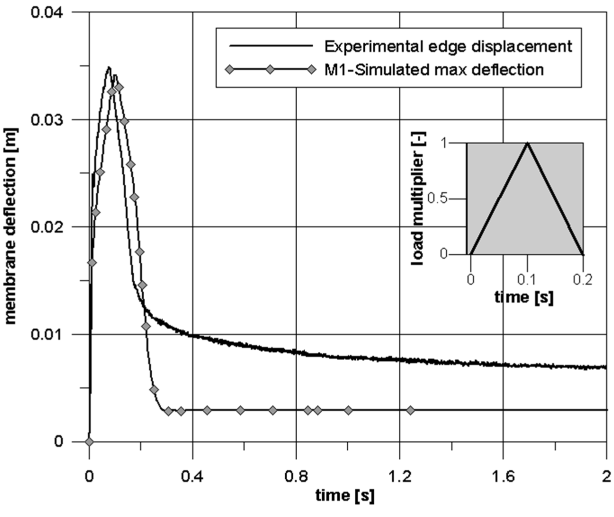

Figure 4. Dynamic analysis of the implanted mesh. Simulation vs. experiments

The registered and calculated values of the maximum deflection of the implant and the displacement of the hernia orifice are shown in Fig. 5. Relatively good accordance between laboratory tests outcomes and the finite element analysis results means that the mechanical model can be applied for modelling of the tissue-implant behaviour.

The junction forces calculated in the points of tacks as the product of the spring stiffness and the tack displacement are used to the assessment of the repair persistence. In the studied case, these extreme forces are R_{max} = 2.25 N and R_{min} = 3 N respectively to the directions of the higher and lower elastic modulus E_1 and E_2 of the orthotropic implant. The difference between both forces is not very significant due to the fact that in this type of implant, the mechanical properties do not differ considerably. The maximum force does not exceed the limit identified for the tissue-implant connection identified in [6].

3. Conclusions

The author developed an orthotropic membrane model of a mesh implanted in a human body in the hernia repair surgery. The model can simulate the behaviour of the ventral hernia repair process under the intaabdominal pressure. The junction forces in the tacks points compared with the limit identified and documented in literature are used to estimate the repair persistence.

The proposed model behaviour matches accurately with the experiment. The maximum reaction forces achieved in this simulation and thus the largest expected values of the junction force in the tissue-implant system do not exceed the limit, what means that the repair should stand the cough pressure.

The presented solution can be applied to estimate the necessary joints number before the laparoscopic surgery when the synthetic implant is used in order to avoid the illness recurrences.

Even if the orthotropy of the implant is not strong, it is reflected in the reaction forces. This fact, together with the anisotropy of the human abdomen observed and described e.g., in [7] should be considered as clinic recommendations when planning the surgeries.

Acknowledgments

The Author wish to acknowledge prof. Czesław Szymczak, prof. Paweł Kłosowski and dr Agnieszka Tomaszewska their support of this contribution.

This study is partially supported by the EU, as part of the Innovative Economy Operational Programme (contract No UDA-POIG.01.03.01-22-086/08-00).

Computations were done in TASK Computer Science Centre, Gdańsk, Poland.

References

1. W.S. Cobb, J.M. Burns, R.D. Peindl, A.M. Carbonell, B.D. Matthews, K.W. Kercher, B.T. Heniford, *Textile Analysis of Heavy Weight, Mid-Weight, and Light Weight Polypropylene Mesh in a Porcine Ventral Hernia Mode,* Journal of Surgical Research, **136** (2006) 1–7, doi:10.1016/j.jss.2006.05.022.

2. C.R. Deeken, M.S. Abdo, M.M. Frisella, B.D. Matthews, *Physicomechanical evaluation of absorbable and nonabsorbable barrier composite meshes for laparoscopic ventral hernia repair*, Surg. Endosc. **212** (2011) 68-79.
3. C. Szymczak, I. Lubowiecka, A. Tomaszewska, M. Śmietański, *Modeling of the fascia-mesh system and sensitivity analysis of a junction force after a laparoscopic ventral hernia repair*, J. Theor. Appl. Mech. **48** (2010) 933-950.
4. I. Lubowiecka, C. Szymczak, A. Tomaszewska, M. Śmietański, *A FEM membrane model of human fascia-synthetic implant system in a case of a stiff ventral hernia orifice*, in: W. Pietraszkieiwcz, I. Kreja (Eds.), Shell Structures. Theory and Applications, CRC Press/Balkema, Londyn, 2010, pp. 311-314.
5. B. Hernandez-Gascon, E. Pena, H. Molero, G. Pascual, M. Doblare, M.P. Ginebra, J.M. Bellon, B. Calvo, *Mechanical behaviour of synthetic surgical mesh: Finite element simulation of th ehernia ab-dominal wall*, Acta Biomatrialia, **7** (2011) 3905-3913.
6. M. Śmietański, J. Bigda, K. Iwan, M. Kołodziejczyk, J. Krajewski, I. Śmietańska, P. Gumiela, K. Bury, S. Bielecki, Z. Śledziński, *Assessment of usefulness of different tacks in laparoscopic ventral hernia repair (IPOM),* Surg. Endosc. **21** (2007) 925-928.
7. C. Szymczak, I. Lubowiecka, A. Tomaszewska, M. Śmietański: *Investigation of abdomen surface deformation due to life excitation: implications for implant selection and orientation in laparoscopic ventral hernia repair.* Clinical Biomechanics, **27** (2012) 105-110.
8. I. Lubowiecka, A. Tomaszewska, C.Szymczak, B. Meronk, M. Śmietański, *Modelling and experimental study of implants used In laparoscopic hernia repair*, in: Proceedings of Nowe Kierunki Rozwoju Mechaniki, Hucisko 2011, Poland (in Polish).
9. E. R. Saberski, S. B. Orenstein, Y. W. Novitsky, *Anisotropic evaluation of synthetic surgical meshes*, Hernia **15** (2011) 47-52.
10. Z.J. Twardowski, R. Khanna, K.D. Nolph, *Intransabdominal pressures during natural activities in pa-tients treated with CAPD*, Nephron, **44** (1986) 129-135.
11. A.P.S. Selvadurai, *Deflections of a rubber membrane*, J. Mech. Phys. Solids, **54** (2006) 1093-1119.
12. D.C. Pamplona, P.B. Goncalves, S.R.X. Lopes, *Finite deformations of cylindrical membrane under internal pressure*, Int. Journal of Mechanical Sciences **48** (2006), 683-696.
13. K. Subbaraj, M.A. Dokainish, *A survey of direct time-integration methods in computational structural dynamics – II. Implicit Methods*, Compt. Struct. **32** (1989) 1387-1401.
14. M. Liu, D.G. Gorman, *Formulation of Rayleigh damping and its extensions*, Compt. Struct. **57** (1995) 277-285.

XXV Symposium *Vibrations in Physical Systems,* Poznan – Bedlewo, May 15-19, 2012

Numerical Aeroacoustic Research of Transmission Loss Characteristics Change of Selected Helicoidal Resonators due to Different Air Flow Velocities

Wojciech ŁAPKA
Poznań University of Technology, Institute of Applied Mechanics
Jan Paweł II 24, 60-965 Poznań, Poland, wojciech.lapka@put.poznan.pl

Abstract

This paper presents the results of aeroacoustic numerical simulations for three types of helicoidal resonators placed inside straight cylindrical duct. The same ratio s/d = 1.976 is considered for three numbers of helicoidal turns n = 0.671, n = 0.695 and n = 1.0. Also three types of transmission loss characteristics are represented. Three-dimensional models were calculated by the use of a finite element method in Comsol Multiphysics Acoustics Module – Aeroacoustics with flow, Frequency Domain. The change of transmission loss characteristics of helicoidal resonators is presented for different air flow velocities in the range from 1 m/s to 20 m/s for cylindrical duct of diameter d = 0.125m.

Keywords: helicoidal resonator, sound attenuation, aeroacoustics.

1. Introduction

Speed of a main flow of air inside ducted system can affect on acoustical properties of applied there passive noise control devices [7,8]. Stronger influence could be observed for resonators. As it has already been well described [3-6], by using helicoidal resonators in ducted systems one can obtain numbers of acoustic resonances inside helicoidal profile, which results in sound reduction at the systems outlet. Also this paper takes under consideration the first approach of solving the problem of helicoidal resonators acoustic attenuation characteristic change due to assuming different speed of a main flow of air inside a straight cylindrical duct. Investigated in this paper models of helicoidal resonators are presented in Fig. 1, where s denotes the length of one helicoidal turn.

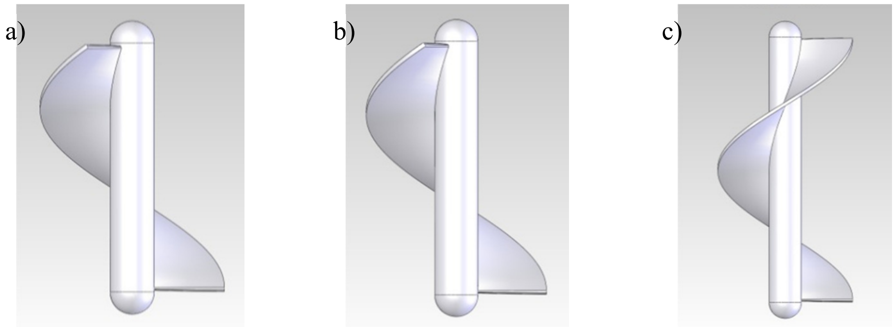

Figure 1. Helicoidal resonators with ratio s/d = 1.976 and number of helicoidal turns n = 0.671 (a), n = 0.695 (b), n = 1.0 (c)

Helicoidal resonators consist of a central axis mandrel with ratio $d_m/d = 0.24$, where d_m denotes the diameter of mandrel, and d is the diameter of cylindrical duct. Helicoidal profile has the ratio $g/d = 0.024$, where g denotes the thickness of helicoidal profile. The cylindrical duct diameter $d = 0.125$ m. Small difference for two selected helicoidal resonators in number of turns $n = 0.671$ and $n = 0.695$ results from representation of two different acoustic attenuation characteristics obtained in previous work [6], which are presented in Fig. 2 and Fig. 3, respectively.

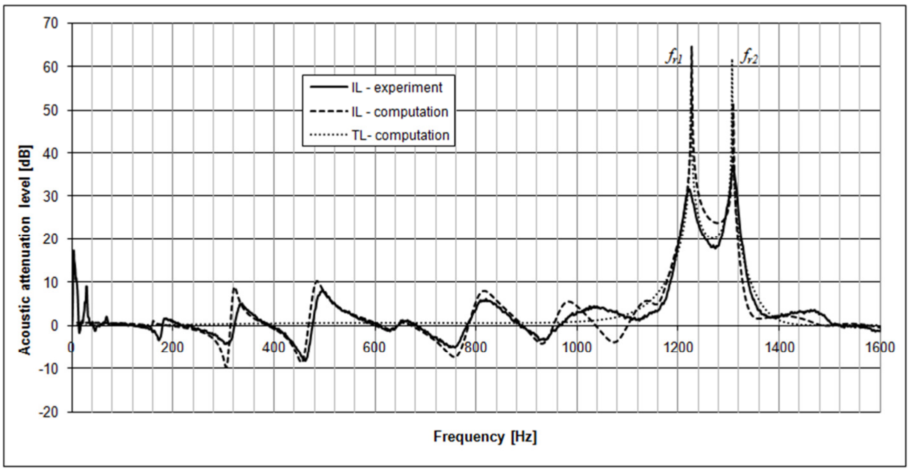

Figure 2. Acoustic attenuation performance parameters levels for helicoidal resonator inside pipe ($d = 0.125$ m) with the number of turns $n = 0.671$ [6]

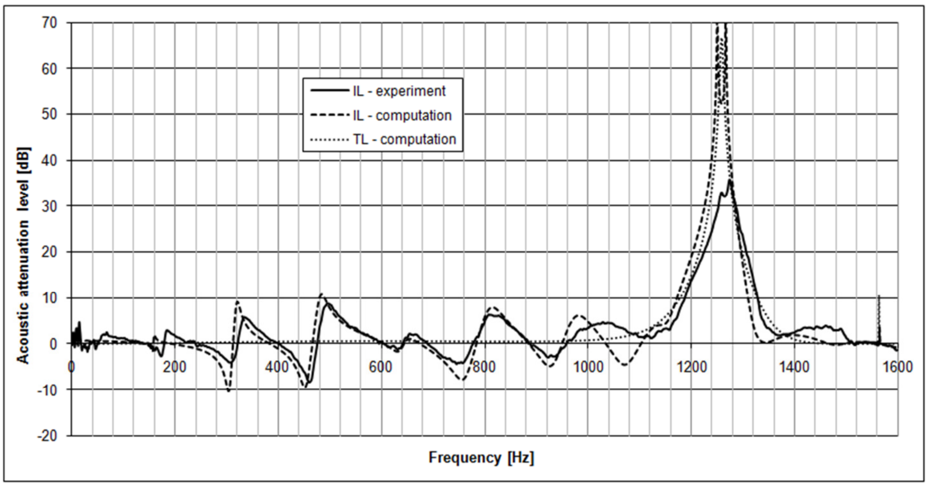

Figure 3. Acoustic attenuation performance parameters levels for helicoidal resonator inside pipe ($d = 0.125$ m) with the number of turns $n = 0.695$ [6]

In Figs. 2 and 3 are presented comparisons between two acoustic attenuation performance parameters, Insertion Loss (IL) and Transmission Loss (TL), obtained in numerical computations (computation) and experimentally (experiment) [6].

2. Basic Characteristics of Numerical Aeroacoustic Simulations

Three-dimensional models were calculated by the use of finite element method in Comsol Multiphysics Acoustics Module – Aeroacoustics with flow, Frequency Domain [1]. Schematic view of investigated cylindrical duct with helicoidal resonator is presented in Fig. 4.

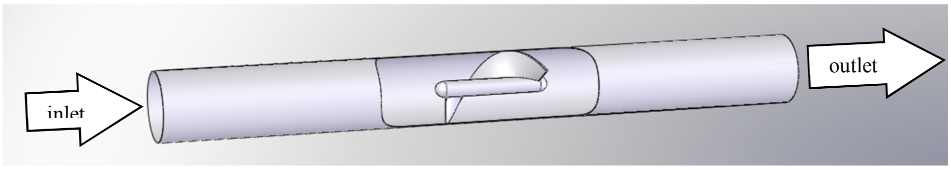

Figure 4. Schematic view of investigated cylindrical duct with helicoidal resonator

To solve aeroacoustic problem in COMSOL flow is assumed to be compressible, inviscid, barotropic, and irrotational [1]. In this paper, for investigated velocities of air flow in range from 1 m/s to 20 m/s, the Reynolds number varies from Re~8333 to Re~166670, respectively. In that case the turbulent flow should be considered [2], but due to fact that COMSOL can solve only CFD turbulent flow without acoustic, the aeroacoustics was used as a weak solution for coupling acoustic with flow, in this case. Also obtained in this paper results can strongly differ from real results, but the aim of this work is to obtain an overview of helicoidal resonators transmission loss change due to different velocities of air flow.

As an acoustical attenuation performance parameter is used the transmission loss (TL) [1, 3-5, 7, 8], which is obtained by integrating the incident nominal acoustic pressures squared at the inlet (*w_in*) and actual transmitted acoustic pressures squared at the outlet (*w_out*) all anechoically terminated, and solving equation:

$$\mathrm{TL} = 10\log(w\_in/w\_out),\ \mathrm{dB} \tag{1}$$

Boundary conditions are described as in COMSOL Multiphysics [1]:

- hard boundary condition - all surfaces of cylindrical duct and helicoidal resonators are hard,
- slip velocity equals zero at all surfaces of cylindrical duct and helicoidal resonators,
- normal flow at the outlet equals zero,
- mass flow at the inlet varies from 1 m/s to 20 m/s,
- plane wave radiation - at the inlet and outlet, while at the inlet the velocity potential equals 1 m^2/s.

Finite element mesh is automatically generated as a free tetrahedral and controlled by physics. The stationary solver is used.

3. Results

In Fig. 5, Fig. 6 and Fig. 7 are presented transmission loss characteristics of helicoidal resonators with $s/d = 1.976$ and $n = 1.0$, $n = 0.695$ and $n = 0.671$, respectively, for different velocities of air flow. Results are presented in the range of frequency from 1200 Hz to 1350 Hz, which is the specific frequency range for investigated models.

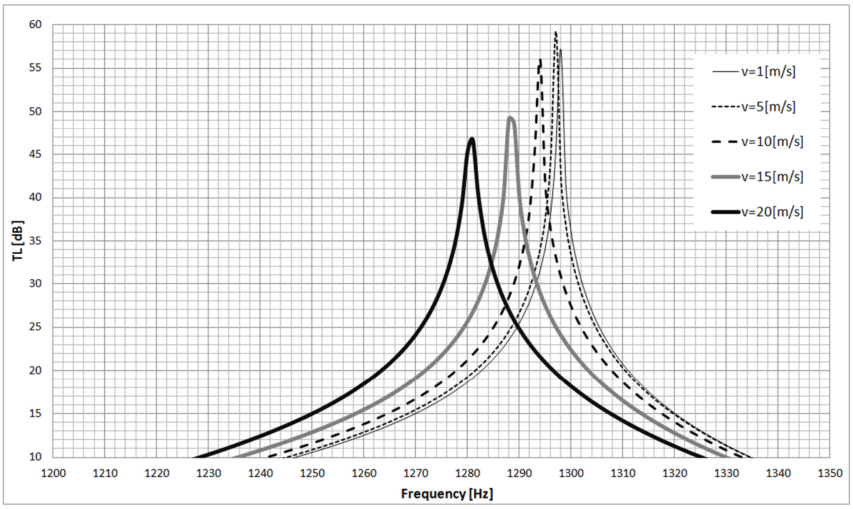

Figure 5. Transmission loss characteristics for helicoidal resonator with *s/d* = 1.976 and *n* = 1.0 for different velocity of air flow *v*

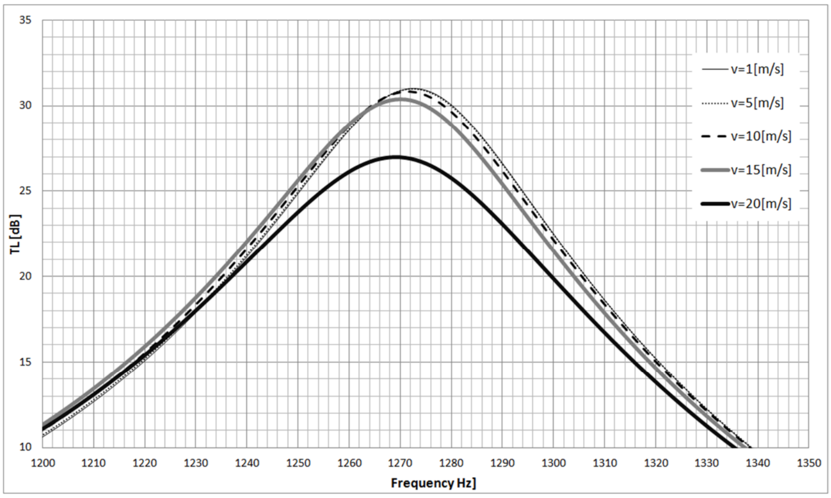

Figure 6. Transmission loss characteristics for helicoidal resonator with *s/d* = 1.976 and *n* = 0.695 for different velocity of air flow v [m/s]

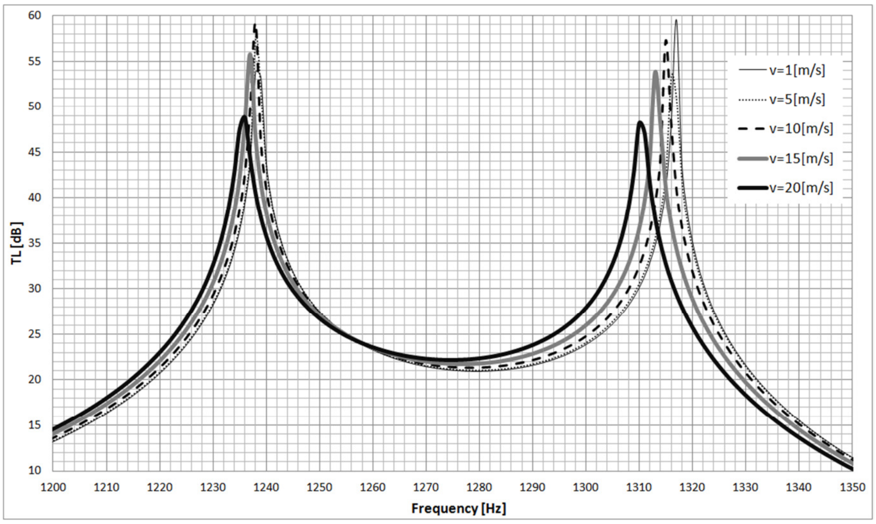

Figure 7. Transmission loss characteristics for helicoidal resonator with *s/d* = 1.976 and *n* = 0.671 for different velocity of air flow v [m/s]

4. Conclusions

In general, for investigated helicoidal resonators, when the velocity of air flow becomes greater the resonance frequencies as well as TL levels become lower.

For helicoidal resonator with $n = 1.0$ can be observed the biggest frequency difference between velocities v = 1 m/s and v = 20 m/s and it equals about 18 Hz. TL level reduces in this case for about 10 dB.

However, for helicoidal resonator with $n = 0.695$ in frequency domain can be observed small difference, which equals about 4 Hz, and similar small difference for TL levels which equals about 5 dB.

For helicoidal resonator with $n = 0.671$ can be observed bigger change for the second resonance frequency, which equals about 7 Hz, than for the first resonance frequency, where the difference equals only about 2 Hz. In this case the reduction of TL levels is similar for both frequencies and it equals about 10 dB. Here interesting is fact, that for the lowest TL level between resonance frequencies, which equals about 21 dB for v = 1-5 m/s, it increases for about 1 dB for v = 20 m/s.

Globally, up to 5 m/s of air flow velocity inside ducted system the resonance frequency does not change. Also, when applying helicoidal resonators for typical ventilation system, where the velocity of main air flow varies up to 5 m/s, there is no need to include any velocity corrections. But for higher velocities, typically in industrial applications, there should take place some air velocity corrections.

In this paper, the obtained numerical results can strongly differ from real results, but the aim of this work was to obtain an overview of helicoidal resonators transmission loss change due to different velocity of air flow, which was here realized. Hence, the experimental researches of the influence of air flow velocity on acoustic attenuation characteristics change of helicoidal resonators should give the exact results.

Acknowledgments

The author gratefully acknowledges the funding by the Polish Ministry of Science and Higher Education in the years 2010-2013 as a research project N N502 4557 39.

References

1. COMSOL Multiphysics version 4.2.a, *Acoustic Module, User's Guide and Model Library Documentation Set*, COMSOL AB, www.comsol.com, Stockholm, Sweden, (2011).
2. Jeżowiecka-Kabsch K., Szewczyk H., *Mechanika płynów*, Oficyna Wydawnicza Politechniki Wrocławskiej, Wrocław, (2001) 386.
3. Łapka W, *Acoustic attenuation performance of a round silencer with the spiral duct at the inlet*, Archives of Acoustics, **32** (2007) 247-252.
4. Łapka W., *Acoustical properties of helicoid as an element of silencers*, Doctoral work, Faculty of Mechanical Engineering and Management, Poznań University of Technology (2009).
5. Łapka W., *Helicoidal resonator*, Proceedings of 39th International Congress and Exposition on Noise Control Engineering INTER-NOISE 2010, 9 pages in CD-ROM, Lisbon, Portugal, (2010) 9 pages in CD-ROM
6. Łapka W., Cempel C., *Acoustic short helicoidal resonator-computational and experimental investigations*, Proceedings of 58th Open Seminar on Acoustics, OSA 2011, Gdańsk-Jurata, Poland, (2011) 9-16.
7. Munjal M. L., *Acoustics of Ducts and Mufflers with Application to Exhaust and Ventilation System Design*, Inc., Calgary, Canada, John Wiley & Sons, (1987) 328.
8. Ver I. L., Beranek L. L., *Noise and vibration control engineering*, 2nd edition, Hoboken, John Wiley & Sons, Inc., New Jersey, USA, (2006) 966.

XXV Symposium *Vibrations in Physical Systems,* Poznan – Bedlewo, May 15-19, 2012

Design and Optimisation of a Control System for Active Vibration Isolators

Igor MACIEJEWSKI
Koszalin University of Technology, 75-453 Koszalin, Śniadeckich 2
igor.maciejewski@tu.koszalin.pl

Abstract

The paper deals with the design and optimisation of a control system for active vibration isolators. This paper presents a control system structure that is based on the inverse dynamics of active force actuator and the primary controller. The primary controller settings are evaluated using the multi-criteria optimisation procedure. In succession, the proposed method of control system design is investigated by using an active seat suspension, as an exemplary vibration isolation system.

Keywords: vibration isolation, active suspension, control system, optimisation

1. Introduction

The design of vibration isolators, constructed at present, is a big challenge for engineers, because of the conflicted criteria that are involved in their design [7]. For example, in the automotive industry it is desired to reduce the vibration of cabin's floor transmitted to operator's seat. On the one hand, the dynamic forces transmitted from the cabin's floor to the seat should approach zero to protect driver's health. On the other hand, the suspension deflection should approach zero as well in order to ensure the controllability of working machines [1, 4].

The active systems provide more effective performance in the vibration isolation, but they are used hardly ever, because of their high constructing costs and complicated structure. However, the permanent development of control algorithms confirms that the control of active systems using the optimisation of multi-objective functional is an effective way to deal with the conflicting suspension performance problem [3].

2. Control system design

A simplified suspension model that consists of the single degree of freedom body mass, the linear spring and damper is shown in Fig. 1a. Such a model has been discussed extensively in the literature and captures many essential characteristics of the real vibration isolators. The passive subsystem is utilized to describe visco-elastic characteristics of the suspension system. The active subsystem is used to determine desired force F_a that should be introduced into the visco-elastic suspension system actively.

The state space model of the hybrid suspension system (Fig. 1a) can be obtained by using the LFT (linear fractional transformation) technique [2] and by grouping signals into sets of external inputs, outputs, an input to the controller and an output from the controller.

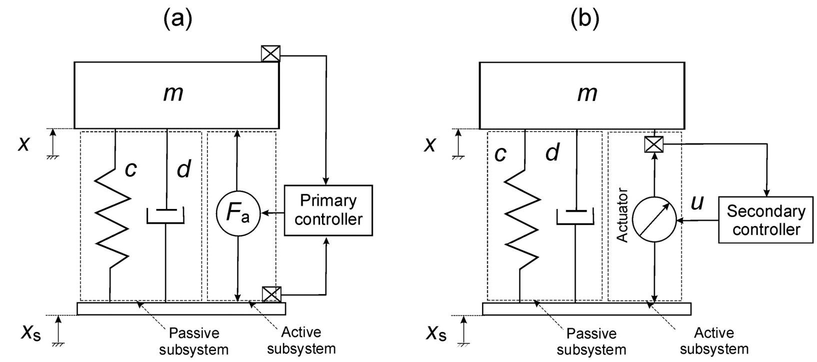

Figure 1. Simplified model of the active suspension with ideal force control (a) and with force tracking control system (b)

Choosing the state variables as: $x_1 := x - x_s$, $x_2 := \dot{x}$, the disturbance caused by road roughness: $w_1 := x_s$, $w_2 := \dot{x}_s$ and the external input force of the suspension system F_a, the state space equation of the hybrid suspension is presented as:

$$\dot{x}(t) = Ax(t) + B_1 w(t) + B_2 F_a(t)$$
$$A = \begin{bmatrix} 0 & 1 \\ -\frac{c}{m} & -\frac{d}{m} \end{bmatrix},\ B_1 = \begin{bmatrix} 0 & -1 \\ 0 & \frac{d}{m} \end{bmatrix},\ B_2 = \begin{bmatrix} 0 \\ \frac{1}{m} \end{bmatrix} \tag{1}$$

In order to satisfy the performance requirement, the acceleration of suspended mass $z_1 := \ddot{x}$ and the suspension deflection $z_2 := x - x_s$ are defined as controlled outputs. Then the output equation reads:

$$z(t) = C_1 x(t) + D_{11} w(t) + D_{12} F_a(t)$$
$$C_1 = \begin{bmatrix} -\frac{c}{m} & -\frac{d}{m} \\ 1 & 0 \end{bmatrix},\ D_{11} = \begin{bmatrix} 0 & \frac{d}{m} \\ 0 & 0 \end{bmatrix},\ D_{12} = \begin{bmatrix} \frac{1}{m} \\ 0 \end{bmatrix} \tag{2}$$

If the suspension deflection $y_1 := x - x_s$ and the velocity of suspended mass $y_2 := \dot{x}$ are measurable, then the measurement equation can be written as:

$$y(t) = C_2 x(t) + D_{21} w(t) + D_{22} F_a(t)$$
$$C_1 = \begin{bmatrix} 1 & 0 \\ 0 & 1 \end{bmatrix},\ D_{11} = \begin{bmatrix} 0 & 0 \\ 0 & 0 \end{bmatrix},\ D_{12} = \begin{bmatrix} 0 \\ 0 \end{bmatrix} \tag{3}$$

A controller is determined by formulating the state feedback control problem in the following form:

$$F_a(t) = Ky(t) = KC_2 x(t) \tag{4}$$

where: $K = [k_1, k_2]$ is the output feedback gain vector to be designed.

If the desired active force is determined than such force has to be reproduced by the active actuator. This can be achieved using the force tracking control system that adjusts the controllable drive. The force tracking control system can be handled by applying an internal force feedback or else by applying a reverse model of the active element [6]. The second approach is employed in this study and the graphical illustration of such principle is presented in Fig. 1b.

The actual control signal u is calculated using a reverse model of the active element in the following form:

$$u = f\left(x - x_s, F_a, \dot{x} - \dot{x}_s, \dot{F}_a\right) \tag{5}$$

where: F_a and $\dot{F}_a$ are the desired active force and its first derivative over the time, $x - x_s$ and $\dot{x} - \dot{x}_s$ are the actual displacement and velocity of the controlled actuator, respectively. The reverse model of an active element has to be calculated for the specific force actuator and its parameters should be evaluated experimentally.

The actuator displacement, the actuator velocity, the desired active force and its first derivative over the time are the reverse model inputs. The model outputs are the control signals to the actuator that should generate the desired active force in the suspension system. Unfortunately, very often efficiency of the force tracking control system is lowered by a phase shift in the feedback loop [6]. This effect might be caused by actuating time of the active element. Therefore the proportional-derivative (PD) controller is utilized in order to speed up the overall control system. The output signal u_c of the PD controller, that controls the active element, finally is described as follows:

$$u_c = t_c \dot{u} + u \tag{6}$$

where: t_c is the actuating time of the actuator, u is the control signal calculated in the basis of a reverse model (input to PD controller).

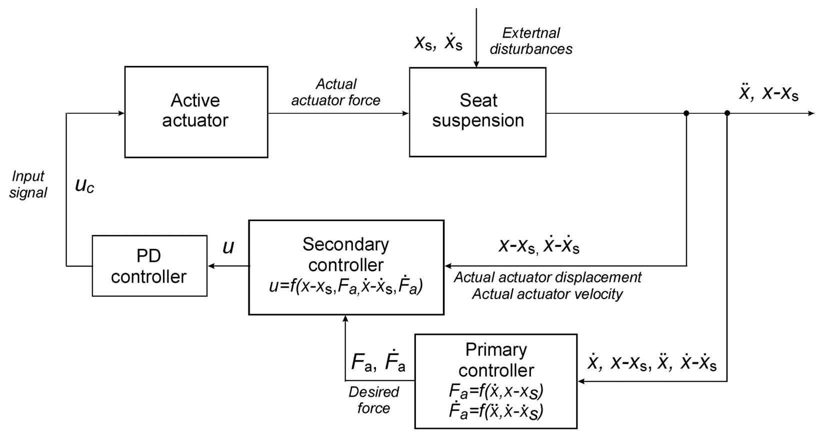

Figure 2. Block diagram of the proposed active control

The block diagram of overall control system of the active suspension is presented in Fig. 2. If the desirable active force is obtained according to the primary controller (Eq. (4)), then the desired force has to be approximately achieved by the active element with calculated input signal using the reverse model (Eq. (5)). The actuating time of the actuator is eliminated because the PD controller speeds up the control signal (Eq. (6)).

3. Multi-criteria optimisation procedure

A different selection of the primary controller settings: k_1, k_2 allows decreasing the forces transmitted to suspended mass at the simultaneous increase of suspension travel and vice versa. The optimization criteria that correspond to the conflicted system requirements are defined as follows:

$$\begin{gathered} \ddot{x}_{RMS} = \sqrt{\frac{1}{t}\int_0^t \ddot{x}^2 dt} \;\; \rightarrow \;\; \text{minimum} \\ (x - x_s)_{\max} = \max_t (x - x_s) - \min_t (x - x_s) \;\; \rightarrow \;\; \text{minimum} \end{gathered} \tag{7}$$

where: $\ddot{x}_{RMS}$ is the effective acceleration of suspended mass, $(x - x_s)_{\max}$ is the maximum relative displacement of suspension system and t is the current computation time instant.

In order to optimize the suspension system vibro-isolating properties, the optimization procedure with the objective function is proposed as:

$$\min_{k_1, k_2} \ddot{x}_{RMS}(k_1, k_2) \tag{8}$$

where: k_1, k_2 are the set of decision variables. The function (Eq. (8)) contains the first criterion $\ddot{x}_{RMS}$ only, because the second criterion $(x - x_s)_{\max}$ is transferred to a nonlinear inequality constraint as follows:

$$(x - x_s)_{\max}(k_1, k_2) \leq (x - x_s)_c \tag{9}$$

where: $(x - x_s)_c$ defines a constraint value of the second criterion. An appropriate selection of such value allows to choose the vibro-isolation properties of the suspension system.

4. Example: Optimisation of the active seat suspension vibro-isolation properties

In Figure 3 a model of the active seat suspension system containing the controlled pneumatic spring and the hydraulic shock-absorber is shown. The active control of an air-flow to the pneumatic spring is applied by means of the directional servo-valve which regulates the inflating/exhausting of the pneumatic spring. Inflating of the pneumatic spring is supplied from an external compressor and its exhausting is driven directly to the atmosphere. In such a solution, the pressure in the pneumatic spring can be changed very fast, and therefore the active force for the suspension system is provided. The equation of motion of this seat suspension has been shown in the author's previous papers [4, 5].

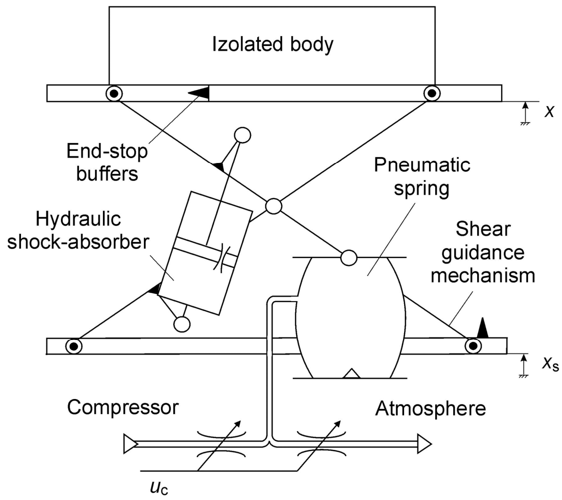

Figure 3. Model of the active seat suspension

In order to enable controlling the vibro-isolation properties of active seat suspension, the primary controller settings and their ranges are taken as follows:

- proportionality factor of the rel. displacement feedback loop $k_1 = 20 - 200 \times 10^3$ N/m
- proportionality factor of the absolute velocity feedback loop $k_2 = 2 - 20 \times 10^3$ Ns/m .

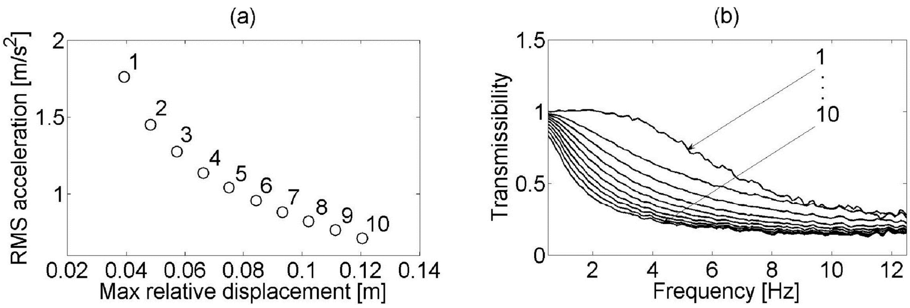

Figure 4. Pareto-optimal points distributions (a) and corresponding transmissibility functions (b) obtained for the active suspension system

The minimization of the constrained objective function (Eqs. (8) and (9)) has allowed finding ten Pareto-optimal points distribution in the conflicted criteria domains. The set of non-dominated solutions is presented in Fig. 4a. A highest limiting of the maximum relative displacement of suspension system is obtained for the Pareto-optimal point number 1, and a highest reduction of the effective acceleration of suspended mass is achieved for Pareto-optimal point number 10. These marginal Pareto-optimal points determine a set of the compromising solutions that are assigned for the Pareto-optimal points from number 2 up to number 9. In Fig. 4b dynamical behaviour of the active suspension system is compared for different Pareto-optimal configurations (point number 1–10). These simulation results are obtained for the random excitation signal (band limited noise) in the 0,5–5 Hz frequency range and for the mass load of suspension system of 100 kg.

6. Conclusions

The obtained results show, that the proposed control method allows to define the overall system structure of active vibration isolators. Moreover, the presented multi-criteria optimisation procedure assists an appropriate selection of the primary controller settings (defined by Pareto-optimal solutions) and allows adjusting the vibro-isolation properties of active suspensions. The very stiff suspension system can be transformed easily to the very soft suspension system only by a change of the controller settings. Each of the Pareto-optimal configurations ensures the optimality of the active vibration isolator in the conflicted criteria domains.

References

1. Alkhatiba R., Nakhaie Jazarb G., Golnaraghi M.F.: *Optimal design of passive linear suspension using genetic algorithm*, Journal of Sound and Vibration **275** (2004) 665-691
2. Gu D., Petkov P., Konstantinov M.: R*obust Control Design with MATLAB*, Springer, Berlin 2005
3. He Y., McPhee J.: *Multidisciplinary design optimization of mechatronic vehicles with active suspensions*, Journal of Sound and Vibration **283** (2005) 217-241
4. Maciejewski I., Meyer L., Krzyzynski T., *Modelling and multi-criteria optimisation of passive seat suspension vibro-isolating properties*, Journal of Sound and Vibration **324** (2009) 520-538
5. Maciejewski I., Meyer L., Krzyzynski T., *The vibration damping effectiveness of an active seat suspension system and its robustness to varying mass loading*, Journal of Sound and Vibration **32**9 (2010) 3898-3914
6. Maślanka M., Sapiński B.: *Experimental study of vibration control of a cable with an attached MR damper*, Journal of Theoretical and Applied Mechanics **45**(4) (2007) 893-917
7. Preumont A.: *Vibration Control of Active Structures An Introduction*, Kluwer Academic Publishers, London 2002

XXV Symposium *Vibrations in Physical Systems,* Poznan – Bedlewo, May 15-19, 2012

Vibration Control of the Rotating Machine Geared Drive System Using Linear Actuators with the Magneto-Rheological Fluid

Maciej MICHAJŁOW, Robert KONOWROCKI, Tomasz SZOLC
Institute of Fundamental Technological Research of the Polish Academy of Sciences
ul. Pawińskiego 5 B, 02-106 Warsaw, Poland
mmich@ippt.gov.pl, rkonow@ippt.gov.pl, tszolc@ippt.gov.pl

Abstract

In this paper there is proposed a semi-active control technique based on the linear actuators with the magneto-rheological fluid (MRF) connecting the drive system planetary gear housing with the immovable rigid support. Here, control damping torques are generated by means of the magneto-rheological fluid of adjustable viscosity. Such actuators can effectively suppress amplitudes of severe transient and steady-state rotational fluctuations of the gear housing position and in this way they are able to minimize dangerous oscillations of dynamic torques transmitted by successive shaft segments in the entire drive system. The general purpose of the considerations is to control torsional vibrations of the real power-station coal-pulverizer geared drive system driven by means of the asynchronous motor. The investigations have been carried out using the experimental test rig based on the real object, where the measurement results were compared with analogous theoretical ones obtained by the use of computer simulations.

Keywords: torsional vibrations, magneto-rheological dampers, semi-active control

1. Introduction

Active vibration control of drive systems of rotating machines, mechanisms and vehicles creates new possibilities of improvement of their effective operation. Torsional vibrations are in general rather difficult to control not only from the viewpoint of proper control torque generation, but also from the point of view of a convenient technique of imposing the control torques on quickly rotating parts of the drive-systems and rotor machines. Unfortunately, one can find not so many published results of research in this field, beyond some attempts performed by an active control of shaft torsional vibrations using piezo-electric actuators, see [4]. But in such cases relatively small values of control torques can be generated and thus the piezo-electric actuators can be usually applied to low-power drive systems.

Thus, for drive systems of high-power machines, mechanisms and vehicles in this paper there is proposed the semi-active control technique based on the linear actuators with the magneto-rheological fluid (MRF) connecting the drive system planetary gear housing with the immovable rigid support. The control torques are generated by means of the magneto-rheological fluid of adjustable viscosity. They interact with reaction torques transmitted by the planetary gear housing due to torsional vibrations of the drive system. Such actuators can effectively suppress amplitudes of severe transient and steady-state rotational fluctuations of the gear housing position and in this way they are able to minimize dangerous oscillations of dynamic torques transmitted by successive shaft segments in the entire drive system.

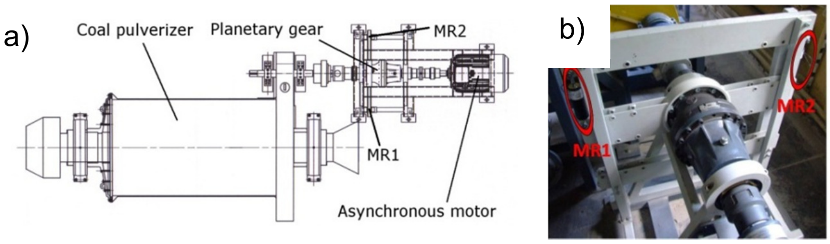

Figure 1. (a) – Scheme of the of the coal pulverizer drive system,
(b) – planetary gear support frame with two MR dampers mounted

The general purpose of the considerations is to control torsional vibrations of the power-station coal-pulverizer drive system driven by means of the asynchronous motor and the double stage planetary gear, as shown in Fig. 1a and 1b. The planetary gear housing is visco-elastically connected with the immovable foundation by means of two or four linear actuators with the magneto-rheological fluid, which is illustrated in Fig. 1b. The actuators support the gear housing at both ends of the proper reaction arm enabling it bounded rotational displacements around the drive system rotation axis. Using such suspension of the gear housing control forces generated by the linear actuators can be imposed on the drive system in the form of control torques.

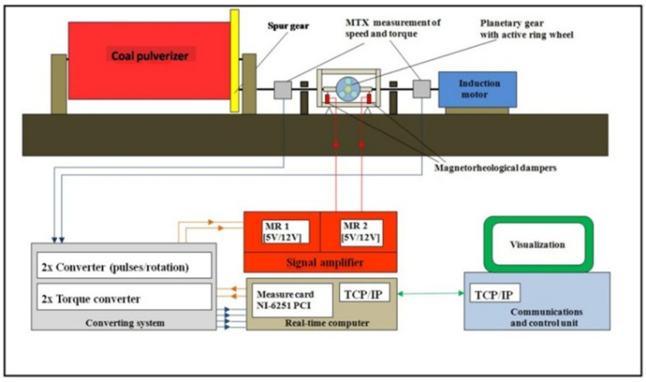

Figure 2. Measurement-control system of the coal pulverizer

In the considered drive system of the coal pulverizer power is transmitted from the asynchronous motor to the driven machine tool by means of the three elastic couplings, double-stage planetary reduction gear, the two torque-meters, electro-magnetic overload coupling and by the shaft segments. Whole stand is observed and controlled in the real-time by the use of dedicated control and data acquisition systems. This setup enables us to perform measurement of dynamic torques and rotational speed fluctuation signals in the input and output shaft, respectively. When needed, additional sensors can be added, as for example the sensor measuring the planetary gear arm position. In dedicated PC units, the real-time processors make use of recorded data, and by means of the user-supplied control algorithm, they generate control signal which is immediately applied to the linear actuators with the magneto-rheological fluid.

2. Assumptions for the mechanical models and formulation of the problem

In order to perform a theoretical investigation of the semi-active control applied for this mechanical system, a reliable and computationally efficient simulation models are required. In this paper dynamic investigations of the entire drive system are performed by means of two structural models consisting of torsionally deformable one-dimensional beam-type finite elements and rigid bodies. These are the classical finite element model and the discrete-continuous (hybrid) model. Both models are characterized by the identical structure resulting in the same division into cylindrical beam elements representing successive drive train components, which can be illustrated in common Fig. 3.

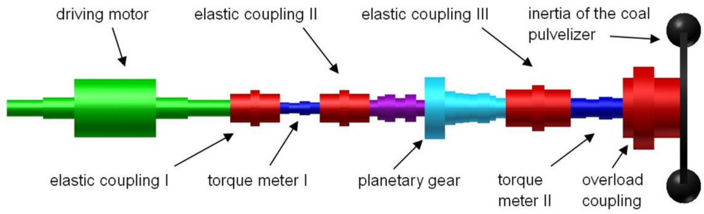

Figure 3. Mechanical model of the coal pulverizer drive system

These models are employed here for eigenvalue analyses as well as for numerical simulations of torsional vibrations of the drive train. In the hybrid model successive cylindrical segments of the stepped rotor-shaft are substituted by the cylindrical macro-elements of continuously distributed inertial-visco-elastic properties, as presented in Fig. 3. However, in the finite element model these continuous macro-elements have been discretized with a proper mesh density assuring a sufficient accuracy of results. In the proposed hybrid and FEM model of the coal pulverizer drive system inertias of the gear wheels, gear housing with the reaction arm, coupling disks and others are represented by rigid bodies attached to the appropriate macro-element extreme cross-sections, which should assure a reasonable accuracy for practical purposes. The time- and response-dependent external active and passive torques are continuously distributed along the respective macro-elements or imposed in the concentrated form on the given macro-element cross-sections.

For the assumed analogous linear finite element model the mathematical description of its motion has the classical form of a set of coupled ordinary differential equations

$$\mathbf{M}\,\ddot{\mathbf{s}}(t)+\mathbf{C}\big(C_0(t)\dot{s}(t)\big)\dot{\mathbf{s}}(t)+\mathbf{K}\,\mathbf{s}(t)=\mathbf{F}\big(t,s(t),\dot{s}(t)\big) \tag{1}$$

where: $\mathbf{s}(t)$ denotes the vector of generalized co-ordinates $s(t)$, $\mathbf{M}$, $\mathbf{C}$ and $\mathbf{K}$ are respectively the mass, damping and stiffness matrices and $\mathbf{F}$ denotes the time – and system response – dependent external excitation vector. By means of Eqs. (1) numerical simulations of the forced torsional vibrations for the passive and controlled system can be carried out. In order to determine natural frequencies and eigenvectors for the FEM model of this drive system it is necessary to reduce (1) into the form of standard eigenvalue problem. The mathematical description and solution for the mentioned hybrid model of drive system have been demonstrated in details in [2]. It is to notice here, that the dynamic responses and their control are going to be investigated in the domain of generalized co-ordinates in the case of the FEM model application and in the space of modal functions in the case of the hybrid model.

Apart from the sufficiently realistic mechanical models of the vibrating object, it is also necessary to introduce a proper mathematical model of the electric motor. In the considered case of the symmetrical three-phase asynchronous motor electric current oscillations in its windings are described by four Park's equations, which can be found e.g. in [3]. Then, the electromagnetic torque generated by such a motor can be expressed by the following formula:

$$T_{el} = \frac{3}{2} pM\left(i_{\beta}^{s} \cdot i_{d}^{r} - i_{\alpha}^{s} \cdot i_{q}^{r} \right), \tag{2}$$

where: M denotes the relative rotor-to-stator coil inductance, p is the number of pairs of the motor magnetic poles and i_{α}^{s}, i_{β}^{s} are the electric currents in the stator reduced to the electric field equivalent axes α and β and i_{d}^{r}, i_{q}^{r} are the electric currents in the rotor reduced to the electric field equivalent axes d and q, see [3]. From the system of Park's equations as well as from formula (2) it follows that the coupling between the electric and the mechanical system is non-linear in character, which leads to complicated analytical description resulting in a rather harmful computer implementation. Thus, this electromechanical coupling has been realized here by means of the step-by-step numerical extrapolation technique, which for relatively small direct integration steps for motion equations derived for both applied drive system yields very effective, stable and reliable results of computer simulation.

3. Computational and experimental examples

Many experiments have been performed using the experimental test-rig, based on the real coal pulverizer drive system shown in Fig.1. In first step, the measured data was used for system parameter identification, results of which are presented in Fig. 3. The FFT analysis of the measured torque signals provided information about the system natural frequencies, see Fig. 3a. To validate the FEM and hybrid models, the modal analysis was carried out. In result, the estimated system structural spectrum was obtained, see Fig. 3b. The good correlation of numerically computed spectrum with that determined from measurement, ensures us that the proposed models sufficiently approximate the real object. Upon an identification of the system, further experiments were performed in order to investigate the worst and the best MR damper efficiency case scenarios. In the sequence, the system has been runned-ahead with several increasing levels of an operational speed. According to the fact that the excitation frequency of the coal pulverizer strictly depends on its rotational speed, the variety of load case scenarios

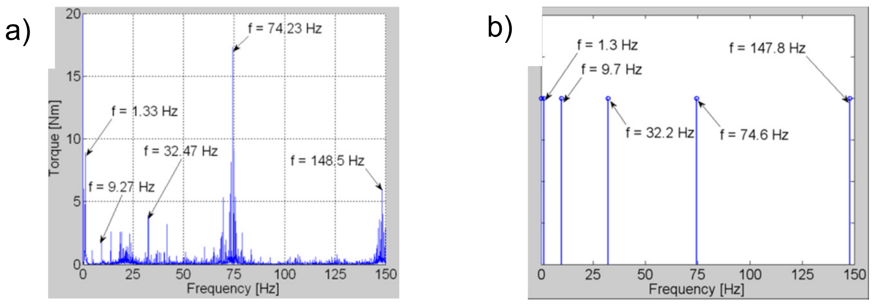

Figure 3. The spectrum: (a) – of the dynamic torque obtained from measurement, (b) – of the system obtained from the FEM model eigenanalysis

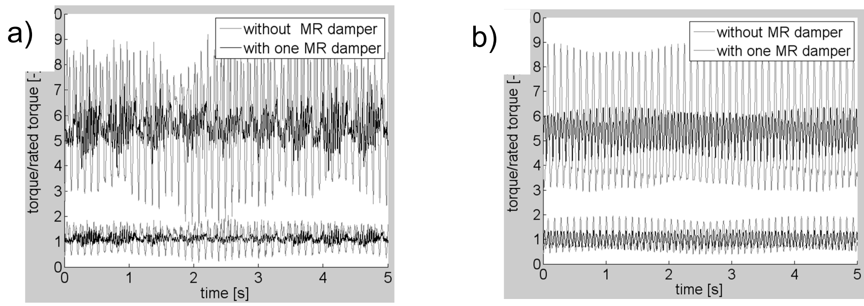

Figure 4.The input and output torque meter signals, with and without MR damper: (a) – obtained from measurement, (b) – obtained from simulation

have been analysed in this way. In Fig. 4 the following example of the MR damper efficiency scenario is presented. As one can see, in this case an application of the linear damper with the MR fluid has benefited in about 60 % measured decrease of dynamic torque amplitude reduction on the real object, Fig. 4a, and in about 65 % in the case of numerical simulation performed using the both applied theoretical models.

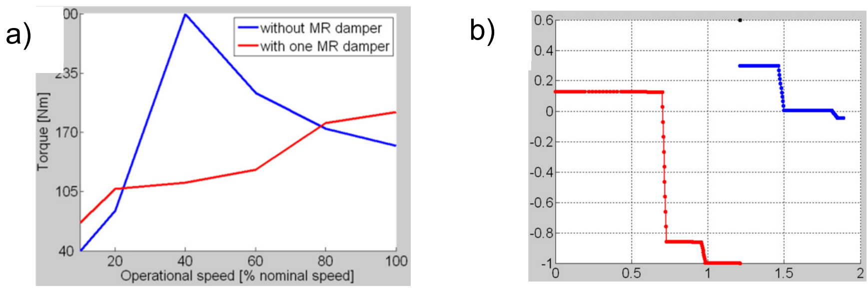

Figure 5. The averaged dynamic torque oscillation amplitude vs. the system average rotational speed (a), the second mode shape of the drive system

The next figure, i.e. Fig. 5a, presents the relationship between the level of the output shaft dynamic torque oscillation amplitudes and the system average nominal operational speed influencing the frequency of system excitation generated by the driven machine. From this figure it follows that the drive system is damped in the most efficient way in the vicinity of 40% of the motor nominal speed. At this speed the second system natural frequency f_2 = 9.7 Hz is being excited the most remarkably. Because the second mode shape shown in Fig. 5b is characterized by a significant modal displacement value at the location of the MR damper in the considered drive train, the attenuation of torsional vibrations is very efficient in this case.

4. Conclusions

In the paper a semi-active control of transient and steady-state torsional vibrations of the coal pulverizer drive system driven by the asynchronous motor and the planetary reduction gear has been performed by means of the linear dampers with the magneto-rheological fluid (MRF). Here, such dampers are able to suppress the torsional vibrations by means of mechanical energy dissipation during relative rotational motion between the planetary gear housing and the immovable foundation. As it follows from the carried out experiments and numerical simulations, such reduction results in a minimization of vibration amplitudes up to 60% in comparison with the passively damped system.

Acknowledgement

This work has been supported by the European Commission through European Regional Development Fund: Project MONIT – “Monitoring of Technical State of Construction and Evaluation of its Lifespan” (POIG 01.01.02-00-013/08).

References

1. Przybyłowicz, P. M., *Torsional vibration control by active piezoelectric system*. Journal of Theoretical and Applied Mechanics, **33**(4) (1995) 809-823.
2. Szolc, T., *On the discrete-continuous modeling of rotor systems for the analysis of coupled lateral-torsional vibrations*, Int. Journal of Rotating Machinery, **6**(2) (2000), 135-149.
3. White, D. C. and Woodson, H. H., *Electromechanical energy conversion*. Wiley, New York 1959.

XXV Symposium *Vibrations in Physical Systems,* Poznan – Bedlewo, May 15-19, 2012

Automatic Recognition of Voice Commands in Car

Marzena MIĘSIKOWSKA
Kielce University of Technology,marzena@tu.kielce.pl

Leszek RADZISZEWSKI
Kielce University of Technology,lradzisz@tu.kielce.pl

Abstract

The aim of this study was to evaluate the recognition process of driver's voice commands spoken in car cabin using Sphinx-4 – the speech recognizer written entirely in Java language. Sphinx-4 recognizer was tested in real-time conditions in standalone car with engine on/off. The speech material consisted of sentences spoken directly to the microphone. Results showed significant differences in recognition accuracy obtained in different conditions (engine on/off).

Keywords: speech recognition, car cabin, telematics systems

1. Introduction

The car interior noise is still problematic and impacts the recognition rates. It has been proposed many solutions to resolve the problem of background interior noise. The automatic speech recognition (ASR) performance degrades substantially when the speech is corrupted by the background noise not seen during training. The reason for this is that the observed speech signal does no longer match the distributions derived from the training material. This mismatch between training and testing conditions is one of the most challenging and important problems in ASR. The main techniques for removing the mismatch fall into the following approaches: robust features, compensation of the noise effect over the representation of the speech, and adaptation of the models to the noisy conditions [1][2].

The first approach is focused on parameterization methods that are fundamentally resistant to noise or minimize the effect of the noise. Cepstral coefficients are not equally affected by noise in linear predictive coding (LPC) cepstrum based representations. The mel-frequency cepstral coefficients (MFCCs) provide significant better results than LPC-cepstrum under noise conditions, and similar results to those provided by parameterizations based on auditory models [3]. Discriminative feature extraction has also been successfully applied to robust speech recognition [4]. High-pass filtering of the speech features tends to remove slow variations of the feature vectors representing speech, which increases accuracy of speech recognizers under noise conditions.

The second approach is based on noise reduction by transforming noisy speech into clean speech – the noise is removing/reducing from the representation of speech. The clean speech is recognized using models trained under clean conditions. This approach includes parameter mapping, spectral subtraction, statistical enhancement, and compensation based on clean speech models.

The third approach includes methods that are based on adoption of clean models to the noisy recognition environment in order to contaminate the models. The mismatch is minimized using a hidden Markov model (HMM) decomposition – also called Parallel Model Combination (PMC), a state dependent Wiener filtering, a statistical adaptation of HMMs, and a contamination of the training database[5, 6].

The Lombard effect is another aspect of the noisy environment [7]. This Lombard effect impacts the performance of speech recognizer and is highly dependent upon the speaker, the context, and the level of noise. As a result, the pronounced sounds are modified in the noisy environment. Mainly for this reasons, robust speech recognition has become an important focus area of speech research.

The aim of this study was to evaluate the recognition process of driver's voice commands spoken in car cabin using Sphinx-4 – the speech recognizer written entirely in Java language [8].

2. Methods

Automatic recognition of speech in car environment was performed in real conditions in standalone car with engine on/off by a single driver. The equipment (Fig. 1) used in the experiment consisted of headphones connected directly to the net book with installed Sphinx-4 framework for speech recognition.

Figure 1. The measuring equipment used in the experiment

Sphinx-4 provides variety of feature extraction methods. These implementations include support for the following: reading from a variety of input formats, preemphasis, windowing with a raised cosine transform, discrete Fourier transform (via FFT), mel frequency filtering, bark frequency warping, discrete cosine transform (DCT), LPC end pointing, CMN, MFCC, and PLP. The components that make up a particular HMM state are Gaussian mixtures, transition matrices, and mixture weights [8].

Speech material consisted of isolated words and sentences spoken in English language. The material included three categories of commands: Internet browsing commands /search Google, go to page …/, navigation commands /my position, find a road to …, give the distance from … to …/, and steering multimedia devices commands /open track, play track, find track digit, close track/. In order to switch between categories of commands, the speech material also included single words such as /navigation, browsing, cd-player/. After choosing the category, the speaker repeated commands relative to the category in a random order.

The speech sounds were transmitted via microphone with 22 kHz sampling rate, and 16-bit signal resolution. The collected speech material was recognized using MFCCs and HMMs applied in Sphinx-4 speech recognizer written in Java language. Sphinx-4 was trained in laboratory conditions with the same speech material.

3. Results

Recognition accuracy obtained in a standalone car with either engine on/off is presented in Table 1.

Table 1. Recognition accuracy obtained in experiment in conditions with engine on/off

Recognition Accuracy (RA) - %				
Categories of commands				Mean RA
Engine	Browsing	Navigation	CD-Player	All categories
Off	89%	78%	83%	83%
On	67%	56%	58%	60%

As presented in Table 1, the recognition accuracy for engine off was higher than for engine on conditions. In conditions with engine off, the highest recognition accuracy was obtained for the commands in the browsing category. The lowest recognition scores were obtained for the commands in navigation category. The recognition accuracy in each category exceeded value of 75%. For the conditions with engine on, the highest recognition accuracy was also obtained for the browsing category commands, and the lowest for the navigation commands. The recognition accuracy in each category exceeded value of 50%.

The mean recognition accuracy obtained for engine off conditions (83%) was significantly higher than the mean recognition accuracy obtained for engine on conditions (60%) – the difference (23%). Higher recognition rates were obtained for the browsing commands in both conditions.

4. Discussion

The aim of this study was to evaluate recognition accuracy of sentences spoken by a single driver in standalone car in conditions with engine off/on. The obtained results suggest that longer sentences obtain lower recognition accuracy than shorter sentences in car cabin. The recognition accuracy hurts and still needs to be improved in the noisy conditions – the value of 60% of mean recognition accuracy with engine on. Higher recognition rates are obtained for browsing commands.

Regardless, it is clear that more automotive companies – both auto manufacturers as well as Original Equipment Manufacturers (OEM) - are implementing speech recognition technology into their systems to provide high-end products to drivers. Speech recognition systems are becoming more and more sophisticated with OEMs combining navigation, media control, point-of-interest search capabilities and phone control. There is strong need to reduce driver distraction. The speech platform must be flexible enough to process both static and dynamic grammars efficiently. This means concealing the complex systems that work together to provide a seamless and complete offering, including speech recognition and text-to-speech capabilities.

Future work will be related to evaluations of recognition accuracy in different noise conditions. It will be tested on how and which of the noise sources influence mostly the recognition accuracy using long sentences speech material in different conditions.

References

1. Y. Gong, *Speech recognition in noisy environments: a survey,* Speech Communication **16**(3) (1995) 261–291.
2. J.R. Bellegarda, *Statistical techniques for robust asr: review and perspectives*, Proceedings of EuroSpeech-97 1997; KN 33–36.
3. C.R. Jankowski, J. Hoang-Doan, R.P. Lippmann, *A comparison of signal processing front ends for automatic word recognition*, IEEE Trans, on Speech and Audio Processing **3**(4) (1995) 286-293.
4. A. Torre, A.M. Peinado, A.J. Rubio, P. Garcia, *Discriminative feature extraction for speech recognition in noise*, Proceedings of EuroSpeech 1997, Rhodes.
5. M.F.J. Gales, S.J. Young, *HMM recognition in noise using parallel model combination*, Proceedings of EuroSpeech-93, 1993.
6. S.V. Vaseghi, B.P., *Noise compensation methods for hidden Markov model speech recognition in adverse environments*, IEEE Trans, on Speech and Audio Processing **5**(1) (1997) 11-21.
7. Evert Ph.J. de Ruiter, *Lombard effect, speech communication and the design of large (public) spaces*, Forum Acusticum 2011, Aalborg, Denmark.
8. W. Walker, P. Lamere, P. Kwok, B. Raj, R. Singh, E. Gouvea, P. Wolf, J. Woelfel, *Sphinx-4: A Flexible Open Source Framework for Speech Recognition*, SMLI TR2004-0811, SUN MICROSYSTEMS INC, 2004.

XXV Symposium *Vibrations in Physical Systems,* Poznan – Bedlewo, May 15-19, 2012

Aplication of Differential Mathieu and Hill Equation to Study the Stability of Selected Mechanical Systems

Waldemar MORZUCH
Wrocław University of Technology, 50-372 Wrocław, Smoluchowskiego 25
waldemar.morzuch@pwr.wroc.pl

Abstract

Following article presents a solution of Mathieu and Hill differential equation describing the vibrations of mechanical systems submitted to force variable in time with damping and without damping. An examples of above systems were presented and selected parameters was set at which the respective solutions of differential equations are unstable.

Keywords: partial Mathieu and Hill equation, dynamic stability

1.Introduction

Vibrations of many mechanical systems are described by Mathieu or Hill differential equation. An example here might be the lateral vibrations of electrical machines rotors [5,7] or the transverse vibrations of spacer rods [6,8].Variability in time during the magnetic tension (in the case of the rotors) or variability of compressive force (in the case of spacer rods) is redacted to examination of issue to solving a differential equation with time variable coefficients.Depending on adopted model differential equations may contain same function (the model without damping) or it first derivative (the model with damping). In this article own methods of solution above differential equations were presented.

2. The solution of Mathieu and Hill differential equations

The issues described in the preceding paragraph reduced to solution of differential equations whose form depends on adopted model of the problem.In the case of adopting the model without damping considered issue reduced to solving the Mathieu differential equation in a form:

$$\ddot{\mathrm{T}}_{\mathrm{n}} + \omega_{\mathrm{n}}^{2}(1 - 2\psi_{n}\mathrm{cospt})\mathrm{T}_{n} = 0 \tag{1}$$

where

T_n - function of time describing dependences of the analised value (eg, deflection) from time t.
ω_n - frequency of a n-th order system for a case when p = 0
p - frequencies of changes, ψ_n – parameter
ψ_n - function which is a ratio of modulation depth.

In the case of adopting the model with damping analogically to (1) differential equation has the form

$$\ddot{T}_n + 2h\dot{T}_n + \Omega^2{}_n[1 - f(t)]T_n = 0 \quad (2)$$

This is a Hill's differential equation. Here coefficient h is the damping factor.

In case absence of damping (h = 0) and after the adoption the function f (t) in form f(t)=2ψ_n cos *pt* obtained by the classical Mathieu equation in the form:

$$\ddot{T}_n + \omega_{on}{}^2(1 - 2\psi_n \cos pt)T_n = 0 \quad (3)$$

where

ω_{on} - is frequency for the n-th order of system without damping at $\psi_n = 0$

A first and also the widest area of instability was obtained by adopting a solution of the differential equation (3) in the form:

$$T(t) = A(t)\cos\frac{pt}{2} + B(t)\sin\frac{pt}{2} \quad (4)$$

where

A(t), B(t)- slowly changing functions of time such that

$$\ddot{A} \ll \dot{A} \ll A \quad \text{and} \quad \ddot{B} \ll \dot{B} \ll B \quad (5)$$

Analyzing further the solution of the differential equation (3) dependence describing boundaries of the first area of instability was obtained.

$$(\frac{1}{4} - z - \psi_n z)(-\frac{1}{4} + z - \psi_n z) \rangle 0 \quad (6)$$

where

$$z = \left(\frac{\omega_{on}}{p}\right)^2 \quad (7)$$

After taking into account the substitution (7) dependence describing the boundary lines of the first area of instability were obtained

$$2\sqrt{1 - \psi_n} \langle \frac{p}{\omega_{on}} \langle 2\sqrt{1 + \psi_n} \quad (8)$$

This area is shown in Figure 1.

Identical to the dependence (8) were obtained dependences administered inmany textbooks, such as in [1,4]. In a similar way the solution of the differential equation (2) for a system with damping was obtained. For this purpose the solution of above equation was adopted as

$$T_n = e^{-ht}\varphi_n \quad (9)$$

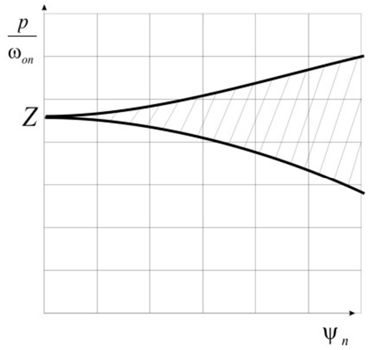

Figure 1. Boundary lines of the first area of instability

Finally a new differential equation describing the function φ_n was obtained

$$\varphi_n + \omega_n{}^2[1 - f_1(t)]\varphi_n = 0 \tag{10}$$

where

$$\omega_n{}^2 = \Omega_n{}^2 - h^2 \tag{11}$$

$$f_1(t) = \frac{\Omega_n{}^2}{\omega_n{}^2} f_1(t) \tag{12}$$

Equation (10) resembles Mathieu equation without damping.

It follows from above that by analyzing this equation can be based on solving the basic Mathieu equations by substituting $f_1(t)$ inspire $f(t)$ and $\Omega_n^2 - h^2$ in a place of ω_n^2.

Proceeding similarly as in the case of Mathieu equation term of the instability for Hill's equations was obtained in form.

$$\lambda^2 \rangle h^2 \tag{13}$$

Proceeding simmilar as in the absence of damping obtained dependences describing boundary lines of the first area of instability

$$\frac{p}{\Omega_1} \langle 2\sqrt{\frac{(1-\zeta_1)^2 - \Psi_1{}^2}{1 - 3\zeta_1 - \sqrt{\Psi_1{}^2 - 4\zeta_1 + 8\zeta_1{}^2}}} \tag{14}$$

$$\frac{p}{\Omega_1} \rangle 2\sqrt{\frac{(1-\zeta_1)^2 - \Psi_1{}^2}{1 - 3\zeta_1 + \sqrt{\Psi_1{}^2 - 4\zeta_1 + 8\zeta_1{}^2}}} \tag{15}$$

Boundary lines describing the first area of instability was shown as visual aid in Fig. 2.

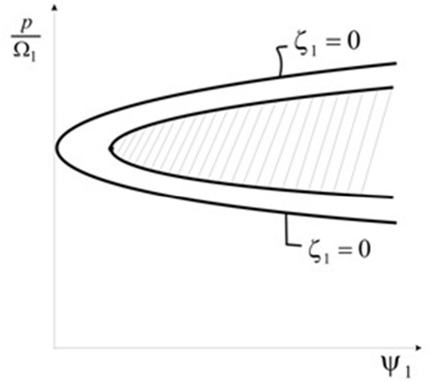

Fig.2 First area of instability

Dependence (14) describes the upper lines, whereas the dependence (15) describes the bottom line.

The solutions outlined above have been used in earlier work of the author [6, 7, 8]

3. Conclusion

As a result of solving the problem described by Mathieu equation without damping a series of so-called. areas of instability is obtained Inclusion of damping insert considered question down to the Hill equation. Here also, areas of instability are obtained which are much narrower. There is a limit value of damping at which parametric resonance occurs.

References

1. Z.Dżygadło, S.Kaliski, L. Solarz, E. Włodarczyk : *Vibrations and waves*, WAT, Warsaw 1965.
2. R.Gryboś: *Drgania maszyn*.Wydawnictwo Politechniki Śląskiej,Gliwice 2009.
3. Kowalski J.:*Zbiór zadań z mechaniki z zastosowaniem do obliczania elementów maszyn*. PWN Warszawa 1980 r.
4. N.W.Mc Lachlan: *Theory and application of Mathieu functions*. Oxford 1947
5. W.Morzuch: *Stateczność dynamiczna wirników dwubiegunowych silników asynchronicznych*. Archiwum Elektrotechniki.1983 t.32,z.3/4.
6. W.Morzuch: *Stateczność dynamiczna pręta przekładkowego ściskanego siłą okresowo-zmienną*. Rozprawy Inżynierskie. 1989 t.37,z.2.
7. W. Morzuch: *Wpływ tłumienia wewnętrznego na drgania giętne wirnika dwubiegunowego silnika elektrycznego*. XII Sympozjum Stateczności Konstrukcji. Zakopane 2009.
8. W. Morzuch: *Stateczność dynamiczna pręta przekładkowego z lepko sprężystym rdzeniem*. XII Sympozjum Stateczności Konstrukcji. Zakopane 2009.

XXV Symposium *Vibrations in Physical Systems,* Poznan – Bedlewo, May 15-19, 2012

Dynamic Stability of the Pendulum with Vibrating Mounting Point

Waldemar MORZUCH
Wrocław University of Technolog, 50-372 Wrocław, Smoluchowskiego 25
waldemar.morzuch@pwr.wroc.pl

Abstract

In the article dynamic analysis of the pendulum whose mounting point performs the vibration was presented. Equation of motion was written and then the stability of this motion was examined . Finally Mathieu equation without suppression was obtained, which solution allowed to designate the frequency bands at which the force of the pendulum motion was unstable.

Keywords: mathematic pendulum, dynamic stability

1.Introduction

The movement of many mechanical systems is described by the Mathieu differential equation. An example here might be the lateral vibrations of electric machines rotors, bipolar [5,6] or transverse vibrations of spacer bars [7,8]. Variability of some parameters like eg. the magnetic tension force in the case of rotors or compressive force in the case of rods, such a issue can be checked by the Mathieu differential equation. As a result of its solution is obtained a range of enforce frequencies at which there is a phenomenon of instability (parametric resonance). Similar situation occurs in the case of a mathematical pendulum with oscillating point of suspension. Differential equation describing such a motion is Mathieu differential equation with coefficients depending on the amplitude forcing and frequency of change. Stability of motion such a pendulum depends on whether the parameters of this work are contained in sedate or unsedate interval. So it was necessary to determine the boundary lines describing a motion stability of an increased pendulum. Based while on our own method of solution of Mathieu equation.

2.Equation of pendulum motion

Considered pendulum is shown in Figure 1. It was assumed that the point of suspension performs vibrations described by dependence

$$\zeta(t) = \zeta_o \cos pt \tag{1}$$

where ζ_o -vibrations amplitude
p- vibration frequency

The motion equation of the pendulum at the direction perpendicular to its length has the form

$$m(\ddot{\zeta}\sin\varphi + l\ddot{\varphi}) = -mg\sin\varphi \tag{2}$$

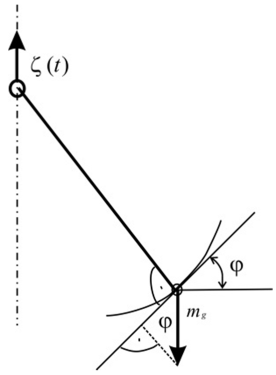

Figure 1 The pendulum with oscillating suspension point

After substituting (1), obtained

$$\ddot{\varphi} + \omega_o{}^2[1 - f(t)]\varphi = 0 \tag{3}$$

where

$$f(t) = -\frac{\ddot{\zeta}}{g},\ \omega_o{}^2 = \frac{g}{l} \tag{4}$$

so

$$\ddot{\varphi} + \omega_o{}^2\left(1 - \frac{p^2\zeta_o \cos pt}{g}\right)\varphi = 0 \tag{5}$$

Differential equation (5) can be written as

$$\ddot{\varphi} + \omega_o{}^2(1 - 2\mu \cos pt)\varphi = 0 \tag{6}$$

where $\mu = \dfrac{p^2\zeta_0}{2g}$

Coefficient μ is a modulation depth factor. Equation (6) is a Mathieu equation (without damping).

Let`s analise the case when $p = 2\Omega$,

where $p = \dfrac{2\pi}{T_p}$

T_p - period of change a parameter μ .

From dependence $p = 2\Omega$ we will receive

$$\frac{2\pi}{T_p} = 2 \cdot \frac{2\pi}{T} \tag{7}$$

where, T - pendulum period of free oscillation

$$T = 2\pi\sqrt{\frac{l}{g}} \tag{8}$$

From equation (7) we have

$$\frac{1}{T_p} = \frac{2}{T} \quad \text{so} \quad T = 2T_p \tag{9}$$

Thus, the period of free oscillation is equal to two periods of change parameter μ .

In order to determine an instability region the solution of equation (6) was presented in the form

$$\varphi_n(t) = A(t)\cos\frac{pt}{2} + B(t)\sin\frac{pt}{2} \tag{10}$$

Where A (t), B (t) - slowly changing functions of time t such that

$$\ddot{A} \langle\langle \dot{A} \langle\langle A \quad , \ \ddot{B} \langle\langle \dot{B} \langle\langle B \tag{11}$$

After differentiating (10) and substituting to (6) the boundary lines of the instability area were obtained

$$2\sqrt{1-\mu} \langle \frac{p}{\omega_o} \langle 2\sqrt{1+\mu} \tag{12}$$

Obtained dependence is identical with dependencies given in other works such as [1,4]

The boundary lines for area described by equation (12) are shown in Fig.2.

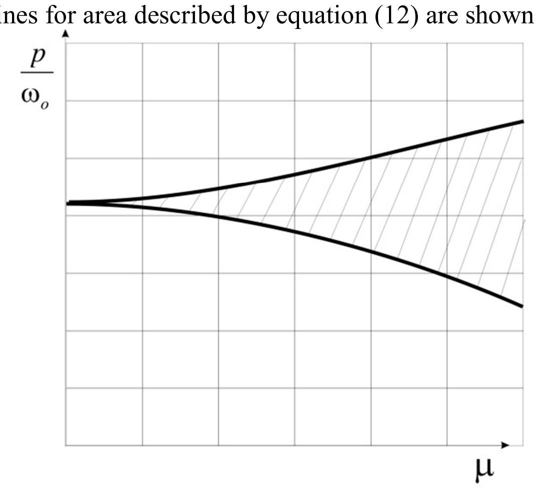

Figure 2. The boundary lines of unstable area

3.Calculation example

Following section analyze of pendulum motion stability with the length $l_1 = 50cm$ and $l_2 = 100cm$ an the amplitude of extortion $\zeta_o = 10cm$. In case of pendulum with length $l_1 = 50cm$ basic on dependence (12) forcing frequency was obtained at which instability occurs.

$$p' = 2\omega_o\sqrt{1+\mu} \text{ (upper line)} \tag{13}$$

$$p'' = 2\omega_o\sqrt{1-\mu} \text{ (down line)} \tag{14}$$

After accepting $l_1 = 50cm$ obtained

$$\omega_o = \sqrt{\frac{g}{l_1}} = 4{,}43\,s^{-1}(T_0 = 1{,}42\,s) \tag{15}$$

Then stability of pendulum motion the near the frequency was examined $p = 2\omega_o = 8{,}86s^{-1}(T_p = 0{,}71s)$
Based on dependences (13) and (14) obtained

$$p' = 10{,}48s^{-1}, p'' = 6{,}86s^{-1}. \tag{16}$$

So in above example dependence was obtained

$$p''\langle p \langle p' \tag{17}$$

where

$$6{,}86s^{-1}\langle 8{,}86s^{-1}\langle 10{,}48s^{-1} \tag{18}$$

In above conduction pendulum move will be unstable.Then adopted pendulum with length $l_2 = 100cm$ Proceeding as above were obtained sequentially

$$\omega_o = 3{,}13\,s^{-1}(T_0 = 2\,s); \mu = 0{,}2; p' = 6{,}81\,s^{-1}; p'' = 5{,}6\,s^{-1} \tag{19}$$

Thus, as previously obtained dependence

$$p''\langle p \langle p' \tag{20}$$

because

$$5{,}6s^{-1}\langle 6{,}28s^{-1}\langle 6{,}81s^{-1} \tag{21}$$

Here pendulum motion will be also unstable

4. Conclusions

Stability of a mathematical pendulum with oscillating point of suspension depends on forcing frequency range. There is a range of frequencies at which the pendulum motion is unstable. Those frequencies determine so-called areas of instability. Width of these areas increases with increasing depth modulation factor.

References

1. Dżygadło Z., Kaliski S., Solarz L., Włodarczyk E. : Vibrations and waves. WAT, Warsaw 1965.
2. Kaliski S.:Vibrations and waves in solids.IPPT PAN,Warsaw,1966 (in Polish)
3. Kowalski J.:Zbiór zadań z mechaniki z zastosowaniem do obliczania elementów maszyn.PWN Warszawa 1980 r.
4. McLachlan N.W : Theory and applications of Mathieu functions. Oxford 1947.
5. Morzuch W.: Stateczność dynamiczna wirników dwubiegunowych silników asynchronicznych. Archiwum Elektrotechniki, Vol XXXII, No.3-4,1983.
6. Morzuch W.: Obszary niestateczności wirników klatkowych dwubiegunowych silników asynchronicznych. Archiwum Budowy Maszyn. Vol XXXIII, No.2, 1986.
7. Morzuch W.: Stateczność dynamiczna pręta przekładowego ściskanego siłą okresowo-zmienną. Rozprawy Inżynierskie. 1989 t.37, z 2.
8. Morzuch W.: Dynamic buckling of sandwich bar compressed with periodic variable force. Engineering Transactions. 2007 Vol.55.

Vibration Analysis of Toothed Gear with Cyclic Symmetry Modelling

Stanisław NOGA
Faculty of Mechanical Engineering and Aeronautics, Rzeszów University of Technology
al. Powstańców Warszawy 12, 35-959 Rzeszów, Poland, noga@prz.edu.pl

Roman BOGACZ
Faculty of Civil Engineering, Cracow University of Technology
and Polish Academy of Science, ul. Pawińskiego 5B, 02-106 Warsaw, Poland
rbogacz@ippt.gov.pl

Kurt FRISCHMUTH
Institute for Mathematics, University of Rostock,
Ulmenstraße 69, D-18055 Rostock, Germany, kurt.frischmuth@uni-rostock.de

Abstract

In the paper the transversal vibration of a toothed gear is studied by means of numerical simulation methods. At first, we focus on preparing a simplified vibration model of a gear, where the teeth are omitted. The accuracy of the approximate model is assessed by the frequency error criterion. Therefore a benchmark solution is calculated by performing the vibration analysis for the full model, which contains all essential elements of the real system. Next, the simplified model of a gear featuring cyclic symmetry is analyzed. All numerical models in this paper are formulated in terms of finite element representations, the computations are carried out in ANSYS. The problems discussed here may be useful for researchers dealing with dynamics of rotating systems.

Keywords: toothed gear, transverse vibration, natural frequencies, cyclic symmetry model

1. Introduction

Problems of transverse vibration of toothed gears are the subject of many recent investigations [2, 3, 6]. This is due to the fact that gears, as systems of rotating bodies, are widely used in various engineering applications, such as aircraft engines, automobiles, machine tools and others. Theoretical investigations of the transverse vibration of gears have been performed in the last century for some problems of fast rotating circular and annular plates. In a recent article [2] the finite element (FE) technique was utilized to work out an algorithm for the identification of the proper distorted mode shapes of a toothed gear, which has the shape of an annular plate with holes. In the work [3] the numerical (by using FE modelling approach) and exerimental analysis of resonant response in aviation gearing were conducted. In the paper [6] the authors analysed free vibration of a planetary gearbox. In [1] dynamic problems concerning the motion of a corrugated circular plate over a wavy base were studied. In the present paper, the free transverse vibration of a toothed gear, considered as an annular plate with geared rim installed on a hollow stepped shaft, is analysed by the finite element method (FEM). A simplified FE model of the toothed gear is proposed. Research into using the cyclic symmetry of the gear for a faster solution of the dynamic problem is presented.

2. Formulation of the problem

The objective of this work is the presentation of a procedure for the derivation of simplified FE models of toothed gears. In the simplified FE model the teeth are omitted. However, satisfactory dynamical behavior of the simplified model of the gear wheel is to be maintained. For that purpose, a set of toothed gears with similar geometry but with different teeth numbers is analyzed. The considered set of toothed gear models is shown in Fig. 1.

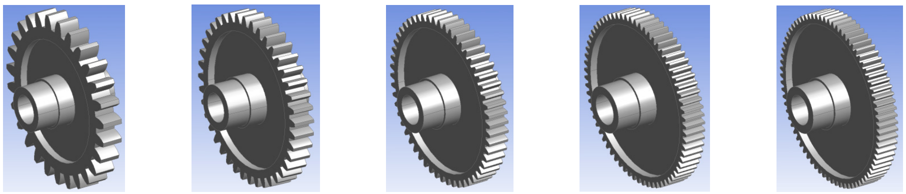

Figure 1. Geometrical models of the systems

Each gear model is composed of an annular plate with a geared rim installed on a hollow stepped shaft. Primary geometrical dimensions of the analysed systems (diameters: d_0, d_w, d_l, d_p; lengths: l_c, l_b, l_w, l_r) are defined as shown in Fig. 2a. The remaining dimensions are taken according to the standard theory of toothed gears. For each gear the simplified model shown in Fig. 2b is adopted.

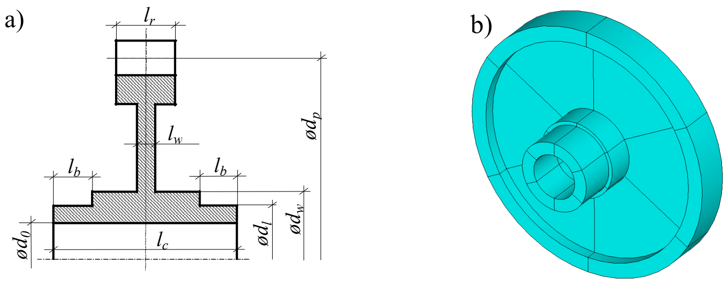

Figure 2. (a) geometrical dimensions, (b) proposed simplified model

The geometrical dimensions of the simplified models are taken from the gear geometry. In each simplified model, the outer diameter of the rim is equal the reference diameter d_p of the corresponding gear. With the exception of Young's modulus of the rim, it is assumed that the simplified models have the same technical data as the gears. For each simplified model, Young's modulus of the rim is selected experimentally to be in accordance with the reference solution. For every single case the problem of free vibration is solved by the FEM. After spatial discretization of the structures under consideration, the ordinary differential equations of motion can be written in each case in the form [4]

$$\mathbf{M}\ddot{\mathbf{u}} + \mathbf{K}\mathbf{u} = 0 \tag{1}$$

where $\mathbf{M}$ is the global mass matrix, $\mathbf{K}$ is the global stiffness matrix, and $\mathbf{u}$ is the nodal displacement vector. Both global mass and stiffness matrices are obtained from the element matrices that are given by [4]

$$\mathbf{M}^{(e)}=\int_{V^{(e)}}\rho^{(e)}\mathbf{N}^T\mathbf{N}\,dV^{(e)},\quad \mathbf{K}^{(e)}=\int_{V^{(e)}}\mathbf{B}^T\mathbf{E}\mathbf{B}\,dV^{(e)} \tag{2}$$

where $\rho^{(e)}$ is the mass density of the element, $\mathbf{N}$ is the matrix of element shape functions, $\mathbf{B}$ is the matrix of derivatives of the element shape functions, $\mathbf{E}$ is the material stiffness matrix, and $V^{(e)}$ is volume of the element. The natural frequencies of the system are obtained by solving the eigenvalue problem

$$\left(\mathbf{K}-\omega^2\mathbf{M}\right)\bar{\mathbf{u}}=0 \tag{3}$$

where ω is the natural frequency and $\bar{\mathbf{u}}$ is the corresponding mode shape vector, which is determined up to a factor by the relation (3). The number of eigenpairs (ω_i, $\bar{\mathbf{u}}_i$) corresponds to the number of degrees of freedom of the system. Because of the discretization and tuning process, the FE models of the simplified toothed gear models have to be treated as approximations of the exact systems. The error between the precise and the FE models is defined by

$$\varepsilon=\left(\omega^f-\omega^e\right)/\omega^e\times 100\,[\%] \tag{4}$$

where ω^f is the natural frequency obtained from the FE solution, while ω^e is the natural frequency of the exact system. The best possibility to determine the accurate values of the natural frequencies is by experimental investigation. For the investigation presented in this paper, exemplary solutions are achieved by vibration analysis of high resolution toothed gear models, which contain all essential elements of the real system.

3. Numerical analysis

In order to obtain reference values for the natural frequencies, for each gear shown in Fig. 1, a high resolution FE model is set up, which contains all essential construction details of the real system. The parameters characterizing the systems used in calculations are shown in Table 1a – b.

Table 1a. Parameters characterizing the system

d_0 [m]	d_w [m]	d_l [m]	l_c [m]	l_b [m]	l_w [m]	l_r [m]	E [Pa]	ρ [kg/m^3]	ν
0.025	0.043	0.039	0.076	0.02	0.006	0.018	$2.08\cdot10^{11}$	$7.83\cdot10^{3}$	0.3

Table 1b. Parameters characterizing the system

No.	1	2	3	4	5
z	27	40	54	67	74
d_p [mm]	140.4	140	140.4	140.7	140.6

In the tables, z is the number of teeth in the gears, whereas E and ν are Young's modulus of elasticity and Poisson ratio, respectively. In accordance with the circular and annular plate vibration theory [5], the particular natural frequencies of vibration are denoted as

ω_{mn} where m refers to the number of nodal circles and n is the number of nodal diame- diameters. Each of these geometrical models is meshed by using standard procedures of the ANSYS software. A 3 – D solid mesh is prepared and the ten node tetrahedral element (solid187) with three degrees of freedom in each node is employed to build each exemplary model. During the mesh generation process, it is assumed that the maximum length of element sides must to be equal or less than 3.5 [mm]. The most complex FE model represents the gear with teeth number $z = 54$ and includes 83124 solid elements. The smallest FE model relates to the gear with teeth number $z = 74$ and comprises 65962 solid elements. Due to space limitation only two elaborated FE models are displayed in Fig. 3a – b.

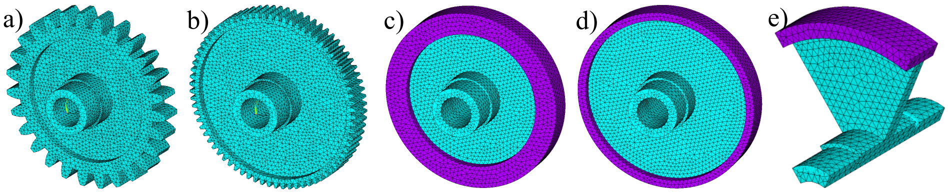

Figure 3. (a – b) complete FE models of the exemplary systems, (c – d) FE models of the simplified gear models, (e) simplified cyclic symmetry FE model of the system

The same procedure as for the exemplary model cases is used to discretise the simplified models of the gears. Two simplified FE models are displayed in Fig. 3c – d. The mass density of the rim is the same as for the related complex model. The proper value of Young's modulus E_i of the rim is selected experimentally to minimize the frequency error (4). The biggest simplified FE model includes 45450 solid elements and it corresponds to the gear with teeth number $z = 27$. Two of the FE models include each no more than 39000 solid elements, and the remaining ones consist of no more than 33600 solid elements. For all models presented here, calculations were continued until the natural frequency ω_{16} was determined. Table 2 shows the values of E_i, for which satisfactory results were achieved by the simplified models. Due to space limitation only the values of natural frequencies related to the gear wheel, for which the gear teeth number is $z = 67$ are presented (see Table 3).

Table 2. Young modulus of elasticity of the rim of the simplified gear models

No.	1	2	3	4	5
z	27	40	54	67	74
E_i [Pa]	$1.15*10^{11}$	$1.2*10^{11}$	$1.3*10^{11}$	$1.36*10^{11}$	$1.38*10^{11}$

Table 3. The reference gear model (1), and the simplified gear model (2) natural frequencies ω_{mn} [Hz] (for $z = 67$), respectively

No.	ω_{11}	ω_{10}	ω_{12}	ω_{13}	ω_{14}	ω_{20}	ω_{21}	ω_{22}	ω_{15}	ω_{23}	ω_{16}
1	1338	1618	1978	4622.5	8325	9523	10028.5	11540.5	12645.5	14322	17308.5
2	1344	1608	2002	4673.5	8463	9598	10105	11666	12966	14531	17943.5

For the other cases only the values of the frequency error are displayed (see Table 4). For each simplified FE model, the largest difference between reference results and simplified FE model solutions is observed in the frequency ω_{16}. With the exception of the simplified model with teeth number $z = 27$, the dimension of the simplified FE model is approximately two times smaller compared with the corresponding high resolution model.

Table 4. Frequency error ε_{mn} [%]

$No.\backslash\varepsilon_{mn}$	ε_{11}	ε_{10}	ε_{12}	ε_{13}	ε_{14}	ε_{20}	ε_{21}	ε_{22}	ε_{15}	ε_{23}	ε_{16}
1	-1.66	-4.91	-0.55	-0.19	2.28	-0.01	-0.22	-0.41	5.88	-0.57	10.5
2	-0.93	-3.25	0.02	-0.63	0.26	-0.17	0	0.54	1.73	0.89	3.61
3	-0.38	-1.61	1.29	1.28	1.95	0.45	0.6	1.25	3.01	1.8	4.29
4	0.45	-0.62	1.21	1.1	1.66	0.79	0.76	1.09	2.53	1.46	3.67
5	0	-0.61	1.34	1.62	2.15	0.66	0.71	1.26	2.93	1.85	4

In the next part, the obtained simplified FE models of the toothed gears undergo verification in the case of fast rotation. We assume that the systems rotate at an angular velocity $\theta = 600$ [*rad/s*]. The reference values of natural frequencies and the simplified FE models natural frequencies are generated. The rotation effect is taken into account by determining stress distributions due to rotation, which for each model is done during the computational step associated with static analysis. This stress distribution is then included in the computation step associated with modal analysis. Table 5 shows the obtained results for the validation. Due to space limitation only the values of the frequency error are displayed.

Table 5. Frequency error ε_{mn} [%] (test data)

$No.\backslash\varepsilon_{mn}$	ε_{11}	ε_{10}	ε_{12}	ε_{13}	ε_{14}	ε_{20}	ε_{21}	ε_{22}	ε_{15}	ε_{23}	ε_{16}
1	-1.66	-4.91	-0.57	-0.18	2.29	-0.01	-0.23	-0.41	5.88	-0.57	10.5
2	-0.89	-3.25	0.02	-0.62	0.26	-0.17	0.01	0.53	1.73	0.89	3.61
3	-0.34	-1.61	1.31	1.28	1.95	0.44	0.61	1.25	2.96	1.8	4.29
4	0.41	-0.62	1.21	1.1	1.67	0.78	0.77	1.09	2.54	1.43	3.67
5	-0.07	-0.61	1.31	1.6	2.15	0.65	0.71	1.27	2.93	1.84	3.99

The table shows that the worst compatibility with the exemplary solution is observed for the simplified FE model case related to the gear for which the teeth number is $z = 27$.

4. Cyclic symmetry modelling

In this section we exploit the cyclic symmetry of the gears. The response behavior of a full circular component may be generated on the basis of solutions achieved for a single symmetric sector, which is a part of the circular component [7]. This allows to reduce the FE model size of the analyzed system considerably. The main point is to achieve good compatibility with the precise solution. The cyclic symmetry analysis is conducted for the gear wheel with the teeth number $z = 67$. The simplified model of the gear, discussed in the previous section, is taken into account. The model of the system consists of six sectors (see Fig. 2), which have the cyclic symmetry feature. Each single symmetric sector is meshed by using the same procedures as for the simplified FE mod-models. The developed FE model is displayed in Fig. 3e, and it consists of only 5855 solid elements. Table 6 shows the natural frequencies and frequency errors obtained by using the FE model presented in Fig. 3e.

Table 6. Natural frequencies ω_{mn} [Hz] (for z = 67) and frequency error ε_{mn} [%] of the cyclic symmetric gear model

	ω_{11}	ω_{10}	ω_{12}	ω_{13}	ω_{14}	ω_{20}	ω_{21}	ω_{22}	ω_{15}	ω_{23}	ω_{16}
ω_{mn}	1336	1604	2006	4704	8521	9580	10099	11685	13053	14580.5	18061.5
	ε_{11}	ε_{10}	ε_{12}	ε_{13}	ε_{14}	ε_{20}	ε_{21}	ε_{22}	ε_{15}	ε_{23}	ε_{16}
ε_{mn}	-0.15	-0.87	1.42	1.76	2.35	0.6	0.7	1.25	3.22	1.81	4.35

The results are a bit worse in comparison with the solution by the simplified model (see Table 3 – 4), but still satisfactory. It is worth pointing out that cyclic symmetry analysis allows to reduce solution time and memory requirements drastically.

5. Conclusions

The present paper deals with free transverse vibration of a toothed gear with complex geometry. A simplified FE model of the gear wheel, where the teeth are omitted, is proposed. The simplified FE models of gears include substantially lower numbers of finite elements compared to the corresponding high resolution reference models. This results in a reduction of the required computation time and computer memory, which in turn allows to employ these models to conduct in advance dynamical simulations with satisfactory accuracy. At this stage of the research, models taking into account cyclic symmetry seem most promising. They provide relatively good results by FE models with moderate numbers of elements.

References

1. R. Bogacz, K. Frischmuth, *On some corrugation related dynamical problems of wheel/rail interaction*, The Archives of Transport, **22** (2010) 27-41.
2. R. Bogacz, S. Noga, *Free transverse vibration analysis of a toothed gear*, Arch. Appl. Mech., (2012) DOI: 10.1007/s00419-012-0608-6.
3. R. Drago, F. Brown, *The analytical and experimental evaluation of resonant response in high-speed, lightweight, highly loaded gearing*, J. Mech. Des. **103** (1981) 346-356.
4. C. de Silva, *Vibration and Shock Handbook*, Taylor & Francis, Boca Raton 2005.
5. S. Kaliski, *Vibration and Waves in Solids*, IPPT PAN, Warsaw, 1966 (in Polish)
6. R. Parker, X. Wu, *Vibration modes of planetary gears with unequally spaced planets and an elastic ring gear*, J. Sound Vib., **329** (2010) 2265-2275.
7. *ANSYS documentation*. 2009. Version 12.1 ANSYS, Ins.

XXV Symposium *Vibrations in Physical Systems,* Poznan – Bedlewo, May 15-19, 2012

In Plane Flexural Vibration of a Ring Interacting with the Winkler Foundation

Stanisław NOGA
Faculty of Mechanical Engineering and Aeronautics, Rzeszów University of Technology
al. Powstańców Warszawy 12, 35 – 959 Rzeszów, Poland, noga@prz.edu.pl

Tadeusz MARKOWSKI
Faculty of Mechanical Engineering and Aeronautics, Rzeszów University of Technology
al. Powstańców Warszawy 12, 35 – 959 Rzeszów, Poland, tmarkow@prz.edu.pl

Abstract

In this study the in plane flexural vibration of a system of circular ring interacting with elastic foundation is presented on the basis of the analytical method and numerical simulation. The elastic foundation is described by the Winkler model. At first the motion of the system is described by partial differential equations. The effect of rotary inertia and shear deformation is included. The general solution of the free vibration is derived by the separation of variable method and the boundary problem is solved. The second model is formulated by using finite element representations. The natural frequencies and natural mode shapes of vibration of the system are determined. The obtained results of calculation are discussed and compared for these two models. FE models are formulated by using ANSYS code.
It is important to note that the data presented in the paper brings practical advice to design engineers.

Keywords: circular ring, in plane flexural vibration, Winkler foundation, Timoshenko's theory

1. Introduction

The problems of in plane flexural vibration of circular rings interacting with foundation find application in several practical problems [1, 7]. The fundamental theory of vibration of circular rings is presented in [6]. Authors of work [1] employed theory of curved beam with foundation to vibration analysis of railway wheels. Free vibrations of Timoshenko beam attached to Winkler foundation are studied in the paper [2]. In the work [7] authors analyse free vibration of a ring gear by using thin ring theory. In the papers [4, 5] the exact solution for the free vibration of annular membrane compound systems with Winkler foundation is given. In this paper the free in plane flexural vibration of a circular ring interacting with Winkler foundation are analyzed using the classical thin and thick ring theory, and the finite element (FE) technique. The obtained results of calculation are discussed and compared for elaborated models. This work continues the recent author's investigations concerning vibration of systems with elastic foundation [3].

2. Theoretical formulation

The mechanical model of the system under consideration consists of circular ring interacting with massless, linear, elastic foundation of a Winkler type. It is assumed that the ring is homogeneous and perfectly elastic, and it has constant cross – sectional area. It is additionally assumed that the neutral line of the ring has radius R and an element of the ring, fixed by angle θ, displaces in the radial and the circumferential direction (see Fig. 1). The small displacements in these directions are denoted as $u(\theta,t)$ and $w(\theta,t)$, respectively. Making use of the classical theory of vibrating thin rings [6], the partial differential equations of motion for the free in – plane flexural vibrations in terms of the radial deflection $u(\theta,t)$, can be combined into a single equation as

$$\frac{\partial^6 u}{\partial\theta^6}+2\frac{\partial^4 u}{\partial\theta^4}+\left(1+\frac{R^4}{EI_1}k_f\right)\frac{\partial^2 u}{\partial\theta^2}-\frac{R}{EI_1}k_p u+\rho A\frac{R^4}{EI_1}\left(\frac{\partial^4 u}{\partial\theta^2\partial^2 t}-\frac{\partial^2 u}{\partial t^2}\right)=0 \tag{1}$$

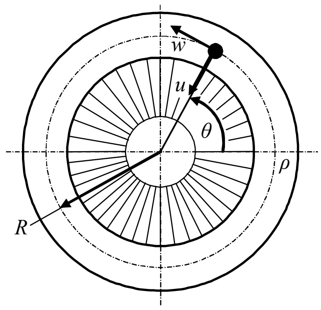

Figure 1. Vibrating system under study

where E denotes Young's modulus of elasticity, I_1 is the area moment of inertia of the rim cross section, ρ is the mass sensity, A is the cross section area, k_f and k_p are the radial and tangential stiffness modulus of a Winkler elastic foundation, respectively.

The solution is assumed to be harmonic, i.e.

$$u(\theta,t)=U(\theta)e^{i\omega t} \tag{2}$$

where ω is the frequency of vibration and $i=\sqrt{-1}$ is the imaginary unit. Then, Eq. (1) becomes

$$\frac{d^6 U}{d\theta^6}+2\frac{d^4 U}{d\theta^4}+\left(1+\frac{R^4}{EI_1}k_f\right)\frac{d^2 U}{d\theta^2}-\frac{R}{EI_1}k_p U-\rho A\frac{R^4}{EI_1}\omega^2\left(\frac{d^2 U}{d\theta^2}-U\right)=0 \tag{3}$$

The general solution of Eq. (3) is assumed in the form

$$U(\theta)=D_1\sin(n\theta+\varphi), \qquad n=2,3,\ldots \tag{4}$$

where D_1 and φ are constants. Substituting solution (4) into (3) yields the natural frequencies of vibration as

$$\omega_n^2=\frac{EI_1\left(n^6-2n^4+n^2\right)+R^4k_f n^2+Rk_p}{\rho AR^4\left(n^2+1\right)} \tag{5}$$

Finally the normal modes of the ring can be written in the following form

$$u_n(\theta,t) = D_1 \sin(n\theta + \varphi)e^{i\omega_n t} \tag{6}$$

where D_1 and φ can be achieved from the initial condition of the ring.

Then the Timoshenko's theory is employed in vibration analysis of the free in – plane flexural vibration of the ring interacting with the Winkler elastic foundation. Taking into account the effects of shear deformation and rotatory inertia, the equation of motion in terms of $u(\theta,t)$ can be expressed as

$$\begin{aligned}&\frac{\partial^6 u}{\partial\theta^6} + 2\frac{\partial^4 u}{\partial\theta^4} + \left(1 + (a_1 - b_1)k_f\right)\frac{\partial^2 u}{\partial\theta^2} + (b_1 - a_1)k_p u - (c_1 + d_1)\frac{\partial^6 u}{\partial\theta^4\partial t^2} - cd\frac{\partial^4 u}{\partial t^4} + \\ &+ cd\frac{\partial^6 u}{\partial\theta^2\partial t^4} + \left(\rho A a_1 + d_1 + h_1 k_f - 2c_1\right)\frac{\partial^4 u}{\partial\theta^2\partial t^2} - \left(c_1 + \rho A a_1 + h_1 k_p\right)\frac{\partial^2 u}{\partial t^2} = 0\end{aligned} \tag{7}$$

where

$$a_1 = \frac{R^4}{EI_1}, \quad b_1 = \frac{R^2}{k'AG}, \quad c_1 = \frac{\rho R^2}{E}, \quad d_1 = \frac{\rho R^2}{k'G}, \quad h_1 = \frac{\rho R^4}{k'EAG} \tag{8}$$

and G is the modulus of elasticity in shear (Kirhoff modulus), k' is the shear correction factor. The rest of the denotations have the same meaning as for in previous case. It is assumed the solution of Eq. (7) to be harmonic in the form (2). This gives the equation

$$\begin{aligned}&\frac{d^6 U}{d\theta^6} + 2\frac{d^4 U}{d\theta^4} + \left(1 + (a_1 - b_1)k_f\right)\frac{d^2 U}{d\theta^2} + (b_1 - a_1)k_p U + (c_1 + d_1)\omega^2\frac{d^4 U}{d\theta^4} - cd\,\omega^4 U + \\ &+ cd\,\omega^4\frac{d^2 U}{d\theta^2} - \left(\rho A a_1 + d_1 + h_1 k_f - 2c_1\right)\omega^2\frac{d^2 u}{d\theta^2} + \left(c_1 + \rho A a_1 + h_1 k_p\right)\omega^2 U = 0\end{aligned} \tag{9}$$

As in the previous case the solution of Eq. (9) is assumed in the form (4). It yields the following frequency equation

$$\begin{aligned}&-n^6 + 2n^4 - \left(1 + (a_1 - b_1)k_f\right)n^2 + (b_1 - a_1)k_p + \Big((c_1 + d_1)n^4 + \\ &+ \left(\rho A a_1 + d_1 + h_1 k_f - 2c_1\right)n^2 + \left(c_1 + \rho A a_1 + h_1 k_p\right)\Big)\omega_n^2 - c_1 d_1\left(n^2 + 1\right)\omega_n^4 = 0\end{aligned} \tag{10}$$

Equation (10) is a quadratic equation in ω_n^2 and hence two frequency values are associated with each value of n. The smaller value of ω_n^2 corresponds to the flexural mode, and the higher value corresponds to the thickness – shear mode. In equations (5) and (10) n must be an integer with a value greater than 1. As for the previous case, the flexural modes of the ring can be determined from the relation (6).

3. The finite element representations

In this section the discrete models of the system under study are formulated using the finite element technique (ANSYS code). These FE models are treated as an approximation of the exact system given by the equations (7) and (10), respectively. To find the eigenpairs (eigenvalue, eigenvector) related to the natural frequencies and natu-natural mode shapes of the ring with elastic foundation, the block Lanczos method is employed [3]. The essential problem of this section is prepared the FE model of the elastic foundation. The first FE model is realized as follows. The foundation is modelled by a finite number of massles spring distributed along the ring in the radial direction. In this model the foundation only in the radial direction is taken into consideration. The spring – damper (combin) element defined by two nodes is employed to realize the elastic layer. The element damping capability are neglected. The proper value of the stiffness moduls k_S of each spring is selected experimentally to minimize the frequency error defined by [3, 4]

$$\varepsilon_n = \left(\omega_n^f - \omega_n^c\right) / \omega_n^c \cdot 100\% \tag{11}$$

where ω_n^f and ω_n^c are the natural freqencies of the FE and precise models, respectively. Ring is modelled as the solid body with by taking into account the structural geometry of the ring. The eight node hexahedron element (solid185) with three degrees of freedom in each node is employed to realize the ring. The prepared model consists of 3744 solid elements, and 288 combin elements, respectively.

a) b)

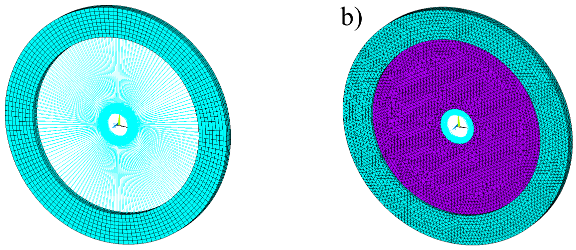

Figure 2. (a) first finite element model, (b) second finite element model

In the second FE model case, both ring and foundation are modelled as the massless solid body with allowing for the structural geometry of the system. The ten node tetrahedral element (solid187) with three degrees of freedom in each node is used to solve the problem. The prepared model is shown in Fig. 2b and it includes 41740 solid elements.

4. Numerical analysis

Numerical analysis results of the circular ring interacting with elastic foundation free vibration are obtained using the models suggested earlier. For all results presented here, the first seven natural frequencies and mode shapes are discussed and compared for these models.

Table 1. Parameters characterizing the circular ring with foundation

d_0 [m]	s_0 [m]	R [m]	d_{if} [m]	I_1 [m^4]	A [m^2]	ρ [kg/m^3]	E [Pa]	ν	k’
0.025	0.008	0.0875	0.03	$1.0417 \cdot 10^{-8}$	$2 \cdot 10^{-4}$	$7.83 \cdot 10^{3}$	$2.08 \cdot 10^{11}$	0.3	5/6

In order to evaluate the accuracy of the ring FE models, in the first instance for each case, the computation for the free ring without the foundation (i.e. $k_f = 0$ and $k_p = 0$) are executed. Table 1 displays the parameters characterizing the system under investigation. In Table 1, d_0 and s_0 are, respectively, the depth and width of the ring; v is the Poisson ratio; d_{if} is the inner diameter of the foundation area.

Table 2. Natural frequencies of the system under study ω_n [Hz]

n / k_f [N/m^2]	2	3	4	5	6	7	8
the exact solution							
0	1982	5296	9483	14243	19373	24739	30254
$6\cdot10^7$	2149	5361	9516	14262	19385	24747	30259
$4\cdot10^9$	7077	8619	11482	15468	20152	25249	30592
the thin ring solution							
0	2074	5868	11252	18197	26695	36742	48337
$6\cdot10^7$	2254	5942	11293	18223	26712	36755	48347
$4\cdot10^9$	7488	9626	13693	19833	27849	37595	48991

At first to evaluate the first ring FE model the computation for the system with the foundation in the radial direction only (i.e. $k_f \neq 0$ and $k_p = 0$) are executed. For the exact model the natural frequencies are determined from numerical solution of the frequency equation (10). For the thin ring model the results are achieved from solution of Eq. (5). The results of calculation of the natural frequencies are shown in Table 2. For each case of k_f the difference between the results of the exact model and the results of the thin ring model grow in parallel with the increase of the number of the natural frequencies.

Table 3. Results of computation related to the first FE model

k_f [N/m^2]	k_S [N/m]	2	3	4	5	6	7	8
natural frequencies of the system under study ω_n [Hz] (the first FE model)								
0	0	2008	5384	9673	14575	19888	25475	31246
$6\cdot10^7$	$4.9\cdot10^4$	2088	5418	9691	14587	19897	25482	31251
$4\cdot10^9$	$6.8\cdot10^6$	6827	8751	11911	16133	21037	26366	31962
frequency error ε_n [%] (the first FE model)								
0	0	1.31	1.66	2	2.33	2.66	2.98	3.28
$6\cdot10^7$	$4.9\cdot10^4$	-2.84	1.06	1.84	2.28	2.64	2.97	3.28
$4\cdot10^9$	$6.8\cdot10^6$	-3.53	1.53	3.74	4.3	4.39	4.42	4.48

Table 4. Results of computation related to the second FE model

n / k_f [N/m^2]	2	3	4	5	6	7	8
natural frequencies of the system under study ω_n [Hz] (the exact solution)							
$9.82\cdot10^9$	10826	11885	13868	17079	21224	25966	31073
natural frequencies of the system under study ω_n [Hz] (the second FE model)							
0	2001	5358	9611	14458	19692	25175	30813
$9.82\cdot10^9$	8692	12916	17221	21801	26665	31749	36984

frequency error ε_n [%] (the second FE model)							
0	0.96	1.17	1.35	1.51	1.65	1.76	1.85
$9.82{\cdot}10^9$	-19.71	8.67	24.18	27.65	25.64	22.27	19.02

Table 3 shows the result obtained for the first FE model case. For each value of k_f (with the exception of $k_f = 0$) the best compatibility with exact solution is obtained for natural frequency ω_3. Results presented in Table 4 are achieved by using the second FE model case. In this instance the results for $k_f = 0$ are better than in the first FE model case. The remaining results related to the second FE model case are compared with exact solution obtained with taking into account the additional foundation in the tangential direction ($k_p = 6{\cdot}10^6$ [N/m^2]). These results are not satisfactory. Too large differences between the achieved results are noticable.

5. Conclusions

Based on the classical theory of vibrating rings, a comprehensive study of the free in – plane flexural vibration analysis of thin and thick rings interacting with the Winkler elastic foundation is investigated. The separation of variables method is applied to solve the eigenvalue problem. Two FE models of the system under consideration are investigated. The numerical solution results demonstrated that further investigations related to the rings interacting with foundation are needed.

References

1. R. Bogacz, S. Dżuła, *Dynamics and stability of a wheelset/track interaction modelled as nonlinear continuous system*, Machine Dynamics Problems, **20** (1998) 23-34.
2. R. Bogacz, S. Noga, *Free vibration of the Timoshenko beam interacting with Winkler foundation*, in: Proceedings of the XVIIIth PTSK Conference, Zakopane, September 26-28, (2011) 14-17.
3. T. Markowski, S. Noga, S. Rudy, *Modelling and vibration analysis of some complex mechanical systems*, In: Baddour N., Recent advances in vibrations, Intech open access publisher, Rijeka, (2011) 143-168.
4. S. Noga, *Free transverse vibration analysis of an elastically connected annular and circular double – membrane compound system*, J. Sound Vib., **329** (2010) 1507-1522.
5. S. Noga, *Free vibrations of an annular membrane attached to Winkler foundation*, Vibrations in Physical Systems, vol. XXIV (2010) 295-300.
6. S. Rao, *Vibration of Continuous Systems*, Wiley, Hoboken 2007.
7. X. Wu, R. Parker, *Vibration of rings on a general elastic foundation*, J. Sound Vib., **295** (2006) 194-213.

XXV Symposium *Vibrations in Physical Systems,* Poznan – Bedlewo, May 15-19, 2012

The Dynamics of Interacting Solitons for the Korteweg-de Vries Equation

Michał OLEJNICZAK
Institute of Applied Mechanics, Poznan University of Technology
ul. Jana Pawła II 24, 60-965 Poznan, Poland, mi.olejniczak@gmail.com

Maciej BŁASZAK
Faculty of Physics, Adam Mickiewicz University
ul. Umultowska 85, 61-614 Poznan, Poland

Abstract

The aim of the paper is to give a new insight into the interaction of soliton particles and their dynamics. We introduce the definition of a soliton, soliton particles (interacting solitons) and a theorem about the decomposition of multi-soliton solutions to soliton particles. In the paper we also give a theorem state that the motion of maxima of interacting solitons (in a special case) are roots of fourth order polynomial.

Keywords: Solitons, Interacting Solitons, Dynamics

1. Introduction

Physics as a science engages in the research of a matter and a phenomenon in the natural way deals with the variance of quantity. When changes propagate in space and time we may talk about waves. Many phenomena such as light, sounds, earthquakes can be described by waves. In 1923 Louis de Broglie gave a hypothesis of the wave-type nature of particles that started a new paradigm and physics crowded Schrödinger equation.

In 1834 Scottish engineer John Scott Russel observed an odd wave in canal boats which propagate with constant speed without changing its shape. He called it 'a solitary wave'. After many years in 1895 Dieterlik Korteweg and Gustaw de Vries explained the strange wave. They found the equation of motion (this is a famous equation called nowadays KdV). Later on, in the twentieth century (1965) Gardner, Greene Kruskal and Miura discovered a method - the inverse scattering transformation of solving particular nonlinear equation (like the KdV). Soon after 1971, Ryogo Hirota proved the existence of the N-soliton solution of KdV.

The properties of solitons encouraged physicists to apply the model of particles. The first theory was Skyrme model that described the interaction of nucleons. Whereas Rybakov and Saha [12] constructed the model of hydrogen atom where electrons were presented as solitons – the solution of a certain nonlinear equation.

In this paper we will present the decomposition of the 2-soliton solution of KdV. We also study dynamics after decomposition (the so-called soliton particles or interacting solitons) and we will obtain numerically *position-time* chart (*x-t* chart). Finally, there will be given a theorem describing the motion of maximum of interacting solitons (in a special case) as the root of fourth order polynomial.

2. Dynamical Field Systems [5]

By the dynamical field system we understand a PDE's of the form

$$u_t = K(u, u_x, u_{xx}, ...) \tag{1}$$

where $u = u(x)$ is a point from manifold and K is a vector field on manifold. In the general case a variable u is a vector.

Nonlinear Hamiltonian field system is integrable when posses a bi-hamiltonian representations. The Hamiltonian vector field is called bi-hamiltonian when exists Poisson operators θ_0, θ_1 and function (functional) H, G that:

$$K(u) = \theta_0 \circ dH = \theta_1 \circ dG\ , \tag{2}$$

where d denotes differential.

For example, for famous equation KdV we have:

$$u_t = u_{xxx} + 6uu_x \tag{3}$$

$$u_t = K(u) = \theta_0 \circ dH(u) = \partial_x \circ \left(d\int \left(-\frac{1}{2}u_x^2 + u^3 \right) dx \right) = \tag{4}$$

$$= \theta_1 \circ dG(u) = \left(\partial_x^3 + 2u\partial_x + 2\partial_x u \right) \circ \left(d\int \left(\frac{1}{2}u^2 \right) dx \right) \tag{5}$$

Many nonlinear integrable systems posse soliton solution and for those systems which has N-soliton solution we can prove following theorem [5], [7].

Theorem 1 On the soliton submanifold hamiltonian vector fields K can be represented as

$$K(u_N) = \sum_i c_i B_i\ , \tag{6}$$

where B_i denotes eigenvector of recursion operator $\Phi(u) = \theta_1 \theta_0^{-1}$ (page 68 in [5]).

3. Solitons and soliton particles

Soliton [6] is the solution of the nonlinear differential equation (or the system of differential equations) which fulfils the properties below:

- the solution is a wave with a permanent shape,
- is localized, decayed or arrived with the constant value at infinity,
- strongly interacts with other solitons; they preserve their shape after a collision.

One of the more simple methods of obtaining the soliton solution from the nonlinear equation is a bilinear Hirota method [4], [9]. The formula of the two-soliton u_2 solution is expressed as

$$u_2 = 2\partial_x^2 \ln(F(x,t)), \qquad F(x,t) = 1 + e^{\eta_1} + e^{\eta_2} + A_{12} e^{\eta_1 + \eta_2} \tag{7}$$

where $\eta_i = 2\chi_i\left(x + q_i + 4\chi_i^2 t\right)$, $\chi_i = \frac{1}{2}\sqrt{c_i}$, q_i – velocity and the asymptotic phase, $i \in \{1,2\}$, A_{12} - an interaction parameter.

The equation interaction parameter for KdV is equal to

$$A_{12} = \left(\frac{\chi_1 - \chi_2}{\chi_1 + \chi_2}\right)^2 \tag{8}$$

The interacting soliton $u^{(i)}$, (or soliton particle) [3] is defined by

$$\partial_x u^{(i)} = B_i \ , \tag{9}$$

In particular for a 2-soliton solution there is: $B_i = \partial_{q_i} u_2, i = 1,2$. From the previous consideration we have the following implications:

$$\partial_x u^{(i)} = B_i \to u^{(i)} = \partial_x^{-1} B_i \to_{(\text{from}\,\mathit{Theorem}\,1)} \to u^{(i)} = \partial_x^{-1}\partial_{q_i} u_2 \tag{10}$$

The last expression in (10) with the arbitrary value of an interaction parameter enables obtained for $u_2 = u^{(1)} + u^{(2)}$ following figures 1, 2 (compare to [8]).

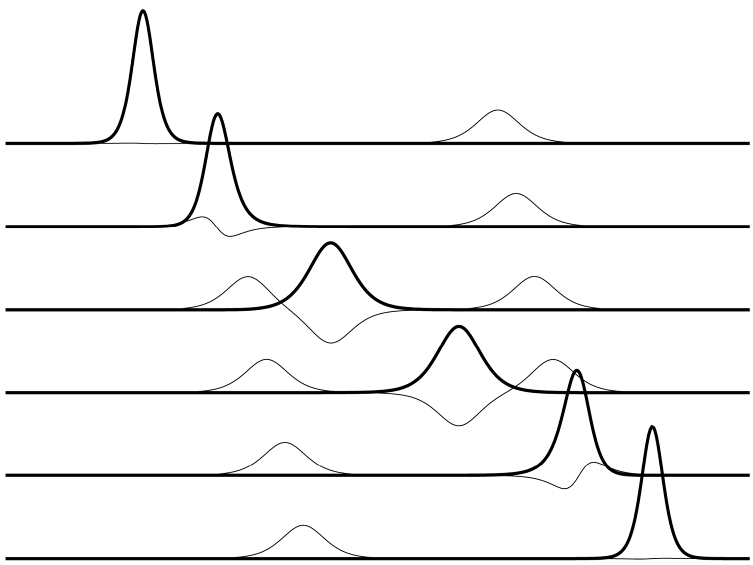

Figure 1. Evolution in time 2 soliton particles $u^{(1)}$, $u^{(2)}$ with $A_{12} = \exp(-20)$ – bold line $u^{(2)}$, thick line $u^{(1)}$

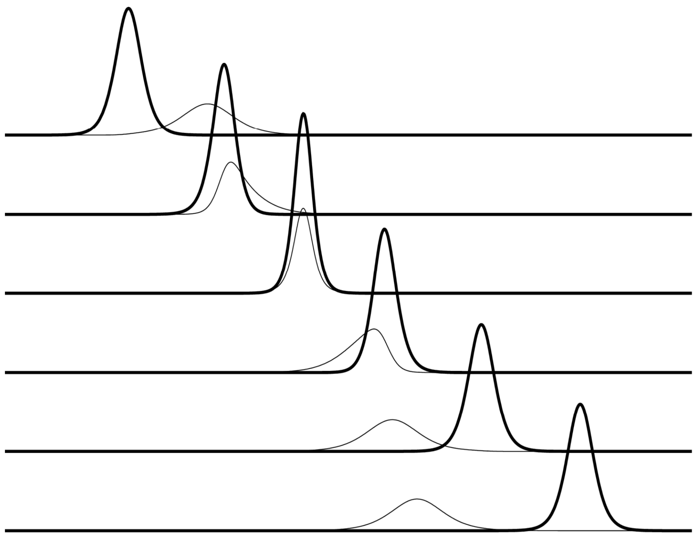

Figure 2. Evolution in time 2 soliton particles for $u^{(1)}$, $u^{(2)}$with $A_{12} = \exp(5)$ – bold line $u^{(2)}$, thin line $u^{(1)}$

4. Dynamics of interacting solitons

By dynamics of interacting solitons we understand motion of peaks (extremes) in time. This problem (for 2-soliton solution) comes down to determinate root of following equation

$$\partial_x u^{(1)}(x,t) = 0, \qquad \partial_x u^{(2)}(x,t) = 0\,. \tag{11}$$

In the case of KdV, (7) with $k_1 = 1$, $k_2 = 2$, $q_1 = q_2 = 0$, results are set in Fig. 3. The numerical computation was done in Maple by means of RealDomain [Solve] command.
In addition, the trajectory of a minimum (curve b) has been also obtained by the analytical method:

$$x(t) = -4\chi_2^2 t + \frac{1}{2\chi_2}\ln\left(\frac{\chi_2 + \chi_1}{\chi_2 - \chi_1}\right) - q_2, \qquad \text{for } \chi_2 > \chi_1 > 0 \tag{12}$$

or

$$x(t) = -4\chi_1^2 t + \frac{1}{2\chi_1}\ln\left(\frac{\chi_1 + \chi_1}{\chi_2 - \chi_1}\right) - q_1, \qquad \text{for } \chi_1 > \chi_2 > 0\,. \tag{13}$$

Finally, in the case $\chi_2 = 2\,\chi_1$ it can be shown that the trajectories of maxima of a slower particle have roots of fourth order polynomial (14).

$$\begin{aligned}&u^4 + 6e^{-8\chi_1^3 t - 2q_1\chi_1}u^3 + 9\left(3e^{-16\chi_1^3 t - 4q_1\chi_1} - e^{-64\chi_1^3 t - 4\chi_1 q_2}\right)u^2 + \\ &-18e^{-72\chi_1^3 t - 4\chi_1 q_2 - 2q_1\chi_1}u - 27e^{-80\chi_1^3 t - 4\chi_1 q_2 - 4q_1\chi_1} = 0\end{aligned} \tag{14}$$

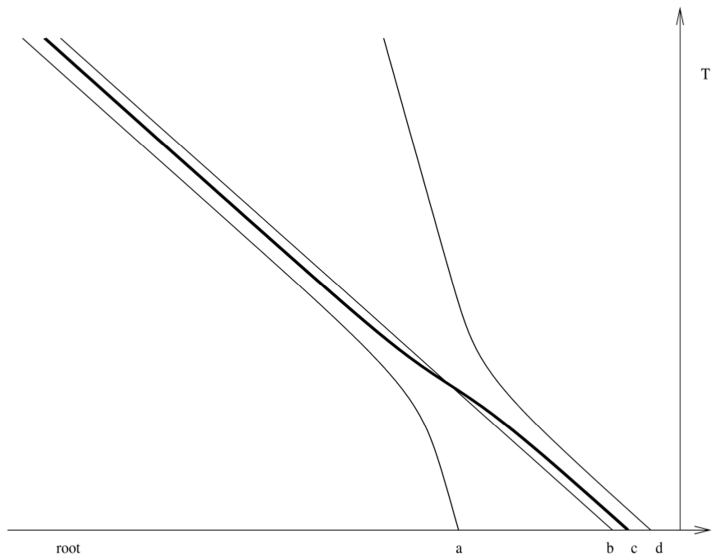

Figure 3. Chart *x-t* for KdV with (8) – bold line - maximum $u^{(2)}$, thin lines – extremes $u^{(1)}$ (3 curves a, b, d, two maxima, one minimum)

5. Conclusions

Various the decomposition of the soliton solution is known from the literature [2], [3], [8], [11]. Nevertheless, the one represented in the paper seems to be more natural than the other (Theorem 1) [8], as its origin is of geometric nature (eigenvector of Φ^*). Assuming the arbitrary value of interaction parameter, it reveals a very interesting phenomenon (figure 1, 2) which can be the new understanding of interaction mechanics.

The authors hope that the presented results will give a new insight. Furthermore, potential applications and the obtained formulas (12), (13), (14) will be helpful to connect the infinite dimensional manifold with the finite dimensional manifold (the differential equation of soliton particles trajectory).

Acknowledgments

The first author contributed to the work presented the paper as a part of a master thesis. He also wishes to thank his supervisor Maciej Błaszak for an interesting theme and guidance. The first author also would like to thank Anita Uściłowska for the motivation and encouragement to write this article.

References

1. Mark J. Ablowitz, Harvey Segur, *Solitons and the Inverse Scattering Transform*, SIAM Studies in Applied Mathematics, 1981
2. Nicholas Benes, Alex Kasman, Kevin Young, *On decomposition of the KdV 2-soliton*, Journal of Nonlinear Science, 16(2):179-200, April 2006
3. Maciej Błaszak, *On interacting solitons*, Acta Phys. Polon, A74:439, 1988
4. Maciej Błaszak, *Theory of classical soliton particles*, UAM Press, 1989
5. Maciej Błaszak, *Multi-Hamiltonian Theory of Dynamics Systems*, Texts and Monographs in Physics, Springer-Verlag, 1998
6. P.G. Drazin, R.S. Johnson, *Soliton: an introduction/ P.G. Drazin/R.S. Johnson*, Cambridge University Press, Cambridge, New York 1989
7. Benno Fuchssteiner, *The Lie algebra structure of nonlinear evolution equations admitting infinite dimensional abelian symmetry group*, Progress of Theoretical Physics, 65(3), March 1981
8. Benno Fuchssteiner, *The dynamical behaviour of interacting solitons, In Nonlinear Evolutions*, pages 13-32, World Scientific Publishers, 1988
9. J. Hietarinta, *Introduction to the Hirota bilinear method*, August 1997
10. Peter J. Olver, *Applications of Lie group to differential equations*, Springer, 2 editions, 1993
11. John Parkers, Fiona Campbell, *The internal structure of two-soliton solution to nonlinear evolutions equations of a certain class*, SOLPHYS, 1997
12. Y. P. Rybakov, B. Saha, *Soliton model of atom*, Foundation of Physics, 25:1723-1731, December 1995.

XXV Symposium *Vibrations in Physical Systems,* Poznan – Bedlewo, May 15-19, 2012

Determining the Parameters of Response of a Discrete System to Stochastic Impulses

Agnieszka OZGA
AGH University of Science and Technology
The Faculty of Mechanical Engineering and Robotics
Department of Mechanics and Vibroacoustics
A. Mickiewicza 30 Ave. 30-059 Krakow, Poland, aozga@agh.edu.pl

Abstract

The paper discusses vibrations of a discrete system with damping, which are caused by impulses with a stochastic value of an impulse and stochastic moments of excitation of the movement. The analysis of the recorded trajectory of vibrations of the oscillator showed that the parameters of the system's responses to subsequent hits undergo changes. The changes of the parameters of the system depend on the duration of work of the oscillator, the intensity of the impulses as well as the temperature of the environment. The study attempts to approximate these changes so that it becomes possible to determine the distribution of stochastic impulses.

Keywords: stochastic impulses, stochastic moments, distributions of impulses

1. Introduction

Methodology by which the distributions of the values of stochastic impulses forcing vibrations of discrete mechanical systems are determined has been presented in the works [1-6]. In the present study a fragment of the above mentioned methodology, namely an approximation of a trajectory recorded during an experiment, which allows for determining of stochastic moments m_n from the motion trajectory of the vibrating system, will be discussed in detail. For $t\to\infty$

$$m_n \cong \frac{1}{k}\sum_{i=1}^{k} x^n\left(ih\right) \tag{1}$$

where:

- $m_n(x)$ is the n-th stochastic moment of the random variable x,
- x is the deviation the mechanical system from the balanced position,
- h is the interval of time between successive measurements.

The problem under consideration is the vibration of a discrete system with damping forced by a series of random impulses. An analysis of vibrations of such a system poses several challenges to the researcher. One of them consists in execution of impulses in a physical system. Another one is approximation of responses of the physical system to a single impulse so that the difference between particular stochastic moments m_n computed from the experiment and from the model is as small as possible. Another difficulty [6] that occurs during an experiment with an RLC system involves the parameters of the system's response to stochastic forcing, which change during the movement. Hence the approximation of the response of the system must be performed separately for each trajectory

2. Approximation of vibrations of a discrete system with damping forced by a single impulse

With the help of a detailed analysis of the character of the load and the response of the oscillator to this load we construct a model of a system that includes substitute rigidity with a definite elasticity constant *k*, substitute damping *c* with the force response proportional to the relative velocity, and substitute mass *M*. Free vibrations of the system are recorded with linear differential equations

$$M\ddot{x}(t) + c\dot{x}(t) + kx(t) = 0 \,. \tag{2}$$

A single hit is modeled [7-9] with the help of mathematical methods using the fact that its duration is much shorter than the duration of the system's own vibrations. This force *F(t)* is substituted with an impulse and recorded with the help of

$$F(t) = I\delta_t(t) \tag{3}$$

where δ_t is a Dirac distribution at t, $\delta_t = \delta(t-\tau)$, I – is the time-effect *F(t)* [9].

In the system which initially was at rest, the impulse [8] working in a short period of time causes an increase of velocity, and therefore the initial conditions assume the form $x(0) = 0,\ \dot{x}(0) = v_0 = I/M$. The parameters of the vibrations are selected so that we have to do with a case of subcritical damping $c/M < \sqrt{k/M}$. Taking into account the above assumptions, the system's vibrations forced by a single impulse have the form

$$x(t) = \frac{I}{M\varpi}\exp(-ht)\sin\left(\omega t\right) \tag{4}$$

where *h=c/2m,* $\varpi = \sqrt{\left(k/m\right)^2 - h^2}$, t is present time.

Using electromechanical analogy, the vibrations of a system forced by a single impulse and by a series of impulses will be executed in an RLC system. A detailed description of the experiment can be found in the studies [4, 6]. The single impulse is executed with the help of single samples of the shortest executable duration of $2\cdot10^{-6}$ s, issuing from the sampling rate of the card NI USB-6251.

Unfortunately, the physical system does not fully satisfy the mathematical assumptions. During the impulse the condenser is being charged (Fig. 1), thus the first sample should be excluded from the data assigned for approximation. Additionally, the recoded signal is burdened with a certain imprecision of measurements.

An approximation of the recorded course is aimed at minimizing of the differences between the stochastic moments calculated from the trajectory of motion taken from the experiment m_{nE} and the model m_{nM}, and it is executed in the MATLAB environment with the help of the function *fit* with the following parameters: '*fourier1*' and '*exp1*'.

In order to minimize the difference fragments of the recorded course were taken into account, due to the noises whose impact increases with the damping of the vibrations (Fig. 1).

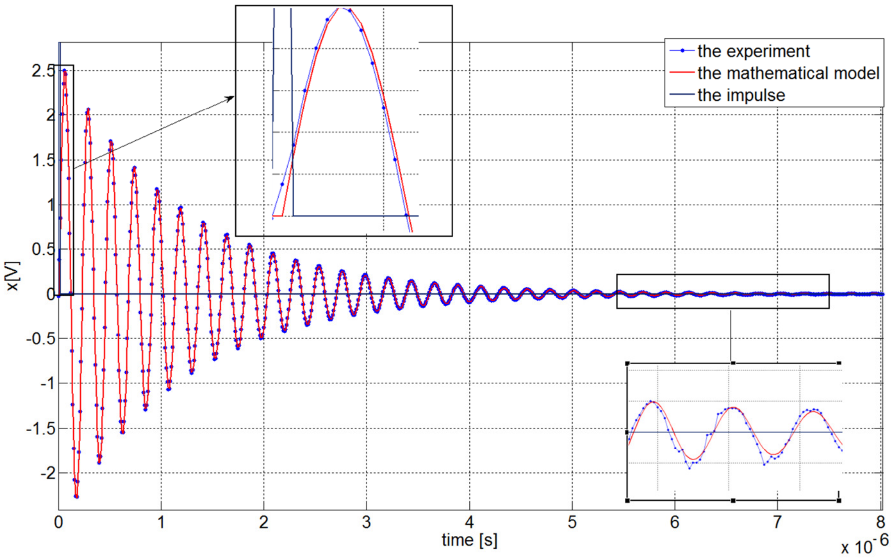

Figure 1. Approximation of the system's response to a single impulse of the value 10[V] for RLC oscillator with capacity C= 2 [nF] and inductivity L=5[mH] that was applied

The calculations that allow for estimation of the impact of the noise on the first two stochastic moments for the system whose approximation is shown in Fig. 1 have been presented in Table 1.

Table 1. An analysis of values for the first and second stochastic moments

Number of elements in the analyzed sample	**900**	**800**	**700**	**600**	**500**	**400**
$\mathbf{m_{1M}}$	0.0104	0.0117	0.0134	0.0157	0.0187	0.0234
m_{1M} - m_{1E}	1.49e-005	-5.23e-006	-3.15e-005	-1.14e-004	-1.44e-004	-4.38e-004
$\mathbf{m_{2M}}$	0.2272	0.2556	0.2921	0.3408	0.4089	0.5106
$m_{2M} - m_{2E}$	-4.94e-004	-5.56e-004	-6.35e-004	-7.39e-004	-8.78e-004	-0.0010

The largest deviations from the actual value occur at m_1, since its value is the least. Hence the greatest difficulties occur at determining of the first stochastic moment. The vibrations of the system decay after 900 measuring samples and all those samples are significant for determining of the moments. Noises occur as early as the 600th measuring sample and if the samples carrying the error are taken into account in the analysis, the difference between m_{1M} and m_{1E} increases ten times. This is a serious difficulty since the subsequent impulse may occur before the former one decays. The higher the intensity of hits is the greater is the error connected with the search for the minimum of m_{IM} - m_{IE}. To cope with this difficulty it is necessary to approximate the responses of the system to all those fragments of trajectory that undergo summation.

3. Movement of a discrete system forced by stochastic impulses.

When the system (1) is forced by stochastic impulses in the form

$$f(t) = \sum_{t_i < t} \eta_i \delta_{t_i} \tag{5}$$

where $\eta_i = I_i / M$, the trajectory of movement of the oscillator is a random variable.

For the following assumptions regarding the stochastic values of impulse η_i and stochastic moments of excitation of the movement of the oscillator t_i :
η_i , i=1,2… is a sequence of independent identically distributed random variables with finite expectation,
$\tau_i = t_i - t_{i-1}$, i=1,2… is the time between two impulses, which is a sequence of independent identically distributed random variables with exponential distribution

$$F(x) = \begin{cases} 1 - \exp(-\lambda x) & \text{if } x \geq 0 \\ 0 & \text{if } x < 0 \end{cases} \tag{6}$$

where the constant λ is the intensity of impulses and sequences $\{t_i\}_{-\infty}^{\infty}, \{\eta_i\}_{-\infty}^{\infty}$ are stochastically independent. The movement of an oscillator with damping *x(t)* is already a stationary process for large *t* [3]. The movement of an oscillator with damping excited by stochastic impulses is expressed by the formula

$$x(t) = \frac{1}{\omega} \sum_{t_i < t} \eta_i \exp(-h(t - t_i)) \sin\left(\omega(t - t_i)\right) \tag{7}$$

The process (7) is also ergodic [5], therefore it is possible to determine the stochastic moments from a single trajectory of movement. Meanwhile the experiments carried out for an RCL system record the parameters of the system's response to the stochastic forcing, which change during the movement. These changes depend on the duration of work of the oscillator, the intensity of the impulses as well as the temperature of the environment. Finding of substitute parameters of the system's response, which could be used in a mathematical model presented above is possible [6] for low intensities of the hits. They should be determined on the basis of stochastic moments calculated from the trajectory of movement of the physical system. For high intensities of the hits the phenomenon of change of the substitute parameters of the system's response (Fig. 2) can be seen after a time.

The same substitute parameters *ω* and *h* were used in the model during the approximation of the whole course. It can be noticed (Fig. 2) that they determine the first stochastic moment correctly only for the fragment of the course of vibrations between the 25th and 35th second of movement, where the difference between m_{1M} - m_{1E} is close to zero.

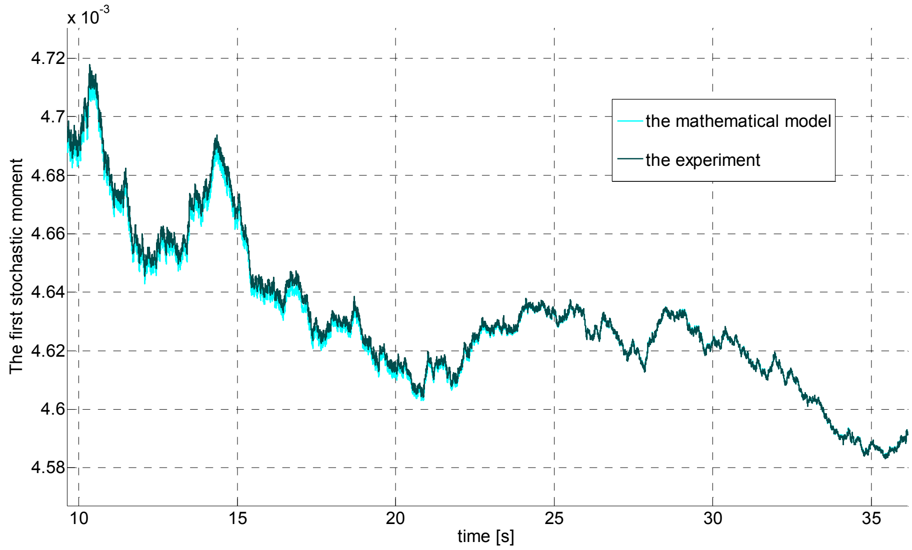

Figure 2. The first moment for an RLC oscillator with capacity C= 2 [nF] and inductivity L=5[mH] and for λ=500

4. Conclusions

The paper discusses the problems encountered by researchers while analyzing the vibrations of a system forced by stochastic impulses. The models used by scientists [2-3, 10-13] are described with the help of linear differential equations and the interpretation of the data obtained in experiments indicates that the vibrations of the systems are nonlinear. The nonlinear model of this phenomenon is an open problem now. Substituting it with a linear model allows for a description and interpretation of the physical phenomenon for low intensity of impulses. For certain systems with high intensity of hits the linear model is merely an approximation of a certain fragment of the trajectory, often too small to be used for determining of distributions of values of stochastic impulses.

Acknowledgments

This work has been financed by the Polish Ministry of Science and Higher Education, research project No. N N501 180636

References

1. M. Jabłoński, A. Ozga, *On statistical parameters characterizing vibrations of damped oscillator forced by stochastic impulses*, Archives of Acoustics, **31**(4 suppl.) (2006) 65-73
2. M. Jabłoński, A. Ozga, *The influence of numerical errors on determining the distribution of values of stochastic impulses forcing an oscillator Mechanics and Control* AGH University of Science and Technology. Faculty of Mechanical Engineering and Robotics, Commission on Applied Mechanics of Polish Academy of Sciences. Cracow Branch, **29(**4) (2010) 163-168.
3. M. Jabłoński, A. Ozga, *Distribution of stochastic impulses acting on an oscillator as a function of its motion*, Acta Physica Polonica A, **118**(1) (2010) 74-77, 2010
4. M. Jabłoński, A,. Ozga, T. Korbiel, P. Pawlik, *Determining the distribution of stochastic impulses acting on a high frequency system through an analysis of its vibrations*, Acta Physica Polonica A, Warszawa; **119**(6A) (2011) Acoustic and biomedical engineering 977-980
5. M. Jabłoński, A. Ozga, *The role of ergodicity in the search for the stochastic distribution of impulses forcing the motion of linear systems*, 10th Conference on Active noise and vibration control methods MARDiH: Krakow-Wojanow 2011.
6. M. Jabłoński, A. Ozga, *Determining the distribution of values of stochastic impulses acting on a discrete system in relation to their intensity*, Acta Physica Polonica A, Warszawa; **121**(1-A) (2012) Acoustic and biomedical engineering. 175A–179A.
7. J. Awrejcewicz, *Drgania deterministyczne układów dyskretnych* [Deterministic vibrations of discrete systems], WNT, Warszawa 1996
8. S. Kaliski, *Drgania i fale* [Vibrations and Waves], Mechanika Techniczna, t. III, PWN, Warszawa 1986.
9. Z., Osiński, *Teoria Drgań* [Theory of Vibrations], PWN, Warszawa 1980.
10. J.B. Roberts, *On the response of a simple oscillator to random impulses*, Journal of Sound and Vibration, **4** (1966) 51-61.
11. J.B. Roberts, *Distribution of the Response of Linear Systems to Poisson Distributed Random Pulses*. Journal of Sound and Vibration, **28** (1973) 93-103
12. J.B. Roberts, P. D. Spanos, *Stochastic averaging: An approximate method of solving random vibration problems*, International Journal of Non-Linear Mechanics **21** (1986) 111-134
13. A. Tylikowski, W. Marowski, *Vibration of a nonlinear single degree of freedom system due to Poissonian impulse excitation*, International Journal of Non-Linear Mechanics, **21**(1986) 229-238.

XXV Symposium *Vibrations in Physical Systems,* Poznan – Bedlewo, May 15-19, 2012

Multilevel Vibration Control System of Aviation Gas-Turbine Engines

Oleksij PAVLOVSKIY
National Technical University of Ukraine "Kiev Polytechnic Institute"
37 Peremogy Pr., Kyiv, Ukraine, a_pav@ukr.net

Nadiia BOURAOU
National Technical University of Ukraine "Kiev Polytechnic Institute"
37 Peremogy Pr., Kyiv, Ukraine, burau@pson.ntu-kpi.kiev.ua

Laslo IATSKO
Joint-Stock Company Scientific and Technical Enterprise "Electronprylad"
27/29 Vandy Vasilevscoy Str., Kyiv, Ukraine, iatsko@i.ua

Abstract

This work is devoted to the development a new multilevel vibration control system of aviation gas-turbine engines (GTE). The bases of the new system are: existing aboard vibration control system for current control and awareness about actual levels of vibration at the harmonics of the rotor rotation (main level); complementary dedicated microcontroller for analysis of “normal vibration” in order to predict or detect small damages of engine systems and details (auxiliary level); signal processing methods for damages diagnosis and decision making about GTE condition. The efficiency of the proposed system and using the signal processing methods is demonstrated by the results of computer simulation of the processes of receiving the information about the GTE vibrating condition, transformation and analysis of it at the main and auxiliary levels.

Keywords: vibration control, gas-turbine engine, dedicated microcontroller, signal processing

1. Introduction

The aircraft gas-turbine engines (GTE) are characterized by the structure and operation complexity. The problem of prolongation of GTE working life and increasing their reliability is the issue of the day. This problem may be solved using the improved existent and new methods and diagnostic instruments. We propose to solve this problem by using the improved techniques of the vibration control system, since the most critical damages of the GTE rotor components are directly connected with the vibration processes which take place in an operating engine. On the other hand, vibration and vibroacoustical methods provide a possibility to diagnose and non-destructive evaluate defects without disassembling the engine [1].

There are many sources of vibration and noise in the GTE, such as the rotor vibration caused by unbalance of rotor elements; turbine and compressor stages; gearboxes; bearings; aerodynamic oscillations; vibration in a gas-air path. The rotating rotor is a basic source of mechanical vibration. It generates vibration on the basic rotor harmonic (it is equal to a rotor rotational frequency) and on multiple harmonics. The character of change of rotor vibration is determined by the inertia-elastic properties of system "rotor-case" at rotational frequency change. The amplitudes of vibration depend on the unbalance magnitude, damping and a relationship of the critical and working rotational frequencies. The amplitudes of rotor vibration components can change considerably in case of change of a rotational frequency at the non-steady-state modes of GTE [1].

The rotor harmonics are the most informative components of a spectrum of the engine vibration. Their levels are analyzed for the estimation of a vibration condition of the GTE. The existing aboard vibration control system is intended for the current control and awareness about the actual levels of vibration at the harmonics of the rotor rotation.

However, many dangerous phenomena (unbalance, unstable oscillatory modes, non-stationary vibration perturbations, etc.) result in occurrence of components on higher rotor harmonics in a spectrum of GTE vibration, while the origination of initial defects of rotor elements (microcracks of shafts, blades, disks) practically do not generate changes in a spectrum of vibration and cannot be detected at early stages of the crack development.

The purpose of this work is the development a new multilevel vibration control system of aviation GTE for the enhancement of sensitivity and diagnostic accuracy.

2. System development

The block scheme of the developed system is shown in Fig. 1.

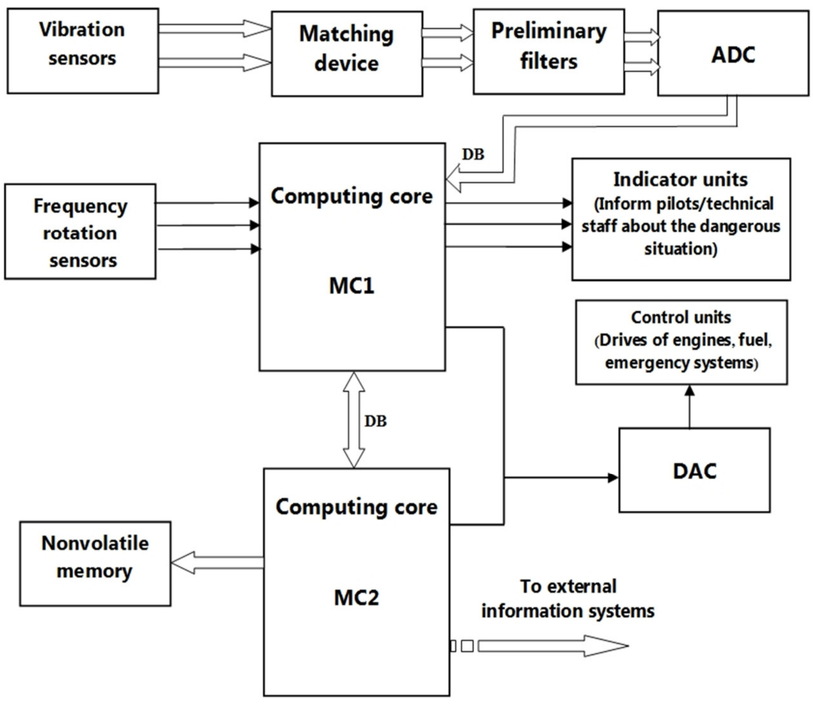

Figure 1. Block scheme of the vibration control system

Generally, the developed vibration control system consists of the following components:

- existing aboard vibration control system for the current control and awareness about the actual levels of vibration at the harmonics of the rotor rotation (main level);
- complementary dedicated microcontroller for analysis of the "normal vibration" in order to predict or detect small damages of engine systems and details (auxiliary level);
- software for signal processing of "normal vibration" for damages diagnosis, prediction and decision making about GTE condition.

On the main level, the signals are conveyed from the sensors of vibration to the analogue-to-digital converter (ADC) after preliminary conversion and filtering, and then the digital data are conveyed to the microcontroller MC1 through the parallel data bus (DB). The signals from sensors of rotation frequency are also conveyed to the microcontroller MC1. The vibration data and signals of rotation frequency are used for determination of magnitudes of vibration on rotor harmonics. The value of current frequency of rotor rotation is used as the central frequency of the tracking band-pass filter for selection of vibration on rotor harmonics. The central frequency of the tracking band-pass filter is changing synchronously with the change of a rotational frequency on non-steady-state modes of GTE. For this purpose the executive signal with variable frequency comes to the digital entries of MC1. The received values of vibration (vibration velocity) on rotor harmonics are compared with the installed threshold values for making the decision on the current vibration condition of the GTE. First of all, the value of vibration is compared to the threshold value of the "dangerous vibration". Then, if the mentioned threshold value is not exceeded, the value of vibration is compared to the threshold value of the "excessive vibration". The signal about the current value of rotor vibration is conveyed to the informational panel of the pilot and, if the vibration signal exceeds the threshold value of the "dangerous vibration" or the "excess vibration", the signal is conveyed from the exit MK1 through a DAC to the engine control units.

The complementary level of the vibration control system is designated for the analysis of the "normal vibration" in order to predict or detect small damages of engine systems and details. For this purpose the complementary dedicated microcontroller MC2 is used with the special software for signal processing. We propose to use the following signal processing methods: a) preliminary Wavelet Decomposition (WD) of signals, and b) determination of spectrum and statistics for each component of WD. In order to detect the initial cracks in turbine engine blades, it is possible to use Higher-Order Spectral analysis and determination of Dimensionless Peak Characteristics [2]. The results of signal processing are conveyed to the external information networks and/or are saved in a non-volatile memory.

The principle of operation of the development system is explained by the algorithm in Fig. 2.

The efficiency of the proposed system and using the signal processing methods is verified by the results of computer simulation and the analysis of vibration at the main and auxiliary levels. The tracking band-pass filter with finite impulse response (equiripple filter [3]) is designed for the main level of the vibration control system. The amplitude-frequency characteristic of narrowband equiripple filter (central frequency of pass band is 100 Hz, minimal order is equal to 250, frequency rejection out of a pass band is 30 dB) is shown in Fig. 3.

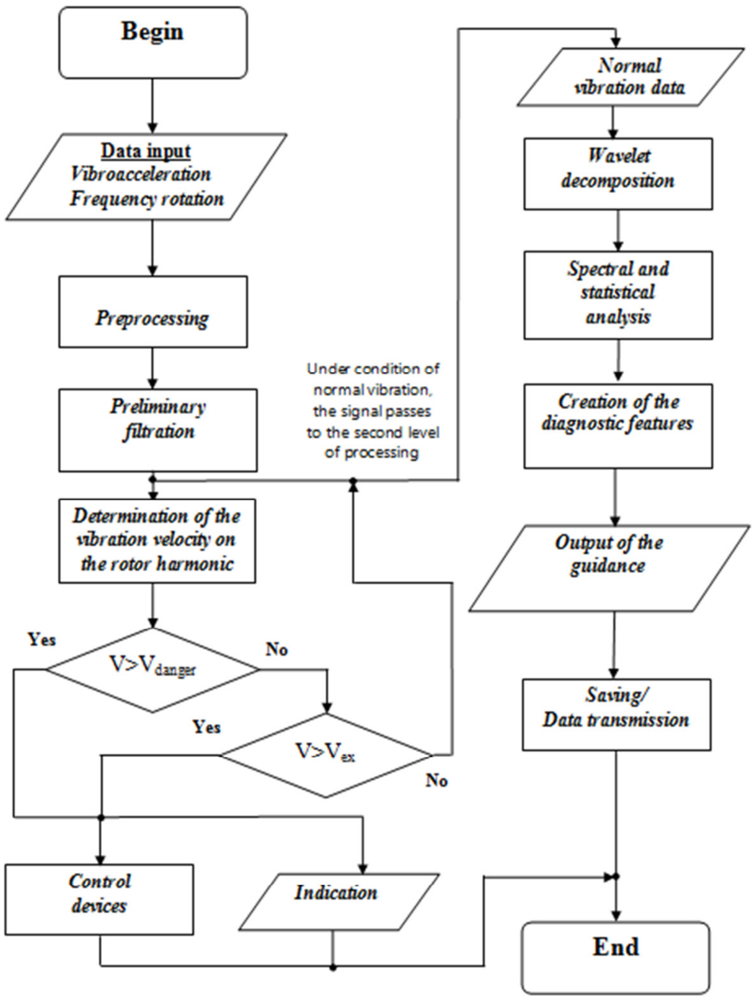

Figure 2. Algorithm of operation of the vibration control system

The software and user interface are designed for simulation and signal processing at the auxiliary level.We used the preliminary WD of vibration signals and signal of frequency rotation, spectral analysis and statistical analysis for auxiliary level. The wave-lets of Daubechies family db10 and 5 levels of decomposition are used for the preliminary WD. The results of WD are used as a sample from each decomposition level for the next spectral analysis and statistical analysis.

For instance, Fig.4 represents the user interface and the results of simulation and signal processing of vibration at the steady-state mode of GTE (constant value of the rotor rotation frequency).

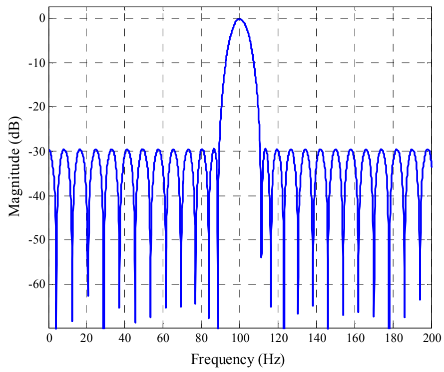

Figure 3. Amplitude-frequency characteristic of designed narrowband equiripple filter

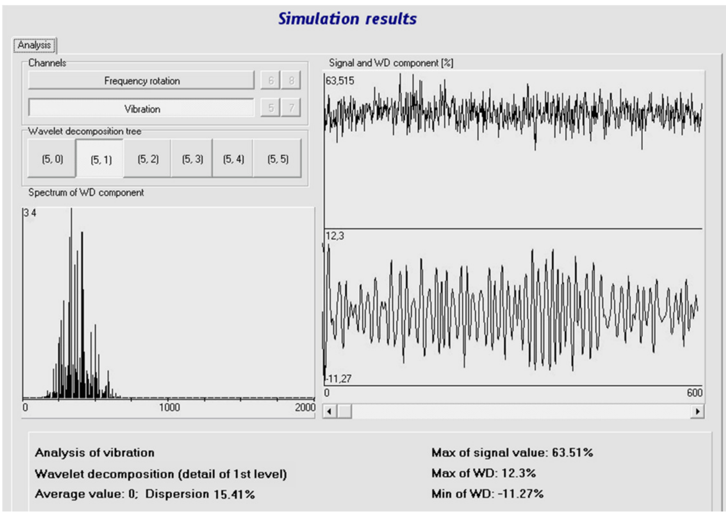

Figure 4. User interface and results of simulation and signal processing of vibration at the steady-state mode of GTE

As shown, the detail of the first level of WD is analyzed (pressed button (5,1)). Fig. 5 represents the user interface and results of simulation and signal processing of the rotor rotation frequency at the non-steady-state mode of GTE (fast increase of the rotor rotation frequency). The detail of the first level of WD is also analyzed in this instance.

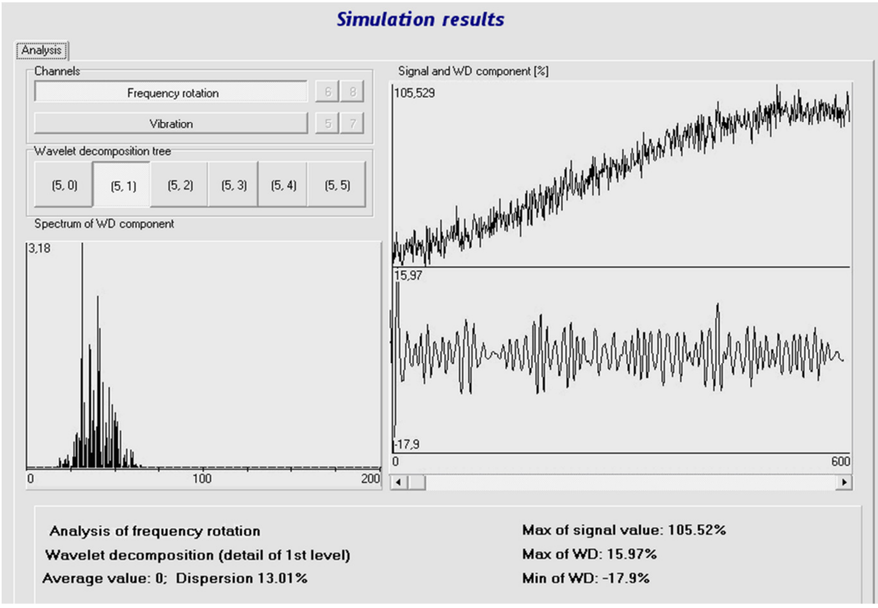

Figure 5. User interface and results of simulation and signal processing of the rotor rotation frequency at the non-steady-state mode of GTE

All time plots (signal and WD component) are represented in the relative scale on the ordinate axis (percentage of maximum value) and in seconds on the abscissa. The dimension of frequency is Hertz for plots of spectrum.

3. Conclusions

The developed multilevel system will allow ensuring the GTE current control and awareness and increasing the reliability and rapidity of detection of the initial damages when the vibration of the GTE is normal.

References

1. S. Doroshko, *The control and diagnosis of a technical condition of gas-turbine engines on vibration parameters*, Transport, Moscow 1984.
2. N. Bouraou, Iu. Sopilka, *Vibroacoustical diagnosis of the crack-like damages of aircraft engine blades at the steady-state and non-steady-state modes*, Vibrations in Physical Systems, **24** (2010) 69-74.
3. A. Sergienko, *Digital signal processing*, Piter, Snt. Petersburg 2006.

XXV Symposium *Vibrations in Physical Systems,* Poznan – Bedlewo, May 15-19, 2012

Experimental Verification of the Semi-Active Control Concepts for Torsional Vibrations of the Electro-Mechanical System Using Rotary Magneto-Rheological Actuators

Agnieszka PRĘGOWSKA, Robert KONOWROCKI, Tomasz SZOLC
Institute of Fundamental Technological Research of the Polish Academy of Sciences
Pawinskiego str. 5b, 02 -106 Warsaw, Poland
aprego@ippt.gov.pl, rkonow@ippt.gov.pl, tszolc@ippt.gov.pl

Abstract

In the paper semi-active control of torsional vibrations of the rotating machine drive system driven by an electric motor is performed by means of rotary actuators with the magneto-rheological fluid. The main purpose of these studies is a minimisation of vibration amplitudes in order to increase the fatigue durability of the most responsible elements, assure possibly precise motion of the driven machine working tool as well as to reduce a generated noise level. For suppression of steady-state torsional vibrations excited by dynamic external torques generated by the motor and by the driven object there are proposed control strategies based on a principle of optimum current damping coefficient values realized by the magneto-rheological fluid. The theoretical control concepts are experimentally verified using the laboratory test rig in the form of drive system co-operating with two asynchronous motors generating properly programmed driving and retarding electromagnetic torques.

Keywords: semi-active control, torsional vibrations, rotary actuators, magneto-rheological fluid

1. Introduction

Active vibration control of drive systems of machines, mechanisms and vehicles creates new possibilities of improvement of their effective operation. From among various kinds of vibrations occurring in the drive systems the torsional ones are very important as naturally associated with their fundamental rotational motion. Torsional vibrations are in general rather difficult to control not only from the viewpoint of proper control torque generation, but also from the point of view of a convenient technique of imposing the control torques on quickly rotating parts of the drive-systems. Unfortunately, one can find not so many published results of research in this field, apart of some attempts performed in [1] by active control of shaft torsional vibrations using piezo-electric actuators. But in such cases relatively small values of control torques can be generated and thus the piezo-electric actuators can be usually applied to low-power drive systems. In [2] there is proposed the semi-active control technique based on the actuators in the form of rotary actuators with the magneto-rheological fluid (MRF). In these actuators between the shaft and the inertial ring, which is freely rotating with a velocity close or equal to the system average rotational speed, the magneto-rheological fluid of adjustable viscosity is used. Such actuators generate control torques that are functions of the shaft actual rotational speed, which consist of the average component corresponding to the rigid body motion and of the fluctuating component caused by torsional vibrations.

The general target of this paper is an experimental verification of the presented in [2] theoretical concept of semi-active control of torsional vibration using the rotary actuators with the magneto-rheological fluid. Thus, for this purpose the proper test-rig has been built, using which the measurement results have been compared with theoretical ones determined by means of two mechanical models of identical structure as the real object.

2. Assumptions for the mechanical models and formulation of the problem

In the considered laboratory drive system imitating operation of the rotating machine power is transmitted from the servo-asynchronous motor to the driven machine tool in the form of electric brake by means of the two multi-disk elastic couplings with built-in torque-meters, electromagnetic overload coupling and by the shaft segments. Moreover, this system is equipped by two rotary magneto-rheological actuators and two inertial disks of adjustable mass moments of inertia and axial positions, which enable us to tune-up the drive train to the proper natural frequency values. The considered real laboratory drive system is presented in Fig. 1.

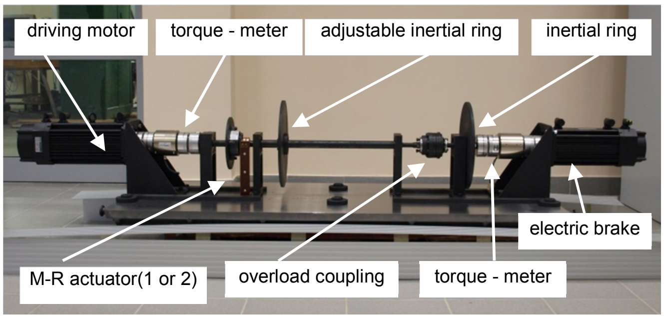

Figure 1. Laboratory drive system

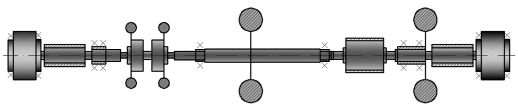
Figure 2. Mechanical model of the laboratory drive system

In order to perform a theoretical investigation of the semi-active control applied for this mechanical system, a reliable and computationally efficient mechanical model is required. In this paper dynamic investigations of the entire drive system are performed by means of two structural models consisting of torsionally deformable one-dimensional beam-type finite elements and rigid bodies, as shown in Fig 2. These are the discrete-continuous (hybrid) model and the classical beam finite element one. Both models are employed here for eigenvalue analyses as well as for numerical simulations of torsional vibrations of the drive train. In the hybrid model successive cylindrical segments of the stepped rotor-shaft are substituted by the cylindrical macro-elements of continuously distributed inertial-visco-elastic properties. However, in the finite element model these continuous macro-elements have been discretized with a proper mesh density assuring a sufficient accuracy of results. In the proposed hybrid and FEM model of the rotating machine drive system inertias of the inertial disks are represented by rigid bodies attached to the appropriate macro-element extreme cross-sections, which should assure a reasonable accuracy for practical purposes. Torsional motion of cross-sections of each visco-elastic macro-element in the hybrid model is governed by the hyperbolic partial differential equations of the wave type. Mutual connections of the successive macro-elements creating the stepped shaft as well as their interactions with the rigid bodies are described by equations of boundary conditions. These equations contain geometrical conditions of conformity for rotational displacements of the extreme cross sections. The second group of boundary conditions are dynamic ones, which contain equations of equilibrium for external and control torques as well as for inertial, elastic and external damping moments.

Similarly as in [2], the solution for forced vibration analysis has been obtained using the analytical - computational approach. Solving the differential eigenvalue problem and an application of the Fourier solution in the form of series in the orthogonal eigenfunctions lead to the set of uncoupled modal equations for time coordinates $\xi_m(t)$. In the assumed model the control damping torques genereded by one rotary actuator with the MRF can be regarded as the response-dependent external excitations. Then, by a transformation of them into the space of modal coordinates $\xi_m(t)$ and upon a proper rearrangements the following set of coupled modal equations is yielded:

$$\mathbf{M}_0\ddot{\mathbf{r}}(t) + \mathbf{D}(k_j(t), \dot{\mathbf{r}}(t))\dot{\mathbf{r}}(t) + \mathbf{K}_0\mathbf{r}(t) = \mathbf{F}(t, \dot{\mathbf{r}}(t)), \tag{1}$$

where $\mathbf{D}(\dot{\mathbf{r}}(t)) = \mathbf{D}_0 + \mathbf{D}_C(k_j(t), \dot{\mathbf{r}}(t)),\ j = 1,2.$

The symbols $\mathbf{M}_0$, $\mathbf{K}_0$ and $\mathbf{D}_0$ denote, respectively, the constant diagonal modal mass, stiffness and damping matrices. The full matrix $\mathbf{D}_C(k_j(t),\dot{\mathbf{r}}(t))$ plays here a role of the semi-active control matrix and the symbol $\mathbf{F}(t,\dot{\mathbf{r}}(t))$ denotes the response dependent external excitation vector due to the electromagnetic torque generated by the electric motor and due to the retarding torque produced by the driven imitated rotating machine. The Lagrange coordinate vector $\mathbf{r}(t)$ consists of the unknown time functions $\xi_m(t)$ in the Fourier solutions, $m = 1,2,\dots$. The number of equations (1) corresponds to the number of torsional eigenmodes taken into consideration in the range of frequency of interest. These equations are mutually coupled by the out-of-diagonal terms in matrix $\mathbf{D}$ regarded as external excitations expanded in series in the base of orthogonal analytical eigenfunctions. A fast convergence of the applied Fourier solution enables us to reduce the appropriate number of the modal equations to solve in order to obtain a sufficient accuracy of results in the given range of frequency. Here, it is necessary to solve only 6÷10 coupled modal equations (1), contrary to the classical one-dimensional rod finite element formulation leading in general to a relatively large number of motion equations in the generalized coordinates.

For the assumed analogous linear finite element model the mathematical description of its motion has the classical form of a set of coupled ordinary differential equations in general coordinates, which can be found e.g. in [2].

In order to develop a proper control algorithm for the given vibrating drive system the electromagnetic external excitation produced by the motor should be described possibly accurately. Thus, the electromechanical coupling between the electric motor and the torsional train ought to be taken into consideration. In the considered case of the symmetrical three-phase asynchronous motor, electric current oscillations in its windings are described by six voltage equations, transformed next into the system of four Park's equations in the so called '$\alpha\beta$-*dq*' reference system, form of which can be found e.g. in [3]. Then, the electromagnetic torque generated by such a motor can be expressed by the following formula

$$T_{el} = \frac{3}{2} pM\left(i_{\beta}^{s} \cdot i_{d}^{r} - i_{\alpha}^{s} \cdot i_{q}^{r}\right), \tag{2}$$

where M denotes the relative rotor-to-stator coil inductance, p is the number of pairs of the motor magnetic poles and i_α^s, i_β^s are the electric currents in the stator reduced to the electric field equivalent axes α and β and i_d^r, i_q^r are the electric currents in the rotor reduced to the electric field equivalent axes d and q, [3].

From the abovementioned system of voltage equations as well as from formula (2) it follows that the coupling between the electric and the mechanical system is non-linear in character, which leads to very complicated analytical description resulting in rather harmful computer implementation. Thus, this electromechanical coupling has been realized here by means of the step-by-step numerical extrapolation technique, which for relatively small direct integration steps for motion equations results in very effective, stable and reliable computer simulation.

4. Computational and experimental example

The experimental investigations are going to be carried out by means of the described above test-rig equipped with the proper measurement-control system, the scheme of which is presented in Fig. 3. This system consists of the voltage amplifier controlled by the real-time computer using the appropriate converting system. Such measurement-control system enables us to monitor and register all results of measurements using the control-communication unit by means of the TCP/IP protocol. Basing on the obtained on-line measurement results of the dynamic torques transmitted by the shown in Fig 1 shaft segments adjacent to the torque-meters, the properly developed control algorithm determines in real time the current values of damping coefficients of the magneto-rheological fluid in both rotary actuators.

The measurement results of dynamic torsional responses have been registered for the steady-state operating conditions at constant nominal rotational speeds, respectively for the passive (without control) and semi-actively controlled drive system excited by the harmonic fluctuating component of the retarding torque within the frequency range 0-150 Hz. Fig. 4 presents exemplary time-histories obtained for the passive system (grey line) and the semi-actively controlled one (black line), both for the excitation frequency 54 Hz corresponding to the first natural system frequency. In Fig. 5 there are shown plots of dynamic response amplitudes of the passive (grey line) and semi-active system (black line) determined by means of measurements, Figs. 4a, and by numerical simulations, Fig. 4b.

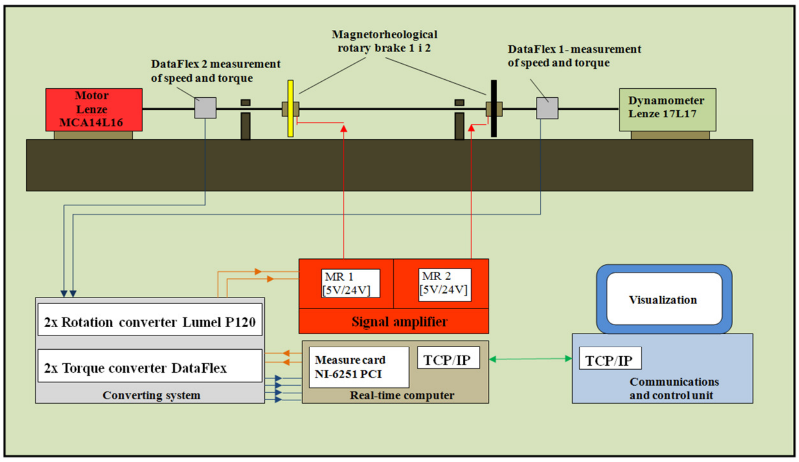

Figure 3. Scheme of the test-rig measurement system

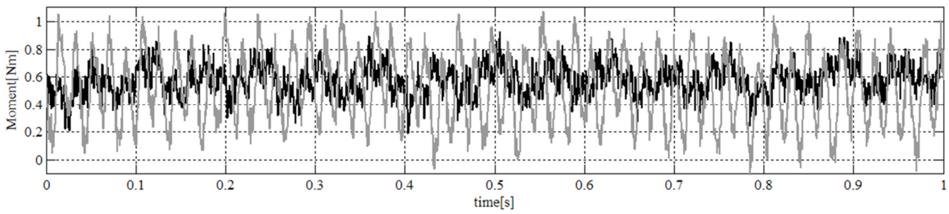

Figure 4. Measured time-histories of the dynamic torque transmitted by the input-shaft

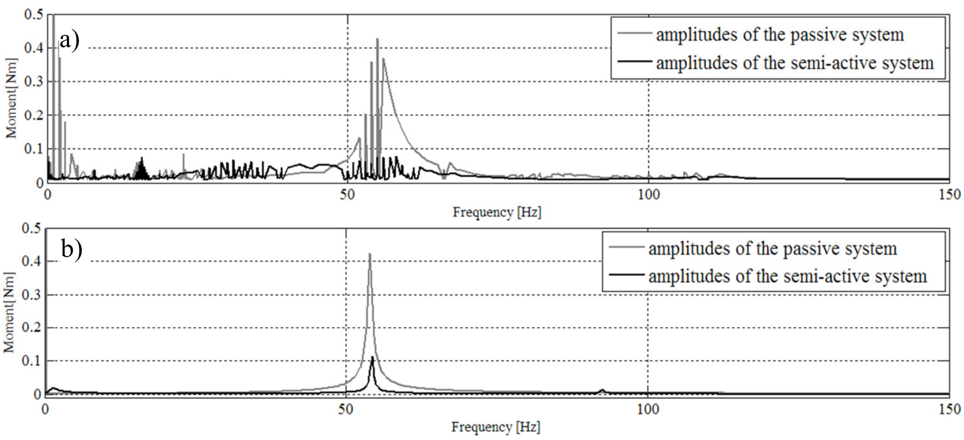

Figure 5. Amplitude characteristics of the dynamic responses of the passive (grey line) and semi-active (black line) system obtained using experiment (a) and simulation (b)

From the experimentally and theoretically obtained plots it follows that the rotary actuators with the magneto-rheological fluid can effectively suppress torsional vibration level, particularly for the resonance oscillation frequencies, e.g. corresponding to the first, fundamental eigenmode, for the properly selected control voltage value based on the respective minimum of the frequency response function determined for the considered mechanical system.

5. Conclusions

In the paper a semi-active control of steady-state torsional vibrations of the laboratory drive system driven by the asynchronous motor has been experimentally and computationally performed by means of rotary actuators with the magneto-rheological fluid (MRF). As it follows from the measurement and numerical examples, in both cases the optimum control carried out by means of the applied actuators with the MRF can effectively reduce the steady-state vibrations of the successive shaft segments to the quasi-static level of the loading transmitted by the drive system, where dynamic amplifications of the responses due to resonance effects have been almost completely suppressed.

Acknowledgments

These investigations are supported by the Polish National Centre of Research and Research Project „Monitoring of Technical State of Construction and Evaluation of its Lifespan MONIT" nr POIG 01.01.02-00-013/08

References

1. Przybyłowicz, P. M., *Torsional vibration control by active piezoelectric system,* J. of Theoretical and Applied Mechanics, **33**(4) (1995) 809-823
2. Szolc T., Jankowski Ł., Pochanke A., Magdziak A., *An application of the magneto-rheological actuators to torsional vibration control of the rotating electro-mechanical systems*, Conference on Rotordynamics, The 8th IFToMM International Conference of Rotor Dynamics, 12-15,09. 2010, KIST, 488-495
3. White, D. C. and Woodson, H. H., *Electromechanical energy conversion*, (1959), New York: Wiley

XXV Symposium *Vibrations in Physical Systems,* Poznan – Bedlewo, May 15-19, 2012

Parametric Vibrations in Printing Unit of Offset Printing Machine

Yuriy PYRYEV
Warsaw University of Technology, ul. Konwiktorska 2,0 0-217 Warszawa, Poland
y.pyryev@wip.pw.edu.pl

Juliusz KRZYŻKOWSKI
Warsaw Univeristy of Technology,ul. Konwiktorska 2,0 0-217 Warszawa, Poland
j.krzyzkowski@gmail.com

Abstract

Vibrations in printing machines are serious problem, which influences on the run of printing process and the quality of the printouts as well. Ones of the most important sources of vibrations are printing units, in which periodically changing stiffness excites parametric vibrations.
In this paper, printing unit of offset printing machine is modelled as a two degree-of-freedom system, which is described by a system of parametric differential equations. Some analyses of this model's behaviour are presented as well as conditions, in which parametric resonance in such systems may occur.

Keywords: parametric vibrations, parametric resonance, two degree-of-freedom, offset printing unit

1. Introduction

Offset printing unit consists of free cylinders: plate, blanket and the impression cylinder (Fig. 1.). The picture, which is going to be printed, is situated on the printing form on the plate cylinder. After inking, the picture is transferred onto blanket cylinder, which is covered with a rubber blanket. Finally, the picture is printed on the paper, which is spread on the impression cylinder.

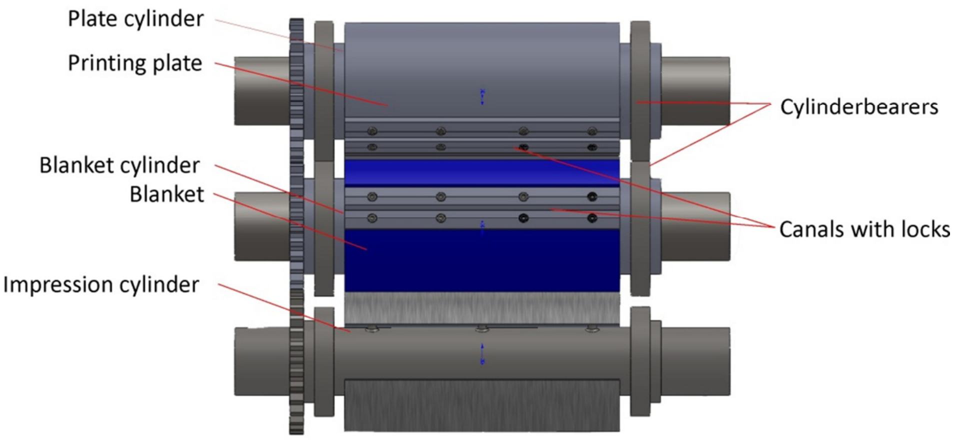

Figure 1 Construction of offset printing unit

2. Model

One of the most frequently mentioned source of vibrations in offset printing units is so called *canal schock effect* [1, 2, 3]. The reason of this phenomenon is rolling over of canals, that are in the plate and blanket cylinders (Fig. 1.). During printing, plate and blanket cylinders are stressed each other. When the canals meet each other, the stress disappears and it comes to sudden change of the stiffness of the printing unit. At this moment vibration exciting force appears.

This phenomenon may be described by the model of printing unit shown in Fig. 2 and system of equations (1)

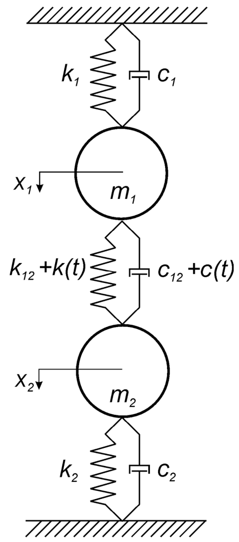

Figure 2 Model of printing unit

$$\hat{\mathbf{M}}\ddot{\mathbf{x}} + \hat{\mathbf{C}}(t)\dot{\mathbf{x}} + \hat{\mathbf{K}}(t)\mathbf{x} = 0 \tag{1}$$

$$\hat{\mathbf{M}} = \begin{Vmatrix} m_1 & 0 \\ 0 & m_2 \end{Vmatrix}, \quad \hat{\mathbf{C}}(t) = \begin{Vmatrix} c_1 + c_{12} + c(t) & -c_{12} - c(t) \\ -c_{12} - c(t) & c_2 + c_{12} + c(t) \end{Vmatrix} \tag{2}$$

$$\hat{\mathbf{K}}(t) = \begin{Vmatrix} k_1 + k_{12} + k(t) & -k_{12} - k(t) \\ -k_{12} - k(t) & k_2 + k_{12} + k(t) \end{Vmatrix}, \quad \mathbf{x} = \begin{Vmatrix} x_1 \\ x_2 \end{Vmatrix} \tag{3}$$

where: m_1, m_2 – masses of the plate and blanket cylinder, respectively; c_{12}, c_1, c_2,– viscous damping coefficients of the dampers, which represent damping properties of the offset blanket and the press frame, respectively; k_{12}, k_1, k_2,– stiffness coefficients of the springs, which represent stiffness of the offset blanket and the press frame, respectively;

$k(t) = kf(t)$ – in time changing stiffness of the blanket force; $c(t) = cf(t)$ – in time changing viscous damping of the blanket.

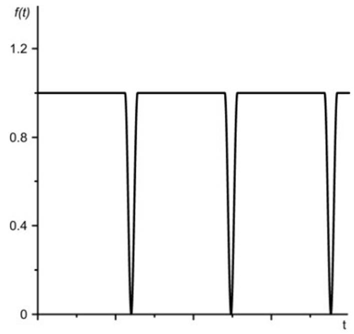

Figure 3 Characteristic of system's stiffness and damping changes

$$\hat{\mathbf{C}}(t+T) = \hat{\mathbf{C}}(t+T)\,,\ \hat{\mathbf{K}}(t+T) = \hat{\mathbf{K}}(t) \tag{4}$$

New variables are introduced: $z_1 = x_1$, $z_2 = x_2$, $z_3 = \dot{x}_1$, $z_4 = \dot{x}_2$

$$\dot{\mathbf{z}} = \hat{\mathbf{A}}(t)\mathbf{z} \tag{5}$$

$$\hat{\mathbf{A}}(t) = \begin{Vmatrix} \mathbf{0} & \hat{\mathbf{I}} \\ -\hat{\mathbf{M}}^{-1}\hat{\mathbf{K}} & -\hat{\mathbf{M}}^{-1}\hat{\mathbf{C}} \end{Vmatrix},\ \hat{\mathbf{I}} = \begin{Vmatrix} 1 & 0 \\ 0 & 1 \end{Vmatrix},\ \mathbf{z} = \begin{Vmatrix} z_1 \\ z_2 \\ z_3 \\ z_4 \end{Vmatrix} \tag{6}$$

Matrix $\hat{\mathbf{A}}(t)$ is a periodic, i.e. $\hat{\mathbf{A}}(t+T) = \hat{\mathbf{A}}(t)$, so equation (5) is a parametric one (Hill's equation) [5, 8, 9].

Matrix $\hat{\mathbf{A}}(t)$ may be written in the following form:

$$\hat{\mathbf{A}}(t) = \hat{\mathbf{A}}_0 + \sum_{n=1}^{\infty}\left(\hat{\mathbf{A}}_n \cos(n\omega t) + \hat{\mathbf{B}}_n \sin(n\omega t)\right) \tag{7}$$

where:

$$\hat{\mathbf{A}}_0 = \begin{Vmatrix} 0 & 0 & 1 & 0 \\ 0 & 0 & 0 & 1 \\ -\dfrac{k_1 + k_{12} + 0{,}5ka_0}{m_1} & \dfrac{k_{12} + 0{,}5ka_0}{m_1} & -\dfrac{c_1 + c_{12} + 0{,}5ca_0}{m_1} & \dfrac{c_{12} + 0{,}5ca_0}{m_1} \\ \dfrac{k_{12} + 0{,}5ka_0}{m_2} & -\dfrac{k_2 + k_{12} + 0{,}5ka_0}{m_2} & \dfrac{c_{12} + 0{,}5ca_0}{m_2} & -\dfrac{c_2 + c_{12} + 0{,}5ca_0}{m_2} \end{Vmatrix}$$

(8)

$$\hat{\mathbf{A}}_n = \left\| \begin{array}{cccc} 0 & 1 & 0 & 0 \\ -\dfrac{k_1 + k_{12} + ka_n}{m_1} & \dfrac{k_{12} + ka_n}{m_1} & -\dfrac{c_1 + c_{12} + ca_n}{m_1} & \dfrac{c_{12} + ca_n}{m_1} \\ 0 & 0 & 0 & 1 \\ \dfrac{k_{12} + ka_n}{m_2} & -\dfrac{k_2 + k_{12} + ka_n}{m_2} & \dfrac{c_{12} + ca_n}{m_2} & -\dfrac{c_2 + c_{12} + ca_n}{m_2} \end{array} \right\| \tag{9}$$

$$\hat{\mathbf{B}}_n = \left\| \begin{array}{cccc} 0 & 1 & 0 & 0 \\ -\dfrac{k_1 + k_{12} + kb_n}{m_1} & \dfrac{k_{12} + kb_n}{m_1} & -\dfrac{c_1 + c_{12} + cb_n}{m_1} & \dfrac{c_{12} + cb_n}{m_1} \\ 0 & 0 & 0 & 1 \\ \dfrac{k_{12} + kb_n}{m_2} & -\dfrac{k_2 + k_{12} + kb_n}{m_2} & \dfrac{c_{12} + cb_n}{m_2} & -\dfrac{c_2 + c_{12} + cb_n}{m_2} \end{array} \right\| \tag{10}$$

In this way modified system with constant parameters is obtained

$$\dot{\mathbf{z}}(t) = \hat{\mathbf{A}}_0 \mathbf{z}(t)\,, \tag{11}$$

for which natural frequencies Ω_1, Ω_2 and roots of characteristic equation $\left| \hat{\mathbf{A}}_0 - s\hat{\mathbf{I}} \right| = 0$ were calculated.

Areas of instability of one degree-of-freedom parametric systems should be looked for parameters which satisfy equation (12). We made an assumption that this condition should be satisfied for two degree-of freedom systems as well. This kind of resonance is called simple resonance [5].

$$\omega = \frac{2\Omega_i}{n}\,,\ n = 1,\ 2,\ 3, \ldots\,;\ i = 1, 2 \tag{12}$$

where: ω – frequency of machine's work, Ω_i – eigenfrequencies of the modified (with constant parameters) system.

Parametric resonance may also occur for parameters satisfying condition (13).

$$\omega = \frac{|\Omega_1 \pm \Omega_2|}{n}\,,\ n = 1,\ 2,\ 3, \ldots \tag{13}$$

Resonances, which satisfy equation (13) are called combination parametric resonances additive or subtractive type [6, 7].

Numerical simulations were carried out for two cases. First, in which cylinder bearers (Fig. 1) were not taken into account and second one – in which plate and blanket cylinders were equipped with cylinder bearers. In calculations following parameters [3, 4] were used:

$m_1 = 85\,\mathrm{kg}$, $m_2 = 105\,\mathrm{kg}$, $k_1 = 2.94 \cdot 10^9\ \mathrm{N\,m^{-1}}$, $k_2 = 3.16 \cdot 10^9\,\mathrm{N\,m^{-1}}$, $k = 2.05 \cdot 10^8\,\mathrm{N\,m^{-1}}$

$k_{12} = 0$, $c_1 = c_2 = 4{,}9 \cdot 10^4\,\mathrm{N\,s^2 m^{-1}}$, $c_{12} = 0$, $c = 1.96 \cdot 10^3\,\mathrm{N\,s^2 m^{-1}}$.

In the first considered case (without cylinder bearers, k_{12}=0 N m^{-1}) natural frequencies of the system are equal Ω_1 = 5585.14 s^{-1} and Ω_2 = 6130.34 s^{-1}.

In figure 3 one can see, that for the lower of system's natural frequencies, parametric resonance does not occur, although condition (12) is satisfied ($\omega = 2\Omega_1/1$, ω = 5585.16 s^{-1}).

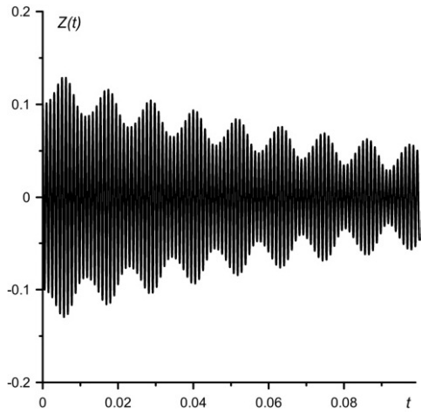

Figure 3 Evolution of cylinders' displacement $Z(t) = z_1(t) - z_2(t)$ for initial conditions $z_1(0)$ = 0.1 mm, $z_2(0) = 0$, $z_3(0) = 0$, $z_4(0) = 0$

However, parametric resonance occurs for the bigger of natural frequencies Ω_2, when condition (12) is satisfied and for n = 1,2,...7. When condition (13) is satisfied – for n = 1,2,...5.

As the examples, numerical analyses for $\omega = 2\Omega_2/2$ (a) and $\omega = (\Omega_1+\Omega_2)/5$ (b) in Fig. 4 are shown.

(a) (b)

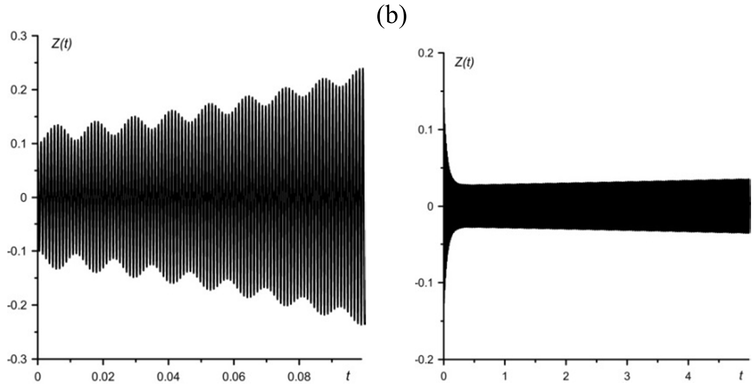

Figure 4 Evolution of cylinders' displacement $Z(t) = z_1(t) - z_2(t)$ for initial conditions $z_1(0)$ = 0.1 mm, $z_2(0) = 0$, $z_3(0) = 0$, $z_4(0) = 0$

For n=8 (eq. (12) satisfied) and n=6 (eq. (13) satisfied) parametric resonance already does not occur.

When stiffness of cylinder bearers is taken into account ($k_{12} = 5.09 \cdot 10^9$ Nm^{-1}), the stiffness of a whole system grows up. In this case parametric resonance does not occur, even when condition (12) and (13) are satisfied.

3. Conclusions

Analyses of parametric two degree-of-freedom system showed, that parametric resonance may occur when the bigger of two natural frequencies of modified system and the sum of system's natural frequencies are multiplicities of the parameters' changes frequency.

Moreover, if offset printing unit were not equipped with cylinder bearers, parametric vibrations and parametric resonance could occur. When cylinder bearers are used, parametric resonance never occurs.

References

1. G.B. Kulikov, *Diagnosing Causes of Increased Vibration of Printing Units of Tower Rotary Printing Machines*, Journal of Machinery Manufacture and Reliability, **37** (2008) 90-96
2. H. Kipphan, *Handbook of Print Media*, Springer Verlag, Heidelberg 2001
3. X. Gao, *Schwingungen von Offsetdruckmaschinen*, PhD dissertation, Technischen Universität Chemnitz 2001
4. V. K. Augustaitis, N. Šešok,, *Analytical investigation metod of the transversal vibration of plate and blanket*, Mechanika, **21** (2000) 46-53
5. Z. Osiński, Teoria drgań, PWN, Warsaw1980
6. V. V. Bolotin, *Vibration in Engineering*, Vol. 1 Vibration of Linear Systems, Mashinostroenie, Moscow 1978
7. G. Schmidt, *Parametererregte Schwingungen*, Deutscher Verl. der Wiss., Berlin 1975
8. V. A. Iakubovic, V.M. Starzinski, *Linear Differential Equations with Periodic Coefficients*, Nauka, Moscow 1972
9. J. Awrejcewicz, *Drgania deterministyczne układów dyskretnych*, WNT, Warsaw 1996

XXV Symposium *Vibrations in Physical Systems,* Poznan – Bedlewo, May 15-19, 2012

Middle Ear Prostheses – Modelling and Simulations

Rafal RUSINEK
Lublin University of Technology, 36 Nabystrzycka St., 20-618 Lublin, Poland
r.rusinek@pollub.pl

Abstract

The paper presents planar model of human middle ear, which is described by differential equations of motion and solved numerically using the MD Adams software. First, dynamic behaviour of intact ossicular chain is analysed, next, incus is removed and partial ossicular replacement prosthesis is used to reconstruct middle ear. Then, natural frequencies of the system are analysed as a function of mass and length of the prosthesis.

Keywords: middle ear model, nonlinear vibrations, middle ear prostheses

1. Introduction

A human middle ear consists of only three small ossicles: the malleus, the incus and the stapes. They create a very complex spatial vibrating system. Therefore, scientists have been looking for a proper model to represent a middle ear since the last half of twenty century. The first study in this field was published in 1961 by Mőller [1]. He presented a simple middle ear mechanism and, on this base, built the first analogue electrical circuit. Similar electrical model has also been investigated by Zwislocki [2]. Both of them based on Bárány theory which claims that the ossicles rotate around an axis lead through the head of the malleus and the short process of the incus. Zwislocki assumed that there is a rigid coupling between malleus and incus, then he omitted this joint in the analog circuit.

In the last decades mechanical models were also developed, where ossicles were represented by lumped masses, connected with springs and dashpots. Usually, in the literature, simple three [3] or four [4] degrees of freedom (dof) models were investigated, but sometimes more advanced – even six dof models [5] were developed. All of them consisted of lumped masses which performed planar translational motion. Although, one can find middle ear model which is built on the grounds of four bar linkage [6] the analysis is in fact limited only to kinematic dependencies.

Generally, models presented in the literature, focus on kinematics of the middle ear, except the work of Feng *et al*. [5], where the authors analyse dynamic behaviour as well. New possibilities of middle ear modelling appeared when Finite Element Method (FEM) was introduced as an engineering tool. In 1978, the first model of FEM was used to study spatial vibrations of tympanic membrane and next also the ossicles. The results of FEM analysis can be found in [1, 2, 7–14]. Despite the fact that FEM can describe geometrical details very accurately, the method cannot explain full dynamics behaviour because this does not give us dynamic equations governing middle ear system. Therefore, it is still very important to find proper mechanical model described by means of mathematical functions. The main problem occurring in modelling is identification of system parameters. Damping and stiffness coefficients cannot be easily found in experimental tests because of many reasons, which make experimental tests difficult. Sometimes, the stiffness and damping coefficient reported in various literature differ meaningfully [15]. Usually, middle ear models present intact ossicular chain. Therefore, there is a lack of models which could simulate middle ear with prostheses. One of the most interesting approaches is presented by Eiber and collaborates [16]. They applied multibody system to investigate dynamical behaviour of middle ear. Their multibody approach assumes, that the motions of each ossicles, as well as of the prosthesis can be treated as a rigid body motion. As far as middle ear model with prosthesis is concerned, the most often FEM is used in order to simulate the ossicles behaviour but there are numerous papers that present experimental investigations as well [17–20].

In this paper, the planar model of human middle ear is analysed where the malleus, the incus and the stapes are treated as rigid bodies connected to each other and fixed to a temporal bone by tendons. Firstly, the intact ossicular chain is investigated, next reconstructed middle ear with prosthesis is analysed with the help of MD Adams.

2. Analysis of middle ear model

The human middle ear mechanism which is very complex system, can be modeled in several ways. Here, planar six degree of freedom (6-dof) model is demonstrated (Fig.1a). Three ossicles: the malleus, the incus, and the stapes are represented by rigid bodies characterised by masses m_m, m_i, m_s suspended with ten springs and dashpots. The malleus (m_M) is jointed to the tympanic membrane (TM) with a spring k_{TM} and a dashpot c_{TM}. The anterior malleal ligament (AML) and the tensor tympani tendon (TT) suspending the malleus are modelled by the springs k_{AML}, k_{TT} and the dashpots c_{AML}, c_{TT}. The malleus is connected with the incus by incudomalleal joint (IMJ) represented by spring k_{IMJ} and dashpot c_{IMJ}. Next, the incus is supported by posterior and superior incudal ligament (PIL and SIL), and the stapes by annular ligament (AL) that are

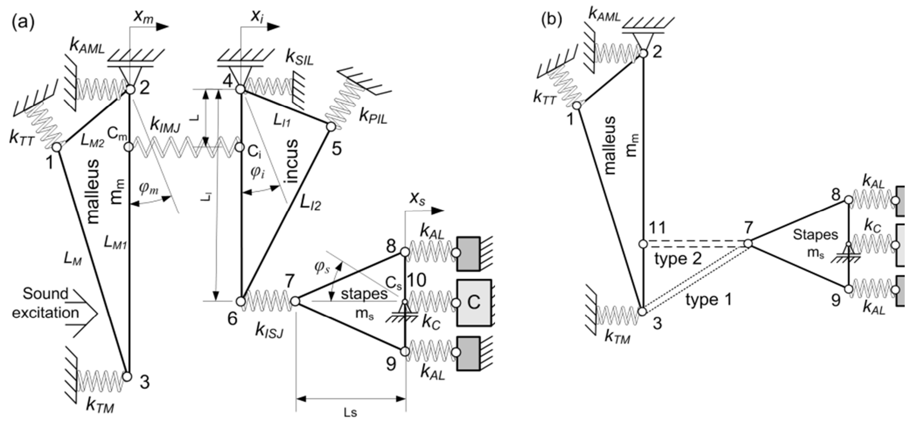

Figure 1. Six degree of freedom model of the middle ear (a), prostheses type 1 and 2 (b)

modelled as springs with stiffness k_{PIL}, k_{SIL} and k_{AL}, and dashpots c_{PIL}, c_{SIL} and c_{AL}. The incudostapedial joint is represented by a spring k_{ISJ} and a dashpot c_{ISJ}. The stapes motion is transferred to the cochlea (C) with stiffness and damping represented by a spring k_C and a dashpot c_C. The malleus motion is stimulated by sound source acting on tympanic membrane. The malleus can translate and rotate about the point 2. The incus similarly can perform translation and rotation about the point 4, whereas the stapes moves like a piston what is described in the literature [3] and additionally can swing around the point 10. Thus, the model possesses 6 degrees of freedom (6-dof): three translations (x_m, x_i, x_s) and three rotations (φ_m, φ_i, φ_s). The system is governed by six differential equations of motion, which can be obtained from the Lagrange equations of the second kind:

$$\frac{d}{dt}\left(\frac{\partial T}{\partial \dot{\varphi}_j}\right) - \frac{\partial T}{\partial \varphi_j} + \frac{\partial V}{\partial \varphi_j} + \frac{\partial \phi}{\partial \dot{\varphi}_j} = 0 \tag{1}$$

where, T and V mean kinetic and potential energy, respectively. D is a dissipation function, which in case of natural vibrations equals zero. φ_j and $\dot{\varphi}_j$ denote the generalized coordinates and the generalized velocities, respectively. For the 6dof system kinetic energy is defined:

$$\begin{aligned} T &= 1/2m_m\left(\dot{x}_m^2 + \dot{\varphi}_m^2(c_m{}^2 + r_m{}^2) + 2\dot{x}_m\dot{\varphi}_m c_m \cos\varphi_m\right) + \\ &1/2m_i\left(\dot{x}_i^2 + \dot{\varphi}_i^2(c_i^2 + r_i^2) + 2\dot{x}_i\dot{\varphi}_i c_i \cos\varphi_i\right) + 1/2m_s\left(\dot{x}_s^2 + \dot{\varphi}_s^2 r_s{}^2\right) \end{aligned} \tag{2}$$

where, c_m, c_i, c_s, determine the distance between centre of mass and the point of rotation, and r_m, r_m, r_m, are gyration radius. Assuming, that k_{TT} and k_{PIL} do not take part in sound transmission, and also that the ossicles mass centre are located as in Fig.1 and that very small ossicles' masses do not influence the change of potential energy, the total potential energy of the system can be presented as follows:

$$\begin{aligned} V &= \frac{1}{2}k_{AML}x_m^2 + \frac{1}{2}k_{SIL}x_i^2 + \frac{1}{2}k_C x_s^2 + \frac{1}{2}k_{TM}\left(4L_{M1}{}^2\sin^2\frac{\varphi_m}{2} + x_m^2 + 4L_{M1}x_m\sin\frac{\varphi_m}{2}\right) + \\ &\frac{1}{2}k_{ISJ}\left(4L_{I3}{}^2\sin^2\frac{\varphi_i}{2} + x_i^2 + 4L_{I3}x_i\sin\frac{\varphi_i}{2}\right) - \frac{1}{2}k_{ISJ}\left(4L_S{}^2\sin^2\frac{\varphi_s}{2} + x_s^2 + 4L_S x_s\sin\frac{\varphi_s}{2}\right) + \\ &\frac{1}{2}k_{IMJ}\left(4L^2\sin^2\frac{\varphi_m}{2} + x_m^2 + 4Lx_m\sin\frac{\varphi_m}{2}\right) - \frac{1}{2}k_{IMJ}\left(4L^2\sin^2\frac{\varphi_m}{2} + x_m^2 + 4Lx_m\sin\frac{\varphi_m}{2}\right) + \\ &\frac{1}{2}k_{AL}\left(4L_{S1}{}^2\sin^2\frac{\varphi_s}{2} + x_s^2 + 4L_{S1}x_s\sin\frac{\varphi_s}{2}\right) \end{aligned} \tag{3}$$

The assumption about the change of potential energy caused by the gravity force is justified because the elastic potential of these springs is about nineteen hundred times bigger than the potential of gravitation. The system presented in Fig. 1 is geometrically nonlinear by nature. The differential equations of natural vibrations, which are obtained after putting equations (2) and (3) into (1), are expressed as:

$$m_m\left(\ddot{x}_m + \ddot{\varphi}_m c_m\cos\varphi_m\right) + x_m\left(k_{AML} + k_{TM} + k_{IMJ}\right) + 2\sin\tfrac{\varphi_m}{2}\left(k_{TM}L_{M1} + k_{IMJ}L\right) = 0 \tag{4}$$

$$m_i\left(\ddot{x}_i+\ddot{\varphi}_i c_i\cos\varphi_i\right)+x_i\left(k_{SIL}-k_{IMJ}+k_{ISJ}\right)+2\sin\tfrac{\varphi_i}{2}\left(k_{ISJ}L_{I3}-k_{IMJ}L\right)=0 \tag{5}$$

$$m_s\ddot{x}_s+x_s\left(k_C-k_{ISJ}+k_{AL}\right)+2\sin\tfrac{\varphi_s}{2}\left(k_{AL}L_{S1}-k_{ISJ}L_S\right)=0 \tag{6}$$

$$\begin{gathered}m_m\left(\ddot{\varphi}_m(c_m{}^2+r_m{}^2)+\ddot{x}_m c_m\cos\varphi_m+\dot{x}_m\dot{\varphi}_m c_m\sin\varphi_m\right)+\left(k_{TM}L_{M1}{}^2+k_{IMJ}L^2\right)\sin\varphi_m+\\ x_m\left(k_{TM}L_{M1}+k_{IMJ}L\right)\cos\tfrac{\varphi_m}{2}=0\end{gathered} \tag{7}$$

$$\begin{gathered}m_i\left(\ddot{\varphi}_i(c_i^2+r_i^2)+\ddot{x}_i c_i\cos\varphi_i+\dot{x}_i\dot{\varphi}_i c_i\sin\varphi_i\right)+\left(k_{ISJ}L_{I3}{}^2-k_{IMJ}L^2\right)\sin\varphi_i+\\ x_i\left(k_{ISJ}L_{I3}-k_{IMJ}L\right)\cos\tfrac{\varphi_i}{2}=0\end{gathered} \tag{8}$$

$$m_s\ddot{\varphi}_s r_s^2+\left(k_{AL}L_{S1}{}^2-k_{ISJ}L_S{}^2\right)\sin\varphi_s+x_s\left(k_{AL}L_{S1}-k_{ISJ}L_S\right)\cos\tfrac{\varphi_s}{2}=0 \tag{9}$$

The equations of motions from (4) to (9) are nonlinear and coupled. Therefore, their analytical solution is a challenging task. Here, the nonlinear model of middle ear is simulated in MD Adams with parameters presented in Tab. 1, which are taken from [15] but some of them marked with an asterisk are assumed on the basis of own numerical researches.

Table 1. Parameters of the middle ear used in simulations

Symbol	Unit	Value	Symbol	Unit	Value	Symbol	Unit	Value
m_m	mg	25	c_{TM}	Ns/m	0.005	k_{TM}	N/m	200
m_i	mg	28	c_{AML}	Ns/m	0.0432	K_{AML}	N/m	620*
m_s	mg	1,78	c_{IMJ}	Ns/m	0.0036	K_{IMJ}	N/m	1000000
			c_{ISJ}	Ns/m	0.6	k_{ISJ}	N/m	1200
			c_{PIL}	Ns/m	0.02	k_{PIL}	N/m	620*
			c_{AL}	Ns/m	0.0036	k_{AL}	N/m	625
			c_C	Ns/m	0.06	k_C	N/m	200
			c_{TT}	Ns/m	0.005*	k_{TT}	N/m	300*
			c_{SIL}	Ns/m	0.005*	k_{SIL}	N/m	62000*

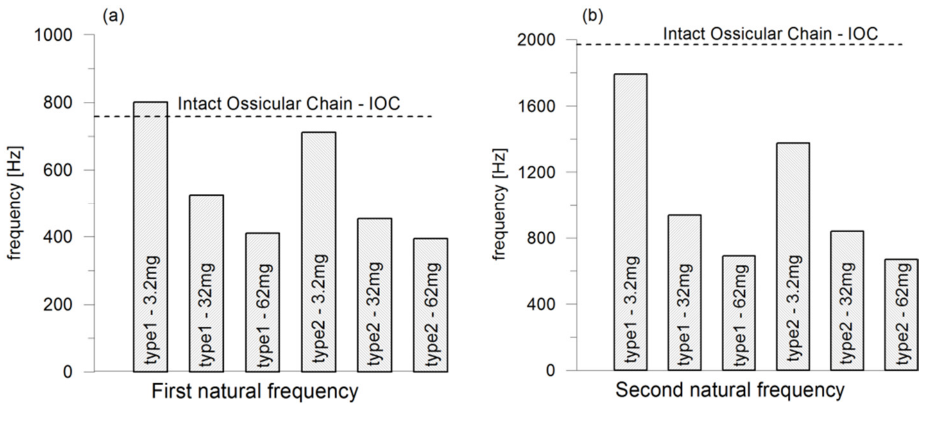

Figure 2. Natural frequencies; the first (a), the second (b)

The natural undamped frequencies of intact ossicular chain (IOC) represented by the model shown in Fig. 1a, are 0.45 kHz, 71 kHz, 0.76 kHz, 1.98 kHz, 9 kHz and 36.8 kHz, but the first two do not exist in the damped system. Therefore, 0.76, 1.98 kHz are the most important in audiology. In case of the incus damage, partially ossicular replacement prosthesis (PORP) is used in medical practice. Then, the position and the mass of the prosthesis is still a disputable problem. Here, two PORP positions are analysed (Fig. 1b) and three prosthesis masses 3.2 mg, 32 mg, and 62 mg, which are typical for ceramics, gold and titanium prostheses, respectively [16]. Comparison of the first and the second natural frequency is depicted in Fig. 2. The lower mass prosthesis is the best because its frequencies are close to those of intact ossicular chain (IOC) which is represented by horizontal dashed line in Fig. 2. As far as prosthesis position is concerned, the position type 1 is better than type 2. Generally, PORP type 2 gives lower natural frequencies than OIC.

3. Conclusions

The planar 6-dof model of the middle ear seems to be adequate to simulate dynamic behaviour of auditory ossicles and useful to estimate the kind of prosthesis and its position in living human body. The results of the numerical simulations are convergent with experimental research reported in the literature [16] which proves that prosthesis mass below 5mg is the best for reconstruction of the ossicular chain.

Acknowledgments

The study is supported by the Polish Ministry of Science and Higher Education grant no. N N518 425936 and partially also N403 065 32/3451.

References

1. A.R. Mőller, *Network Model of the Middle Ear*, Journal of the Acoustical Society of America **33** (1961) 168-176.
2. J. Zwislocki, *Analysis of the Middle-Ear Function. Part I: Input Impedance*, Journal of the Acoustical Society of America **34** (1962) 1514-1523.
3. M.E. Ravicz, W.T. Peake, H.H. Nakajima, S.N. Merchant, J.J. Rosowski, *Modeling Flexibility in the Human Ossicular Chain:Comparision to Ossicular Fixation Data*, in: Gyo K, Wada H (Eds.), Middle Ear Mechanics in Research and Otology, Word Scientific, Singapore, 2004.
4. H.H. Nakajima, M.E. Ravicz, S.N. Merchant, W.T. Peake, J.J. Rosowski, *Experimental ossicular fixations and the middle ears response to sound: Evidence for a flexible ossicular chain*, Hearing Research **204** (2005) 60-77.
5. B. Feng, R.Z. Gan, *Lumped parametric model of the human ear for sound transmission*, Biomech Model Mechanobiol **3** (2004) 33-47.
6. M. Iwaniec, D. Marszalik, *Vibrations analysis of ossicles mechanism*, Vibrations in Phisical Systems XXIV (2010) 29-34.
7. M. Bornitz, T. Zahnert, H.J. Hardtke, K.B. Huttenbrink, *Identyfication of Parameters for the Middle Ear Model*, Audiology & Neuro-Otology **4** (1999) 163-169.

8. C. Dai, T. Cheng, M. W. Wood, R.Z. Gan, *Fixation and detachment of superior and anterior malleolar ligaments in human middle ear: Experiment and modeling*, Hearing Research **230** (2007) 24-33.
9. A. Eiber, H.-G. Freitag, Burkhardt C., Hemmert W, Maassen M., J. Rodriguez Jorge, H.-P. Zenner, *Dynamics of Middle Ear Prostheses - Simulations and Measurements*, Audiol Neurootol **4** (1999) 178-184.
10. R.Z. Gan, Q. Sun, *Finite element modeling of human ear with external ear canal and middle ear cavity*, Second Joint Embs-Bmes Conference 2002, Vols 1-3, Conference Proceedings (2002) 264-265.
11. R.Z. Gan, Q.L. Sun, R.K. Dyer, K.H. Chang, K.J. Dormer, *Three-dimensional modeling of middle ear biomechanics and its applications*, Otology & Neurotology **23** (2002) 271-280.
12. Q.L. Sun, K.H. Chang, K.J. Dormer, R.K. Dyer, R.Z. Gan, *An advanced computer-aided geometric modeling and fabrication method for human middle ear*, Medical Engineering & Physics **24** (2002) 595-606.
13. Q. Sun, R.Z. Gan, K.H. Chang, K.J. Dormer, *Computer-integrated finite element modeling of human middle ear*, Biomech Model Mechanobiol 1 (2002) 109-122.
14. H. Taschke, C. Weistenhofer, H. Hudde, *A full-size physical model of the human middle ear*, Acustica **86** (2000) 103-116.
15. M. Kringlebotn, *Network Model for the Human Middle Ear*, Scandinavian Audiology **17** (1988) 75-85.
16. H.P. Zenner, H.-G. Freitag, C. Linti, U. Steinhardt, J.R. Jorge, S. Preyer, P.-S. Mauz, M. Surth, H. Planck, I. Baumann, R. Lehner, A. Eiber, *Acoustomechanical properties of open TTP titanium middle ear prostheses*, Hearing Research **192** (2004) 36-46.
17. Asai M., Heiland K. E., Huber A. M., Goode R. L., *Evaluation of a Cement Incus Replacement Prosthesis in a Temporal Bone Model*, Acta Otolaryngol (Stockh) **119** (1999) 573-576.
18. M. Asai, A.M. Huber, R.L. Goode, *Analysis of the Best Site on the Stapes Footplate for Ossicular Chain Reconstruction*, Acta Otolaryngol **119** (1999) 355-361.
19. D.P. Morris, M. Bance, R.G. van Wijhe, M. Kiefte, R. Smith, *Optimum Tension for Partial Ossicular Replacement Prosthesis Reconstruction in the Human Middle Ear*, The Laryngoscope **114** (2004) 305-308.
20. S. Zhao, N. Hato, R.L. Goode, *Experimental study of an adjustable-length titanium ossicular prosthesis in a temporal bone model*, Acta Oto-Laryngologica **125** (2005) 33-37.

XXV Symposium *Vibrations in Physical Systems,* Poznan – Bedlewo, May 15-19, 2012

An Influence of Auditory Chain Components' Stiffness on Vibrations Characteristics Measured by a Finite-Element Model of the Middle Ear Structure

Sylwester SAMBORSKI
Lublin University of Technology, 36 Nadbystrzycka St., Lublin 20-618, Poland
s.samborski@pollub.pl

Rafal RUSINEK
Lublin University of Technology, 36 Nabystrzycka St., 20-618 Lublin, Poland
r.rusinek@pollub.pl

Marcin SZYMANSKI
Department of Otolaryngology, Head and Neck Surgery, Medical University of Lublin
8 Jaczewskiego St., 20-854 Lublin, Poland, marcinszym@poczta.onet.pl

Abstract

The problem of modelling of middle ear auditory chain functioning is still very difficult to be made precisely in comparison with the real ossicles' behaviour observed experimentally. The main reason for this is geometrical complexity and a number of material characteristics of the ossicles themselves. Here, FEM is engaged to model human middle ear work because this method allows for reconfiguring of complex auditory chain geometry, various material models etc. and provides good accuracy.

Keywords: auditory chain mechanics, middle ear dynamics, FE model, modal analysis

1. Introduction

The Finite Elements Method (FEM) allows for detailed modelling of the human ear complicated auditory chain [1]. It allows for changing and comparing different configurations (angles) of the ossicles, changing material models (e.g. tympanic membrane can by isotropic, anisotropic, hyper elastic etc.). Also some details of ossicles' suspension (tendons and ligaments) as well as other agents (air inertia, the cochlear fluid etc.) can be taken into account [1,2]. From practical point of view, a special importance has the possibility of simulating work of any prostheses incorporated into the human auditory chain [3–5].

Even though in the open literature one can find many approaches to modelling of the middle ear dynamics [1–10] there are still some important problems to be solved, such as bypassing difficulties connected with individual differences of human being ossicular chain. As indicated by other researchers (e.g. [1]) the identification of parameters by in situ measurements are difficult to perform for many reasons. Even though there is a number of material data given in the literature [1, 2,4,6,7,9], there is still an unsolved problem of individual variety of characteristics of human beings. The method of FE gives here a strong and desirable possibilities to vary many characteristics of the auditory chain, what is enormously advantageous in understanding the dynamics of the ossicles and the whole system.

As it was observed during the STL generation by tomography, even though the ossicles are very small they are not solid, as it is generally accepted in modelling [2,6]. Namely, they can have empty spaces (pores) inside, what has significant influence on their strength [11,12] and other mechanical characteristics (for example the center of mass can be moved from the geometrical center) and thus the common assumption of the homogeneity, isotropy etc. are no longer valid. Again, in this situation FE modelling in connection with tomography gives many possibilities to simulate precisely auditory chain mechanics.

As other authors say, the most important variables in middle-ear modelling is the behaviour of the eardrum (tympanic membrane) and the interaction of the stapedius with the cochlear fluid [1,4,6,7,9]. Of course a number of studies can be found on precise modelling of the ossicles' suspension – muscles, tendons and ligaments [1–4,6–10]. However, it is hard to find in the open literature wider studies on the eigenproblems of the whole auditory chain, even though some researchers performed modal analysis of the eardrum [1,4,6]. Our model covers estimation of eigenmodes and eigenfrequencies for the whole middle-ear auditory chain.

2. Method

The geometry of ossicles were obtained from computer micro-tomography. Next, the IGES files containing the main parts of the auditory chain were imported into ABAQUS/CAE® environment ver. 6.10.2. Then, the ossicles were joined together in the ossicular chain and meshed using automated seeding process. The mesh consisted of C3D4 linear tetrahedral elements of total number of 44119 with smaller elements around bigger curvatures and so on. Having all parts (ossicles and tissues) read, meshed and prepared for analysis a complete auditory chain was established in one assembly. The mutual location and orientation of the parts was tuned to the one given in a separate IGES file containing the spatial configuration of all ossicles. The only way to improve the geometry was to disassemble the auditory chain, to improve all parts separately and to assemble them again without redundant geometrical entities, what in fact was done. The material data for all elements of the auditory chain was taken from the literature [1,2,4,6,7,9] in order to match them to requirements of our model (see Table 1). All ossicles, the eardrum and the two joint tissues were assumed to be isotropic and homogeneous solids. It is worth notifying, that there is a great difference between the two joint tissues: maleo-incudeal and incudeo-stapedial, what has an important influence on the movement at different frequency level (different eigenmodes). Namely, at lower frequencies the malleus-incus couple moves as one body, as it was indicated in [1] among others. At higher frequencies (generally above 3kHz) the incus tends to rotate because of its considerable inertia and a tendency to minimize the energy used to move and this is specific for human ear, as other – smaller mammals have simpler kinematics of the ossicles [4,7].

A set of suspensory elements was added to the ossicles in the form of springs S_1-S_7, where S_1 stands for superior malleal ligament, S_2 – lateral malleal ligament, S_3 – posterior incudal ligament, S_4 – anterior malleal ligament, S_5 – posterior stapedial tendon, S_6

reflects cochlear fluid elasticity (only for this part damping is also considered) and S_7 simulates the reaction of tensor tympani tendon.

Table 1. Material characteristics of the human middle-ear ossicles

Auditory-chain element	Material characteristics		
	Modulus of elasticity, MPa	Poisson ratio	Mass density, kg/m^3
Eardrum	35.0	0.35	1 200
Malleus, Incus, Stapedius	14 100.0	0.30	3 590, 3 230, 2 200
maleo-incudeal tissue	14 100.0	0.30	3 200
incudeo-stapedial tissue	0.6	0.30	1 200

Note, that stapedial annular ligament was included in S6 for simplicity, which is one of the desired features of our model. All suspensory elements were attached and oriented similarly to [9] and each spring S_i (i=1...7) was characterized by its respective stiffness coefficient k_i. The basic mechanical data for S_6 was taken from [9], i.e. the stiffness coefficient K_6=209N/m and the damping coefficient c=0.06Ns/m. Here, capital "K" means the reference constant value, as k_6 is a variable stiffness and also other k_i (i=1...5, 7) were given various values, as farther described. The D_6 damper was connected in a series with the S_6 spring (Maxwell model).

As it was mentioned before, the stapedial annular ligament was incorporated in the S6 spring. However, the piston-like movement of the stapedius [1,4,6,7,9] was enforced by restraining respective degrees of freedom. This kind of stapedius movement is observed at least within the 0-3000Hz frequency interval [4] and in our paper we consider only first five eigenfrequencies, generally not exceeding 3kHz. In addition the eardrum was encastered (for simplicity) at the whole tympanic ring. Such approach is used by some authors (e.g. [4]), even though other treatments are possible [1,3]. All elements were joined by tie constraints with surface to node region method. The last element in the middle-ear auditory chain was the stapedius. In reality it is connected to the inner ear (cochlea) and this connection can be modelled in several ways [1,9]. In this paper a visco-elastic joint was used, as described above. Some authors say [4], that this is the best modelling of the fluid inertia of the cochlea.

During the FE simulation six values of k_i to K_6 ratio were used: 1/3, 1, 10/3, 10, 100/3, 100, in order to analyze the influence of springs' stiffnesses on eigenfrequencies of the whole auditory chain. This analysis was the main goal of our research at this stage and it was realized as a Static-Linear Perturbation step in Abaqus/CAE by the following procedure. First, eigenfrequencies of the connected ossicles was performed with boundary conditions for the eardrum and the stapedius footplate as described above and no suspensory springs at all. Next, the S_6 spring was introduced and again the first five eigenfrequencies were found numerically for different values of k_6, i.e. k_6=(1/3, 1, ... 100)xK_6. In the third step different values of the damping coefficient of D_6 were tested, but they had no effect on eigenfrequencies at all. This raises doubts about the necessity of considering damping of the cochlea with the accepted model assumptions. Subsequently, a comparison of other springs was performed in two ways:

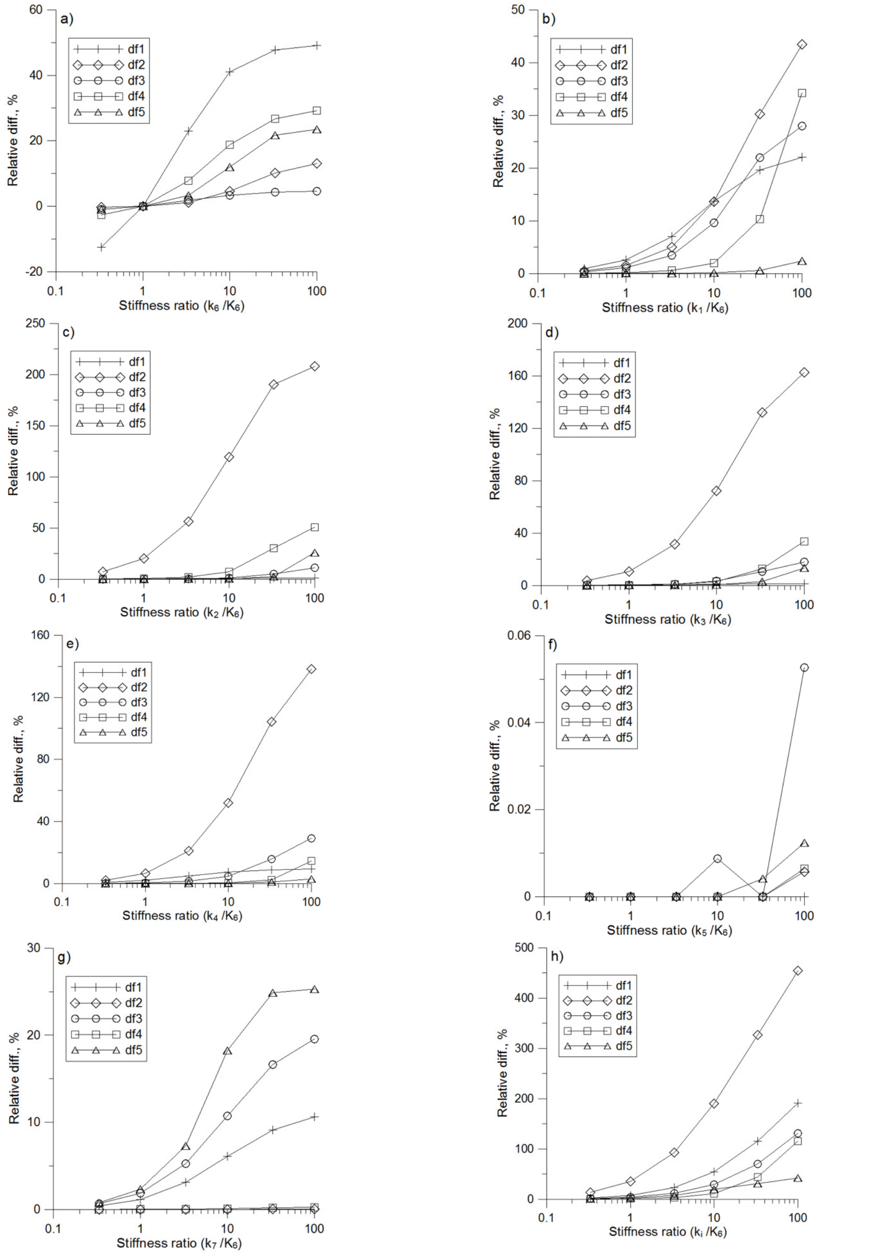

Figure 1. Comparison of the suspensory element stiffness' influence on the auditory chain eigenfrequencies

1. each spring $S_1 – S_5$ and S_7 employed simultaneously with S_6 at $k_6=K_6$ and the k_i to K_6 ratios equal 1/3, 1, 10/3, ..., 100, subsequently (6x6=36 cases),
2. all springs working at a time, with S_6 at $k_6=K_6$ and all other springs having the same stiffnesses $k_1=k_2=k_3=k_4=k_5=k_7$, changed subsequently from $1/3xK_6$ up to $100xK_6$, as in the previous item, which gave another 6 analysis cases.

The results of these analyses are presented in the next section (see Fig. 1).

3. Results and discussion

The first five eigenfrequencies for the auditory chain with ascribed boundary conditions and no suspension were f_1=177.01Hz, f_2=350.66Hz, f_3=1121.50Hz, f_4=1495.20Hz and f_5=2394.50Hz. After introducing the S_6 spring all the frequencies increased, the more the stiffness was enlarged. For k_6=209N/m (=K_6) the respective frequencies were f_1=223.86Hz, f_2=352.07Hz, f_3=1138.70Hz, f_4=1559.40Hz and f_5=2427.50Hz and they were subsequently used as reference values at the graphs in Fig. 1. As shown in Fig. 1 the influence of the suspension in the form of springs was successfully found with the FE model of the human middle-ear auditory chain. Fig. 1a depicts the influence of the cochlea elastic properties on the relative difference (df_j, j=1, 2, ..., 5) of the first five eigenfrequencies ($f_1 – f_5$) in comparison to the frequencies of the system with only boundary conditions and the S_6 spring activated ($k_6=K_6$=209N/m). This influence is particularly strong in case of the first eigenfrequency. Note, that the intensity of the influence is not proportional to the subsequent number of the frequency. Consecutive graphs (b – g) say, that the influence of the separate springs ($S_1 – S_5$, S_7) working at the same time with the S_6 spring is generally important, even though in each case the five eigenfrequencies are differently sensitive to the change of the particular spring's stiffness. For example, the highest frequency (f_5) is affected only by tensor tympani tendon stiffness (S_7) more seriously. In other cases ($S_1 – S_5$) the value of f_5 is practically untouched by any change of these springs' stiffness coefficients. On the other hand the second eigenfrequency (f_2) reacts strongly for stiffening of the four ligaments ($S_1 – S_4$) and the posterior stapedial tendon (S_5), but not for the tensor tympani tendon (S_7).

Figure 1f exhibits, that S_5 has no influence on the eigenfrequencies irrespective to its stiffness. The last plot (Fig. 1h) indicates the influence of the stiffness' changes of all the springs acting simultaneously, when only the stiffness of S_6 is kept constant and equal to K_6=209N/m is strong (or even huge - for the second frequency (f_2)) over a wide span of k_i to K_6 ratio (up to 100). This can be treated as a proof, that even the simplest FE model can give significant information about the complicated mechanics of the human auditory chain.

4. Conclusions

The FE modal analysis of the human middle-ear auditory chain showed, that FE is a powerful, convenient and reliable technique of modelling complicated dynamic behaviour of biomechanical systems [13,14]. It is known, that on the contrary to other mammals' ear system [4], the movement of the human one is more complicated and behaves in various ways, depending on the transmitted frequency [4]. This is connected to the fact, that the human ossicles are heavier and have higher moments of inertia [4]. Thus, the ossicles move in such a way that is the most effective from the energetical point of view at different frequencies [4]. The results presented here are in good agreement with the reality and the other authors' results, as subsequent eigenmodes show different moves of the ossicles. Introducing a simplified set of suspension in the form of springs having different properties, where directions of them and attachment points were similar to those given in [9] shows that considering suspension does substantially change the eigenfrequencies and the dynamical behaviour of the human auditory chain. If only the lower frequencies are taken into account, when the stapedius moves like a piston, the cochlear fluid's damping properties can be neglected. In that case the proposed simplified middle-ear model can give satisfactory results.

Acknowledgments

The study is supported by the Polish Ministry of Science and Higher Education grant no. N N518 425936 and partially also N403 065 32/3451.

References

1. T. Koike, H. Wada, T. Kobayashi, Modeling of the human middle ear using the finite-element method, J. Acoust. Soc. Am. 111 (2002) 1306.
2. W.-j. Yao, J.-w. Ma, B.-l. Hu, Numerical Model on Sound-Solid Coupling in Human Ear and Study on Sound Pressure of Tympanic Membrane, Mathematical Problems in Engineering 2011 (2011) 1–13.
3. A. Eiber, H.G. Freitag, C. Burkhardt, W. Hemmert, M. Maassen, J. Rodriguez Jorge, H.P. Zenner, Dynamics of Middle Ear Prostheses - Simulations and Measurements, Audiol Neurootol 4 (1999) 178–184.
4. P. Ferris, P. Prendergast, Middle-ear dynamics before and after ossicular replacement, Journal of Biomechanics 33 (2000) 581–590.
5. M. Neudert, M. Berner, M. Bornitz, T. Beleites, M. Ney, T. Zahnert, Osseointegration of Prostheses on the Stapes Footplate: Evaluation of the Biomechanical Feasibility by Using a Finite Element Model, JARO 8 (2007) 411–421.
6. Bornitz M, Zahnert T, Hardtke H. J, Huttenbrink K. B, Identyfication of Parameters for the Middle Ear Model, Audiology & Neuro-Otology 4 (1999) 163–169.
7. H. Cai, R.P. Jackson, C. Steele, S. Puria, A Biological Gear in the Human Middle Ear, in: Proceedings of the COSMOL Conference, 2010.
8. T. Cheng, R.Z. Gan, Mechanical properties of anterior malleolar ligament from experimental measurement and material modeling analysis, Biomech Model Mechanobiol 7 (2008) 387–394.
9. R.Z. Gan, Q.L. Sun, R.K. Dyer, K.H. Chang, K.J. Dormer, Three-dimensional modeling of middle ear biomechanics and its applications, Otology & Neurotology 23 (2002) 271–280.
10. W.-j. Yao, H.-c. Zhou, B.-l. Hu, X.-s. Huang, X.-q. Li, Research on Ossicular Chain Mechanics Model, Mathematical Problems in Engineering 2010 (2010) 1–15.

11. T. Sadowski, S. Samborski, Modeling of Porous Ceramics Response to Compressive Loading, Journal of the American Ceramic Society 86 (2003) 2218–2221.
12. T. Sadowski, S. Samborski, Development of damage state in porous ceramics under compression: Proceedings of the 16th International Workshop on Computational Mechanics of Materials IWCMM-16, Computational Materials Science 43 (2008) 75–81.
13. E. Skrodzka, J. Modławska, Modelling of some mechanical malfunctions of the human tympanic membrane. Polish J. Environmental Stud. 15 4a(2006) 140-144.
14. E. Skrodzka, J. Modławska, Modal Analysis of the Human Tympanic Membrane of The Middle Ear Using the Finite-Element Method. Archives of Acoustics 31 4(2006) 23-28.

XXV Symposium *Vibrations in Physical Systems,* Poznan – Bedlewo, May 15-19, 2012

Assessing the Wear of Friction Pads in Disc Braking System of Rail Vehicle by Using Selected FrequencyCharacteristics of Vibration Signal

Wojciech SAWCZUK
Poznan University of Technology, Institute of Combustion Engines and Transport Division of Rail Vehicles, wojciech.sawczuk@put.poznan.pl

Abstract

Attempt to raise train speed involves application of greater braking power i.e. braking systems rapidly absorbing and dispersing stored heat energy. To maintain high efficiency of braking system in the whole operational process, it is necessary to control the friction set: brake and pad before reaching limit wear particularly of friction pads [5]. The purpose of this article is to present possibility to diagnose the friction set of disc brake by using selected frequency characteristics of vibration signal generated by brake caliper with friction pads.

Keywords: railway disc brake, wear of friction pad, diagnostics of brake, frequency analysis.

1. Introduction

Because of complex braking system in rail cars and locomotive, most often consisting of 8 individual brake cylinders, application of one diagnostic system to assess the wear of all friction sets is impeded [7]. A system for visual inspection and diagnostics worked out in Rail Vehicle Institut *TABOR* in Poznan is the most advanced system do diagnose disc brake. Diagnosing system [1] provides complete information about the wear of friction pads and brake disc in each operation moment. Worked out solutions, becasue of complex and expensive measuring set consisting of a digital film camera and a software to convert the picture, after successful tests at reasearch station, have not been applied by railway industry yet.

In rail technique, also rail track stations are used to diagnose the wear of friction pad. At these stations friction set consisting of disc brake and friction pad is photograhed during train ride. However, it is not a very precise method because, on the basis of recorded pictures the thickness of frction pads of disc brake is only assessed. When pads' thickness amounts to approx. 10 mm tram driver receives information that limit acceptable wear of pads on a certain axle of axle set has been reached. Rail track stations to diagnose the wear of friction pads are used by German, British and French railways.

In railway vehicles, systems signaling braking process and turning off braking process, visible for the service from the inside and outside of the vehicle, are the most often applied. Those systems enable to check during train ride in which car braking system is bloked. Nevertheless, rail technique lacks an objective method of quantitive assessment of the wear of friction pads.

The purpose of this research is to apply vibration signal of pad calipers to assess the wear of friction pads of disc brake.

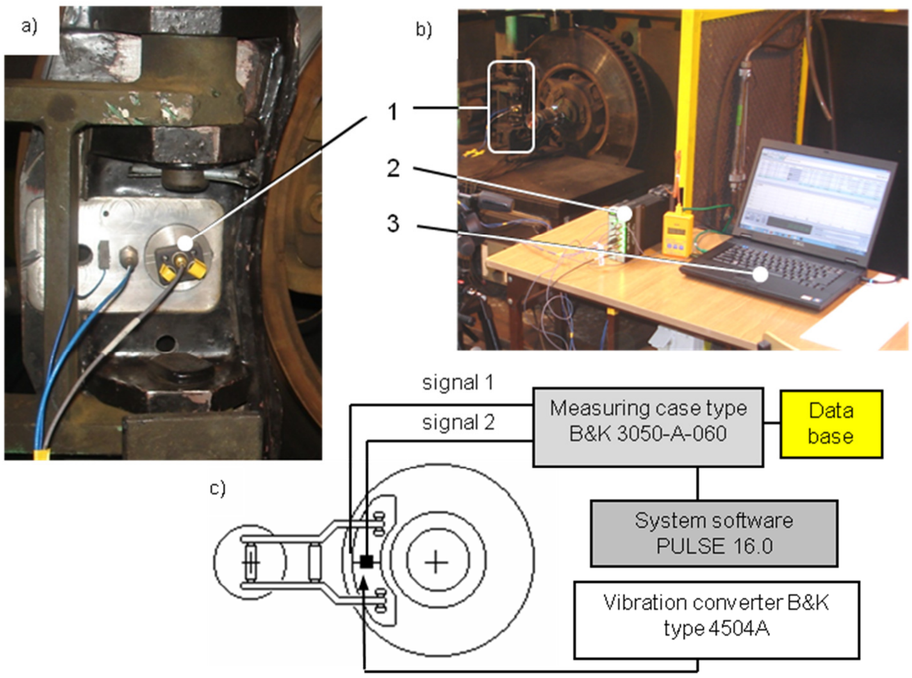

Figure. 1. Station for tests of railway brakes; a) pad caliper with accelerometer, b) view of equipment set of vibrations generated by caliper with pads, c) diagram of measurement track of vibrations generated by caliper with pads, 1-accelerometer, 2-measuring case type B&K 3050-A-060 , 3- System software PULSE 16.0

2. Methodology and research object

The research was carried out at internal testing for tests of railway brakes. A brake disc type 610×110 with ventilation vanes made by Kovis and three sets of pads type 200 FR20H.2 made by Frenoplast constitute the research object. One set was new - 35 mm thick and two sets were worn to thickness of 25 mm and 15 mm. A reasearch program C (fast ride) according to instructions of UIC 541-3 was applied. The brakings were carried out from speed of 50, 80, 120, 160 and 200 km/h. During the research pad's pressures to disc N of 28 and 44kN were realized as well as braking masses per one disc of M=4.4T and 7.5T. Vibration transducer were mounted on pad calipers with a mounting clip, which is presented in Fig. 1a. During the research signals of vibration accelerations were registered in three reciprocally orthogonal directions. To acquire vibration signal a measuring system consisting of piezoelectric vibration accelerations transducer and measuring case type B&K 3050-A-060 with system software PULSE 16.0 was used. Fig. 1b presents the view of the measuring track.

Brüel&Kjær's the vibration transducer type 4504 were selected on the basis of instructions included in paper [3], the linear frequency of converter transit amounted to 13 kHz. During diagnostic tests signals in frequency from 0.7 Hz to 9 kHz [2] were registered. Sampling frequency was set at 32 kHz. This means that the frequency that was subject of the analysis in accordance with Nyquist relation amounted to 16 kHz.

This research was carried out in accordance with principles of active experiment. After carrying out a series of brakings at set speeds at the beginning of braking, pads' pressures to the disc and braking masses, the friction pads were changed and values of instantenuous vibration accelerations were registered.

3. Analysis of results of vibration accelerations by defining in frequency domain

The purpose of spectrum analysis of signals of vibration accelerations was to determine frequency bands connected with change of pad's thickness during operation of braking system. Figure 2 presents exemplary amplitude spectra of vibration accelerations for various pad's thicknesses received during braking from speed of 160 km/h. Spectrum received on measurement of vibrations in direction perpendicular to friction surface of the disc (direction *Y*) with pad's clamp to the disc N=44kN and braking mass M=4,4t.

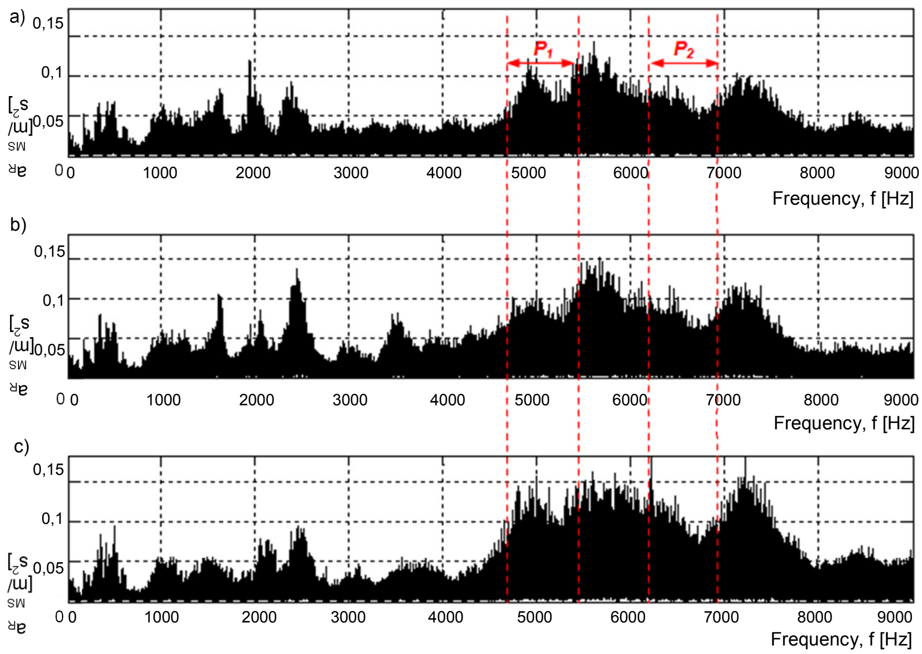

Figure. 2. Dependence of amplitude of vibration accelerations on frequencies for different pad's thicknesses for speed at the beginning of braking v=120km/h in direction Y2:

P1-frequency band 4600-5100 Hz, P2-frequency band 6000-6700 Hz: a) pad's thickness G1=35mm, b) pad's thickness G2=25mm, c) pad's thickness G3=15mm

Research on measurement of vibration accelerations of brake calipers in frequency domain showed that it is possible to find frequency bands, in which dependence of RMS value of vibration accelerations a_{RMS} (equation (1)) [4] on various pad's thicknesses in considered range of speeds at the beginning of braking is observed.

$$a_{RMS} = \sqrt{\frac{1}{T}\int_{0}^{T}\left[a^{2}(t)\right]dt} \tag{1}$$

where:

T - average time [s],

a(t) - instantaneous value of vibration accelerations [m/s²].

Additionally, dynamics of changes according to dependence in [6] of an examined diagnostic parameter for a certain frequency band and at a certain speed at the beginning of braking and values of correlation coefficients for linear dependence of amplitude value of vibration accelerations on examined friction pad's thicknesses is presented. On this basis it was concluded that diagnosing the wear of frictions pads can be carried out independently from the speed at the beginning of braking for certain frequency bands.

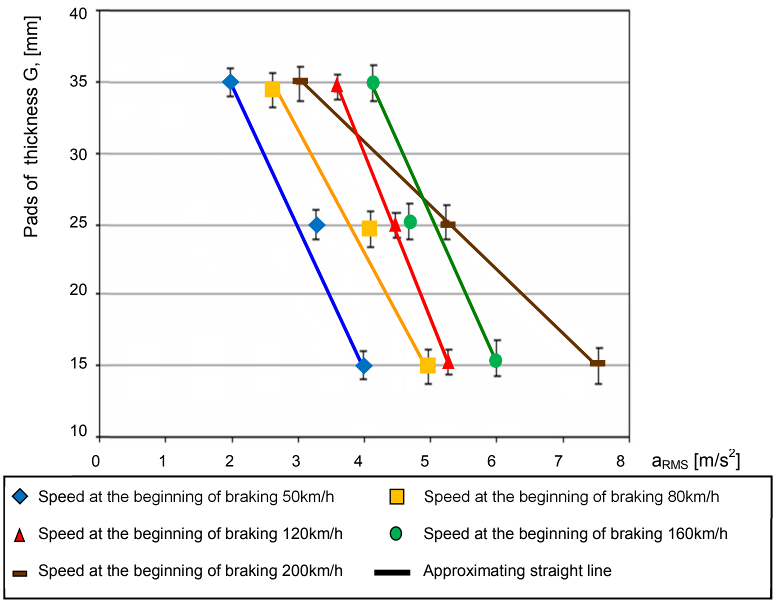

Figure. 3. Dependence of pad's thickness in function of RMS value of vibrations accelerations for frequency band 4600-5100Hz

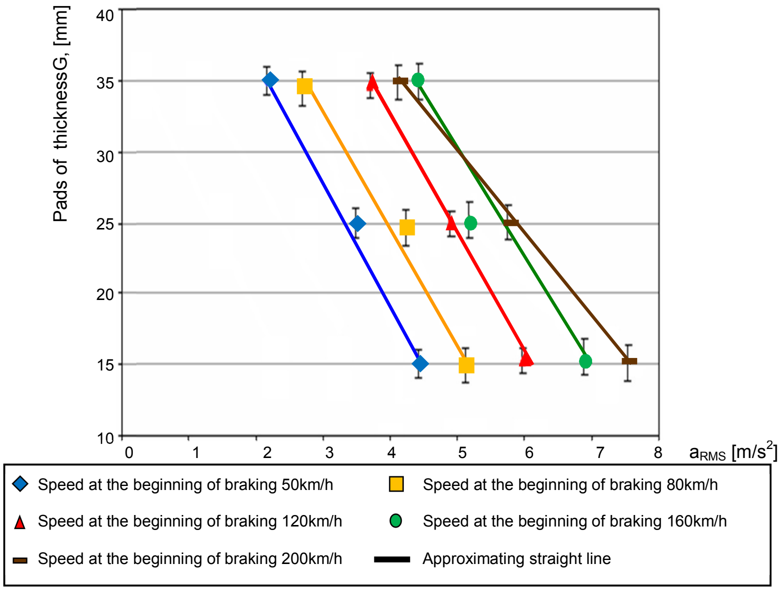

Figure. 4. Dependence of pad's thickness in function of RMS value of vibrations accelerations for frequency band 6000-6700Hz

Figure 3 and 4 presents dependence of friction pad's thickness of disc brake G on RMS value of vibration accelerations a_{RMS} in considered frequency bands.

On the basis of approximation function of the wear of friction pads against RMS value of vibration accelerations, linear dependences (2-7) were implemented for considered speeds at the beginning of braking enabling defining current friction pad's thickness.

$$G_{(v=50,\,4600-5100)} = -8{,}028 \cdot a_{RMS(v=50)} + 50{,}395, \tag{2}$$

$$G_{(v=80,\,4600-5100)} = -7{,}929 \cdot a_{RMS(v=80)} + 56{,}032, \tag{3}$$

$$G_{(v=120,\,4600-5100)} = -11{,}585 \cdot a_{RMS(v=120)} + 76{,}09, \tag{4}$$

$$G_{(v=50,\,6000-6700)} = -9{,}07 \cdot a_{RMS(v=50)} + 56{,}203, \tag{5}$$

$$G_{(v=80,\,6000-6700)} = -8{,}922 \cdot a_{RMS(v=80)} + 61{,}638, \tag{6}$$

$$G_{(v=120,\,6000-6700)} = -11{,}01 \cdot a_{RMS(v=120)} + 80{,}528, \tag{7}$$

Verification of stationary research on pads' thicknesses: G4=21.1mm and G5=16.2mm showed that diagnose error stemming from application of dependencies (2-

7) equaled 4-7% for pad G5 and 7-12% for pad G4. Lower values of diagnose error were obtained for band 6000-6700Hz.

3. Conclusions

The reseach at internal testing of railway brakes showed that it is possible to diagnose the wear of friction pads by using analysis of the values of the vibration acceleration caliper by defining in frequency domain.

Analysis of caliper vibrations in frequency domain enables to diagnose the wear of friction pads in two bands: 4600-5100 and 6000-6700Hz independently of speed at the beginning of braking.

For analysis in frequency domain, coefficients of dynamics of changes equals 2.7-7.6dB depending on the speed at the beginning of braking. Using RMS value of vibration accelerations it is possible to use diagnostic models to define the wear of friction pads at considered speeds at the beginning of braking.

Analyzing signals a(t) for considered pads' thickness, occurrence of self-excitation vibrations for pads worn to thickness of 15mm was observed. The effect of self-excitation vibrations may be connected with change of dynamics properties of the system caused by change of caliper and pad's mass, which is particularly visible at the end of braking.

References

1. Bocian, S., Boguś, P., Kaluba, M., Kardacz A., *Pozyskanie obrazu przez komputerowe systemy graficzne do wizyjnej kontroli i diagnostyki hamulca tarczowego*. Pojazdy Szynowe 2000, nr **2**, s. 37-53.
2. Brüel & Kjær, *Measuring Vibration*. Revision September 1982.
3. Brüel & Kjær, *Piezoelectric Accelerometer Miniature Triaxial Delta Tron Accelerometer* – Type 4504A, oferta firmy Brüel & Kjær.
4. Cempel, C., *Podstawy wibroakustycznej diagnostyki maszyn*. WNT Warszawa 1982.
5. Gruszewski, M., *Wybrane zagadnienia eksploatacji hamulca tarczowego*. Technika Transportu Szynowego 1995, nr **6-7**, s. 84-86.
6. Gryboś, R., *Drgania maszyn*. Wydawnictwo Politechniki Śląskiej, Gliwice 2009, s. 214.
7. Sawczuk, W., Szymański, M.G., *Application of selected time and amplitude characteristics of vibration Signac to diagnose railway disc brake*, Modern Electric Traction – Vehicles, s. 129-141.

XXV Symposium *Vibrations in Physical Systems,* Poznan – Bedlewo, May 15-19, 2012

Semiactive Damping of a Three-Layered Cantilever Beam with MR Fluid Embedded in Its Structure

Jacek SNAMINA, Bogdan SAPIŃSKI , Mateusz ROMASZKO
AGH University of Science and Technology, al. A. Mickiewicza 30, 30-059 Krakow
snamina@agh.edu.pl

Abstract

The subject of the paper is vibration control of a cantilever beam with magnetorheological (MR) fluid. Based on the results of identification and energy analysis, a control algorithm for free vibrations damping of the beam was proposed. The algorithm was realized by controlling the current supplying the electromagnet. The free vibrations of beam were investigated for constant current and current varied according to the assumed control algorithm.

Keywords: cantilever beam, MR fluid, vibration, control

1. Introduction

The interaction between an MR fluid and a system with continuously distributed mass and stiffness is in the form of a distributed load. It is realized by providing an MR fluid layer to continuous systems such as beams, plates and shells for the purpose of vibration reduction [1, 2, 5].

In theory, damping layers, being an integral part of a continuous system, have a great possibility for vibration reduction. However, problems arise associated with introduction of an MR fluid layer to the system, its sealing and maintenance in the service conditions.

In the first place an algorithm has to be developed for controlling the current in electromagnet coil so that properties of MR fluid could be varied under the action. The analysis of motion is mostly associated with discretization of a continuous system [6] and the control strategy is developed basing on the modal control approach [3, 7].

2. Experimental set-up

Three-layered cantilever beam is shown schematically in Fig. 1. Two outer layers made of aluminium are $l = 400$ mm long, $b = 30$ mm wide and $h_1 = 2$ mm high. The space between the two layers is sealed with silicone rubber $h_2 = 2$ mm thick and $g = 1.5$ mm wide. The beam interior is filled with MR fluid of the type 132DG (Lord Corporation).

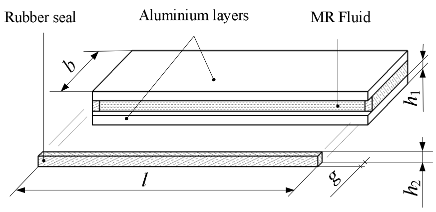

Figure 1. Structure of the beam

Semiactive damping of the beam's free vibrations is tested in the experimental setup (see Figs. 2 and 3). The magnetic field acting upon the beam is generated by an electromagnet whose position is defined by distance y_m between the beam attachment point and the centre of the electromagnet core. The electromagnet is supplied with current i from a power amplifier.

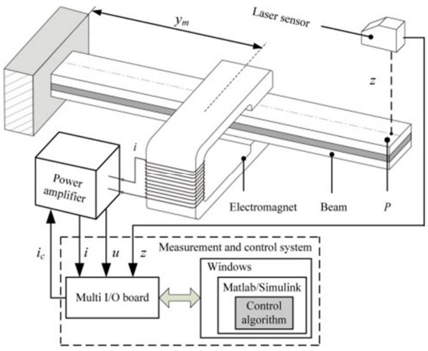

Figure 2. Schematic diagram of the experimental setup

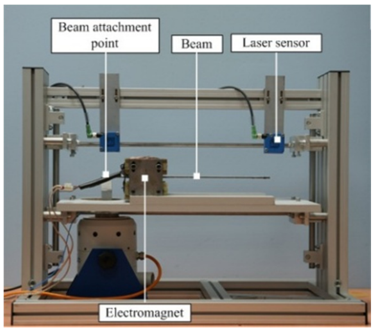

Figure 3.View of the experimental setup

The measuring and control system incorporates a PC computer, and I/O card RT-DAC4 (Inteco Ltd), supported by MATLAB/Simulink. A laser sensor is used to measure the displacement z of the beam's end point P.

The power amplifier [4] was used to generate magnetic field and control its strength. Two modes of amplifier operation are available: the voltage mode and the current mode (with an analogue PID controller embedded). The amplifier incorporates sensors for measuring the output signal u and the current i in the electromagnet coil.

3. Reduction of the beam's vibration

In most cases, the free vibrations of a cantilever beam involve the first mode. Accordingly, the beam displacement is given by the formula:

$$w(y,t) = Y(y)z(t) \tag{1}$$

where $Y(y)$ is the vibration mode and $z(t)$ is the displacement of the beam's free end. The equation of the beam's vibration can be reduced to the following differential equation:

$$m\ddot{z} + b\dot{z} + kz = 0 \tag{2}$$

where coefficients m, b, k stand for the modal mass, damping and stiffness, respectively.

Reduction of the beam's vibration through the control of its parameters consists in selecting the parameters b and k, depending on the state of the beam's motion. As the interaction between magnetic field and the beam with MR fluid give rise to the change of the beam's damping and stiffness, there is a possibility for controlling those parameters such that the vibration amplitude should be reduced as quickly as possible.

One approach to vibration reduction of the beam is that based on cyclic changes of the beam's stiffness such that its potential energy should be reduced in each cycle [3, 8].

This concept can be implemented through the control of magnetic field which causes the change of the MR fluid properties. A simple analysis of the beam's potential and kinetic energy during its movement with the first mode of vibration leads to formulate the stiffness switching principles. At the instant when the dead point is reached, the velocity becomes zero and the total energy of the system is associated only with the potential energy of elasticity. Reduction of stiffness at that moment gives rise to reduction of potential energy without an increase of kinetic energy, hence the total beam's energy is decreasing. The increase of the beam's stiffness should occur at the instant when the beam is not deformed. At that moment the potential energy of beam equals zero and kinetic energy reaches maximal level. The change in stiffness in the condition of no deformation does not lead to an increase of potential energy and kinetic energy does not change, either. Therefore, the stiffness switch should be performed four times within one cycle of vibration [8], in accordance with the following algorithm:

$$\begin{aligned} z\dot{z} \geq 0 \rightarrow k = k_h \\ z\dot{z} < 0 \rightarrow k = k_l \end{aligned} \tag{3}$$

where z is displacement of the end point of a vibrating beam, k is the modal stiffness of the beam, k_h denotes a high value of stiffness realised as a result of the control action, k_l stands for the low stiffness. Assuming the vibration amplitude to be A, the energy dissipated during one full cycle can be estimated from the formula:

$$W_s = \left(k_h - k_l\right) A^2 \tag{4}$$

The effectiveness of this algorithm depends on the difference between the high and low beam's stiffness ($k_h - k_l$) associated with the change of magnetic field. The rate of the decay of vibration is proportional to this difference.

Controlling the magnetic field causes not only variations of the beam's modal stiffness but the change of modal damping too. At each moment the damping force dissipates the energy of a vibrating beam. Assuming the sine vibrations with the amplitude A and frequency ω, energy dissipated within one full cycle is obtained from the formula:

$$W_t = \pi A^2 b \omega \tag{5}$$

where b is the modal damping coefficient for the first vibration mode. Eq (5) indicates that the dissipated energy will be maximal when the value of the coefficient b becomes as high as possible.

When the proposed algorithm is executed, the damping coefficient takes two values. Let b_l denote the damping coefficient realised when the stiffness coefficient equals k_l and b_h – the damping coefficient realised when the stiffness coefficient equals k_h. Hence, the dissipated energy is given by the formula:

$$W_t = 0.5\pi A^2 (b_h + b_l)\omega \tag{6}$$

This expression takes a value lower than that based on (5), when the magnetic field strength is assumed to be maximal value. Then the damping coefficient can be calculated as b=max (b_l, b_h).

It appears that in the case when the stiffness and damping cannot be separately controlled, the algorithm using the stiffness changes to reduce the beam's free vibration causes the decrease of energy dissipation associated with the damping coefficient. Practical application of the stiffness control algorithm will be merited if the 'profit' from the stiffness switch exceeds the 'loss' associated with simultaneous change of the damping coefficient, otherwise the free vibration will be well reduced when the value of the damping coefficient is assumed as high as possible. The final conclusions will be drawn after an experiment taking into account the non-ideal switching of the stiffness coefficient.

4. Experiments

The setup for testing the vibrations of sandwich beams with MR fluid and the system for controlling the current supplying the electromagnet are now used in testing the effects of control action in accordance with the control algorithm (see section 3) on the reduction of beam's free vibration. Before the algorithm can be used in practical applications, further tests are required to find out how variation of current flowing in the electromagnet coil should affect the beam's stiffness. This relationship shown in Fig. 4 is based on research data described in [2].

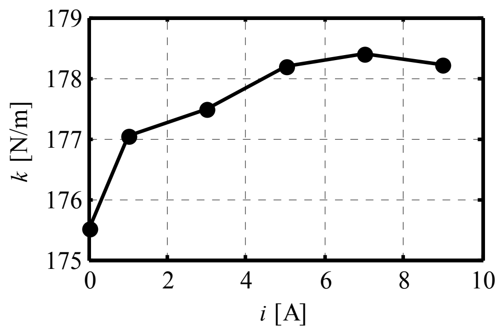

Figure 4. MR beam modal stiffness k vs. current i in the electromagnet coil

The effectiveness of the control algorithm can be evaluated basing on the plots of the beam's end displacement (Fig. 5). With control, the beam's end displacement tends to decrease faster than in the case when no current flows through the electromagnet coil (i = 0 A). However, the displacement decreases more slowly than in the case when the electromagnet coils are supplied with maximal current (i = 2 A).

Figure 6 presents the plots of the beam's end displacement, the current i_c predicted by control algorithm and the current i flowing in electromagnet coil. The current flowing in electromagnet coil differs from the predicted value due to the dynamic behaviour of the control system and of the power-supply.

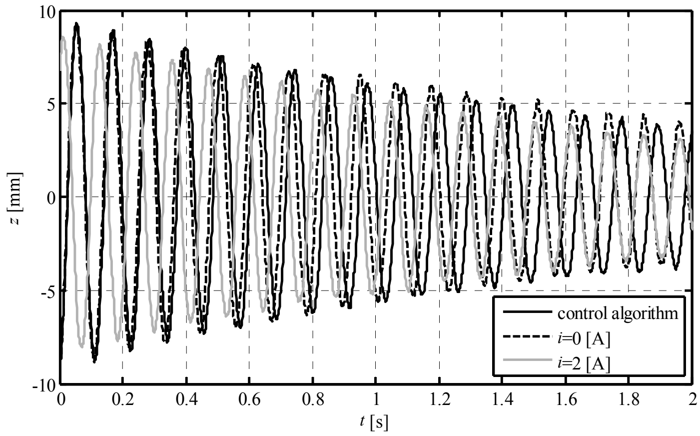

Figure 5. Displacement of the beam’s end

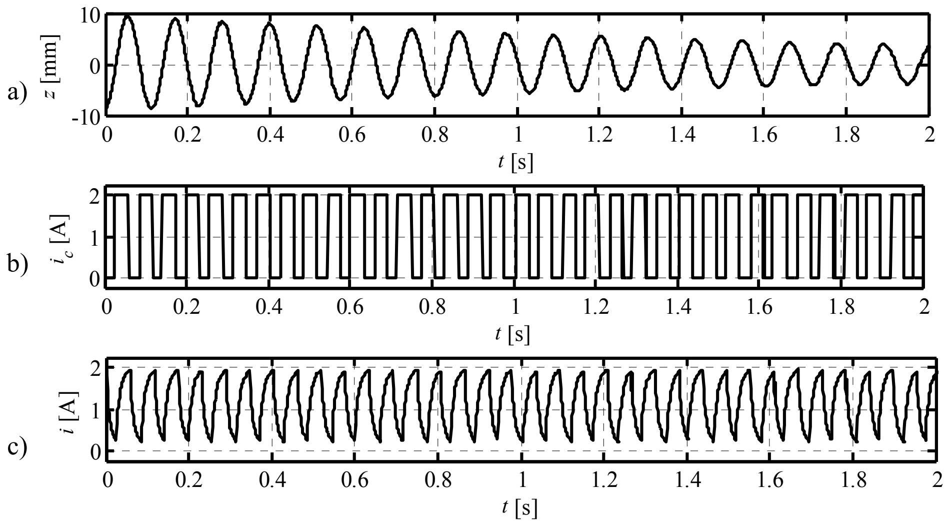

Figure 6. Displacement of the beam’s end a), current predicted by algorithm b), current in the electromagnet coil c)

5. Conclusions

Application of MR fluid in the sandwich beam allows the beam’s vibration to be actively reduced through the control of magnetic field surrounding the beam. The proposed algorithm for controlling the current supplying the electromagnet utilises the changes of the stiffness and damping coefficients to effect the fast reduction of the vibration amplitude. The purpose of this research was to determine whether the change of the beam's stiffness induced by variations of magnetic field should be sufficiently large to be effectively used in vibration reduction algorithms. Results show that application of a stiffness control algorithm to vibration reduction is ineffective due to concurrent changes of damping coefficients, decreasing the efficiency of the control algorithm. A simple algorithm whereby magnetic field is generated by the maximal current supplying the electromagnet seems to be a better solution for vibration reduction. One has to bear in mind, however, that this algorithm consumes more power than the switching algorithm.

Further work concerning new effective algorithm should focus on stiffness control algorithms admitting only slight modifications of the effects of variations in the damping coefficient.

Acknowledgments

This study is a part of research program no N501 223337.

References

1. V. Rajamohan, R. Sedaghati, S. Rakheja, *Optimal vibration control of beams with total and partial MR-fluid treatments*, Smart Materials and Structures, 20, 2011
2. M. Romaszko, S. Pakuła, B. Sapiński, J. Snamina, *Vibration parameters of sandwich beams with two types of MR fluid*, Mechanics And Control, **30(**3) (2011) 151-156, 2011
3. B. Sapiński, J, Snamina, *Vibration control capabilities of a cantilever beam with a magnetorheological fluid*, Mechanics, **27**(2) (2008).
4. B. Sapiński, M. Rosół, Ł. Jastrzębski, *Power amplifier for semi-active actuators based on MR fluid,* 13th International Carpathian Control Conference - ICCC´2012, Podbanské, 2012 (to be published)
5. B. Sapinski, J. Snamina, M. Romaszko, *Identification of model parameters of a sandwich beam incorporating magnetorheological fluid*, Vibration in Physical Systems, Poznan-Bedlewo, 24, 2010
6. J. Snamina, B. Sapiński, M. Romaszko, *Modeling of the sandwich beam incorporating magnetorheological fluid using FE method*, Engineering Modeling, **8(**39) (2010) 185-192.
7. J. Snamina, *Redukcja drgań układów ciągłych w wyniku oddziaływania tłumików i warstw tłumiących zawierających ciecz magnetoreologiczną*, Prace Komisji Nauk Technicznych PAU, 2010
8. P.L. Walsh, J.S. Lamancusa, *A variable stiffness vibration absorber for minimization of transient vibration*, Journal of Sound and Vibration, **120**(4) (1992), 1291-1305.

XXV Symposium *Vibrations in Physical Systems,* Poznan – Bedlewo, May 15-19, 2012

The Dynamic Stability of a Simply Supported Stepped Beam with Additional Discrete Elements

Wojciech SOCHACKI
Częstochowa University of Technology
Institute of Mechanics and Machine Design Foundations, Częstochowa, Poland
sochacki@imipkm.pcz.czest.pl

Abstract

The dynamic stability of a simply supported stepped beam with additional discrete elements was investigated in the paper. These elements are a rotational spring and a rotary inertia, both of which are connected to the beam. The discrete elements can be mounted at any chosen position along the beam length. The influence of step changes in the cross-section of the beam on its dynamic stability was also investigated in the paper. The problem of dynamic stability was solved by applying the mode summation method. Applying an orthogonal condition of eigenfunctions, the dynamic of the system was described with the use of the Mathieu equation. The obtained equation allowed the dynamic stability of the tested system to be analysed. The considered beam was treated as Euler- Bernoulli beam.

Keywords: Dynamic stability, Mathieu equation, eigenfunctions, stepped beam.

1. Introduction

Many works dealing with the dynamic stability of beams with additional discrete elements and with step changes in the cross-section can be found in the literature. Aldraihem and Baz [1] considered the dynamic stability of beams with step changes in the cross-section under moving loads. The dynamic stability of an elastic beam was analysed by Cederbaum and Mond [2]. Chen and Yeh [3] analysed the parametric instability of an electromagnetically excited beam. Evensen and Evan-Iwanowski [5] carried out analytical and experimental research into the influence of a mass mounted at the end of a beam on the dynamic stability of the beam. Gürgöze [6] analysed the influence of a mass mounted at the end of a beam elastically supported along its axis. Majorana and Pellegrino [7] analysed the dynamic stability of an elastically supported beam (rotation and translation springs at the ends). Sato et al. [8] investigated the parametric vibrations of a horizontal beam loaded by a concentrated mass, which showed the influence of the beam weight and the inertia of a rotational mass on the beam vibrations. Sochacki [9] investigated a simply supported beam axially loaded by a harmonic force, showing the destabilising effect of the concentrated mass, spring and harmonic oscillator.

This paper considers a simply supported stepped beam loaded by a longitudinal force in the form $P(t)= P_0+S\cos \nu t$. Additionally, a rotational spring and rotary inertia were connected to the beam at a chosen position between the supports. A change in the cross-section was made at a selected place on the beam length. The considered beams were treated as Bernoulli – Euler beams. The problem of dynamic stability was solved using the mode summation method. The applied research procedure allowed the dynamics of the tested systems to be described with the use of the Mathieu equation. The influence of the rotational spring and rotary inertia (values of coefficients c and I_o) and their positions on the beam on the value of coefficient b in the Mathieu equation was investigated. Similarly, the influence of step changes in the cross-section of the beams and its position along the beam length on the value of coefficient b was investigated. In this way the possibility of a loss of dynamic stability by the investigated systems was determined.

2. Mathematical model of beam vibrations

A diagram of the considered beam is presented in Fig. 1.

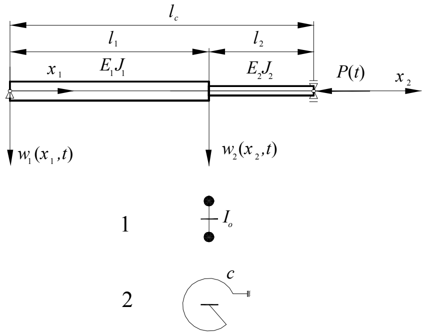

Figure 1. Model of the beam with step changes in the cross-section with rotary inertia (1) and rotational spring (2)

The vibration equation for two parts of a beam is known and has the following form:

$$E_i J_i \frac{\partial^4 w_{in}(x_i,t)}{\partial x_i^4} + P(t)\frac{\partial^2 w_{in}(x_i,t)}{\partial x_i^2} + \rho_i A_i \frac{\partial^2 w_{in}(x_i,t)}{\partial t^2} = 0 \tag{1}$$

where : $P(t) = P_0 + S\cos \nu t$, ν - forcing frequency,

ρ_i – density, A_i – cross-section area, i = 1,2 i-th part of the beam

Substituting into equations (1)

$$w_{in}(x_i,t) = W_{in}(x_i)\cos(\omega_n t)\,, \quad (i = 1,2) \tag{2}$$

where: ω_n is n-th natural frequency of the beam,

and into boundary conditions one can obtain (for S = 0):

$$E_i J_i W_{in}^{IV}(x_i) + P_0 W_{in}^{II}(x_i) - \rho_i A_i \omega_n^2 W_{in}(x_i) = 0\,, \quad (i = 1,2) \tag{3}$$

and

$$W_1(0) = 0\,, \qquad W_2(l_2) = 0 \tag{4, 5}$$

$$W_1(l_1) = W_2(0) \tag{6}$$

$$W_1^I(l_1)=W_2^I(0) \tag{7}$$

$$E_1J_1W_1^{II}(l_1)-E_2J_2W_2^{II}(0)=I_o\omega^2 W_1^I(l_1) \tag{8}$$

$$E_1J_1W_1^{III}(l_1)-cW_1^I(l_1)-E_2J_2W_2^{III}(0)=0 \tag{9}$$

$$W_1^{II}(0)=0\,, \quad W_2^{II}(l_2)=0 \tag{10, 11}$$

where the Roman numerals denote differentiation with respect to x.
The general solution to equations (3) takes the form:

$$W_{in}(x_i)=C_{i1}\cosh(\alpha_{in}x_i)+C_{i2}\sinh(\alpha_{in}x_i)+C_{i3}\cos(\beta_{in}x_i)+C_{i4}\sin(\beta_{in}x_i) \tag{12}$$

where C_{ik} are integration constants (k = 1, 2, 3, 4) and:

$$\alpha_{in}^2=-\frac{\lambda_i}{2}+\sqrt{\frac{\lambda_i^2}{4}+\Omega_{in}}\,, \qquad \beta_{in}^2=\frac{\lambda_i}{2}+\sqrt{\frac{\lambda_i^2}{4}+\Omega_{in}} \tag{13, 14}$$

where: $\Omega_{in}^2=\omega_n^2\dfrac{\rho_i A_i}{E_iJ_i}$, $\lambda_i=\dfrac{P_0}{E_iJ_i}$, $i=1,2$

The equations of vibrations (3) together with the boundary conditions (4-11) allow the boundary value problem of the investigated beam to be formulated. The natural frequency ω_n and eigenfunctions of the beam $W_{in}(x_i)$ are determined by solving the boundary value problem.

3. The solution to the problem of the dynamic stability of the beam

The solution to equation (1) is assumed to be in the form of an eigenfunction series [4].

$$w_i(x_i,t)=\sum_{n=1}^{\infty}W_{in}(x_i)T_n(t) \tag{15}$$

where: $T_n(t)$ are unknown time functions and $W_{in}(x_i)$ are normalized eigenfunctions of free frequencies of i-th parts of the beams which satisfies

$$\sum_{i=1}^{2}\rho_i^*\int_0^{l_i}W_{in}(x_i)W_{im}(x_i)dx_i+I_oW_{1n}^I(l_1)W_{1m}^I(l_1)\Big|\begin{matrix}=0 & gdy \quad m\neq n\\ =\gamma_m^2 & gdy \quad m=n\end{matrix} \tag{16}$$

Substituting solution (15) into equation (1) one can obtain:

$$\sum_{n=1}^{\infty}\left[E_iJ_iW_{in}^{IV}(x_i)T_{in}(t)+(P_0+S\cos\nu t)W_{in}^{II}(x_i)T_{in}(t)+\rho_iA_iW_{in}(x_i)\ddot{T}_{in}(t)\right]=0 \tag{17}$$

After multiplying by $W_{im}(x_i)$, one can receive from equation (17):

$$\sum_{n=1}^{\infty}\Big[E_iJ_iW_{in}^{IV}(x_i)W_{im}(x_i)\;T_n(t)+P_0W_{in}^{II}(x_i)W_{im}(x_i)T_n(t)+ \\ +S\cos\nu t\,W_{in}^{II}(x_i)W_{im}(x_i)T_n(t)+\rho_iA_iW_{in}(x_i)W_{im}(x_i)\ddot{T}_n(t)\Big]=0 \tag{18}$$

From equations (3), after multiplying by $W_{im}(x_i)$, one can obtain:

$$E_iJ_iW_{in}^{IV}(x_i)W_{im}(x_i)+P_0W_{in}^{II}(x_i)W_{im}(x_i)=\rho_iA_i\omega_n^2W_{in}(x_i)W_{im}(x_i) \tag{19}$$

then (18) takes the following form:

$$\sum_{n=1}^{\infty}\Big[\rho_iA_i\omega_n^2W_{in}(x_i)W_{im}(x_i)T_n(t)+ \\ +S\cos\nu t\,W_{in}^{II}(x_i)W_{im}(x_i)T_n(t)+\rho_iA_iW_{in}(x_i)W_{im}(x_i)\ddot{T}_n(t)\Big]=0 \tag{20}$$

As only the basic parametric resonance with the first natural frequency of the beam is taken into account in this paper, further analysis considers the first term of the sum from equation (20). Hence, after integrating equations (20), the following form was obtained for the whole beam and the first term:

$$T_1(t)\left(\omega_1^2\rho_iA_i\int_0^l W_{i1}^2(x_i)dx_i+S\cos\nu t\int_0^l W_{i1}^{II}(x_i)W_{i1}(x_i)dx_i\right)+\ddot{T}_1(t)\rho_iA_i\int_0^l W_{i1}^2(x_i)dx_i=0 \tag{21}$$

Appropriate transformations of equation (21) and the substitution of t by a new variable $\tau = \nu t$ lead to the following form of the Mathieu equation (the subscripts i and 1 were omitted).

$$\ddot{T}(\tau)+(a+b\cos\tau)T(\tau)=0 \tag{22}$$

where: $a=\dfrac{\omega_1^2}{\nu^2}$, $b=\dfrac{S}{\nu^2}\dfrac{\sum_{i=1}^{2}\int_0^l W_{i1}^{II}(x_i)W_{i1}(x_i)dx_i}{\sum_{i=1}^{2}\rho_iA_i\int_0^l W_{i1}^2(x_i)dx_i}$, dots denote differentiation with respect to τ.

The periodical solutions to the Mathieu equation (22) are known [10]. These solutions allow us to determine the stable and unstable regions of the solutions. It must be stated that the probability of obtaining a stable solution is higher in case of a lower value of coefficient *b,* at the determined value of *a*.

4. The results of numerical computations and discussion

Computations were carried out assuming the following dimensionless quantities:

$$C=\frac{cl_c}{EJ},\quad I=\frac{I_o}{A_1\,l_c^3},\quad J=\frac{J_2}{J_1},\quad l=\frac{l_1}{l_c},\quad p=\frac{P_0}{P_c},\quad s=\frac{S}{P_c} \tag{23}$$

where: P_c – the critical load of the tested beam with a constant cross-section, $p = 0.05$ and $s = 0.05$ was assumed for computations.

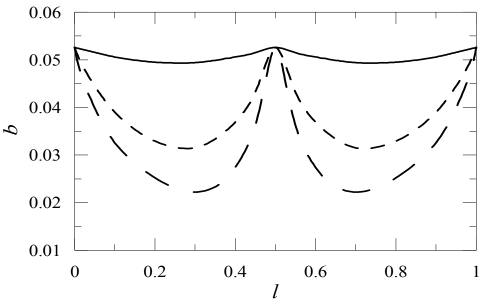

Figure 2. The influence of the position of a spring with elasticity coefficient C mounted on the beam on the value of coefficient b for a = 1: C = 1— —, C = 10- - -, C = 20——.

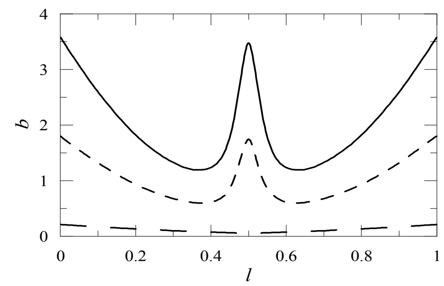

Figure 3. The influence of the position of an element with rotary inertia I mounted on the beam on the value of coefficient b for a = 1: I = 0.1— —, I = 1- - -, I = 2—— .

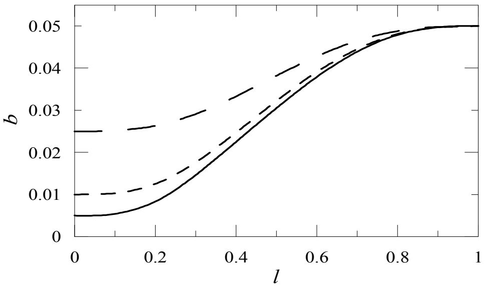

Figure 4. The influence of the location of changes in the cross-section l of the beam on the value of coefficient b for a = 1: J = 2 — —, J = 5 - - -, J = 10 ——.

The results of the solution to the dynamic stability problem allows us to determine the values of coefficient b in the Mathieu equation for changeable coefficient of rotational spring C mounted at a randomly selected position on the beam (Fig. 2) and the changeable values of rotary inertia I (Fig. 3). Additionally, the solution to the problem of the dynamic stability of the tested beams allowed us to determine the values of coefficient b in the Mathieu equation at changeable values of moments of inertia J_1 and J_2 for two parts of the beam (Fig. 4).

5. Conclusions

The following conclusions can be drawn from the analysis of the presented results:

- The most disadvantageous position to mount the rotational spring is in the centre and on the supports of the beam (independently of the values *C*). Each of the intermediate positions of the rotational spring between the supports and the midpoint of the beam leads to a stabilization of the tested systems (lowers *b*).
- The mounting position of the element with rotary inertia *I* on the beam has a significant influence on the value of coefficient *b*. If its position is closer to the midpoint or to the ends of the beam, the value of coefficient *b* is higher.
- An increase in the values of coefficients *C* and *I* leads to an increase in coefficient *b* in the Mathieu equation (this leads to a destabilization of the system).
- The smaller difference between moments of inertia J_1 and J_2 (less *J*) the easier is for the tested systems to lose dynamic stability (higher *b*) an increase in the beam lengths with a higher moment of inertia leads to a stabilization of the tested systems.

Acknowledgments

This research was supported by the Ministry of Science and Higher Education in 2012, Warsaw, Poland.

References

1. O. J. Aldraihem, A. Baz, *Dynamic stability of stepped beams under moving loads*, Journal of Sound and Vibration, **205**, 5, (2002) 835-848.
2. G. Cederbaum, M. Mond, *Stability Properties of a Viscoelastic Column Under a Periodic Force*, Journal of Applied Mechanics, **59**, (1992) 16-19.
3. C.-C. Chen, M.-K. Yeh, *Parametric instability of a beam under electromagnetic excitation*, Journal of Sound and Vibration, **240**, 4, (2001) 747-764.
4. R. R. Craig Jr., *Structural Dynamics*, New York, Wiley 1981.
5. H. A. Evensen, R. M. Evan-Iwanowski, *Effects of Longitudinal Inertia Upon the Parametric Response of Elastic Columns*, ASME Journal of Applied Mechanics, **33**, (1966) 141-148.
6. M. Gürgöze, Parametric vibrations of restrained beam with an end mass under displacement excitation, Journal of Sound and Vibration, **108**, 1, (1986) 73-84.
7. C. E. Majorana, C. Pellegrino, *Dynamic stability of elastically constrained beams: an exact approach,* Engineering Computations, **14**, 7, (1997) 792-805.
8. K. Sato, V. Saito, V. Otomi, *The Parametric Response of a Horizontal Beam Carrying a Concetrated Mass Under Gravity*, ASME Journal of Applied Mechanics, **45**, 10 (1978) 643-648.
9. W. Sochacki, 2008, The dynamic stability of a simply supported beam with additional discrete elements, Journal of Sound and Vibration, **314**, 180-193.
10. S. P. Timoshenko, V. Gere, *Theory of Elastic Stability*, Mc Graw–Hill – INC 1961.

XXV Symposium *Vibrations in Physical Systems,* Poznan – Bedlewo, May 15-19, 2012

Differential Evolution in System Parameters Identification

Tomasz STRĘK, Maria NIENARTOWICZ
Institute of Applied Mechanics, Poznan University of Technology
Piotrowo 3, 60-965 Poznan, Poland
maria.nienartowicz@gmai.com, tomasz.strek@put.poznan.pl

Abstract

In this paper the Differential Evolution (DE) optimization algorithm is presented and applied in benchmark problem: minimization of Rosenbrock's function and identification of mechanical systems parameters. DE optimization algorithm is also used in conjunction with a squared error measure to identify the optimal model parameter values of mass-spring-damper (MSD) using time series experimental data.

Keywords: optimization, parameters identification, differential evolution

1. Introduction

In recent years, the technical literature has seen a significant increase of reported methods for identifying parameters of systems (modeled by ordinary or partial differential equations) from time series data. A natural way to evaluate the performance of such methods is to try them on a sufficient number of realistic test cases. However, weak practices in specifying identification problems and lack of commonly accepted benchmark problems makes it difficult to evaluate and compare different methods [1]. In paper [1] authors present a collection of more than 40 benchmark problems for ODE model identification of cellular systems. Authors consider both problems with simulated data from known systems, and problems with real data.

D'Ambrosio and coauthors discuss the problem of system identification and parameters monitoring for a general class of non-linear systems [2]. Authors introduce a new method based on Lie series expansion. In order to use this approach, the system features must be modeled by analytic or sufficiently smooth functions of the state variables, including the time parameter.

Methods for determination of the dynamic characteristics and parameters of mechanical vibrating systems by processing experimental data on controlled vibrations are presented in paper [3]. These methods are intended for construction of mathematical models of objects to be identified and classed as parametric and nonparametric methods.

2. Nonlinear optimization

Numerical algorithms for constrained nonlinear optimization can be broadly categorized into gradient-based methods and direct search methods [4]. Gradient-based methods use first derivatives (gradients) or second derivatives (Hessians). Examples are the sequential quadratic programming (SQP) method, the augmented Lagrangian method, and the (nonlinear) interior point method. Direct search methods do not use derivative information. Examples are Nelder–Mead, genetic algorithm and differential evolution, and simulated annealing [5, 6]. Direct search methods tend to converge more slowly, but can be more tolerant to the presence of noise in the function and constraints.

Typically, algorithms only build up a local model of the problems. Furthermore, many such algorithms insist on certain decrease of the objective function, or decrease of a merit function which is a combination of the objective and constraints, to ensure convergence of the iterative process. Such algorithms will, if convergent, only find local optima, and are called local optimization algorithms.

Global optimization algorithms attempt to find the global optimum, typically by allowing decrease as well as increase of the objective/merit function. Such algorithms are usually computationally more expensive.

In this paper the differential evolution (DE) algorithm is presented and applied in benchmark problem: minimization of Rosenbrock's function and identification of mechanical systems parameters using amplitude versus frequency experimental data. DE optimization algorithm is also used in conjunction with a squared error measure to identify the optimal model parameter values of mass-spring-damper (MSD) using time series data experimental data. MSD system is modeled by system of ordinary differential equations (ODEs).

3. Differential Evolution (DE) algorithm

A new heuristic approach for minimizing possibly nonlinear and non-differentiable continuous space functions is presented in papers of Storn and Price [7]. Authors demonstrated that the new method converges faster and with more certainty than many other acclaimed global optimization methods. The new method requires few control variables, is robust, easy to use, and lends itself very well to parallel computation [7].

Differential Evolution is distinguished from other direct search optimization procedures by the biologically inspired process which produces the trial vector. A parent vector ($\mathbf{x}_{parent}$) from the population of the primary array is mutated by adding noise to its parameters, thus helping to explore new areas of parameter space and to escape from local minima. The noise is taken to be the scaled difference between two other vectors ($\mathbf{x}_1$ and $\mathbf{x}_2$) chosen randomly from the population of the primary array $\mathbf{x}_{mutated} = \mathbf{x}_{parent} + s(\mathbf{x}_1 - \mathbf{x}_2)$, where s is a scaling factor which must be in the range $0 \le s \le 1.2$ for stability and whose optimal value for most problems lies in the range $0.4 \le s \le 1.0$. The vector produced by mutation and the original target vector are then used in a crossover operation designed to resemble the process by which a child inherits DNA from its two parents.

There exists another methods generating new mutated population $\mathbf{x}_{mutated} = \mathbf{x}_{best} + s(\mathbf{x}_1 - \mathbf{x}_2)$ or $\mathbf{x}_{mutated} = \mathbf{x}_{parent} + s(\mathbf{x}_1 - \mathbf{x}_2 + \mathbf{x}_3 - \mathbf{x}_4)$. Differential evolution is a simple stochastic function minimizer. The algorithm maintains a population of *pop* points, $\{\mathbf{x}_1, \mathbf{x}_2, \ldots \mathbf{x}_j, \ldots, \mathbf{x}_{pop}\}$, where typically $pop > n$, with n being the number of variables. Points are from range from $\mathbf{x}_{\min}$ to $\mathbf{x}_{\max}$.

During each iteration of the algorithm, a new population of m points is generated. The *j-th* new point is generated by picking three random points, $\mathbf{x}_w, \mathbf{x}_u \mathbf{x}_v$, from the old population, and forming $\mathbf{x}_s = \mathbf{x}_w + s(\mathbf{x}_u - \mathbf{x}_v)$ or $\mathbf{x}_s = \mathbf{x}_{best} + s(\mathbf{x}_u - \mathbf{x}_v)$, where s is a real scaling factor and $\mathbf{x}_{best}$ is best points at given population. Then a new point $\mathbf{x}_{new}$ is constructed from $\mathbf{x}_j$ and $\mathbf{x}_s$ by taking the *i-th* coordinate from $\mathbf{x}_s$ with probability *prob* and otherwise taking the coordinate from $\mathbf{x}_j$. If $f(\mathbf{x}_{new}) < f(\mathbf{x}_j)$, then $\mathbf{x}_{new}$ replaces $\mathbf{x}_j$ in the population. The probability *prob* is controlled by the cross probability option.

Moreover, $f_{best} = f(\mathbf{x}_{best})$. If any *i-th* coordinate of new point is outside the range, the new *i-th* coordinate of point is generated from $x_{\min,j}$ to $x_{\max,j}$ range.

The process is assumed to have converged if the difference between the best function values in the new and old populations, as well as the distance between the new best point and the old best point, are less than the tolerances provided by `eps`. Iteration process is limited also by maximum number of steps – *maxstep*. The differential evolution method is computationally expensive, but is relatively robust and tends to work well for problems that have more local minima.

4. Numerical results and conclusions

Quality of optimization procedures (those known and proposed) are frequently evaluated by using common standard literature benchmarks. There are several classes of such test functions, all of them are continuous, e.g. Rosenbrock function [8]. In this paper DE algorithm is applied to solve three problems: minimization of Rosenbrock function, parameters identification of nonlinear driven mechanical vibrating system and system parameters identification from time series.

Let us consider function $y = f(x,\mathbf{p})$, where parameters are as follow $\mathbf{p} = \lfloor p_1,...,p_{nofp} \rfloor$. Let us assume that experimental data of function with unknown set of parameters is represented by set $sol = \{(x_i, \bar{y}(x_i)), i = 1,2,...,nofx\}$. For set of parameters $\mathbf{p}$ the function is represented by set $solp = \{(x_i, y_i = y(x_i,\mathbf{p})), i = 1,2,...,nofx\}$. Let us define error as function of $\mathbf{p}$: $err(\mathbf{p}) = \left(\sum_{i=1}^{nofx} (\bar{y}\ (x_i) - y\ (t_i,\mathbf{p}))^2\right)^{1/2} = \left(\sum_{i=1}^{nofx} (\bar{y}_i - y_i)^2\right)^{1/2}$.

To find optimal values of unknown parameters we should minimize $err(\mathbf{p})$. This can be done using, for example, DE algorithm.

Problem 1. The Rosenbrock function minimization

In mathematical optimization, the Rosenbrock function is a non-convex function used as a performance test problem for optimization algorithms introduced by Howard H. Rosenbrock in 1960 [8]. There are many ways to extend this function stochastically:

$$f(\mathbf{p})=\sum_{i=1}^{n-1}\left((1-p_i)^2+100\varepsilon_i\left(p_{i+1}-p_i^2\right)^2\right), \tag{1}$$

where the random variables ε obey a uniform distribution from range <0,1>.

Using DE algorithm (s = 0.5, $prob$ = 0.8 and eps = $1e\text{-}15$) one can find minimized parameters $\mathbf{p}_{best}$ of the Rosenbrock function. Results of minimization of the Rosenbrock function using DE algorithm are presented in Table 1.

Table 1. Bounds for parameters, best parameters, error and DE quantities

No.	$p_{\min,i}$	$p_{\max,i}$	ε_i	n	pop	$err(\mathbf{p}_{best})$	$steps$
1	-10	10	1e-2	20	150	4.92e-05	500
2	-10	10	1e-2	50	150	3.36e+00	500
3	-10	10	1e-2	50	200	6.27e-03	1000

Problem 2. The intensity of oscilations

Let us consider mechanical system described by following equation

$$m\frac{d^2x}{dt^2}+b\frac{dx}{dt}+kx=F\cos(\omega t). \tag{2}$$

Solution of the above equation is in the form

$$x(t)=A(\omega)\cos(\omega t+\phi), \tag{3}$$

where the expression for the displacement amplitude is

$$A(\omega)=\frac{F/m}{\sqrt{\left(\omega^2-\omega_0^2\right)^2+(b\omega/m)^2}}, \tag{4}$$

with natural frequency $\omega_0=\sqrt{k/m}$. Vector of optimized parameters is $\mathbf{p}=[F,m,\omega_0,b]$. Using DE algorithm ($s$ = 0.1, $prob$ = 0.8 and eps = $1e\text{-}15$) one can find optimized parameters $\mathbf{p}_{best}$ using experimental data for amplitude. Three cases of problem were considered in this subsection. Cases are different due to bounds for parameters. Results are presented in Table 2 and in Fig. 1. Figure presents experimental amplitude of vibrating system and error between experimental and optimized data.

Table 2. Bounds for parameters, best parameters, error and DE quantities

No.	$\mathbf{p}_{\min}$	$\mathbf{p}_{\max}$	$\mathbf{p}_{best}$	$err(\mathbf{p}_{best})$	pop	$steps$
1	1.0, 0.1, 5.0, 0.1	100, 1, 500, 10	52.28, 0.52, 49.99, 5.22	1.25e-06	50	500
2	5, 0.05, 25, 0.5	50, 0.5, 250, 5	35.48, 0.35, 49.99, 3.54	1.25e-06	50	500
3	9, 0.09, 45, 0.9	11, 0.11, 55, 0.1	9.38, 0.09, 49.99, 0.93	1.25e-06	50	500

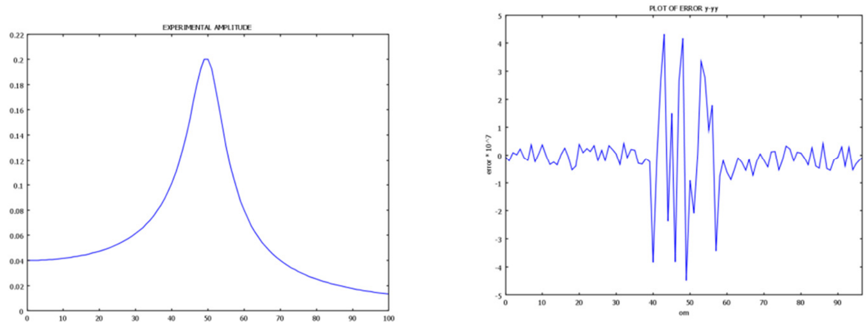

Figure 1. Experimental amplitude (left) and error between experimental and optimized amplitude (right) for parameters $\mathbf{p}_{best} = [9.38, 0.09, 49.99, 0.93]$ (vertical axis - amplitude value (left) and error (right); horizontal axis - frequency)

Problem 3. Identification of system parameters from time series

In recent years, the technical literature has seen a significant increase of reported methods for identifying parameters of systems (modeled by ordinary or partial differential equations) from time series data.

Let us consider first order ODEs system $\dot{\mathbf{y}} = f(t, \mathbf{y}, \mathbf{p})$ with initial conditions $\mathbf{y}(t_0) = \mathbf{y}_0$ where $\mathbf{y} = [y_1, y_2, ..., y_N]$ and vector of parameters $\mathbf{p} = [p_1, p_2, ..., p_{nofp}]$. Let us assume that time series data (experimental data or solution of system of ODEs with unknown set of parameters) is represented by set $sol = \{(t_i, \overline{\mathbf{y}}(t_i)), i = 1,2,..., noft\}$. For set of parameters $\mathbf{p}$ the solution of system of ODEs is as it follows $solp = \{(t_i, \mathbf{y}_i = \mathbf{y}(t_i, \mathbf{p})), i = 1,2,..., noft\}$. Let us define error as function of $\mathbf{p}$: $err(\mathbf{p}) = \left(\sum_{i=1}^{noft} \sum_{j=1}^{N} (\overline{y}_j(t_i) - y_j(t_i, \mathbf{p}))^2 \right)^{1/2} = \left(\sum_{i=1}^{noft} \sum_{j=1}^{N} (\overline{y}_{ji} - y_{ji})^2 \right)^{1/2}$. To find optimal values of unknown parameters we should minimize $err(\mathbf{p})$.

DE algorithms can be used for example for identification of chosen parameters of mechanical systems. Dynamical and advanced mechanics problems are stated, illustrated and discussed in book [9]. In Figure. 2 a simple mechanical system MSD is presented.

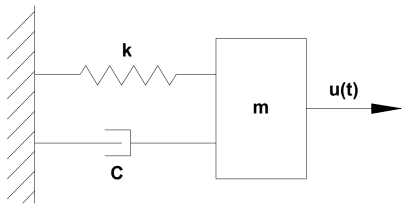

Figure 2. Simple mechanical system MSD

The behavior of MSD system can be described by differential equation

$$m\frac{d^2y(t)}{dt}+c\frac{dy(t)}{dt}+ky(t)=u(t) \tag{5}$$

where: $y(t)$ – an instantaneous displacement of mass m, c – coefficient of damping, k – spring constant. We assumed that a force acting on this system is: $u(t)=p\sin(\omega t)$.
Above equation one can write in matrix form

$$\frac{d}{dt}\begin{bmatrix} y_1 \\ y_2 \end{bmatrix}=\begin{bmatrix} 0 & 1 \\ -k/m & -c/m \end{bmatrix}\begin{bmatrix} y_1 \\ y_2 \end{bmatrix}+\begin{bmatrix} 0 \\ 1/m \end{bmatrix}u(t)\,. \tag{6}$$

It is easy to implement DE algorithm and optimize parameters like m, c, k, p and ω using the Differential Evolution Algorithm. Vector of optimized parameters is $\mathbf{p}=[m,c,k,p,\omega]$. Using DE algorithm ($s$=0.1 and $prob$=0.8) one can find optimized parameters $\mathbf{p}_{best}$ using experimental data for y_1 and y_2. In this paper ODEs system was solved using COMSOL Script and the implicit time-stepping scheme DAE solver DASPK [10]. Results are presented in Table 3 and in Fig. 3. Figure 3 presents experimental time series of vibrating system and error between experimental and optimized data for MSD system.

Table 3. Bounds for parameters, best parameters, error and DE quantities

Quantity	$\mathbf{p}_{min}$	$\mathbf{p}_{max}$	$\mathbf{p}_{best}$	$err(\mathbf{p}_{best})$	pop	$steps$
m	0.5	1.5	0.8722	6.5832e-005	50	200
c	0.05	0.15	0.0872			
k	0.05	0.15	0.0872			
p	5.0	15	8.7223			
ω	1.0	3.0	1.9999			

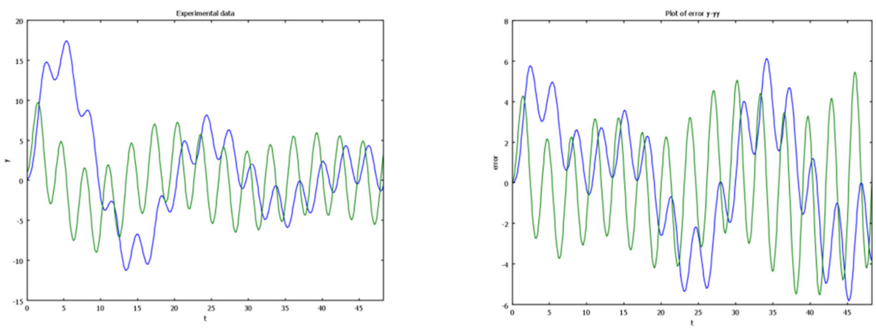

Figure 3. Experimental data (left) and error of optimized shape (right) for y_1 and y_2 for parameters $\mathbf{p}_{best}$ from Table 3 (vertical axis - value of y_1 and y_2 (left) and optimized error (right); horizontal axis - time). Error is mulitplied by 10^6.

The Differential Evolution heuristic algorithm offers an easy and efficient way to optimize or identify parameters of different systems. In the present paper we have shown explicitly its applicability to the function and system parameters identification.

References

1. Peter Gennemark, Dag Wedelin, *Benchmarks for identification of ordinary differential equations from time series data*, Bioinformatics, **25(**6) (2008) 780-786.
2. D'Ambrosio S., Guarnaccia C., Guida D., Lenza T.L.L., Quartieri J., *System Parameters Identification in a General Class of Non-linear Mechanical Systems*, International Journal of Mechanics, **4(**1) (2007) 76-79.
3. N. P. Plakhtienko, *Methods of Identification of Nonlinear Mechanical Vibrating Systems*, International Applied Mechanics, **36(**12) (2000) 1565-1594.
4. J.S. Arora, *Introduction to Optimum Design*, Elsevier Academic Press, London, 2004.
5. J.H. Holland., *Adaptation in natural and artificial systems*, The University Michigan Press, 1975.
6. J.R. Koza, *Genetic programming. On the Programming of Computers by Means of Natural Selection*, MIT Press, Cambridge, 1992.
7. R. Storn, K. Price, *Differential Evolution – A Simple and Efficient Heuristic for Global Optimization over Continuous Spaces*, Journal of Global Optimization, **11** (1997) 341-359.
8. H.H. Rosenbrock., *An automatic method for finding the greatest or least value of a function*, The Computer Journal, **3** (1960) 175-184.
9. J. Awrejcewicz, *Classical Mechanics. Dynamics*, Springer, New York, 2012.
10. P.N. Brown, A.C. Hindmarsh, L.R. Petzold, *Using Krylov Methods in the Solution of Large-Scale Differential-Algebraic Systems*, SIAM J. Sci. Comput., **15** (1994) 1467-1488.

XXV Symposium *Vibrations in Physical Systems,* Poznan – Bedlewo, May 15-19, 2012

Acoustic Study of Two Modern Churches

Anna SYGULSKA
Poznań University of Technology, Faculty of Architecture
ul. Nieszawska 13 C, 61-021 Poznań, anna.sygulska@wp.eu

Abstract

The acoustics of churches is a very important issue, especially because of the speech intelligibility. This aspect is very often neglected during the designing process in modern sacral architecture. Too long reverberation time and acoustic defects such as echo result in the lack of verbal intelligibility. Two modern churches were investigated in this paper. Acoustic parameters were measured and analyzed in terms of their function. The results of the measurements in the objects were compared and analyzed in terms of the influence of the architecture on the acoustics. The results of the measurements show considerable differences in acoustic parameters in both churches.

Keywords: church acoustics, reverberation time in church, acoustic investigation in church.

1. Introduction

The architecture of some churches is a cause of acoustic problems. It is especially seen in modern church architecture solutions. Above all, inappropriate architectural design causes lack of understanding of the spoken word. We should specifically remember that the word is a priority in a liturgy of a Catholic church; therefore, the basic function of the liturgy cannot be fulfilled. Hence, it is very important to see what architectural factors influence such a situation. The problem of church acoustics is discussed inter alia in papers [2-6].

The main problem is excessive reverberance of church interiors, i.e. too long reverberation time. Reverberation time is proportional to cubature, i.e the bigger cubature, the longer reverberation time is. The influence of applied materials is connected with α coefficient. Absorption coefficients are used to rate material's effectiveness in absorbing sound. The absorption coefficient of a material varies with frequency. [4]. The required reverberation time of a particular interior depends on its function. The greater participation of speech, the lower reverberation time the room should have (Table 1).

Table 1. Recommended values of reverberation time for different kinds of sound production according to Meyer and Neuman [5].

Type of sound production	Reverberation time [s]
Speech: cabaret	0.8
performances, lectures	1.0
Music: chamber music	1. to 1.5
opera	1.3 to 1.6
concert	1.7 to 2.1
organ music	2.5 to 3.0

Figure 1 shows recommended reverberation time for churches. The line graph shows mutual dependence between the optimum reverberation time and the cubature of an interior. The upper section of the graph refers to cathedrals and churches with a considerable amount of organ music; the lower section refers to churches where speech is more important.

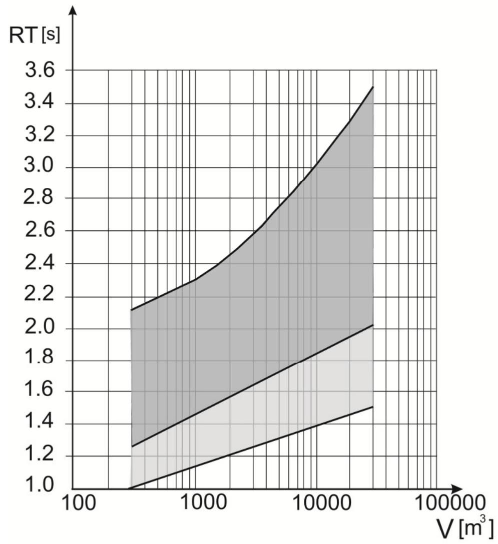

Figure 1. Range of optimum reverberation time for churches [on the basis of 4]

Minimalism in architecture, vast areas and application of traditional materials such as stone, glass, and plaster contribute to the fact that contemporary churches excess recommended reverberation time values. Architectural styles of historic churches, particularly the Baroque style rich in detail, facilitate sound diffusion. Likewise, transepts and aisles as sub-areas influence the decrease of reverberation time in church. Contemporary designs of churches offer aisless interiors with scanty detailing, while they disregard workable contemporary solutions, such as application of acoustic plaster**.**

The question of acoustics in churches is a complex issue as church interiors must facilitate functions with entirely different acoustic requirements. First and foremost, an utterance must be understood since the spoken word is the foundation of liturgy in the Catholic Church. The liturgy, however, is often accompanied by the pipe organ. The recommended acoustic parameters for organ music entirely differ from the parameters suitable for a speech. The recommended reverberation time for churches is more suitable for organ music; yet, with the introduction of artificial reinforcement, a church provides favourable conditions for speeches too. In contrast, if the recommended reverberation time in a church interior is exceeded, organ music may sound good enough, but sound reinforcement applied in order to facilitate comprehension of an utterance will pose a considerable difficulty (in most cases, it can be virtually impossible due to prohibitive costs).

2. Acoustic investigation of churches

Two contemporary churches – the Name of Mary Church in Poznan (Fig. 2) and the Christ the Only Saviour Church in Swarzedz (Fig. 4) – underwent acoustic investigation.

The Name of Mary Church in Poznan was erected in place of a former church founded in 1937. The consecration of the newer and bigger temple took place in 1982. The walls of the old choir were preserved, but the new walls do not correspond with the style of the former building. The cubature of the church is about 5100 m³. The walls are covered with traditional plaster and fleecy texture plaster. The side walls have huge windows, between which there are wooden pillars. The suspended ceiling is made of bulky wooden panels. Wood is also part of the choir banister in the back of the church. The wood is a system of panels, constituting sound diffusing structure. In the church there is also a vast pipe organ. Its pipes are both in the choir and on the back wall. Figure 3 shows a view of the church with the distribution of measuring points and the sound source.

The Christ the Only Saviour Church is at the final finishing stage. In 2005, the erection of the church was accomplished. At present, its ceiling is covered with oiled wood; the floor is made of marble; the walls are plastered and have huge windows; the benches have upholstered seats. The choir, situated at the back of the church, changes into narrow side balconies along the aisle. The church does not have a pipe organ as an electronic instrument is used. The cubature of the church is about 7100 m³. Figure 5 shows a view with the distribution of measuring points. Both churches are of an aisleless type. Due to the symmetry in both churches, measuring points were determined on one side only. The sound source was placed at the altar.

The measuring equipment consists of a sound measuring device SVAN 945A, connected to the DIRAC programme. The Brüel & Kjær ZE-0948 USB Audio Interface was used. To receive the impulse response of the room, a gun shot was applied. The DIRAC programme calculates the following acoustic parameters: *RT, Ts, C80, C50, STI.*

Table 2 shows the results of the measurements taken in both churches. Figure 6 shows frequency characteristic of mean reverberation time.

Table 2. Results of the measurements

Parameters	Name of Mary Church	Christ the Only Saviour Church
RT [s]	1.82	4.65
$RT_{500-1000}$ [s]	1.97	5.17
Ts [ms]	148	344
C80 [dB] *first row*	- 2.0	- 8.1
C80 [dB] *back row*	- 4.6	- 8.6
C50 [dB]	- 5.2	-12.5
STI female, first row	0.47	0.33
STI male, first row	0.47	0.33

Figure 2.The Name of Mary Church in Poznan [8]

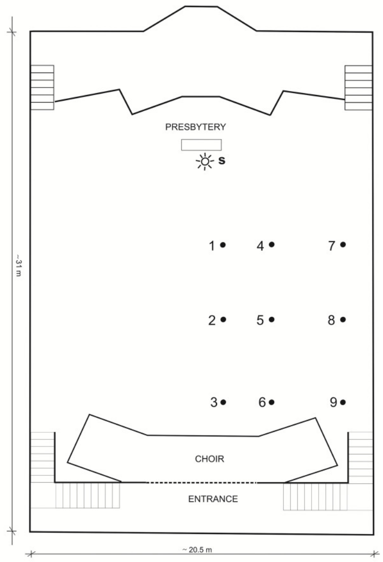

Figure 3. View of the church with marked points of the observation and the sound source

Figure 4. The Christ the Only Saviour Church [7]

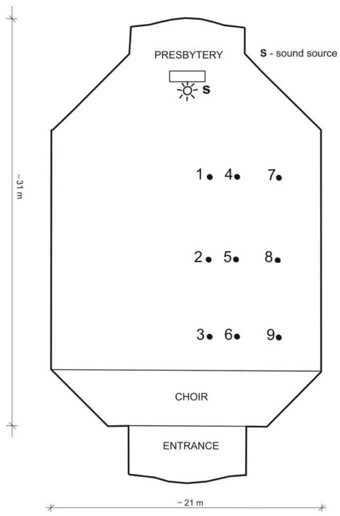

Figure 5. View of the church with marked points of the observation and the sound source

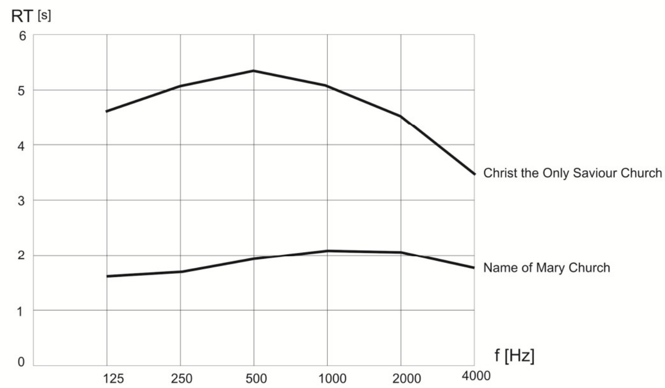

Figure 6. Frequency characteristic of mean reverberation time

3. The analysis of the results

For the Name of Mary Church, reverberation time *RT* amounts to 1.82 s and remains in accordance with recommended values (Fig. 1). For the Christ the Only Saviour Church, reverberation Time *RT* amounts to 4.65 s, which considerably exceeds recommended values. For the frequency of 500-1000 Hz, results for reverberation time are similar, $RT_{500-1000}$ is 1.97 s and 5.17 s respectively. The recommended $RT_{500-1000}$ for churches with prevalence of organ music amounts to 1.5 s – 2.2 s. For churches where speech and music are equally important, *RT* amounts to 1.3 s – 1.75 s.

Center time *Ts* is the center of gravity along the time axis of the squared impulse response [1]. It is used for evaluation of sound clarity of music. The recommended value for liturgic churches with cubature up to 15 000 m³ amounts to 70-120 ms. For organ music, the value is *Ts* = 180 ms. In the Christ the Only Saviour Church, *Ts* amounts to 344 ms, which exceeds acceptable values. In contrast, in the Name of Mary Church, *Ts* amounts to 148 ms, which is within the permissible range for organ music in churches.

The clarity indicator *C80* is used to determine the quality of music sound. It consists in the capability of differentiating between details in a received piece of music. The indicator is calculated from the impulse response of an interior. Clarity, measured in decibels is the difference between the sound energy in the first 80 ms, and the late reverberation energy arriving after the first 80 ms [4]. According to the recommendations in reference books C80 was averaged for 0.5, 1, 2 kHz. It is recommended that *C80* > 2 for front rows and *C80* > 0 for back rows. The measurements in both churches show that their interiors do not fulfill the criterion; moreover, the Christ the Only Saviour Church in Swarzedz considerably exceeds recommended values with its *C80* amounting to -8 dB. By contrast, Marshall suggests that *C80* < -3 dB for organ music [6]. The Name of Mary Church fulfils the criterion for front rows.

To evaluate intelligibility of an utterance, an array of parameters is applied. In this paper, two parameters, *C50* and *STI*, were applied. The clarity indicator *C50* is analogically defined in the same way as *C80*. The measurements are used to calculate a weighted value of the *C50* coefficient. Octave bands 0.5, 1, 2, 4 kHz are multiplied by the weight coefficient amounting to 0.15, 0.25, 0.35, 0.25 for each octave band respectively. It is recommended that thus calculated parameter *C50* > -2. The *STI* parameter (Speech Transmission Index) amounts from 0 to 1, where *STI* = 1 indicates that the intelligibility of speech is perfect, while *STI* = 0 indicates complete unintelligibility. The recommended *STI* is 0.45 for speech without reinforcement systems for front rows [6]. In the Name of Mary Church, the *STI* = 0.47 fulfils the recommendations, while *C50* = -5.2 dB exceeds the recommended value. In the Christ the Only Saviour Church, neither of the recommended values is fulfilled: *STI* = 0.33, *C50* = -12.5 dB. Especially the *C50* substantially exceeds the allowed values.

4. Conclusions

The results indicate huge acoustic differences between the churches. The Name of Mary Church meets acoustic recommendations for such parameters as *RT*, *STI*, *Ts* for organ music, and *C80* for front rows. The other parameters are close to the recommended values. In contrast, in the Christ the Only Saviour Church, no acoustic parameter meets the recommendations. The main parameter, which is reverberation time *RT* is substantially exceeded. Also, *Ts* and *C50* considerably deviate from the recommended values. A series of factors has an impact on such results. First of all, the cubature of the Christ the Only Saviour Church is bigger than the one of the Name of Mary Church. In addition, finishes of the interior, such as big surfaces of plain walls and an inconsiderable amount of surface texture in the church in Swarzedz, have an impact on the results. In the Name of Mary Church, the interior is more diverse. Here, the sound diffusion elements are pipe organs, finishes of the back wall and of the banisters of the choir with extended panels, and pillars between the windows.

References

1. M. Barron, *Auditorium acoustics and architectural design,* Taylor & Francis, London; New York 2005.
2. Z. Engel, J. Engel, K. Kosała, J. Sadowski, *Podstawy akustyki obiektów sakralnych,* ITE, Kraków 2007.
3. Z. Engel, K. Kosała, *Acoustic properties of the selected churches in Poland,* MECHANICS Vol. 24 No. 3 2005.
4. F. A. Everest, K. C. Pohlmann, *Master handbook of acoustics,* Fifth edition, Mc Graw Hill, USA 2009.
5. A. Kulowski, *Akustyka sal, zalecenia projektowe dla architektów,* Wydawnictwo Politechniki Gdańskiej, Gdańsk 2011.
6. D. Wróblewska, A. Kulowski, *Czynniki akustyki w architektonicznym projektowaniu kościołów,* Wydawnictwo Politechniki Gdańskiej, Gdańsk 2007.
7. *Kościoły Archidiecezji Poznańskiej*, Pomorska Oficyna Wydawniczo-Reklamowa, Bydgoszcz 2010.
8. *Kościoły Poznania*, Pomorska Oficyna Wydawniczo-Reklamowa, Bydgoszcz 2010.

XXV Symposium *Vibrations in Physical Systems,* Poznan – Bedlewo, May 15-19, 2012

The Free Vibrations of a Column with an Optimum Shape with Regard to the Value of the Critical Load Subjected to a Generalized Load by a Force Directed Towards the Positive Pole

Janusz SZMIDLA
Częstochowa University of Technology
Institute of Mechanics and Machine Design Foundations
ul. Dąbrowskiego 73, 42 – 200 Częstochowa, szmidla@imipkm.pcz.czest.pl

Abstract

The results of numerical computations and theoretical research into the free vibrations of a column subjected to the generalized load by a force directed towards the positive pole are presented in this paper. The total mechanical energy of the column was formulated by taking into account the physical model of the system and the constructional solution of the loading head. The equations of motion and the boundary conditions of the considered system are determined. The curve courses of changes in the eigenvalues in the plane: load – natural frequency are shown on the basis of the solution to the boundary problem, which is obtained by considering the kinetic criterion of the stability. The changes in natural frequencies were determined for the chosen values of the geometrical parameters of the loading head. The accepted distribution of the bending rigidity along the length of the column corresponds to the systems with maximum values of the critical load at the assumed optimization condition of constant volume of the structure.

Keywords: column, specific load, free vibrations

1. Introduction

Many scientific publications have been dedicated to analysis of the free transverse vibrations of columns and beams with changeable cross-section. The problems of the free vibrations of systems consisting of segments with changeable cross-sectional area (comp. [1-3]) and columns or beams where the cross-section was changed continuously along the length (comp. [4, 5]) were considered. Detailed literature review of specified subject area has been presented in monograph [6]. The solution to the vibration problem is also considered in research into the optimisation of slender system forms (comp. [3, 7]).

2. The physical model of the column.

The physical model of the column for the chosen version of specific load which was formulated by L. Tomski (comp. [8]) is presented in Fig. 1a. Column ③ is subjected to the generalized load by the force directed towards the positive pole in the constructional solution of the loading head ① and receiving head ② with circular profile (constant curvature). Direction of an external force P passes through the constant point O_1 (the centre of curvature of the receiving head) and through the constant point O (the centre of curvature of the loading head). Points O and O_1 are placed in the distance R and r from the free end of the column, respectively. The column is rigidly mounted from one side

($x_1 = 0$) and is connected to the receiving head at the free end ($x_n = l$) (elements of the loading head are infinitely rigid). The system is divided into smaller segments (Fig. 1b) with flexural rigidity (EJ_i) (indexes $i = 1.. n$), where J_i is a moment of inertia of the cross section of the i – th segment of the column in relation to the neutral bending axis. Segments are described by the length l and by transverse displacement $W_i(x_i, t)$. The following assumptions and denotations are applied in work (comp. [3, 7]):

- constant total length of column L and constant length of its elements $l_i = l$ ($L = n\,l$),
- constant value of Young's modulus E and material density ρ of all segments of the column,
- constant total volume v of all segments describing form of the column (comp. equation (1a)).

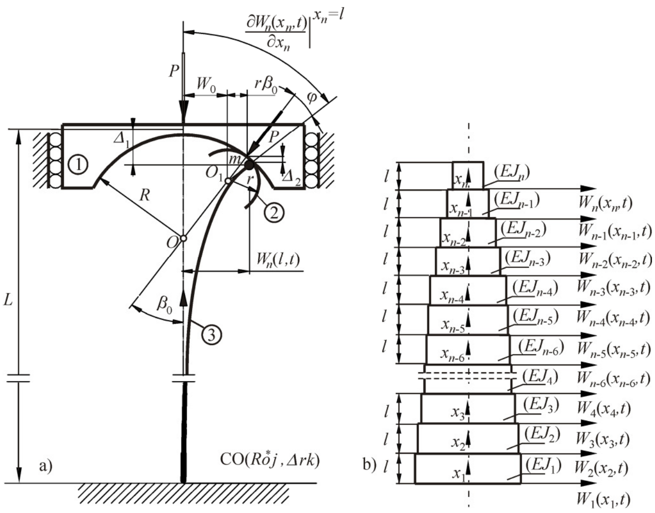

Figure 1. The physical model of the column: a) at the generalized load by the force directed towards the positive pole, b) division of the columns into segments (comp. [7,8])

Exemplary denotations of the columns considered in this paper are introduced:

- CO(R_o^*0.3,Δr0.1) – optimized column subjected to the generalized load by the force directed towards the positive pole with the changeable bending rigidity at the parameter of the loading head $R_o^* = 0.3$ and at the parameter of the receiving head Δr=0.1,
- CP(R_o^*0.2,Δr0.1) – column with the constant bending rigidity $(EJ)_p$ (comparative) subjected to the generalized load by the force directed towards the positive pole at the parameter of the loading head $R_o^* = 0.2$ and at the parameter of the receiving head Δr=0.1.

Dimensionless parameters R_o^*, Δr of the heads subjected to the load are described by equations (1b,c).

$$v=\sum_{i=1}^{n} v_i,\; R_o^*=\frac{R}{L},\; \Delta r=\frac{R-r}{L} \tag{1a÷c}$$

Volume of the column CP(R_o^*j,Δrk) is identical to the total volume of all segments describing the form of the system CO(R_o^*j,Δrk) (comp. equation (1a)).

3. Formulation of and solution to the boundary problem

The boundary problem is formulated on the basis of the Hamilton's principle which for conservative systems takes the form:

$$\delta\int_{t_1}^{t_2}(T-V)dt=0, \tag{2}$$

where: δ is operator of variation.

The kinetic energy T of the considered column CO(R_o^*j,Δrk) is a sum of kinetic energy of its individual segments and kinetic energy of elements going into composition of the receiving head (body with mass m):

$$T=\sum_{i=1}^{n}\frac{(\rho A_i)}{2}\int_0^l\left[\frac{\partial W_i(x_i,t)}{\partial t}\right]^2 dx_i+\frac{m}{2}\left[\frac{\partial W_n(l,t)}{\partial t}\right]^2, \tag{3}$$

where A_i is cross-sectional area of the i – th segment of the optimized column.

The total potential energy V is described by the relationship:

$$V=-P\Delta_1+P\Delta_2+\frac{1}{2}P\beta_0\left[W_0+r\beta_0\right]. \tag{4}$$

Displacements Δ_1, Δ_2 and angles β, φ are given by the relationships:

$$\Delta_1=\frac{P}{2}\sum_{i=1}^{n}\int_0^l\left[\frac{\partial W_i(x_i,t)}{\partial x_i}\right]^2 dx_i,\qquad \Delta_2=\frac{r}{2}\left[\left[\left.\frac{\partial W_n(x_n,t)}{\partial x_n}\right|^{x_n=l}\right]^2-\beta_0^2\right]$$

$$\varphi=\frac{W_0}{R-r}=\frac{R\left.\frac{\partial W_n(x_n,t)}{\partial x_n}\right|^{x_n=l}-W_n(l,t)}{R-r},\quad \beta_0=\frac{W_n(l,t)-r\left.\frac{\partial W_n(x_n,t)}{\partial x_n}\right|^{x_n=l}}{R-r}. \tag{5a÷d}$$

Commutation of integration (in relation to space coordinates x_i and time t) and computation of variation is used in Hamilton's principle (2). After computing variation of the kinetic energy (3), variation of potential energy (4) and after separation of variables of function $W_i(x_i, t)$ in relation to variables x_i and t :

$$W_i(x_i,t)=y_i(x_i)\cos(\omega t), \tag{5}$$

one can obtain:

- equations of motion for the considered system:

$$y_i^{IV}(x_i)+k_i^2\, y_i^{II}(x_i)-\Omega_i^2 y_i(x_i)=0, \qquad i=1...n, \tag{6}$$

- the boundary conditions for the column: in relation to mounting point ($x_0 = 0$), at the free end ($x_n = l$) and continuity conditions between individual segments of the column:

$$y_1(0)=y_1^I(0)=0,\; y_\zeta(l)=y_{\zeta+1}(0),\; y_\zeta^I(l)=y_{\zeta+1}^I(0), \tag{7a-d}$$

$$y_\zeta^{II}(l)=\chi_{\zeta+1}y_{\zeta+1}^{II}(0),\;\; y_\zeta^{III}(l)=\chi_{\zeta+1}y_{\zeta+1}^{III}(0), \tag{7e-f}$$

$$\begin{aligned} &y_n^{II}(l)+k_n^2\left[\frac{Rr}{R-r}y_n^I(l)-\frac{r}{R-r}y_n(l)\right]=0,\\ &y_n^{III}(l)+k_n^2\left[\frac{R}{R-r}y_n^I(l)-\frac{1}{R-r}y_n(l)\right]+\frac{m\omega^2}{(EJ_n)}y_n(l)=0, \end{aligned} \tag{7g-h}$$

where: $\zeta = 1,...,(n\text{-}1)$, $k_i^2 = P/(EJ_i)$, $\Omega_i^2 = (\rho A_i)\omega^2/(EJ_i)$, $\chi_{j+1} = (EJ_{j+1})/(EJ_j)$.
Substitution of equation solutions (6) into the boundary conditions (7a-h) leads into transcendental equation for natural frequency ω.

4. Results of numerical computations

The results of computations concerning optimization of the form of the column CO(R_o^*j,Δrk) are presented in work [7]. Taking into account the static criterion of the stability and modified algorithm of simulated annealing, the values of geometrical parameters of the individual segments of the column were determined. Maximal value of the critical load was obtained for the mentioned above parameters.

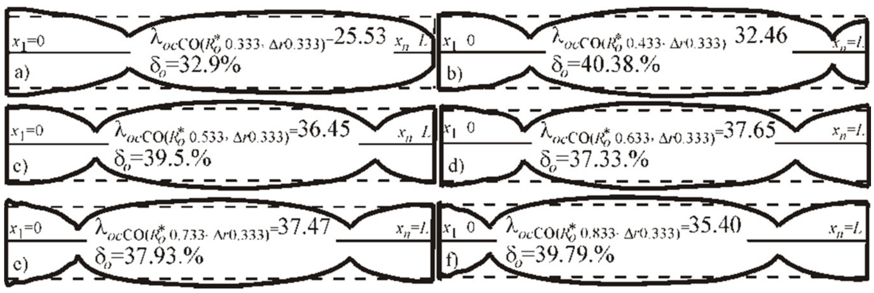

Figure 2. The form of optimized column CO(R^*_oj, Δr 0.333) for changeable value of parameter R_o^* of the loading head [7]

Exemplary forms of the optimized column at division into n = 128 segments and for chosen parameters R, r of the loading head are presented in Fig. 2. The form of comparative column CP($R_o^* j$,Δrk) is shown by broken lines.

Additionally, the value of critical load λ_{oc} of the considered system (comp. equation (8a)) and percentage increase δ_o (comp. equation (8b)) in the critical force of the column CO($R_o^* j$,Δrk) in relation to prismatic column were given. The value of critical load refers to the total length of the column L and flexural rigidity of comparative column EJ, that is:

$$\lambda_{oc} = \frac{P_{kr} L^2}{(EJ)_p}, \quad \delta_o = \frac{\lambda_{oc\mathrm{CO}(R_o^* j,\Delta r)} - \lambda_{oc\mathrm{CP}(R_o^* j,\Delta r)}}{\lambda_{oc\mathrm{CP}(R_o^* j,\Delta r)}} 100\% . \tag{8a,b}$$

The course of changes in natural frequencies ω of the column CO($R_o^* j$,Δrk) in relation to external load taking into account changeable flexural rigidity along the column length is determined in this paper (comp. Fig. 2) on the basis of publication [7]. Research was limited (Fig. 3) to determination of the first two basic natural frequencies in dimensionless form (Ω_{o1}, Ω_{o2}) in relation to dimensionless load parameter λ_o for the chosen values of geometrical parameters of the loading head. In numerical computations zero value of the concentrated mass m at the free end of the column was assumed, which is to say:

$$\lambda_o = \frac{PL^2}{(EJ)_p}, \; \Omega_o = \frac{(\rho A)_p \, \omega^2 L^4}{(EJ)_p}, \; m_o = \frac{m}{(\rho A)_p \, L} . \tag{9a,b}$$

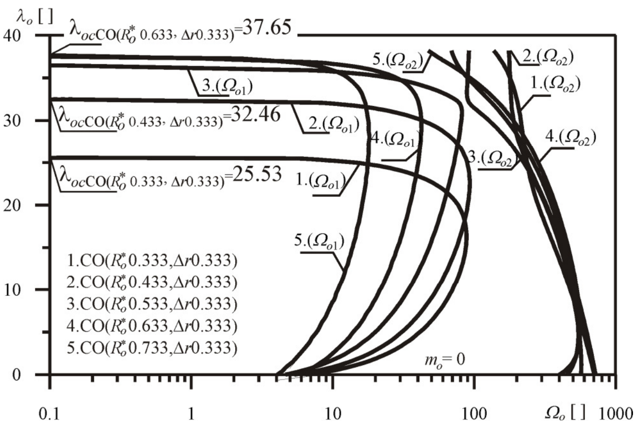

Figure 3. Curves in the plane: load parameter λ_o - parameter of natural frequency Ω_o (system CO(R_o^* j, Δr 0.333)) [7]

The value of critical load of the considered column in the case of given geometrical parameters of the loading heads was obtained at parameter Ω_{o1} = 0. The presented courses of base natural frequency Ω_{o1} can have negative, positive or zero slope in the plane λ_o - Ω_o in dependence on the values of geometrical parameters of the loading and receiving heads.

5. Conclusions

Regarding the influence of the external load and the geometrical parameters of the loading and receiving heads on the changes in natural frequencies, the considered column was rated as divergence or divergence pseudo-flutter type of the systems. The values of critical parameter of the load obtained on the basis of the kinetic criterion of stability are identical as for application of the static criterion.

Acknowledgments

The study has been carried out within Research Project No. N N501 117236 awarded by the Ministry of Science and Higher Education and the statutory funds of the Czestochowa University of Technology (BS-1-101-302/99/P).

References

1. S. Kukla, I. Zamojska, *Frequency analysis of axially loaded stepped beams by Green's function method*, Journal of Sound and Vibration, **300** (2007) 1034-1041.
2. S. Naguleswaran, *Natural frequencies, sensitivity and mode shape details of an Euler-Bernoulli beam with one-step change in cross-section and with ends on classical supports*, Journal of Sound and Vibration, **252** (2002) 751-767.
3. J. Szmidla, A. Wawszczak, *Drgania swobodne kolumn o optymalnym kształcie ze względu na wartość obciążenia krytycznego poddanych obciążeniu eulerowskiemu*, Modelowanie Inżynierskie, **38** (2009) 205 - 212.
4. S. Abrate, *Vibration of non-uniform rods and beams*, Journal of Sound and Vibration, **185** (1995) 703-716.
5. N. Auciello, *Transverse vibrations of a linearly tapered cantilever beam with tip mass of rotary inertia and eccentricity*, Journal of Sound and Vibration, **194**(1) (1996) 25- 34.
6. Posiadała B, *Modelowanie i analiza zjawisk dynamicznych maszyn roboczych i ich elementów jako dyskretno–ciągłych układów mechanicznych*, Seria Monografie, Nr 61, Wydawnictwo Politechniki Częstochowskiej, Częstochowa, (1999).
7. J. Szmidla, *Drgania swobodne i stateczność układów smukłych poddanych obciążeniu swoistemu*, Seria Monografie, Nr 165, Wydawnictwo Politechniki Częstochowskiej, Częstochowa (2009).
8. L. Tomski, *Obciążenia układów oraz układy swoiste. Rozdział 1: Drgania swobodne i stateczność obiektów smukłych jako układów liniowych lub nieliniowych.* Praca zbiorowa wykonana pod kierunkiem naukowym i redakcją L. Tomskiego, WNT, Fundacja „Książka Naukowo-Techniczna", Warszawa (2007) 17-46.

XXV Symposium *Vibrations in Physical Systems,* Poznan – Bedlewo, May 15-19, 2012

The Free Vibrations and Optimization of the Shape of a Column Subjected to a Load by a Follower Force Directed Towards the Positive Pole Applying the Variational Method

Janusz SZMIDLA
Częstochowa University of Technology
Institute of Mechanics and Machine Design Foundations
ul. Dąbrowskiego 73, 42-200 Częstochowa, szmidla@imipkm.pcz.czest.pl

Denys YATSENKO
Częstochowa University of Technology
Institute of Mechanics and Machine Design Foundations
ul. Dąbrowskiego 73, 42-200 Częstochowa, dennis7@poczta.fm

Abstract

The results of numerical computations and theoretical research into optimization of the shape and the free vibrations of a cantilever column subjected to a load by the follower force directed towards the positive pole are presented in this paper. The systems of equations: of motion and of cross-sectional area of the considered column were determined on the basis of the total mechanical energy and Hamilton's principle. Taking into account the formulated boundary conditions, optimized shapes of the systems were determined for the chosen values of geometrical parameter of a head subjected to a load. The values of natural frequency of the considered system were obtained taking into account distribution of flexural rigidity along the column length while the values of critical load of optimized column were obtained on the basis of curves of changes in the basic natural frequency in relation to external load. The results of numerical computations were presented in the case of one from three classes of the systems – versatile uniformly convergence column for the assumed criterion of constant volume of the system.

Keywords: column, specific load, free vibrations, optimization

1. Introduction

The critical load is a base quantity describing stability of slender systems. The critical force, which value is indispensable for correct design of mechanical systems, is determined using one from two criteria of stability determination: energetic method and vibration method (comp. [1, 2]). In the case of energetic method, such a load of the system is being sought for which potential energy of the system stops being positively determined. Applying vibration method, such a load value is being determined for which the free movement of the system stops being limited. Research into optimization of the shape of slender systems is aimed to find maximum critical load at the given constant mass of the system (comp. [3]) or is aimed to find a solution to reciprocal problem. In this case, the lowest weight of the column is determined for the assumed constant value of critical load (comp. [4]). In [5] a modified algorithm of simulated annealing was applied to determine an optimum shape of the column loaded by the follower force directed towards the positive pole (the case of specific load formulated by L. Tomski (comp. [6])). The values of the critical load of the optimised system were obtained on the basis of energetic method. In this paper, research into optimization of the shape was carried out using the variational method on the basis of A. Gajewski and M. Życzkowski publications (comp. [7]). The value of the critical force was received on the basis of a vibration method.

2. The physical model of the column

The physical model of the column loaded by the follower force directed towards the positive pole (comp. [5, 6]) in the constructional version of loading head and receiving load built of circular elements (constant curvature) is presented in Fig. 1. The column was loaded by the force P passing through the constant point O – the centre of loading ① and receiving ② heads. Pole O is placed in the distance R from the free end of the column. It was assumed that elements of receiving heads are infinitely rigid. Rod of the column ③ was rigidly mounted from one side ($x = 0$) and connected to the receiving head at the free end ($x = l$).

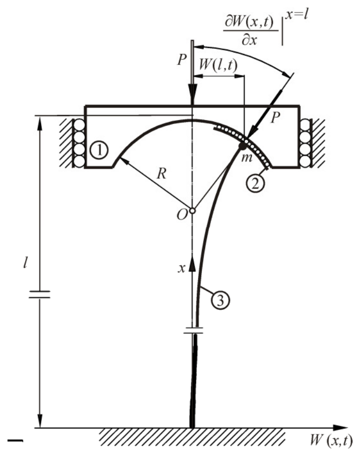

Figure 1. The physical model of the column loaded by the force directed towards the positive pole

Exemplary denotations of the considered system are introduced:

- COi(0.1) – optimized column with the continuously changeable bending rigidity along the system length at the parameter of loading and receiving heads $R^* = 0.1$.
- CP(0.2) – prismatic column (comparative) with the constant bending rigidity along the system length, at the parameter of loading and receiving heads $R^* = 0.2$, where: $R^* = R/l$.

Additionally, the following constants: total length l, volume V_{obj}, value of Young's modulus E and material density ρ of the optimized column and corresponding comparative column were assumed. The column was described by moment of inertia of cross-section $J(x)$, cross-sectional area $A(x)$ and transverse displacement $W(x,t)$.

3. Formulation of and solution to the boundary problem

The boundary problem is formulated on the basis of the Hamilton's principle (1a) together with condition of constant volume of the column (1b):

$$\delta\int_{t_1}^{t_2}(T-H)\,dt=0,\quad H=V+\lambda_1(t)\left(V_{obj}-\int_0^l A(x)\,dx\right), \tag{1a,b}$$

where: $\delta(.)$ is operator of variation, $\lambda_1(t)$ is a certain function dependent on time.

Kinetic energy T and potential energy V of the considered column COi(R^*) are equal to:

$$T=\frac{\rho}{2}\int_0^l A(x)\left[\dot{W}(x,t)\right]^2 dx+\frac{m}{2}\left[\dot{W}(x,t)\big|_{x=l}\right]^2,$$
$$V=\frac{E}{2}\int_0^l J(x)\left[W''(x,t)\right]^2 dx-\frac{P}{2}\int_0^l\left[W'(x,t)\right]^2 dx+\frac{PR}{2}\left[W'(x,t)\big|_{x=l}\right]^2, \tag{2a,b}$$

where m is the reduced mass of the receiving head.

Applying relationships (1b), (2a,b) in Hamilton's principle (1a) the system of equations was received:

$$\begin{cases}\rho A(x)\ddot{W}(x,t)+E\left[J(x)W''(x,t)\right]''+PW''(x,t)=0\\ \rho\left[J(x)\right]^{-0.5}W(x,t)\ddot{W}(x,t)-E\left[W''(x,t)\right]^2-\lambda_2(t)\left[J(x)\right]^{-0.5}=0.\end{cases} \tag{3a,b}$$

After separation of variables of function $W(x, t)$ in relation to variables x and t (4a) and after substitution of (4b):

$$W(x,t)=y(x)\cos(\omega t),\ \lambda_1(t)=\frac{\lambda_2}{2\sqrt{\pi}}\cos(\omega t), \tag{4a,b}$$

one can obtain:

$$E\left[J(x)y''(x)\right]''+Py''(x)-\omega^2\rho A(x)y(x)=0\,, \tag{5a}$$

$$\rho\left[J(x)\right]^{-0.5}\omega^2\left[y(x)\right]^2+E\left[y''(x)\right]^2+\lambda_2\left[J(x)\right]^{-0.5}=0\,, \tag{5b}$$

where: ω - natural frequency of the system, λ_2 is a certain constant dependent on the boundary conditions.

The geometrical boundary conditions of the considered column are described by the relationships:

$$y(0)=y'(0)=0,\quad y(l)-Ry'(l)=0 \tag{6a÷c}$$

Missing natural boundary condition was obtained on the basis of equation (1a) after considering relationships (6a÷c):

$$\left[R\left(J\left(x\right)y''\left(x\right)\right)' - J\left(x\right)y''\left(x\right) - \frac{Rm\omega^2}{E}y\left(x\right)\right]\Bigg|_{x=l} = 0 \tag{6d}$$

Taking into account the considered case of load, column loses its stability due to buckling. Therefore the value of the critical load is obtained for condition $\omega = 0$. Distribution of moment of inertia along the column length in relation to maximum of critical force for the assumed criterion of the constant volume of the system was determined on the basis of equations (5a,b) considering the described character of stability loss. Adequate relationships were written in the parametric form:

$$\begin{cases} J\left(\varphi\right) = J_o \sin^4\left(\varphi\right) \\ x\left(\varphi\right) = l\left(B_3 + B_2\left(\varphi - \frac{1}{2}\sin\left(2\varphi\right)\right)\right), \end{cases} \tag{7a,b}$$

where: J_o – moment of inertia in relation to neutral bending axis in the reference point $x_{od} = x(\pi/2)$.

Constants B_2, B_3 were determined on the basis of the boundary conditions (6a÷d). The values φ_0, φ_1 of independent variable $\varphi \in \langle \varphi_0, \varphi_1 \rangle$ (connected to variable x), corresponding to mounting and loading points of the column, were obtained on the basis of relationship (7b).

4. Results of numerical computations

As a result of solution of the boundary problem the range of changes in critical load $(P_c)_o$ of the optimized column COi(R^*) and its shape for the rod of versatile uniformly convergence system was determined. Numerical computations were carried out for the chosen value of radius R of the loading head in the range from zero to the length of the column l ($R^* \in \langle 0,1 \rangle$). The shapes of models of optimized columns obtained on the basis of equations (7a,b) for the assumed criterion of the constant volume of the system are presented in Fig. 2. Contour of the prismatic column (comparative) is stated by broken line. The shape of column model for Euler's load is presented in special case $R^* = 0$ (Fig. 2a). Presence of singular points of cross-section ($J(x(\varphi)) = 0$) along the column length is the characteristic feature of the all presented shapes. Placement of these points is dependent on the value of geometrical parameter R^* of the head subjected to the discussed case of the specific load.

Carried out numerical computations were aimed to display the course of changes in the values of natural frequency ω in relation to the function of external load P of columns COi(R^*) and CP(R^*) for zero value of mass m of the loading head, taking into account the obtained distribution of moment of inertia ($J(x(\varphi))$) (comp. Fig. 2). Character of changes in the basic natural frequency of the system in dimensionless form (Ω_{o1}), in relation to dimensionless load parameter β_o (comp. equation (8c,d)), for the chosen values of parameter R^*, was determined considering equation (5a), whereas:

$$\left(\beta_c\right)_{pr} = \frac{\left(P_c\right)_{pr} l^2}{EJ_p},\ \left(\beta_c\right)_o = \frac{\left(P_c\right)_o l^2}{EJ_p},\ \beta_o = \frac{Pl^2}{EJ_p},\ \Omega_{o1} = \frac{\rho A_p \omega_1^2 l^4}{EJ_p} \qquad (8a\div d)$$

The value of critical parameter of critical load of optimized $(\beta_c)_o$ and prismatic $(\beta_c)_{pr}$ systems (comp. eqs. (8a,b)) of the discussed column was obtained for parameter $\Omega_{o1}= 0$. The range of changes in critical parameter of column load in relation to parameter R^* of the head subjected to the load is presented in Fig. 4 on the basis of the obtained curves of eigenvalues.

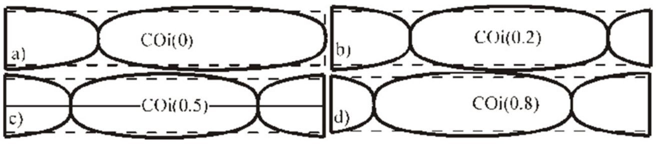

Figure 2. Shape of optimized column COi(R^*) for the chosen values of parameter R^* of the loading head

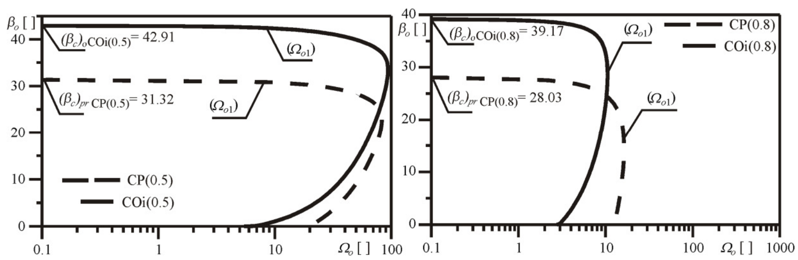

Figure 3. Curves in the plane load parameter β_o - parameter of natural frequency Ω_{o1} (the systems: COi(R^*), CP(R^*))

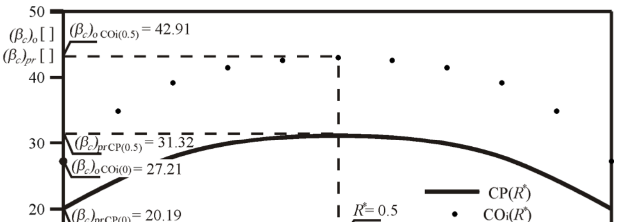

Figure 4. Change in the critical parameter of load $(\beta_c)_o$, $(\beta_c)_{pr}$ in relation to the value of parameter R^* of the systems COi(R^*), CP(R^*)

5. Conclusions

Determined character of changes in the critical load of the optimised and prismatic columns was characterised by a presence of maximum values of the critical force for the considered range of the values of radius R of the loading head. The values of the critical load presented in work [5] and obtained in this paper by variational method are comparable. As a result of carried out theoretical research and numerical computations into optimization of the system, the shapes of the column were obtained, which were characterised by a presence of the zero cross-section along its length.

Acknowledgments

The study has been carried out within Research Project No. N N501 117236 awarded by the Ministry of Science and Higher Education and the statutory funds of the Czestochowa University of Technology (BS-1-101-302/99/P).

References

1. Wesołowski Z., *Zagadnienia dynamiczne nieliniowej teorii sprężystej*, PWN, Warszawa 1974.
2. Ziegler H., *Principles of Structural Stability*, Waltham 1968.
3. Prager W., Taylor I. E., *Problems of optimal structural design, Journal of Applied Mechanics*, **35** (1968) 102-106.
4. Langthjem M. A., Sugiyama Y., *Optimum design of cantilevered columns under the combined action of conservative and nonconservative loads. Part I: The undamped case*; Computers and Structures, **74(4)** (2000) 385-398.
5. Szmidla J., *Drgania swobodne i stateczność układów smukłych poddanych obciążeniu swoistemu*, Seria Monografie, Nr 165, Wydawnictwo Politechniki Częstochowskiej, Częstochowa 2009.
6. Tomski, L., *Obciążenia układów oraz układy swoiste. Rozdział 1: Drgania swobodne i stateczność obiektów smukłych jako układów liniowych lub nieliniowych.* Praca zbiorowa wykonana pod kierunkiem naukowym i redakcją L. Tomskiego, WNT, Fundacja „Książka Naukowo-Techniczna", Warszawa 2007, 17-46.
7. Gajewski A., Życzkowski M., *Optimal shaping of an elastic homogeneous bar compressed by polar force*, Biulletyn de L`Academie Polonaise des Sciences, **17, 10** (1969) 479-488.

XXV Symposium *Vibrations in Physical Systems,* Poznan – Bedlewo, May 15-19, 2012

An Influence of the Asynchronous Motor Driving Torque on Dynamic Properties of the Rotating Machine Drive Systems

Tomasz SZOLC
Department of Mechatronics of the Warsaw University of Technology
ul. Św. A. Boboli 8, 02-525 Warsaw, Poland, t.szolc@mchtr.pw.edu.pl

Andrzej POCHANKE
Department of Electrical Engineering of the Warsaw University of Technology
Pl. Politechniki 1, 00-661 Warsaw, Poland, andrzej.pochanke@ee.pw.edu.pl

Abstract

Drive systems of several machines driven by the electric motors commonly indicate diverse sensitivity to resonances resulting from their purely mechanical eigenvibration properties. Thus, in order to explain better these phenomena, in the paper dynamic electromechanical interaction between the rotating machine drive system and the asynchronous motor is considered. The investigations are performed by means of the circuit model of the asynchronous motor as well as using an advanced structural hybrid (discrete-continuous) model of the drive system. By means of the analytical-computational approach the electromechanical interaction between the successive torsional eigenmodes and the driving and retarding torques are studied in order to determine the frequency zones of greater sensitivity to amplification of torsional vibrations as well as the frequency zones of significant attenuating activity of the electromagnetic damping.

Keywords: drive system, electromechanical interaction, asynchronous motor, dynamic analysis

1. Introduction

Currently observed fast development of machines and mechanisms driven by electric motors requires bigger and bigger knowledge about dynamic interaction between the mechanical and electrical part of the entire system. This problem has been already studied for many years and by many authors, but in majority of cases using insufficiently accurate electromechanical models, where usually the drive system was represented in a very simplified form of one or at most few rigid disks mutually connected by torsional springs. In the case of synchronous motors the complex torque coefficients method is commonly applied in order to determine the torsional vibration frequency dependent electromagnetic stiffness and damping coefficient, where negative value zones of the latter indicate a probability of dynamic instabilities, [1]. The abovementioned stiffness and damping coefficient have been also determined in [2] for the synchronous and several asynchronous motors using the spatial finite element model of the electromagnetic flux between the stator and the rotor, where the torsional perturbations were excited by the use of test impulses.

As it follows from numerous observations, drive systems of several working machines driven by the asynchronous motors commonly indicate diverse sensitivity to resonances resulting from mechanical eigenvibration properties. It is suspected that for almost complete attenuation of resonances at resonant frequencies of excitation induced by the driven object retarding torque as well as for unexpected severe amplification of torsional vibration amplitudes at non-resonant excitation there are responsible the abovementioned additional torsional elasticity and viscosity introduced into the mechanical system by the electromagnetic flux generated in the electric motor. In order to explain better such dynamic behavior, in the paper there is performed a qualitative analysis of the electromechanical coupling effects for the drive system of the rotating machine driven by the asynchronous motor during its steady-state operation. The investigations are carried out by means of the circuit model of the electric motor and using the advanced structural hybrid model of the mechanical system.

2. Modeling of the electromechanical system

In order to investigate a character of the electromechanical coupling, the possibly realistic and reliable physical and mathematical model of the mechanical system should be applied. Majority of commonly applied in an engineering practice methods of modeling, e.g. hybrid (discrete-continuous), multi-body or finite-element modeling, upon solving their differential eigenvalue problems for the orthogonal linear systems, usually lead to the set of modal ordinary differential equations:

$$\ddot{\xi}_m(t) + \left(\beta + \tau\omega_m^2\right)\dot{\xi}(t) + \omega_m^2\xi(t) = \frac{1}{\gamma_m^2}\left(X_m^S \cdot T_{el}(t) - X_m^R \cdot M_r(t)\right), \quad m = 1,2,... \tag{1}$$

where ω_m are the successive natural frequencies of the mechanical system, β denotes the coefficient of external damping assumed here as proportional one to the modal masses γ_m^2, τ is the shaft material retardation time, $T_{el}(t)$ denotes the external torque generated by the electric motor, $M_r(t)$ is the driven machine retarding torque and X_m^S, X_m^R are the modal displacements corresponding respectively to the electric motor and driven machine working tool locations in the physical model.

From the viewpoint of electromechanical coupling investigation, the properly advanced circuit model of the electric motor seems to be sufficiently accurate. In the case of the symmetrical three-phase asynchronous motor electric current oscillations in its windings are described by the six circuit voltage equations transformed next into the system of four Park's equations in the so called '$\alpha\beta$-dq' reference system, form of which can be found e.g. in [3]. Then, the electromagnetic torque generated by such a motor can be expressed by the following formula

$$T_{el} = \frac{3}{2} pM\left(i_\beta^s \cdot i_d^r - i_\alpha^s \cdot i_q^r\right), \tag{2}$$

where M denotes the relative rotor-to-stator coil inductance, p is the number of pairs of the motor magnetic poles and i_α^s, i_β^s are the electric currents in the stator reduced to the electric field equivalent axes α and β and i_d^r, i_q^r are the electric currents in the rotor reduced to the electric field equivalent axes d and q, [3].

From the system of Park's equations, [3], as well as from formula (2) it follows that the coupling between the electric and the mechanical system is non-linear in character, particularly for significantly varying motor rotational speed $\Omega(t)$, which leads to very complicated analytical description resulting in rather harmful computer implementation. Nevertheless, for steady-state operating conditions with the constant average motor rotational speed Ω_n, i.e. for $\Omega(t)=\Omega_n+\Theta(t)$, where $|\Theta(t)|<<\Omega_n$, in order to obtain more qualitative information about the character of electromechanical coupling in the drive system, the harmonic balance method has been applied for an approximate analytical solution for currents in Park's equations. In the first step, this solution used for various rotational speeds $\Omega(t)=\Omega_n$=const enables us to determine by means of (2) the static torque characteristic of the asynchronous motor. In the next step, for the assumed sinusoidal external excitation generated by the driven machine $M_r(t)=R\cdot\sin(\omega t)$, the fluctuating component of the motor rotational speed $\Omega(t)$ is expected also in the harmonic form: $\Theta(t)=G\cdot\sin(\omega t)+H\cdot\cos(\omega t)$, where $|G|,|H|<<\Omega_n$. Then, for $\Omega(t)=\Omega_n+\Theta(t)$ an application of the harmonic balance method leads to the following system of 16×16 linear algebraic equations:

$$\mathbf{C}(\Omega_n, \omega_e, \omega) \cdot \mathbf{D} = \mathbf{E}(\mathbf{B}, G, H)\,, \tag{3}$$

where **C** denotes the matrix of circuit resistances and inductances, ω_e is the circular frequency of the power supply, $\mathbf{D}$=col($\ldots C_\mu^{\nu}\ldots,\ldots D_\mu^{\nu}\ldots,\ldots E_\mu^{\nu}\ldots,\ldots F_\mu^{\nu}\ldots$), C_μ^{ν}, D_μ^{ν}, E_μ^{ν}, F_μ^{ν} are the constant unknown coefficients standing in the assumed analytical solution for $\Omega(t)=\Omega_n+\Theta(t)$, $\mathbf{B}$=col($\ldots\Phi_\mu^{\nu}\ldots,\ldots \Psi_\mu^{\nu}\ldots$), Φ_μ^{ν}, Ψ_μ^{ν} are the already determined constant coefficients standing in the analytical solution which satisfies Park's equations for $\Omega(t)=\Omega_n$=const, $\mu=\alpha$, β for $\nu=s$ and $\mu=d$, q for $\nu=r$, and **E** is the input vector of the sine- and cosine-amplitudes of the fluctuating component of the motor rotational speed $\Theta(t)$. By solving (3), substituting components of vector **D** into (2) and upon neglecting small terms of higher order, the sine- and cosine-amplitude of the fluctuating component of the motor torque is obtained in the following form:

$$T_{el}^{\mathrm{var}}(t) = S(\omega)\cdot\sin(\omega t) + T(\omega)\cdot\cos(\omega t), \tag{4}$$

where:

$$S(\omega) = \frac{3}{2}pM\left(\Psi_\beta^s E_d^r + \Psi_d^r E_\beta^s - \Psi_\alpha^s E_q^r - \Psi_q^r E_\alpha^s\right),$$

$$T(\omega) = \frac{3}{2}pM\left(\Psi_\beta^s F_d^r + \Psi_d^r F_\beta^s - \Psi_\alpha^s F_q^r - \Psi_q^r F_\alpha^s\right).$$

In this way the fluctuating component of the electromagnetic torque induced by the drive system torsional oscillations has been separated from the average torque value. For the abovementioned harmonic retarding torque generated by the driven machine and for the obtained harmonic electromagnetic motor torque, the external excitation of modal equations (1) becomes also harmonic. By means of the well known analytical solutions of such ordinary differential equations and using the Fourier solution dynamic responses of the considered mechanical system can be determined. For example, the sine- and cosine-amplitudes of the fluctuating component of the motor rotational speed $\Theta(t)$ are then obtained in the following form:

$$G = -\omega W,\; W = \sum_{m=0}^{\infty} \frac{(X_m^S)^2 T(\omega)(\omega_m^2 - \omega^2) - \left[(X_m^S)^2 S(\omega) - X_m^S X_m^R R\right](\beta + \tau\omega_m^2)\omega}{\gamma_m^2 \left[(\omega_m^2 - \omega^2)^2 + (\beta + \tau\omega_m^2)^2 \omega^2\right]},$$

$$H = \omega U,\; U = \sum_{m=0}^{\infty} \frac{\left[(X_m^S)^2 S(\omega) - X_m^S X_m^R R\right](\omega_m^2 - \omega^2) + (X_m^S)^2 T(\omega)(\beta + \tau\omega_m^2)\omega}{\gamma_m^2 \left[(\omega_m^2 - \omega^2)^2 + (\beta + \tau\omega_m^2)^2 \omega^2\right]}. \tag{5}$$

Then, by expressing $S(\omega)$ and $T(\omega)$ as in (4), substituting them into (5) and by inserting (5) into (3), upon proper rearrangements one obtains the following system of 16×16 linear algebraic equations describing electromechanical coupling in the drive system:

$$\mathbf{C}(\Omega_n, \omega_e, \omega, \omega_m, \gamma_m^2, \beta, \tau) \cdot \mathbf{D} = \mathbf{F}(\omega_m, \gamma_m^2, \beta, \tau, \omega, R). \tag{6}$$

Here, matrix **C** as well as input vector **F** became functions of the mechanical system dynamic parameters. Solutions of (6) for various retarding torque fluctuation frequencies ω and amplitudes R enables us to determine using (4) the sine- and cosine-amplitude of the oscillating component of the asynchronous motor torque. By projecting the sine- and cosine-components of the electromagnetic torque and of the rotor rotation angle respectively on the complex plane real and imaginary axes and using the definitions given e.g. in [2] the electromagnetic torsional stiffness $k_e(\omega)$ and coefficient of damping $d_e(\omega)$ generated by the asynchronous motor are determined in the following form:

$$k_e(\omega) = -\frac{U \cdot S(\omega) + W \cdot T(\omega)}{U^2 + W^2}, \qquad d_e(\omega) = -\frac{1}{\omega} \cdot \frac{U \cdot T(\omega) - W \cdot S(\omega)}{U^2 + W^2}, \tag{7}$$

where the sine- and cosine- angular displacement amplitudes U and W have been already defined in (5). The above expressions (3)-(7) derived by means of the proposed analytical-computational approach enable us to determine dynamic characteristics of the coupled electromechanical system, which are going to be presented below.

3. Computational example

In the computational example the rotating machine drive system is considered. This machine is driven by the 22 kW asynchronous motor by means of the reduction planetary gear. The static characteristic of this motor as well as the drive system first torsional eigenform of frequency 4.2 Hz are shown in Figs. 1a and 1b, respectively. The considerations are going to be focused on the interaction frequency range ω containing the fundamental first torsional eigen-frequency induced by sinusoidal external excitation generated by the driven machine with the assumed test amplitude R. From results of numerical simulation performed for the resonant frequency of the retarding torque fluctuation it follows that completely no resonance effects are obtained, The maximal amplification of the system dynamic response has been obtained for the retarding torque fluctuation frequency 2.2 Hz. In order to explain this phenomenon the qualitative analysis of the considered electromechanical system has been carried out, results of which are presented in Fig. 2. Here, in Fig. 2a for a comparison the frequency response function of the purely mechanical system is shown with the significant peak corresponding to the first torsional natural frequency 4.2 Hz. Also in the retarding torque

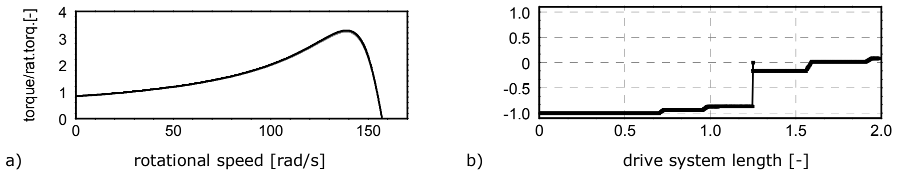

Figure 1: Static characteristic of the driving motor (a) and the drive system first eigenform (b)

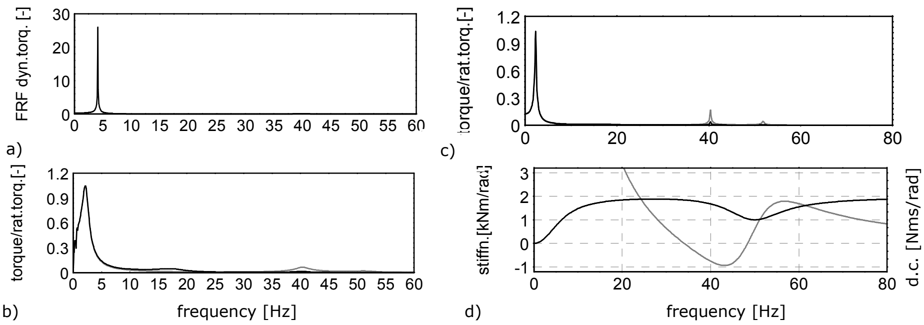

Figure 2: Frequency response function of the mechanical system (a), amplitude characteristics of the electromagnetic torque (black) and mechanical torque (grey) obtained using simulation (b) and the analytical solution (c), electromagnetic stiffness (black) and damping coefficient (grey) (d)

fluctuation frequency domain in Fig. 2b the plots of steady-state dynamic response oscillation amplitudes determined by simulations are shown, where by the black and grey lines respectively the motor-torque and the input shaft dynamic torque amplitudes are plotted. These almost entirely mutually overlying curves are characterized by the predominant amplitude peak of the abovementioned frequency 2.2 Hz. The simulation result presented in Fig. 2b has been confirmed analytically by solving Eqs. (6), which follows from the analogous plots in Fig. 2c. Moreover, in Fig. 2d, also in the retarding torque fluctuation frequency domain, there are presented by the black and grey lines, respectively, the plots of electromagnetic stiffness and damping coefficient determined using formulae (7). From the stiffness characteristic in Fig. 2d it follows that at the maximum dynamic response frequency 2.2 Hz the electromagnetic stiffness introduced by the asynchronous motor is equal ca. 0.180 kNm/rad, which exceeds the mechanical system first modal torsional stiffness $\omega_1^2 \cdot \gamma_1^2$=0.169 kNm/rad, to reach much greater values for higher interaction frequencies. Thus, the considered drive system is not a so called ‘free-free’ one, but it becomes visco-elastically clamped by the electromagnetic flux between the motor rotor and the stator. In general, this feature can significantly change system natural frequency values and corresponding to them torsional eigneforms. In the considered case such electromagnetic visco-elastic spring has completely attenuated the resonance effect with the first eigenfrequency because of relatively very high electromagnetic damping generated at low interaction frequencies, see Fig. 2d. It is to emphasize that the plot of the electromagnetic damping shown in Fig. 2d indicates a negative damping zone in the range between 35-50 Hz, which for very small drive system mechanical damping can lead to operational instabilities. In the considered case the assumed level of shaft material damping protects the entire electromechanical system against instabilities and severe resonances, which follows from the respective amplitude characteristics shown in Figs. 2b and 2c. However, for very small material damping typical for majority of torsionally vibrating shafts, the negative electromagnetic damping becomes significant and leads to gradual rise of the electromechanical dynamic response amplitudes obtained for the second resonant interaction frequency 40.3 Hz.

4. Final remarks

In the paper dynamic electromechanical coupling between the structural model of the mechanical system and the circuit model of the asynchronous motor has been investigated. By means of the analytical-computational approach an interaction between the fundamental torsional eigenmodes and the driving electromagnetic torque was studied in order to determine the frequency zones of greater sensitivity to amplification of torsional vibrations as well as the frequency zones of significant attenuating activity of the electromagnetic damping. For this purpose an influence of electromagnetic and retarding torque fluctuation on torsional vibration amplitudes was investigated for given eigenmodes of the mechanical system. As objects of considerations there was applied the rotating machine drive system driven by the asynchronous motor. From the obtained results of computations it follows that the coupling effects between the mechanical and electrical part are significant because of drive system very small fundamental torsional natural frequency resulting in relatively small modal stiffness becoming sensitive to effective stiffening by the electromagnetic stiffness generated by the driving motor. Moreover, also negative electromagnetic damping occurred, which can lead to dangerous instabilities for weakly damped mechanical systems.

References

1. A. Tabesh, R. Iravani, *On the application of the complex torque coefficients method to the analysis of torsional dynamics*, IEEE Transactions on Energy Conversion, **20**(2) (2005) 268-275.
2. T. P. Holopainen, A.-K. Repo, J. Järvinen, *Electromechanical interaction in torsional vibrations of drive train systems including an electrical machine*, Proc. of the 8th IFToMM Int. Conf. on Rotordynamics, Sept., 2010, KIST, Seoul, Korea, 986-993.
3. K. L. Shi, T. F. Chan, Y. K. Wong, L. S. Ho, *Modelling and simulation of the three-phase induction motor using SIMULINK*, Int. Journal of Electrical Engineering Education, **36** (1999) 163-172.

XXV Symposium *Vibrations in Physical Systems,* Poznan – Bedlewo, May 15-19, 2012

Acoustic Properties of Small Wind Turbines

Jacek SZULCZYK, Czesław CEMPEL
University of Technology, Institute of Applied Mechanics
Division biodynamics Vibroacoustics and Systems, Piotrowo St. 3, 60-965 Poznan
jacek.szulczyk@doctorate.put.poznan.pl, czeslaw.cepmel@put.poznan.pl

Abstract

The study of vibroacoustic properties of small wind turbines with a vertical axis laboratory test conditions used in the form of an anechoic chamber in the Acoustics Laboratory, Institute of Energy, Department of Heat in. Anechoic chamber design allowed the installation of a duct through which the airflow is adjusted by means of a centrifugal fan mounted at the inlet of the waveguide. The paper presents the identification of the acoustic parameters of acoustic small wind turbines with a vertical axis comprising:

a) determination of sound power levels for different classes of frequency characteristics and test wind turbines work
b) identification of the components of the spectrum frequency - amplitude associated mainly with turbine speeds and frequencies of their own, such as duct

The result of research was to obtain input data to define a more dedicated to the identification of measurement noise and vibration characteristics of wind turbines such as the efficiency of vibroacoustic, cepstrum analysis or dimensional analysis.

Keywords: wind turbines noise, VAWT turbines, sound power level, sound preesure level.

1. Research methodology

The study of acoustic properties of small turbines VAWT work took place on the PULSE system platform from B & K, using the four channels. Metrics used for the analysis of the sound spectrum was 1/12 octave in the measurement range from 1 Hz - 10 kHz. In addition, for each class of wind speed measured with the FFT in the range 1 Hz - 1 kHz, with a fixed bandwidth, resulting resolution 6400 line measurements. During the study examined identification turbine noise for 12 classes of wind speed by adjusting the air stream by means of a centrifugal fan inverter. Physical parameters recorded during the study included the current reading speed turbines, voltage produced by the turbine generator working and reading speed centrifugal fan generating airflow.Preparation of test bench generation assumed the air stream in a very limited area.

The tunnel itself had dimensions for indoor square with sides of 0.4 mx 0.4 m, which meant that the location of measuring microphones on the floor was "free" from the influence of wind.

Diagram of the measuring platform production PULSE B&K included the use of four channels of low-frequency microphones production GRAS 40AN and 26AK preamplifier, enabling linear audio recording levels on the frequency of 0.5 Hz with an accuracy of +/- 2 dB.

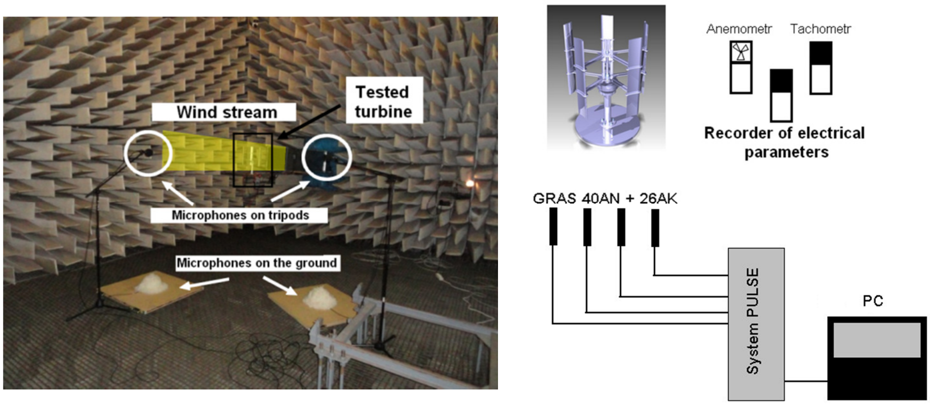

Figure 1. Location of measurement points in an anechoic chamber and a diagram of the measuring circuit.

The measurement procedure was based on an analysis of the research work of the acoustic small wind turbine mounted on a shaft for ventilation supplied to an anechoic chamber. Variable speed drive centrifugal fan inlet air stream into the chamber followed by the inverter. This allowed to obtain stable wind speed on the forehead channel, which was measured manually using a digital anemometer anemometer's Testo 410-2. Measured the rotational speed of the turbine digital tachometer NDN-838 with a resolution of 0.1 rev/min and a sampling time of 1 second. Range of wind speeds ranged from 6 m/s to about 14 m/s.

2. The scope and frequency analysis of sound power levels of the turbines for different wind speeds

As previously mentioned acoustic tests were performed for the frequency range from 1 Hz to 10 kHz in the analysis of 1/12 octave and 1 kHz using FFT analysis with a fixed bandwidth. All signals presented a linear measurement of sound levels, which were made on the basis of further analysis and acoustic correction. One such analysis was to provide sound levels obtained for different wind speeds to determine the levels and further equivalent sound power level for the frequency A, C and G.

Selection of measurement points was to place them on a special plate on the substrate located at a distance from the turbine, related to its dimensions. The microphone was on the plate was measured and sheltered from the wind with additional transmitters for the purpose of eliminating the acoustic impact of wind on the outcome of the study. The following is a graphic guidelines for the location of the microphone relative to the turbine and the scheme of arrangement of the measuring board. For the tests concerned the distance Ro was 2 meters (1.7 meters from the axis of the turbine to the ground and 0.3 meters in diameter turbine), while distance R1 was 2.62 meters. ISO 61400-11 specifies the method of acoustic analysis, which is further used to determine the sound power level, the designation of source directivity and its tonality.

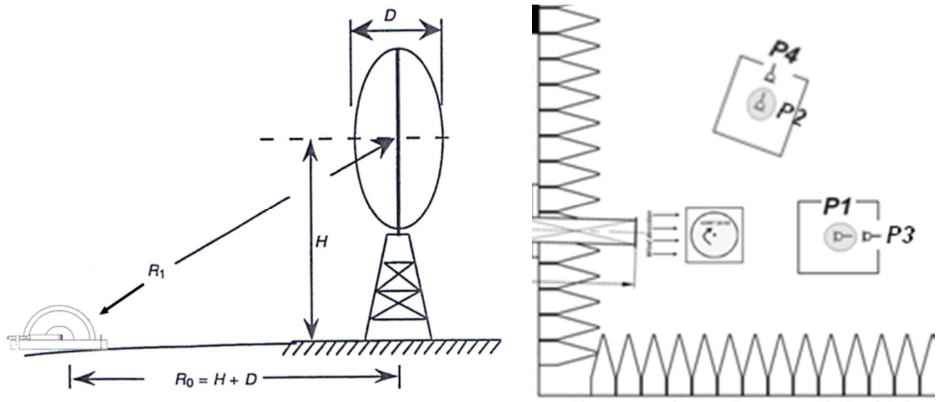

Figure 2. The distance measuring points and their location relative to the test turbine

To determine the sound power level used for sound levels obtained from the measurement point 1 (channel 1), considered as a reference point according to the guidelines standard 61400-11. The sound power level, L_W, are based on sound pressure levels obtained from the measurement point P1 (position of reference - the turbine), for the studied range of wind speed, using the following formula:

$$L_W = L_{i,eq} - 6 + 10\log\left(\left(4\pi R_1^2\right)/\left(S_0\right)\right), \tag{1}$$

where:

$L_{i,eq}$ is a linear sound pressure level,
R_1 is measured in an oblique direction and distance in meters from the microphone inside the rotor ,
S_o is the reference surface $S_o = 1$ m^2.

Constant 6 dB, in equation (1), with around two-fold increase in pressure when the sound level measurements on the ground.

3. Conclusions from the study

Using equation (1) enabled the determination of sound power levels for the studied range of turbines VAWT wind stream velocity of 6 m/s to 14 m/s Determination of sound power levels for each frequency characteristics allowed the fuller reasoning associated with different wind speeds and studied stream turbines.

The x-axis contains the *Frequency [Hz],* in the range from 1 Hz to 10 kHz, and the y-axis, the left graph shows the *Sound pressure level in [dB]* on the right side of the chart-weighted *Sound power level [dB]* for different frequency characteristics.

For the turbine H-rotor 3-arm images and spectral sound power levels are as follows:

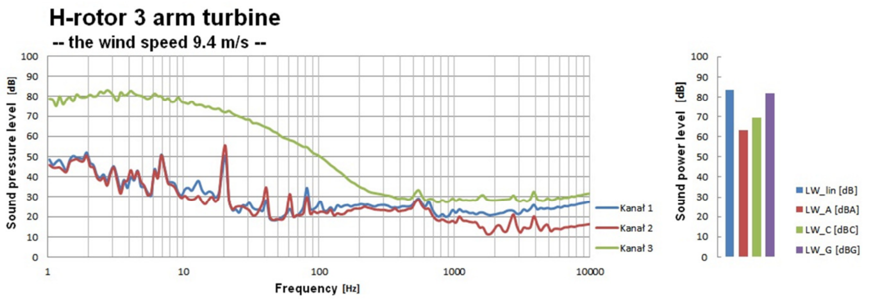

Figure 3. The spectrum of sound and sound power level
of the turbine 3 arm of the wind speed 9.4 m/s

Analyzing these results it should be noted both on the same spectral shape and sound levels for different frequencies. Next on the difference in sound pressure level for the different channels of sound power levels, the corrected line-level frequency characteristics.

For the turbine H-rotor 3-arm images and spectral sound power levels are as follows:

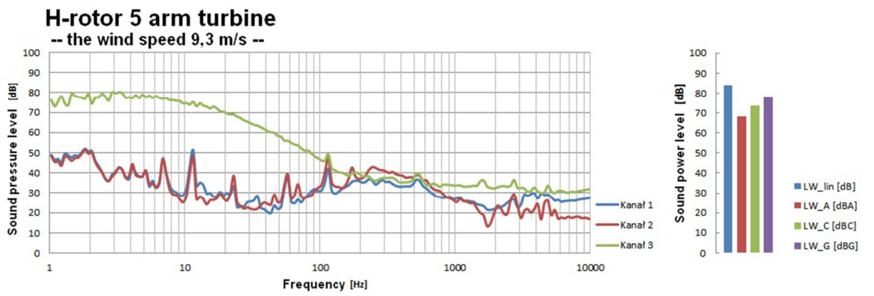

Figure 4. The spectrum of sound and sound power level
of the turbine 3 arm of the wind speed 9.3 m/s

The obtained results the following conclusions:

1. The spectrum of the amplitude - frequency can be clearly seen "moving" peak sound levels associated with the rotational frequency of the turbine. The relationship particularly evident for the higher speed wind stream.
2. Sound power levels, the designated sound level of a linear channel 1 (reference point) behave under different values of the frequency characteristics, and only vary in their levels for the next stream velocity of the wind. These changes are linear with respect to the increasing wind.
3. The sound power level A corrected for wind classes from 1 to 5 is a very similar, only the 5 class wind speed turbine with five arms is characterized by higher levels of approximately 7 - 9 dB, the highest class of wind. Higher sound power level for the frequency A, 5 class wind speed is caused by the fact more likely to

five arms turbine compared with the three arms turbine. Acoustic Interaction turbine with five arms for wind speeds above 5 stream class, seems to be the most dominant right for the audible range. It can be concluded after analyzing the sound power levels without adjustment of frequency, where the power levels are in those classes of wind look very similar.

4. Comparing the characteristics of the sound level for a test turbines, the analysis performed at the measuring point No. 1 show that the initial speed wind stream sound level is 40 dB and forth for a turbine with three arms is about 50 dB, and for the turbine of the five arms of about 55 dB . The result is that for higher wind speed turbine with five arms is louder. This is due to the shape of the sound spectrum and larger amplitudes in the audible range, for analyzing the audio level for the tested rope turbine does not differ substantially among themselves.

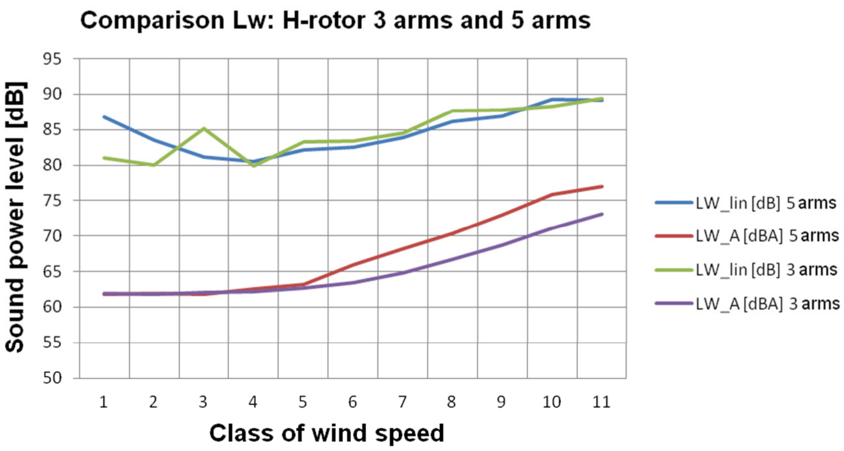

Figure 5. Comparison of linear sound power levels
and A levelsof H-rotor turbine 5 and 3 arm.

Acknowledgments

The work carried out with financial support from the Ministry of Science and Higher Education, contract No. 2683/B/T02/2009/37.

References

1. Cempel Cz., *Wibroakustyka Stosowana*, Wyd. PWN, Poznan-Warszawa 1978.
2. Engel Z., *Ochrona środowiska przed drganiami i hałasem*, Wyd. PWN, W-wa 2001.
3. Ferreira C., van Bussel G., van Kuik G., *2D CFD simulation of dynamics stall on a vertical axis wind turbine: verification and validation with PIV measurements*, Delf Univ. of Technology, Netherland 2007.

4. Makarewicz R. *Hałas w środowisku*, Ośrodek Wydawnictw Naukowych, Poznań 1996.
5. Oerlemans Stefan, „*Wind Tunnel Aeroacoustic Tests of Six Airfoils for Use on Small Wind Turbines"*, National Renewable Energy Laboratory, Period of Performance: August 23, 2002 through March 31, 2004.
6. Pedersen E., *Human response to wind turbine noise – perception, annoyance and moderating factors*, Gegetorg 2007.
7. Szulczyk J., Cempel C., *Acoustic analysis of a wind turbine with vertical axis under "In-situ" in the urban area,* Fourth International Meeting on Wind Turbine Noise, Rome Italy 12-14 April 2011- conference publications.
8. Szulczyk J., Cempel C., KarłowskiJ., Górka T., *The possibility of using wind turbines with a vertical axis in urban and rural areas*, International Scientific Conference „Generating and Use of Renewable Energy in Agricultural Farms" 20-21 September 2010 - conference publications.
9. Szulczyk J., Cempel C., *Ocena akustyczna modeli turbin wiatrowych o pionowej osi obrotu*, 38 Krajowa Konferencja Badań Nieniszczących 2009 - conference publications.
10. Wegner S., Bareiss R., Guidati G,. *Wind Turbine Noise*, Springer, Berlin, 1996.
11. Timouchev S., CFD-CAA *Study of Generic Savonius Wind Turbine Rotor*, Wind Turbine Noise 2005, Berlin 2005.

XXV Symposium *Vibrations in Physical Systems,* Poznan – Bedlewo, May 15-19, 2012

Modelling and Identification of Tower Type Historic Buildings

Czesław SZYMCZAK
Gdansk University of Technology, Faculty of Ocean Engineering and Ship Technology
Narutowicza 11/12, 80- 233 Gdansk, Poland, szymcze@pg.gda.pl

Agnieszka TOMASZEWSKA
Gdansk University of Technology, Faculty of Civil and Environmental Engineering
Narutowicza 11/12, 80- 233 Gdansk, Poland, atomas@pg.gda.pl

Abstract

In this paper the problem of parametric identification of a historic masonry tower model is discussed. The tower leans and its foundation stiffness is a concern to authorities. The authors identified some modal characteristics of the tower, natural frequencies and mode shapes. It is known, based on the first mode shape identified, that the structure behaves like a stiff solid on elastic foundation. Thus, a simple, five parameter plane model is considered. The unknown parameters are identified to be the solution to an optimisation problem, in which the sensitivity analysis and scatters of the modal identification are applied. A hierarchical process is formulated, where two natural frequencies are assumed to be the input data. In this approach, the number of unknown parameters increases incrementally, and the process changes from even-posed to under-posed successively. Such approach allows one to control the final under-posed identification problem and leads to an increasingly better solution.

Keywords: Identification, Modelling, Optimisation, Sensitivity analysis, Masonry tower

1. Introduction

This paper discusses the problem of parameters identification of the Vistula Mounting tower model (see Fig.1). The tower dates back to the 15th century, however it was damaged several times in military conflicts. Nowadays it is 22.65 m high, and its external diameter is 7.7 m. The structure has seven floors with concrete reinforced ceilings. Its walls were built using masonry and were restored at different times. The average wall thickness is 1.25 m. The tower was founded on weak and layered subsoil. The foundations were made of boulders and lie just below the ground level. This is probably a cause, why the tower leans. This behaviour of the structure is now a concern of authorities.

The author's task is to estimate foundation stiffness of the tower and create the model of the structure. For that purpose dynamic measurements were taken and some modal characteristics have been identified. Basing on the first mode shape a the type of a tower model was selected. A rigid solid body resting upon elastic foundation is considered to be a good approximation of the structure, since a considerable rotation - in comparison to the tower structural deformation - about the tower base is observable. Natural frequencies of the first and the second coplanar mode shapes, and two coordinates of the first mode shape are used as the data in the model parameters identification. In order to solve this problem, a least square error function was formulated as the objective function. Important elements of this task are scatters of the structure's measured modal characteristics. They are used to accurately define the optimisation problem.

2. Experimental modal identification

The Peak Picking method (see [1]) was used for modal identification of the tower. The method is suitable for any signals, also for low-energy vibrations, which occur in the tower. The method was selected for the investigation also because of the possibility of determining statistical errors of identified modal characteristics. This feature of the method was useful for this investigation.

The mode shapes errors arise from the fact that only estimates of the auto-spectra, which are basic functions in the Peak Picking method, can be calculated. Real values of the functions could be obtained for signals infinite in time and that is practically impossible. The estimates are affected by statistical errors, bias ε_b and random ε_r, which give a final error $\varepsilon = \varepsilon_b + \varepsilon_r$. They are presented in [1] and [2]. The formulae are:

$$\varepsilon_b\left[\hat{G}_{pp}(f)\right] \approx \frac{\Delta f^2}{24}\left[\frac{\left(\hat{G}_{pp}(f)\right)''}{\hat{G}_{pp}(f)}\right]; \qquad \varepsilon_r\left[\hat{G}_{pp}(f)\right] \approx \frac{1}{\sqrt{n_d}}, \tag{1}$$

where $\hat{G}_{pp}(f)$ is the estimate of auto-spectrum calculated for signal measured in a structural point p, Δf denotes the frequency resolution of the analyzed spectra, $\left(\hat{G}_{pp}(f)\right)''$ is the second derivative of the function $\hat{G}_{pp}(f)$ and n_d is a number of signals $p(t)$ analyzed.

If coordinates of a mode shape associated with the resonant frequency f_m are calculated according to the formula (2) (see [1]):

$$\hat{\phi}_p(f_m) = \sqrt{\frac{\hat{G}_{pp}(f_m)}{\hat{G}_{rr}(f_m)}}, \tag{2}$$

where $\hat{\phi}_p(f_m)$ denotes the estimated mode shape coordinate at a discretization point p and $\hat{G}_{rr}(f_m)$ is the auto-spectrum value for f_m, calculated for a signal $r(t)$, measured at the structural reference point r, then the statistical error of the mode shape coordinates is calculated from the following formula:

$$\varepsilon\left[\hat{\phi}_p\right] = \frac{1}{2}\left(\varepsilon\left[\hat{G}_{pp}\right] + \varepsilon\left[\hat{G}_{rr}\right]\right) \tag{3}$$

The error of the measured natural frequencies has two components: the digitalisation error equal to the half of the spectrum resolution, and the random error calculated using dispersion of the measured resonant frequencies.

Accelerations of points selected across the tower were measured during ambient vibrations according to the above-presented rules of the Peak Picking method. Wind and water waves from the nearby situated river (Fig. 1) caused major environmental excitation. The measuring points were arranged along two opposite walls at the tower height on nine levels. Accelerations in two horizontal directions, East-West (parallel to the wall surfaces) and North-South (perpendicular to the wall surfaces) were recorded at each point. Thus, 36 measuring points were set. Each measurement took 1024 seconds, 256 samples were collected per second, so each signal consisted of 262144 samples. In order to estimate the signal spectra, time histories were divided into 32 sections ($n_d = 32$).

Only one resonant frequency of the tower was identified using signals measured across the North-South plane, whereas three were determined using time series measured in the East-West direction. Nature of related mode shapes was also specified using the analysis of phase shifts between signals measured at different structural points. Additionally, coordinates of two first mode shapes in two perpendicular planes were determined. Hence, it is known that $f_1^{N-S} = 1.416$ Hz and $f_1^{E-W} = 1.446$ Hz refer to the first two lateral mode shapes in two perpendicular directions: North-South and East-West, respectively. The mode shape associated with f_1^{E-W} is presented in Fig.2. Then, frequencies identified in the East-West direction are $f_t = 4.485$ Hz , which relates to the torsional mode, and $f_2^{E-W} = 6.570$ Hz , connected with the second lateral mode shape in this plane.

The following values of the errors were obtained for the tower's natural frequencies $\varepsilon\left[f_1^{N-S}\right] = 0.00322$, $\varepsilon\left[f_1^{E-W}\right] = 0.00337$, $\varepsilon\left[f_t\right] = 0.00689$ and $\varepsilon\left[f_2^{E-W}\right] = 0.00871$. The error for all the modes is the same and amounts to $\varepsilon[\phi] = \varepsilon_r[\phi] = 0.177$, because $\varepsilon_b[\phi]$ is negligibly small as it is of the 0.001 order (see also [3]).

Figure 1. The Vistula Mounting Fortress

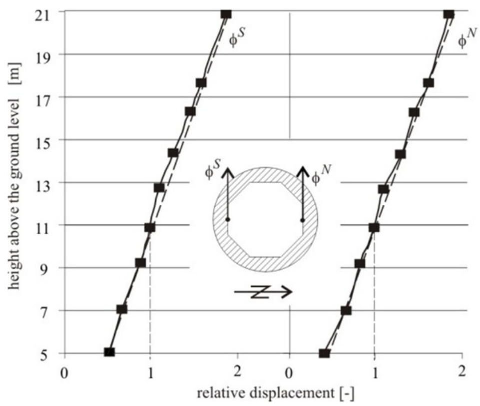

Figure 2. Mode shape of the first resonant frequency of the tower in the East-West plane

3. Mathematical model of the tower and its identification

In case of the Vistula Mounting Fortress tower the type of model is determined based on first mode shapes measured. The mode shape (Fig. 2) shows that the tower leans almost like a stiff solid therefore a model of a rigid solid body resting on an elastic foundations can be a reasonable mathematical approximation of the building's behaviour. A small number of parameters is the advantage of this model. It is convenient because only a few modal characteristics of the tower are to be used as state variables in the model parametric identification.

The plane model is the subject of interest. Therefore there are two dynamic degrees of freedom, namely: the displacement across the x axis and rotation φ, relative to the y axis. The foothold of the Cartesian coordinate system xyz is placed in the centre of gravity of the structure. The following equation of motion is valid:

$$\underbrace{\begin{bmatrix} m & 0 \\ 0 & J_y \end{bmatrix}}_{\boldsymbol{M}} \begin{Bmatrix} \ddot{x} \\ \ddot{\varphi} \end{Bmatrix} + \underbrace{\begin{bmatrix} k_x & -k_x z_c \\ -k_x z_c & k_\varphi + k_x z_c^2 \end{bmatrix}}_{\boldsymbol{K}} \begin{Bmatrix} x \\ \varphi \end{Bmatrix} = \mathbf{0}\,, \tag{4}$$

with the following five parameters: m mass of the tower, J_y the tower mass moment of inertia with respect to y axis, z_c coordinate of the tower's centre of gravity, and k_φ, k_x foundation stiffness modules. Those five parameters are to be determined based on measured tower modal characteristics

In the task of parametric identification of the mathematical model, an optimisation problem was formulated. The square error function is assumed to be the objective function:

$$F(\boldsymbol{b}) = \sum_{i=1}^{i=S} \alpha_i \left(s_i(\boldsymbol{b}) - \hat{s}_i \right)^2 , \tag{5}$$

where $\boldsymbol{b}$ denotes a vector of the design variables (the sought-after parameters of the model), $s_i(\boldsymbol{b})$ stands for the state variables of the model, $\hat{s}_i$ represents measured state variables of the tower and α_i is a weight coefficient determined for each state variable. In order to find the minimum of the objective function (5) an iterative procedure is proposed and the optimization problem is reformulated as minimisation of the objective function in relation to the design variables vector variations:

$$\min_{\delta \boldsymbol{b}} F(\delta \boldsymbol{b}^k) = \min_{\delta \boldsymbol{b}} \sum_{i=1}^{i=S} \alpha_i \left(s_i^k(\boldsymbol{b}^k) + \delta s_i^k(\boldsymbol{b}^k, \delta \boldsymbol{b}^k) - \hat{s}_i \right)^2 , \tag{6}$$

where $\delta s_i^k \left(\boldsymbol{b}^k, \delta \boldsymbol{b}^k \right)$ is the first variation of the state variable with respect to the design variable vector. Variations $\delta \boldsymbol{b}^k$, calculated at each stage k are used for updating the $\boldsymbol{b}$ vector. Calculations continue until the relative variations $\delta \boldsymbol{b}^k$ are smaller than the assumed accuracies. The mathematically complicated relation $\delta s_i(\boldsymbol{b}, \delta \boldsymbol{b})$ is substituted by approximation $\delta s_i = \left(\boldsymbol{w}_{sb} \right)^{\mathrm{T}} \delta \boldsymbol{b}$ determined by means of sensitivity analysis.

In this approach the radial natural frequencies squared λ_i and the coordinates of the first mode shape $\boldsymbol{\phi}_{n1}$ are the state variables. Thus, the objective function is formulated as follows:

$$\min_{\delta \boldsymbol{b}} F(\delta \boldsymbol{b}^k) = \min_{\delta \boldsymbol{b}} \left(\sum_{i=1}^{i=2} \alpha_j \left(\frac{\lambda_i^k(\boldsymbol{b}^k) - \hat{\lambda}_i}{\lambda_i^k(\boldsymbol{b}^k)} + \left(\overline{\boldsymbol{w}}_{\lambda b}^k \right)^{\mathrm{T}} \delta \overline{\boldsymbol{b}}^k \right)^2 + \sum_{n=1}^{n=2} \alpha_n \left(\frac{\phi_{n1}^k(\boldsymbol{b}^k) - \hat{\phi}_{n1}}{\phi_{n1}^k(\boldsymbol{b}^k)} + \overline{\boldsymbol{W}}_{\boldsymbol{\phi} b}^k \delta \overline{\boldsymbol{b}}^k \right)^2 \right) \tag{7}$$

where the vector $\overline{\boldsymbol{w}}_{\lambda b}$ and the matrix $\overline{\boldsymbol{W}}_{\boldsymbol{\phi} b}$ consist of the relative first variations of the radial natural frequency squared λ and of the mode shape $\boldsymbol{\phi}$ relative to the variations of the design variables, respectively. The coefficients are derived from the equation of motion for a discrete system and are presented for example in [4]

The following values of state variables $\hat{\lambda}_1 = \left(2\pi f_1^{E-W}\right)^2 = 81.99\left(\text{rad/ s}\right)^2$ determined from experiments were used in the optimisation procedure: $\hat{\lambda}_2 = \left(2\pi f_2^{E-W}\right)^2 = 1703.34\left(\text{rad/ s}\right)^2$, $,\hat{\phi}_{t1}^{E-W} = 1.806\,[-]$, $\hat{\phi}_{b1}^{E-W} = 0.453\,[-]$. Errors in measured state variables are used to specify weighted coefficients of state variables so that their sum is equal to 1. Hence, the values are: $\alpha\left(\hat{\lambda}_1\right) = 0.869$, $\alpha\left(\hat{\lambda}_2\right) = 0.119$ and $\alpha\left(\hat{\phi}_{t1}^{E-W}\right) = \alpha\left(\hat{\phi}_{b1}^{E-W}\right) = 0.00588$.

The final criterion for identification is defined by a relative difference between the measured and the calculated state variables. For each variable this difference must be smaller than its error obtained from the modal identification. Therefore, the criterion consists of the following conditions: $\varepsilon\left(\phi_{n1}^{E-W}\right) = \dfrac{\hat{\phi}_{n1}^{E-W} - \phi_{n1}^{E-W}}{\hat{\phi}_{n1}^{E-W}} \le 0.177;\quad n = b, t$,

$\varepsilon\left(\lambda_1\right) = \dfrac{\hat{\lambda}_1 - \lambda_1}{\hat{\lambda}_1} \le 0.00337$ and $\varepsilon\left(\lambda_2\right) = \dfrac{\hat{\lambda}_2 - \lambda_2}{\hat{\lambda}_2} \le 0.00871$.

The result obtained in the optimization is assessed by calculating the Normalized Modal Difference (*NMD*) between the first mode shape calculated for the model and the measured mode shape of the tower.

Acknowledgments

This work has been supported by the Centre for Urban Construction and Rehabilitation CURE, founded by the 5-th EU Framework Programme, acting at the Gdansk University of Technology in Poland – this support is kindly acknowledged.

	Identified parameters / The parameter name	Starting value	Boundary condition	Identification result	Number of itera-tion steps	*NMD* [%]
Starting values	k_{φ} [Nm]	$1.00 \cdot 10^{10}$	100 - ∞	$1.239 \cdot 10^{10}$	10	4.666
	k_x [N/m]	$4.00 \cdot 10^{8}$	100 - ∞	$4.264 \cdot 10^{8}$		
	z_c [m]	10.00	0 – 15.00	9.921		
	J_y [kg·m^2]	$4.30 \cdot 10^{7}$	10^6- ∞	$4.115 \cdot 10^{7}$		
	m [kg]	$9.000 \cdot 10^{5}$	(9-10) $\cdot 10^5$	$9.202 \cdot 10^{5}$		

References

1. Bendat JS, Piersol AG. *Engineering applications of correlation and spectral analysis*. John Wiley & Sons, Inc.; 1980.
2. Bendat JS. *Statistical errors in measurement of coherence functions and input/output quantities*. J. Sound and Vibration 1978;59:405-21.
3. Tomaszewska A. *Influence of statistical errors on damage detection based on structural flexibility and mode shape curvatures*. Computers and Structures, 2010;88:154-64.
4. Szymczak C. *Elem teorii projektowania*

XXV Symposium *Vibrations in Physical Systems,* Poznan – Bedlewo, May 15-19, 2012

Application of Frequency Analysis of the Vibration Signal in Order to Evaluate Technical Condition of Vehicle Suspension Elements

Franciszek TOMASZEWSKI
Poznan University of Technology, Institute of Combustion Engines and Transport
60-965 Poznań, Piotrowo 3, franciszek.tomaszewski@put.poznan.pl

Grzegorz M. SZYMAŃSKI
Poznan University of Technology, Institute of Combustion Engines and Transport
60-965 Poznań, Piotrowo 3, grzegorz.m.szymanski@put.poznan.pl

Roman FILIPIAK
Poznan University of Technology, Institute of Machines and Motor Vehicles
60-965 Poznań, Piotrowo 3, roman.filipiak@doctorate.put.poznan.pl

Abstract

This paper presents the possibilities in using of vibration signal parameters to evaluate the clearance in fastening of suspension elements to the body of an automobile. The application of spectrum of vibration signal to determine frequency band connected with proper vibrations of the car body generated by impacts of vehicle suspension elements in case of clearance in fastening of suspension elements to the car body.

Keywords: vibroacoustic diagnostics, vehicle suspension

1. Introduction

Technical test of the vehicle suspension system performed at the Vehicles Inspection Station is done by means of the equipment constituting diagnostic line. Repeatability of results achieved by means of the above mentioned equipment is not satisfactory in all cases – therefore, to find new and more precise examination methods which would allow to do detailed analysis of vehicle suspension system efficiency, the specific researching attempts were taken.

The method which can be used in this area of examination is a method focused on analysis of vehicle body vibration signals, i.e. the changes in frequency of the vibrations.

2. Analysis of signals in the domain of frequency

In the domain of frequency a spectrum selection was performed and it was carried out in order to isolate and expose the frequency bands or its respective components in the signal. Apart from spectrum selecting performed with the low-pass and high-pass filters, band elimination filters, and comb filters, the following things are also used: tracking filters and advanced techniques (among others order analysis) or polyharmonic recurrent filtration [1].

Frequency characteristics present amplitude or signal phase in the frequency domain. In vibration diagnostic testing, in order to evaluate technical condition of the object, the relation of the amplitude with the frequency (amplitude spectra, power spectra, product spectra, power density spectra and others) is used. On the basis of spectral analysis, the damaged technical assembly can be easily identified, because those technical assemblies generate vibrations of different frequencies. To analyse the vibration signals in the domain of frequency, various types of analysers are used. The spectral analysis can be performed with absolute or relative constant of analysis band. Vibration signals spectra can be achieved in analogue manner or signal timing digital processing.

The analysis of signals by analogue means includes sequential or parallel filtration the band of signals. Filter parameters and details of this type of signal processing is presented in works [3, 5].

In relation to dynamic development the IT technologies, nowadays the digital methods of processing and analysis of vibration signals are used. In digital methods of signal analysis for the transformation of timing in the domain of frequency, expansion of function into Fourier's series is used in accordance with the relationship:

$$s(t) = a_0 + \sum_{k=1}^{\infty}\left[a_k \cos\left(\frac{2\cdot\pi\cdot k\cdot t}{T}\right) + b_k \sin\left(\frac{2\cdot\pi\cdot k\cdot t}{T}\right)\right], \tag{1}$$

The a_0, a_k and b_k coefficients of expansion of function into Fourier's series can be determined as coefficients of correlation between the x(t) function, and orthogonal base functions by means of the following relationship [4]:

$$a_0 = \frac{1}{T}\int_0^T s(t)\,dt, \tag{2}$$

$$a_k = \frac{1}{T}\int_0^T s(t)\cdot\cos\left(\frac{2\cdot\pi\cdot k\cdot t}{T}\right)dt, \tag{3}$$

$$b_k = \frac{1}{T}\int_0^T s(t)\cdot\sin\left(\frac{2\cdot\pi\cdot k\cdot t}{T}\right)dt, \tag{4}$$

where:

$s(t)$ – time history,
t – time,
T – time range,
k – harmonic number (k = 1,2,3…),
f – frequency
a_0 – constant component of signal,
a_k, b_k – coefficients of expanding the function into Fourier's series.

The amplitude and frequency estimation error for local maximum values of a map can be minimized by using amplitude – frequency correction AFC [2].

In order to enable presentation of the timing in the form of Fourier's series, one factor has to be met i.e. signal timing has to fulfill the Dirchlet's conditions which are formulated in the following manner [4]:

1. Any given time range "t" with the "T" width can be divided into finite number of ranges in which this function is determined, continuous and monotonic.
2. The number of discontinuity points must be specified, and in each point of discontinuity, there is a right and left-hand side limit.
3. The value of the function in a singular point is equal to an arithmetic average of the limits.

In this dissertation [1] the author states that every vibroacoustic signal meets the Dirchlet's conditions.

The a_k and b_k coefficients are composite spectra of the signal. The amplitude spectrum is described by the equation (5) whereas phase spectrum can be determined pursuant to the dependence (6).

$$A(k) = \sqrt{a_k^2 + b_k^2}\,, \tag{5}$$

$$\theta(k) = arctg\left(\frac{b_k}{a_k}\right), \tag{6}$$

where:

A(k) – amplitude spectrum,

θ(k) – phase spectrum,

k – harmonic number (k = 1,2,3…),

a_k, b_k – coefficients of expanding the function into Fourier's series.

3. Methodology and course of research

The examination was performed for a medium class motor car – Renault Clio III, 2008 year of manufacture, engine cubic capacity of 1 200 cm^3. The vehicle had chassis systems, including suspension, in good working order. The tyres met required technical conditions (the depth of tyre tread and pressure inside tyre) – all those elements conformed to the legal requirements. The tyre dimensions were compliant with the vehicle manufacturer's recommendations.

The examination was performed with active experiment principles. The experiment was conducted by means of MAHA diagnostic equipment which is used for testing technical condition of dampers embedded in vehicles. That equipment allowed us to get the frequency of vibrations within the range of 0 to 15 Hz. For an analysis of vibrations in the suspension system, the PULSE 3050 A60 and 4504 type Brüel & Kjaar vibration converters [5, 6, 7] were used. The equipment was located on the body of the vehicle (Fig. 1a). Suspension system vibrations were forced by means of the diagnostic station panel. The scope of frequencies generated by the station's panel was in the range of 0-15 Hz.

Vibrations measurements were made for the upper part of the left front absorber’s column (Fig. 1a). Each time, the clearance of the nut and the column was increased by a half of the turn, which was equal to the pitch of the thread of 0.5 mm. Vehicle on the inspection station is presented in Fig. 2b. The test was repeated till the moment when the absorber’s clearance was 5 mm.

a) b)

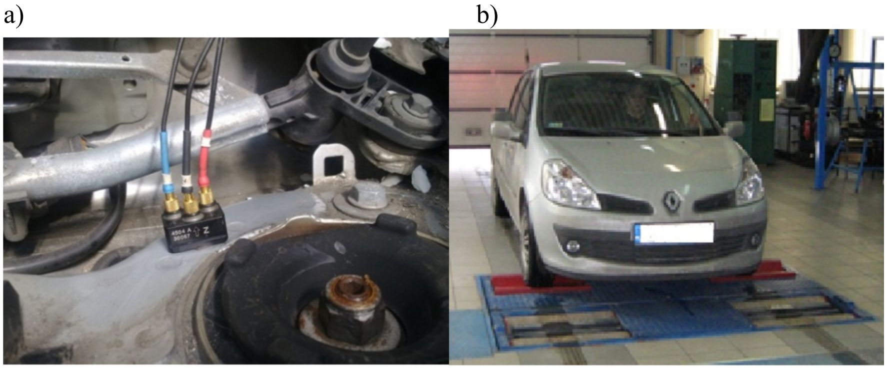

Figure 2. The view of: a) the location of accelerometer, b) the vehicle at the test station

4. Results and their analysis

In order to determine the impact of the clearance between the absorber and the body, the analyses of the recorded vibration signal were conducted. Such analyses comprised of determining frequency characteristics. The analyses results are presented in Figures 2 and 3. On the basis of spectral characteristics presented in Figure 2, it has been stated that in order to determine the relationship between the absorber’s clearance fastening with the chassis, the frequency band of 1.2 – 1.6 kHz is the most appropriate.

a) b)

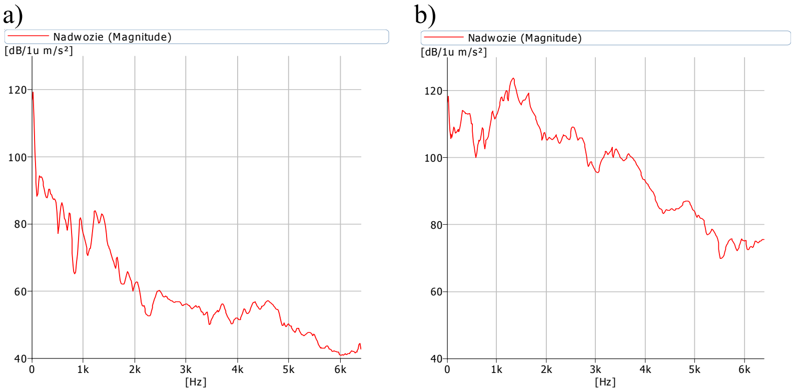

Figure 2. Vibration signal spectrum in case: a) when there is no clearance, b) with maximum clearance

In order to develop a model of diagnostic testing to evaluate absorber's chassis fastening clearance, the spectral analysis was performed for different values of the clearance. Frequency characteristics in the band from 1.2 to 1.6 kHz for various clearance values are presented in Figure 3a.

Figure 3b presents the maximum value of A $_{max}$ from vibrations spectrum in the band of 1.2-1.6 kHz, in the domain of clearance, for the upper column of the left front absorber of the examined vehicle. The calculated maximum values of vibration spectrum are circled.

a) b)

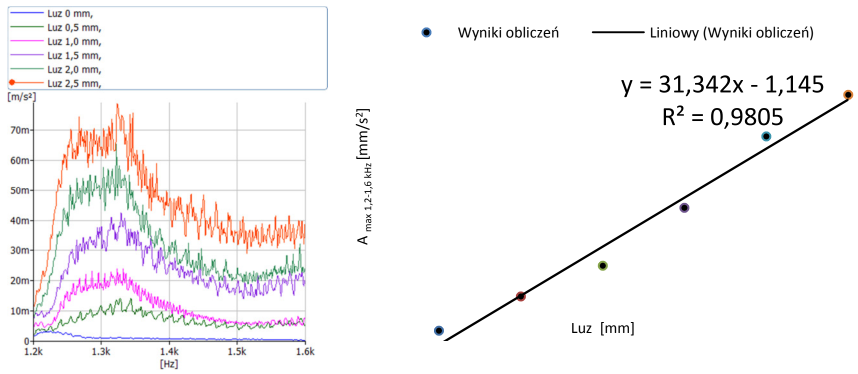

Figure 3. Vibration signal spectrum for different clearance values in the band of 1.2-1.6 kHz (a); the dependence of A $_{max}$ 1.2-1.6 kHz on the clearance (b)

The presented dependencies were approximated (by means of the least squares method) with the linear function. As a result of approximation, a mathematical model was achieved which is described with the equation (7). The approximation curve is presented in Figure 4b, as a full line.

$$A_{\max 1.2\text{-}1.6\,\mathrm{kHz}} = 31.342 \cdot L - 1.145 \tag{7}$$

where:

$A_{\max\ 1.2\text{-}1.6\ \mathrm{kHz}}$ – maximum value from vibrations acceleration spectrum in the band of 1.2-1.6 kHz [mm/s^2],

L – clearance [mm].

A basic element of the aforementioned test, based on the known vibration acceleration values was to achieve the relationship between the maximum value of acceleration of the vibrations and the clearance in the place where the upper column of the vehicle's front absorber is fastened. For that purpose, the clearance calculations were performed on the basis of approximation curves, in order to determine functions helping estimate McPherson's column clearance on the basis of calculated values of vibrations $A_{\max\ 1,2\text{-}1,6\ \mathrm{kHz}}$. In the equation, the maximum value of vibrations acceleration was assumed as explanatory variable. The response variable was the clearance between the absorber and the chassis. As a result of approximation coefficients calculations, we obtained a curve described by the following dependence (8):

$$L = 0.0313 \cdot A_{\max 1.2\text{ - }1.6\,\mathrm{kHz}} + 0.0602 \tag{8}$$

where:

$A_{\max 1.2\text{-}1.6\,\mathrm{kHz}}$ – maximum value of vibration acceleration spectrum in the band of 1.2-1.6 kHz [mm/s^2],

L – clearance [mm].

The value of R^2 coefficient obtained is based on the comparison of clearance measurement results between the absorber and chassis with the use of relationship (8) – clearance between the absorber and the chassis was 0.98, which means a very good representation of actual measurements in the mathematical model describing changes of the clearance depending on the maximum value of vibrations acceleration. Diagnostic parameter of dynamics changes in the band of 1.2-1.6 kHz was approximately 27 dB.

5. Conclusion

From the performed tests, it has been concluded that in order to estimate the clearance between the absorber and the body, for the presented object a method focused on the vibration spectral analysis can be used.

Figure 5 presents that in order to assess the clearance between the absorber and the body, vibration signal in the band of 1.2-1.6 kHz must be filtered.

On the basis of the recorded vibration signals analyses, it has been concluded that for the purpose of clearance assessment (between left front absorber and the body) in a model based on the peak value of the vibration acceleration in the band of 1.2-1.6 kHz, dynamics in instance of the peak value is approximately 27 dB.

References

1. R. Barczewski: *Poliharmoniczna filtracja rekurencyjna – diagnostycznie zorientowana metoda analizy sygnału*. Diagnostyka ’92, Materiały X Szkoły Diagnostyki Poznań – Zajączkowo 1992.
2. R. Barczewski: *AFC - the method of amplitude spectrum correction*. Congress of Technical Diagnostics, Gdańsk 1996.
3. C. Cempel: *Podstawy wibroakustycznej diagnostyki maszyn*, WNT Warszawa 1982.
4. G.M. Fichtenholtz: *Rachunek różniczkowy i całkowy III*. PWN Warszawa 1985.
5. R.B. Randall, B.A. Tech: *Frequency analysis*. Brüel & Kjær 1987.
6. M. Serridge, T.R. Licht: *Piezoelectric accelerometers and vibration preamplifiers*. Brüel & Kjær 1987.
7. http://www.bksv.com/products/transducersconditioning/vibration-transducers/accelerometers/accelerometers/4504a.aspx (January 2012)

XXV Symposium *Vibrations in Physical Systems,* Poznan – Bedlewo, May 15-19, 2012

The Regions of Divergence and Flutter Instability of a Column Subjected to Beck's Generalized Load Taking into Account an Elastic Support at the Loaded End

Lech TOMSKI
Częstochowa University of Technology
Institute of Mechanics and Machine Design Foundations
ul. Dąbrowskiego 73, 42-200 Częstochowa, email: sekr@imipkm.pcz.czest.pl

Sebastian UZNY
Częstochowa University of Technology
Institute of Mechanics and Machine Design Foundations
ul. Dąbrowskiego 73, 42-200 Częstochowa, email: uzny@imipkm.pcz.czest.pl

Abstract

The boundary value problem concerning the free vibrations of a slender system subjected to Beck's generalized load was formulated and solved in the work. The considered column was elastically supported by a spring with linear characteristic at the loaded end. The critical load of the system, both divergence and flutter, and the regions of presence of divergence and flutter instability were determined on the basis of the boundary problem concerning the free vibrations (the kinetic criterion of stability). Numerical calculations have been assigned to different values of the parameters of the considered system for which the follower factor, the rigidity parameter of a spring supporting column, the parameter of the translational inertia of the body mounted at the loaded end of the column are ranked.

Keywords: column, free vibrations, kinetic criterion of stability, flutter and divergence instability

1. Introduction

Slender systems subjected to non-conservative compression load can lose stability due to oscillations with growing amplitude (flutter instability) or due to buckling (divergence instability). These systems were called hybrid systems by Leipholz [1]. The method of stability losing is dependent on parameters of the system. The parameters can be divided into two groups: parameters connected to the load and structural parameters. The follower factor η [2] is the parameter connected to load. Hybrid system can be subjected to simultaneous action of two forces: follower force (Beck's) and Euler's force [3].

The structural parameters are as follows: rigidities of translational [2, 4] or rotational [5] springs, a system of translational and rotational dampers [6], mass of the body mounted at the loaded end of the column (comp. [7]), and in the case of complex systems - pre-stressing [8] and flexural rigidity asymmetry factor [9].

Sundararajan [4] considered the column subjected to the follower force (Beck's) supported by a linear spring at the loaded end of this column. Sundararajan determined the critical load, both flutter and divergence, of the system in relations to the rigidity of the spring supporting the column. Tomski and Przybylski [2] also considered the column supported by a spring with linear characteristic at the loaded end subjected to Beck's generalized load. The authors determined the divergence critical forces depending on the support rigidity for different values of the follower coefficient η. The rotational spring limiting the rotation of the loaded end also has an influence on the way in which stability is lost (divergence or flutter) (comp. [5]). In work [5] the authors determined the divergence and flutter critical loads depending on the system parameters, and identified regions of occurrence of divergence and flutter instability. Research into influence of mass and the mass moment of inertia of the body present at the loaded end of the column on the value of flutter critical load can be found in [5, 7]. An increase in the value of mass of the body mounted at the loaded end of the column leads to an increase in the value of flutter critical load. The mass moment of inertia destabilizes the system (flutter critical force lowers together with a rise in the mass moment of inertia).

Damping, both external and internal, is the next parameter influencing the value of the critical flutter load. External damping caused an increase in the critical flutter load (por. [10]). The extent of this increase is dependent on the values of the remaining parameters of the considered system. Internal damping destabilizes the system (comp. [11]) (flutter critical force lowers together with a rise in this type of damping).

2. The boundary problem connected to free vibrations

The system shown in Fig. 1 is considered in this paper. This system was presented by Tomski and Przybylski in [2]. Detailed numerical research into determination of system parameters corresponding to divergence and flutter instability is the aim of this paper. The considered column is subjected to Beck's generalized load and elastically supported by a spring with linear characteristic (C – spring rigidity). The direction of force P is determined by the follower factor η.

The kinetic criterion of stability was applied to define the critical load and regions of divergence and flutter instability. The differential equation of motion and the boundary conditions of the considered system are as follows (comp. [2]):

- differential equation of motion:

$$\frac{\partial^4 w(\xi,\tau)}{\partial \xi^4} + k^2 \frac{\partial^2 w(\xi,\tau)}{\partial \xi^2} + \Omega^2 \frac{\partial^2 w(\xi,\tau)}{\partial \tau^2} = 0 \tag{1}$$

- geometrical boundary condition:

$$w(0,\tau) = 0 \tag{2}$$

- natural boundary conditions:

$$\left.\frac{\partial^2 w(\xi,\tau)}{\partial \xi^2}\right|_{\xi=0} - c_0 \left.\frac{\partial w(\xi,\tau)}{\partial \xi}\right|_{\xi=0} = 0 \tag{3}$$

$$\left.\frac{\partial^2 w(\xi,\tau)}{\partial \xi^2}\right|^{\xi=1} = 0 \tag{4}$$

$$\left.\frac{\partial^3 w(\xi,\tau)}{\partial\xi^3}\right|^{\xi=1}+k^2(1-\eta)\left.\frac{\partial w(\xi,\tau)}{\partial\xi}\right|^{\xi=1}-cw(\xi,\tau)\Big|^{\xi=1}-\Omega^2\zeta_m\left.\frac{\partial^2 w(\xi,\tau)}{\partial\tau^2}\right|^{x=l}=0 \qquad (5)$$

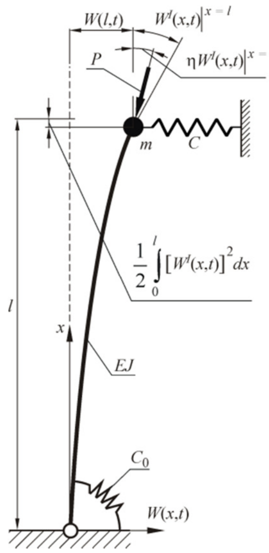

Figure 1. Considered column loaded by generalized Beck's load

Considerations were carried out taking into account the following dimensionless quantities:

$$\lambda=k^2=\frac{Pl^2}{EJ},\ \Omega^*=\Omega^2=\frac{\rho A\omega^2 l^4}{EJ},\ \tau=\omega t,\ w(\xi,\tau)=\frac{W(x,t)}{l}$$

$$\xi=\frac{x}{l},\ c_0=\frac{C_0 l}{EJ},\ c=\frac{Cl^3}{EJ},\ \zeta_m=\frac{m}{\rho Al},\ \lambda_{kr}=\frac{P_{kr}l^2}{EJ}$$

where: EJ – the flexural rigidity of the column, ω – free vibration frequency, m – mass of the body mounted at the loaded end of the column, t – time, ρAl – mass of the column, C_0 – rigidity of the mounting.

After separation of variables using relationship:

$$w(\xi,\tau)=y(\xi)\cos\tau \qquad (6)$$

the solution to differential equation is defined by the following dependence:

$$y(\xi)=A_d\cosh(\alpha\xi)+B_d\sinh(\alpha\xi)+C_d\cos(\beta\xi)+D_d\sin(\beta\xi) \qquad (7)$$

In the solution (7), A_d, B_d, C_d, D_d are integration constants of differential equation (1), while quantities α, β are given by equations:

$$\alpha = \sqrt{-\frac{k^2}{2} + \sqrt{\frac{k^4}{4} + \Omega^2}}\ ,\ \beta = \sqrt{\frac{k^2}{2} + \sqrt{\frac{k^4}{4} + \Omega^2}} \tag{8}$$

By substituting formulae (7) into the boundary conditions (2)-(5) and after separating variables, a system of equations is obtained:

$$\left[a_{ij}\right]\left\{A_d, B_d, C_d, D_d\right\} = 0 \tag{9}$$

The matrix determinant of coefficients of the above equation, as equated to zero, is the transcendental equation for the natural frequency:

$$\left|a_{ij}\right| = 0 \tag{10}$$

3. Results of numerical research

The boundary value of rigidity parameter of spring supported system for which the change in the type of instability (divergence and flutter instability) took place is presented in Figs. 2 and 3. The considered system can be characterised by two boundary rigidities (c_{bI} i c_{bII}) or by only one boundary rigidity (c_{bII}).

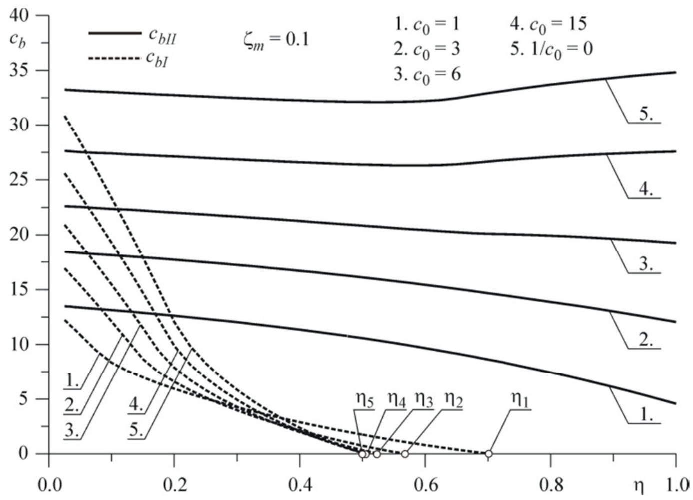

Figure 2. Boundary value of spring rigidity parameter c_b in relation to parameter η

In the case of the system characterised by two boundary rigidities c_{bI} and c_{bII} flutter instability, flutter instability of the column is present for $c \in (c_{bI}, c_{bII})$ while divergence instability is present for $c < c_{bI}$ and for $c > c_{bII}$. In the case of the system characterised by only one boundary rigidity c_{bII}, flutter instability is present for $c < c_{bII}$, while divergence instability is present for $c > c_{bII}$. If the rigidity of a spring supported the system is equal to the boundary rigidity ($c = c_{bI}$ lub $c = c_{bII}$), two critical forces (flutter and divergence) exist at the same time. The boundary values of rigidity of spring supporting the system c_{bI} lorc_{bII} in relation to the follower factor of a load η are presented in Fog. 2. The numerical computations were carried out for different values of the rigid mounting of the column c_0.

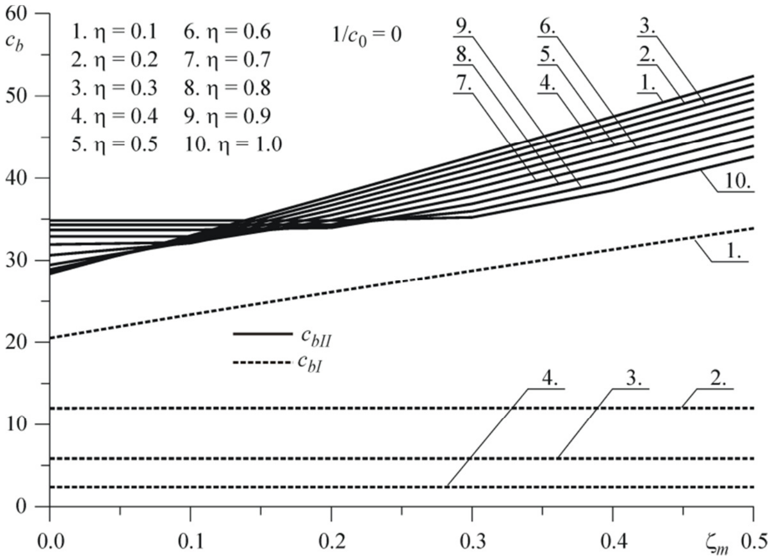

Figure 3. Boundary value of spring rigidity parameter c_b in relation to parameter ζ_m

The influence of mass parameter of the body mounted at the loaded end of the column ζ_m on the value of the boundary rigidity parameter of the spring supported c_b is presented in figure 3. In this case, the numerical computations were carried out for different values of the follower factor η and for rigid mounting of the column $1/c_0 = 0$. In Figs. 2 and 3, the rigidities c_{bII} are denoted by solid lines while rigidities c_{bI} are denoted by broken lines.

4. Conclusions

The problem applied to the free vibrations of a slender system subjected to Beck's generalized load and supported at the loaded end by translational spring with linear characteristics was solved in this paper. The boundary values of rigidities of the spring supporting column were determined on the basis of the kinetic criterion of stability where the change in instability type (divergence and flutter) took place. Numerical computations were carried out for different values of the system parameters such as: the follower factor, parameter of mounting rigidity and mass parameter of the body mounted at the loaded end of the column. One (c_{bII}) or two (c_{bI}, c_{bII}) values of the boundary rigidity of the spring supported the column are present in relation to the system parameters. Divergence instability is present if $c < c_{bI}$ and $c > c_{bII}$, while flutter instability is present if $c_{bI} < c <$

c_{bII} and $c < c_{bII}$. The value c_{bI} decreases with an increase in the follower factor η. The value c_{bII} is changing less intensively in relation to the follower factor comparing to c_{bI}.

Acknowledgments

The study has been carried out within the statutory funds of the Czestochowa University of Technology (BS-1-101-302/99/P) and Research Project No. N N501 117236 awarded by the Ministry of Science and Higher Education, Warsaw, Poland.

References

1. H. Leipholz, *Aspects of Dynamic Stability of Structures*, Journal of the Engineering Mechanics Division, **101**(2) (1975), 109-124.
2. L. Tomski, J. Przybylski, *Static Instability of an Elastically Restrained Cantilever Under a Partial Follower Force*, AIAA Journal **23**(10) (1985) 1637-1639.
3. J. A. Hernández-Urrea, J. Dario Aristizábal-Ochoa, *Static and dynamic stability of an elastically restrained Beck column with an attached end mass*, J. Sound Vib., **312** (2008) 789-800.
4. C. Sundararajan, *Influence of an elastic end support on the vibration and stability of Beck's column*, Int. J. Mech. Sci. **18** (1976) 239-241.
5. L. Tomski, S. Uzny, *The regions of flutter and divergence instability of a column subjected to Beck's generalized load taking into account the torsional flexibility of the loaded end of the column*, Mech. Res. Com., **38** (2011) 95-100.
6. A. Di Egidio, A. Luongo, A. Paolone, *Linear and non-linear interactions between static and dynamic bifurcations of damped planar beams*, Int. J. Non-linear Mech., **42** (2007) 88-98.
7. A.N. Kounadis, *Stability of elastically restrained Timoshenko cantilevers with attached masses subjected to a follower force*, J. Appl. Mech., **44** (1977) 731-736.
8. J. Przybylski, *The role of prestressing in establishing regions of instability for a compound column under conservative or nonconservative load*, J. Sound Vib., **231**(2) (2000) 291-305.
9. J. Przybylski, *Vibrations and stability of initially prestressed two-member rod systems under nonconservative load*, Publishing House of Częstochowa University of Technology, series Monographs, Nr 92, Częstochowa 2002.
10. P. Pedersen, *Influence of boundary conditions on the stability of a column under non-conservative load*, Int. J. Solids Struct., **13** (1977) 445-455.
11. M.A. Langthjem, Y. Sugiyama, *Dynamic stability of columns subjected to follower loads: a survey*, J. Sound Vib., **238**(5) (2000) 809-851.

XXV Symposium *Vibrations in Physical Systems,* Poznan – Bedlewo, May 15-19, 2012

The Calculation of the Eigenfrequencies of the Torsional Free Vibrations of the Bars Using the Method of Fundamental Solutions

Anita UŚCIŁOWSKA, Agnieszka FRASKA
Institute of Applied Mechanics, Poznan University of Technology
ul Piotrowo 3, 60-965 Poznan, POLAND
anita.uscilowska@put.poznan.pl, agnieszka.fraska@put.poznan.pl

Abstract

This work concerns an application of the method of fundamental solutions to the calculation of the eigenfrequencies of the torsional natural vibrations of the bars. The problem of the torsional free vibrations of the bar is an initial-boundary value problem. In the solution process of this problem, the method of variables separation is used. The boundary value problem is solved by the method of fundamental solutions. The different shapes of the bar cross-section are taken into account. The numerical calculations are performed for the rods made of the materials with the different characteristics (mass, density, shear modulus, etc.). To check the accuracy of the proposed methods the results of numerical experiment are included.

Keywords: method of fundamental solutions; eigenfrequencies problem, Bessel functions

1. Introduction

Taking into account in calculations the various type of vibrations is a challenging issue and often requires the complicated mathematical or the numerical method using. The vibrations of the bars belong to the important problems of dynamic, because the bars are elements of many machines and constructions. In our considerations we concentrate on the free torsional vibrations of a prismatic bar. A formulation of this problem one can find in some monographies [1, 3, 8, 16]. Here we use the formulae based on elasticity equations of motion according to Nowacki [16]. The problem of the torsional waves propagating in a bar is described by a partial differential equation of second order and appropriate initial and boundary conditions. In the solution process of this problem, the method of variables separation is used. The boundary value problem is solved by the method of fundamental solutions. The method of fundamental solutions (MFS) is a meshfree numerical method [14].The idea for MFS was first proposed by Kupradze and Aleksidze [13] in 1964, and Mathon and Johnston carried out its numerical implementation [15]. In MFS the assumed solution is a linear combination of the fundamental solutions. The comprehensive reviews of the MFS for the various applications can be found in [4, 5, 20]. The method of fundamental solutions has been also used for solving torsion problems of bars. An implementation of MFS for elasto-statics torsion of prismatic homogenous bars is presented in works [6, 7] and in case of inhomogeneous bars, made with functionally graded materials (FGM) in [21, 22]. Recently the work [12] about an application the methods of fundamental solutions for torsion of homogeneous prismatic bars in the area of elasto-plastic static was publicated too. As regards the application of MFS for solving the dynamic torsion of bars, we undertook the problem of free torsional vibrations of a functionally graded bar in paper from 2010 [19]. In this paper the method of finite differences was used in order to approximation of the time derivation. In this way for each time step the boundary value problem has been obtained. The method of fundamental solutions supported by the Picard iterations and approximation by radial basis functions and monomials was proposed for solving the problem. The influence of the method's parameters on the convergence of this complex procedure, was investigated.

The aim of this study is an application of the method of fundamental solutions for calculation of the eigenfrequencies of the natural vibrations of a bar subjected the dynamic torsion. The knowledge of the eigenfrequencies problem is helpful in engineering practice, in designing structural elements of constructions and exploiting of the machines. The concept of using MFS for the calculation of eigenvalues of the Helmholtz equation was presented by Karageorghis in his paper [10] and Reutskiy applied the MFS in physical problem of free vibrations of plates [18]. The undoubtedly advantage of the MFS consists in avoiding the integration over the boundary. Therefore the implementation of the MFS is quite easy on the contrary to the method of boundary elements (BEM), the one of the most popular method used in analysis of torsional free vibrations of bars [2, 9, 17].

2. Formulation of the initial-boundary value problem

The problem of the torsional vibrations of a bar is formulated on the ground of theory of elasticity. A homogeneous and an infinitely long cylinder with a solid circular cross-section of radius a is taken into account. In the cylindrical coordinates the components of displacement are u_r, u_θ, u_z and the components of stress are σ_{rr}, $\sigma_{r\theta}$, σ_{rz}, etc. The torsional waves propagating in a cylinder involve only a u_θ - circumferential displacement which is independent of θ.

The partial differential equation of the dynamical torsion of a bar, in the axi-symmetric case, has the following form (see [1, 16]):

$$\left(\frac{\partial^2}{\partial r^2}+\frac{1}{r}\frac{\partial}{\partial r}-\frac{1}{r^2}+\frac{\partial^2}{\partial z^2}\right)u_\theta=\frac{\rho}{\mu}\frac{\partial^2 u_\theta}{\partial t^2} \tag{1}$$

for $(r,z)\in\Omega$ and $t\geq 0$, where $\Omega=\{(r,z):0\leq r\leq a,\ z\in\Re\}$, μ is a shear modulus, ρ is a density of a bar.

An absence of tractions on the lateral surface of the cylinder implicates next boundary condition:

$$\sigma_{r\theta}(a,z,t)=\mu\left(\frac{\partial}{\partial r}-\frac{1}{r}\right)u_\theta(r,z,t)=0 \quad \text{for} \quad (r,z)\in\partial\Omega \tag{2}$$

where $\partial\Omega$ is the boundary of the region Ω.
Moreover it is necessary to assume that the displacement at $r = 0$ is finite.
The initial conditions are given as:

$$u_\theta(r,z,t_0) = u_o(r,z) \tag{3}$$

and

$$\left.\frac{\partial u_\theta(r,z,t)}{\partial t}\right|_{t=t_0} = \dot{u}_0(r,z) \tag{4}$$

for $(r,z)\in\Omega$.

3. The method of solution

The considered problem is solved by the method of variables separation. The assumed solution has the form:

$$u_\theta(r,z,t) = U_\theta(r,z)\cdot e^{-\omega t} \text{ for } (r,z)\in\Omega \text{ and } t\geq 0. \tag{5}$$

As a result of substituting the above formula to the equation (1) and dividing by $e^{-\omega t}$ we get the following equation:

$$\left(\frac{\partial^2}{\partial r^2}+\frac{1}{r}\frac{\partial}{\partial r}+\frac{\partial^2}{\partial z^2}\right)U_\theta(r,z)-k^2U_\theta(r,z)=0 \text{ for } (r,z)\in\Omega, \tag{6}$$

where

$$k^2=\frac{1}{r^2}+\omega^2\frac{\rho}{\mu}. \tag{7}$$

Now the boundary condition (2) has the form:

$$\left.\left(\mu\left(\frac{\partial}{\partial r}-\frac{1}{r}\right)U_\theta(r,z)\right)\right|_{r=a}=0 \text{ for } (r,z)\in\partial\Omega. \tag{8}$$

Of course, we still remember that the displacement U_θ, is finite for $r = 0$.

So, in this way we obtained the boundary value problem to solve, which leads to eigenvalues problem. The problem is described by modified Helmholtz equation in axi-symmetric case and the boundary condition. This problem is solved by the Method of Fundamental Solutions (MFS) (see [10]). The aim of this study is to find the values k for which the problem has a nontrivial solution.

In the Method of Fundamental Solutions the assumed solution is a linear combination of fundamental solutions:

$$U_\theta(r,z)\approx u_N(k,r,z)=\sum_{i=1}^{Ns}c_i\, fs_i(k,r,z), \tag{9}$$

where $fs_i(k,r,z) = fs\left(k, \left\|\left(r - r_i^s, z - z_i^s\right)\right\|\right)$ is the fundamental solution of the equation (9), where $\|\cdot\|$ is a distance in sense of an Euclidean norm. Points $(r,z) \in \Omega \cup \partial\Omega$ are approximation points and $\left\{\left(r_i^s, z_i^s\right)\right\}_{i=1}^{Ns}$ is a set of points outside the region Ω. The points $\left\{\left(r_i^s, z_i^s\right)\right\}_{i=1}^{Ns}$ called source points are presented in Figure 1 [13].

The points of the set $\left\{\left(r_j^b, z_j^b\right)\right\}_{j=1}^{Nb}$ are the boundary points (see Fig. 1).

In case of axisymmetric problems with modified Helmholtz operator the fundamental solution is expressed in terms of complete elliptic integrals (see [11]).

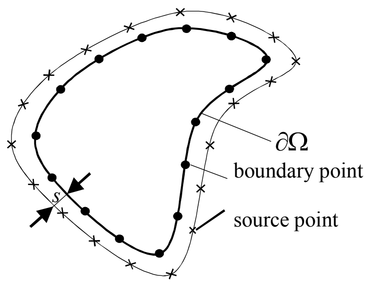

Figure 1. The sets of boundary and source points [13]

The unknown coefficients c_i are determined from the boundary condition (8):

$$\left. \left(\mu \left(\frac{\partial}{\partial r} - \frac{1}{r} \right) \sum_{i=1}^{Ns} c_i\, fs\left(k, \left\|\left(r - r_i^s, z - z_i^s\right)\right\|\right) \right) \right|_{\left\{\left(r_j^b, z_j^b\right)\right\}_{j=1}^{Nb}} = 0\,. \tag{10}$$

The above homogeneous linear system of equation can be written in the general form:

$$\mathbf{A}(k) \cdot \mathbf{c} = \mathbf{0}\,, \tag{11}$$

where

$$\mathbf{c} = \{c_i\}_{i=1,\dots,Ns}\,,\ \mathbf{A}(k) = \{a_{ij}(k)\}_{\substack{i=1,\dots,Ns \\ j=1,\dots,Nb}}\,, \tag{12}$$

and elements of matrix $\mathbf{A}$ have the form:

$$a_{ij}(k) = \left. \left(\mu \left(\frac{\partial}{\partial r} - \frac{1}{r} \right) fs\left(k, \left\|\left(r - r_i^s, z - z_i^s\right)\right\|\right) \right) \right|_{\left(r_j^b, z_j^b\right)}\,, \tag{13}$$

for $i=1,\dots,Ns$ and $j=1,\dots,Nb$.
In order to obtain a nontrivial solution of equation (6) the determinant of the matrix $\mathbf{A}(k)$ must be equal zero:

$$\det(\mathbf{A}(k)) = 0\,, \tag{14}$$

Therefore the values of parameter k are the eigenvalues of problem (6)-(8).
Finally, the values of the eigenfrequencies ω we calculate from a condition (7).

4. Summary

The method of fundamental solutions has been applied to the calculation of eigenfrequencies of free torsion vibrations of a bar. To check the accuracy of the proposed methods the numerical experiment has been performed. The obtained results agree with expected ones and they will be presented during the symposium. The proposed method shows a high precision and this is a good tool for solved problem. An implementation of the MFS for investigated problem is quite easy and the computer calculations are not very time-consuming.

Acknowledgements

The researches carried out within the limits of this paper are supported by Poznan University of Technology from the Grant 21-381/2012 DS.

References

1. J. D. Achenbach, *Wave propagation in elastic solids*, North-Holland Publishing Company, 1975.
2. J. P. Agnantiaris, D. Polyzos, D. E. Beskos, *Free vibration analysis of non-axisymmetric and axisymmetric structures by the dual reciprocity BEM*, Engineering Analysis with Boundary Elements **25** (2001) 713-723.
3. R. Bąk, T. Burczyński, *Wytrzymałość materiałów z elementami ujęcia komputerowego*, Wydawnictwa Naukowo-Techniczne, Warszawa 2001
4. G. Fairweather, A. Karageorghis, *The method of fundamental solutions for elliptic boundary value problems.* Advances in Computational Mathematics, 9 (1998) 69-95.
5. M. A. Golberg, C. S. Chen, *The method of fundamental solutions for potential, Helmholtz and diffusion problems.* In: Golberg MA, editor. Boundary integral methods - numerical and mathematical aspects. Boston, Computational Mechanics Publications, 1998, 103-176.
6. P. Gorzelańczyk, J. A. Kołodziej, *Some remarks concerning the shape of the source contour with application of the method of fundamental solutions*, Engineering Analysis with Boundary Elements, **31** (2007) 200-208.
7. P. Gorzelańczyk, H. Tylicki, J. A. Kołodziej, *The torsional stiffness of bars with L, [, +, I, and ⌡ cross-section,* Steel and Composite Structures, **7** (2007) 441-456.

8. R. Gutowski, A. Swietlicki, *Dynamika i drgania układów mechanicznych*, PWN, Warszawa 1986.
9. M. Itagaki, S. Nishiyama, S. Tomioka, T. Enoto, N. Sahashi, *Power iterative multiple reciprocity boundary element method for solving three-dimensional Helmholtz eigenvalue problems*, Engineering Analysis with Boundary Elements **20** (1997) 113-121.
10. A. Karageorghis, *The method of fundamental solutions for the calculation of the eigenvalues of the Helmholtz equation*, Applied Mathematics Letters, **14** (2001) 837-842.
11. A. Karageorghis, G. Fairweather, *The method of fundamental solutions for axisymmetric potential problems, International Journal for Numerical Methods in Engineering*, **44** (1999) 1653-1669.
12. J. A. Kołodziej, P. Gorzelańczyk, *Application of method of fundamental solutions for elasto-plastic torsion of prismatic rods*, Engineering Analysis with Boundary Elements, **36** (2012) 81-86.
13. V. D. Kupradze, M. A. Aleksidze, *The method of functional equations for the approximate solution of certain boundary-value problems*, USRR*,* Computational Mathematics and Mathematical Physics, **4** (1964) 82-126.
14. G. R. Liu, *Mesh free methods. Moving beyond finite element method*, CRC Press, Boca Raton 2003
15. R. Mathon, R. L. Johnston, *The approximate solution of elliptic boundary-value problems by fundamental solutions*. SIAM Journal on Numerical Analysis, **14** (1977) 638-650.
16. W. Nowacki, *Teoria sprężystości*, PWN, Warszawa 1970
17. E. J. Sapountzakis, *Torsional vibrations of composite bars by BEM*, Composite Structures, **70** (2005) 229-239.
18. S. Yu. Reutskiy, *The method of fundamental solutions for problems of free vibrations of plates*, Engineering Analysis with Boundary Elements, **31** (2007) 10-21.
19. A. Uscilowska, A. Fraska, *An investigation of functionally graded material parameters effects on free torsional vibrations of a bar using meshfree methods*, Vibrations in Physical Systems, **24** (2010) 435-440.
20. A. Uściłowska, *Rozwiązywanie wybranych zagadnień nieliniowych mechaniki metodą rozwiązań podstawowych*, Wydawnictwo Politechniki Poznańskiej, Poznań 2008
21. A. Uściłowska, A. Fraska, *Implementation of the method of fundamental solutions for solving a torsion problem of a rod made with functionally graded material*, Reviews on Advanced Materials Science, in press
22. A. Uściłowska, A. Fraska, *Mesh-free method based numerical experiment for estimation of torsional stiffness of a long bone*, Journal of Mechanics of Materials and Structures, in press

XXV Symposium *Vibrations in Physical Systems,* Poznan – Bedlewo, May 15-19, 2012

Vibrations of a Column Consisting of a Pipe and Rod with a Viscoelastic Layer Subjected to Euler's Load

Sebastian UZNY
Częstochowa University of Technology
Institute of Mechanics and Machine Design Foundations
ul. Dąbrowskiego 73, 42-200 Częstochowa, email: sekr@imipkm.pcz.czest.pl

Abstract

The boundary problem concerning the free vibrations of a geometrically non-linear slender system subjected to a load by a force, unchanging in its direction (Euler's force), is formulated and solved in the work. The considered column is a pipe with a focally mounted rod. A layer made of viscoelastic material is placed between the pipe and the rod. The Kelvin-Voigt model of this layer is taken into account to formulate the boundary problem. Numerical calculations connected to the free vibrations of the considered system are carried out on the basis of the boundary problem. Numerical simulations are assigned to different values of the parameters of the system for which the rigidity and damping parameters of the viscoelastic layer are ranked.

Keywords: column, free vibrations, Euler load, Kelvin-Voigt model

1. Introduction

Slender systems consisting of two elements with different flexural and compressional rigidities are geometrically non-linear systems due to application of non-linear theory to formulate the boundary problem (comp. [1-6]). The solution to the boundary problem concerning stability of geometrically non-linear system was first presented by Tomski in work [1]. The considered systems are characterised by rectilinear and curvilinear form of static equilibrium, local and global instability and non-linear natural frequency in dependence on amplitude. Non-linear natural frequency of geometrically non-linear system (in dependence on amplitude of vibrations) was determined in works [4, 5]. The geometrically non-linear system can consist of symmetrically located rods (flat frame – comp. [2, 3, 5]) or of a pipe and coaxially located rod (comp. [1, 4, 6]).

Many authors carried out research into influence of additional discrete elements in the form of springs or dampers on the stability and the free vibrations of the columns as well as on the free vibrations of beams (comp. [7-10]). The Kelvin-Voigt model is frequently used to formulate the boundary problems of the systems built of viscoelastic elements. The rigidity parameter of viscoelastic element has an influence on the value of critical load and on natural frequency while the damping parameter can have influence only on natural frequency.

Research into influence of parameters of viscoelastic layer on the value of natural frequency for geometrically non-linear system is the aim of this paper.

2. The boundary problem connected to the free vibrations

The considered in the paper geometrically non-linear system, built of a pipe and rod, is presented in Fig. 1. An elastic layer of δ in length (where $\delta << l$) made of viscoelastic material is taken into account in the system. This layer is placed between a pipe and the central rod. The Kelvin-Voigt model was applied to formulate the boundary problem of the considered system. This model is built of connected in parallel: spring (rigidity parameter *C*) and damper (damping parameter *D*). The column is hinged at two ends and subjected to Euler's load (external force *P* does not change direction of action).

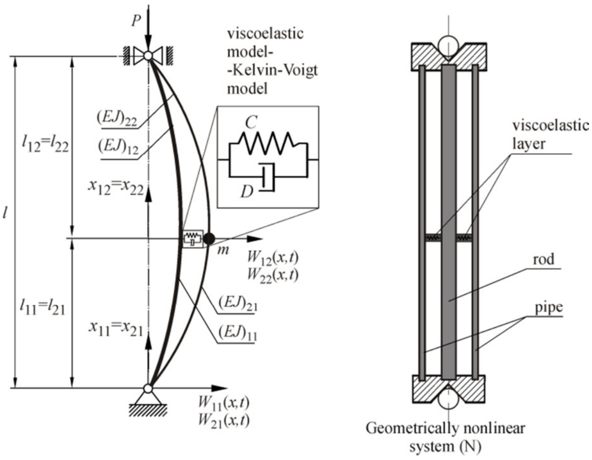

Figure 2. Considered slender system

The boundary problem connected to the free vibrations of the considered non-conservative system (the system is non-conservative due to damping) was formulated on the basis of Hamilton's principle in the following form:

$$\delta \int_{t_1}^{t_2} (T - V) dt + \int_{t_1}^{t_2} \delta L = 0 \tag{1}$$

where: T – kinetic energy, V – potential energy, δL – virtual work of non-conservative forces originating from damping. Energies: kinetic, potential and virtual work of non-conservative forces are defined by the following relationships:

$$T = \frac{1}{2} \sum_i \sum_k (\rho A)_{ik} \int_0^{l_{ik}} \left(\dot{W}_{ik}(x_{ik}, t) \right)^2 dx_{ik} + \frac{1}{2} m \left(\dot{W}_{21}(x_{21}, t) \Big|^{x_{21} = l_{21}} \right)^2 \tag{2}$$

$$\begin{gathered} V = \frac{1}{2} \sum_i \sum_k (EJ)_{ik} \int_0^{l_{ik}} \left(W_{ik}^{II}(x_{ik}, t) \right)^2 dx_{ik} + P U_{12}(l_{12}, t) \\ \frac{1}{2} (EA)_{ik} \int_0^{l_{ik}} \left[U_{ik}^{I}(x_{ik}, t) + \frac{1}{2} \left(W_{ik}^{I}(x_{ik}, t) \right)^2 \right]^2 dx_{ik} + \frac{1}{2} C \left(W_{11}(l_{11}, t) - W_{21}(l_{21}, t) \right)^2 \end{gathered} \tag{3}$$

$$\delta L = D\left(\dot{W}_{21}(x_{21},t)\Big|^{x_{21}=l_{21}} - \dot{W}_{11}(x_{11},t)\Big|^{x_{11}=l_{11}} \right)\delta W_{11}(l_{11},t) + \\ + D\left(\dot{W}_{11}(x_{11},t)\Big|^{x_{11}=l_{11}} - \dot{W}_{21}(x_{21},t)\Big|^{x_{21}=l_{21}} \right)\delta W_{21}(l_{21},t) \tag{4}$$

In this paper an order of partial derivative in relations to a space coordinate is denoted by Roman numeral while an order of partial derivative in respect of time is denoted by dots. The following denotations were introduced: $U_{ik}(x_{ik},t)$, $W_{ik}(x_{ik},t)$ – displacement longitudinal and transversal, respectively, of the individual elements of the column corresponding to coordinate x_{ik}, $(EJ)_{ik}$, $(EA)_{ik}$, $(\rho A)_{ik}$ – flexural rigidity, compressional rigidity, mass per unit length of the individual elements of the column (while $(EJ)_{11} = (EJ)_{12}$, $(EJ)_{21} = (EJ)_{22}$, $(EA)_{11} = (EA)_{12}$, $(EA)_{21} = (EA)_{22}$, $(\rho A)_{11} = (\rho A)_{12}$, $(\rho A)_{21} = (\rho A)_{22}$ and $(EJ)_{11} + (EJ)_{21} = idem$), m – mass of viscoelastic layer, t – time, i – index corresponding to pipe (i = 1) or rod (i = 2), k – index corresponding to an adequate segment of the pipe and rod (k = 1 – segment below viscoelastic layer, k = 2 – segment above viscoelastic layer).

Geometrical boundary conditions of the considered system are as follows:

$$W_{i1}(0,t) = W_{i2}(l_{i2},t) = U_{i1}(0,t) = 0 \tag{5}$$

$$W_{1k}^{I}((k-1)l_{1k},t) = W_{2k}^{I}((k-1)l_{2k},t) \tag{6}$$

$$W_{i1}^{I}(l_{i1},t) = W_{i2}^{I}(0,t)\,;\; W_{i1}(l_{i1},t) = W_{i2}(0,t) \tag{7}$$

$$U_{12}(l_{12},t) = U_{22}(l_{22},t);\; U_{i1}(l_{i1},t) = U_{i2}(0,t) \tag{8}$$

By substituting the kinetic energy (3) and potential energy (4) into Hamilton's principle (2) and using geometrical boundary conditions, the following relationships were obtained

By substituting relationships (2), (3) i (4) into Hamilton's principle and after taking into account the geometrical boundary conditions the following relationships were obtained:

- the differential equation of motion in the transversal direction

$$(EJ)_{ik} W_{ik}^{IV}(x_{ik},t) + S_{ik}(t) W_{ik}^{II}(x_{ik},t) + (\rho A)_{ik} \ddot{W}_{ik}(x_{ik},t) = 0 \tag{9}$$

- the differential equation of longitudinal displacements (non-linear equation)

$$\left(U_{ik}^{I}(x_{ik},t) + \frac{1}{2}\left(W_{ik}^{I}(x_{ik},t)\right)^2 \right)^{I} = 0 \tag{10}$$

- natural boundary conditions

$$\sum_i (EJ)_{i1} W_{i1}^{II}(x_{i1},t)\Big|_{x_{i1}=0} = 0\,;\; \sum_i (EJ)_{i2} W_{i2}^{II}(x_{i2},t)\Big|^{x_{i2}=l_{i2}} = 0 \tag{11}$$

$$\sum_k (-1)^k (EJ)_{ik} W_{ik}^{II}(x_{ik},t)\Big|_{x_{ik}=(2-j)l_{ik}} = 0 \; ; \; i,k=1,2 \tag{12}$$

$$\begin{gathered}(EJ)_{11} W_{11}^{III}(x_{11},t)\Big|^{x_{11}=l_{11}} - (EJ)_{12} W_{12}^{III}(x_{12},t)\Big|_{x_{12}=0} - \\ - C\big(W_{11}(l_{11},t) - W_{21}(l_{21},t)\big) - D\left(\dot{W}_{11}(x_{11},t)\Big|^{x_{11}=l_{11}} - \dot{W}_{21}(x_{21},t)\Big|^{x_{21}=l_{21}}\right) = 0\end{gathered} \tag{13}$$

$$\begin{gathered}(EJ)_{21} W_{21}^{III}(x_{21},t)\Big|^{x_{21}=l_{21}} - (EJ)_{22} W_{22}^{III}(x_{22},t)\Big|_{x_{22}=0} + C\big(W_{11}(l_{11},t) - W_{21}(l_{21},t)\big) + \\ + D\left(\dot{W}_{11}(x_{11},t)\Big|^{x_{11}=l_{11}} - \dot{W}_{21}(x_{21},t)\Big|^{x_{21}=l_{21}}\right) - m\ddot{W}_{21}(x_{21},t)\Big|^{x_{21}=l_{21}} = 0\end{gathered} \tag{14}$$

$$S_{11}(t) = S_{12}(t), \; S_{21}(t) = S_{22}(t), \; S_{11}(t) - S_{22}(t) - P = 0 \tag{15}$$

After integrating twice, and after considering the geometrical boundary conditions connected to longitudinal displacement, the equation of longitudinal displacement can be written in the following form:

$$U_{ik}(x_{ik},t) - U_{ik}(0,t) = -\frac{S_{ik}(t)}{(EA)_{ik}} x_{ik} - \frac{1}{2}\int_0^{x_{ik}} \left(W_{ik}^{I}(x_{ik},t)\right)^2 dx_{ik} \tag{16}$$

Due to the non-linearity occurring in Eq. (16), the straightforward expansion method is used to formulate finally the boundary problem. This method relies on the expansion of all non-linear terms of the differential equations into a power series of small parameter. In this paper, the considerations were limited to rectilinear form of static equilibrium corresponding to external load changing from zero to bifurcation force. The considerations were also limited to determination the linear term of natural vibrations irrespectively of amplitude of vibrations. Only the terms of expansions into a power series of the small parameter of the individual non-linear expressions, which make it possible to carry out numerical computations of the linear term of the free vibrations in the case of rectilinear form of the static equilibrium, are presented in this paper. The considered terms of expansions are as follows:

$$W_{ik}(x_{ik},t) = \varepsilon W_{ik(1)}(x_{ik},t), \; U_{ik}(x_{ik},t) = U_{ik(0)}(x_{ik}), \; S_{ik}(t) = S_{ik(0)}, \; \omega = \omega_0 \tag{17}$$

where:

$$W_{ik(1)}(x_{ik},t) = \overset{(1)}{W}_{ik(1)}(x_{ik})e^{j\omega_0 t} \tag{18}$$

In the solution (18) j is the imaginary unit and natural frequency ω_0 is a complex number in the form:

$$\omega_0 = \omega_{0\,\mathrm{Re}} + j\omega_{0\,\mathrm{Im}} \tag{19}$$

Equations (17) are substituted into the differential equations and into boundary conditions. After grouping the terms of obtained relationships in relation to identical powers of small parameter (ε^0 and ε^1), the final form of the boundary problem connected to the free vibrations was received. Internal forces in the individual elements of the system were determined on the basis of equations connected to the zero power of the small parameter (ε^0) in the case of rectilinear form of the static equilibrium. Linear (independent on amplitude) component of natural frequency ω_0 (both real ($\omega_{0\mathrm{Re}}$) and imaginary ($\omega_{0\mathrm{Im}}$)) was determined on the basis of equations connected to the first power of the small parameter (ε^1) in the case rectilinear form of the static equilibrium.

3. The results of numerical computations

The results of numerical computations connected to natural frequency were presented using dimensionless quantities defined in the following way:

$$c = \frac{Cl^3}{\sum_i (EJ)_{i1}},\; d = \frac{Dl^3}{\sum_i (EJ)_{i1}} \frac{\omega_{ref}}{2\pi};\; \lambda = \frac{Pl^2}{\sum_i (EJ)_{i1}},\; \lambda_b = \frac{P_b l^2}{\sum_i (EJ)_{i1}} \tag{20}$$

$$\Omega = \frac{\omega^2 \sum_i (\rho A)_{i1} l^4}{\sum_i (EJ)_{i1}},\; \zeta_A = \frac{l_{11}}{l},\; \zeta_\lambda = \frac{\lambda}{\lambda_b},\; \mu_a = \frac{(EJ)_{21}}{(EJ)_{11}},\; \zeta_\omega = \frac{\Omega_{0\mathrm{Re}}}{\Omega_{0ND}} \tag{21}$$

where: $\omega_{ref} = 1$ [rad/s], Ω_{0ND} is the parameter of natural frequency at zero value of damping, P_b is bifurcation load of the system.

Change in parameter ζ_ω in relations to parameter ζ_λ is shown in Figure 3. The results of numerical computations are presented in the load range corresponding to the value of parameter $\zeta_\omega > 1$.

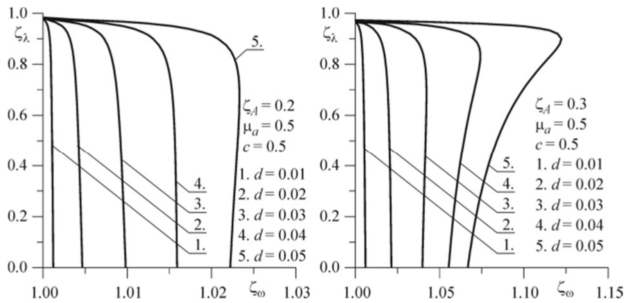

Figure 2. Parameter ζ_λ in relation to parameter ζ_ω

4. Conclusions

The problem of the free vibrations of a geometrically non-linear slender system, which consists of a pipe and a focally mounted rod considering viscoelastic layer, was formulated in the paper. The Kelvin-Voigt model of viscoelastic layer was applied to build mathematical model. Natural frequencies for different parameters of the system were determined on the basis of the boundary problem. Value of external load, location coefficient of viscoelastic layer, asymmetry factor of the flexural rigidity for pipe and rod, the rigidity and damping parameters of the viscoelastic layer are ranked for the parameters of the system. On the basis of carried out numerical computations, it was stated that parameter ζ_ω is dependent on the value of external load of the system. Rapid decrease in the value of parameter ζ_ω is observed for the load closed to the bifurcation load. Influence of damping on natural frequency is more significant if viscoelastic layer is located further from mounting of the system.

Acknowledgments

The study has been carried out within the statutory funds of the Czestochowa University of Technology (BS-1-101-302/99/P) and Research Project No. N N501 117236 awarded by the Ministry of Science and Higher Education, Warsaw, Poland.

References

1. L. Tomski, Prebuckling Behaviour of Compound Column – Direct Nonlinear Analysis, Z. Angew. Math. U. Mech. **65**(1) (1985) 59-61.
2. L. Tomski, J. Szmidla, S. Uzny, The Local and Global Instability and Vibration of Systems Subjected to Non-Conservative Loading, Thin-Walled Struct., **45(**10-11) (2007) 945-949.
3. L. Tomski L., S. Uzny, Free vibration and the stability of a geometrically non-linear column loaded by a follower force directed towards the positive pole, Int. J. Solids Struct., **45**(1) (2008) 87-112.
4. J. Przybylski, L. Tomski, Vibration of an Initially Prestressed Compound Column under Axial Compression, Elsevier Science Publishers B.V. (1992) 263-268.
5. S. Uzny, Nieliniowa składowa częstości drgań własnych kolumny poddanej obciążeniu Eulera (krzywoliniowa postać równowagi statycznej), Modelowanie Inżynierskie, **11**(42) (2011) 441-448.
6. S. Uzny, Local and global instability and vibrations of a slender system consisting of two coaxial elements, Thin-Walled Struct., **49** (2011) 618-626.
7. A. Di Egidio, A. Luongo, A. Paolone, Linear and non-linear interactions between static and dynamic bifurcations of damped planar beams, Int. J. Non-linear Mech., **42** (2007), 88-98.
8. K. A. Mladenov, Y. Sugiyama, Stability of a jointed free-free beam under end rocket thrust, J. Sound Vib., **199**(1) (1997) 1-15.
9. A. Luongo, A. Di Egidio, Bifurcation Equations Through Multiple-Scales Analysis for a Continuous Model of a Planar Beam**,** Nonlinear Dyn., **41** (2005) 171-190.
10. M. Abu-Hilal, Dynamic response of a double Euler–Bernoulli beam due to a moving constant load, J. Sound Vib., **297** (2006) 477-491.

XXV Symposium *Vibrations in Physical Systems,* Poznan – Bedlewo, May 15-19, 2012

Free Vibration Analysis of Shear Wall Structures with Stiffening Beams

Jacek WDOWICKI
Poznan University of Technology, 60-965 Poznań, ul. Piotrowo 5, Poland
jacek.wdowicki@put.poznan.pl

Elżbieta WDOWICKA
Poznan University of Technology, 60-965 Poznań, ul. Piotrowo 5, Poland
elzbieta.wdowicka@put.poznan.pl

Abstract

The paper presents the free vibration analysis of non-planar asymmetric shear wall structures with connecting and stiffening beams. The stiff beams incorporated at various levels of coupled shear walls improve the stiffness of the structural system of the building. The analysis is based on a variant of the continuous connection method for three-dimensional shear wall structures having stepwise changes in cross-section. The mass matrix including flexural and torsional inertia is generated. As a result of solving eigenproblem, which corresponds to free vibration equation, natural frequencies and mode shapes of vibration have been received. The results obtained by this method have been compared with those available in literature and a satisfactory match has been observed.

Keywords: dynamic analysis, coupled shear walls, continuous connection method, stiffening beams

1. Introduction

Reinforced concrete coupled shear walls are structural members that are widely used in multi-storey buildings to increase the overall rigidity and resist the lateral loads due to wind and earthquakes. The free vibration response of such structures is of interest in force vibration predictions using the modal analysis.

For the dynamic analysis of the shear wall structures it is convenient to use a continuous-discrete approach [8, 1, 10, 6, 11]. In this approach the continuous connection method is employed to find the structural flexibility matrix, whereas the structure mass matrix is found with the lumped mass assumption. In the continuous connection method (CCM) the shear forces in connecting beams are modelled as continuously distributed functions along the height of a structure.

In practice the depth of connecting beams is limited and coupling effect provided by the lintel beams on structural walls may not be sufficient. The behaviour of coupled shear walls can be improved by incorporating deep stiffening beams, called “stiffeners”, at various levels along the structure height. The dynamic analysis of planar coupled shear walls with stiffening beams has been presented in many papers [8, 6, 7, 1, 3, 2, 4]. Turkozer *et al.* [9] has studied the dynamic analysis of stiffened non-planar coupled shear walls with one band of connecting beams.

The aim of this paper is to present the free-vibration analysis of non-planar shear wall structures with connecting and stiffening beams, using a variant of the continuous connection method for structures of variable cross-section [12].

2. Theoretical background

The analysis is based on the following main assumptions:

- The floor slabs are taken as diaphragms with infinite in-plane stiffness.
- The out-of-plane stiffness of the floor slabs can be modelled by connecting beams of appropriate stiffness spanning between shear walls.
- Vlasov's theory for thin walled beams of an open section is taken to be valid for the individual shear walls.
- The walls and beams are assumed to be linearly elastic.
- The geometric and mechanical properties of the structure are constant throughout the height of each segment.

In our analysis the continuous connection method has been used in conjunction with Vlasov's theory of thin-walled beams. To simplify the analysis, the effect of St. Venant's torsion has been neglected. The dynamic model with masses in the form of rigid floor slabs has been adopted since over a half of building total mass is usually concentrated on the floor levels. The coupled torsional-flexural vibrations have been taken into consideration because torsional response of buildings during ambient and earthquake response is significant.

For shear wall multi-storey structure it is more natural to determine the flexibility matrix **D** rather than stiffness matrix **K** [5]**.** To find the flexibility matrix **D** each lumped mass is loaded with a unit horizontal generalized force and the corresponding horizontal displacement vector is found by the continuous connection method. The following relation describes the free vibration of a structure:

$$\mathbf{D}\mathbf{M}\ddot{\mathbf{u}} + \mathbf{u} = 0 \tag{1}$$

Where: **D** and **M** are flexibility and mass matrices, respectively; **u** is d-element vector of generalised coordinates; and d is the number of dynamic degrees of freedom of a structure.

3. Analysis

The flexibility matrix **D** is generated from the solution of the governing differential equations for three-dimensional continuous model of the shear wall structure with variable cross-section [12]. A structure, which changes its cross-section along the height, can be divided into n_h segments, each one of the constant cross-sections. For k-th segment, the differential equations can be stated as follows:

$$\mathbf{B}\,\mathbf{n}''_{\mathbf{N}}(z) = \mathbf{A}\,\mathbf{n}_{\mathbf{N}}(z) + \mathbf{f}(z) \tag{2}$$

$$\mathbf{v}'''_{\mathbf{G}}(z) = \mathbf{V}_{\mathbf{T}}\mathbf{t}_{\mathbf{K}}(z) - \mathbf{V}_{\mathbf{N}}\mathbf{n}_{\mathbf{N}}(z) \tag{3}$$

where the following notation applies: $z \in (h_{k-1}, h_k>$, h_k is the height of the upper boundary of k-th segment of the constant cross-section, ($k = 1, \ldots n_h$), n_h is the number of segments of the constant cross-section; n_w is the number of continuous connections; **B** is $n_w \times n_w$ diagonal matrix containing flexibilities of connecting beams; $\mathbf{n}_{\mathbf{N}}(z)$ is the vector containing unknown functions of the shear force intensity in continuous connections which substitute connecting beams; $\mathbf{A}$, $\mathbf{V_T}$, $\mathbf{V_N}$ are the matrices dependent on a structure, $\mathbf{f}(z)$ is a vector formed on the basis of given lateral loads; $\mathbf{t_K}(z)$ is the vector of the functions of shear forces and a torque due to the action of lateral loads, $\mathbf{t_K}(z) = col\ [t_X(z), t_Y(z), m_S(z)]$ and $\mathbf{v_G}(z)$ is the vector containing the functions of horizontal displacements of the structure measured in the global coordinate system *OXYZ*, $\mathbf{v_G}(z) = col\ [v_X(z), v_Y(z), \varphi(z)]$.

The boundary conditions for Eq. (2) and Eq. (3) at the bottom and at the top of the shear wall structure can be stated as follows:

$$\mathbf{n}'_{\mathbf{N}}(H) = 0, \qquad \mathbf{n}_{\mathbf{N}}(0) = 0, \tag{4}$$

$$\mathbf{v_G}(0) = 0, \qquad \mathbf{v}'_{\mathbf{G}}(0) = 0, \qquad \mathbf{v}''_{\mathbf{G}}(H) = 0. \tag{5}$$

The boundary conditions for shear force intensity functions at the plane of contiguity, at which a change in cross-section occurs, have been derived on the basis of compatibility conditions at the mid-points of the connecting beams and equilibrium consideration in shear walls [12].

In the analysis of stiffened shear wall structures, storeys with stiffening beams are considered as the individual segments of the constant cross-section.

The mass matrix $\mathbf{M}$ is generated exactly according to real distribution of floor slabs, walls, connecting and stiffening beams, including flexural and torsional inertia, in the following form:

$$\mathbf{M} = diag(\mathbf{M_k}), \quad (k = 1, \ldots, n_k), \tag{6}$$

where: n_k – number of storeys, $\mathbf{M_k}$ – symmetrical matrix of the order three.

The generalized eigenvalue problem corresponding to the Eq. (1) is solved by using the procedure *geig*, created on thy basis of the procedures: *reduc2, tred2, tql2 , rebaka* , included in [13]. On the basis of the prepared algorithm the software in Object Pascal of Delphi 5 environment has been implemented and included in the DAMB (Dynamic Analysis of Multi-Storey Buildings) program for the dynamic analysis of shear wall tall buildings [10, 11].

4. Numerical results

To verify the present method the non-planar, non-symmetrical coupled shear wall with and without the stiffening beam, solved previously in [9], has been analysed (Fig. 1). The total height of the shear wall is 48 m and the storey height is 3 m.

The mass density and the elasticity and shear modules are as follows: ρ = 2400kg/m^3, E = 2.85GPa and G = 1.056 GPa. The height of the connecting beams is 0.4 m. The thickness of the connecting beams and walls in the right part is 0.4 m and 0.2 m in the left part. The stiffening beam of 3.0 m height was placed at the height of 30 m on the tenth storey.

The mass of the typical storey, including a connecting beam, equals to 104.3×10^3 kg and the total mass of building, including stiffener, is 1673.9×10^3 kg. The mass of floor slabs has not been considered in this example for comparison purposes.

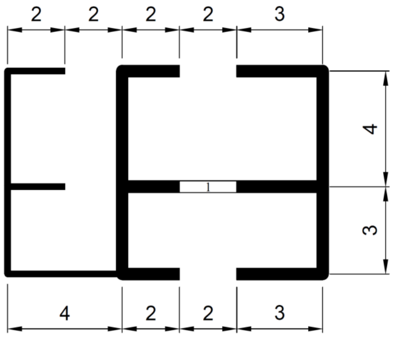

Figure 1. Cross-sectional view of the non-planar shear wall structure [9]

It may be noted, that in the present analysis the shear deformation of the walls has been neglected due to the assumption in Vlasov's theory. The same assumption has been made in the analysis presented in [9] and for comparison purposes the shear deformation was neglected in SAP2000 applications as well.

Table 1 and Table 2 compare the first ten natural frequencies corresponding to each mode found by the present method (program DAMB) and given in [9], obtained by SAP2000 structural analysis program, using MacLeod's frame method, for unstiffened and stiffened case, respectively.

The torsional modes are omitted in the results given in [9] because of the assumption that the mass is lumped in nodes, which have no rotational inertia [9], but for the other frequencies a good match has been observed.

Table 1. Comparison of the first ten natural frequencies (NF) found by present method (CCM) and SAP2000 [9] for unstiffened case

Mode	Predominant mode	Present method (CCM) NF (Hz)	SAP2000 [9] NF (Hz)	% Difference
1	First mode X	0.4748	0.50047	-5.13
2	First mode Y	0.6656	0.66117	0.67
3	First torsional mode	1.0022		
4	Second mode X	2.4180	2.46396	-1.87
5	Second mode Y	4.1799	4.11839	1.49
6	Second torsional mode	6.2020		
7	Third mode X	6.4394	6.47507	-0.55
8	Third mode Y	11.729	11.45595	2.38
9	Fourth mode X	12.456	12.37532	0.65
10	Third torsional mode	17.265		

Table 2. Comparison of the first ten natural frequencies (NF) found by present method (CCM) and SAP2000 [9] for stiffened case

Mode	Predominant mode	Present method (CCM) NF (Hz)	SAP2000 [9] NF (Hz)	Diff.(%) (CCM-SAP) /SAP
1	First mode X	0.5751	0.62284	-7.58
2	First mode Y	0.6663	0.66030	0.91
3	First torsional mode	1.0852		
4	Second mode X	2.5131	2.58037	-2.61
5	Second mode Y	4.1700	4.11147	1.42
6	Second torsional mode	6.2229		
7	Third mode X	6.6740	6.57733	1.47
8	Third mode Y	11.721	11.43606	2.49
9	Fourth mode X	12.827	12.77066	0.44
10	Third torsional mode	17.324		

It is demonstrated that the natural frequencies of coupled shear walls increase with the contribution of stiffening beams, which indicates the improvement in stiffness of coupled shear walls due to the incorporation of stiffening beams.

Figure 2 presents the first, second and third mode shapes of the non-planar shear wall structure with stiffening beam found by the present method, using DAMB program.

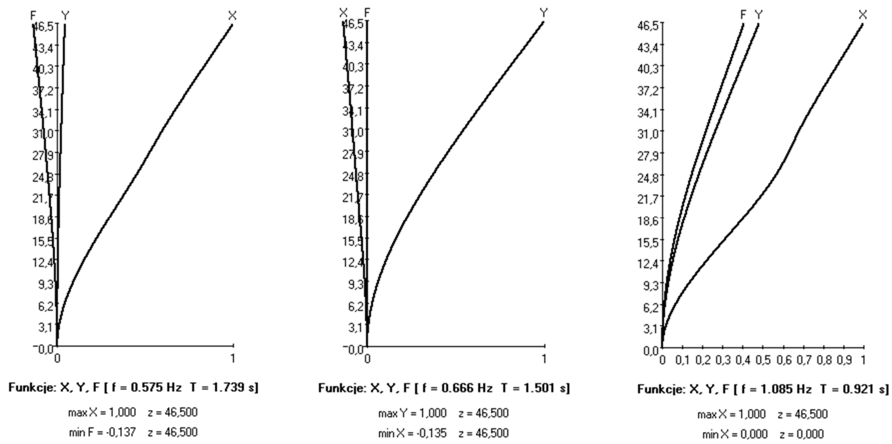

Figure 2. The first, second and third mode shapes of the non-planar shear wall structure with stiffening beam, obtained by the present method

5. Conclusions

The paper presents the free vibration analysis of non-planar shear wall structures with stiffening beams, using a variant of the continuous connection method for structures of variable cross section. The results obtained by the above-mentioned method have been compared with those obtained using the SAP2000 structural analysis program, given in literature, and a satisfactory match has been observed. The proposed method is efficient and can be very useful, particularly, at the preliminary design stage when quick checks with different structural arrangements and dimensions are needed.

References

1. O. Aksogan, H.M. Arslan, B.S. Choo, *Forced vibration analysis of stiffened coupled shear walls using continuous connection method*, Engineering Structures, **25** (2003) 499-506.
2. O. Aksogan, M. Bikce, E. Emsen, H.M. Arslan, *A simplified analysis of multi-bay stiffened coupled shear walls*, Advances in Eng. Software , **38** (2007) 552-560.
3. H.M. Arslan, O. Aksogan, B.S. Choo, *Free vibrations of flexibility connected elastically supported stiffened coupled shear walls with stepwise changes in width,* Iranian Journal of Science and Technology, Transaction B: Engineering, **28** (2004). 605-614.
4. K.B. Bozdogan, D. Ozturk, *A method for static and dynamic analyses of stiffened multi-bay coupled shear walls,* Structural Engineering and Mechanics, **28** (2008) 479-489.
5. R.W. Clough, J. Penzien, *Dynamics of Structures*, McGraw-Hill, New York 1993.
6. J.S. Kuang, C.K. Chau, *Free vibrations of stiffened coupled shear walls*,The Structural Design of Tall Buildings, **7** (1998) 135-145.
7. J.S.Kuang, C.K. Chau, *Dynamic behaviour of stiffened coupled shear walls with flexible bases*, Computers and Structures, **73** (1999) 327-339.
8. G.Q. Li, B.S. Choo, *A continuous-discrete approach to the free vibration analysis of stiffened pierced walls on flexible foundations*, Int. J. Solids and Structures. **33** (1996) 249-263.
9. C.D. Turkozer, O. Aksogan, E. Emsen, R. Resatoglu, *Dynamic Analysis of Non-Planar Coupled Shear Walls with Stiffeners using a Continuous Connection Method,* in: B.H.V. Topping, J.M. Adam, F.J. Pallarés, R. Bru, M.L. Romero, (Editors), "Proceedings of the Tenth International Conference on Computational Structures Technology", Civil-Comp Press, Stirlingshire, UK, Paper 364, 2010.
10. J. Wdowicki, E. Wdowicka, *Integrated system for analysis of three-dimensional shear wall structures*, Comp. Meth. in Civil Engineering, **1** (1991) 53-60.
11. J. Wdowicki: *Continuous connection method in dynamic analysis of composite tall building structures*, in: Vibrations in Physical Systems, Vol. XXIV, Editors: Cz. Cempel, M. W. Dobry, Poznań, (2010) 465-470.
12. J. Wdowicki, E. Wdowicka, *Analysis of shear wall structures of variable cross-section,* The Structural Design of Tall and Special Buildings **21** (2012) 1-15.
13. J.H. Wilkinson, C. Reinsch, *Linear Algebra. Handbook for Automatic Computation vol.II*, Springer-Verlag , Berlin, Heidelberg, New York 1971.

XXV Symposium *Vibrations in Physical Systems,* Poznan – Bedlewo, May 15-19, 2012

Analysis of Local Vibrations in a Vehicle

Małgorzata WOJSZNIS
Institute of Applied Mechanic, Poznan University of Technology
3 Piotrowo Street, 60-965 Poznań, Malgorzata.Wojsznis@put.poznan.pl

Abstract

The paper presents a problem of local vibrations in a vehicle as one of physical factors occurring at the driver's place. Influence of tires used in a car on local vibrations generated in a steering mechanism has been considered here. The analysis of local vibration hazards was carried out based on experimental results published in [1]. The measurement results obtained for five types of tires differing, among other things, from one another in tread depth, degree of wear and use were analyzed. The analysis has revealed significant influence of tires on the level of local vibrations transmitted through the steering mechanism into driver's hands.

Keywords: local vibrations, steering mechanism, physical factors in the workplace

1. Introduction

In the workplaces the work is adjusted to psychophysical capabilities of a human being considering improvement of working conditions at a minimum biological cost. The improvement is achieved mainly by elimination of sources of occupational diseases [2, 3]. Different types of harmful factors occur in the workplace. These can be divided into three groups: chemical substances, dust, and physical factors. In case of drivers the first two groups may appear, but they do not pose any direct danger. The most important here are physical factors, such as general vibrations, local vibrations and noise. They occur in the discussed workplace simultaneously and have a significant influence on assessment of occupational hazard related to the exposure to them [4, 5].

The paper presents results of measurements obtained for local vibrations occurring while driving a vehicle. Operators of hand-held tools used, for example, in construction industry are mainly exposed to mechanical vibrations acting locally on a human body. Drivers, however, who have contact with a vibrating element, such as a steering wheel of a vehicle, may also be rated among the exposed ones.

Mechanical vibrations may cause many ailments and diseases, even irreversible ones. One of the diseases caused by vibrations is *vibration syndrome*, which in Poland has already been rated among occupational diseases since 1968. Research with human beings as research participants has confirmed that the neural system and cardiovascular system are the most sensible to vibrations [4, 6]. Ailments caused by vibrations may, therefore, manifest themselves in paroxymal vasoconstrictions, dysaesthesia, labyrinth disorders, dystrophic changes of muscles, and formation of bone cysts. A complex of such disorders depends on individual susceptibility [7].

In the process of creation of ergonomic conditions in the workplace one should fulfill strong requirements set by the human being included in ergonomics principles and safety regulations [8]. Minimization or eliminations of hazards are the main activities performed to meet these requirements.

Occurrence of general and local vibrations and noise at the driver's place is conditioned on several factors. Aside from the construction and technical state of the vehicle they may include the state of the pavement, where the vehicular traffic occurs and the type of tires in use. The state of pavement depends on the type of the road (e.g. on the material it is made of), its wear, and, in particular, on weather conditions.

Based on experimental results presented in [1] only local vibrations have been analyzed and results of experimental research carried out for a small commercial vehicle are presented (Figure 1). The influence of tires on the levels of vibration acceleration transmitted through the steering wheel into driver's hands was investigated. The measurements were performed for three ranges of speed, including driving in built-up areas and on local roads.

Figure 1. Commercial vehicle used for research and the road used for measurements [1]

Five types of commonly used tires with different treads, different purpose, and having been used for two seasons were used during research.

2. Field research

Field research was performed on an asphalt concrete pavement (Fig. 1), and it consisted of recording values of steering wheel vibration acceleration for three ranges of vehicle speed: 50-60 km/h, 60-70 km/h and 70-80 km/h. The measurements were carried out at constant weather conditions, which guaranteed good driving conditions (dry pavement). The outdoor temperature was +25˚C, and the relative humidity was about 21%.

Five types of tires classified according to their purpose, depth and shape of tread, tested on the same steel R14 rims were used for the investigation (Table 1). Air pressure was selected individually for each tire, according to producer's recommendations. The tires were installed and removed using specialist machinery. After every change of tires the wheels were balanced.

Table 1. Tires used for research [1]

Pos.	Type	Tread depth [mm]	Tread shape
I	summer	4,5	asymmetric
II	all-season	6	directional
III	summer	5,5	asymmetric
IV	summer	6	directional
V	winter	6	directional

An all-season tire, winter tire, and summer tires, appropriate for the period of time, when the research was performed were examined. The summer tires had asymmetric and directional tread shapes and they differed from one another in tread depth.

The analysis of local vibrations was carried out based on the research presented in [1], which contains results of measurement of weighted values of acceleration of vibrations transmitted through the steering system into driver's hands, measured in three perpendicular directions. The measurements shown in [1] were carried out according to ISO 5349 standard [9] and based on [10], using Brüel&Kjær Integrating Vibration Meter Type 2513 and vibration acceleration sensors. The sensors were mounted on a clamping ring installed on the vehicle steering wheel (Fig. 2).

The asphalt concrete pavement was free from bends and unevenness that could influence the measurement results significantly. The length of the road section used for measurement was equal to about 7 kilometers. For each type of tires five measurements of the weighted value of vibration acceleration were taken, and than they were averaged.

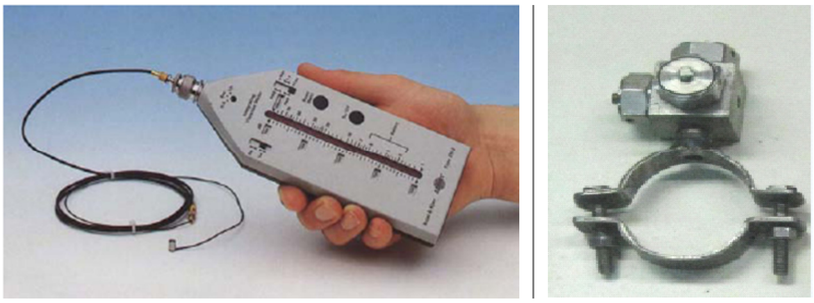

Figure 2. B&K meter used for research

The mean value determined in [1] was used to compute the quantity characterizing vibrations occurring in the workplaces, i.e. the vector sum of frequency weighted rms values of vibration acceleration measured in three directions x, y and z. The obtained results were compared with the permissible value of 2.8 m/s^2, valid for eight-hour exposure of the human body to local vibrations [4].

3. Analysis of research results

Table 2 shows the vector sum of weighted rms values of vibration acceleration in x, y and z directions obtained for three ranges of speed for different types of tires measured on the steering wheel of the investigated vehicle. From the directional components the vector sum for each tire was determined using the formula:

$$a_{w,s} = \sqrt{a_{w,x,RMS}^2 + a_{w,y,RMS}^2 + a_{w,z,RMS}^2} \tag{1}$$

where: $a_{w,x,RMS}$, $a_{w,y,RMS}$, $a_{w,z,RMS}$, – weighted rms values of vibration acceleration measured in x, y and z directions [11].

Table 2. The vector sum of vibration acceleration of three directional components x, y, z for three ranges of speed for the investigated tires

Tire number	**Vector sum for directions x, y and z [m/s^2]**		
	50 – 60 km/h	**60 – 70 km/h**	**70 – 80 km/h**
I	5,9	5,9	5,6
II	6,3	5,0	3,3
III	3,2	3,0	2,4
IV	3,8	4,2	2,8
V	5,8	4,0	2,9

Analyzing the results obtained for different types of tires one can observe small influence of tread shape on the level of the recorded vibrations (see Table 2 – tires III and IV). The results also indicate, that in case of summer tires (I and IV) the tread depth may be of great importance in propagation of vibrations through the steering system.

Computation results put together in Table 2 show that different purpose tires (summer tire IV and winter tire V) having the same tread shape and depth have similar values of vector sums, aside from the speed range of 50-60 km/h. To complete the analysis it would be worthwhile to examine the winter tire in conditions it has been made for. For safety reasons (pavement covered with ice or snow), however, such an attempt has not been made.

Table 2 and Fig. 3 show that the higher speed the lower are the vibration levels independently of the type of the tire in use. There is one exception, tire IV, for which at the speed range 60 – 70 km/h a little higher value of vibration acceleration was obtained.

The obtained values of the vector sum for the chosen speed ranges were compared with the permissible value of 2.8 m/s^2 shown in Fig. 3.

Analyzing the results for different types of tires it can be observed that the winter tire (V) and the all-season tire (II) behave similarly. For both types of tires the decrease in vibrations is almost identical. Between tires (III) and (IV) significant differences in vibration levels can be observed for speed ranges of 50 – 60 km/h and 60 – 70 km/h. For the speed range of 70 – 80 km/h the permissible value has not been exceeded.

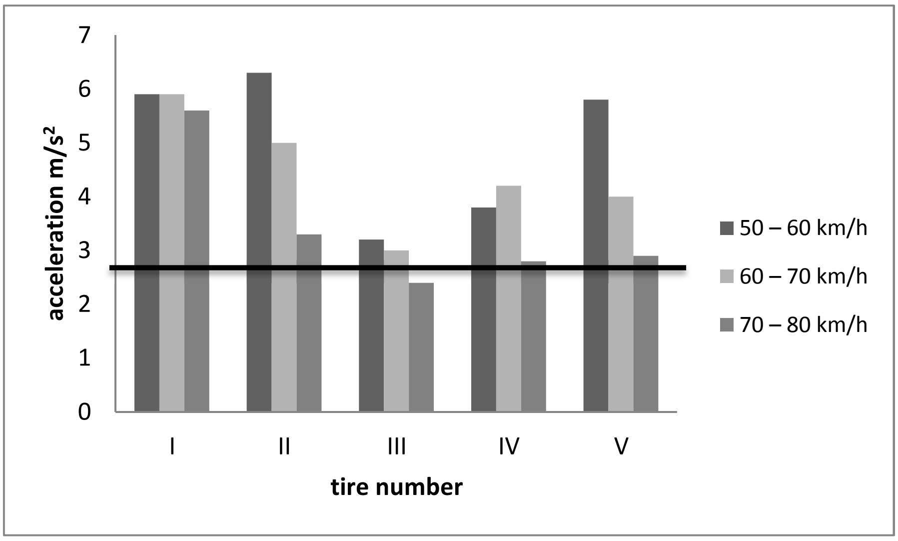

Figure 3. Vibration acceleration of the steering wheel for the investigated tires obtained for three speed ranges referenced to the permissible level

The most unfavorably appears the summer tire (I) for which almost twofold excess of the permissible value can be observed independently of the vehicle speed. For tire (III) small excesses of the permissible value can be observed.

5. Conclusions

The paper has shown that local vibrations occurring in a vehicle are closely dependent on tires in use and also on vehicle speed.

The obtained values of vibration acceleration of the steering wheel depend only to a small degree on tire tread shape and tire type (summer, winter, all-season). The choice of tires is determined, however, by the season and driving safety. Hence, it is impossible to choose the type of tires using only the local vibrations criterion. The analysis has shown that only one of the five investigated tires meets the requirements of the standard. Thus, the problem exists and cannot be solved in a simple way, because when designing tires many factors should be taken into account simultaneously. The overriding goal is safety, and the driving comfort is less important.

The performed investigations confirm the need for taking local vibrations into account when assessing the occupational risk connected with the exposure to this factor.

References

1. Ł. Bąbelek, *Drgania układu kierowniczego w samochodzie osobowym*, Praca dyplomowa magisterska, Poznań 2010;
2. E. Górska, *Diagnoza ergonomiczna stanowisk pracy*, Oficyna Wydawnicza Politechniki Warszawskiej, Warszawa1998;
3. E. Tytyk, *Projektowanie ergonomiczne*, PWN Warszawa – Poznań 2001;
4. D. Augustyńska, M. Pośniak, *Czynniki szkodliwe w środowisku pracy (wartości dopuszczalne),* Międzyresortowa Komisja ds. Najwyższych Stężeń i Natężeń Czynników Szkodliwych dla Zdrowia w Środowisku Pracy, CIOP – PIB, ISBN 83-7373-130-X, Warszawa 2003;
5. P. Kowalski, *Drgania i hałas w pojazdach drogowych*, Bezpieczeństwo Pracy 5/2007, pp 10 – 13.
6. K. Marek*, Choroby zawodowe*, Wydawnictwo Lekarskie PZWL, Warszawa2003;
7. Praca zbiorowa *Mała encyklopedia medycyny*, PWN, 1987;
8. J. Olszewski, *Podstawy ergonomii i fizjologii pracy*, Wydawnictwo Akademii Ekonomicznej, Poznań 1997;
9. ISO 5349. Mechanical vibrations - Guidelines for the measurement and assessment of human exposure to the hand-transmitted vibration, 1986;
10. T. Kucharski, *System pomiaru drgań mechanicznych,* Wydawnictwo Naukowo-Techniczne, Warszawa 2002, ISBN 83-204-2739-4;
11. PN-91/N-01352. Drgania. Zasady wykonywania pomiarów na stanowiskach pracy.
12. PN-91/N-01353. Drgania. Dopuszczalne wartości przyspieszenia drgań oddziałujących na kończyny górne.

XXV Symposium *Vibrations in Physical Systems,* Poznan – Bedlewo, May 15-19, 2012

Vibration Research on a Demolition Hammer Using a High-Speed Camera

Małgorzata WOJSZNIS
Institute of Applied Mechanics, Poznań University of Technology
3 Piotrowo Street, 60-965 Poznań
Malgorzata.Wojsznis@put.poznan.pl

Maciej TABASZEWSKI
Institute of Applied Mechanics, Poznań University of Technology
3 Piotrowo Street, 60-965 Poznań
Maciej.Tabaszewski@put.poznan.pl

Marian W. DOBRY
Institute of Applied Mechanics, Poznań University of Technology
3 Piotrowo Street, 60-965 Poznań
Marin.Dobry@put.poznan.pl

Abstract

The paper presents methodology of measurements and results of vibration research on a demolition hammer weighing 15.5 kg. The measurements of vibrations for the chosen measuring points have been carried out using a Photron FastCam 1024 PCI high-speed camera on a stand prepared for testing hand-held tools. To ensure signal stability and to reduce the influence of an operator the research was carried out with the hammer mounted in a special fixture enabling holding a tool with symmetric layout of handles. The measurement results are to be used for verification of a model assumed for a human being – tool system.

Keywords: local vibrations, hand-held tools, high-speed camera

1. Introduction

Hand-held tools commonly used, for example, in construction industry are sources of vibrations of very high levels exceeding many times acceptable norms. Work in such conditions may contribute to many illnesses and deterioration of health. One of the first symptoms of harmful influence of local vibrations entering the human body through the upper limbs is the loss of sensation in palms and finger whitening as a result of vascular disturbances [1, 2, 10].

Depending on the character of work performed tools with different types of handles are used. The layout of handles determines arising of pain in both limbs equally or in each one differently. Harmfulness of vibrations transmitted into the human body causes that research involving human beings should, if possible, be avoided. In such cases real objects, such as machines or tools, are replaced by physical or mathematical models. The models should then be verified experimentally, which enables to continue research and to carry out analyses without doing harm to any human being. On the other hand, performing appropriate measurements enables, at least partially, such adjustment of model parameters, that its behavior is to the highest degree similar to the behavior of the modeled object.

The paper presents results of vibration research on a demolition hammer weighing over 10 kg and having a T-shape handle, which means that it is a big tool requiring the use of both hands to operate it (Fig. 1). Such a posture of operator at work causes symmetric force distribution and vibration propagation in both upper limbs.

The performed measurements were meant to be used for verification of a model built to analyze a human being – tool system described in [3, 4, 5, 6, 7, 8].

2. Laboratory research

The experimental research was carried out for a pneumatic demolition hammer with a symmetric handle, weighing 15,5 kg. The tool was mounted on a test stand for testing hand-held impact tools using a special two-jaw fixture (Fig. 1). The research was carried out on the foundation made according to ISO/FDIS 8662 [9] (Fig. 1).

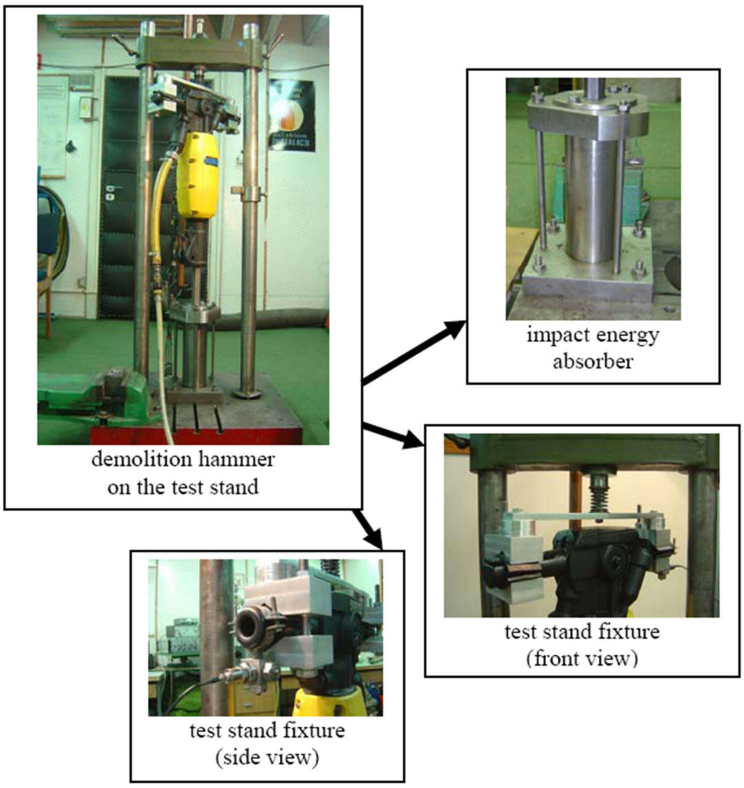

Figure. 1. Test stand for testing hand-held impact tools

The fixture enables fastening the hammer handles and work with a controlled force of pressuring the hammer against the foundation generated by the initial spring tension. The fixture ensured stability of signals and elimination of the operator's influence, which guaranteed repeatability of measurements on a satisfactory level.

On the test stand displacements of different points on the object and test stand marked with markers were recorded. The locations of markers are shown in Figure 2.

The research was carried out using a Photron 1024 PCI 100KC camera with a Nikon 50 mm, 1: 1,4D lens (see Fig. 2). Acquisition parameters 1000 frames per second, display resolution 256 x 1024. The operating frequency of the hammer was about 25 Hz. Finally, only two components of the displacement signal were significant in the recorded signal (about 25 Hz and 50 Hz – see Fig. 3). Thanks to the chosen recording speed one vibration period with the fundamental frequency of motion of the hammer was represented by about 40 samples and the second harmonic by about 20 samples. It was assumed, that the quantities which would be used for initial adjustment (initial verification) of the model were rms values of the signal (and not the time function itself). Thus, the obtained digital representation was assumed as sufficient to obtain good estimation of the rms value.

The measuring system was equipped with the camera, two sources of strong halogen light with power of 500 W each, and a computer with a software for data acquisition (Fig. 2).

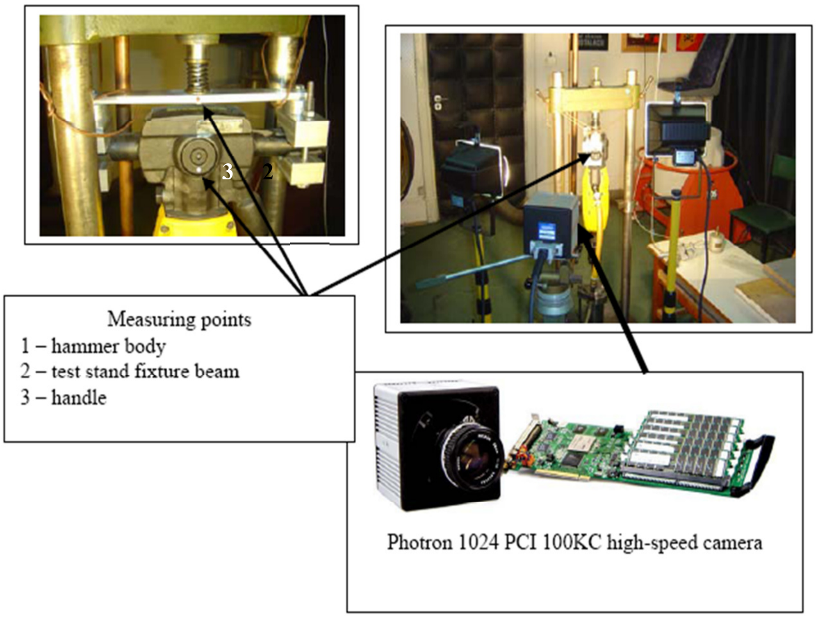

Figure 2. Measuring apparatus used for research

The camera recorded displacements only in Z-direction, because of restrictions of motion in other directions caused by the used fixture. It was assumed that it was the direction, where the biggest displacements could be expected and also the only one, where the displacements were measurable using a camera with the previously mentioned resolution and with the available lens.

3. Analysis of the research results

Figure 3 shows examples of displacement, velocity and acceleration values obtained for the marker placed on the demolition hammer handle, recorded in Z-direction.

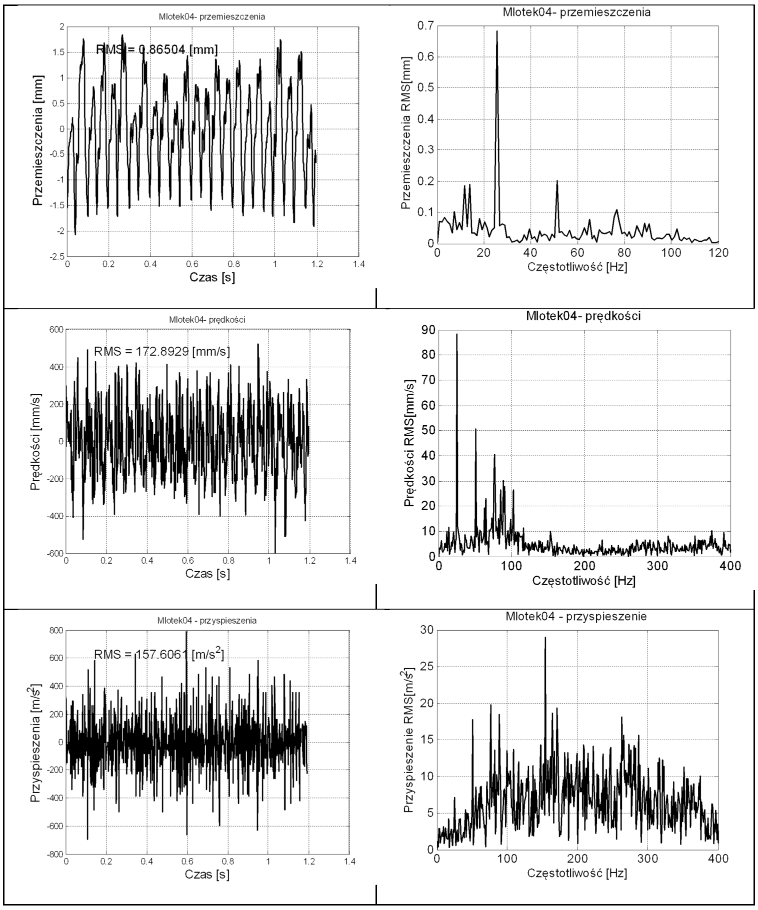

Figure 3. Displacement, velocity and acceleration of the **handle**, and their spectra

The camera enables direct measurement of vibration displacement only. To obtain velocity and acceleration it is necessary to compute respective time derivatives.

The computations may be done in frequency domain using a complex spectrum, and in the next step using the reverse Fourier transform, determining the time courses of vibration velocities or accelerations (after applying the procedure twice).

The table shows the rms values of displacement, velocity and acceleration of vibrations of the hammer handle, its body, and the fixture.

Table 1. RMS values of displacement, velocity and acceleration of vibrations of the hammer handle and its body determined in Z-direction

Measuring point	Displacement [m]	Velocity [m/s]	Acceleration [m/s^2]
Handle	0.0009 0.0003	0.172 0.137	157 160
Hammer body	0.0005 0.0002	0.240 0.152	411 267
Fixture	0.0017 0.0010	0.196 0.168	293 231

The table shows the results for different tests (with different values of pressure supplied to the hammer). The hammer was operated under laboratory conditions (lack of influence of an operator). Hence, differences in results were caused only by differences in pressure supplied to the hammer. It concerns, however, mainly the vibration displacement. In case of acceleration, because of the fact that higher frequency bands also become significant, this difference decreases. It should, however, be mentioned that the process of computation of consecutive derivatives of displacement itself introduces some numerical errors.

4. Conclusions

The conducted vibration research on a hammer mounted in a stable fixture on a laboratory test stand have confirmed the impulse character of force exciting vibrations of the hammer body.

The recorded values of acceleration, velocity and displacement enable simulative generation of impulse forces exciting vibrations of the demolition hammer body. Obtaining conformity of rms amplitudes of the determined parameters will enable adjustment of the model to a real object and continuation of research on minimization of vibrations generated by a tool.

One of advantages of a measurement performed by means of a high-speed camera is that it can be simply carried out for any point on the structure, which motion can be observed. It is not always possible to mount transducers directly to any point of a structure. Contactless measurement using a camera eliminates this inconvenience. Another advantage is a relatively low cost of such a solution in comparison with methods based on laser measurements. Among significant disadvantages one can rate low accuracy of direct measurements caused by resolution of the camera transducer and lens in use.

Acknowledgments

The work was partially funded by the Polish Ministry of Science and Higher Education in research project No. N503 017 32/2558.

References

1. K. Marek, *Choroby zawodowe*, Wydawnictwo Lekarskie PZWL, Warszawa 2003;
2. M. W. Dobry, M. Wojsznis*, Oddziaływanie drgań miejscowych na organizm ludzki-ocena analizy dynamicznej i energetycznej*, Diagnostyka vol. 30, tom 1, ISSN 641-6414, Polskie Towarzystwo Diagnostyki Technicznej, pp. 151-154, 2004;
3. M. W. Dobry, M. Wojsznis, *Energy model of a spatial Human-being – Demolition Hammer System with WoSSO vibroisolation*, Vibrations in Physical Systems, vol. XXIII, Poznan University of Technology, Poznan 2008, pp. 103-108;
4. M. Wojsznis, M. W. Dobry*, Spatial model of a Human-being – Demolition Hammer System,* Vibrations in Physical systems, vol. XXIII, Poznan University of Technology, Poznan 2008, pp. 429-434;
5. M. Wojsznis, M. W. Dobry, *3D vibrations in a Human Being – Tool Structure, Structural Dynamics Recent Advances*, Proceedings of the X International Conference, Institute of Sound and Vibration Research, University of Southampton, UK, pp. 05, 2010;
6. M. W. Dobry, M. Wojsznis, *Energy flow in a Human Being – Tool Structure (3D Model),* Structural Dynamics Recent Advances, Proceedings of the X International Conference, Institute of Sound and Vibration Research, University of Southampton, UK, pp.07, 2010;
7. M. W. Dobry, M. Wojsznis, *Przepływ energii w strukturze człowiek-narzędzie*, Wybrane zagadnienia analizy modalnej konstrukcji, Praca zbiorowa pod redakcją Tadeusza UHLA, Kraków 2010, ISBN 978-83-7204-983-4, pp 51-58;
8. M. Wojsznis, M. W. Dobry, *Drgania w strukturze Człowiek-Narzędzie*, Wybrane zagadnienia analizy modalnej konstrukcji, Praca zbiorowa pod redakcją Tadeusza UHLA, Kraków 2010, ISBN 978-83-7204-983-4, pp 301-308.
9. ISO/FDIS 8662 (EN28662). Hand-held portable power tools – Measurement of vibrations at handle. Part 5: Pavement breakers and hammers for construction work.
10. L. Markiewicz, *Fizjologia i higiena pracy*, Wibracja, Instyt. Wyd. CRZZ, Warszawa 1980;